Mathematical Problems in Engineering

New Challenges in Fractional Systems

Guest Editors: Jocelyn Sabatier, Clara Ionescu, József K. Tar, and José A. Tenreiro Machado

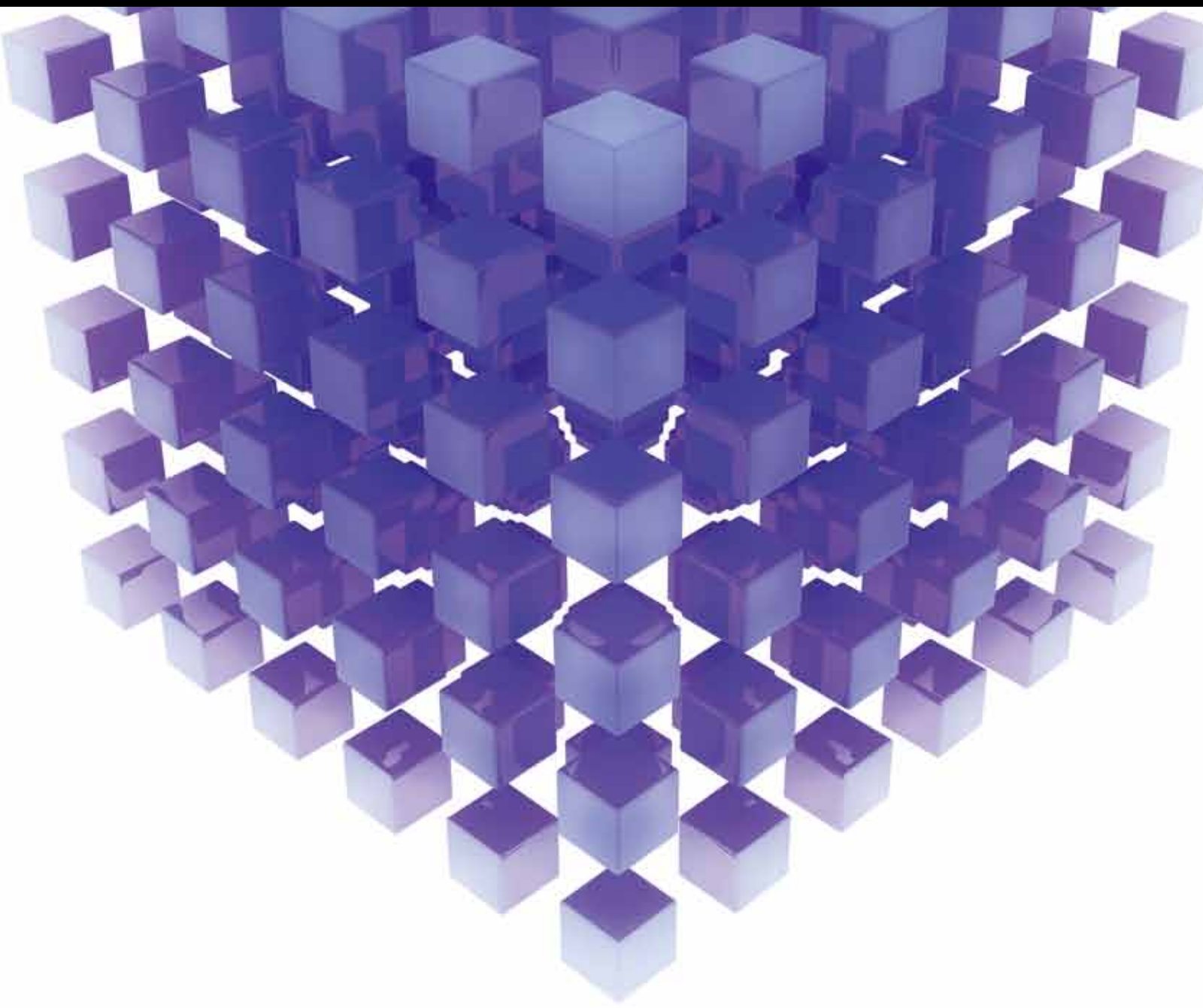

New Challenges in Fractional Systems

Mathematical Problems in Engineering

New Challenges in Fractional Systems

Guest Editors: Jocelyn Sabatier, Clara Ionescu, József K. Tar, and José A. Tenreiro Machado

Editorial Board

Contents

Hindawi Publishing Corporation
Mathematical Problems in Engineering
Volume 2013, Article ID 239378, 2 pages
http://dx.doi.org/10.1155/2013/239378

Editorial

New Challenges in Fractional Systems

Jocelyn Sabatier,[1] Clara Ionescu,[2] József K. Tar,[3] and José A. Tenreiro Machado[4]

[1] *IMS Laboratory, Bordeaux 1 University, 351 Cours de la Liberation, 33400 Talence, France*
[2] *Ghent University, Technologiepark 913, B9052 Zwijnaarde, Belgium*
[3] *John von Neumann Faculty of Informatics, Óbuda University, H-1034 Budapest, Hungary*
[4] *Department of Electrical Engineering, Institute of Engineering, Polytechnic of Porto, 4200-072 Porto, Portugal*

Correspondence should be addressed to Jocelyn Sabatier; jocelyn.sabatier@u-bordeaux1.fr

Received 9 May 2013; Accepted 9 May 2013

Without any doubt, the recently emerging tools from fractional calculus became successful in a manifold of applications and currently the playground of modern engineering sciences. Fractional order differentiation consists in the generalisation of classical integer differentiation to real or complex orders. From a mathematical point of view, several interpretations of fractional differentiation were proposed, but there is still a deep debate about it. However, all these interpretations demonstrate that fractional order differentiation cannot simply be connected to the slope at one point of the derived function for instance. This lack of interpretation is in fact due to the definition of the fractional order operator. This is a nonlocal operator based on an integral with a singular kernel. The same conclusion can be made for the fractional integrator operator; fractional differentiation operator definition being based on the fractional integrator operator definition. This situation explains why these operators are still not well defined and that several definitions still coexist, which impedes the process of becoming standard tools. Since the first recorded reference work in 1695 up to the present day, many articles have been published on this subject, but much progress is still to be done particularly on the relationship of these different definitions with the physical reality of a system (through taking into account the initial conditions for instance).

A fractional order system is a system described by an integro-differential equation involving fractional order derivatives of its input(s) and/or output(s). From a physical point of view, linear fractional order systems are not quite conventional linear systems, and not quite conventional distributed parameter systems. They are in fact halfway between these two classes of systems. Fractional order systems exhibit long memory or hereditary effects. Hence, they are a modelling tool well suited to a wide class of phenomena with nonstandard dynamic behaviour and the applications of fractional order systems are now well accepted in the following disciplines:

(i) electrical engineering (modelling of motors, modelling of transformers, skin effect, etc.);

(ii) electronics, telecommunications (phase-locking loops, etc.);

(iii) electromagnetism (modelling of complex dielectric materials, etc.);

(iv) electrochemistry (modelling of batteries and ultracapacitors, etc.);

(v) thermal engineering (modelling and identification of thermal systems, etc.);

(vi) mechanics, mechatronics (vibration insulation, etc.);

(vii) rheology (behaviour identification of materials, etc.);

(viii) automatic control (robust control, system identification, observation and control of fractional systems, etc.);

(ix) robotics (modelling, path tracking, path planning, etc.);

(x) signal processing (filtering, restoration, reconstruction, analysis of fractal noises, etc.);

(xi) image processing (fractal environment modelling, pattern recognition, edge detection, etc.);

(xii) biology, biophysics (electric conductance of biological systems, fractional models of neurons, muscle modelling, etc.);

(xiii) physics (analysis and modelling of diffusion phenomenon, etc.);

(xiv) economy (analysis of stock exchange signals, etc.).

The goal of the present special issue is to give an overview of recent results obtained in the field. This special issue is only a sample of the work carried out throughout the world, but we hope it is representative of the broached themes and is a useful source of information to begin with fractional differentiation and its applications or to develop new researches. The 19 papers are grouped in six major areas:

(i) mathematical tools, analytical and numerical solutions, and approximation of fractional order systems,

(ii) fractional order systems properties analysis,

(iii) applications in system modelling,

(iv) applications in system identification,

(v) applications in control theory and robotics,

(vi) applications in signal and image processing.

Jocelyn Sabatier
Clara Ionescu
József K. Tar
José A. Tenreiro Machado

Hindawi Publishing Corporation
Mathematical Problems in Engineering
Volume 2013, Article ID 932150, 14 pages
http://dx.doi.org/10.1155/2013/932150

Research Article

A New Model of the Fractional Order Dynamics of the Planetary Gears

Vera Nikolic-Stanojevic,[1] Ljiljana Veljovic,[2] and Cemal Dolicanin[1]

[1] *State University of Novi Pazar, Novi Pazar, Serbia*
[2] *Faculty of Engineering Science, University of Kragujevac, Serbia*

Correspondence should be addressed to Vera Nikolic-Stanojevic; veranikolic1@gmail.com

Received 9 November 2012; Revised 25 March 2013; Accepted 31 March 2013

Academic Editor: Jocelyn Sabatier

A theoretical model of planetary gears dynamics is presented. Planetary gears are parametrically excited by the time-varying mesh stiffness that fluctuates as the number of gear tooth pairs in contact changes during gear rotation. In the paper, it has been indicated that even the small disturbance in design realizations of this gear cause nonlinear properties of dynamics which are the source of vibrations and noise in the gear transmission. Dynamic model of the planetary gears with four degrees of freedom is used. Applying the basic principles of analytical mechanics and taking the initial and boundary conditions into consideration, it is possible to obtain the system of equations representing physical meshing process between the two or more gears. This investigation was focused to a new model of the fractional order dynamics of the planetary gear. For this model analytical expressions for the corresponding fractional order modes like one frequency eigen vibrational modes are obtained. For one planetary gear, eigen fractional modes are obtained, and a visualization is presented. By using MathCAD the solution is obtained.

1. Introduction

Planetary gears are a great application in modern engineering systems as a replacement for the conventional manual transmission complex because it has a compact structure and high transmission ratios. Due to the structure of planetary gears and the fact that the so-called planetary gear-satellites simultaneously perform two current trends in the work of planetary gears, there are even extreme vibration, that is, dynamic loads, which cause damage to the gears, bearings, and other elements of the transmission. Precise study of the dynamic behavior of planetary gear is often a difficult mathematical problem, because there are no adequate models. In the idealization of the attached planetary transmission and selection of appropriate dynamic models usually first allocate primary properties, which are maintained in solving the task, and then in future work neglect less important characteristics.

In the first papers on the dynamic behavior of gears in use, one notes a great simplification, for example, that all changes have linear character. However, subsequent experimental studies have shown that this approach is not realistic and that the dynamic behavior of gears in the paper is influenced by many factors that cannot be described by linear relationships [1]. These studies have shown that it is especially important to separate the effects that occur between the gear teeth in mesh, the dynamic effects that result in the load bearing of the engine, dynamic errors in transmission, and so forth. Therefore, a number of important research results of the dynamic behavior of gear transmission will be given, with special reference to the planetary gear.

Although gear dynamics has been studied for decades, few studies present a formulation intended for the dynamic response of full gear systems that contain multiple gear meshes, flexible shafts, bearings, and so forth. There are few reliable computational tools for the dynamic analysis of general gear configurations. Some models exist, but they are limited by simplified modeling of gear tooth mesh interfaces, two-dimensional models that neglect out of plane behavior, and models specific to a single gear configuration.

In a series of papers that follow, the fundamental task of analytical gear research is to build a dynamic model. For different analysis purposes, there are several modelling

choices such as a simple dynamic factor model, compliance tooth model, torsional model, and geared rotor dynamic model, for example, [2, 3].

The simplest models are found in a number of textbooks used in education in this field. So, the teeth in meshing action can be modelled as an oscillatory system [4–6] and so forth. This model consists of concentrated masses (each of which represents one gear) connected with elastic and dump element. Applying the basic principles of analytical mechanics and taking the initial and boundary conditions into consideration, it is possible to obtain the system of equations representing physical meshing process between the two or more gears. In order to obtain better results, it is possible to model the elastic element as a nonlinear spring.

Dynamic transmission error is taken as the parameter for modelling of noise in geared transmission. In the last two decades, there is plenty of work concetrated on modelling of the dynamic transmission error for spur and helical gears and representing the influence of the dynamic transmission errors on the level of noise in the geared transmission. Lately, there has been experiments conducted in order to isolate particular noise effects like noise coming from bearing, housing noise, meshing action noise, and backlash noise simply by measuring the dynamic transmission error. Some of the earliest models are represented in [7–10].

Using the free vibration analysis, one calculates critical parameters such as natural frequencies and vibration modes that are essential for almost all dynamic investigations. The free vibration properties are very useful for further analyses of planetary gear dynamics, including eigensensitivity to design parameters, natural frequency veering, planet mesh phasing, and parametric instabilities from mesh stiffness variations [11, 12].

Based on the results of the experiments conducted during the gear vibration research, it is to conclude that the excitation is restored every time when a new pair of teeth enters the mesh. Vibrations with natural frequencies dominate the vibration spectrums. The internal dynamic forces in teeth mesh, vibration, and noise are consequences of the change in teeth deformation, teeth impact, gear inertia due to measure, and teeth shape deviation [13].

Paper [14, 15] aims to provide insight into the three-dimensional vibration of gears by investigating the mechanisms of excitation and nonlinearity coming from the gear tooth mesh.

For different analysis purposes, there are several modelling choices such as a simple dynamic factor model, compliance tooth model, torsional model, and geared rotor dynamic model [6]. Using the free vibration analysis one calculates critical parameters such as natural frequencies and vibration modes that are essential for almost all dynamic investigations. The free vibration properties are very useful for further analyses of planetary gear dynamics, including eigensensitivity to design parameters, natural frequency veering, planet mesh phasing, and parametric instabilities from mesh stiffness variations [16–22]. It is also necessary to systematically study natural frequency and vibration mode sensitivities and their veering characters to identify the parameters critical to gear vibration. In addition, practical gears may be mistuned by mesh stiffness variation, manufacturing imperfections, and assembling errors. For some symmetric structures, such as turbine blades, space antennae, and multispan beams, small disorders may dramatically change the vibration [18, 19]. The following articles [10, 23] are related to the nonlinear analysis of dynamic behavior of gears, using experimental methods and the application of finite element method (FEM).

Paper [24, 25] examines the nonlinear dynamics of planetary gears by numerical and analytical methods over the meaningful mesh frequency ranges. Concise, closed-form approximations for the dynamic response are obtained by perturbation analysis.

By using three-dimensional finite element analysis, it is possible to model the whole planetary gear and get adequate solutions. Such a solution to the classic gear transmissions is given in the paper [26]. General three-dimensional finite element models for dynamic response are rare because they require significant computational effort. This is accomplished by many time steps required for the transient response to diminish so that steady-state data can be obtained. This study attempts to fill this gap with a general finite element formulation that can be used for full gearbox dynamic analyses.

A finite element formulation for the dynamic response of gear pairs is proposed in [24, 26, 27] and so forth. Following an established approach in lumped parameter gear dynamic models, the static solution is used as the excitation in a frequency domain solution of the finite element vibration model. The nonlinear finite element/contact mechanics formulation provides an accurate calculation of the static solution and average mesh stiffness that are used in the dynamic simulation. The frequency domain finite element calculation of dynamic response compares well with numerically integrated (time domain) finite element dynamic results and previously published experimental results. Simulation time with the proposed formulation is two orders of magnitude lower than numerically integrated dynamic results. This formulation admits system level dynamic gearbox response, which may include multiple gear meshes, flexible shafts, rolling element bearings, housing structures, and other deformable components.

In the latest research, light fractional order coupling element is used to describe the dynamic behavior of gears and set of constitutive relationships, so the fractional calculus can be successfully applied to obtain results.

The monograph [28–31] contains a basic mathematical description of fractional calculus and some solutions of the fractional order differential equations necessary for applications of the corresponding mathematical description of a model of gear transmission based on the teeth coupling by standard light fractional order element.

In the series of references [32–40], the mixed discrete-continuum or continuum mechanical systems with fractional order creep properties are mathematically described and analytically solved.

Paper [40] presents two models of the geared transmission with two or more shafts. First approach gives a model based on the rigid rotors coupled with rigid gear teeth, with mass distributions not balanced and in the form of the mass

particles as the series of the mass disturbance of the gears in multistep gear transmission. Using very simple model it is possible and useful to investigate the nonlinear dynamics of the multistep gear transmission and nonlinear phenomena in free and forced dynamics. This model is suitable to explain source of vibrations and big noise, as well as no stability in gear transmission dynamics. Layering of the homoclinic orbits in phase plane is source of a sensitive dependence nonlinear type of regime of gear transmission system dynamics. Second approach gives a model based on the two-step gear transmission taking into account deformation and creeping and also viscoelastic teeth gears coupling. This investigation was focused to a new model of the fractional order dynamics of the gear transmission. For this model we obtain analytical expressions for the corresponding fractional order modes like one frequency eigen vibrational modes. Generalization of this model to the similar model of the multistep gear transmission is very easy.

The model in this paper represents dynamic model of the planetary gears with four degrees of freedom. Our investigation was focused to a new model of the fractional order dynamics of the planetary gears. For this model we obtain analytical expressions for the corresponding fractional order modes like one frequency eigen vibrational modes.

2. Mathematical Model of the Planetary Gear

In the practice, planetary gears are very often exposed to action of forces that change with time (dynamic load). There are also internal dynamic forces present. The internal dynamic forces in gear teeth meshing are the consequence of elastic deformation of the teeth and defects in manufacture such as pitch differences of meshed gears and deviation of shape of tooth profile. Deformation of teeth results in the so-called collision of teeth which is intensified at greater difference in the pitch of meshed gears. Occurrence of internal dynamic forces results in vibration of gears so that the meshed gears behave as an oscillatory system. This model consists of reduced masses of the gear with elastic and damping connections (see [6, 14, 15, 26, 27]). By applying the basic principles of mechanics and taking into consideration initial and boundary conditions, the system of equation is established which describes physicality of the gear meshing process. On the other hand, extremely cyclic loads (dynamic forces) can result in breakage of teeth, thus causing failure of the mechanism or system.

Primary dependences between geometrical and physical quantities in the mechanics of continuum (and with planetary gear as well) include mainly establishing the constitutive relation between the stress state and deformation state of the tooth's material in the two teeth in contact for each particular case. Thus, solving this task, it is necessary to reduce numerous kinetic parameters to minimal numbers and obtain a simple abstract model describing main properties for investigation of corresponding dynamical influences.

Based on previous, at starting this part, we take into account that contact between two teeth is possible to be constructed by standard light element with constitutive stress-strain state relations which can be expressed by fractional order derivatives.

The papers [29, 39] analyzed in details the standard light coupling elements of negligible mass in the form of axially stressed rod without bending, which has the ability to resist deformation under static and dynamic conditions.

Figure 1 shows the model planetary gear when the coupling between the teeth (sun-planet and ring-planet meshes) was obtained from a standard light fractional element. The planetary gear model consists of three members (the sun, 3 planets, and ring).

The motion of the sun gear and the ring gear is given by translations that is expressed as y_i, $i = 1, 2$ ($\vec{r}_i$, $i = 1, 2$), and rotations that is expressed as φ_i, $i = 1, 2$. The kinetic energy E_K of the planetary stage can be written as

$$E_K = \sum_{i=1}^{2} E_{Ki}. \tag{1}$$

The kinetic energy for the each element is represented by

$$E_{Ki} = \frac{1}{2} m_i \vec{v}_i \cdot \vec{v}_i + \frac{1}{2} J_i \omega_i^2, \quad i = 1, 2, \tag{2}$$

where m_i are masses of the sun gear and ring gear, J_i are mass moments of the inertia, $\vec{v}_i$ are velocities of mass centers, and ω_i are angular velocities of the sun gear and ring gear.

So, the total kinetic energy of the planetary stage is given by

$$E_K = \frac{1}{2} m_1 \dot{y}_1^2 + \frac{1}{2} J_1 \dot{\varphi}_1^2 + \frac{1}{2} m_2 \dot{y}_2^2 + \frac{1}{2} J_2 \dot{\varphi}_2^2. \tag{3}$$

Sun gear is supported with bearing which is modeled as linear spring c_{10}, and planet gear is supported with bearing which is modeled as linear spring c_{20}, but the meshes of sun gear-planet gear and ring gear-planet gear are described by standard light fractional element with restitution forces $P_1(t)$ and $P_2(t)$. Thus, the potential energies of the bearings are

$$E_P = \frac{1}{2} c_{10} y_1^2 + \frac{1}{2} c_{20} y_2^2. \tag{4}$$

The restitution forces are in the function of element elongation $x_i(t)$, and they are in the form

$$P_i(t) = -\left\{ c_i x_i(t) + c_\alpha D_\alpha^{/} \left[x_i(t) \right] \right\}, \quad i = 1, 2. \tag{5}$$

The fractional order differential operator $D_\alpha^{/}[*]$ of the αth derivative with respect to time t is given in following form: [32, 33, 39]

$$D_\alpha^{/} \left[x_i(t) \right] = \frac{d^\alpha x_i(t)}{dt^\alpha} = \frac{1}{\Gamma(1-\alpha)} \frac{d}{dt} \int_0^t \frac{x_i(\tau)}{(t-\tau)^\alpha} d\tau, \tag{6}$$

where c_i, c_α are rigidity momentary and prolonged coefficients and α is rational number ($0 < \alpha < 1$).

The equations of motion for the planetary gear are derived from Lagrange's equation given by well-known form

$$\frac{d}{dt}\left(\frac{\partial E_K}{\partial \dot{q}_j} \right) - \frac{\partial E_K}{\partial q_j} + \frac{\partial E_P}{\partial q_j} = Q_j^* - \frac{\partial \Phi}{\partial \dot{q}_j}, \quad j = 1, 2, \ldots, 4, \tag{7}$$

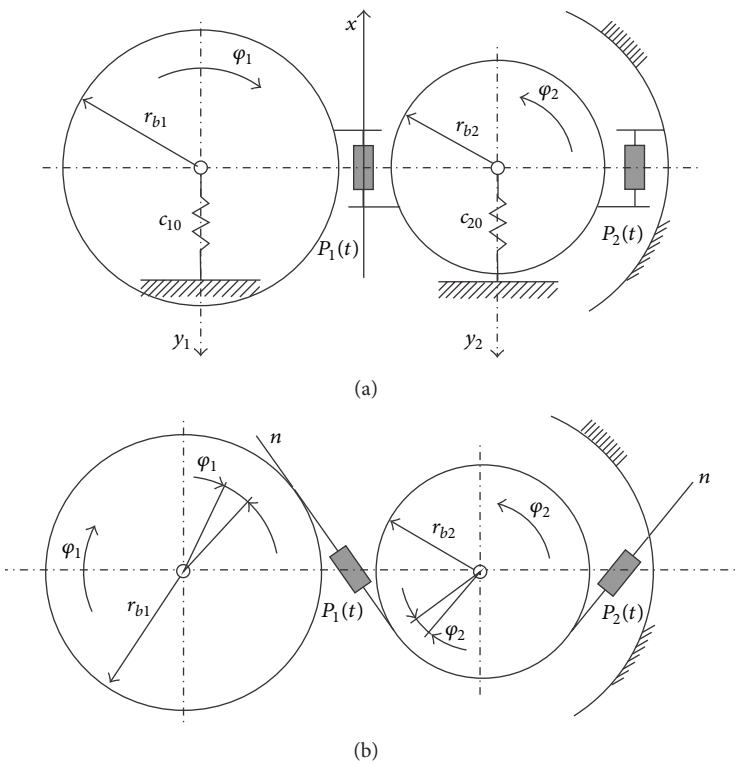

Figure 1: The model of the planetary gear with viscoelastic fractional order tooth coupling: (a) the frontal plane, (b) the direction of contact.

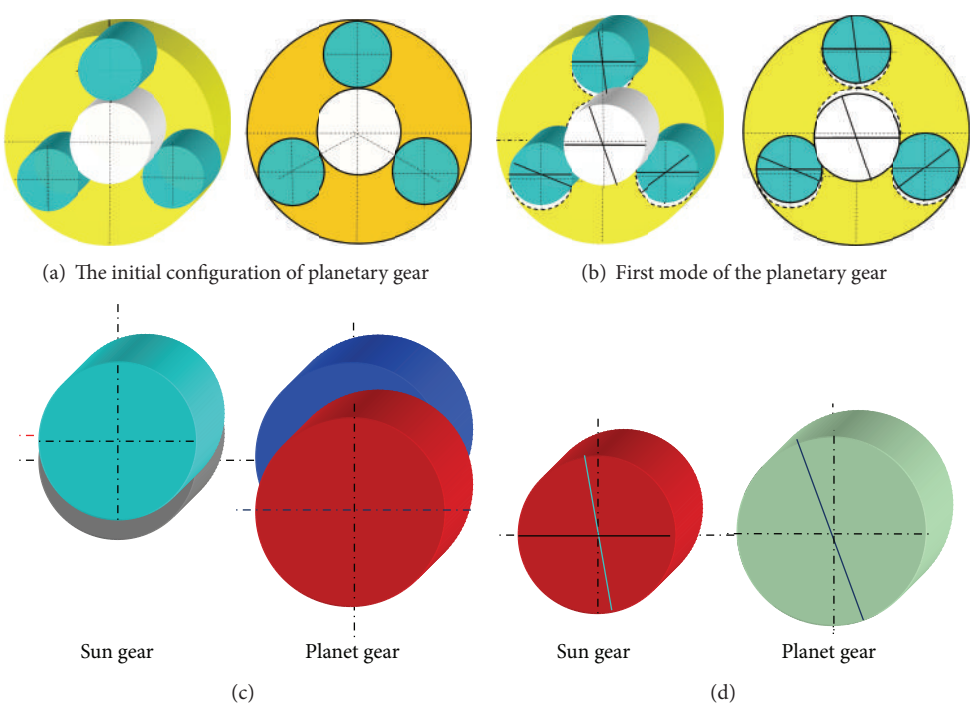

Figure 2: First rotational-axial modes of the planetary gear system defined in Table 1. Translational (a) and angular (b) displacements-eigen amplitudes for $\omega_1 = 215{,}546$ Hz.

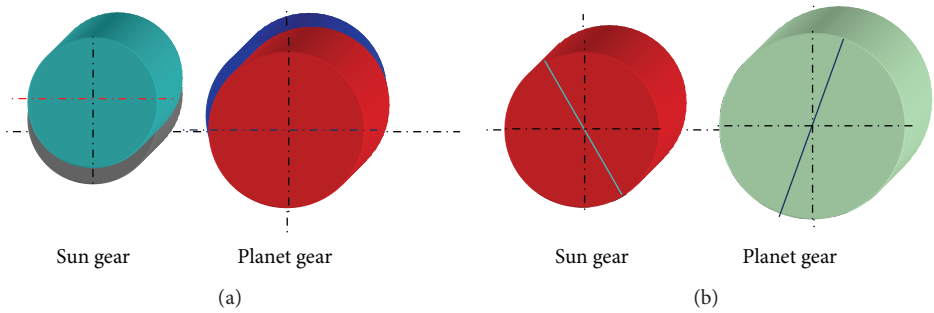

Figure 3: A pair of degenerate translational (a) and angular (b) displacements-eigen amplitudes for second modes of the planetary gear system defined in Table 1. Translational (a) and angular (b) displacements-eigen amplitudes for $\omega_2 = 2901$ Hz.

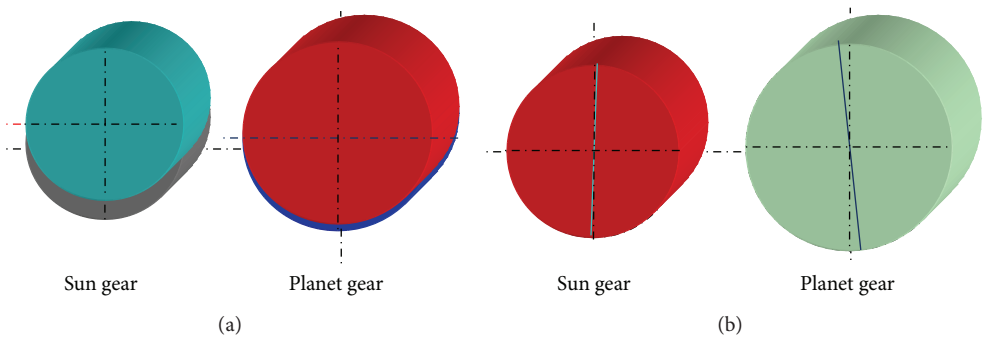

Figure 4: A pair of degenerate translational (a) and angular (b) displacements-eigen amplitudes for second modes of the planetary gear system defined in Table 1. Translational (a) and angular (b) displacements-eigen amplitudes for $\omega_3 = 40890$ Hz.

where q_j are generalized coordinates, Q_j^* are generalized forces, and Φ is Rayleigh dissipation function (in our case Rayleigh dissipation function is zero because damping effects are taken into consideration). Generalized coordinates for the given system are y_1, y_2, φ_1, and φ_2.

Therefore, the dynamic behavior will be governed by four independent equations of motion. In matrix form they are

$$\mathbf{M}\{\ddot{q}\} + \mathbf{C}\{q\} = Q_j^* - \frac{\partial \Phi}{\partial \dot{q}_j}, \quad j = 1, 2, \ldots, 4, \tag{8}$$

where the matrix $\mathbf{M}$ is diagonal inertia matrix and the matrix $\mathbf{C}$ is stiffness matrix.

Light standard creep constraint element between sun gear and planet gear is strained for $x_1 = y_2 - y_1 + r_{b2}\varphi_2 - r_{b1}\varphi_1$, and light standard creep constraint element between planet gear and ring gear is strained for $x_2 = y_2 - r_{b2}\varphi_2$.

So, due to the constitutive relation of the standard light fractional order coupling elements, the generalized forces as a function of elongation of elements are

$$\begin{aligned} Q_1^* &= -c_1 x_1 - c_\alpha D_\alpha^{/}[x_1] \\ &= -c_1[(y_2 + r_{b2}\varphi_2) - (y_1 + r_{b1}\varphi_1)] \\ &\quad - c_\alpha D_\alpha^{/}[(y_2 + r_{b2}\varphi_2) - (y_1 + r_{b1}\varphi_1)], \\ Q_2^* &= -c_2 x_2 - c_\alpha D_\alpha^{/}[x_2] \\ &= -c_2[y_2 - r_{b2}\varphi_2] - c_\alpha D_\alpha^{/}[y_2 - r_{b2}\varphi_2]. \end{aligned} \tag{9}$$

Lagrange equations of motion are obtained following substitution (9) into (7), and they can be expressed as

$$\begin{aligned} &m_1\ddot{y}_1 + c_{01}y_1 + c_1[(y_1 + r_{b1}\varphi_1) - (y_2 + r_{b2}\varphi_2)] \\ &\quad = c_\alpha D_\alpha^{/}[(y_2 + r_{b2}\varphi_2) - (y_1 + r_{b1}\varphi_1)], \\ &J_1\ddot{\varphi}_1 + c_1[(y_1 + r_{b1}\varphi_1) - (y_2 + r_{b2}\varphi_2)]r_{b1} \\ &\quad = c_\alpha D_\alpha^{/} r_{b1}[(y_2 + r_{b2}\varphi_2) - (y_1 + r_{b1}\varphi_1)], \\ &m_2\ddot{y}_2 + c_{02}y_2 \\ &\quad + c_1[(y_2 + r_{b2}\varphi_2) - (y_1 + r_{b1}\varphi_1)] \\ &\quad + c_2[(y_2 - r_{b2}\varphi_2)] \\ &\quad = c_\alpha D_\alpha^{/}[(y_1 + r_{b1}\varphi_1) - (y_2 + r_{b2}\varphi_2)] \\ &\quad - c_\alpha D_\alpha^{/}[(y_2 - r_{b2}\varphi_2)], \\ &J_2\ddot{\varphi}_2 + c_1[(y_2 + r_{b2}\varphi_2) - (y_1 + r_{b1}\varphi_1)]r_{b2} \\ &\quad + c_2[r_{b2}\varphi_2 - y_2]r_{b2} \\ &\quad = c_\alpha D_\alpha^{/}[(y_1 + r_{b1}\varphi_1) - (y_2 + r_{b2}\varphi_2)] \\ &\quad + c_\alpha D_\alpha^{/}[(y_2 - r_{b2}\varphi_2)]. \end{aligned} \tag{10}$$

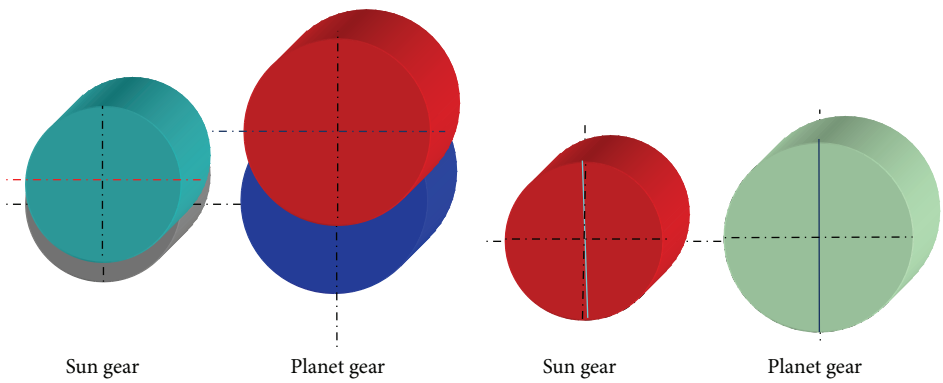

(a) (b)

Figure 5: Fourth rotational-axial modes of the planetary gear system defined in Table 1. Translational (a) and angular (b) displacements-eigen amplitudes for $\omega_4 = 50000$ Hz.

The diagonal inertia matrix $\mathbf{M}$ is

$$\mathbf{M} = \operatorname{diag}(m_1, J_1, m_2, J_2). \tag{11}$$

The stiffness matrix $\mathbf{C}$ is

$$\mathbf{C} = \begin{bmatrix} c_{10} + c_1 & c_1 r_{b1} & -c_1 & -c_1 r_{b2} \\ & c_1 r_{b1}^2 & -c_1 r_{b1} & -c_1 r_{b1} r_{b2} \\ \text{Symmetric} & & c_{20} + c_1 + c_2 & (c_1 - c_2) r_{b2} \\ & & & (c_1 + c_2) r_{b2}^2 \end{bmatrix}. \tag{12}$$

3. Modal Analysis of the Planetary Gear

The system is tuned, that is, all sun-planet and ring-planet mesh stiffnesses, and their centers of stiffnesses, are identical among all planets; the planet bearing stiffnesses, the axial locations of the planet bearings, and the planet inertias are the same for all planets.

3.1. Eigenvalue Problem. The proposed solutions are in the form of

$$\{q\} = \{A\} \cos(\omega t + \varepsilon). \tag{13}$$

The eigenvalue problem is

$$(\mathbf{C} - \lambda \mathbf{M}) \{q\} = 0 \tag{14}$$

with natural frequencies $\sqrt{\lambda}$.

It is known that to have nontrivial solutions the matrix on the left side must be singular. It follows that the determinant of the matrix must be equal to 0, so

$$\det(\mathbf{C} - \lambda \mathbf{M}) = 0 \tag{15}$$

or, in the developed form,

$$\begin{bmatrix} (c_{10} + c_1) - \lambda m_1 & c_1 r_{b1} & -c_1 & -c_1 r_{b2} \\ & (c_1 r_{b1}^2) - \lambda J_1 & -c_1 r_{b1} & -c_1 r_{b1} r_{b2} \\ \text{Symmetric} & & (c_{20} + c_1 + c_2) - \lambda m_2 & (c_1 - c_2) r_{b2} \\ & & & ((c_1 + c_2) r_{b2}^2) - \lambda J_2 \end{bmatrix} = 0. \tag{16}$$

Corresponding frequency equation in the polynomial form is

$$a_4 \lambda^4 + a_3 \lambda^3 + a_2 \lambda^2 + a_1 \lambda + a_0 = 0, \tag{17}$$

where, for instance, $a_4 = \operatorname{trace} \mathbf{M}$, $a_0 = \det \mathbf{C}$, and so forth.

Solving this polynomial four roots λ_j, $j = 1, 2, 3, 4$ and corresponding eigen circular frequencies $\omega_j = \sqrt{\lambda_j}$, $j = 1, 2, 3, 4$, can be obtained.

The solution of basic linear differential equation is

$$q_j(t) = \sum_{s=1}^{4} q_j^{(s)}(t) = \sum_{s=1}^{4} A_j^{(s)} \cos(\omega_s t + \varepsilon_s), \tag{18}$$

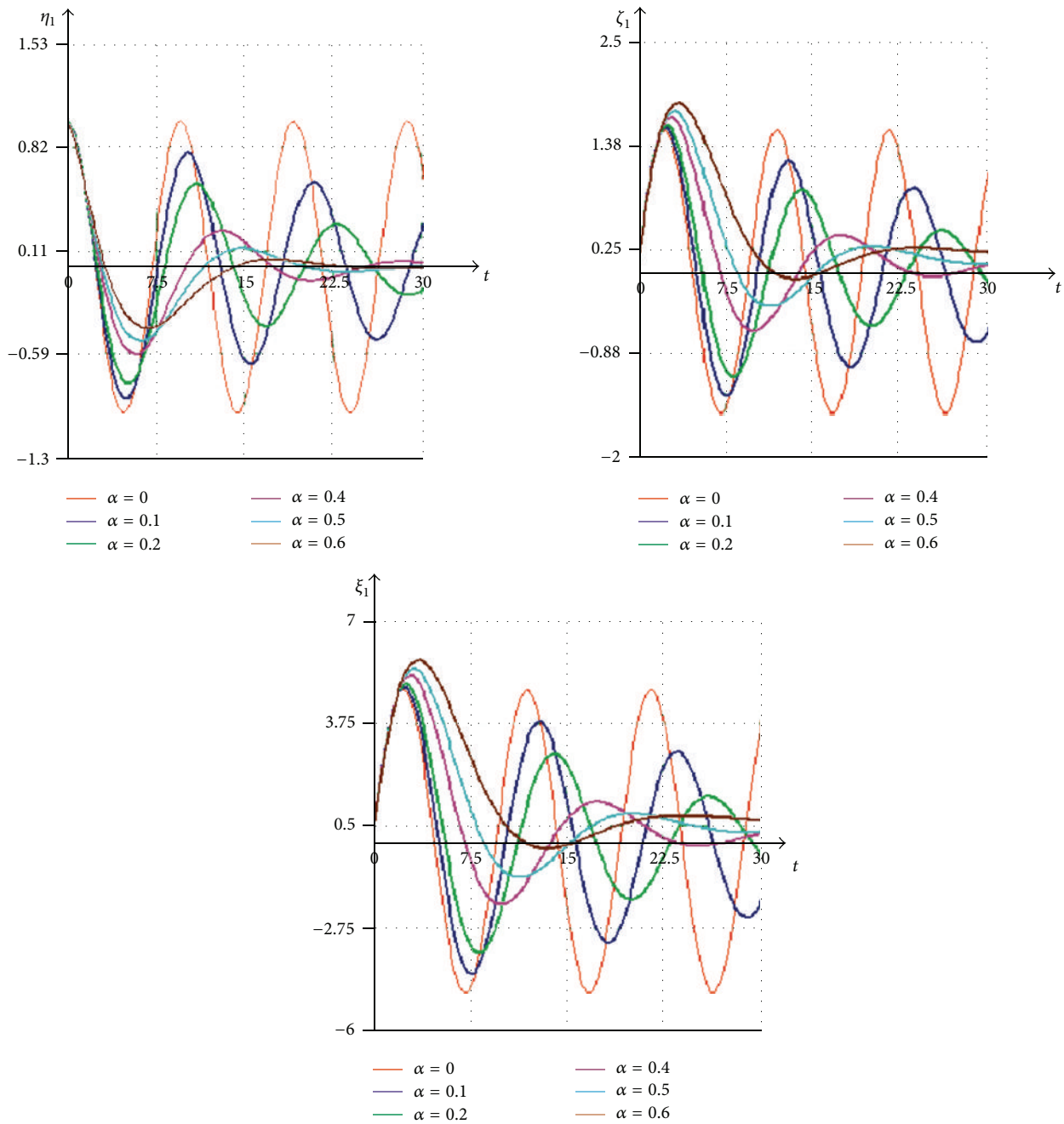

FIGURE 6: First eigen fractional mode $\xi_1(t)$ with corresponding first fractional order time components $\eta_1(t)$ and $\zeta_1(t)$ for different system kinetic and geometric parameter values.

and in matrix presentation

$$\{q(t)\} = \mathbf{R}\{C_s \cos(\omega_s t + \varepsilon_s)\}, \tag{19}$$

where $\mathbf{R}$ is modal matrix defined by the corresponding cofactors, $\xi_s = C_s \cos(\omega_s t + \varepsilon_s)$, and $s = 1, 2, 3, 4$ are main coordinates of the linear system.

With this expression, the system of the fractional differential equation (10) can be transformed in the form of [39]

$$\ddot{\xi}_s + \omega_s^2 \xi_s = -\omega_{\alpha s}^2 D_\alpha^{/}[\xi_s], \quad s = 1, 2, 3, 4. \tag{20}$$

This resulted the system of the fractional differential equation. Analytical solution of these fractional order differential equations is obtained using the approach presented in

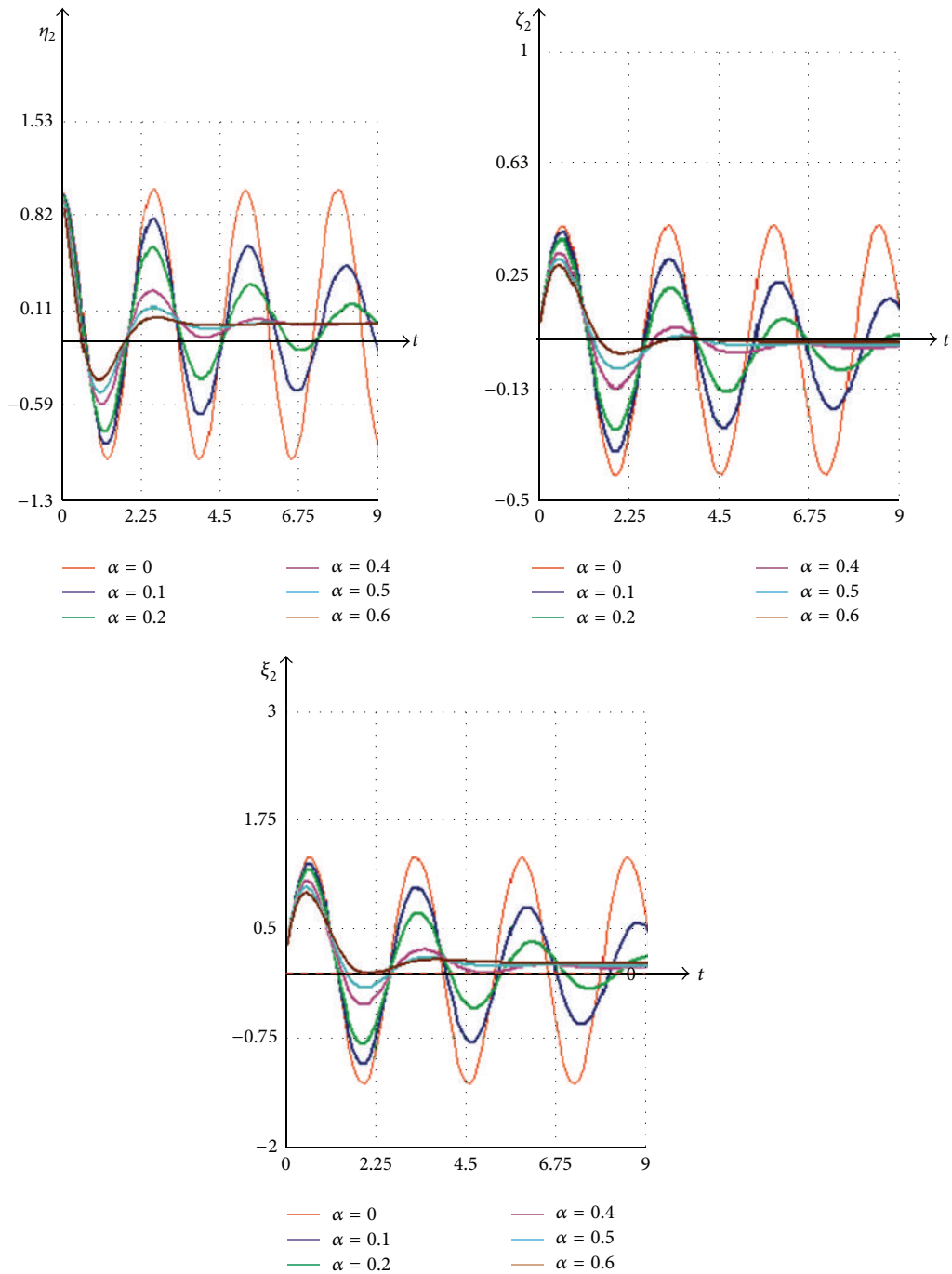

FIGURE 7: Second eigen fractional mode $\xi_2(t)$ with corresponding second fractional order time components $\eta_2(t)$ and $\zeta_2(t)$ for different system kinetic and geometric parameter values.

[37, 39]. Therefore, each fractional differential equation can be written in the form of

$$\xi_s(t) = \xi_{0s} \sum_{k=0}^{\infty} (-1)^k \omega_{\alpha s}^{2k} t^{2k} \times \sum_{j=0}^{k} \binom{k}{j} \frac{(\mp 1)^j \omega_{\alpha s}^{2j} t^{-\alpha j}}{\omega_s^{2j} \Gamma(2k+1-\alpha j)} + \dot{\xi}_{0s} \sum_{k=0}^{\infty} (-1)^k \omega_{\alpha s}^{2k} t^{2k+1} \times \sum_{j=0}^{k} \binom{k}{j} \frac{(\mp 1)^j \omega_{\alpha s}^{-2j} t^{-\alpha j}}{\omega_s^{2j} \Gamma(2k+2-\alpha j)}, \quad s = 1, 2, 3, 4, \tag{21}$$

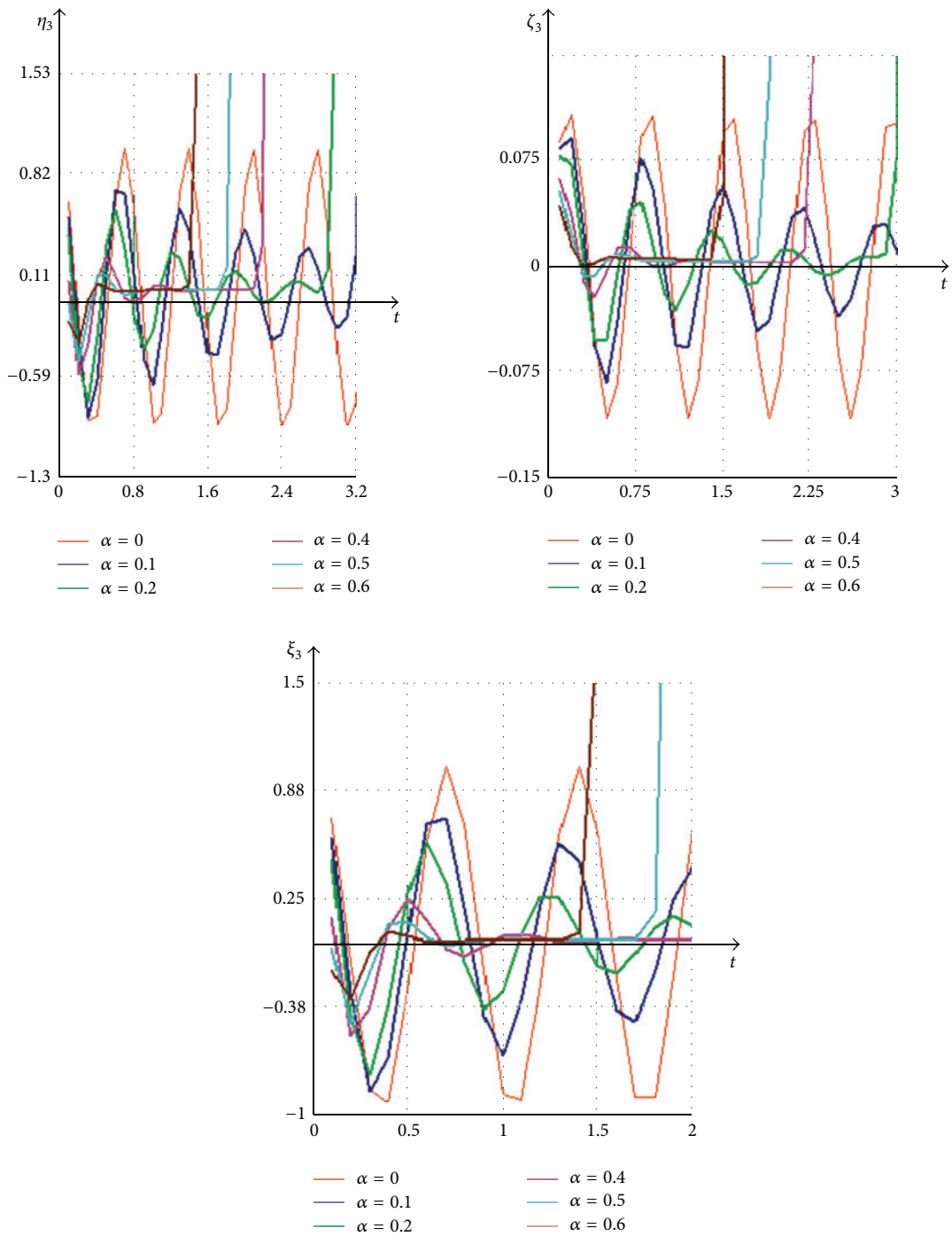

FIGURE 8: Third eigen fractional mode $\xi_3(t)$ with corresponding third fractional order time components $\eta_3(t)$ and $\zeta_3(t)$ for different system kinetic and geometric parameter values.

where $\xi_s(0) = \xi_{0s}$ and $\dot{\xi}_s(0) = \dot{\xi}_{0s}$ are initial values of main coordinates defined by initial conditions and α is rational number $(0 < \alpha < 1)$.

The solution of the basis system [39] can be expressed in the following form:

$$\begin{aligned} q_j(t) &= \sum_{s=1}^{4} K_{pk}^{(s)} \xi_s(t) \\ &= \sum_{s=1}^{4} K_{pk}^{(s)} \xi_{0s} \sum_{k=0}^{\infty} (-1)^k \omega_{\alpha s}^{2k} t^{2k} \\ &\quad \times \sum_{j=0}^{k} \binom{k}{j} \frac{(\mp 1)^j \omega_{\alpha s}^{2j} t^{-\alpha j}}{\omega_s^{2j} \Gamma(2k+1-\alpha j)} \\ &\quad + \sum_{s=1}^{4} K_{pk}^{(s)} \dot{\xi}_{0s} \sum_{k=0}^{\infty} (-1)^k \omega_{\alpha s}^{2k} t^{2k+1} \\ &\quad \times \sum_{j=0}^{k} \binom{k}{j} \frac{(\mp 1)^j \omega_{\alpha s}^{-2j} t^{-\alpha j}}{\omega_s^{2j} \Gamma(2k+2-\alpha j)}, \quad s = 1, 2, 3, 4. \end{aligned} \tag{22}$$

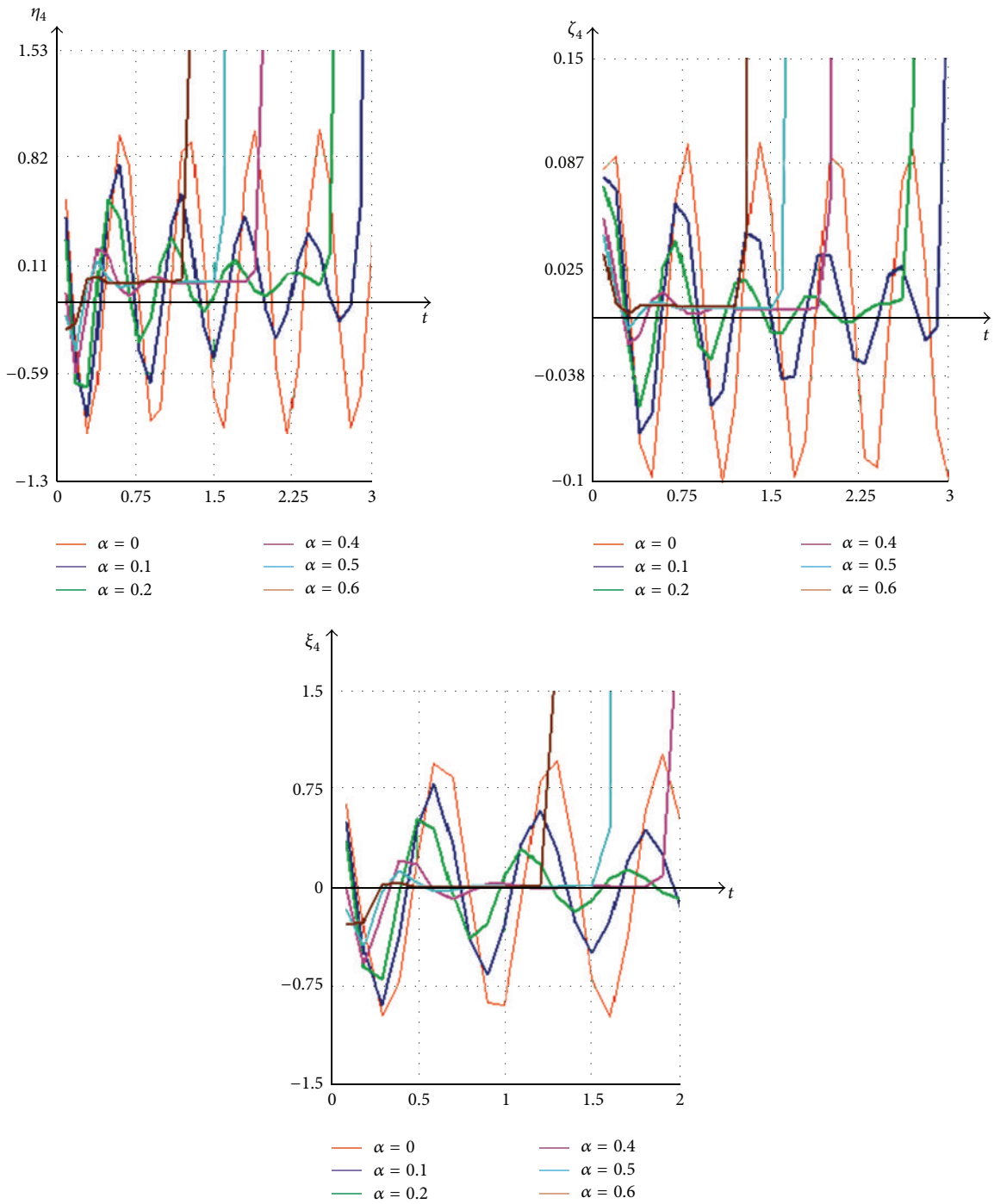

FIGURE 9: Fourth eigen fractional mode $\xi_4(t)$ with corresponding third fractional order time components $\eta_4(t)$ and $\zeta_4(t)$ for different system kinetic and geometric parameter values.

3.2. Numerical Visualisation. Eigensolutions of a sample system [20, Table 1], with four degrees of freedom are evaluated numerically to expose the modal properties.

Eigensolutions of a sample system (Table 1) with three equally spaced planets are evaluated numerically to expose the modal properties. Four natural frequencies and their corresponding mode types are given in Figures 2, 3, 4, and 5. In Figure 2(a), the initial configuration of planetary gear is shown, and Figure 2(b) shows the planetary gear first mode. In order to better consideration of modes of individual elements of the gear in the following Figures 2(c), 2(d), 3, 4 and 5, separate elements of planetary gear are shown.

The vibration modes exhibit distinctive characteristics. The central member rotates and translates axially and planets do same. Regardless of the system parameters the modal deflection of planet gears are zero for $\omega_4 = 50000$ Hz.

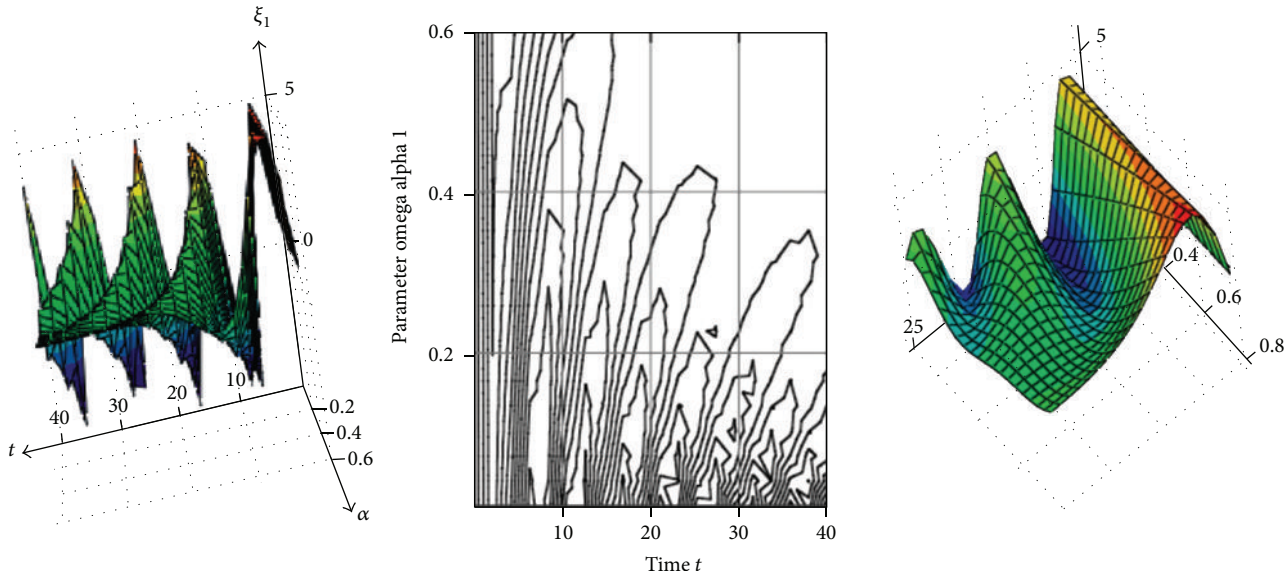

(a) First mode of the planetary gear system $\xi_1(\alpha, t)$

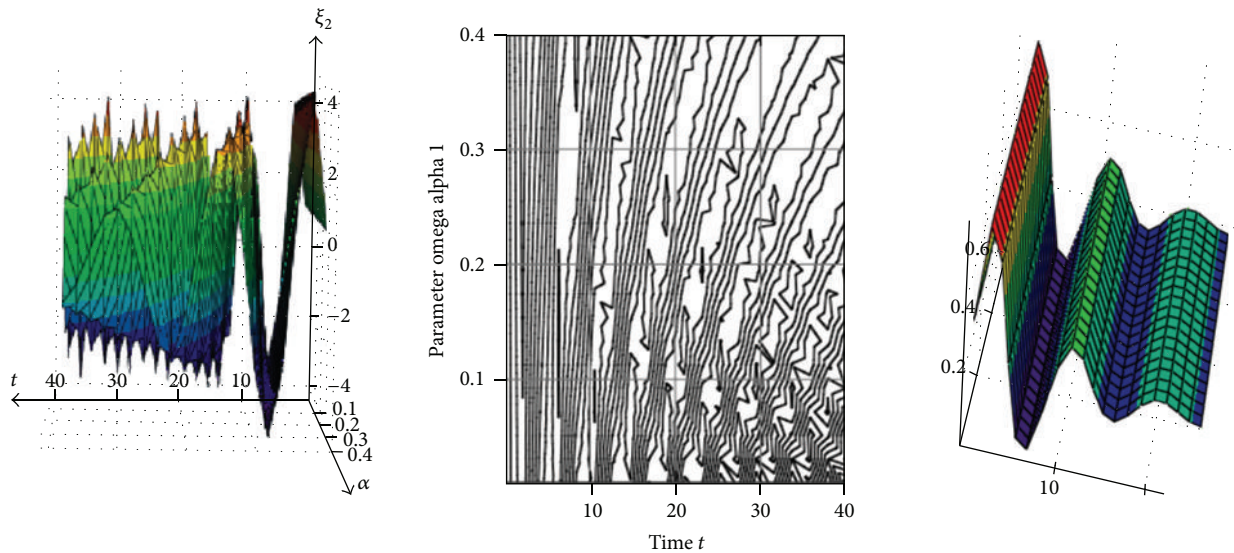

(b) Second mode of the planetary gear system $\xi_2(\alpha, t)$

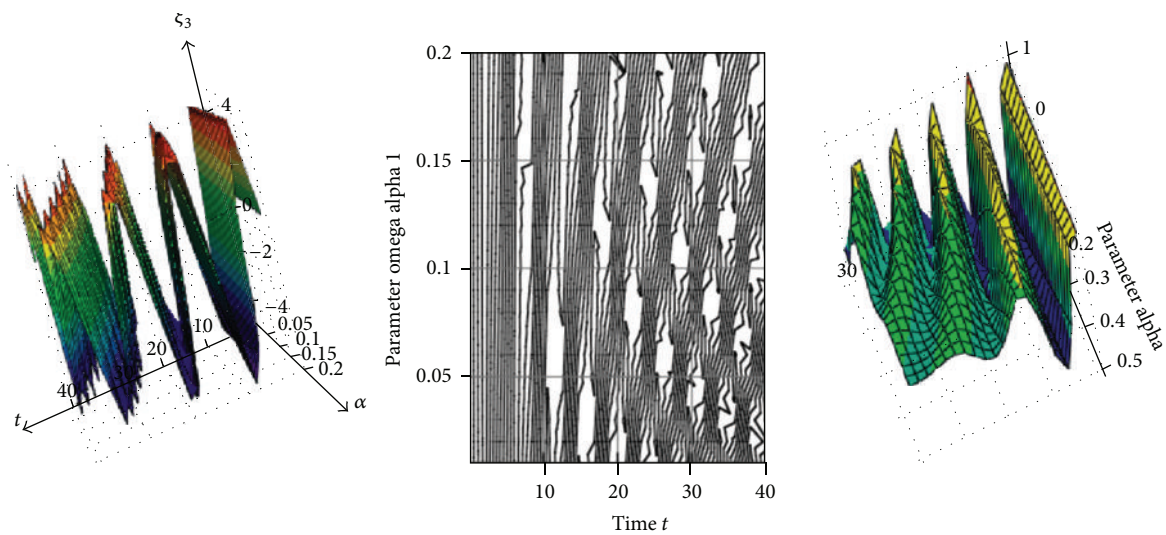

(c) Third mode of the planetary gear system $\xi_3(\alpha, t)$

Figure 10: Continued.

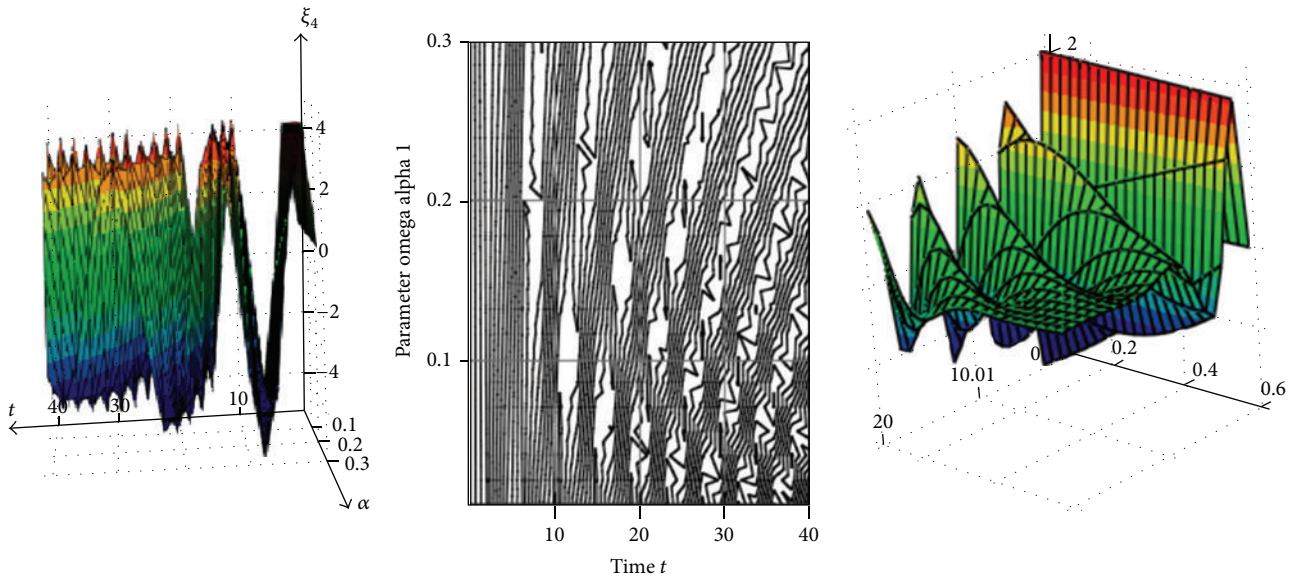

(d) Fourth mode of the planetary gear system $\xi_4(\alpha, t)$

Figure 10: Four eigen fractional modes, $\xi_1(\alpha, t)$, $\xi_2(\alpha, t)$, $\xi_3(\alpha, t)$, and $\xi_4(\alpha, t)$ presented by surfaces.

Table 1: Parameters of the planetary gear.

Parameter	Sun	Planet
Base radius r_b, mm	24	16
Radial bearing stiffnesses c_{10} and c_{20}, N/m	0.5×10^9	0.5×10^9
Stiffness of teeth c_1 and c_2, N/m	2.91×10^8	1.81×10^8
Mass m, kg	0.3	0.20
Rotational inertia, J_1, kg m^2	10×10^{-3}	100×10^{-6}

Based on (18), the first normal mode corresponds to both masses moving in the opposite direction while angular displacements are in the same direction. The second normal mode corresponds to the masses moving in the opposite directions and angular displacements are in the opposite directions also. The masses, for ω_3 and ω_4, move in the same direction, but angular displacements are in the opposite directions or equal zero (fourth mode). The general solution is a superposition of the normal modes where the initial conditions of the problem must be used.

By using different numerical values of the kinetic and geometrical parameters of the planetary gear model, the series of the graphical presentation of the four sets of the two time components $\eta_s(t)$ and $\zeta_s(t)$, $s = 1, 2, 3, 4$ of the solutions, by using expressions (21) are obtained. In the series Figures 6–10 are presented characteristic modes for different values of the α coefficient of the fractional order of the used standard light fractional order element for describing teeth coupling between sun-planet and planet-ring. Time t is in sec, and all values on the vertical axis are in μm.

First eigen fractional order mode $\xi_1(t)$ with corresponding first eigen fractional order time components $\eta_1(t)$ and $\zeta_1(t)$ for different system kinetic and geometric parameter values is presented in Figure 6.

In Figure 7, we can see second eigen fractional mode $\xi_2(t)$ with corresponding second fractional order time components $\eta_2(t)$ and $\zeta_2(t)$ for different system kinetic and geometric parameter values.

In Figure 8, third eigen fractional mode $\xi_3(t)$ with corresponding third fractional order time components $\eta_3(t)$ and $\zeta_3(t)$ for different system kinetic and geometric parameter values is presented.

Fourth eigen fractional mode $\xi_4(t)$ with corresponding third fractional order time components $\eta_4(t)$ and $\zeta_4(t)$ for different system kinetic and geometric parameter values, in Figure 9, is presented.

In Figure 10, first, second, third, and fourth eigen fractional modes $\xi_1(\alpha, t)$, $\xi_2(\alpha, t)$, $\xi_3(\alpha, t)$, and $\xi_4(\alpha, t)$ are presented by surfaces. Also, the family trajectory in the plane (α, t) is shown.

Based on the obtained results in this paper, we can conclude that eigen fractional order modes are like one frequency vibration modes similar to single frequency eigen mode of the corresponding linear system [29, 38, 39, 41].

The fractional order dynamic system is like dumping system. With the increase of the parameter α, the period of oscillation increases but the amplitude becomes smaller. So we can say that parameter α has the same influence as dumping coefficient in the corresponding system.

4. Conclusions

This paper presents a new dynamic model of a planetary gear. The planetary gear system is represented by a model that allows for four degrees of freedom per gear-shaft body supported by bearings at arbitrary axial positions and with

standard creep constraint element. The standard light fractional order coupling element is between sun-planet and planet-ring. A novel approach for the planetary gear dynamic analysis is developed. So, in this paper it is shown how the new model of the fractional order dynamic planetary gear can be applied to study dynamic behavior. This model simulates the real behavior of the planetary gear.

With this simple model, it is possible to research the nonlinear dynamics of the planetary gear and nonlinear phenomena in free and forced dynamics. The model is suitable to explain source of vibrations and big noise, as well as no stability in planetary gear.

A new method, using MATCAD software, is used in this paper for the obtaining of the eigen values and for analysis results.

In the literature, similar procedures are presented in introduction, and they were used as reference material for the composition and verification of models and results.

On the basis of the numerical results, shown in this paper, it has been concluded that the methodology developed to study the dynamic behaviour of planetary gear is very efficient. It gives a lot of possibilities and can be easily upgraded for analysis of other effects.

The dynamic behavior and analysis of results suggest that the gear transmission is very complex and that it is almost impossible to include all the effects by such and similar research. This paper considers planetary gear with 3 planet gears, which makes the problem more complex.

Further research should be directed at studying the effects of mutual dynamic impact of teeth in mesh, as well as at including more effects [42]. So, it is possible to study eigen frequency of planetary gear with moving excentric masses on the body of one of the gears or with holes on the body, by using finite element method.

In accordance with the present trend of application of new materials, authors will, in future studies, simulate the dynamic behavior of a gear made of composite materials and study the life of the gears at the load. Also, future research should focus on the study of planetary gears life using low cycle fatigue properties and so forth.

Results in this paper can be taken as relevant for further research, because this model simulates the real behavior of the planetary gear, more than earlier models.

Acknowledgments

Parts of this research were supported by the Ministry of Sciences of Republic Serbia through Mathematical Institute SANU Belgrade Grant no. ON 174001 "Dynamics of hybrid systems with complex structures. Mechanics of materials" and also through the Faculty of Mechanical Engineering University of Niš and the State University of Novi Pazar.

References

[1] F. Cunliffe, D. J. Smith, and D. B. Welbourn, "Dynamic tooth loads in epicyclic gears," *Journal of Engineering For Industry*, vol. 95, no. 2, pp. 578–584, 1974.

[2] G. W. Blankenship and R. Singh, "Dynamic force transmissibility in helical gear pairs," *Mechanism and Machine Theory*, vol. 30, no. 3, pp. 323–339, 1995.

[3] G. W. Blankenship and R. Singh, "A new gear mesh interface dynamic model to predict multi-dimensional force coupling and excitation," *Mechanism and Machine Theory*, vol. 30, no. 1, pp. 43–57, 1995.

[4] G. Liu and R. G. Parker, "Impact of tooth friction and its bending effect on gear dynamics," *Journal of Sound and Vibration*, vol. 320, no. 4-5, pp. 1039–1063, 2009.

[5] G. Niemann and H. Winter, *Maschinen-Elemente II and III*, Springer, Berlin, Germany, 1989.

[6] V. Nikolic, *Machine Elements, Theory, Calculation, Examples*, Faculty of Mechanical Engineering, Prizma, Kragujevac, Serbia, 2004.

[7] V. Nikolic, *Mechanical Analysis of Gears*, Faculty of Mechanical Engineering, Cimpes, Kragujevac, Serbia, 1999.

[8] G. Liu and R. G. Parker, "Nonlinear dynamics of idler gear systems," *Nonlinear Dynamics*, vol. 53, no. 4, pp. 345–367, 2008.

[9] A. Kahraman and G. W. Blankenship, "Experiments on nonlinear dynamic behavior of an oscillator with clearance and periodically time-varying parameters," *Journal of Applied Mechanics*, vol. 64, no. 1, pp. 217–226, 1997.

[10] A. Kahraman and R. Singh, "Non-linear dynamics of a spur gear pair," *Journal of Sound and Vibration*, vol. 142, no. 1, pp. 49–75, 1990.

[11] R. G. Parker, S. M. Vijayakar, and T. Imajo, "Non-linear dynamic response of a spur gear pair: modelling and experimental comparisons," *Journal of Sound and Vibration*, vol. 237, no. 3, pp. 435–455, 2000.

[12] J. Lin and R. G. Parker, "Analytical characterization of the unique properties of planetary gear free vibration," *Journal of Vibration and Acoustics*, vol. 121, no. 3, pp. 316–321, 1999.

[13] L. Vedmar and A. Andersson, "A method to determine dynamic loads on spur gear teeth and on bearings," *Journal of Sound and Vibration*, vol. 267, no. 5, pp. 1065–1084, 2003.

[14] M. F. Agemi and M. Ognjanović, "Gear vibration in supercritical mesh-frequency range," *FME Transactions*, vol. 32, no. 2, pp. 87–94, 2004.

[15] D. Dimitrijević and V. Nikolić, "Eigenfrequencies analysis for the deep drilling machine gear set," *The Scientific Journal FACTA UNIVERSATES*, vol. 1, no. 5, pp. 629–636, 1998.

[16] D. Dimitrijevic and V. Nikolic, "Eigenfrequence analysis of the spur gear pair with moving excentric masses on the body of one of the gears," *FME Transactions*, vol. 35, no. 3, pp. 157–163, 2007.

[17] H. Vinayak and R. Singh, "Multi-body dynamics and modal analysis of compliant gear bodies," *Journal of Sound and Vibration*, vol. 210, no. 2, pp. 171–212, 1998.

[18] J. Lin and R. G. Parker, "Analytical characterization of the unique properties of planetary gear free vibration," *Journal of Vibration and Acoustics*, vol. 121, no. 3, pp. 316–321, 1999.

[19] J. Lin and R. G. Parker, "Natural frequency veering in planetary gears," *Mechanics of Structures and Machines*, vol. 29, no. 4, pp. 411–429, 2001.

[20] J. Lin and R. G. Parker, "Planetary gear parametric instability caused by mesh stiffness variation," *Journal of Sound and Vibration*, vol. 249, no. 1, pp. 129–145, 2002.

[21] T. Eritenel and R. G. Parker, "Modal properties of three-dimensional helical planetary gears," *Journal of Sound and Vibration*, vol. 325, no. 1-2, pp. 397–420, 2009.

[22] Y. Guo and R. G. Parker, "Sensitivity of general compound planetary gear natural frequencies and vibration modes to model parameters," *Journal of Vibration and Acoustics*, vol. 132, no. 1, 13 pages, 2010.

[23] T. Hidaka, Y. Terauchi, and K. Nagamura, "Dynamic behavior of planetary gear," *Bulletin of the JSME*, vol. 22, no. 169, pp. 1017–1025, 1979.

[24] R. G. Parker, V. Agashe, and S. M. Vijayakar, "Dynamic response of a planetary gear system using a finite element/contact mechanics model," *Journal of Mechanical Design*, vol. 122, no. 3, pp. 304–310, 2000.

[25] C. J. Bahk and R. G. Parker, "Analytical solution for the nonlinear dynamics of planetary gears," *Journal of Computational and Nonlinear Dynamics*, vol. 6, no. 2, Article ID 021007, 15 pages, 2011.

[26] T. Sun and H. Hu, "Nonlinear dynamics of a planetary gear system with multiple clearances," *Mechanism and Machine Theory*, vol. 38, no. 12, pp. 1371–1390, 2003.

[27] V. Nikolić, C. Dolićanin, and D. Dimitrijević, "Numerical modelling of gear set dynamic behaviour," *Scientific Technical Review*, no. 3-4, pp. 48–54, 2010.

[28] V. Nikolić, Ć. Dolićanin, and D. Dimitrijević, "Dynamic Model for the Stress and Strain State Analysis of a Spur Gear Transmission, StrojniŔki vestnik," *Journal of Mechanical Engineering*, vol. 58, no. 1, pp. 56–67, 2012.

[29] O. A. I. Goroško and K. Hedrih, *Analitička Dinamika (Mehanika) Diskretnih Naslednih Sistema, (Analytical Dynamics (Mechanics) of Discrete Hereditary Systems)*, Monograph, University of Niš, 2001.

[30] O. A. Goroško and K. Hedrih, "Advances in development of the analytical dynamics of the hereditary discrete systems," *Journal of Physics*, vol. 96, Article ID 012143, 2008.

[31] B. S. Bačlić and T. M. Atanacković, "Stability and creep of a fractional derivative order viscoelastic rod," *Bulletin*, no. 25, pp. 115–131, 2000.

[32] M. T. Atanacković, C. D. Dolićanin, and S. Pilipović, "Forced oscillations of a single degree of freedom system with fractional dissipation," *Scientific Publications of the State University of Novi Pazar*, vol. 3, no. 1, pp. 1–11, 2011.

[33] K. Hedrih and R. Knežević, "Structural stability of the planetary reductor nonlinear dynamics phase portrait," *Facta Universitatis*, vol. 1, no. 7, pp. 911–923, 2000.

[34] K. Hedrih, K. Knežević, and R. Cvetković, "Dynamics of planetary reductoe with turbulent damping," *International Journal of Nonlinear Sciences and Numerical Simulations*, vol. 2, no. 3, pp. 265–262, 2001.

[35] R. G. Parker, "On the eigenvalues and critical speed stability of gyroscopic continua," *Journal of Applied Mechanics*, vol. 65, no. 1, pp. 134–140, 1998.

[36] K. Hedrih and L. J. Veljović, "Nonlinear dynamic of heavy gyro-rotor with two skew rotating axes," *Journal of Physics*, vol. 96, Article ID 012221, 2008.

[37] K. Hedrih and L. J. Veljović, "Nonlinear dynamic of heavy gyro-rotor with two rotating axes, facta universitates series mechanics," *Automatic Control and Robotics*, vol. 14, no. 16, pp. 55–68, 2004.

[38] K. R. Hedrih and L. Veljović, "Vector rotators of rigid body dynamics with coupled rotations around axes without intersection," *Mathematical Problems in Engineering*, vol. 2011, Article ID 351269, 26 pages, 2011.

[39] K. R. Hedrih, "Dynamics of multi-pendulum systems with fractional order creep elements," *Journal of Theoretical and Applied Mechanics*, vol. 46, no. 3, pp. 483–509, 2008.

[40] K. S. Hedrih and V. Nikolić-Stanojević, "A model of gear transmission fractional order system dynamics," *Mathematical Problems in Engineering*, vol. 2010, Article ID 972873, 23 pages, 2010.

[41] S. Vijayakar, "Combined surface integral and finite element solution for a three-dimensional contact problem," *International Journal for Numerical Methods in Engineering*, vol. 31, no. 3, pp. 525–545, 1991.

[42] S. Y. T. Lang, "Graph-theoretic modelling of epicycle gear systems," *Mechanism and Machine Theory*, vol. 40, no. 5, pp. 511–529, 2005.

Hindawi Publishing Corporation
Mathematical Problems in Engineering
Volume 2013, Article ID 642101, 10 pages
http://dx.doi.org/10.1155/2013/642101

Research Article

Parametric Analysis of a Heavy Metal Sorption Isotherm Based on Fractional Calculus

Enrico M. Gomes,[1] Rosana R. L. Araújo,[1] Marcelo K. Lenzi,[1] Fernanda R. G. B. Silva,[2] and Ervin K. Lenzi[2]

[1] *Departamento de Engenharia Química, Universidade Federal do Paraná, Caixa Postal 19011, 81531-980 Curitiba, PR, Brazil*
[2] *Departamento de Física, Universidade Estadual de Maringá, 87020-900 Maringá, PR, Brazil*

Correspondence should be addressed to Ervin K. Lenzi; ervinklenzi@gmail.com

Received 5 October 2012; Revised 5 April 2013; Accepted 14 April 2013

Academic Editor: Jocelyn Sabatier

Heavy metals are widely recognized as being hazardous to human health and environmentally aggressive. The literature reports different approaches for lead removal, for example, water hyacinths. Heavy metal sorption isotherm modeling represents an important tool towards the study of equilibrium conditions. Fractional calculus represents a novel approach and a growing research field for process modeling, based on derivatives of arbitrary order. Recently, a novel isotherm based on fractional calculus was proposed for lead sorption using water hyacinth (*Eichhornia crassipes*). This paper reports a general procedure on error analysis and its influence on parameter estimation. It was applied to mathematical models based on fractional differential equations, focusing on a heavy metal novel isotherm sorption model. Parameter variance was calculated by using two different approaches (with the complete Hessian matrix and with a simplified Hessian matrix), and joint parameter confidence regions were generated, being successfully able to show that the fractional nature of the model is statistically valid.

1. Introduction

Heavy metals are widely recognized as being hazardous to human health and environmentally aggressive, being continuously generated by different chemical plants. The use of lead in the battery industry [1] is an important example. The literature reports different approaches for heavy metals removal, such as chemical precipitation [2], ion exchange [3], and electrochemical [4] and water hyacinths [5]. Mathematical models represent an essential tool for in-depth process studies, design, optimization, and control [6]. Therefore, heavy metal sorption isotherm modeling represents an important way towards the study of equilibrium conditions, which play a key role in sorption process design. The most common approach for this task consists in the use of classical models [7], such as Langmuir, Freundlich, and Redlich-Peterson among others, followed by proper parameter estimation and model discrimination analysis.

Fractional calculus represents a novel approach and a growing research field for process modeling, being based on derivatives of arbitrary order [8–14]. The literature reports a broad range of applications, concerning systems engineering [15], diffusion processes [16], heat transfer [17], solid mixing [18], biological systems [19], and fluid mechanics [20] among others [21]. Recently, dos Santos et al. [22] proposed a novel isotherm based on fractional calculus for lead sorption using water hyacinths (*Eichhornia crassipes*). The reported isotherm can successfully predict equilibrium concentrations of lead between the aqueous solution and the water hyacinth after. The model was validated using synthetic effluent [1]. It is important to highlight that the proposed model also leads to better performances when compared to classical models (Langmuir, Freundlich, and Redlich-Peterson), which were used for sake of comparison.

Error analysis represents a crucial step in model validation and further applications [23]. Recently, Joshi et al. [24] presented a detailed model analysis concerning classical sorption models. Regarding fractional-calculus-based models, Gabano and Poinot [25], Khemane et al. [26], and Isfer et al. [15] report the calculation of parametric variance.

It is important to state that one may identify a mathematical model of fractional order for a given set of experimental data [27]; however, only a precise error analysis can ensure that the derivative is in fact fractional. If the variance of the estimated fractional order of the derivative is large enough, the fractional order can be statistically regarded as integer order for a given confidence level. Consequently, the analysis of parameter joint confidence region becomes an essential tool, as the region indicates, for a given confidence level, the possible set of parameters that could generate the experimental data [28]. To the best of our knowledge, the generation and analysis of joint confidence regions have not yet been reported for models based on fractional calculus. This paper reports a detailed study on an error analysis procedure applied to mathematical models based on fractional differential equations. After the development of a theoretical framework concerning parameter estimation, parameter variance estimation and joint confidence region determination, the fractional model proposed by dos Santos [22] was used as a case study for validation purposes.

2. Theoretical Framework

2.1. Mathematical Model. Further details regarding the experimental data set can be obtained from dos Santos and Lenzi [1]. It needs to be highlighted that experimental data was normalized in the interval $[0,1]$ for proper parameter estimation [22, 29]. The mathematical model used in this work was firstly proposed by dos Santos et al. [22] for describing the lead equilibrium sorption. According to the authors, a large number of experimental results on equilibrium systems dealing with heavy metals have the following behavior: when the heavy metal concentration in the aqueous phase is low, the equilibrium concentration in the solid phase may largely change for a given modification in the concentration of the fluid phase. On the other hand, for higher concentrations of the heavy metal in the fluid phase, the equilibrium concentration in the solid may be less sensitive, indicating some kind of saturation. These features resemble to a certain degree in an exponential behavior, obtained, for example, from first-order differential equations. Consequently, an exponential model for heavy metal sorption isotherm, as given by (1), can explain some normalized experimental results, where parameters θ_1 and θ_2 depend on the sorption process features, like the type of heavy metal, solid matrix used for sorption process, and so on:

$$\begin{aligned} &\theta_1 \cdot \frac{dy}{dx} + \theta_2 \cdot y = 1, \quad y(x=0) = 0 \\ &\Longrightarrow y = \left(\frac{1}{\theta_2}\right) \cdot \left(1 - e^{-(\theta_2/\theta_1)\cdot x}\right). \end{aligned} \tag{1}$$

Therefore, by using fractional calculus, the previous model can be generalized to (2), by considering a fractional order θ_3 for the differential equation. One can note that parameter θ_3 also depends on the features of the sorption process:

$$\begin{aligned} &\theta_1 \cdot \frac{d^{\theta_3} q}{dx^{\theta_3}} + \theta_2 \cdot y = 1, \quad y(x=0) = 0 \\ &\Longrightarrow y = \left(\frac{1}{\theta_1}\right) \cdot \varepsilon_0 \left(x, \frac{-\theta_2}{\theta_1}; \theta_3, \theta_3 + 1\right), \end{aligned}$$

Epsilon function:

$$\varepsilon_0(m_1, m_2; m_3, m_4) = (m_1)^{(m_4-1)} \cdot E_{m_3,m_4}\left(m_2 \cdot (m_1)^{m_3}\right),$$

Mittag-Leffler function:

$$E_{n_1,n_2}(n_3) = \sum_{j=0}^{\infty} \frac{(n_3)^j}{\Gamma(n_1 \cdot j + n_2)}, \tag{2}$$

where ε_0 is the 0th-order Epsilon function defined by Podlubny [30], which uses the Mittag-Leffler function; m_i $i = \{1,\ldots,4\}$ and n_i $i = \{1,\ldots,3\}$ are dummy variables. Details regarding the Gamma function (Γ) can be found in the appendix.

2.2. Parameter Estimation. Parameter estimation was carried out using a genetic algorithm procedure as reported by Isfer et al. [15]. More specifically, the initial population consisted of 250 sets of values for parameters $\underline{\theta} = \{\theta_1; \theta_2; \theta_3\}$, which iterated until the difference of each parameter θ_i, the best set of two consecutive iterations, was lower than 10^{-6}. Crossover and mutation probabilities were of 80% assuring a good macroscopic search and of 10% assuring a good microscopic (refinement), respectively. In order to avoid a local optimum solution, estimation was performed using different initial populations. Parameters θ_1, θ_2, and θ_3 were estimated using (3) as the objective function of the optimization problem, representing a normalized quadratic error analysis [31]. Experimental variances were considered constant and equal to $\delta^2_{y^E}$ for all experiments and experimental covariances were assumed equal to zero. Consequently, matrix $\underline{\underline{[V_{y^E}]}}_{(\mathrm{NE}\times\mathrm{NE})}$ is a diagonal matrix. According to Bard [32], $\delta^2_{y^E}$ can be approximated by (4):

$$\begin{aligned} F_{\mathrm{OBJ}} &= \left[\left(\underline{y}^E - \underline{y}^M\right)^T\right]_{(1\times\mathrm{NE})} \cdot \left[\left(\underline{\underline{V_{y^E}}}\right)^{-1}\right]_{(\mathrm{NE}\times\mathrm{NE})} \\ &\quad \cdot \left(\underline{y}^E - \underline{y}^M\right)_{(\mathrm{NE}\times 1)} \\ &= \left(\frac{1}{\delta^2_{y^E}}\right) \cdot \sum_{i=1}^{\mathrm{NE}} \left(y_i^E - y_i^M(\underline{\theta}; x_i)\right)^2, \end{aligned} \tag{3}$$

$$\delta^2_{y^E} = \sum_{i=1}^{\mathrm{NE}} \frac{\left(y_i^E - y_i^M(\underline{\theta}; x_i)\right)^2}{\mathrm{NE} - \mathrm{NP}}. \tag{4}$$

2.3. Parameter Variance. According to Bard [32], for the objective function defined by (3), the parametric variance

matrix $[\underline{\underline{V_\theta}}]_{(\mathrm{NP}\times\mathrm{NP})}$ is given by (5), which uses the Hessian matrix $[\underline{\underline{H_\theta}}]_{(\mathrm{NP}\times\mathrm{NP})}$ and matrix $[\underline{\underline{G_y}}]_{(\mathrm{NP}\times\mathrm{NE})}$, given by (6):

$$\begin{aligned}\left[\underline{\underline{V_\theta}}\right]_{(\mathrm{NP}\times\mathrm{NP})} &= \left[\left(\underline{\underline{H_\theta}}\right)^{-1}\right]_{(\mathrm{NP}\times\mathrm{NP})} \\ &\quad\cdot\left(\left[\underline{\underline{G_y}}\right]_{(\mathrm{NP}\times\mathrm{NE})}\cdot\left[\underline{\underline{V_{y^E}}}\right]_{(\mathrm{NE}\times\mathrm{NE})}\cdot\left[\underline{\underline{G_y^T}}\right]_{(\mathrm{NE}\times\mathrm{NP})}\right) \\ &\quad\cdot\left[\left(\underline{\underline{H_\theta}}\right)^{-1}\right]_{(\mathrm{NP}\times\mathrm{NP})}\end{aligned} \tag{5}$$

$$\begin{aligned}\left[\underline{\underline{H_\theta}}\right]_{(\mathrm{NP}\times\mathrm{NP})} &= \begin{bmatrix}\dfrac{\partial^2 F_{\mathrm{OBJ}}}{\partial\theta_1^2} & \cdots & \dfrac{\partial^2 F_{\mathrm{OBJ}}}{\partial\theta_1\partial\theta_{\mathrm{NP}}} \\ \vdots & \ddots & \vdots \\ \dfrac{\partial^2 F_{\mathrm{OBJ}}}{\partial\theta_1\partial\theta_{\mathrm{NP}}} & \cdots & \dfrac{\partial^2 F_{\mathrm{OBJ}}}{\partial\theta_{\mathrm{NP}}^2}\end{bmatrix}, \\ \left[\underline{\underline{G_y}}\right]_{(\mathrm{NP}\times\mathrm{NE})} &= \begin{bmatrix}\dfrac{\partial^2 F_{\mathrm{OBJ}}}{\partial\theta_1\partial y_1^E} & \cdots & \dfrac{\partial^2 F_{\mathrm{OBJ}}}{\partial\theta_1\partial y_{\mathrm{NE}}^E} \\ \vdots & \ddots & \vdots \\ \dfrac{\partial^2 F_{\mathrm{OBJ}}}{\partial\theta_{\mathrm{NP}}\partial y_1^E} & \cdots & \dfrac{\partial^2 F_{\mathrm{OBJ}}}{\partial\theta_{\mathrm{NP}}\partial y_{\mathrm{NE}}^E}\end{bmatrix}.\end{aligned} \tag{6}$$

It can be observed that matrix $[\underline{\underline{G_y}}]_{(\mathrm{NP}\times\mathrm{NE})}$ can also be obtained by using a sensitivity matrix [23], $[\underline{\underline{B}}]_{(\mathrm{NE}\times\mathrm{NP})}$, which is given by (8):

$$\begin{aligned}\left[\underline{\underline{G_y}}\right]_{(\mathrm{NP}\times\mathrm{NE})} &= 2\cdot\left[\left(\underline{\underline{B}}\right)^T\right]_{(\mathrm{NP}\times\mathrm{NE})}\cdot\left[\left(\underline{\underline{V_{y^E}}}\right)^{-1}\right]_{(\mathrm{NE}\times\mathrm{NE})}, \\ \left[\left(\underline{\underline{B}}\right)^T\right]_{(\mathrm{NP}\times\mathrm{NE})} &= \left(\frac{1}{2}\right)\cdot\left[\underline{\underline{G_y}}\right]_{(\mathrm{NP}\times\mathrm{NE})}\cdot\left[\underline{\underline{V_{y^E}}}\right]_{(\mathrm{NE}\times\mathrm{NE})},\end{aligned} \tag{7}$$

$$\left[\underline{\underline{B}}\right]_{(\mathrm{NE}\times\mathrm{NP})} = \begin{bmatrix}\dfrac{\partial y_1^M}{\partial\theta_1} & \cdots & \dfrac{\partial y_1^M}{\partial\theta_{\mathrm{NP}}} \\ \vdots & \ddots & \cdots \\ \dfrac{\partial y_{\mathrm{NE}}^M}{\partial\theta_1} & \cdots & \dfrac{\partial y_{\mathrm{NE}}^M}{\partial\theta_{\mathrm{NP}}}\end{bmatrix}. \tag{8}$$

Also, according to Bard [32], the elements $[h_{ij}]$ of the Hessian matrix $[\underline{\underline{H_\theta}}]_{(\mathrm{NP}\times\mathrm{NP})}$ are given by

$$\begin{aligned}&\frac{\partial^2 F_{OBJ}}{\partial\theta_i\partial\theta_j} \\ &= \underbrace{2\cdot\left[\left(\frac{\partial \underline{\underline{y^M}}}{\partial\theta_i}\right)^T\right]_{(1\times NE)}\cdot\left[\left(\underline{\underline{V_{y^E}}}\right)^{-1}\right]_{(NE\times NE)}\cdot\left(\frac{\partial \underline{\underline{y^M}}}{\partial\theta_j}\right)_{(NE\times 1)}}_{TERM1} \\ &\quad\underbrace{-2\cdot\left(\frac{\partial^2 \underline{\underline{y^M}}}{\partial\theta_i\partial\theta_j}\right)_{(1\times NE)}\cdot\left[\left(\underline{\underline{V_{y^E}}}\right)^{-1}\right]_{(NE\times NE)}\cdot\left(\underline{y^E}-\underline{y^M}\right)_{(NE\times 1)}}_{TERM2}.\end{aligned} \tag{9}$$

For linear estimation problems, TERM2 automatically vanishes. However, this is not the case for nonlinear problems, but, according to Alberton et al. [23], this term can be neglected in some scenarios. Therefore, the parametric variance matrix is usually approximated by

$$\begin{aligned}\left[\underline{\underline{V_\theta}}\right]_{(\mathrm{NP}\times\mathrm{NP})} &= \left(\left[\left(\underline{\underline{B}}\right)^T\right]_{(\mathrm{NP}\times\mathrm{NE})}\cdot\left[\left(\underline{\underline{V_{y^E}}}\right)^{-1}\right]_{(\mathrm{NE}\times\mathrm{NE})}\cdot\left[\underline{\underline{B}}\right]_{(\mathrm{NE}\times\mathrm{NP})}\right)^{-1} \\ &= 4\cdot\left(\left(\left[\underline{\underline{G_y}}\right]_{(\mathrm{NP}\times\mathrm{NE})}\cdot\left[\underline{\underline{V_{y^E}}}\right]_{(\mathrm{NE}\times\mathrm{NE})}\cdot\left[\underline{\underline{G_y^T}}\right]_{(\mathrm{NE}\times\mathrm{NP})}\right)\right)^{-1}.\end{aligned} \tag{10}$$

2.4. Parameter Confidence Interval and Joint Confidence Region. According to Himmelblau [33], parameter confidence intervals can be obtained by using (11) for a given confidence level of $100\cdot(1-\alpha)\%$, but the use different values of ρ has been reported. For a small number of experimental data, the use of $\rho = t_{(1-\alpha/2),(\mathrm{NE}-\mathrm{NP})}$, obtained from Student's t-distribution, is recommended. On the other hand, $\rho = z_{(1-\alpha/2)}$, obtained from the normal distribution, can be used for a large number of experimental data:

$$\theta_i^{\#} - \rho\cdot\delta_{\theta_i} < \theta_i^{\#} < \theta_i^{\#} + \rho\cdot\delta_{\theta_i}. \tag{11}$$

Based on parametric variance, joint confidence region also needs to be obtained. For a given confidence level, this region provides the set of parameters that could actually generate the experimental data set. This is an important analysis tool, as although a given set of parameter may be within the confidence interval, it may not be inside the joint confidence region [33]. Usually, these joint confidence regions can be obtained by (12), which considers a linearization of the estimation problem [28]. Thus, a key issue to be addressed is concerns on the influence of the approach used to calculate

matrix $[\underline{\underline{V_\theta}}]_{(\mathrm{NP}\times\mathrm{NP})}$ ((5) or (10)) on the shape of the confidence region:

$$\left[\left(\underline{\theta}-\underline{\theta}^{\#}\right)^T\right]_{(1\times\mathrm{NP})}\cdot\left[\left(\underline{\underline{V_\theta}}\right)^{-1}\right]_{(\mathrm{NP}\times\mathrm{NP})}\cdot\left[\left(\underline{\theta}-\underline{\theta}^{\#}\right)\right]_{(\mathrm{NP}\times 1)} \leq F_{\mathrm{OBJ}}\left(\underline{\theta}^{\#}\right)\cdot\frac{\mathrm{NP}}{\mathrm{NE}-\mathrm{NP}}\cdot F^{(1-\alpha)}_{\mathrm{NP},(\mathrm{NE}-\mathrm{NP})}. \tag{12}$$

It needs to be stressed that (12) is only an approximation for nonlinear problems. A much more realistic approach [28, 34] given by (13) which considers the intrinsic nonlinear features of the estimation problem, leading to joint confidence regions usually larger than the ones obtained by (12):

$$F_{\mathrm{OBJ}}\left(\underline{\theta}\right)\leq F_{\mathrm{OBJ}}\left(\underline{\theta}^{\#}\right)\cdot\left(1+\frac{\mathrm{NP}}{\mathrm{NE}-\mathrm{NP}}\cdot F^{1-\alpha}_{\mathrm{NP},(\mathrm{NE}-\mathrm{NP})}\right). \tag{13}$$

2.5. Model Prediction Variance. Pinto and Schwaab [35] report that the variance of the model predictions of the experimental data used for parameter estimation is given by (14). The main feature of this equation is that not only experimental and modeling error themselves are taken into account, but also the correlation between them is also considered for the variance prediction:

$$\begin{aligned}\left[\underline{\underline{V_{y^{M\#}}}}\right]_{(\mathrm{NE}\times\mathrm{NE})} &= \underbrace{\left[\underline{\underline{B}}\right]_{(\mathrm{NE}\times\mathrm{NP})}\cdot\left[\underline{\underline{V_\theta}}\right]_{(\mathrm{NP}\times\mathrm{NP})}\cdot\left[\left(\underline{\underline{B}}\right)^T\right]_{(\mathrm{NP}\times\mathrm{NE})}}_{\text{modeling errors}}+\underbrace{\left[\underline{\underline{V_{y^E}}}\right]_{(\mathrm{NE}\times\mathrm{NE})}}_{\text{experimental errors}}\\ &\quad-\underbrace{\left(\left[\underline{\underline{B}}\right]_{(\mathrm{NE}\times\mathrm{NP})}\cdot\left(\left[\left(\underline{\underline{H_\theta}}\right)^{-1}\right]_{(\mathrm{NP}\times\mathrm{NP})}\cdot\left[\underline{\underline{G_y}}\right]_{(\mathrm{NP}\times\mathrm{NE})}\cdot\left[\underline{\underline{V_{y^E}}}\right]_{(\mathrm{NE}\times\mathrm{NE})}\right)+\left(\left[\left(\underline{\underline{H_\theta}}\right)^{-1}\right]_{(\mathrm{NP}\times\mathrm{NP})}\cdot\left[\underline{\underline{G_y}}\right]_{(\mathrm{NP}\times\mathrm{NE})}\cdot\left[\underline{\underline{V_{y^E}}}\right]_{(\mathrm{NE}\times\mathrm{NE})}\right)^T\cdot\left[\left(\underline{\underline{B}}\right)^T\right]_{(\mathrm{NP}\times\mathrm{NE})}\right)}_{\text{correlation between experimental and modeling errors}}.\end{aligned} \tag{14}$$

For prediction of the variance either of future experiments (for a given value of x_i) or available experimental data not used during parameter estimation, (15) needs to be used. Only used data for parameter estimation contribute to the correlation between experimental and modeling errors:

$$\delta^2_{y_i^{M\otimes}}=\left(\left[\underline{\underline{B^\otimes}}\right]_{(1\times\mathrm{NP})}\cdot\left[\underline{\underline{V_\theta}}\right]_{(\mathrm{NP}\times\mathrm{NP})}\cdot\left[\left(\underline{\underline{B^\otimes}}\right)^T\right]_{(\mathrm{NP}\times 1)}\right)+\left(\delta^2_{y^E}\right), \tag{15}$$

where $[\underline{\underline{B^\otimes}}]_{(1\times\mathrm{NP})}$ is the model gradient vector given by (16) and evaluated for x_i:

$$\left[\underline{\underline{B^\otimes}}\right]_{(1\times\mathrm{NP})}=\left[\frac{\partial y^M}{\partial\theta_1}\quad\frac{\partial y^M}{\partial\theta_2}\quad\cdots\quad\frac{\partial y^M}{\partial\theta_{\mathrm{NP}}}\right]. \tag{16}$$

2.6. Analytical Expressions. By using the definitions of ε_0 and the Mittag-Leffler function, the mathematical model given by (2) can be rewritten as

$$y_i^M=\sum_{j=0}^{\infty}\left[\frac{(-1)^j\cdot(\theta_2)^j\cdot x_i^{((\theta_3)\cdot(j+1))}}{(\theta_1)^{j+1}\cdot\Gamma((\theta_3)\cdot(j+1)+1)}\right]. \tag{17}$$

The objective function used for estimating the parameter set $\underline{\theta}=\{\theta_1;\theta_2;\theta_3\}$ is given by (18)

$$F_{\mathrm{OBJ}}=\sum_{i=1}^{\mathrm{NE}}\left(y_i^E-\left(\sum_{j=0}^{\infty}\left[\frac{(-1)^j\cdot(\theta_2)^j\cdot x_i^{((\theta_3)\cdot(j+1))}}{(\theta_1)^{j+1}\cdot\Gamma((\theta_3)\cdot(j+1)+1)}\right]\right)\right)^2. \tag{18}$$

The elements of matrix $[\underline{\underline{B}}]_{(\mathrm{NE}\times\mathrm{NP})}$ and matrix $[\underline{\underline{B^\otimes}}]_{(1\times\mathrm{NP})}$ are given by

$$\begin{aligned}\frac{\partial y_i^M}{\partial\theta_1}&=\sum_{j=0}^{\infty}\left[-\frac{(-1)^j\cdot(\theta_2)^j\cdot x_i^{((\theta_3)\cdot(j+1))}\cdot(j+1)}{(\theta_1)^{j+2}\cdot\Gamma((\theta_3)\cdot(j+1)+1)}\right],\\ \frac{\partial y_i^M}{\partial\theta_2}&=\sum_{j=0}^{\infty}\left[\frac{(-1)^j\cdot(\theta_2)^{(j-1)}\cdot x_i^{((\theta_3)\cdot(j+1))}\cdot j}{(\theta_1)^{j+1}\cdot\Gamma((\theta_3)\cdot(j+1)+1)}\right],\\ \frac{\partial y_i^M}{\partial\theta_3}&=\sum_{j=0}^{\infty}\left[\left((-1)^j\cdot(\theta_2)^j\cdot x_i^{((\theta_3)\cdot(j+1))}\cdot(j+1)\right.\right.\\ &\qquad\left.\cdot\left(\ln(x_i)-\Psi((\theta_3)\cdot(j+1)+1)\right)\right)\\ &\qquad\left.\times\left((\theta_1)^{j+1}\cdot\Gamma((\theta_3)\cdot(j+1)+1)\right)^{-1}\right].\end{aligned} \tag{19}$$

The objective function gradient is given by

$$\begin{aligned}
\frac{\partial F_{\mathrm{OBJ}}}{\partial \theta_1} &= \sum_{i=1}^{\mathrm{NE}} \left(-2 \cdot \left(y_i^E - \left(\sum_{j=0}^{\infty} \left[\frac{(-1)^j \cdot (\theta_2)^j \cdot x_i^{((\theta_3)\cdot(j+1))}}{(\theta_1)^{j+1} \cdot \Gamma((\theta_3)\cdot(j+1)+1)} \right] \right) \right) \right) \cdot \frac{\partial y_i^M}{\partial \theta_1}, \\
\frac{\partial F_{\mathrm{OBJ}}}{\partial \theta_2} &= \sum_{i=1}^{\mathrm{NE}} \left(-2 \cdot \left(y_i^E - \left(\sum_{j=0}^{\infty} \left[\frac{(-1)^j \cdot (\theta_2)^j \cdot x_i^{((\theta_3)\cdot(j+1))}}{(\theta_1)^{j+1} \cdot \Gamma((\theta_3)\cdot(j+1)+1)} \right] \right) \right) \right) \cdot \frac{\partial y_i^M}{\partial \theta_2}, \\
\frac{\partial F_{\mathrm{OBJ}}}{\partial \theta_3} &= \sum_{i=1}^{\mathrm{NE}} \left(-2 \cdot \left(y_i^E - \left(\sum_{j=0}^{\infty} \left[\frac{(-1)^j \cdot (\theta_2)^j \cdot x_i^{((\theta_3)\cdot(j+1))}}{(\theta_1)^{j+1} \cdot \Gamma((\theta_3)\cdot(j+1)+1)} \right] \right) \right) \right) \cdot \frac{\partial y_i^M}{\partial \theta_3}.
\end{aligned} \tag{20}$$

The elements of matrix $\underline{\underline{[G_y]}}_{(\mathrm{NP}\times\mathrm{NE})}$ are obtained by

$$\begin{aligned}
\frac{\partial^2 F_{\mathrm{OBJ}}}{\partial \theta_1 \partial y_i^E} &= -2 \cdot \left(\sum_{j=0}^{\infty} \left[-\frac{(-1)^j \cdot (\theta_2)^j \cdot x_i^{((\theta_3)\cdot(j+1))} \cdot (j+1)}{(\theta_1)^{j+2} \cdot \Gamma((\theta_3)\cdot(j+1)+1)} \right] \right), \\
\frac{\partial^2 F_{\mathrm{OBJ}}}{\partial \theta_2 \partial y_i^E} &= -2 \cdot \left(\sum_{j=0}^{\infty} \left[\frac{(-1)^j \cdot (\theta_2)^{(j-1)} \cdot x_i^{((\theta_3)\cdot(j+1))} \cdot j}{(\theta_1)^{j+1} \cdot \Gamma((\theta_3)\cdot(j+1)+1)} \right] \right), \\
\frac{\partial^2 F_{\mathrm{OBJ}}}{\partial \theta_3 \partial y_i^E} &= -2 \cdot \left(\sum_{j=0}^{\infty} \left[\left((-1)^j \cdot (\theta_2)^j \cdot x_i^{((\theta_3)\cdot(j+1))} \cdot (j+1) \cdot (\ln(x_i) - \Psi((\theta_3)\cdot(j+1)+1)) \right) \times \left((\theta_1)^{j+1} \cdot \Gamma((\theta_3)\cdot(j+1)+1) \right)^{-1} \right] \right).
\end{aligned} \tag{21}$$

Finally, the elements of $\underline{\underline{[H_\theta]}}_{(\mathrm{NP}\times\mathrm{NP})}$ result from

$$\begin{aligned}
\frac{\partial^2 F_{\mathrm{OBJ}}}{\partial \theta_1^2} &= \sum_{i=1}^{\mathrm{NE}} \left(\left(2 \cdot \left(\frac{\partial y_i^M}{\partial \theta_1} \right)^2 \right) - 2 \cdot \left(\left(y_i^E - \left(\sum_{j=0}^{\infty} \left[\frac{(-1)^j \cdot (\theta_2)^j \cdot x_i^{((\theta_3)\cdot(j+1))}}{(\theta_1)^{j+1} \cdot \Gamma((\theta_3)\cdot(j+1)+1)} \right] \right) \right) \cdot \sum_{j=0}^{\infty} \left[\left((-1)^j \cdot (\theta_2)^j \cdot x_i^{((\theta_3)\cdot(j+1))} \cdot \left((j+1)^2 + (j+1) \right) \right) \times \left((\theta_1)^{j+3} \cdot \Gamma((\theta_3)\cdot(j+1)+1) \right)^{-1} \right] \right) \right), \\
\frac{\partial^2 F_{\mathrm{OBJ}}}{\partial \theta_2^2} &= \sum_{i=1}^{\mathrm{NE}} \left(\left(2 \cdot \left(\frac{\partial y_i^M}{\partial \theta_2} \right)^2 \right) - 2 \cdot \left(\left(y_i^E - \left(\sum_{j=0}^{\infty} \left[\frac{(-1)^j \cdot (\theta_2)^j \cdot x_i^{((\theta_3)\cdot(j+1))}}{(\theta_1)^{j+1} \cdot \Gamma((\theta_3)\cdot(j+1)+1)} \right] \right) \right) \cdot \sum_{j=0}^{\infty} \left[\frac{(-1)^j \cdot (\theta_2)^{(j-2)} \cdot x_i^{((\theta_3)\cdot(j+1))} \cdot (j^2 - j)}{(\theta_1)^{j+1} \cdot \Gamma((\theta_3)\cdot(j+1)+1)} \right] \right) \right), \\
\frac{\partial^2 F_{\mathrm{OBJ}}}{\partial \theta_3^2} &= \sum_{i=1}^{\mathrm{NE}} \left(\left(2 \cdot \left(\frac{\partial y_i^M}{\partial \theta_3} \right)^2 \right) - 2 \cdot \left(\left(y_i^E - \left(\sum_{j=0}^{\infty} \left[\frac{(-1)^j \cdot (\theta_2)^j \cdot x_i^{((\theta_3)\cdot(j+1))}}{(\theta_1)^{j+1} \cdot \Gamma((\theta_3)\cdot(j+1)+1)} \right] \right) \right) \cdot \sum_{j=0}^{\infty} \left[\left((-1)^j \cdot (\theta_2)^j \cdot x_i^{((\theta_3)\cdot(j+1))} \cdot (j+1)^2 \cdot \left((\ln(x_i) - \Psi((\theta_3)\cdot(j+1)+1))^2 - \Psi(1, (\theta_3)\cdot(j+1)+1) \right) \right) \times \left((\theta_1)^{j+1} \cdot \Gamma((\theta_3)\cdot(j+1)+1) \right)^{-1} \right] \right) \right), \\
\frac{\partial^2 F_{\mathrm{OBJ}}}{\partial \theta_1 \partial \theta_2} &= \sum_{i=1}^{\mathrm{NE}} \left(\left(2 \cdot \left(\frac{\partial y_i^M}{\partial \theta_1} \right) \cdot \left(\frac{\partial y_i^M}{\partial \theta_2} \right) \right) - 2 \cdot \left(\left(y_i^E - \left(\sum_{j=0}^{\infty} \left[\frac{(-1)^j \cdot (\theta_2)^j \cdot x_i^{((\theta_3)\cdot(j+1))}}{(\theta_1)^{j+1} \cdot \Gamma((\theta_3)\cdot(j+1)+1)} \right] \right) \right) \right)
\end{aligned}$$

$$\cdot \sum_{j=0}^{\infty}\Bigg[-\Big((-1)^{j}\cdot(\theta_2)^{(j-1)}\cdot x_i^{((\theta_3)\cdot(j+1))} \cdot (j\cdot(j+1))\Big) \times \Big((\theta_1)^{j+2}\cdot\Gamma((\theta_3)\cdot(j+1)+1)\Big)^{-1}\Bigg]\Bigg)\Bigg),$$

$$\frac{\partial^2 F_{\mathrm{OBJ}}}{\partial\theta_1\partial\theta_3} = \sum_{i=1}^{\mathrm{NE}}\left(\left(2\cdot\left(\frac{\partial y_i^M}{\partial\theta_1}\right)\cdot\left(\frac{\partial y_i^M}{\partial\theta_3}\right)\right) - 2\cdot\left(\left(y_i^E-\left(\sum_{j=0}^{\infty}\left[\frac{(-1)^{j}\cdot(\theta_2)^{j}\cdot x_i^{((\theta_3)\cdot(j+1))}}{(\theta_1)^{j+1}\cdot\Gamma((\theta_3)\cdot(j+1)+1)}\right]\right)\right) \cdot \sum_{j=0}^{\infty}\Bigg[\Big((-1)^{j}\cdot(\theta_2)^{j}\cdot x_i^{((\theta_3)\cdot(j+1))}\cdot(j+1)^2 \cdot(-\ln(x_i)+\Psi((\theta_3)\cdot(j+1)+1))\Big) \times\Big((\theta_1)^{j+2}\cdot\Gamma((\theta_3)\cdot(j+1)+1)\Big)^{-1}\Bigg]\right)\right),$$

$$\frac{\partial^2 F_{\mathrm{OBJ}}}{\partial\theta_2\partial\theta_3} = \sum_{i=1}^{\mathrm{NE}}\left(\left(2\cdot\left(\frac{\partial y_i^M}{\partial\theta_2}\right)\cdot\left(\frac{\partial y_i^M}{\partial\theta_3}\right)\right) - 2\cdot\left(\left(y_i^E-\left(\sum_{j=0}^{\infty}\left[\frac{(-1)^{j}\cdot(\theta_2)^{j}\cdot x_i^{((\theta_3)\cdot(j+1))}}{(\theta_1)^{j+1}\cdot\Gamma((\theta_3)\cdot(j+1)+1)}\right]\right)\right) \cdot \sum_{j=0}^{\infty}\Bigg[\Big((-1)^{j}\cdot(\theta_2)^{(j-1)}\cdot x_i^{((\theta_3)\cdot(j+1))}\cdot(j\cdot(j+1)) \cdot(\ln(x_i)-\Psi((\theta_3)\cdot(j+1)+1))\Big) \times\Big((\theta_1)^{j+1}\cdot\Gamma((\theta_3)\cdot(j+1)+1)\Big)^{-1}\Bigg]\right)\right). \tag{22}$$

Further details regarding Gamma (Γ) and Psi (Ψ) functions can be found in the appendix.

3. Results

Heavy metal sorption processes involve a solid phase, which in many scenarios consist in irregular and disordered structures; consequently, many classical models usually cannot adequately explain observed experimental behavior. Towards this, fractional calculus plays a key role in mathematical modeling of transport phenomena in irregular structure, mainly due to memory effects as already reported in the literature [36, 37]. It is important to note that the model proposed by dos Santos et al. [22] presents a novel characteristic as according to the value of parameter θ_3, the Epsilon function turns into a different mathematical function; for example, if θ_3 is equal to 1, an exponential form is obtained [30].

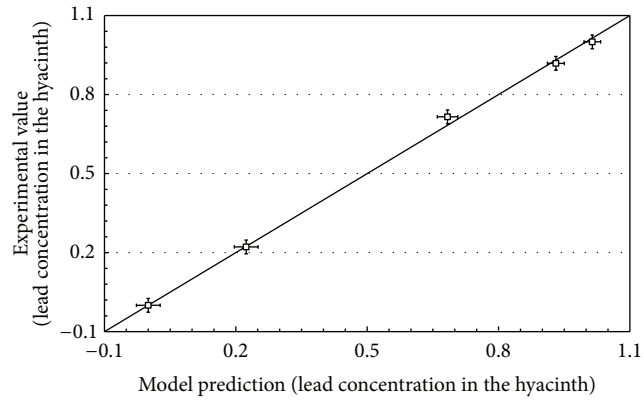

Figure 1: Experimental values versus model predictions.

Table 1 presents a summary of the parameter estimation procedure. The row EPSILON 1 presents the results considering (5) to calculate the parameter variance matrix. The results in row EPSILON 2 considered (10) to calculate the parameter variance matrix. Firstly, it can be seen that the model reported by dos Santos et al. [22] presents a very good correlation coefficient and a low value of the objective function.

It can also be observed that the parameter variance is small when compared to the value of the parameter; consequently, all the parameters can be considered significant. This fact occurred independently of the approach used for the calculations of the parametric variance. This conclusion is also obtained after analyzing the parameter confidence intervals calculated for 95% of confidence level, regardless of the value used for ρ in (11). It can be seen that all parameters are significant as they are all statistically different from zero. However, it is important to emphasize that for this nonlinear parameter estimation study, the choice of the approach used to calculate the parameter variance led to differences of one order of magnitude for parameters θ_1 and θ_3. Besides, some interesting effects regarding parameter correlation showed up; more specifically, by choosing the simplified approach, correlation between parameters θ_1 and θ_3 and parameters θ_1 and θ_2 considerably increased.

Figure 1 presents the experimental values plotted against the model predictions. Bar errors were obtained using (4) to obtain an approximation of the experimental error and (14) to obtain the error of the model predictions of the experimental data used in the parameter estimation task. It can be observed that model predictions are in good agreement with the experimental values as the points are close to the straight line, which indicates the ideal case that model predictions are equal to the experimental values. Figure 2 presents a comparison of experimental data and model predictions plotted against the independent variable. As mentioned before, experimental error was calculated using (4). Again, one can see that the fractional model adequately describes the experimental data, especially for low concentrations of lead in the aqueous solutions, where low variations cause large variations in the lead concentration in the hyacinth. Besides,

Table 1: Parameter estimation results[@].

	Parameter		δ_{θ_i}	$\theta_i \pm t_{(1-(\alpha/2)),(\mathrm{NE-NP})} \cdot \delta_{\theta_i}$ $\theta_i \pm z_{(1-(\alpha/2))} \cdot \delta_{\theta_i}$	$[[\underline{\underline{V_\theta}}]]$	$[[\underline{\underline{V_{r_\theta}}}]]$	r	F_{OBJ}
EPSILON 1	θ_1	0.169	$2.66 \cdot 10^{-3}$	0.169 ± 0.011 0.169 ± 0.005	$\begin{bmatrix} 7.08 \cdot 10^{-6} & -2.02 \cdot 10^{-6} & -5.36 \cdot 10^{-6} \\ -2.02 \cdot 10^{-6} & 3.83 \cdot 10^{-4} & 9.37 \cdot 10^{-5} \\ -5.36 \cdot 10^{-6} & 9.37 \cdot 10^{-5} & 2.89 \cdot 10^{-5} \end{bmatrix}$	$\begin{bmatrix} 1 & -0.039 & -0.38 \\ -0.039 & 1 & 0.89 \\ -0.38 & 0.89 & 1 \end{bmatrix}$	0.999	$1.38 \cdot 10^{-3}$
	θ_2	0.884	$1.96 \cdot 10^{-2}$	0.884 ± 0.084 0.884 ± 0.038				
	θ_3	0.488	$5.38 \cdot 10^{-3}$	0.488 ± 0.023 0.488 ± 0.010				
EPSILON 2	θ_1	0.169	$3.12 \cdot 10^{-2}$	0.169 ± 0.134 0.169 ± 0.061	$\begin{bmatrix} 9.74 \cdot 10^{-4} & -1.57 \cdot 10^{-3} & -1.34 \cdot 10^{-3} \\ -1.57 \cdot 10^{-3} & 3.31 \cdot 10^{-3} & 1.93 \cdot 10^{-3} \\ -1.34 \cdot 10^{-3} & 1.93 \cdot 10^{-3} & 2.05 \cdot 10^{-3} \end{bmatrix}$	$\begin{bmatrix} 1 & -0.87 & -0.95 \\ -0.87 & 1 & 0.74 \\ -0.95 & 0.74 & 1 \end{bmatrix}$		
	θ_2	0.884	$5.76 \cdot 10^{-2}$	0.884 ± 0.247 0.884 ± 0.112				
	θ_3	0.488	$4.52 \cdot 10^{-2}$	0.488 ± 0.194 0.488 ± 0.088				

[@] $100 \cdot (1-\alpha)\% = 95\%$: $t_{(1-(\alpha/2)),(\mathrm{NE-NP})} = t_{0.975;(5-3)} = t_{0.975;\,2} = 4.3030$; $t_{(1-(\alpha/2)),(\mathrm{NE-NP})} = t_{0.975;(5-2)} = t_{0.975;\,3} = 3.182$; and $t_{(1-(\alpha/2)),(\infty)} = z_{(1-(\alpha/2))} = z_{0.975} = 1.96$.

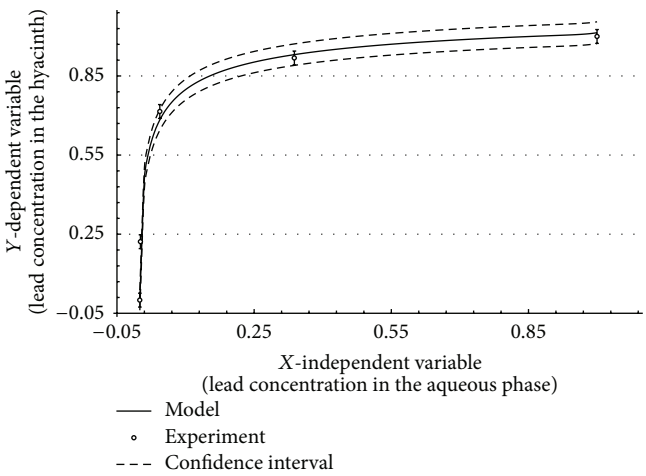

Figure 2: Isotherm behavior.

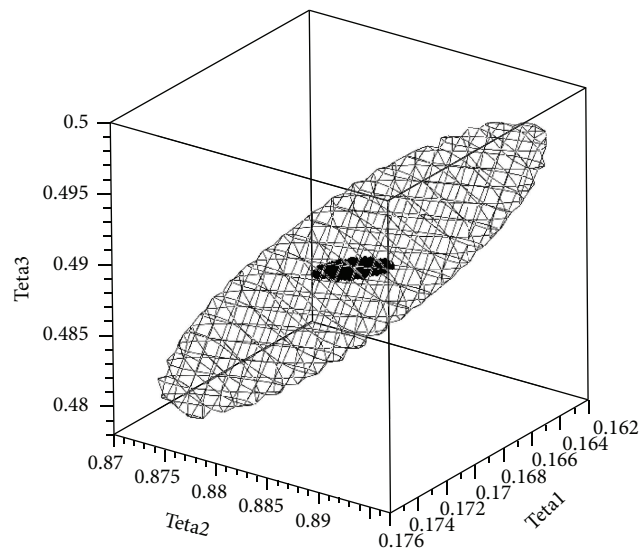

Figure 3: Confidence region—Approach 1.

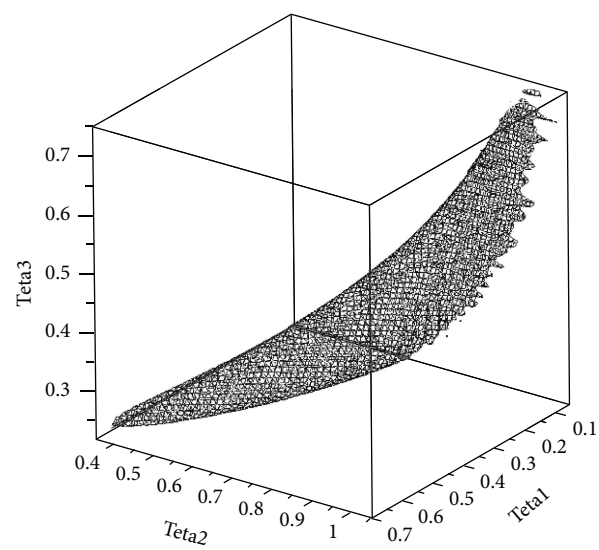

Figure 4: Confidence region—Approach 2.

Figure 2 also presents the confidence interval limits $(1 \cdot \sigma)$ considering (15) to calculate the model prediction error and using the complete Hessian to calculate $\underset{(\mathrm{NP}\times\mathrm{NP})}{[\underline{\underline{V_\theta}}]}$.

Parameter θ_3 plays a key role in the model because, as mentioned before, according to its value the equation can assume a different form. Besides, it is the order of the fractional differential equation (see (2)). Therefore, it is important to prove that θ_3 is statistically different from 1, otherwise an integer order differential equation would be a model with the same efficiency. Initially, this analysis considers the confidence interval presented in Table 1. However, this may not be enough, as the parameter joint confidence region plays a key role. Figure 3 presents the region obtained by (12) considering the parametric variance matrix obtained by (5) (solid region) and considering the parametric variance matrix obtained by (9) (wired region). One can observe that θ_3 is different from 1; consequently, the use of fractional order derivative is significant. Secondly, the approach used for calculating the parameter variance significantly influences the parameter confidence region as it can be seen by the difference in size and shape of the ellipsoids. This is an important consequence as a set of parameters which is inside the wired region may be outside the solid region; therefore, it may not be statistically significant.

Finally, it needs to be remembered that the joint confidence regions shown in Figure 3 were obtained by a simplified though useful approach. For nonlinear parameter estimation problems, a more accurate parameter confidence region is obtained by (13), which is presented by Figure 4. It is essential to stress that the size and the shape of the region may considerably change as (13) preserves the nonlinear features of the problem, remembering that (12) is somehow a linearization of (13). Moreover, it must be emphasized that parameter θ_3 is still lower than 1 (see Figure 4); consequently, the model nature and experimental data behavior can be adequately described by a fractional order model.

It is important to analyze the variance of the model predictions of future experiments, which can be obtained by (15). Figure 5 presents the variance predictions plotted against the independent variable, that is, lead concentration in the aqueous solution. The variances were calculated using the different parametric variance matrixes; that is, Epsilon1 used (5) and Epsilon2 used (10). One can observe that using (10) the variance of future experiments predictions considerably changes. It must be remembered that, although often used, (10) is an approximation of the calculation of the parametric variance. Therefore, for nonlinear problems as the one present in fractional calculus applications, (5) should be chosen. It is also important to note that the minimum values of variance are obtained for lower values of the independent variable. For higher values, the variance tends to increase.

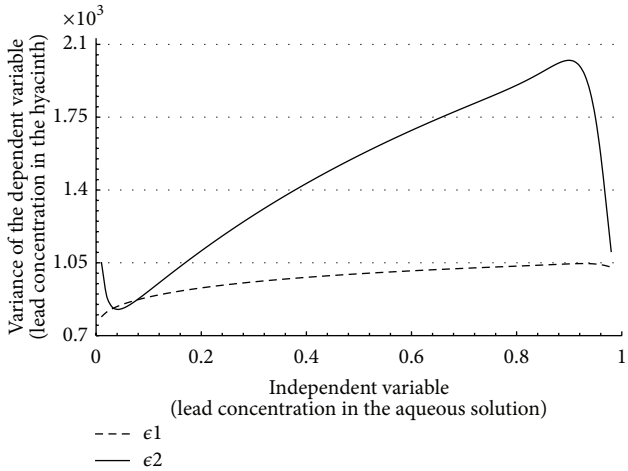

Figure 5: Variance behavior for different values of the independent variable.

4. Conclusions

The availability of mathematical models plays a key role in understanding heavy metal equilibrium phenomena. The literature reports different approaches for modeling the sorption process, particularly lead. Recently, a model based on fractional calculus was proposed to describe experimental data concerning lead sorption by hyacinths. This paper reported the use of an error analysis procedure for mathematical models based on fractional order differential equations in order to show that the fractional order is in fact fractional.

Parametric variance matrix was calculated by two different approaches, one considering the complete Hessian matrix and the other considering a simplification of its elements. It was observed that the use of the complete Hessian matrix leads to different results; consequently, the simplified approach may not be recommended for some nonlinear parameter estimation problems, such as the one reported in this paper. Joint confidence regions played a key role in the analysis of parameter confidence intervals, especially in the order of the fractional differential equation. It is also important to conclude that the fractional model considered was in fact fractional, as the estimated order of the derivative was higher than its error and also statistically different from 1, showing that the fractional nature of the model is valid.

Appendix

Gamma function is defined by $\Gamma(x) = \int_0^\infty e^{-t} \cdot t^{x-1} dt$ and Psi function, and some properties can be obtained from Lebedev [38]:

$$\Psi(x) = \frac{\Gamma'(x)}{\Gamma(x)}, \tag{A.1}$$

$$\Gamma'(x) = \int_0^\infty e^{-t} \cdot t^{x-1} \cdot \ln(t)\, dt, \tag{A.2}$$

$$\Gamma''(x) = \int_0^\infty e^{-t} \cdot t^{x-1} \cdot (\ln(t))^2 dt, \tag{A.3}$$

$$\Psi(1, 1+x) = \Psi(1, x) - \frac{1}{x^2}, \tag{A.4}$$

$$\Psi(1, x) = \frac{\Gamma''(x)}{\Gamma(x)} - (\Psi(x))^2. \tag{A.5}$$

Nomenclature

F_{OBJ}:	Objective function
$F^{1-\alpha}_{\mathrm{NP},(\mathrm{NE-NP})}$:	Value of F distribution considering $(1-\alpha)$ as confidence level and NP and NE−NP as degrees of freedom and $0 < \alpha < 1$
NE:	Number of experiments
NP:	Number of parameters
r:	Correlation coefficient
$t_{(1-\alpha/2),(\mathrm{NE-NP})}$:	Value of the Student t-distribution for a confidence level of $(1-\alpha/2)$ and (NE−NP) degrees of freedom, where $0 < \alpha < 1$
x:	Independent variable-lead concentration in the aqueous solution
y:	Dependent variable-lead concentration in the hyacinth
$z_{(1-\alpha/2)}$:	Value of the normal distribution for a confidence level of $(1-\alpha/2)$, where $0 < \alpha < 1$.

Greek Letters

ρ: Dummy variable
δ^2: Variance
θ_i: ith parameter.

Superscript

−1: Inverse
T: Transpose
M: Model
E: Experiment
#: Optimized or estimated value
⊗: Predicted value of the dependent variable of a given future experiment.

Acknowledgments

The authors thank CNPQ, CAPES, and Fundação Araucária for providing financial support and scholarships.

References

[1] M. C. dos Santos and E. Lenzi, "The use of aquatic macrophytes (*Eichhornia crassipes*) as a biological filter in the treatment of lead contaminated effluents," *Environmental Technology*, vol. 21, no. 6, pp. 615–622, 2000.

[2] M. D. Machado, E. V. Soares, and H. M. V. M. Soares, "Selective recovery of chromium, copper, nickel, and zinc from

an acid solution using an environmentally friendly process," *Environmental Science and Pollution Research*, vol. 18, pp. 1279–1285, 2011.

[3] T. S. Mthombo, A. K. Mishra, S. B. Mishra, and B. B. Mamba, "The adsorption behavior of Cu(II), Pb(II), and Co(II) of ethylene vinyl acetate-clinoptilolite nanocomposites," *Journal of Applied Polymer Science*, vol. 121, no. 6, pp. 3414–3424, 2011.

[4] J. G. Ibanez, P. Balderas-Hernandez, E. Garcia-Pintor et al., "Laboratory experiments on the electrochemical remediation of the environment—part 9: microscale recovery of a soil metal pollutant and its extractant," *Journal of Chemical Education*, vol. 88, no. 8, pp. 1123–1125, 2011.

[5] E. Tel-Or and C. Forni, "Phytoremediation of hazardous toxic metals and organics by photosynthetic aquatic systems," *Plant Biosystems*, vol. 145, no. 1, pp. 224–235, 2011.

[6] M. Asteasuain, M. Soares, M. K. Lenzi et al., "'Living' free radical polymerization in tubular reactors. I. Modeling of the complete molecular weight distribution using probability generating functions," *Macromolecular Reaction Engineering*, vol. 1, no. 6, pp. 622–634, 2007.

[7] D. D. Do, *Adsorption Analysis: Equilibria and Kinetics*, Imperial College Press, London, UK, 1st edition, 1998.

[8] J. T. Machado, V. Kiryakova, and F. Mainardi, "Recent history of fractional calculus," *Communications in Nonlinear Science and Numerical Simulation*, vol. 16, no. 3, pp. 1140–1153, 2011.

[9] V. Z. Povstenko, "Fractional heat conduction equation and associated thermal stress," *Journal of Thermal Stresses*, vol. 28, no. 1, pp. 83–102, 2005.

[10] I. S. Jesus and J. A. Tenreiro Machado, "Application of integer and fractional models in electrochemical systems," *Mathematical Problems in Engineering*, vol. 2012, Article ID 248175, 17 pages, 2012.

[11] J. Klafter, S. C. Lim, and R. Metzler, Eds., *Fractional Dynamics: Recent Advances*, World Scientific Publishing Company, Singapore, 2011.

[12] K. Tas, J. A. T. Machado, and D. Baleanu, Eds., *Mathematical Methods in Engineering*, Springer, Dordrecht, The Netherlands, 2007.

[13] J. Sabatier, O. P. Agrawal, and J. A. T. Machado, Eds., *Advances in Fractional Calculus: Theoretical Developments and Applications in Physics and Engineering*, Springer, Dordrecht, The Netherlands, 2007.

[14] D. Baleanu, J. A. T. Machado, and Z. B. Guvenc, Eds., *New Trends in Nanotechnology and Fractional Calculus Applications*, Springer, Dordrecht, The Netherlands, 2010.

[15] L. A. D. Isfer, M. K. Lenzi, and E. K. Lenzi, "Identification of biochemical reactors using fractional differential equations," *Latin American Applied Research*, vol. 40, no. 2, pp. 193–198, 2010.

[16] J. Hristov, "A short-distance integral-balance solution to a strong subdiffusion equation: a weak power-law profile," *International Review of Chemical Engineering*, vol. 2, pp. 555–563, 2010.

[17] J. Hristov, "Heat-balance integral to fractional (half-time) heat diffusion sub-model," *Thermal Science*, vol. 14, no. 2, pp. 291–316, 2010.

[18] R. A. Pfaffenzeller, M. K. Lenzi, and E. K. Lenzi, "Modeling of granular material mixing using fractional calculus," *International Review of Chemical Engineering*, vol. 3, pp. 818–821, 2011.

[19] R. L. Magin, "Fractional calculus models of complex dynamics in biological tissues," *Computers & Mathematics with Applications*, vol. 59, pp. 1586–1593, 2010.

[20] M. Khan, S. H. Ali, C. Fetecau, and H. Qi, "Decay of potential vortex for a viscoelastic fluid with fractional Maxwell model," *Applied Mathematical Modelling*, vol. 33, no. 5, pp. 2526–2533, 2009.

[21] R. F. Camargo, E. C. de Oliveira, and J. Vaz Jr., "On the generalized Mittag-Leffler function and its application in a fractional telegraph equation," *Mathematical Physics, Analysis and Geometry*, vol. 15, pp. 1–16, 2012.

[22] M. C. dos Santos, E. Lenzi, E. M. Gomes, M. K. Lenzi, and E. K. Lenzi, "Development of heavy metal sorption isotherm using fractional calculus," *International Review of Chemical Engineering*, vol. 3, pp. 814–817, 2011.

[23] A. L. Alberton, M. Schwaab, M. Schmal, and J. C. Pinto, "Experimental errors in kinetic tests and its influence on the precision of estimated parameters—part I: analysis of first-order reactions," *Chemical Engineering Journal*, vol. 155, pp. 816–823, 2009.

[24] M. Joshi, A. Kremling, and A. Seidel-Morgenstern, "Model based statistical analysis of adsorption equilibrium data," *Chemical Engineering Science*, vol. 61, no. 23, pp. 7805–7818, 2006.

[25] J. D. Gabano and T. Poinot, "Fractional modelling and identification of thermal systems," *Signal Processing*, vol. 91, no. 3, pp. 531–541, 2011.

[26] F. Khemane, R. Maltia, T. Raïssic, and X. Moreaua, "Robust estimation of fractional models in the frequency domain using set membership methods," *Signal Processing*, vol. 92, pp. 1591–1601, 2012.

[27] A. Almusharff and N. Nguyen, "A combination of time-scale calculus and a cross-validation technique used in fitting and evaluating fractional models," *Applied Mathematics Letters*, vol. 25, no. 3, pp. 550–554, 2012.

[28] G. E. P. Box and W. G. Hunter, "A useful method for model-building," *Technometrics*, vol. 4, pp. 301–318, 1962.

[29] G. E. P. Box and P. W. Tidwell, "Transformation of the independent variables," *Technometrics*, vol. 4, pp. 531–550, 1962.

[30] I. Podlubny, *Fractional Differential Equations*, Academic Press, New York, NY, USA, 1st edition, 1999.

[31] P. Englezos and N. Kalogerakis, *Applied Parameter Estimation for Chemical Engineers*, Marcel Dekker, New York, NY, USA, 1st edition, 2001.

[32] Y. Bard, *Nonlinear Parameter Estimation*, Academic Press, New York, NY, USA, 1st edition, 1974.

[33] D. M. Himmelblau, *Process Analysis by Statistical Methods*, John Wiley & Sons, New York, NY, USA, 1st edition, 1970.

[34] I. Guttman and D. A. Meeter, "On Beale's measures of nonlinearity," *Technometrics*, vol. 7, pp. 623–637, 1965.

[35] J. C. Pinto and M. Schwaab, *Análise de Dados Experimentais. I. Fundamentos de Estatística e Estimação de Parâmetros*, Editora e-Papers, Rio de Janeiro, Brazil, 1st edition, 2007.

[36] M. Giona and H. E. Roman, "A theory of transport phenomena in disordered systems," *The Chemical Engineering Journal*, vol. 49, no. 1, pp. 1–10, 1992.

[37] E. K. Lenzi, H. V. Ribeiro, J. Martins, M. K. Lenzi, G. G. Lenzi, and S. Specchia, "Non-Markovian diffusion equation and diffusion in a porous catalyst," *Chemical Engineering Journal*, vol. 172, pp. 1083–1087, 2011.

[38] N. N. Lebedev, *Special Functions and Their Applications*, Dover Publications, New York, NY, USA, 1st edition, 1972.

Hindawi Publishing Corporation
Mathematical Problems in Engineering
Volume 2013, Article ID 356215, 14 pages
http://dx.doi.org/10.1155/2013/356215

Review Article

Stability of Fractional Order Systems

Margarita Rivero,[1] Sergei V. Rogosin,[2] José A. Tenreiro Machado,[3] and Juan J. Trujillo[4]

[1] *Departamento de Matemática Fundamental, University of La Laguna, Tenerife 38271 La Laguna, Spain*
[2] *Department of Economics, Belarusian State University, Nezavisimosti Avenue 4, 220030 Minsk, Belarus*
[3] *Department of Electrical Engineering, Institute of Engineering, Polytechnic of Porto, 4200-072 Porto, Portugal*
[4] *Departamento de Análisis Matemático, University of La Laguna, Tenerife 38271 La Laguna, Spain*

Correspondence should be addressed to José A. Tenreiro Machado; jtm@isep.ipp.pt

Received 26 December 2012; Revised 8 April 2013; Accepted 11 April 2013

Academic Editor: Clara Ionescu

The theory and applications of fractional calculus (FC) had a considerable progress during the last years. Dynamical systems and control are one of the most active areas, and several authors focused on the stability of fractional order systems. Nevertheless, due to the multitude of efforts in a short period of time, contributions are scattered along the literature, and it becomes difficult for researchers to have a complete and systematic picture of the present day knowledge. This paper is an attempt to overcome this situation by reviewing the state of the art and putting this topic in a systematic form. While the problem is formulated with rigour, from the mathematical point of view, the exposition intends to be easy to read by the applied researchers. Different types of systems are considered, namely, linear/nonlinear, positive, with delay, distributed, and continuous/discrete. Several possible routes of future progress that emerge are also tackled.

1. Classical Stability Analysis

The study of stability of polynomial and related questions for differential equations goes back to XIX century. Hurwitz (or Routh-Hurwitz) criterion [1] is a necessary and sufficient condition for all the roots of a polynomial

$$P(z) = a_n z^n + a_{n-1} z^{n-1} + \cdots + a_0, \quad (z \in \mathbb{C}) \tag{1}$$

with real coefficients and $a_n > 0$ to have negative real parts. It consists of the following: *all principal minors* Δ_k, $k = 1, 2, \ldots, n$, *of the Hurwitz matrix* H *are positive*.

Here H is a matrix of order n whose jth row is of the form

$$a_{2n-j}, a_{2n-2-j}, \ldots, a_{4-j}, a_{2-j}, \tag{2}$$

where $a_k = 0$ if $k > n$ or $k < 0$. Polynomial $P(z)$ satisfying the Hurwitz condition is called a Hurwitz polynomial or, in applications of the Routh-Hurwitz criterion in the stability theory of oscillating systems, a stable polynomial. Exact and approximate methods of Hurwitz factorization were developed intensively (see, e.g., [2, 3]).

Among other criteria concerning zeros distribution of polynomials, we have to mention Mikhailov stability criterion [4]. It states that *all roots of a polynomial*

$$P(z) = z^n + a_{n-1} z^{n-1} + \cdots + a_0, \quad (z \in \mathbb{C}) \tag{3}$$

with real coefficients have strictly negative real part if and only if the complex-valued function $\zeta = P(i\omega)$, $i = \sqrt{-1}$, *of a real variable* $\omega \in [0, \infty)$ *describes a curve (the Mikhailov hodograph) in the complex* ζ*-plane which starts on the positive real semiaxis and does not cross the origin and successively generates an anticlockwise motion through* n *quadrants.*

An equivalent condition is as follows: *the radius vector* $P(i\omega)$, *as* ω *increases from* 0 to $+\infty$, *never vanishes and monotonically rotates in a positive direction through an angle* $n\pi/2$.

The Mikhailov criterion gives a necessary and sufficient condition for the asymptotic stability of a linear differential equation of order n

$$x^{(n)} + a_{n-1} x^{(n-1)} + \cdots + a_0 x = 0 \tag{4}$$

with constant coefficients or of a linear system (where the prime symbol denotes first derivative with respect to time):

$$X' = AX, \quad X \in \mathbb{R}^n, \tag{5}$$

with a constant matrix A, the characteristic polynomial of which is $P(z)$.

A very general result on the zero location problem for the polynomial is the Hermite-Biehler theorem [5], which states that the roots of $g(z) + ih(z)$ are all on the same side of the real axis when $g(z)$ and $h(z)$ are polynomials with real coefficients if and only if the zeros of $g(z)$ and $h(z)$ are real and alternate. The Hermite-Biehler theorem provides necessary and sufficient conditions for Hurwitz stability of real polynomials in terms of an interlacing (alternating) property [6–8]. Notice that if a given real polynomial is not a Hurwitz one, then the Hermite-Biehler theorem does not provide information on its roots distribution.

During the last years, several surveys addressed this topic; see, for instance, [9–12]. This paper, without being exhaustive, is complementary to the contents of such other works. In our paper, we introduced formally a selected set of methods to characterize the stability of fractional systems. It is intended to form a comprehensive text so that readers can follow easily the concepts. Furthermore, the limitations of the known methods are also pointed out, giving readers the opportunity to consider the open problems.

Bearing these ideas in mind, this paper is organized as follows. Sections 2 and 3 introduce fundamental aspects, namely, the concepts of quasi-polynomials and fractional quasi-polynomials, respectively. Section 4 addresses the main core of the paper, the stability of fractional order systems, and is divided into eight subsections. The section starts by presenting general fractional order systems. In the next subsections issues associated with linear time-invariant systems are discussed in more details, such as controllers, positive systems, systems with delay, and distributed, discrete-time, and nonlinear systems. Stability of closed-loop linear control systems becomes a major motivation of the paper. Therefore, four examples in Section 5 deal with this topic. Finally, Section 6 outlines several techniques that are presently emerging and draws the main conclusions.

2. Quasi-Polynomials

Pontryagin [13] gave a generalization of the Hermite-Biehler Theorem, which appeared to be very relevant formal tool for the mathematical analysis of stability of quasi-polynomials, that is, of the functions of the following type:

$$F(z) = \sum_{k=0}^{n} f_k(z)\, e^{\lambda_k z}, \tag{6}$$

where $f_k(z)$ are polynomials in z with constant coefficients, and λ_k, $k = 0, \ldots, n$, are real (or complex) numbers. By other words, $F(z)$ is a sum, where the terms are the product of and exponential and polynomial function with constant coefficients. In control theory, such exponentials correspond to delays. If λ_k are commensurable real numbers, that is, $\lambda_k = \lambda \cdot k$, $k = 0, \ldots, n$, and $\lambda > 0$, then the quasi-polynomial (6) can be written in the form

$$\delta(z) = P(z, e^z), \tag{7}$$

with

$$P(z, s) = \sum_{j=0}^{m} \sum_{k=0}^{n} a_{jk} z^j s^{\lambda k}, \quad z, s \in \mathbb{C}, \tag{8}$$

where $P(z, s)$ is a polynomial function of two variables, and then, if $s = e^z$, we get $\delta(z)$.

Thus, from this point of view, the determination of the zeros of a quasi-polynomial (7) by means of Pontryagin theorem can be considered to be a mathematical method for analysis of stabilization of a class of linear time invariant systems with time delay (see, e.g., [14]):

$$\sum_{j=0}^{m} \sum_{k=0}^{n} a_{jk} x^{(j)}(t + \lambda \cdot k) = 0, \tag{9}$$

where a_{jk} are constant coefficients.

Pontryagin Theorem (see [13]). *Let $\delta(z) = P(z, e^z)$ be a quasi-polynomial of the type (7), where $P(z, s)$ is a polynomial function in two variables with real coefficients. Suppose that the "oldest" coefficient $a_{mn} \neq 0$. Let $\delta(i\omega)$ be the restriction of the quasi-polynomial $\delta(z)$ to imaginary axis. One can express $\delta(i\omega) = f(\omega) + ig(\omega)$, where the real functions (of a real variable) $f(\omega)$ and $g(\omega)$ are the real and imaginary parts of $\delta(i\omega)$, respectively. Let one denote by ω_r and ω_i, respectively, the zeros of the functions $f(\omega)$ and $g(\omega)$. If all the zeros of the quasi-polynomial $\delta(z)$ lie to the left side of the imaginary axis, then the zeros of the functions $f(\omega)$ and $g(\omega)$ are real, alternating, and*

$$g'(\omega) f(\omega) - g(\omega) f'(\omega) > 0 \tag{10}$$

for each $\omega \in \mathbb{R}$.

Reciprocally, let one of the following conditions be satisfied:

(1) *all the zeros of the functions $f(\omega)$ and $g(\omega)$ are real and alternate, and the inequality (10) is satisfied for at least one value ω;*

(2) *all the zeros of the function $f(\omega)$ are real, and for each zero of $f(\omega)$ the inequality (10) is satisfied; that is, $g(\omega_r) f'(\omega_r) < 0$;*

(3) *all the zeros of the function $g(\omega)$ are real, and for each zero of $g(\omega)$ the inequality (10) is satisfied; that is, $g'(\omega_i) f(\omega_i) > 0$.*

Then all the zeros of the quasi-polynomial $\delta(z)$ lie to the left side of the imaginary axis.

In [15] quasi-polynomial of the type

$$F(z) = A(z) + B(z)\, e^{-\tau z} \tag{11}$$

is studied where $A(z)$ and $B(z)$ are polynomials with constant coefficients given by

$$A(z) = \sum_{k=0}^{m} a_{m-k} z^k, \qquad B(z) = \sum_{k=0}^{n} b_{n-k} z^k. \tag{12}$$

A notion of the principal term, closely connected with the stability problem, is used in this study; namely, the principal term of quasi-polynomial (11) after premultiplying it by $e^{\tau z}$ is the term $c_k z^k e^{\tau z}$ in which the argument of the power z and τ has the highest value for some $k = 0, 1, \ldots, n$. From the Pontryagin criterion, follows that a quasi-polynomial with no principal term has infinitely many roots with arbitrary large, positive real parts. Hence, the presence of principal term in a quasi-polynomial is a necessary condition for its stability. In [15] the following formula, related zeros of quasi-polynomials z_j and it coefficients are proved:

$$\sum_{j=1}^{\infty} \frac{1}{z_j} = \frac{1}{2}\left[\frac{F'(z)}{F(z)}\right]_{z=\infty} - \left[\frac{F'(z)}{F(z)}\right]_{z=0}. \tag{13}$$

Stability of systems of differential equations with delay (or, in other words, systems of differential-difference equations)

$$x'(t) = Ax(t-\tau), \quad x \in \mathbb{R}^n \tag{14}$$

with a constant matrix A was also investigated by using properties of quasi-polynomials.

Thus, in [16] the following criterion was proved: *let A be a 2×2 matrix of real constants. Then all zeros of the quasi-polynomial $\Delta(z) = z^2 e^{2z} - \operatorname{tr}(A) z e^z + |A|$ have negative real parts if and only if*

$$\begin{gathered} \left(\frac{\pi}{2}\right)^2 + \frac{\pi}{2} \operatorname{tr}(A) + |A| > 0, \\ 0 < |A| < \zeta^2 < \left(\frac{\pi}{2}\right)^2, \end{gathered} \tag{15}$$

where ζ is the smallest positive root of the equation $y \sin y = -(1/2)\operatorname{tr}(A)$.

Distribution of zeros of quasi-polynomials, related to the coupled renewal-differential system

$$\begin{gathered} w(t) = f(t) + \int_0^t A(t-\tau) w(\tau)\, d\tau + by(t), \\ y'(t) = Cw(t) + Dy(t), \qquad y(0) = y_0, \end{gathered} \tag{16}$$

is discussed in [17]). A numerical method for calculation of zeros of quasi-polynomials is proposed, for example, in [18].

Special attention was paid in the last years to (finite and infinite) Dirichlet series. In [19] it was proved that if

$$\begin{gathered} \sum_{k=0}^{\infty} P_k(z) e^{-\lambda_k z}, \\ z = \sigma + it, \quad \lambda_k \in \mathbb{C}, \\ P_k(z) \in \mathbb{C}[z], \quad \operatorname{Re} \lambda_k \uparrow \infty \end{gathered} \tag{17}$$

is a convergent Taylor-Dirichlet series, where, as usual, $\mathbb{C}[z]$ means the set of polynomial with constant complex coefficients. The symbol $\lambda_k \uparrow \infty$ denotes $\lambda_1 < \lambda_2 < \cdots < \lambda_n < \cdots \to \infty$, when $n \to \infty$, and satisfies an algebraic differential-difference equation

$$\begin{gathered} G\left(x, f^{(m_1)}(x+h_1), \ldots, f^{(m_r)}(x+h_r)\right) = 0, \\ G(x, x_1, \ldots, x_r) = \sum C_{k_1,\ldots,k_r} x^{k_1} \cdots x^{k_r}, \end{gathered} \tag{18}$$

where $C_{k_1,\ldots,k_r}$ are constant coefficients, and then the set of its exponents $\{\lambda_k\}_{k=0}^{\infty}$ has a finite, linear, integral basis.

Different questions related to the series of polynomial of exponents were discussed in [20] (see also references therein and [21]). In [22] the large n asymptotic of zeros of sections of a generic exponential series are derived, where the nth section of the mentioned series mean the the sum of the first n terms of it. In [23] it is given an answer on the question when the reciprocal to the product of Gamma-functions coincide with a quasi-polynomial of type (6).

3. Fractional Quasi-Polynomials

Recently, an attention is paid to the study of linear fractional systems with delays described by the transfer function

$$P(z) = \frac{q_0(z) + \sum_{j=1}^{m_2} q_j(z) \exp\left(-z^r \gamma_j\right)}{p_0(z) + \sum_{j=1}^{m_1} p_j(z) \exp\left(-z^r \delta_j\right)} = \frac{N(z)}{D(z)}, \tag{19}$$

where r is such a real number ($0 < r \leq 1$), and the fractional degree nontrivial polynomials $p_j(z)$ and $q_j(z)$ with real coefficients have the forms

$$\begin{gathered} p_j(z) = \sum_{k=0}^{n} a_{jk} z^{\alpha_k}, \quad j = 0, 1, \ldots, m_1, \\ q_j(z) = \sum_{k=0}^{m} b_{jk} z^{\beta_k}, \quad j = 0, 1, \ldots, m_2, \end{gathered} \tag{20}$$

where α_k, β_k are real nonnegative numbers and $a_{0n} \neq 0$, $b_{0m} \neq 0$.

The fractional degree characteristic quasi-polynomial of the system (19) has the form

$$D(z) = p_0(z) + \sum_{j=1}^{m_1} p_j(z) \exp\left(-z^r \delta_j\right). \tag{21}$$

In the case of a system with delays of a fractional commensurate order (i.e., when $\alpha_k = \alpha \cdot k$ ($k = 0, 1, \ldots, n$); $\beta_k = \alpha \cdot k$ ($k = 0, 1, \ldots, m$)), one can consider the natural degree quasi-polynomial

$$\widetilde{D}(\lambda) = \widetilde{p}_0(\lambda) + \sum_{j=1}^{m_1} \widetilde{p}_j(\lambda) \exp\left(-\lambda^{r/\alpha} \delta_j\right), \quad \lambda = z^{\alpha}, \tag{22}$$

associated with the characteristic quasi-polynomial (21) of a fractional order.

In [24] new frequency domain methods for stability analysis of linear continuous-time fractional order systems with delays of the retarded type are proposed. The methods

are obtained by generalization to the class of fractional order systems with delays of the Mikhailov stability criterion and the modified Mikhailov stability criterion known from the theory of natural order systems without and with delays.

The following results concerning stability of the considered system are proved in [24].

(1) The fractional quasi-polynomial (21) of commensurate degree satisfies the condition $D(z) \neq 0$, $\operatorname{Re} z \geq 0$ if and only if all the zeros of the associated natural degree quasi-polynomial (22) satisfy the condition

$$\left|\arg(\lambda)\right| > \frac{\alpha\pi}{2}, \tag{23}$$

where $\arg(\lambda)$ means the principal branch of the multivalued function $\operatorname{Arg}(\lambda)$, $\lambda \in \mathbb{C}$; that is, $\arg(\lambda) \in (-\pi, \pi]$.

(2) The fractional quasi-polynomial (21) of commensurate degree is not stable for any $\alpha > 1$.

(3) The fractional characteristic quasi-polynomial (21) of commensurate degree is stable if and only if

$$\Delta_{0\leq\omega<+\infty} \arg(D(i\omega)) = \frac{n\pi}{2}, \tag{24}$$

which means that the plot of $D(i\omega)$ with ω increasing from 0 to $+\infty$ runs in the positive direction by n quadrants of the complex plane, missing the origin of this plane.

(4) The fractional characteristic quasi-polynomial (21) (of commensurate or noncommensurate degree) is stable if and only if

$$\Delta_{-\infty<\omega<+\infty} \arg(\psi(i\omega)) = 0, \tag{25}$$

where

$$\psi(z) = \frac{D(z)}{w_r(z)}, \tag{26}$$

and $w_r(z)$ can be chosen, for example, as

$$w_r(z) = a_{0n}(z+c)^{\alpha_n}, \quad c > 0. \tag{27}$$

Remark 1. Stability of fractional polynomials is related to the stability of ordinary quasi-polynomials due to the following relation:

$$\begin{aligned} a_0 + a_1 z^{\alpha_1} + \cdots + a_n z^{\alpha_n} = a_0 + a_1 \cdot e^{\alpha_1 w} + \cdots \\ + a_n \cdot e^{\alpha_n w}, \end{aligned} \tag{28}$$

where $w = \log z$. Application of formula (28) needs to be very careful since w is now the point on the Riemann surface of the logarithmic function (see, e.g., [22]).

An approach describing the stability of fractional quasi-polynomials in terms of zeros distribution of these polynomials on certain Riemann surfaces is widely used now (see, e.g., survey paper [10] and references therein). Sometimes it is called "root-locus method." The characteristic result obtained with the application of this method is the following [25].

(5) The fractional order system with characteristic polynomial $w(z)$ is stable if and only if $w(z)$ has no zeros in the closed right-half of the Riemann surface; that is,

$$w(z) \neq 0 \quad \forall \operatorname{Re} z \geq 0. \tag{29}$$

The fractional order polynomial $w(z)$ is a multivalued function whose domain is a Riemann surface. In general, this surface has an infinite number of sheets, and thus the fractional polynomial has (in general) an infinite number of zeros. We are interested only in those zeros which are situated on the main sheet of the Riemann surface which can be fixed in the following way: $-\pi < \arg(z) < \pi$.

Recently the notion of robust stability was introduced for systems with characteristic polynomials dependent on uncertainty parameter (see [26–29]). In [25] this notion is applied to the convex combination of two fractional degrees polynomials

$$W(z,q) = \{w(z,q) : q \in Q = [0,1]\}, \tag{30}$$

$$w(z,q) = (1-q)\, w_a(z) + q w_b(z), \tag{31}$$

where q is uncertainty parameter, and $w_a(z)$, $w_b(z)$ are fractional degree polynomials.

The family (30) of fractional degree polynomials is called robust stable if polynomial $w(z,q)$ is stable for all $q \in Q$.

Generalization of the Mikhailov-type criterion (see [24]) to this case has the following form [25].

(6) Let the nominal polynomial $w_a(z)$ be stable. The family of polynomials (30) is robust stable if and only if the plot of the function

$$\vartheta(j\omega) = \frac{w_b(j\omega)}{w_a(j\omega)}, \quad \omega \in \Omega = [0,\infty) \tag{32}$$

does not cross the nonpositive part $(-\infty, 0]$ of the real axis in the complex plane.

4. Stability of Fractional Order Systems

Several applications of the results on stability of the fractional polynomials to the systems describing different processes and phenomena are presented, for example, [30, 31]. Some of these results are closely related to the recent achievements and the theory and applications of fractional calculus and fractional differential equations (see [32–34]). The results in this area need to be systematized as from the point of the ideas, technical point of view.

4.1. General Fractional Order Systems. A general fractional order system can be described by a fractional differential equation of the form

$$\begin{aligned} a_n D^{\alpha_n} y(t) + a_{n-1} D^{\alpha_{n-1}} y(t) + \cdots + a_0 D^{\alpha_0} y(t) \\ = b_m D^{\beta_m} y(t) + b_{m-1} D^{\beta_{m-1}} y(t) + \cdots + b_0 D^{\beta_0} y(t), \end{aligned} \tag{33}$$

where $D^\gamma = {}_0D_t^\gamma$ denotes the Riemann-Liouville ${}_0^{\mathrm{RL}}D_t^\gamma$ or Caputo ${}_0^{C}D_t^\gamma$ fractional derivative [32, 33]. Another form of general fractional order system is due to properties of the Laplace transform [32, 34]. This form represents the system in terms of corresponding transfer function

$$G(s) = \frac{b_m s^{\beta_m} + b_{m-1} s^{\beta_{m-1}} + \cdots + b_0 s^{\beta_0}}{a_n s^{\alpha_n} + a_{n-1} s^{\alpha_{n-1}} + \cdots + a_0 s^{\alpha_0}} = \frac{Q(s)}{P(s)}, \tag{34}$$

where s is the Laplace variable. Here $a_n, \ldots, a_0$, $b_m, \ldots, b_0$ are given real constants, and $\alpha_n, \ldots, \alpha_0$, $\beta_m, \ldots, \beta_0$ are given real numbers (usually positive). Without loss of generality, these sets of parameters can be ordered as $\alpha_n > \cdots > \alpha_0$, $\beta_m > \cdots > \beta_0$.

If both sets α-s and β-s constitute an arithmetical progression with the same difference, that is, $\alpha_k = k\alpha$, $k = 0, \ldots, n$, $\beta_k = k\alpha$, $k = 0, \ldots, m$, then system (33) is called *commensurate order system*. Usually it is supposed that parameter α satisfies the inequality $0 < \alpha < 1$. In all other cases system (33) is called *incommensurate order system*. Anyway, if parameters α and β are rational numbers, then this case can be considered as commensurate one, with $\alpha = 1/N$ being a least common multiple of denominators of fractions $\alpha_n, \ldots, \alpha_0$, $\beta_m, \ldots, \beta_0$ [35].

For commensurate order system, its transfer function can be thought as certain branch of the following multivalued function:

$$G(s) = \frac{\sum_{k=0}^{m} b_k (s^\alpha)^k}{\sum_{k=0}^{n} a_k (s^\alpha)^k} = \frac{\widetilde{Q}(s^\alpha)}{\widetilde{P}(s^\alpha)}. \tag{35}$$

Since the right hand-side of this relation is a rational function of s^α, then one can represent $G(s)$ in the form of generalized simple fractions. The most descriptive representation of such a type is that for $n > m$,

$$G(s) = \left\{ \sum_{i=1}^{p} \sum_{j=1}^{r_i} \frac{A_{ij}}{(s^\alpha + \lambda_i)^j} \right\}, \tag{36}$$

where $-\lambda_i$ is a root of polynomial $P(z)$ of multiplicity r_i. In particular, if all roots are simple, then the representation (36) has the most simple form

$$G(s) = \left\{ \sum_{i=1}^{n} \frac{B_i}{s^\alpha + \lambda_i} \right\}. \tag{37}$$

In this case an analytic solution to system (33) is given by the formula

$$\begin{aligned} y(t) &= \mathscr{L}^{-1} \left\{ \sum_{i=1}^{n} \frac{B_i}{s^\alpha + \lambda_i} \cdot (\mathscr{L}u)(s) \right\} \\ &= \mathscr{L}^{-1} \left\{ \sum_{i=1}^{n} \frac{B_i}{s^\alpha + \lambda_i} \right\} * u(t) \\ &= \left(\sum_{i=1}^{n} B_i t^\alpha E_{\alpha,\alpha}(-\lambda_i t^\alpha) \right) * u(t), \end{aligned} \tag{38}$$

where the symbol "$*$" means the Laplace-type convolution, and $E_{\mu,\nu}$ is the two-parametric Mittag-Leffler function [36]

$$E_{\mu,\nu}(z) = \sum_{k=0}^{\infty} \frac{z^k}{\Gamma(\mu k + \nu)}. \tag{39}$$

In the case of homogeneous fractional order system

$$a_n D^{\alpha_n} y(t) + a_{n-1} D^{\alpha_{n-1}} y(t) + \cdots + a_0 D^{\alpha_0} y(t) = 0, \tag{40}$$

the analytical solution is given by the following formula (see, e.g., [10, 37]):

$$\begin{aligned} y(t) &= \frac{1}{a_n} \sum_{k=0}^{\infty} \frac{(-1)^k}{k!} \sum_{\substack{k_0+\cdots+k_{n-2}=k \\ k_0 \geq 0, \ldots, k_{n-2} \geq 0}} (k; k_0, \ldots, k_{n-2}) \\ &\quad \times \prod_{i=0}^{n-2} \left(\frac{a_i}{a_n} \right)^{k_i} \mathscr{E}_k \\ &\quad \times \left(t, -\frac{a_{n-1}}{a_n}; a_n - a_{n-1}, a_n + \sum_{j=0}^{n-2} (a_{n-1} - a_j) k_j + 1 \right), \end{aligned} \tag{41}$$

where $(k; k_0, \ldots, k_{n-2})$ are the multinomial coefficients, and $\mathscr{E}_k(t, y; \mu, \nu)$ is defined by the formula [33]

$$\begin{aligned} \mathscr{E}_k(t, y; \mu, \nu) &= t^{\mu k + \nu - 1} E_{\mu,\nu}^{(k)}(y t^\mu), \quad (k = 0, 1, 2, \ldots), \\ E_{\mu,\nu}^{(k)}(z) &= \sum_{j=0}^{\infty} \frac{(j+k)! z^j}{j! \Gamma(\mu j + \mu k + \nu)} \quad (k = 0, 1, 2, \ldots) \end{aligned} \tag{42}$$

is the kth derivative of two-parametric Mittag-Leffler function [32, 38]

$$E_{\mu,\nu}(z) = \sum_{j=0}^{\infty} \frac{z^j}{\Gamma(\mu j + \nu)} \quad (k = 0, 1, 2, \ldots). \tag{43}$$

The stability analysis of the fractional order system gives the following results (see [10, 24, 39, 40]).

Theorem 2. *A commensurate order system with transfer function* (37) *is stable if and only if*

$$|\arg(\lambda_i)| > \alpha \frac{\pi}{2} \quad \forall i = 1, \ldots, n, \tag{44}$$

with $-\lambda_i$ being the ith root of the generalized polynomial $P(s^\alpha)$.

To formulate the result in incommensurate case, we use the concept of bounded input-bounded output (BIBO) or external stability (see [10, 39]).

Theorem 3. *Let the transfer function of an incommensurate order system be represented in the form*

$$G(s) = \left\{ \sum_{i=1}^{p} \sum_{j=1}^{r_i} \frac{A_{ij}}{(s^{q_i} + \lambda_i)^j} \right\}, \tag{45}$$

for some complex numbers A_{ij}, λ_i, positive q_i, and positive integer r_i.

Such system is BIBO stable if and only if parameters q_i and arguments of numbers λ_i satisfy the following inequality:

$$0 < q_i < 2, \quad |\arg(\lambda_i)| < \pi \left(1 - \frac{q_i}{2} \right) \quad \forall i = 1, \ldots, p. \tag{46}$$

The result of Theorem 3 was obtained by using the stability results given in [40, 41].

4.2. Fractional Order Linear Time-Invariant Systems. Besides the conception of stability, for fractional order linear time-invariant systems

$$\begin{aligned} {}_0D_t^{\mathbf{q}}\mathbf{x}(t) &= \mathbf{A}\mathbf{x}(t) + \mathbf{B}\mathbf{u}(t), \\ \mathbf{y}(t) &= \mathbf{C}\mathbf{x}(t), \end{aligned} \tag{47}$$

the conceptions of *controllability* and *observability* (known as linear and nonlinear differential systems [42, 43]) are introduced too.

In (47) $\mathbf{x} \in \mathbb{R}^n$ is an unknown state vector, and $\mathbf{u} \in \mathbb{R}^r$, $\mathbf{y} \in \mathbb{R}^p$ are the control vector and output vector, respectively. Given (constant) matrices $\mathbf{A}$, $\mathbf{B}$, and $\mathbf{C}$ are of the following size $\mathbf{A} \in \mathbb{R}^{n\times n}$, $\mathbf{B} \in \mathbb{R}^{n\times r}$, and $\mathbf{C} \in \mathbb{R}^{p\times n,}$. Positive vector $\mathbf{q} = [q_1, \ldots, q_n]^T$ denotes the (fractional) order of system (47). If $q_1 = \cdots = q_n = q$, then system (47) is called a commensurate order system.

As in case of ordinary linear differential time-invariant systems, controllability and observability conditions [44] are represented in terms of controllability $C_a = [B|AB|A^2B|\cdots|A^{n-1}B]$ and observability $O_a = [C|CA|CA^2|\cdots|CA^{n-1}]$ matrices, respectively.

We have to mention also the stability criterion for the system (47) (see [40, 45–48]).

Theorem 4. *Commensurate system* (47) *is stable if the following conditions are satisfied:*

$$\left|\arg\left(eig\left(\mathbf{A}\right)\right)\right| > q\frac{\pi}{2}, \quad 0 < q < 2, \tag{48}$$

for all eigenvalues eig($\mathbf{A}$) *of the matrix* $\mathbf{A}$.

Several new results on stability, controllability, and observability of system (47) are presented in the recent monograph [49] (see also [37, 50–52]) is proposed. We can say that control theory for fractional order systems becomes a special branch of fractional order systems and mention in this connection several important papers developing this theory [53–67]. A number of applications of the fractional order systems are presented in [30, 31, 68].

4.3. Fractional Order Controllers. The fractional-order controller (FOC) $\mathrm{PI}^\lambda\mathrm{D}^\delta$ (also known as $\mathrm{PI}^\lambda\mathrm{D}^\mu$ controller) was proposed in [33] as a generalization of the PID controller with integrator of real order λ and differentiator of real order δ. The transfer function of such controller in the Laplace domain has this form

$$C(s) = \frac{U(s)}{E(s)} = K_p + T_i s^{-\lambda} + T_d s^{\delta} \quad (\lambda, \delta > 0), \tag{49}$$

where K_p is the proportional constant, T_i is the integration constant, and T_d is the differentiation constant.

In [69] a classification of different modifications of the fractional $\mathrm{PI}^\lambda\mathrm{D}^\delta$ controllers (see also [49, 70–72]):

(i) *CRONE controller* (1st generation), characterized by the bandlimited lead effect:

$$C(s) = C_0 \frac{\left(1 + s/\omega_b\right)^r}{\left(1 + s/\omega_h\right)^{r-1}}. \tag{50}$$

There are a number of real-life applications of three generations of the CRONE controller [73].

(ii) *Fractional lead-lag compensator* [49], which is given by

$$C(s) = k_c\left(\frac{s + 1/\lambda}{s + 1/\lambda}\right)^r, \tag{51}$$

where $0 < s < 1$, $\lambda \in \mathbb{R}$, and $r \in \mathbb{R}$.

(iii) *Noninteger integral* and its application to control as a reference function [74, 75]; Bode suggested an ideal shape of the loop transfer function in his work on design of feedback amplifiers in 1945. Ideal loop transfer function has the form

$$L(s) = \left(\frac{s}{\omega_{gc}}\right)^\alpha, \quad (\alpha < 0), \tag{52}$$

where ω_{gc} is desired crossover frequency and α is the slope of the ideal cut-off characteristic. The Nyquist curve for ideal Bode transfer function is simply a straight line through the origin with $\arg(L(j\omega)) = \alpha\pi/2$.

(iv) *TID compensator* [76], which has structure similar to a PID controller but the proportional component is replaced with a tilted component having a transfer function s to the power of $(-1/n)$. The resulting transfer function of the TID controller has the form

$$C(s) = \frac{T}{s^{1/n}} + \frac{I}{s} + Ds, \tag{53}$$

where T, I, and D are the controller constants, and n is a non-zero real number, preferably between 2 and 3. The transfer function of TID compensator more closely approximates an optimal transfer function, and an overall response is achieved, which is closer to the theoretical optimal response determined by Bode [74].

Different methods for determination of $\mathrm{PI}^\lambda\mathrm{D}^\delta$ controller parameters satisfying the given requirements are proposed (see, e.g., [69] and references therein).

4.4. Positive Fractional Order Systems. A new concept (notion) of the practical stability of the positive fractional 2D linear systems is proposed in [77]. Necessary and sufficient conditions for the practical stability of the positive fractional 2D systems are established. It is shown that the positive fractional 2D systems are practically unstable (1) if a corresponding positive 2D system is asymptotically unstable and (2) if some matrices of the 2D system are nonnegative.

Simple necessary and sufficient conditions for practical stability independent of the length of practical implementation are established in [78]. It is shown that practical stability of the system is equivalent to asymptotic stability of the corresponding standard positive discrete-time systems of the same order.

4.5. Fractional Order Systems with Delay. Fractional order systems with delay meet a number of important applications (see, e.g., [31, 49]). There are several important works about stability of closed-loop fractional order systems/controllers with time delays. Some relevant examples can be found in [79–81].

To describe simplest fractional order systems with delay, let us introduce some notations (see [82]).

Let $\mathscr{C}([a,b],\mathbb{R}^n)$ be the set of continuous functions mapping the interval $[a,b]$ to $\mathbb{R}^n$). One may wish to identify a maximum time delay r of a system. In this case, we are interested in the set of continuous function mapping $[-r,0]$ to $\mathbb{R}^n$), for which we simplify the notation to $\mathscr{C} = \mathscr{C}([-r,0],\mathbb{R}^n)$. For any $A > 0$ and any continuous function of time $\mathbf{x} \in \mathscr{C}([t_0 - r, t_0 + A],\mathbb{R}^n)$, $t_0 \le t_0 + A$, let $\mathbf{x}_t(\theta) \in \mathscr{C}$ be a segment of function defined as $\mathbf{x}_t(\theta) = \mathbf{x}(t+\theta)$, $-r \le \theta \le 0$.

Let the fractional nonlinear time-delay system be the system of the following type:

$$ {}_{t_0}^{C}D_t^{\mathbf{q}}\mathbf{x}(t) = \mathbf{f}(t, \mathbf{x}_t(t)), \tag{54} $$

where $\mathbf{x} \in \mathscr{C}([t_0 - r, t_0 + A],\mathbb{R}^n)$ for any $A > 0$, $\mathbf{q} = (q,\ldots,q)$, $0 < q < 1$, and $f : \mathbb{R}\times\mathscr{C} \to \mathbb{R}^n$. To determine the future evolution of the state, it is necessary to specify the initial state variables $\mathbf{x}(t)$ in a time interval of length r, say from $t_0 - r$ to t_0; that is,

$$ \mathbf{x}(t_0) = \varphi, \tag{55} $$

where $\varphi \in \mathscr{C}$ is given. In other words $\mathbf{x}(t_0)(\theta) = \varphi(\theta)$, $-r \le \theta \le 0$.

Several stability results for fractional order systems with delay were obtained in [82–84]. In particular, in [84], the linear and time-invariant differential-functional Caputo fractional differential systems of order α are considered:

$$ \begin{aligned} {}^{C}D_{0t}^{\alpha}\mathbf{x}(t) &:= \frac{1}{\Gamma(k-\alpha)}\int_0^t \frac{\mathbf{x}^{(k)}(\tau)}{(t-\tau)^{\alpha+1-k}}d\tau \\ &= \sum_{i=0}^{p}\mathbf{A}_i\mathbf{x}(t-h_i) + \mathbf{B}\mathbf{u}(t), \end{aligned} \tag{56} $$

$k-1 < \alpha \le k$, $k-1 \in \mathbb{Z}_{0+}$, $0 < h_0 < h_1 < \cdots < h_p = h < \infty$. $\mathbf{A}_0$, $\mathbf{A}_i \in \mathbb{R}^{n\times n}$ are matrices of dynamics for each delay h_i, and $\mathbf{B} \in \mathbb{R}^{n\times m}$ is the control matrix. Under standard initial conditions, the solution to this problem is represented via Mittag-Leffler function, and the dependence of the different delay parameters is studied.

4.6. Distributed Order Fractional Systems. An example of *distributed order* fractional systems is the system of the following type (see, e.g., [85]) containing the so-called *distributed order fractional derivative*:

$$ {}_{do}^{C}D_t^{\alpha}x(t) = A\,{}_{do}^{C}D_t^{\beta}x(t) + Bu(t), \qquad x(0) = x_0, \tag{57} $$

where $0 < \beta < \alpha \le 1$,

$$ {}_{do}D_t^{\alpha}(\cdot) = \int_t^{\gamma} b(\alpha)\frac{d^{\alpha}(\cdot)}{dt^{\alpha}}d\alpha, \quad \gamma > l \ge 0,\ b(\alpha) \ge 0, \tag{58} $$

and ${}_{so}D_t^{\alpha}(\cdot) = d^{\alpha}(\cdot)/dt^{\alpha}$ is a standard (single order) fractional derivative.

Application of such systems to the description of the *ultraslow diffusion* is given in series of articles by Kochubei (see, e.g., [86]).

4.7. Discrete-Time Fractional Systems. There are different definitions of the fractional derivative (see, e.g., [34, 87]). The Grünwald-Letnikov definition, which is the discrete approximation of the fractional order derivative, is used here. The Grünwald-Letnikov fractional order derivative of a given function $f(t)$ is given by

$$ {}_{a}^{\mathrm{GL}}D_t^{\alpha}f(t) = \lim_{h\to 0}\frac{{}_{a}\Delta_h^{\alpha}f(t)}{h^{\alpha}}, \tag{59} $$

where the real number α denotes the order of the derivative, a is the initial time, and h is a sampling time. The difference operator Δ is given by

$$ {}_{a}\Delta_h^{\alpha}f(t) = \sum_{j=0}^{[(t-a)/h]}(-1)^j\binom{\alpha}{j}f(t-jh), \tag{60} $$

where $\binom{\alpha}{j}$ is the Pochhammer symbol and $[\cdot]$ denotes an integer part of a number.

Traditional discrete-time state-space model of integer order, that is, when α is equal to unity has the form,

$$ \begin{gathered} \mathbf{x}(k+1) = \mathbf{A}\mathbf{x}(k) + \mathbf{B}\mathbf{u}(k), \qquad x(0) = x_0, \\ \mathbf{y}(k) = \mathbf{C}\mathbf{x}(k) + \mathbf{D}\mathbf{u}(k), \end{gathered} \tag{61} $$

where $\mathbf{u}(k) \in \mathbb{R}^p$ and $\mathbf{y}(k) \in \mathbb{R}^q$ are, respectively, the input and the output vectors, and $\mathbf{x}(k) = [x_1(k),\ldots,x_n(k)] \in \mathbb{R}^n$ is the state vector. Its initial value is denoted by $x_0 = x(0)$ and can be set equal to zero without loss of generality. $\mathbf{A}$, $\mathbf{B}$, $\mathbf{C}$, and $\mathbf{D}$ are the conventional state space matrices with appropriate dimensions.

The generalization of the integer-order difference to a noninteger order (or fractional-order) difference has been addressed in [88] where the discrete fractional-order difference operator with the initial time taken equal to zero is defined as follows:

$$ \Delta^{\alpha}\mathbf{x}(k) = \frac{1}{h^{\alpha}}\sum_{j=0}^{k}(-1)^j\binom{\alpha}{j}\mathbf{x}(k-j). \tag{62} $$

In the sequel, the sampling time h is taken equal to 1. These results conducted to conceive the linear discrete-time fractional-order state-space model, using

$$ \Delta^{\alpha}\mathbf{x}(k+1) = \mathbf{A}_d\mathbf{x}(k) + \mathbf{B}\mathbf{u}(k), \qquad \mathbf{x}(0) = \mathbf{x}_0. \tag{63} $$

The discrete-time fractional order system is represented by the following state space model:

$$ \begin{gathered} \mathbf{x}(k+1) = \sum_{j=0}^{k}\mathbf{A}_j\mathbf{x}(k-j) + \mathbf{B}\mathbf{u}(k), \qquad \mathbf{x}(0) = \mathbf{x}_0, \\ \mathbf{y}(k) = \mathbf{C}\mathbf{x}(k) + \mathbf{D}\mathbf{u}(k), \end{gathered} \tag{64} $$

where $\mathbf{A}_0 = \mathbf{A}_d - c_1\mathbf{I}_n$ and $\mathbf{A}_j = -c_{j+1}I_n$ for $j \geq 2$ with $c_j = -(-1)^j\binom{\alpha}{j}$. This description can be extended to the case of noncommensurate fractional-order systems modeled in [88] by introducing the following vector difference operator:

$$\begin{gathered}\Delta^{\Upsilon}\mathbf{x}(k+1) = \mathbf{A}_d\mathbf{x}(k) + \mathbf{B}\mathbf{u}(k),\\ \mathbf{x}(k+1) = \Delta^{\Upsilon}\mathbf{x}(k+1) + \sum_{j=1}^{k+1}\mathbf{A}_j\mathbf{x}(k-j+1),\\ \Delta^{\Upsilon}\mathbf{x}(k+1) = \begin{bmatrix}\Delta^{\alpha_1}x_1(k+1)\\ \Delta^{\alpha_2}x_2(k+1)\\ \vdots\\ \Delta^{\alpha_n}x_n(k+1)\end{bmatrix}.\end{gathered} \tag{65}$$

Stability analysis of such system is performed, for example, [89] (see also [90, 91]).

The paper [92] is devoted to controllability analysis of discrete-time fractional systems.

4.8. Fractional Nonlinear Systems. The simplest fractional nonlinear system in the incommensurate case is the system of the type

$$\begin{gathered}{}_0D_t^{\mathbf{q}}\mathbf{x}(t) = \mathbf{f}(\mathbf{x}(t), t),\\ \mathbf{x}(0) = \mathbf{c}.\end{gathered} \tag{66}$$

It has been mentioned in [39] that exponential stability cannot be used to characterize the asymptotic stability of fractional order systems. A new definition of power law stability was introduced [93].

Definition 5. Trajectory $\mathbf{x}(t) = \mathbf{0}$ of the system (66) is power law t^{-q} asymptotically stable if there exists a positive $q > 0$ such that

$$\begin{gathered}\forall\,\|\mathbf{x}(t)\| \quad \text{with } t \leq t_0, \qquad \exists N = N(\mathbf{x}(\cdot)),\\ \text{such that } \forall t \geq t_0 \Longrightarrow \|\mathbf{x}(t)\| \leq Nt^{-q}.\end{gathered} \tag{67}$$

Power law t^{-q} asymptotic stability is a special case of the Mittag-Leffler stability [94], which has the following form.

Definition 6 (definition of the Mittag-Leffler stability). The solution of the nonlinear problem

$$\begin{gathered}{}_{t_0}D_t^{\mathbf{q}}\mathbf{x}(t) = f(\mathbf{x}(t), t),\\ \mathbf{x}(t_0) = \mathbf{c}\end{gathered} \tag{68}$$

is said to be Mittag-Leffler stable if

$$\|x(t)\| \leq \left\{m[x(t_0)]\,E_q(-\lambda(t-t_0)^q)\right\}^b, \tag{69}$$

where $E_q(u)$ is the classical Mittag-Leffler function, $\mathbf{q} = (q, \ldots, q)$, $q \in (0,1)$, $\lambda > 0$, $b > 0$, and $m(\mathbf{0}) = 0$, $m(\mathbf{x}) \geq 0$, m is locally Lipschitz on $\mathbf{x} \in \mathbb{B} \subseteq \mathbb{R}^n$ with Lipschitz constant m_0.

Among the many methods that have been proposed for the study of "different kinds of stability definitions" of nonlinear fractional order systems (66), we mention perturbation analysis.

Thus, in [95], it is investigates the qualitative behaviour of a perturbed fractional order differential equations with Caputo derivatives that differs in initial position and initial time with respect to the unperturbed fractional order differential equation with Caputo derivatives. In [96], the stability of n-dimensional linear fractional differential systems with commensurate order and the corresponding perturbed systems is investigated. By using the Laplace transform, the asymptotic expansion of the Mittag-Leffler function, and the Grönwall's inequality, some conditions on stability and asymptotic stability are given. In [97], the stability of nonlinear fractional differential systems with Caputo derivatives by utilizing a Lyapunov-type function is studied. Taking into account the relation between asymptotic stability and generalized Mittag-Leffler stability, the condition on Lyapunov-type function is weakened.

5. Some Examples

In this section, we analyze the stability of the four systems by means of the root locus and the polar diagram. For calculating the root-locus, the algorithm proposed in [98] is adopted. The closed-loop system is constituted by a controller and a plant with transfer functions $C(s)$ and $G(s)$, respectively, and unit feedback.

For studying the stability, the following classical criteria are applied

(i) ultimate (or critical) gain K_u: $1 + K_uC(s)G(s) = 0$, $\mathrm{Re}(s) = 0$,

(ii) phase margin PM: $|CG(i\omega_1)| = 1$, $\mathrm{PM} = \arg\{CG(i\omega_1)\} + \pi$,

(iii) gain margin GM: $\arg\{CG(i\omega_\pi)\} = -\pi$, $\mathrm{GM} = |CG(i\omega_\pi)|^{-1}$.

5.1. Example 1. This example was discussed in [10]. In this case we have $C(s) = K(64.47 + 12.46s)$ and $G(s) = 1/(0.598 + 39{,}96s^{1.25})$. Figure 1 depicts the root locus where the white circles represent the roots for $K = 1$, $s_{1,2} = -1.0788 \pm i\ 0.6064$. The system is always stable.

Figure 2 shows the polar diagram for $K = 1$. The corresponding phase margin is $\mathrm{MF} = 1.4720$ rad for $\omega_1 = 1.5195$. Varying the gain, we verify again that the system is always stable.

5.2. Example 2. This example was discussed in [99]. In this case we have $C(s) = K(1 + 1.1694(1/s^{1.1011}) - 0.1517s^{0.1855})$ and $G(s) = e^{-0.5s}/(1 + s^{0.5})$. Figure 3 depicts the root locus where the white circles represent the roots for $K = 1.4098$; namely, $s_{1,2} = -0.6620 \pm i\ 0.4552$, $s_{3,4} = -2.0323 \pm i\ 4.1818$. The limit of stability occurs for $K_u = 3.5549$, $s_{1,2} = 0 \pm i\ 4.5124$.

Figure 4 shows the polar diagram for $K = 1.4098$. The corresponding phase margin is $\mathrm{PM} = 1.1854$ rad for $\omega_1 =$

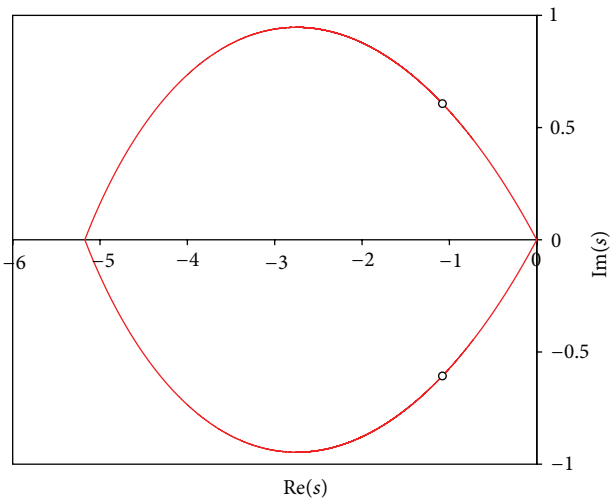

Figure 1: Root locus for $C(s) = K(64.47 + 12.46s)$ and $G(s) = 1/(0.598 + 39{,}96s^{1.25})$.

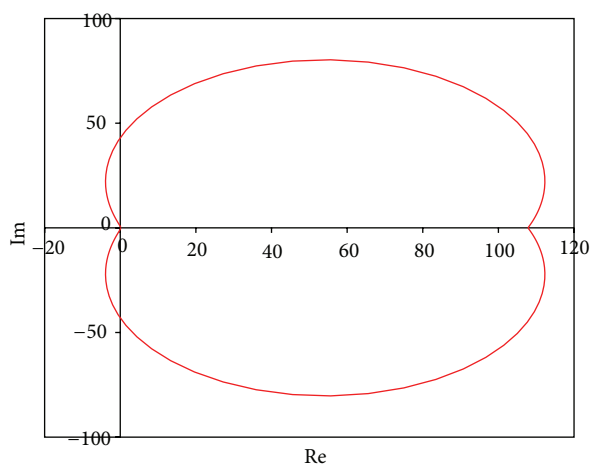

Figure 2: Polar diagram for $C(s) = K(64.47 + 12.46s)$, $G(s) = 1/(0.598 + 39{,}96s^{1.25})$, and $K = 1$.

1.0478, and gain margin GM = 2.5201 for $\omega_\pi = 4.5062$ rad which leads to $K_u = 3.5549$ as the ultimate gain.

5.3. Example 3. This example analyzes the system $K/s(s+1)^\alpha(s+2)$ for $\alpha \in \{0, 1/2, 1, 3/2, 2, 5/2, 3\}$. Since the integer-order cases are trivial, in Figures 5, 6, and 7 are only depicted the fractional-order cases. Table 1 shows the corresponding gain in the limit of stability K_u, the phase margin PM, and gain margin GM for several values of α.

5.4. Example 4. This example analyzes the nonminimum phase system $K((s+2)^{\alpha_2}/(s-1)^{\alpha_1})$ for $\alpha_1 = 3.3$, $\alpha_2 = 2.3$. Figure 8 depicts the root locus. The limit of stability occurs for $K_u = 4.3358$, $s_{1,2} = 0 \pm i\,4.8493$.

Figure 9 shows the polar diagram for $K = 1.0$. The corresponding gain margin is GM = 4.3358 for $\omega_\pi = 4.8493$ rad which leads to $K_u = 4.3358$ as the ultimate gain.

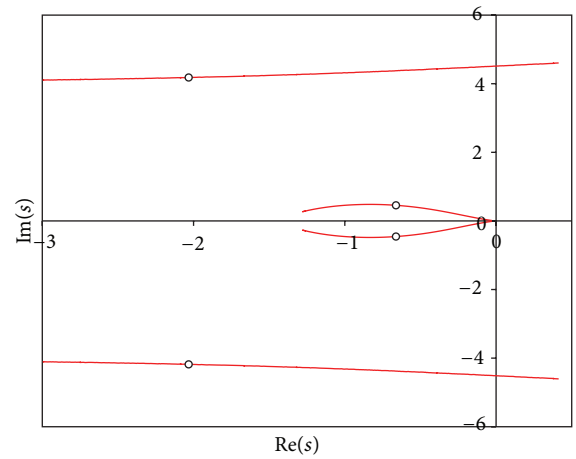

Figure 3: Root locus for $C(s) = K(1 + 1.1694(1/s^{1.1011}) - 0.1517s^{0.1855})$ and $G(s) = e^{-0.5s}/(1 + s^{0.5})$.

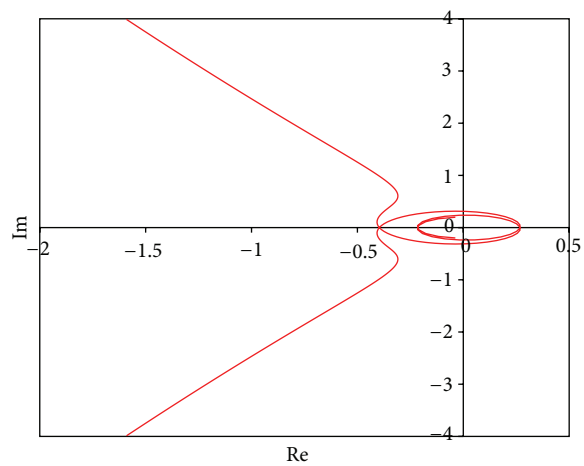

Figure 4: Polar diagram for $C(s) = K(1 + 1.1694(1/s^{1.1011}) - 0.1517s^{0.1855})$, $G(s) = e^{-0.5s}/(1 + s^{0.5})$, and $K = 1.4098$.

6. Future Directions of Research and Conclusions

In the previous discussion, one can outline the main methods applied at the study of stability of ordinary and fractional order systems. These directions are as follows:

(i) complex analytic methods related to the properties of single- and multivalued analytic functions;

(ii) methods of geometric functions theory describing the behaviour of polynomials or systems in geometrical terms;

(iii) methods of linear algebra (mainly matrix analysis);

(iv) methods of stochastic analysis;

(v) methods of fuzzy data analysis;

(vi) perturbation analysis of nonlinear systems;

(vii) methods of differential equations of fractional order.

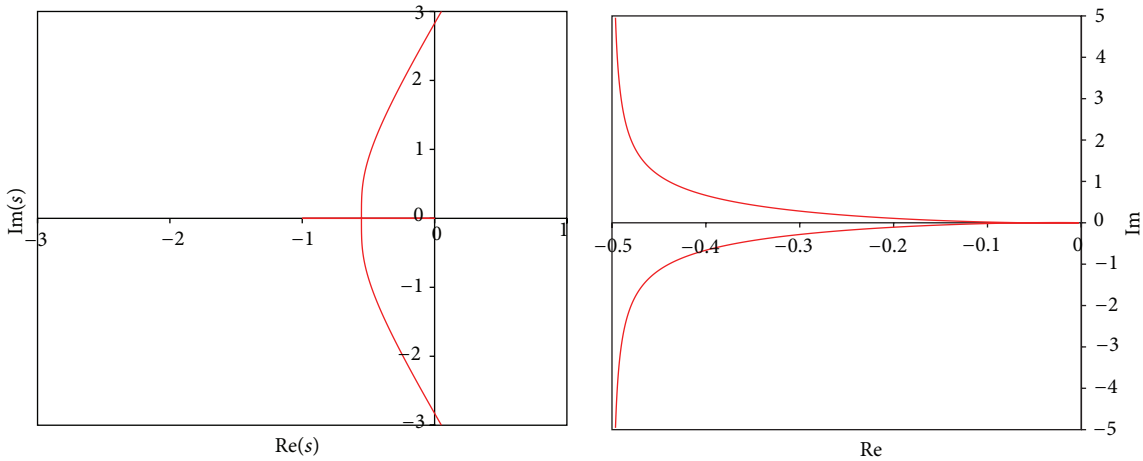

(a) (b)

FIGURE 5: Root locus and polar diagram for $K/s(s+1)^{\alpha}(s+2)$, $\alpha = 0.5$.

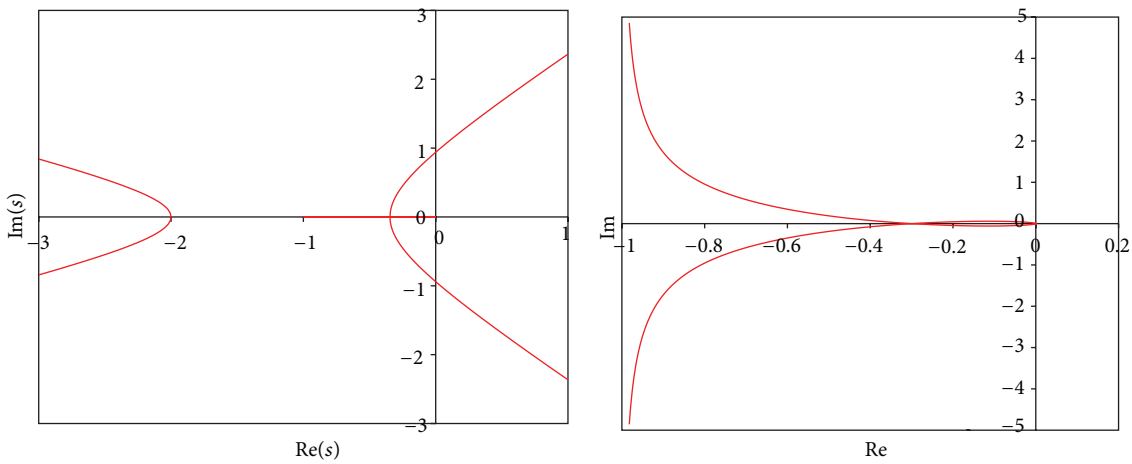

(a) (b)

FIGURE 6: Root locus and polar diagram for $K/s(s+1)^{\alpha}(s+2)$, $\alpha = 1.5$.

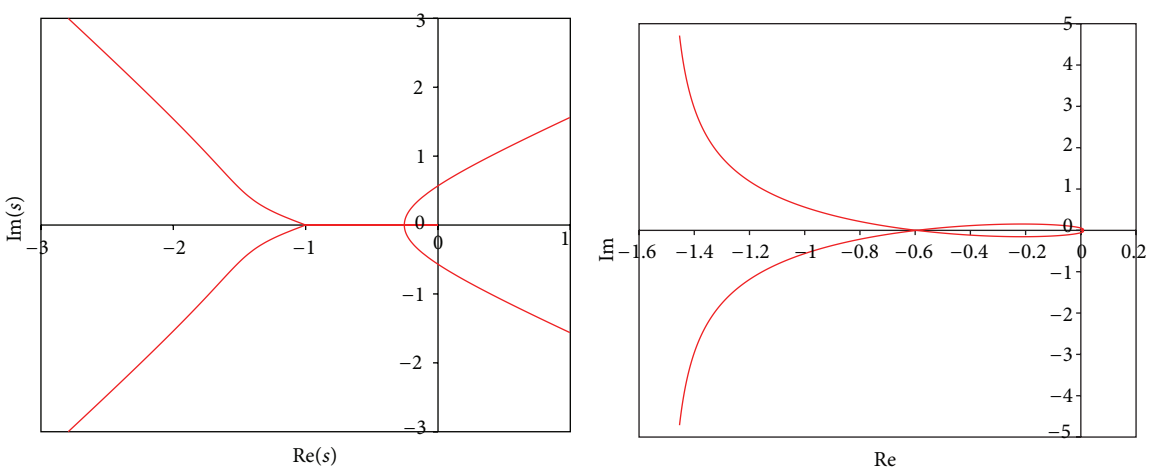

(a) (b)

FIGURE 7: Root locus and polar diagram for $K/s(s+1)^{\alpha}(s+2)$, $\alpha = 2.5$.

Table 1: Stability indices of $K/(s(s+1)^{\alpha}(s+2))$ for $\alpha \in \{0, 1/2, 1, 3/2, 2, 5/2, 3\}$.

α	K_u	PM	ω_1	GM	ω_π
0		1.332478866	0.4858682677		
0.5	17.0542240216776	1.125696835	0.4639038816	16.97056274	2.828427124
1	6	0.9321940595	0.4457479715	6	1.414213562
1.5	3.3537212820799	0.7492952635	0.4303313791	3.338364465	0.9397638161
2	2.25	0.5751435644	0.4169759154	2.25	0.7071067811
2.5	1.69381413351661	0.4083841882	0.4052247852	1.680695653	0.5691429584
3	1.347	0.2479905647	0.3947560116	1.33607116	0.4774914945

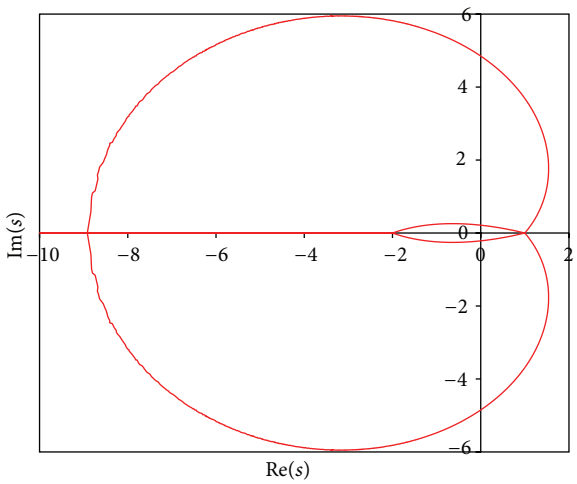

Figure 8: Root locus for $K((s+2)^{\alpha_2}/(s-1)^{\alpha_1})$ for $\alpha_1 = 3.3$, $\alpha_2 = 2.3$.

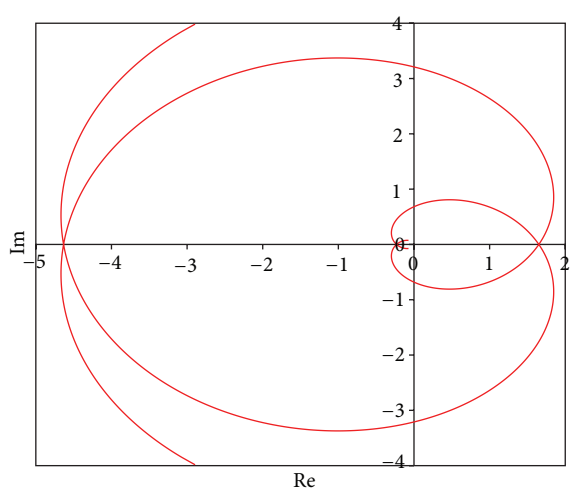

Figure 9: Polar diagram for $K((s+2)^{\alpha_2}/(s-1)^{\alpha_1})$ for $\alpha_1 = 3.3$, $\alpha_2 = 2.3$.

We can also mention the possibility to apply the study of fractional order stability methods of Padé (or Hermite-Padé) approximation (see, e.g., [100–102]).

In conclusion, this paper reviewed the main contributions that were proposed during the last years for analysing the stability of fractional order systems. Different problems were addressed such as control, systems including a delay or with a distributed nature, as well as discrete-time and nonlinear systems. The paper presented in a comprehensive and concise way many details that are scattered in the literature and provide researchers a reference text for work in this area.

Acknowledgments

The authors thank the anonymous referees for their valuable suggestions that helped to improve the paper. The work was done in the framework of cooperation between Belarusian State University and University La Laguna. The work is partly supported by Project MTM2010-16499 from the Government of Spain.

References

[1] A. Hurwitz, "Ueber die Bedingungen, unter welchen eine Gleichung nur Wurzeln mit negativen reellen Theilen besitzt," *Mathematische Annalen*, vol. 46, no. 2, pp. 273–284, 1895.

[2] F. J. MacWilliams, "An iterative method for the direct hurwitz-factorization of a polynomial," *IRE Transactions on Circuit Theory*, vol. 5, no. 4, pp. 347–352, 1958.

[3] M. Wunch, *Hurwitz-Faktorisierung von Polynomen und Ganzen Funktionen*, Giessen University: Selbstverlag des Mathematischen Instituts, 1993.

[4] A. V. Mikhailov, "Methods for harmonic analysis in automatic control systems," *Avtomat i Telemekh*, vol. 3, pp. 27–81, 1938 (Russian).

[5] N. G. Čebotarev and N. N. Meĭman, "The Routh-Hurwitz problem for polynomials and entire functions," *Trudy Matematicheskogo Instituta imeni V. A. Steklova*, vol. 26, p. 331, 1949.

[6] R. Caponetto and G. Dongola, "A numerical approach for computing stability region of FO-PID controller," *Journal of the Franklin Institute*, vol. 350, no. 4, pp. 871–889, 2013.

[7] A. Datta, M. Ho, and S. Bhattacharyya, *Structure and Synthesis of PID Controllers*, Springer, London, UK, 2000.

[8] M.-T. Ho, A. Datta, and S. P. Bhattacharyya, "Generalizations of the Hermite-Biehler theorem," *Linear Algebra and its Applications*, vol. 302/303, pp. 135–153, 1999, Special issue dedicated to Hans Schneider (Madison, WI, 1998).

[9] C. P. Li and F. R. Zhang, "A survey on the stability of fractional differential equations," *European Physical Journal*, vol. 193, no. 1, pp. 27–47, 2011.

[10] I. Petráš, "Stability of fractional-order systems with rational orders: a survey," *Fractional Calculus & Applied Analysis*, vol. 12, no. 3, pp. 269–298, 2009.

[11] I. Petráš, *Fractional-Order Nonlinear Systems: Modelling, Analysis and Simulation*, Springer, Dordrecht, The Netherlands, 2011.

[12] J. C. Trigeassou, N. Maamri, J. Sabatier, and A. Oustaloup, "A Lyapunov approach to the stability of fractional differential equations," *Signal Processing*, vol. 91, no. 3, pp. 437–445, 2011.

[13] L. S. Pontryagin, "On the zeros of some elementary transcendental functions," *American Mathematical Society Translations*, vol. 1, no. 2, pp. 95–110, 1955.

[14] L. Cossi, "Introduction to stability of quasipolynomials," in *Time-Dealay Systems*, D. Debeljkovich, Ed., pp. 1–14, InTech, 2001.

[15] H. Gorecki and S. Bialas, "Relations between roots and coefficients of the transcendental equations," *Bulletin of the Polish Academy of Sciences*, vol. 58, no. 4, pp. 631–634, 2010.

[16] T. Hara and J. Sugie, "Stability region for systems of differential-difference equations," *Funkcialaj Ekvacioj*, vol. 39, no. 1, pp. 69–86, 1996.

[17] R. P. Rhoten and J. K. Aggarwal, "The location of zeros of finite exponential series," *SIAM Journal on Applied Mathematics*, vol. 20, pp. 44–50, 1971.

[18] È. O. Movsesyan, "Calculation of zeros of a quasipolynomial by the method of the derivative of the argument," *Zhurnal Vychislitel'noi Matematiki i Matematicheskoi Fiziki*, vol. 26, no. 8, pp. 1132–1140, 1986 (Russian).

[19] F. Wadleigh, "Taylor-Dirichlet series and algebraic differential-difference equations," *Proceedings of the American Mathematical Society*, vol. 80, no. 1, pp. 83–89, 1980.

[20] A. F. Leont'ev, *Posledovatelnosti Polinomov iz Eksponent*, Nauka, Moscow, Russia, 1980.

[21] A. F. Leont'ev, "Series and sequences of polynomials of exponentials," *Trudy Matematicheskogo Instituta imeni V.A. Steklova*, vol. 176, pp. 308–325, 1987 (Russian).

[22] P. Bleher and R. Mallison Jr., "Zeros of sections of exponential sums," *International Mathematics Research Notices*, vol. 2006, Article ID 38937, 49 pages, 2006.

[23] V. V. Napalkov and S. G. Merzlyakov, "Entire functions of exponential type represented by using the gamma function," *Doklady Mathematics*, vol. 74, no. 2, pp. 748–750, 2006.

[24] M. Busłowicz, "Stability of linear continuous-time fractional order systems with delays of the retarded type," *Bulletin of the Polish Academy of Sciences*, vol. 56, no. 4, pp. 319–324, 2008.

[25] M. Buslowicz, "Robust stability of convex combination of two fractional degree characteristic polynomials," *Acta Mechanica et Automatica*, vol. 2, no. 2, pp. 5–10, 2008.

[26] M. Busłowicz, "Robust stability of positive continuous-time linear systems with delays," *International Journal of Applied Mathematics and Computer Science*, vol. 20, no. 4, pp. 665–670, 2010.

[27] M. Busłowicz, "Simple conditions for robust stability of positive discrete-time linear systems with delays," *Control and Cybernetics*, vol. 39, no. 4, pp. 1159–1171, 2010.

[28] T. Kaczorek, *Selected Problems of Fractional Systems Theory*, Springer, Berlin, Germany, 2011.

[29] T. Kaczorek and M. Busłowicz, "Minimal realization for positive multivariable linear systems with delay," *International Journal of Applied Mathematics and Computer Science*, vol. 14, no. 2, pp. 181–187, 2004.

[30] J. Sabatier, O. P. Agraval, and J. A. T. Machado, Eds., *Advances in Fractional Calculus*, Springer, Dordrecht, The Netherlands, 2007.

[31] D. Baleanu, Z. B. Güvenç, and J. A. T. Tenreiro Machado, Eds., *New Trends in Nanotechnology and Fractional Calculus Applications*, Springer, Dordrecht, The Netherlands, 2010.

[32] A. A. Kilbas, H. M. Srivastava, and J. J. Trujillo, *Theory and Applications of Fractional Differential Equations*, vol. 204 of *North-Holland Mathematics Studies*, Elsevier, Amsterdam, The Netherlands, 2006.

[33] I. Podlubny, *Fractional Differential Equations*, Academic Press, New York, NY, USA, 1999.

[34] S. G. Samko, A. A. Kilbas, and O. I. Marichev, *Fractional Integrals and Derivatives: Theory and Applications*, Gordon and Breach Science Publishers, New York, NY, USA, 1993.

[35] F. Merrikh-Bayat and M. Afshar, "Extending the root-locus method to fractional-order systems," *Journal of Applied Mathematics*, vol. 2008, Article ID 528934, 13 pages, 2008.

[36] R. Gorenflo and F. Mainardi, "Fractional calculus: integral and differential equations of fractional order," in *Fractals and Fractional Calculus in Continuum Mechanics*, vol. 378 of *CISM Courses and Lectures*, pp. 223–276, Springer, Berlin, Germany, 1997.

[37] R. Caponetto, G. Doongola, L. Fortuna, and I. Petras, *Fractional Order Systems: Modeling and Control Applications*, World Scientific, Singapore, 2010.

[38] A. M. Mathai and H. J. Haubold, *Special Functions for Applied Scientists*, Springer, New York, NY, USA, 2008.

[39] D. Matignon, "Stability result on fractional differential equations with applications to control processing," in *Proceedings of the International Meeting on Automated Compliance Systems and the International Conference on Systems, Man, and Cybernetics (IMACS-SMC '96)*, pp. 963–968, Lille, France, 1996.

[40] D. Matignon, "Stability properties for generalized fractional differential systems," in *Proceedings of the Fractional Differential Systems: Models, Methods and Applications*, pp. 145–158, 1998.

[41] H. Akcay and R. Malti, "On the completeness problem for fractional rationals with incommensurable differentiation orders," in *Proceedings of the 17th World Congress, International Federation of Automatic Control (IFAC '08)*, pp. 15367–15371, Soul, Korea, July 2008.

[42] L. S. Pontryagin, V. G. Boltyanskii, R. V. Gamkrelidze, and E. F. Mishchenko, *The Mathematical Theory of Optimal Processes*, John Wiley & Sons, New York, NY, USA, 1962.

[43] Y. Y. Liu, J. J. Slotine, and A. L. Barabasi, "Controllability of complex networks," *Nature*, vol. 473, pp. 167–173, 2011.

[44] D. Matignon and B. D'Andrea-Novel, "Some results on controllability and observability of nite-dimensional fractional differential systems," in *Proceedings of Computational Engineering in Systems Applications*, pp. 952–956, Lille, France, 1996.

[45] M. Aoun, R. Malti, F. Levron, and A. Oustaloup, "Numerical simulations of fractional systems: an overview of existing methods and improvements," *Nonlinear Dynamics*, vol. 38, no. 1–4, pp. 117–131, 2004.

[46] M. S. Tavazoei and M. Haeri, "Unreliability of frequency-domain approximation in recognising chaos in fractional-order systems," *IET Signal Processing*, vol. 1, no. 4, pp. 171–181, 2007.

[47] M. S. Tavazoei and M. Haeri, "A necessary condition for double scroll attractor existence in fractional-order systems," *Physics Letters A*, vol. 367, no. 1-2, pp. 102–113, 2007.

[48] M. S. Tavazoei and M. Haeri, "Limitations of frequency domain approximation for detecting chaos in fractional order systems," *Nonlinear Analysis. Theory, Methods & Applications A*, vol. 69, no. 4, pp. 1299–1320, 2008.

[49] C. A. Monje, Y. Chen, B. M. Vinagre, D. Xue, and V. Feliu, *Fractional-Order Systems and Controls: Fundamentals and Applications*, Springer, New York, NY, USA, 2010.

[50] S. Das, *Functional Fractional Calculus for System Identification and Controls*, Springer, Berlin, Germany, 2008.

[51] S. Das and I. Pan, *Fractional Order Signal Processing: Introductory Concepts and Applications*, Springer, Heidelberg, Germany, 2012.

[52] W. M. Haddad and V. Chellaboina, *Nonlinear Dynamical Systems and Control: A Lyapunov-Based Approach*, Princeton University Press, Princeton, NJ, USA, 2008.

[53] K. Balachandran, J. Y. Park, and J. J. Trujillo, "Controllability of nonlinear fractional dynamical systems," *Nonlinear Analysis. Theory, Methods & Applications A*, vol. 75, no. 4, pp. 1919–1926, 2012.

[54] A. Debbouche and D. Baleanu, "Controllability of fractional evolution nonlocal impulsive quasilinear delay integro-differential systems," *Computers & Mathematics with Applications*, vol. 62, no. 3, pp. 1442–1450, 2011.

[55] R. Dorville, G. M. Mophou, and V. S. Valmorin, "Optimal control of a nonhomogeneous Dirichlet boundary fractional diffusion equation," *Computers & Mathematics with Applications*, vol. 62, no. 3, pp. 1472–1481, 2011.

[56] M. Hazi and M. Bragdi, "Controllability of fractional integrodifferential systems via semigroup theory in Banach spaces," *Mathematical Journal of Okayama University*, vol. 54, pp. 133–143, 2012.

[57] V. Kavitha and M. M. Arjunan, "Controllability of impulsive quasi-linear fractional mixed Volterra-Fredholm-type integrodifferential equations in Banach spaces," *Journal of Nonlinear Science and its Applications*, vol. 4, no. 2, pp. 152–169, 2011.

[58] G. M. Mophou, "Optimal control of fractional diffusion equation," *Computers & Mathematics with Applications*, vol. 61, no. 1, pp. 68–78, 2011.

[59] D. Mozyrska and D. F. M. Torres, "Minimal modified energy control for fractional linear control systems with the Caputo derivative," *Carpathian Journal of Mathematics*, vol. 26, no. 2, pp. 210–221, 2010.

[60] R. Sakthivel, Y. Ren, and N. I. Mahmudov, "On the approximate controllability of semilinear fractional differential systems," *Computers & Mathematics with Applications*, vol. 62, no. 3, pp. 1451–1459, 2011.

[61] J. Si and W. Jiang, "The optimal control for a class of fractional differential equations," *International Journal of Biomathematics*, vol. 26, no. 1, pp. 17–24, 2011.

[62] N. Sukavanam and S. Kumar, "Approximate controllability of fractional order semilinear delay systems," *Journal of Optimization Theory and Applications*, vol. 151, no. 2, pp. 373–384, 2011.

[63] Z. Tai, "Controllability of fractional impulsive neutral integrodifferential systems with a nonlocal Cauchy condition in Banach spaces," *Applied Mathematics Letters*, vol. 24, no. 12, pp. 2158–2161, 2011.

[64] J. Wang and Y. Zhou, "Existence and controllability results for fractional semilinear differential inclusions," *Nonlinear Analysis. Real World Applications*, vol. 12, no. 6, pp. 3642–3653, 2011.

[65] J. Wang and Y. Zhou, "Analysis of nonlinear fractional control systems in Banach spaces," *Nonlinear Analysis. Theory, Methods & Applications A*, vol. 74, no. 17, pp. 5929–5942, 2011.

[66] J. Wang, Y. Zhou, W. Wei, and H. Xu, "Nonlocal problems for fractional integrodifferential equations via fractional operators and optimal controls," *Computers & Mathematics with Applications*, vol. 62, no. 3, pp. 1427–1441, 2011.

[67] C. Yeroglu and N. Tan, "Absolute stability of uncertain fractional order control systems," *Journal of Applied Functional Analysis*, vol. 6, no. 3, pp. 211–218, 2011.

[68] V. E. Tarasov, *Fractional Dynamics: Applications of Fractional Calculus to Dynamics of Particles, Fields and Media*, Springer, New York, NY, USA, 2010.

[69] I. Petráš, "Tuning and implementation methods for fractional-order controllers," *Fractional Calculus and Applied Analysis*, vol. 15, no. 2, pp. 282–303, 2012.

[70] Y. Luo and Y. Q. Chen, "Fractional-order [proportional derivative] controller for robust motion control: tuning procedure and validation," in *Proceedings of the American Control Conference (ACC '09)*, pp. 1412–1417, Hyatt Regency Riverfront, St. Louis, Mo, USA, June 2009.

[71] C. A. Monje, B. M. Vinagre, V. Feliu, and Y. Chen, "Tuning and auto-tuning of fractional order controllers for industry applications," *Control Engineering Practice*, vol. 16, no. 7, pp. 798–812, 2008.

[72] B. M. Vinagre, C. A. Monje, A. J. Caldern, and J. I. Surez, "Fractional PID controllers for industry application: a brief introduction," *Journal of Vibration and Control*, vol. 13, no. 9-10, pp. 1419–1429, 2007.

[73] A. Oustaloup, *La Derivation Non Entiere: Theorie, Synthese et Applications*, Hermes, Paris, France, 1995.

[74] H. W. Bode, *Network Analysis and Feedback Amplifier Design*, Tung Hwa Book Company, 1949.

[75] S. Manabe, "The non-integer integral and its application to control systems," *ETJ of Japan*, vol. 6, no. 3-4, pp. 83–87, 1961.

[76] B. J. Lurie, "Three-parameter tunable Tilt-Integral-Derivative (TID) controller," United States Patent, 5371670, 1994.

[77] T. Kaczorek, "Practical stability of positive fractional 2D linear systems," *Multidimensional Systems and Signal Processing*, vol. 21, no. 3, pp. 231–238, 2010.

[78] M. Busłowicz and T. Kaczorek, "Simple conditions for practical stability of positive fractional discrete-time linear systems," *International Journal of Applied Mathematics and Computer Science*, vol. 19, no. 2, pp. 263–269, 2009.

[79] S. E. Hamamci, "An algorithm for stabilization of fractional-order time delay systems using fractional-order PID controllers," *IEEE Transactions on Automatic Control*, vol. 52, no. 10, pp. 1964–1968, 2007.

[80] S. E. Hamamci and M. Koksal, "Calculation of all stabilizing fractional-order PD controllers for integrating time delay systems," *Computers & Mathematics with Applications*, vol. 59, no. 5, pp. 1621–1629, 2010.

[81] T. Liang, J. Chen, and C. Lei, "Algorithm of robust stability region for interval plant with time delay using fractional order $PI^{\lambda}D^{\mu}$ controller," *Communications in Nonlinear Science and Numerical Simulation*, vol. 17, no. 2, pp. 979–991, 2012.

[82] D. Baleanu, S. J. Sadati, R. Ghaderi, A. Ranjbar, T. Abdeljawad, and F. Jarad, "Razumikhin stability theorem for fractional systems with delay," *Abstract and Applied Analysis*, vol. 2010, Article ID 124812, 9 pages, 2010.

[83] D. Baleanu, A. Ranjbar N., S. J. Sadati R., H. Delavari, T. Abdeljawad, and V. Gejji, "Lyapunov-Krasovskii stability theorem for fractional systems with delay," *Romanian Journal of Physics*, vol. 56, no. 5-6, pp. 636–643, 2011.

[84] M. De la Sen, "Positivity and stability of the solutions of Caputo fractional linear time-invariant systems of any order with internal point delays," *Abstract and Applied Analysis*, vol. 2011, Article ID 161246, 25 pages, 2011.

[85] H. S. Najafi, A. Refahi Sheikhani, and A. Ansari, "Stability analysis of distributed order fractional differential equations," *Abstract and Applied Analysis*, vol. 2011, Article ID 175323, 12 pages, 2011.

[86] A. N. Kochubei, "Distributed order calculus and equations of ultraslow diffusion," *Journal of Mathematical Analysis and Applications*, vol. 340, no. 1, pp. 252–281, 2008.

[87] A. V. Letnikov and V. A. Chernykh, *The Foundations of Fractional Calculus*, Neftegaz, Moscow, Russia, 2011 (Russian).

[88] A. Dzieliński and D. Sierociuk, "Adaptive feedback control of fractional order discrete state-space systems," in *Proceedings of the International Conference on Computational Intelligence for Modelling, Control and Automation and the International Conference on Intelligent Agents, Web Technologies and Internet Commerce (CIMCA-IAWTIC'05)*, pp. 804–809, November 2005.

[89] S. Guermah, S. Djennoune, and M. Bettayeb, "A new approach for stability analysis of linear discrete-time fractional-order systems," in *New Trends in Nanotechnology and Fractional Calculus Applications*, D. Baleanu, Z. B. Güvenç, and J. A. Tenreiro Machado, Eds., pp. 151–162, Springer, Dordrecht, The Netherlands, 2010.

[90] F. Chen and Z. Liu, "Asymptotic stability results for nonlinear fractional difference equations," *Journal of Applied Mathematics*, vol. 2012, Article ID 879657, 14 pages, 2012.

[91] P. Ostalczyk, "Stability analysis of a discrete-time system with variablefractional-order control," *Bulletin of the Polish Academy of Sciences*, vol. 58, no. 4, pp. 613–619, 2010.

[92] J. Klamka, "Controllability and minimum energy control problem of fractional discrete-time systems," in *New Trends in Nanotechnology and Fractional Calculus Applications*, D. Baleanu, Z. B. Güvenç, and J. A. Tenreiro Machado, Eds., pp. 503–509, Springer, New York, NY, USA, 2010.

[93] A. Oustaloup, J. Sabatier, P. Lanusse, R. Malti, P. Melchior, and M. Moze, "An overview of the CRONE approach in system analysis, modeling and identification, observation and control," in *Proceedings of the 17th World Congress, International Federation of Automatic Control (IFAC '08)*, pp. 14254–14265, Soul, Korea, July 2008.

[94] Y. Li, Y. Chen, and I. Podlubny, "Mittag-Leffler stability of fractional order nonlinear dynamic systems," *Automatica*, vol. 45, no. 8, pp. 1965–1969, 2009.

[95] C. Yakar, "Fractional differential equations in terms of comparison results and Lyapunov stability with initial time difference," *Abstract and Applied Analysis*, vol. 2010, Article ID 762857, 16 pages, 2010.

[96] F. Zhang and C. Li, "Stability analysis of fractional differential systems with order lying in (1,2)," *Advances in Difference Equations*, vol. 2011, Article ID 213485, 2011.

[97] F. Zhang, C. Li, and Y. Chen, "Asymptotical stability of nonlinear fractional differential system with Caputo derivative," *International Journal of Differential Equations*, vol. 2011, Article ID 635165, 12 pages, 2011.

[98] J. A. Tenreiro Machado, "Root locus of fractional linear systems," *Communications in Nonlinear Science and Numerical Simulation*, vol. 16, no. 10, pp. 3855–3862, 2011.

[99] D. Valério and J. S. da Costa, "Tuning of fractional PID controllers with Ziegler-Nichols-type rules," *Signal Processing*, vol. 86, no. 10, pp. 2771–2784, 2006.

[100] A. I. Aptekarev and W. Van Assche, "Scalar and matrix Riemann-Hilbert approach to the strong asymptotics of Padé approximants and complex orthogonal polynomials with varying weight," *Journal of Approximation Theory*, vol. 129, no. 2, pp. 129–166, 2004.

[101] A. I. Aptekarev, "Asymptotics of Hermite-Padé approximants for a pair of functions with branch points," *Doklady Mathematics*, vol. 78, no. 2, pp. 717–719, 2008.

[102] A. I. Aptekarev, A. Kuijlaars, and W. Van Assche, "Asymptotics of Hermite-Pade rational approximants for two analytic functions with separated pairs of branch points (case of genus 0)," *International Mathematics Research Papers*, vol. 2008, Article ID rpm007, p. 128, 2008.

Hindawi Publishing Corporation
Mathematical Problems in Engineering
Volume 2013, Article ID 498781, 21 pages
http://dx.doi.org/10.1155/2013/498781

Research Article

Existence Results for a Coupled System of Nonlinear Singular Fractional Differential Equations with Impulse Effects

Yuji Liu,[1] Juan J. Nieto,[2,3] and Óscar Otero-Zarraquiños[2]

[1] *Department of Mathematics, Guangdong University of Business Studies, Guangzhou 510320, China*
[2] *Departamento de Análisis Matemático, Facultad de Matemáticas, Universidad de Santiago de Compostela, 15782 Santiago de Compostela, Spain*
[3] *Department of Mathematics, Faculty of Science, King Abdulaziz University, P.O. Box 80203, Jeddah 21589, Saudi Arabia*

Correspondence should be addressed to Juan J. Nieto; juanjose.nieto.roig@usc.es

Received 2 October 2012; Accepted 15 February 2013

Academic Editor: Jocelyn Sabatier

A boundary value problem for the singular fractional differential system with impulse effects is presented. By applying Schauder's fixed point theorem in a suitably Banach space, we obtain the existence of at least one solution for this problem. Two examples are presented to illustrate the main theorem.

1. Introduction

Fractional differential equations have received increasing attention during recent years since the behavior of many physical, chemical, and engineering processes can be properly described by using fractional differential equations theory; see the books [1–3], papers [4, 5] and references therein. For details on the geometric and physical interpretation of the derivatives of noninteger order, see, for example, [6–11]. For some recent works with applications to engineering we refer the reader to [12–15].

For an introduction of the basic theory of impulsive differential equation, we refer the reader to [16]. Among previous research, little is concerned with differential equations with fractional order with impulses [17]. Ahmad and Sivasundaram [18, 19] gave some existence results for two-point boundary value problems involving nonlinear impulsive hybrid differential equations of fractional order $1 < \alpha \leq 2$. Ahmad and Nieto in [20] establish sufficient conditions for the existence of solutions of the antiperiodic boundary value problem for impulsive differential equations with the Caputo derivative of order $q \in (1,2]$. Some recent results on impulsive initial value problems or boundary value problems for fractional differential equations on a finite interval can be found in [21–23] and references therein. The memory property of fractional calculus makes studies more complicated.

This paper is motivated by [24] in which the following boundary value problem for the fractional differential equation

$$\begin{gathered} D_{0^+}^{\alpha} x(t) = f\left(t, y(t), D_{0^+}^{p} y(t)\right), \quad t \in (0,1), \\ D_{0^+}^{\beta} y(t) = g\left(t, x(t), D_{0^+}^{q} x(t)\right), \quad t \in (0,1), \\ x(0) = 0, \quad y(0) = 0, \quad x(1) - \gamma x(\eta) = 0, \\ y(1) - \gamma y(\eta) = 0 \end{gathered} \tag{1}$$

was studied, where $1 < \alpha, \beta < 2$, $0 < p \leq \beta - 1$ and $0 < q \leq \alpha - 1$, $\gamma > 0$, $1 > \gamma\eta^{\alpha-1}$, $1 > \gamma\eta^{\beta-1}$ and $f, g : [0,1] \times R^2 \to R$ are continuous functions, and D_{0^+} is the Riemann-Liouville fractional derivative. An existence result was proved for BVP (1) in [24]. The growth assumptions imposed on f and g are sublinear cases (see [25, Theorem 3.1]); that is, there exist functions $a, b \in L^1(0,1)$, nonnegative constants $\epsilon_1, \epsilon_2 > 0$, $\delta_1, \delta_2 \geq 0$ and $\rho_1, \rho_2, \sigma_1, \sigma_2 \in (0,1)$ such that

$$\begin{gathered} \left|f(t,x,y)\right| \leq a(t) + \epsilon_1 |x|^{\rho_1} + \epsilon_2 |y|^{\rho_2}, \\ \left|g(t,x,y)\right| \leq b(t) + \delta_1 |x|^{\sigma_1} + \delta_2 |y|^{\sigma_2}. \end{gathered} \tag{2}$$

In [25], the following boundary value problem for the fractional differential equation

$$\begin{aligned} &D_{0^+}^{\alpha} x(t) = f\left(t, y(t), D_{0^+}^{p} y(t)\right), \quad t \in (0,1), \\ &D_{0^+}^{\beta} y(t) = g\left(t, x(t), D_{0^+}^{q} x(t)\right), \quad t \in (0,1), \\ &x(0) = 0, \quad y(0) = 0, \quad x(1) = 0, \quad y(1) = 0 \end{aligned} \tag{3}$$

was studied, where $1 < \alpha, \beta < 2$, $0 < p \le \beta - 1$ and $0 < q \le \alpha - 1$, and $f, g : [0,1] \times R^2 \to R$ are continuous functions, and D_{0^+} is the Riemann-Liouville fractional derivative. The growth assumptions imposed on f and g are sublinear cases (see [25, Theorem 3.1]), that is, there exist functions $a, b \in L^1(0,1)$, nonnegative constants $\epsilon_1, \epsilon_2 > 0$, $\delta_1, \delta_2 \ge 0$, and $\rho_1, \rho_2, \sigma_1, \sigma_2 \in (0,1]$ such that

$$\begin{aligned} &\left|f(t,x,y)\right| \le a(t) + \epsilon_1 |x|^{\rho_1} + \epsilon_2 |y|^{\rho_2}, \\ &\left|g(t,x,y)\right| \le b(t) + \delta_1 |x|^{\sigma_1} + \delta_2 |y|^{\sigma_2}, \end{aligned} \tag{4}$$

or sublinear cases, that is, there exist nonnegative constants $\epsilon_1, \epsilon_2 > 0$, $\delta_1, \delta_2 \ge 0$ and $\rho_1, \rho_2, \sigma_1, \sigma_2 \in (1, \infty)$ such that

$$\begin{aligned} &\left|f(t,x,y)\right| \le \epsilon_1 |x|^{\rho_1} + \epsilon_2 |y|^{\rho_2}, \\ &\left|g(t,x,y)\right| \le \delta_1 |x|^{\sigma_1} + \delta_2 |y|^{\sigma_2}. \end{aligned} \tag{5}$$

We find that in the superlinear cases, BVP (3) has a pair of solutions $(x, y) = (0, 0)$ without needing any other assumptions. Hence, these cases are trivial ones discussed in [25].

It is interesting to consider the solvability of BVP (1) when the growth assumptions imposed on f, g are superlinear cases. Furthermore, the solvability of BVP (1) is not studied when $q > \alpha - 1$ or $p > \beta - 1$.

In this paper we consider the following nonlinear boundary value problem for the singular multiterm fractional differential equation with impulse effects whose boundary conditions are of integral form

$$\begin{aligned} &D_{0^+}^{\alpha} x(t) = \phi(t) f\left(t, y(t), D_{0^+}^{p} y(t)\right), \\ &\qquad t \in (0,1), \quad t \ne t_1, \\ &D_{0^+}^{\beta} y(t) = \psi(t) g\left(t, x(t), D_{0^+}^{q} x(t)\right), \\ &\qquad t \in (0,1), \quad t \ne t_1, \\ &\lim_{t \to 0} t^{2-\alpha} x(t) = \int_0^1 u(s) G\left(s, y(s), D_{0^+}^{p} y(s)\right) ds, \\ &\lim_{t \to 0} t^{2-\beta} y(t) = \int_0^1 v(s) H\left(s, x(s), D_{0^+}^{q} x(s)\right) ds, \\ &x(1) = \int_0^1 m(s) M\left(s, y(s), D_{0^+}^{p} y(s)\right) ds, \\ &y(1) = \int_0^1 n(s) N\left(s, x(s), D_{0^+}^{q} x(s)\right) ds, \end{aligned} \tag{6}$$

$$\begin{aligned} &\Delta x(t_1) = \lim_{t \to t_1^+} x(t) - \lim_{t \to t_1^-} x(t) = I\left(t_1, y(t_1), D_{0^+}^{p} y(t_1)\right), \\ &\Delta y(t_1) = \lim_{t \to t_1^+} y(t) - \lim_{t \to t_1^-} y(t) = J\left(t_1, x(t_1), D_{0^+}^{q} x(t_1)\right), \\ &\Delta D_{0^+}^{q} x(t_1) = \lim_{t \to t_1^+} D_{0^+}^{q} x(t) - \lim_{t \to t_1^-} D_{0^+}^{q} x(t) \\ &\qquad = I_1\left(t_1, y(t_1), D_{0^+}^{p} y(t_1)\right), \\ &\Delta D_{0^+}^{p} y(t_1) = \lim_{t \to t_1^+} D_{0^+}^{p} y(t) - \lim_{t \to t_1^-} D_{0^+}^{p} y(t) \\ &\qquad = J_1\left(t_1, x(t_1), D_{0^+}^{q} x(t_1)\right), \end{aligned} \tag{7}$$

where

(a) $1 < \alpha, \beta \le 2$, $0 < p < \beta$ and $0 < q < \alpha$, D_{0^+} is the Riemann-Liouville fractional derivative,

(b) $\phi, \psi : (0,1) \to R$, f, g defined on $(0,1) \times R^2$,

(c) $m, n, u, v : (0,1) \to R$ with $m, n, u, v \in L^1(0,1)$, G, H, M, N defined on $(0,1) \times R^2$,

(d) $0 = t_0 < t_1 < t_2 = 1$,

(e) $I, I_1, J, J_1 : (0,1) \times R^2 \to R$.

A pair of functions (x, y) defined on $(0,1)$ is called a solution of BVP (1) and BVP (3), if $x|_{(t_k, t_{k+1}]}$, $D_{0^+}^{q} x|_{(t_k, t_{k+1}]}$ and $y|_{(t_k, t_{k+1}]}$, $D_{0^+}^{p} y|_{(t_k, t_{k+1}]}$ $(k = 0, 1)$ are continuous, there exists the limits

$$\begin{aligned} &\lim_{t \to t_k^+} t^{2-\alpha} x(t), \qquad \lim_{t \to t_k^+} t^{2-\beta} y(t), \\ &\lim_{t \to t_k^+} t^{2+q-\alpha} D_{0^+}^{q} x(t), \qquad \lim_{t \to t_k^+} t^{2+p-\beta} D_{0^+}^{p} y(t), \\ &\qquad k = 0, 1, \end{aligned} \tag{8}$$

$D_{0^+}^{\alpha} x, D_{0^+}^{\beta} y \in L^1(0,1)$ and (x, y) satisfies all equations in (6) and (7).

The novelty of this paper is as follows: first, the fractional differential equations in (6) are multiterm ones and their nonlinearities f, g depend on the lower fractional derivatives; second, both ϕ and ψ may be singular at $t = 0$ and $t = 1$, that is, $\phi(t) f(t, x, y)$ and $\psi(t) g(t, x, y)$ may be not continuous functions on $[0,1] \times R^2$, the boundary conditions are integral boundary conditions, and we obtain the results on the existence of at least one solution of BVP (6)-(7); third, $0 < p < \beta$ and $0 < q < \alpha$ are supposed; the growth assumptions imposed on f, g, G, H, M, N and I, I_1, J, J_1 are allowed to be sublinear cases. Finally, two examples are given to illustrate the efficiency of the main theorem.

The remainder of this paper is as follows: in Section 2, we present preliminary results. In Section 3, the main theorem and its proof are given. In Section 4, two examples are given to illustrate the main results.

2. Preliminaries

In this section, we present some background definitions and preliminary results.

Definition 1 (see [1]). The Riemann-Liouville fractional integral of order $\alpha > 0$ of a function $g : (0,\infty) \to R$ is given by

$$I_{0^+}^{\alpha} g(t) = \frac{1}{\Gamma(\alpha)} \int_0^t (t-s)^{\alpha-1} g(s)\, ds, \tag{9}$$

provided that the right-hand side exists.

Definition 2 (see [1]). The Riemann-Liouville fractional derivative of order $\alpha > 0$ of a continuous function $g : (0,\infty) \to R$ is given by

$$D_{0^+}^{\alpha} g(t) = \frac{1}{\Gamma(n-\alpha)} \frac{d^n}{dt^n} \int_0^t \frac{g(s)}{(t-s)^{\alpha-n+1}} ds, \tag{10}$$

where $n-1 \le \alpha < n$, provided that the right-hand side is pointwise defined on $(0,\infty)$.

Definition 3. $K : (0,1) \times R^2 \to R$ is called a β-Caratheodory function if K satisfies that

(i) $t \to K(t, t^{\beta-2}U, t^{\beta-p-2}V)$ is continuous on $(t_k, t_{k+1}]$ $(k = 0,1)$ for every $(U,V) \in R^2$;

(ii) $(U,V) \to K(t, t^{\beta-2}U, t^{\beta-p-2}V)$ is continuous on R^2 for every $t \in (0,1)$;

(iii) for each $r > 0$ there exists a constant $A_r > 0$ such that $|K(t, t^{\beta-2}U, t^{\beta-p-2}V)| \le A_r$, $t \in (0,1)$, $|U|, |V| \le r$.

Definition 4. $Q : (0,1) \times R^2 \to R$ is called a α-Caratheodory function if Q satisfies that

(i) $t \to Q(t, t^{\alpha-2}U, t^{\alpha-q-2}V)$ is continuous on $(t_k, t_{k+1}]$ $(k = 0,1)$ for every $(U,V) \in R^2$;

(ii) $(U,V) \to Q(t, t^{\alpha-2}U, t^{\alpha-q-2}V)$ is continuous on R^2 for every $t \in (0,1)$;

(iii) for each $r > 0$ there exists a constant $B_r > 0$ such that $|Q(t, t^{\alpha-2}U, t^{\alpha-q-2}V)| \le B_r$, $t \in (0,1)$, $|U|, |V| \le r$.

Lemma 5 (the Leray-Schauder nonlinear alternative [23]). *Let X be a Banach space and $T : X \to X$ be a completely continuous operator. Suppose Ω is a nonempty open subset of X centered at zero. Then either there exists $x \in \partial\Omega$ and $\lambda \in (0,1)$ such that $x = \lambda Tx$ or there exists $x \in \overline{\Omega}$ such that $x = Tx$.*

Let the gamma and beta functions $\Gamma(\alpha)$ and $\mathbf{B}(p,q)$ be defined by

$$\Gamma(\alpha) = \int_0^{+\infty} x^{\alpha-1} e^{-x} dx,$$

$$\mathbf{B}(p,q) = \int_0^1 x^{p-1}(1-x)^{q-1} dx, \tag{11}$$

$$\|m\|_1 = \int_0^1 |m(s)|\, ds \quad \text{for } m \in L^1(0,1).$$

Choose

$$X = \left\{ x : (0,1] \longrightarrow R \;\; \begin{array}{l} x|_{(t_k,t_{k+1}]} \in C^0(t_k, t_{k+1}]\ (k=0,1), \\ D_{0^+}^q x|_{(t_k,t_{k+1}]} \in C^0(t_k, t_{k+1}]\ (k=0,1), \\ \text{there exist the limits} \\ \lim\limits_{t\to t_k^+} t^{2-\alpha} x(t), \\ \lim\limits_{t\to t_k^+} t^{2+q-\alpha} D_{0^+}^q x(t) \end{array} \right\},$$

$$Y = \left\{ y : (0,1] \longrightarrow R \;\; \begin{array}{l} y|_{(t_k,t_{k+1}]} \in C^0(t_k, t_{k+1}]\ (k=0,1), \\ D_{0^+}^p x|_{(t_k,t_{k+1}]} \in C^0(t_k, t_{k+1}]\ (k=0,1), \\ \text{there exist the limits} \\ \lim\limits_{t\to t_k^+} t^{2-\beta} y(t), \\ \lim\limits_{t\to t_k^+} t^{2+p-\beta} D_{0^+}^p y(t) \end{array} \right\}. \tag{12}$$

For $x \in X$, define the norm by

$$\begin{aligned} \|x\| &= \|x\|_X \\ &= \max\left\{ \sup_{t\in(0,1)} t^{2-\alpha} |x(t)|,\ \sup_{t\in(0,1)} t^{2+q-\alpha} \left|D_{0^+}^q x(t)\right| \right\}. \end{aligned} \tag{13}$$

It is easy to show that X is a real Banach space. For $y \in Y$, define the norm by

$$\begin{aligned} \|y\| &= \|y\|_Y \\ &= \max\left\{ \sup_{t\in(0,1)} t^{2-\beta} |y(t)|,\ \sup_{t\in(0,1)} t^{2+p-\beta} \left|D_{0^+}^p y(t)\right| \right\}. \end{aligned} \tag{14}$$

It is easy to show that Y is a real Banach space. Thus, $(X \times Y, \|\cdot\|)$ is a Banach space with the norm defined by $\|(x,y)\| = \max\{\|x\|_X, \|y\|_Y\}$ for $(x,y) \in X \times Y$.

In this paper, we suppose the following:

(A) ϕ satisfies that there exist constants $L_1 > 0$, $k > -1$, $\delta \in (q-\alpha, 0]$ such that $\alpha + 2\delta - q > 0$, $\alpha + k + \delta - q \ge 0$, and $|\phi(t)| \le L_1 t^k (1-t)^{\delta}$ for all $t \in (0,1)$; ψ satisfies that there exist constants $L_2 > 0$, $l > -1$, $\theta \in (p-\beta, 0]$ such that $\beta + 2\theta - p > 0$, $\beta + l + \theta - p \ge 0$, and $|\psi(t)| \le L_2 t^l (1-t)^{\theta}$ for all $t \in (0,1)$.

(B) f, G, M, I, I_1 are β-Caratheodory functions and g, H, N, J, J_1 are α-Caratheodory functions.

Remark 6. Suppose that f is a β-Caratheodory function. For example, $\alpha = 7/4$, $q = 1/8$, choose $k = -1/2$, $\delta = -3/4$ and $\phi(t) = t^k(1-t)^{\delta}$, then $k > -1$, $\delta \in (-\alpha, 0]$ such that $\alpha + 2\delta - q > 0$, $\alpha + k + \delta - q \ge 0$, and $|\phi(t)| \le t^k(1-t)^{\delta}$ for all $t \in (0,1)$. It is easy to see that ϕ is singular at $t = 0$ and $t = 1$.

Lemma 7. *Suppose that $y \in Y$, and (a)–(e), (A)-(B) hold. Then $x \in X$ is a solution of*

$$\begin{aligned} D_{0^+}^{\alpha} x(t) &= \phi(t) f\left(t, y(t), D_{0^+}^{p} y(t)\right), \quad t \in (0,1),\ t \neq t_1, \\ \lim_{t \to 0} t^{2-\alpha} x(t) &= \int_0^1 u(s) G\left(s, y(s), D_{0^+}^{p} y(s)\right) ds, \\ x(1) &= \int_0^1 m(s) M\left(s, y(s), D_{0^+}^{p} y(s)\right) ds, \\ \Delta x(t_1) &= I\left(t_1, y(t_1), D_{0^+}^{p} y(t_1)\right), \\ \Delta D_{0^+}^{q} x(t_1) &= I_1\left(t_1, y(t_1), D_{0^+}^{p} y(t_1)\right), \end{aligned} \tag{15}$$

if and only if $x \in X$ satisfies the integral equation

$$x(t) = \begin{cases} \displaystyle\int_0^t \frac{(t-s)^{\alpha-1}}{\Gamma(\alpha)} \phi(u) f\left(u, y(u), D_{0^+}^{p} y(u)\right) du \\ \quad - \dfrac{t^{\alpha-1}}{\Gamma(\alpha)} \\ \quad \times \displaystyle\int_0^1 (1-s)^{\alpha-1} \phi(s) f\left(s, y(s), D_{0^+}^{p} y(s)\right) ds \\ \quad + t^{\alpha-2} \displaystyle\int_0^1 u(s) G\left(s, y(s), D_{0^+}^{p} y(s)\right) ds \\ \quad + t^{\alpha-1} \displaystyle\int_0^1 m(s) M\left(s, y(s), D_{0^+}^{p} y(s)\right) ds \\ \quad + \dfrac{t^{\alpha-1}}{\Pi} \\ \quad \times \left(\dfrac{\Gamma(\alpha)}{\Gamma(\alpha-q)} t_1^{\alpha-q-1} - \dfrac{\Gamma(\alpha-1)}{\Gamma(\alpha-q-2)} t_1^{\alpha-q-2} \right) \\ \quad \times I\left(t_1, y(t_1), D_{0^+}^{p} y(t_1)\right) \\ \quad + \dfrac{t^{\alpha-1}\left(t_1^{\alpha-2} - t_1^{\alpha-1}\right)}{\Pi} \\ \quad \times I_1\left(t_1, y(t_1), D_{0^+}^{p} y(t_1)\right), \quad t \in (0, t_1], \\ \displaystyle\int_0^t \frac{(t-s)^{\alpha-1}}{\Gamma(\alpha)} \phi(s) f\left(s, y(s), D_{0^+}^{p} y(s)\right) ds \\ \quad - \dfrac{t^{\alpha-1}}{\Gamma(\alpha)} \\ \quad \times \displaystyle\int_0^1 (1-s)^{\alpha-1} \phi(s) f\left(s, y(s), D_{0^+}^{p} y(s)\right) ds \\ \quad + \left(t^{\alpha-2} - t^{\alpha-1}\right) \\ \quad \times \displaystyle\int_0^1 u(s) G\left(s, y(s), D_{0^+}^{p} y(s)\right) ds \\ \quad + t^{\alpha-1} \displaystyle\int_0^1 m(s) M\left(s, y(s), D_{0^+}^{p} y(s)\right) ds \\ \quad + \dfrac{t^{\alpha-1} - t^{\alpha-2}}{\Pi} \dfrac{\Gamma(\alpha)}{\Gamma(\alpha-q)} t_1^{\alpha-q-1} \\ \quad \times I\left(t_1, y(t_1), D_{0^+}^{p} y(t_1)\right) \\ \quad + \dfrac{t^{\alpha-2} - t^{\alpha-1}}{\Pi} t_1^{\alpha-1} I_1\left(t_1, y(t_1), D_{0^+}^{p} y(t_1)\right), \\ \qquad\qquad t \in (t_1, 1], \end{cases} \tag{16}$$

where

$$\Pi = \left(\frac{\Gamma(\alpha-1)}{\Gamma(\alpha-q-1)} - \frac{\Gamma(\alpha)}{\Gamma(\alpha-q)} \right) t_1^{2\alpha-q-3}. \tag{17}$$

Proof. If $y \in Y$ is a solution of BVP (15), then

$$\begin{aligned} \|y\| &= \max\left\{ \sup_{t \in (0,1)} t^{2-\beta} |y(t)|,\ \sup_{t \in (0,1)} t^{2+p-\beta} \left|D_{0^+}^{p} y(t)\right| \right\} \\ &= r < +\infty, \end{aligned} \tag{18}$$

and x satisfies all equations in (31) From (B), f is a β-Caratheodory function, then there exists $A_r > 0$ such that

$$\begin{aligned} &\left| f\left(t, y(t), D_{0^+}^{p} y(t)\right) \right| \\ &\quad = \left| f\left(t, t^{\beta-2} t^{2-\beta} y(t), t^{\beta-p-2} t^{2+p-\beta} D_{0^+}^{p} y(t)\right) \right| \le A_r. \end{aligned} \tag{19}$$

Similarly we get that there exist constants $A_r', A_r'', B_r', B_r'' > 0$ such that

$$\begin{aligned} \left| G\left(t, y(t), D_{0^+}^{p} y(t)\right) \right| &\le A_r', \\ \left| M\left(t, y(t), D_{0^+}^{p} y(t)\right) \right| &\le A_r'', \\ & t \in (0,1), \\ \left| I\left(t_1, y(t_1), D_{0^+}^{p} y(t_1)\right) \right| &\le B_r', \\ \left| I_1\left(t_1, y(t_1), D_{0^+}^{p} y(t_1)\right) \right| &\le B_r''. \end{aligned} \tag{20}$$

It follows from (15) that, for $t \in (t_k, t_{k+1}] (k = 0, 1)$, there exist constants $c_k, d_k \in R$ such that

$$\begin{aligned} x(t) = &\frac{1}{\Gamma(\alpha)} \int_0^t (t-s)^{\alpha-1} \phi(s) f\left(s, y(s), D_{0^+}^{p} y(s)\right) ds \\ &+ c_k t^{\alpha-1} + d_k t^{\alpha-2}, \quad t \in \left(t_k, t_{k+1}\right],\ k = 0, 1. \end{aligned} \tag{21}$$

From $\lim_{t \to 0} t^{2-\alpha} x(t) = \int_0^1 u(s) G(s, y(s), D_{0^+}^{p} y(s)) ds$, we get

$$d_0 = \int_0^1 u(s) G\left(s, y(s), D_{0^+}^{p} y(s)\right) ds. \tag{22}$$

From $x(1) = \int_0^1 m(s) M(s, y(s), D_{0^+}^{p} y(s)) ds$, we get

$$\begin{aligned} &\frac{1}{\Gamma(\alpha)} \int_0^1 (1-s)^{\alpha-1} \phi(s) f\left(s, y(s), D_{0^+}^{p} y(s)\right) ds + c_1 + d_1 \\ &\quad = \int_0^1 m(s) M\left(s, y(s), D_{0^+}^{p} y(s)\right) ds. \end{aligned} \tag{23}$$

From $\Delta x(t_1) = I(t_1, y(t_1), D_{0^+}^{p} y(t_1))$, we get

$$\left(c_1 - c_0\right) t_1^{\alpha-1} + \left(d_1 - d_0\right) t_1^{\alpha-2} = I\left(t_1, y(t_1), D_{0^+}^{p} y(t_1)\right). \tag{24}$$

From $\Delta D_{0^+}^{q} x(t_1) = I_1(t_1, y(t_1), D_{0^+}^{p} y(t_1))$, we get

$$(c_1 - c_0)\frac{\Gamma(\alpha)}{\Gamma(\alpha-q)}t_1^{\alpha-q-1} + (d_1 - d_0)\frac{\Gamma(\alpha-1)}{\Gamma(\alpha-q-2)}t_1^{\alpha-q-2} = I_1\left(t_1, y(t_1), D_{0^+}^{p} y(t_1)\right). \tag{25}$$

It follows that

$$\begin{aligned} c_1 - c_0 &= \left(\frac{\Gamma(\alpha-1)}{\Gamma(\alpha-q-2)}t_1^{\alpha-q-2} I\left(t_1, y(t_1), D_{0^+}^{p} y(t_1)\right) - t_1^{\alpha-2} I_1\left(t_1, y(t_1), D_{0^+}^{p} y(t_1)\right)\right) \times (\Pi)^{-1}, \\ d_1 - d_0 &= \left(t_1^{\alpha-1} I_1\left(t_1, y(t_1), D_{0^+}^{p} y(t_1)\right) - \frac{\Gamma(\alpha)}{\Gamma(\alpha-q)}t_1^{\alpha-q-1} I\left(t_1, y(t_1), D_{0^+}^{p} y(t_1)\right)\right) \times (\Pi)^{-1}. \end{aligned} \tag{26}$$

Then

$$\begin{aligned} d_1 = {} & \left(t_1^{\alpha-1} I_1\left(t_1, y(t_1), D_{0^+}^{p} y(t_1)\right) - \frac{\Gamma(\alpha)}{\Gamma(\alpha-q)}t_1^{\alpha-q-1} I\left(t_1, y(t_1), D_{0^+}^{p} y(t_1)\right)\right) \times (\Pi)^{-1} \\ & + \int_0^1 u(s) G\left(s, y(s), D_{0^+}^{p} y(s)\right) ds. \end{aligned} \tag{27}$$

So

$$\begin{aligned} c_1 = {} & \int_0^1 m(s) M\left(s, y(s), D_{0^+}^{p} y(s)\right) ds \\ & - \frac{1}{\Gamma(\alpha)}\int_0^1 (1-s)^{\alpha-1}\phi(s) f\left(s, y(s), D_{0^+}^{p} y(s)\right) ds \\ & - \left(t_1^{\alpha-1} I_1\left(t_1, y(t_1), D_{0^+}^{p} y(t_1)\right) - \frac{\Gamma(\alpha)}{\Gamma(\alpha-q)}t_1^{\alpha-q-1} I\left(t_1, y(t_1), D_{0^+}^{p} y(t_1)\right)\right) \times (\Pi)^{-1} \\ & - \int_0^1 u(s) G\left(s, y(s), D_{0^+}^{p} y(s)\right) ds, \\ c_0 = {} & \int_0^1 m(s) M\left(s, y(s), D_{0^+}^{p} y(s)\right) ds \\ & - \frac{1}{\Gamma(\alpha)}\int_0^1 (1-s)^{\alpha-1}\phi(s) f\left(s, y(s), D_{0^+}^{p} y(s)\right) ds \\ & - \left(t_1^{\alpha-1} I_1\left(t_1, y(t_1), D_{0^+}^{p} y(t_1)\right) - \frac{\Gamma(\alpha)}{\Gamma(\alpha-q)}t_1^{\alpha-q-1} I\left(t_1, y(t_1), D_{0^+}^{p} y(t_1)\right)\right) \times (\Pi)^{-1} \\ & - \int_0^1 u(s) G\left(s, y(s), D_{0^+}^{p} y(s)\right) ds \\ & - \left(\frac{\Gamma(\alpha-1)}{\Gamma(\alpha-q-2)}t_1^{\alpha-q-2} I\left(t_1, y(t_1), D_{0^+}^{p} y(t_1)\right) - t_1^{\alpha-2} I_1\left(t_1, y(t_1), D_{0^+}^{p} y(t_1)\right)\right) \times (\Pi)^{-1}. \end{aligned} \tag{28}$$

Hence, for $t \in (0, t_1]$, we have

$$\begin{aligned} x(t) = {} & \int_0^t \frac{(t-s)^{\alpha-1}}{\Gamma(\alpha)}\phi(u) f\left(u, y(u), D_{0^+}^{p} y(u)\right) du \\ & - \frac{t^{\alpha-1}}{\Gamma(\alpha)}\int_0^1 (1-s)^{\alpha-1}\phi(s) f\left(s, y(s), D_{0^+}^{p} y(s)\right) ds \\ & + t^{\alpha-2}\int_0^1 u(s) G\left(s, y(s), D_{0^+}^{p} y(s)\right) ds \\ & + t^{\alpha-1}\int_0^1 m(s) M\left(s, y(s), D_{0^+}^{p} y(s)\right) ds \\ & + \frac{t^{\alpha-1}}{\Pi}\left(\frac{\Gamma(\alpha)}{\Gamma(\alpha-q)}t_1^{\alpha-q-1} - \frac{\Gamma(\alpha-1)}{\Gamma(\alpha-q-2)}t_1^{\alpha-q-2}\right) \times I\left(t_1, y(t_1), D_{0^+}^{p} y(t_1)\right) \\ & + \frac{t^{\alpha-1}\left(t_1^{\alpha-2} - t_1^{\alpha-1}\right)}{\Pi} I_1\left(t_1, y(t_1), D_{0^+}^{p} y(t_1)\right). \end{aligned} \tag{29}$$

And for $t \in (t_1, 1]$, we have

$$\begin{aligned} x(t) = {} & \int_0^t \frac{(t-s)^{\alpha-1}}{\Gamma(\alpha)}\phi(s) f\left(s, y(s), D_{0^+}^{p} y(s)\right) ds \\ & - \frac{t^{\alpha-1}}{\Gamma(\alpha)}\int_0^1 (1-s)^{\alpha-1}\phi(s) f\left(s, y(s), D_{0^+}^{p} y(s)\right) ds \\ & + \left(t^{\alpha-2} - t^{\alpha-1}\right)\int_0^1 u(s) G\left(s, y(s), D_{0^+}^{p} y(s)\right) ds \\ & + t^{\alpha-1}\int_0^1 m(s) M\left(s, y(s), D_{0^+}^{p} y(s)\right) ds \\ & + \frac{t^{\alpha-1} - t^{\alpha-2}}{\Pi}\frac{\Gamma(\alpha)}{\Gamma(\alpha-q)}t_1^{\alpha-q-1} \times I\left(t_1, y(t_1), D_{0^+}^{p} y(t_1)\right) \\ & + \frac{t^{\alpha-2} - t^{\alpha-1}}{\Pi} t_1^{\alpha-1} I_1\left(t_1, y(t_1), D_{0^+}^{p} y(t_1)\right). \end{aligned} \tag{30}$$

Hence, $x \in X$ satisfies (16).

On the other hand, if $y \in Y$ and $x \in X$ is a solution of (16), then we can prove that $x \in X$ is a solution of BVP (6)-(7). The proof is completed. □

Lemma 8. *Suppose that $x \in X$, and (a)–(e), (A)-(B) hold. Then $y \in Y$ is a solution of*

$$\begin{aligned} D_{0^+}^{\beta} y(t) &= \psi(t)\, g\left(t, x(t), D_{0^+}^{q} x(t)\right), \quad t \in (0,1),\ t \neq t_1, \\ \lim_{t\to 0} t^{2-\beta} y(t) &= \int_0^1 v(s)\, H\left(s, x(s), D_{0^+}^{q} x(s)\right) ds, \\ y(1) &= \int_0^1 n(s)\, N\left(s, x(s), D_{0^+}^{q} x(s)\right) ds, \\ \Delta y(t_1) &= J\left(t_1, x(t_1), D_{0^+}^{q} x(t_1)\right), \\ \Delta D_{0^+}^{p} y(t_1) &= J_1\left(t_1, x(t_1), D_{0^+}^{q} x(t_1)\right), \end{aligned} \tag{31}$$

if and only if $y \in Y$ satisfies the integral equation

$$y(t) = \begin{cases} \displaystyle\int_0^t \frac{(t-s)^{\beta-1}}{\Gamma(\beta)} \psi(u)\, g\left(u, x(u), D_{0^+}^{q} x(u)\right) du \\ \quad - \dfrac{t^{\beta-1}}{\Gamma(\beta)} \\ \quad \times \displaystyle\int_0^1 (1-s)^{\beta-1} \psi(s)\, g\left(s, x(s), D_{0^+}^{q} x(s)\right) ds \\ \quad + t^{\beta-2} \\ \quad \times \displaystyle\int_0^1 v(s)\, H\left(s, y(s), D_{0^+}^{p} y(s)\right) ds \\ \quad + t^{\beta-1} \\ \quad \times \displaystyle\int_0^1 n(s)\, N\left(s, x(s), D_{0^+}^{q} x(s)\right) ds \\ \quad + \dfrac{t^{\beta-1}}{\Xi} \\ \quad \times \left(\dfrac{\Gamma(\beta)}{\Gamma(\beta-p)} t_1^{\beta-p-1} - \dfrac{\Gamma(\beta-1)}{\Gamma(\beta-p-2)} t_1^{\beta-p-2} \right) \\ \quad \times J\left(t_1, x(t_1), D_{0^+}^{q} x(t_1)\right) \\ \quad + \dfrac{t^{\beta-1}\left(t_1^{\beta-2} - t_1^{\beta-1}\right)}{\Xi} \\ \quad \times J_1\left(t_1, x(t_1), D_{0^+}^{q} x(t_1)\right), \quad t \in (0, t_1], \\ \displaystyle\int_0^t \frac{(t-s)^{\beta-1}}{\Gamma(\beta)} \psi(s)\, g\left(s, x(s), D_{0^+}^{q} x(s)\right) ds \\ \quad - \dfrac{t^{\beta-1}}{\Gamma(\beta)} \\ \quad \times \displaystyle\int_0^1 (1-s)^{\beta-1} \psi(s)\, g\left(s, x(s), D_{0^+}^{q} x(s)\right) ds \\ \quad + \left(t^{\beta-2} - t^{\beta-1}\right) \\ \quad \times \displaystyle\int_0^1 v(s)\, H\left(s, y(s), D_{0^+}^{p} y(s)\right) ds \\ \quad + t^{\beta-1} \\ \quad \times \displaystyle\int_0^1 n(s)\, N\left(s, x(s), D_{0^+}^{q} x(s)\right) ds \\ \quad + \dfrac{t^{\beta-1} - t^{\beta-2}}{\Xi} \dfrac{\Gamma(\beta)}{\Gamma(\beta-p)} t_1^{\beta-p-1} \\ \quad \times J\left(t_1, x(t_1), D_{0^+}^{q} x(t_1)\right) \\ \quad + \dfrac{t^{\beta-2} - t^{\beta-1}}{\Xi} t_1^{\beta-1} \\ \quad \times J_1\left(t_1, x(t_1), D_{0^+}^{q} x(t_1)\right), \quad t \in (t_1, 1], \end{cases} \tag{32}$$

where

$$\Xi = \left(\frac{\Gamma(\beta-1)}{\Gamma(\beta-p-1)} - \frac{\Gamma(\beta)}{\Gamma(\beta-p)} \right) t_1^{2\beta-p-3}. \tag{33}$$

Proof. The proof is similar to that of the proof of Lemma 7 and is omitted.

Now, we define the operator T on $X \times Y$ by $T(x, y)(t) = ((T_1 y)(t), (T_2 x)(t))$ with

$$(T_1 y)(t) = \begin{cases} \displaystyle\int_0^t \frac{(t-s)^{\alpha-1}}{\Gamma(\alpha)} \phi(u)\, f\left(u, y(u), D_{0^+}^{p} y(u)\right) du \\ \quad - \dfrac{t^{\alpha-1}}{\Gamma(\alpha)} \displaystyle\int_0^1 (1-s)^{\alpha-1} \phi(s)\, f\left(s, y(s), D_{0^+}^{p} y(s)\right) ds \\ \quad + t^{\alpha-2} \displaystyle\int_0^1 u(s)\, G\left(s, y(s), D_{0^+}^{p} y(s)\right) ds \\ \quad + t^{\alpha-1} \displaystyle\int_0^1 m(s)\, M\left(s, y(s), D_{0^+}^{p} y(s)\right) ds \\ \quad + \dfrac{t^{\alpha-1}}{\Pi} \left(\dfrac{\Gamma(\alpha)}{\Gamma(\alpha-q)} t_1^{\alpha-q-1} - \dfrac{\Gamma(\alpha-1)}{\Gamma(\alpha-q-2)} t_1^{\alpha-q-2} \right) \\ \quad \times I\left(t_1, y(t_1), D_{0^+}^{p} y(t_1)\right) \\ \quad + \dfrac{t^{\alpha-1}\left(t_1^{\alpha-2} - t_1^{\alpha-1}\right)}{\Pi} \\ \quad \times I_1\left(t_1, y(t_1), D_{0^+}^{p} y(t_1)\right), \quad t \in (0, t_1], \\ \displaystyle\int_0^t \frac{(t-s)^{\alpha-1}}{\Gamma(\alpha)} \phi(s)\, f\left(s, y(s), D_{0^+}^{p} y(s)\right) ds \\ \quad - \dfrac{t^{\alpha-1}}{\Gamma(\alpha)} \displaystyle\int_0^1 (1-s)^{\alpha-1} \phi(s)\, f\left(s, y(s), D_{0^+}^{p} y(s)\right) ds \\ \quad + \left(t^{\alpha-2} - t^{\alpha-1}\right) \displaystyle\int_0^1 u(s)\, G\left(s, y(s), D_{0^+}^{p} y(s)\right) ds \\ \quad + t^{\alpha-1} \displaystyle\int_0^1 m(s)\, M\left(s, y(s), D_{0^+}^{p} y(s)\right) ds \\ \quad + \dfrac{t^{\alpha-1} - t^{\alpha-2}}{\Pi} \dfrac{\Gamma(\alpha)}{\Gamma(\alpha-q)} t_1^{\alpha-q-1} I\left(t_1, y(t_1), D_{0^+}^{p} y(t_1)\right) \\ \quad + \dfrac{t^{\alpha-2} - t^{\alpha-1}}{\Pi} t_1^{\alpha-1} I_1\left(t_1, y(t_1), D_{0^+}^{p} y(t_1)\right), \\ \qquad t \in (t_1, 1], \end{cases} \tag{34}$$

$$
\begin{aligned}
&(T_2x)(t)\\
&= \begin{cases}
\displaystyle\int_0^t \frac{(t-s)^{\beta-1}}{\Gamma(\beta)}\psi(u)\, g\left(u, x(u), D_{0^+}^q x(u)\right) du \\
\quad -\displaystyle\frac{t^{\beta-1}}{\Gamma(\beta)}\int_0^1 (1-s)^{\beta-1}\psi(s)\, g\left(s, x(s), D_{0^+}^q x(s)\right) ds \\
\quad +t^{\beta-2}\displaystyle\int_0^1 v(s)\, H\left(s, y(s), D_{0^+}^p y(s)\right) ds \\
\quad +t^{\beta-1}\displaystyle\int_0^1 n(s)\, N\left(s, x(s), D_{0^+}^q x(s)\right) ds \\
\quad +\displaystyle\frac{t^{\beta-1}}{\Xi}\left(\frac{\Gamma(\beta)}{\Gamma(\beta-p)}t_1^{\beta-p-1} - \frac{\Gamma(\beta-1)}{\Gamma(\beta-p-2)}t_1^{\beta-p-2}\right) \\
\quad \times J\left(t_1, x(t_1), D_{0^+}^q x(t_1)\right) \\
\quad +\displaystyle\frac{t^{\beta-1}\left(t_1^{\beta-2}-t_1^{\beta-1}\right)}{\Xi} J_1\left(t_1, x(t_1), D_{0^+}^q x(t_1)\right), \\
\qquad\qquad t \in (0, t_1], \\
\displaystyle\int_0^t \frac{(t-s)^{\beta-1}}{\Gamma(\beta)}\psi(s)\, g\left(s, x(s), D_{0^+}^q x(s)\right) ds \\
\quad -\displaystyle\frac{t^{\beta-1}}{\Gamma(\beta)}\int_0^1 (1-s)^{\beta-1}\psi(s)\, g\left(s, x(s), D_{0^+}^q x(s)\right) ds \\
\quad +\left(t^{\beta-2}-t^{\beta-1}\right)\displaystyle\int_0^1 v(s)\, H\left(s, y(s), D_{0^+}^p y(s)\right) ds \\
\quad +t^{\beta-1}\displaystyle\int_0^1 n(s)\, N\left(s, x(s), D_{0^+}^q x(s)\right) ds \\
\quad +\displaystyle\frac{t^{\beta-1}-t^{\beta-2}}{\Xi}\frac{\Gamma(\beta)}{\Gamma(\beta-p)}t_1^{\beta-p-1} \\
\quad \times J\left(t_1, x(t_1), D_{0^+}^q x(t_1)\right) \\
\quad +\displaystyle\frac{t^{\beta-2}-t^{\beta-1}}{\Xi}t_1^{\beta-1} J_1\left(t_1, x(t_1), D_{0^+}^q x(t_1)\right), \\
\qquad\qquad t \in (t_1, 1].
\end{cases}
\end{aligned}
\tag{35}
$$

□

Remark 9. By Lemmas 7 and 8, $(x, y) \in X \times Y$ is a solution of BVP (6)-(7) if and only if $(x, y) \in X \times Y$ is a fixed point of the operator T.

Lemma 10. *Suppose that (a)–(e) and (A)-(B) hold. Then $T : X \times Y \to X \times Y$ is well defined and is completely continuous.*

Proof. The proof is very long, so we list the steps. First, we prove that T is well defined; second, we prove that T is continuous, and, finally, we prove that T is compact. So T is completely continuous. Thus, the proof is divided into three steps.

Step 1. Prove that $T : X \times Y \to X \times Y$ is well defined.

For $(x, y) \in X \times Y$, we have $||(x, y)|| = r > 0$. Then

$$
\max\left\{\sup_{t\in(0,1)} t^{2-\alpha}|x(t)|,\ \sup_{t\in(0,1)} t^{2+q-\alpha}\left|D_{0^+}^q x(t)\right|\right\} \le r < +\infty,
$$

$$
\max\left\{\sup_{t\in(0,1)} t^{2-\beta}|y(t)|,\ \sup_{t\in(0,1)} t^{2+p-\beta}\left|D_{0^+}^p y(t)\right|\right\} \le r < +\infty. \tag{36}
$$

From (B), f, G, M, I, I_1 are β-Caratheodory functions, then there exist constants $A_r > 0$ such that

$$
\begin{aligned}
&\left|f\left(t, y(t), D_{0^+}^p y(t)\right)\right| \le A_r, \quad t \in (0,1),\\
&\left|G\left(t, y(t), D_{0^+}^p y(t)\right)\right| \le A_r, \quad t \in (0,1),\\
&\left|M\left(t, y(t), D_{0^+}^p y(t)\right)\right| \le A_r, \quad t \in (0,1),\\
&\left|I\left(t_1, y(t_1), D_{0^+}^p y(t_1)\right)\right| \le A_r, \quad t \in (0,1),\\
&\left|I_1\left(t_1, y(t_1), D_{0^+}^p y(t_1)\right)\right| \le A_r, \quad t \in (0,1).
\end{aligned}
\tag{37}
$$

Hence,

$$
\begin{aligned}
&\left|\int_0^t \frac{(t-s)^{\alpha-1}}{\Gamma(\alpha)}\phi(u)\, f\left(u, y(u), D_{0^+}^p y(u)\right) du\right| \\
&\quad \le \int_0^t \frac{(t-s)^{\alpha-1}}{\Gamma(\alpha)}\left|\phi(u)\, f\left(u, y(u), D_{0^+}^p y(u)\right)\right| du \\
&\quad \le A_r L_1 \frac{\mathbf{B}(\alpha+\delta, k+1)}{\Gamma(\alpha)} < \infty.
\end{aligned}
\tag{38}
$$

From (34), (37), and (38), we see that $(T_1 y)(t)$ is defined on $(0, 1]$, continuous on $(0, t_1]$ and $(t_1, 1]$, respectively. One sees that

$$
\begin{aligned}
&\lim_{t\to 0} t^{2-\alpha}(T_1 y)(t) \\
&= \lim_{t\to 0}\left[t^{2-\alpha}\int_0^t \frac{(t-s)^{\alpha-1}}{\Gamma(\alpha)}\phi(u)\, f\left(u, y(u), D_{0^+}^p y(u)\right) du\right. \\
&\qquad -\frac{t}{\Gamma(\alpha)}\int_0^1 (1-s)^{\alpha-1}\phi(s)\, f\left(s, y(s), D_{0^+}^p y(s)\right) ds \\
&\qquad +\int_0^1 u(s)\, G\left(s, y(s), D_{0^+}^p y(s)\right) ds \\
&\qquad +t\int_0^1 m(s)\, M\left(s, y(s), D_{0^+}^p y(s)\right) ds \\
&\qquad +\frac{t}{\Pi}\left(\frac{\Gamma(\alpha)}{\Gamma(\alpha-q)}t_1^{\alpha-q-1} - \frac{\Gamma(\alpha-1)}{\Gamma(\alpha-q-2)}t_1^{\alpha-q-2}\right) \\
&\qquad \times I\left(t_1, y(t_1), D_{0^+}^p y(t_1)\right) \\
&\qquad \left.+\frac{t\left(t_1^{\alpha-2}-t_1^{\alpha-1}\right)}{\Pi} I_1\left(t_1, y(t_1), D_{0^+}^p y(t_1)\right)\right] \\
&= \int_0^1 u(s)\, G\left(s, y(s), D_{0^+}^p y(s)\right) ds,
\end{aligned}
\tag{39}
$$

and there exits the limit $\lim_{t\to t_1^+}(T_1 y)(t)$.

On the other hand, we have

$$
\begin{aligned}
&D_{0^+}^{q}\left(T_1 y\right)(t) \\
&= \begin{cases}
\displaystyle\int_0^t \frac{(t-s)^{\alpha-q-1}}{\Gamma(\alpha-q)}\phi(u) f\left(u, y(u), D_{0^+}^{p} y(u)\right) du \\
\quad -\dfrac{t^{\alpha-q-1}}{\Gamma(\alpha-q)} \\
\quad \times \displaystyle\int_0^1 (1-s)^{\alpha-1}\phi(s) f\left(s, y(s), D_{0^+}^{p} y(s)\right) ds \\
\quad +t^{\alpha-q-2}\dfrac{\Gamma(\alpha-1)}{\Gamma(\alpha-q-1)} \\
\quad \times \displaystyle\int_0^1 u(s) G\left(s, y(s), D_{0^+}^{p} y(s)\right) ds \\
\quad +t^{\alpha-q-1}\dfrac{\Gamma(\alpha)}{\Gamma(\alpha-q)} \\
\quad \times \displaystyle\int_0^1 m(s) M\left(s, y(s), D_{0^+}^{p} y(s)\right) ds \\
\quad +\dfrac{t^{\alpha-q-1}}{\Pi}\dfrac{\Gamma(\alpha)}{\Gamma(\alpha-q)} \\
\quad \times\left(\dfrac{\Gamma(\alpha)}{\Gamma(\alpha-q)} t_1^{\alpha-q-1}-\dfrac{\Gamma(\alpha-1)}{\Gamma(\alpha-q-2)} t_1^{\alpha-q-2}\right) \\
\quad \times I\left(t_1, y(t_1), D_{0^+}^{p} y(t_1)\right) \\
\quad +\dfrac{\Gamma(\alpha)}{\Gamma(\alpha-q)}\dfrac{t^{\alpha-q-1}\left(t_1^{\alpha-2}-t_1^{\alpha-1}\right)}{\Pi} \\
\quad \times I_1\left(t_1, y(t_1), D_{0^+}^{p} y(t_1)\right), \qquad t \in\left(0, t_1\right], \\
\displaystyle\int_0^t \frac{(t-s)^{\alpha-q-1}}{\Gamma(\alpha-q)}\phi(s) f\left(s, y(s), D_{0^+}^{p} y(s)\right) ds \\
\quad -\dfrac{t^{\alpha-q-1}}{\Gamma(\alpha-q)} \\
\quad \times \displaystyle\int_0^1 (1-s)^{\alpha-1}\phi(s) f\left(s, y(s), D_{0^+}^{p} y(s)\right) ds \\
\quad +\left(t^{\alpha-q-2}\dfrac{\Gamma(\alpha-1)}{\Gamma(\alpha-q-1)}-t^{\alpha-q-1}\dfrac{\Gamma(\alpha)}{\Gamma(\alpha-q)}\right) \\
\quad \times \displaystyle\int_0^1 u(s) G\left(s, y(s), D_{0^+}^{p} y(s)\right) ds \\
\quad +t^{\alpha-q-1}\dfrac{\Gamma(\alpha)}{\Gamma(\alpha-q)}\displaystyle\int_0^1 m(s) M\left(s, y(s), D_{0^+}^{p} y(s)\right) ds \\
\quad +\dfrac{1}{\Pi}\left(t^{\alpha-q-1}\dfrac{\Gamma(\alpha)}{\Gamma(\alpha-q)}-t^{\alpha-q-2}\dfrac{\Gamma(\alpha-1)}{\Gamma(\alpha-q-1)}\right) \\
\quad \times\dfrac{\Gamma(\alpha)}{\Gamma(\alpha-q)} t_1^{\alpha-q-1} I\left(t_1, y(t_1), D_{0^+}^{p} y(t_1)\right) \\
\quad +\dfrac{1}{\Pi}\left(t^{\alpha-q-2}\dfrac{\Gamma(\alpha-1)}{\Gamma(\alpha-q-1)}-t^{\alpha-q-1}\dfrac{\Gamma(\alpha)}{\Gamma(\alpha-q)}\right) \\
\quad \times t_1^{\alpha-1} I_1\left(t_1, y(t_1), D_{0^+}^{p} y(t_1)\right), \qquad t \in\left(t_1, 1\right],
\end{cases}
\end{aligned}
$$

$$
\begin{aligned}
&D_{0^+}^{p}\left(T_2 x\right)(t) \\
&= \begin{cases}
\displaystyle\int_0^t \frac{(t-s)^{\beta-p-1}}{\Gamma(\beta-p)}\psi(u) g\left(u, x(u), D_{0^+}^{q} x(u)\right) du \\
\quad -\dfrac{t^{\beta-p-1}}{\Gamma(\beta-p)} \\
\quad \times \displaystyle\int_0^1 (1-s)^{\beta-1}\psi(s) g\left(s, x(s), D_{0^+}^{q} x(s)\right) ds \\
\quad +t^{\beta-p-2}\dfrac{\Gamma(\beta-1)}{\Gamma(\beta-p-1)} \\
\quad \times \displaystyle\int_0^1 v(s) H\left(s, y(s), D_{0^+}^{p} y(s)\right) ds \\
\quad +t^{\beta-p-1}\dfrac{\Gamma(\beta)}{\Gamma(\beta-p)} \\
\quad \times \displaystyle\int_0^1 n(s) N\left(s, x(s), D_{0^+}^{q} x(s)\right) ds \\
\quad +\dfrac{t^{\beta-p-1}}{\Xi}\dfrac{\Gamma(\beta)}{\Gamma(\beta-p)} \\
\quad \times\left(\dfrac{\Gamma(\beta)}{\Gamma(\beta-p)} t_1^{\beta-p-1}-\dfrac{\Gamma(\beta-1)}{\Gamma(\beta-p-2)} t_1^{\beta-p-2}\right) \\
\quad \times J\left(t_1, x(t_1), D_{0^+}^{q} x(t_1)\right) \\
\quad +\dfrac{t^{\beta-p-1}\left(t_1^{\beta-2}-t_1^{\beta-1}\right)}{\Xi}\dfrac{\Gamma(\beta)}{\Gamma(\beta-p)} \\
\quad \times J_1\left(t_1, x(t_1), D_{0^+}^{q} x(t_1)\right), \qquad t \in\left(0, t_1\right], \\
\displaystyle\int_0^t \frac{(t-s)^{\beta-p-1}}{\Gamma(\beta-p)}\psi(s) g\left(s, x(s), D_{0^+}^{q} x(s)\right) ds \\
\quad -\dfrac{t^{\beta-p-1}}{\Gamma(\beta)}\dfrac{\Gamma(\beta)}{\Gamma(\beta-p)} \\
\quad \times \displaystyle\int_0^1 (1-s)^{\beta-1}\psi(s) g\left(s, x(s), D_{0^+}^{q} x(s)\right) ds \\
\quad +\left(t^{\beta-p-2}\dfrac{\Gamma(\beta-1)}{\Gamma(\beta-p-1)}-t^{\beta-p-1}\dfrac{\Gamma(\beta)}{\Gamma(\beta-p)}\right) \\
\quad \times \displaystyle\int_0^1 v(s) H\left(s, y(s), D_{0^+}^{p} y(s)\right) ds \\
\quad +t^{\beta-p-1}\dfrac{\Gamma(\beta)}{\Gamma(\beta-p)}\displaystyle\int_0^1 n(s) N\left(s, x(s), D_{0^+}^{q} x(s)\right) ds \\
\quad +\dfrac{1}{\Xi}\left(t^{\beta-p-1}\dfrac{\Gamma(\beta)}{\Gamma(\beta-p)}-t^{\beta-p-2}\dfrac{\Gamma(\beta-1)}{\Gamma(\beta-p-1)}\right) \\
\quad \times\dfrac{\Gamma(\beta)}{\Gamma(\beta-p)} t_1^{\beta-p-1} J\left(t_1, x(t_1), D_{0^+}^{q} x(t_1)\right) \\
\quad +\dfrac{1}{\Xi}\left(t^{\beta-p-2}\dfrac{\Gamma(\beta-1)}{\Gamma(\beta-p-1)}-t^{\beta-p-1}\dfrac{\Gamma(\beta)}{\Gamma(\beta-p)}\right) \\
\quad \times t_1^{\beta-1} J_1\left(t_1, x(t_1), D_{0^+}^{q} x(t_1)\right), \qquad t \in\left(t_1, 1\right].
\end{cases}
\end{aligned}
\tag{40}
$$

It is easy to see that

$$\left|\int_0^t \frac{(t-s)^{\alpha-q-1}}{\Gamma(\alpha-q)}\phi(u) f\left(u, y(u), D_{0^+}^p y(u)\right) du\right| \le A_r L_1 \frac{\mathbf{B}(\alpha+\delta-q, k+1)}{\Gamma(\alpha-q)} < \infty. \tag{41}$$

From (37) and (41), we see that $D_{0^+}^q(T_1 y)(t)$ is defined on $(0,1]$, continuous on $(0,t_1]$ and $(t_1,1]$, respectively. One sees that

$$\begin{aligned}
&\lim_{t\to 0} t^{2+q-\alpha} D_{0^+}^q (T_1 y)(t) \\
&= \lim_{t\to 0}\Bigg[t^{2+q-\alpha} \\
&\quad \times \int_0^t \frac{(t-s)^{\alpha-q-1}}{\Gamma(\alpha-q)}\phi(u) f\left(u, y(u), D_{0^+}^p y(u)\right) du \\
&\quad - \frac{t}{\Gamma(\alpha-q)} \\
&\quad \times \int_0^1 (1-s)^{\alpha-1}\phi(s) f\left(s, y(s), D_{0^+}^p y(s)\right) ds \\
&\quad + \frac{\Gamma(\alpha-1)}{\Gamma(\alpha-q-1)}\int_0^1 u(s) G\left(s, y(s), D_{0^+}^p y(s)\right) ds \\
&\quad + t\frac{\Gamma(\alpha)}{\Gamma(\alpha-q)}\int_0^1 m(s) M\left(s, y(s), D_{0^+}^p y(s)\right) ds \\
&\quad + \frac{t}{\Pi}\frac{\Gamma(\alpha)}{\Gamma(\alpha-q)} \\
&\quad \times\left(\frac{\Gamma(\alpha)}{\Gamma(\alpha-q)} t_1^{\alpha-q-1} - \frac{\Gamma(\alpha-1)}{\Gamma(\alpha-q-2)} t_1^{\alpha-q-2}\right) \\
&\quad \times I\left(t_1, y(t_1), D_{0^+}^p y(t_1)\right) \\
&\quad + \frac{\Gamma(\alpha)}{\Gamma(\alpha-q)}\frac{t\left(t_1^{\alpha-2} - t_1^{\alpha-1}\right)}{\Pi} \\
&\quad \times I_1\left(t_1, y(t_1), D_{0^+}^p y(t_1)\right)\Bigg] \\
&= \frac{\Gamma(\alpha-1)}{\Gamma(\alpha-q-1)}\int_0^1 u(s) G\left(s, y(s), D_{0^+}^p y(s)\right) ds,
\end{aligned} \tag{42}$$

and there exits the limit $\lim_{t\to t_1^+} D_{0^+}^q (T_1 y)(t)$.

From the above discussion, we have $(T_1 y) \in X$. Similarly, we can show that $(T_2 x) \in Y$. Hence, $((T_1 y), (T_2 x)) \in X \times Y$. Then $T : X \times Y \to X \times Y$ is well defined.

Step 2. We prove that T is continuous. Let $(x_n, y_n) \in X \times Y$ with $(x_n, y_n) \to (x_0, y_0)$ as $n \to \infty$. We will show that $T(x_n, y_n) \to T(x_0, y_0)$ as $n \to \infty$, that is, prove that $T_1 y_n \to T_1 y_0$ and $T_2 x_n \to T_2 x_0$ as $n \to \infty$.

In fact, we have $r > 0$ such that $\|(x_n, y_n)\| = r > 0$. Then

$$\begin{aligned}
&\max\left\{\sup_{t\in(0,1)} t^{2-\alpha}\left|x_n(t)\right|, \sup_{t\in(0,1)} t^{2+q-\alpha}\left|D_{0^+}^q x_n(t)\right|\right\} \\
&\quad \le r < +\infty, \quad n = 0, 1, 2, \ldots, \\
&\max\left\{\sup_{t\in(0,1)} t^{2-\beta}\left|y_n(t)\right|, \sup_{t\in(0,1)} t^{2+p-\beta}\left|D_{0^+}^p y_n(t)\right|\right\} \\
&\quad \le r < +\infty, \quad n = 0, 1, 2, \ldots.
\end{aligned} \tag{43}$$

From (B), f, G, M, I, I_1 are β-Caratheodory functions, then there exist constants $A_r > 0$ such that

$$\begin{aligned}
&\left|f\left(t, y_n(t), D_{0^+}^p y_n(t)\right)\right| \le A_r, \\
&\quad t \in (0,1), \quad n = 0, 1, 2, \ldots, \\
&\left|G\left(t, y_n(t), D_{0^+}^p y_n(t)\right)\right| \le A_r, \\
&\quad t \in (0,1), \quad n = 0, 1, 2, \ldots, \\
&\left|M\left(t, y_n(t), D_{0^+}^p y_n(t)\right)\right| \le A_r, \\
&\quad t \in (0,1), \quad n = 0, 1, 2, \ldots, \\
&\left|I\left(t_1, y_n(t_1), D_{0^+}^p y_n(t_1)\right)\right| \le A_r, \\
&\quad t \in (0,1), \quad n = 0, 1, 2, \ldots, \\
&\left|I_1\left(t_1, y_n(t_1), D_{0^+}^p y_n(t_1)\right)\right| \le A_r, \\
&\quad t \in (0,1), \quad n = 0, 1, 2, \ldots, \\
&\sup_{t\in(0,1)} t^{2-\alpha}\left|x_n(t) - x_0(t)\right| \longrightarrow 0, \\
&\sup_{t\in(0,1)} t^{2-\beta}\left|y_n(t) - y_0(t)\right|, \\
&\sup_{t\in(0,1)} t^{2+q-\alpha}\left|D_{0^+}^q x_n(t) - D_{0^+}^q x_0(t)\right| \longrightarrow 0, \\
&\sup_{t\in(0,1)} t^{2+p-\beta}\left|D_{0^+}^p y_n(t) - D_{0^+}^p y_0(t)\right| \longrightarrow 0,
\end{aligned} \tag{44}$$

as $n \to \infty$. We have

$$
\begin{aligned}
&D_{0^+}^{q}\left(T_1 y_n\right)(t) \\
&= \begin{cases}
\displaystyle\int_0^t \frac{(t-s)^{\alpha-q-1}}{\Gamma(\alpha-q)}\phi(u) f\left(u, y_n(u), D_{0^+}^{p} y_n(u)\right) du \\
\quad -\dfrac{t^{\alpha-q-1}}{\Gamma(\alpha-q)} \\
\quad \times \displaystyle\int_0^1 (1-s)^{\alpha-1}\phi(s) f\left(s, y_n(s), D_{0^+}^{p} y_n(s)\right) ds \\
\quad +t^{\alpha-q-2}\dfrac{\Gamma(\alpha-1)}{\Gamma(\alpha-q-1)} \\
\quad \times \displaystyle\int_0^1 u(s) G\left(s, y_n(s), D_{0^+}^{p} y_n(s)\right) ds \\
\quad +t^{\alpha-q-1}\dfrac{\Gamma(\alpha)}{\Gamma(\alpha-q)} \\
\quad \times \displaystyle\int_0^1 m(s) M\left(s, y_n(s), D_{0^+}^{p} y_n(s)\right) ds \\
\quad +\dfrac{t^{\alpha-q-1}}{\Pi}\dfrac{\Gamma(\alpha)}{\Gamma(\alpha-q)} \\
\quad \times\left(\dfrac{\Gamma(\alpha)}{\Gamma(\alpha-q)} t_1^{\alpha-q-1}-\dfrac{\Gamma(\alpha-1)}{\Gamma(\alpha-q-2)} t_1^{\alpha-q-2}\right) \\
\quad \times I\left(t_1, y_n(t_1), D_{0^+}^{p} y_n(t_1)\right) \\
\quad +\dfrac{\Gamma(\alpha)}{\Gamma(\alpha-q)}\dfrac{t^{\alpha-q-1}\left(t_1^{\alpha-2}-t_1^{\alpha-1}\right)}{\Pi} \\
\quad \times I_1\left(t_1, y_n(t_1), D_{0^+}^{p} y_n(t_1)\right), \quad t \in (0, t_1], \\
\displaystyle\int_0^t \frac{(t-s)^{\alpha-q-1}}{\Gamma(\alpha-q)}\phi(s) f\left(s, y_n(s), D_{0^+}^{p} y_n(s)\right) ds \\
\quad -\dfrac{t^{\alpha-q-1}}{\Gamma(\alpha-q)} \\
\quad \times \displaystyle\int_0^1 (1-s)^{\alpha-1}\phi(s) f\left(s, y(s), D_{0^+}^{p} y(s)\right) ds \\
\quad +\left(t^{\alpha-q-2}\dfrac{\Gamma(\alpha-1)}{\Gamma(\alpha-q-1)}-t^{\alpha-q-1}\dfrac{\Gamma(\alpha)}{\Gamma(\alpha-q)}\right) \\
\quad \times \displaystyle\int_0^1 u(s) G\left(s, y_n(s), D_{0^+}^{p} y_n(s)\right) ds \\
\quad +t^{\alpha-q-1}\dfrac{\Gamma(\alpha)}{\Gamma(\alpha-q)} \\
\quad \times \displaystyle\int_0^1 m(s) M\left(s, y_n(s), D_{0^+}^{p} y_n(s)\right) ds \\
\quad +\dfrac{1}{\Pi}\left(t^{\alpha-q-1}\dfrac{\Gamma(\alpha)}{\Gamma(\alpha-q)}-t^{\alpha-q-2}\dfrac{\Gamma(\alpha-1)}{\Gamma(\alpha-q-1)}\right) \\
\quad \times\dfrac{\Gamma(\alpha)}{\Gamma(\alpha-q)} t_1^{\alpha-q-1} I\left(t_1, y_n(t_1), D_{0^+}^{p} y_n(t_1)\right) \\
\quad +\dfrac{1}{\Pi}\left(t^{\alpha-q-2}\dfrac{\Gamma(\alpha-1)}{\Gamma(\alpha-q-1)}-t^{\alpha-q-1}\dfrac{\Gamma(\alpha)}{\Gamma(\alpha-q)}\right) \\
\quad \times t_1^{\alpha-1} I_1\left(t_1, y_n(t_1), D_{0^+}^{p} y_n(t_1)\right), \quad t \in (t_1, 1].
\end{cases}
\end{aligned}
\tag{45}
$$

From the Lebesgue dominated convergence theorem, we get

$$
\begin{aligned}
&\sup_{t\in(0,1)} t^{2-\beta}\left|\left(T_1 y_n\right)(t)-\left(T_1 y_0\right)(t)\right|, \\
&\sup_{t\in(0,1)} t^{2+p-\beta}\left|D_{0^+}^{p}\left(T_1 y_n\right)(t)-D_{0^+}^{p}\left(T_1 y_0\right)(t)\right| \longrightarrow 0,
\end{aligned}
\tag{46}
$$

as $n \to \infty$. Similarly, we can show that

$$
\begin{aligned}
&\sup_{t\in(0,1)} t^{2-\alpha}\left|\left(T_2 x_n\right)(t)-\left(T_2 x_0\right)(t)\right| \longrightarrow 0, \\
&\sup_{t\in(0,1)} t^{2+q-\alpha}\left|D_{0^+}^{q}\left(T_2 x_n\right)(t)-D_{0^+}^{q}\left(T_2 x_0\right)(t)\right| \longrightarrow 0,
\end{aligned}
\tag{47}
$$

as $n \to \infty$. It follows from (46) and (47) that T is continuous.

Step 3. We prove that T is compact, that is, for each nonempty open bounded subset Ω of $X \times Y$, prove that $T(\overline{\Omega})$ is relatively compact. We must prove that $T(\overline{\Omega})$ is uniformly bounded, equicontinuous on each subinterval $[a,b] \subseteq (t_k, t_{k+1}](k = 0,1)$, $T(\overline{\Omega})$ is equiconvergent as $t \to 0$, and equiconvergent as $t \to t_1$.

Let Ω be a bounded open subset of Y. We have $r > 0$ such that

$$
\begin{aligned}
&\max\left\{\sup_{t\in(0,1)} t^{2-\beta}\left|y(t)\right|, \sup_{t\in(0,1)} t^{2+p-\beta}\left|D_{0^+}^{p} y(t)\right|\right\} \\
&\quad \le r < +\infty, \quad y \in \overline{\Omega}.
\end{aligned}
\tag{48}
$$

From (B), f, G, M, I, I_1 are β-Caratheodory functions, then there exist constants $A_r > 0$ such that

$$
\begin{aligned}
&\left|f\left(t, y(t), D_{0^+}^{p} y(t)\right)\right| \le A_r, \quad t \in (0,1), \\
&\left|G\left(t, y(t), D_{0^+}^{p} y(t)\right)\right| \le A_r, \quad t \in (0,1), \\
&\left|M\left(t, y(t), D_{0^+}^{p} y(t)\right)\right| \le A_r, \quad t \in (0,1), \\
&\left|I\left(t_1, y(t_1), D_{0^+}^{p} y(t_1)\right)\right| \le A_r, \quad t \in (0,1), \\
&\left|I_1\left(t_1, y(t_1), D_{0^+}^{p} y(t_1)\right)\right| \le A_r, \quad t \in (0,1).
\end{aligned}
\tag{49}
$$

Substep 3.1. Prove that $T(\overline{\Omega})$ is uniformly bounded.

In fact, for $t \in (0, t_1]$, use (49), we have

$$
\begin{aligned}
&t^{2-\alpha}\left|\left(T_1 y\right)(t)\right| \\
&\quad \le t^{2-\alpha}\int_0^t \frac{(t-s)^{\alpha-1}}{\Gamma(\alpha)}\left|\phi(u) f\left(u, y(u), D_{0^+}^{p} y(u)\right)\right| du \\
&\qquad + \frac{t}{\Gamma(\alpha)}\int_0^1 (1-s)^{\alpha-1}\left|\phi(s) f\left(s, y(s), D_{0^+}^{p} y(s)\right)\right| ds \\
&\qquad + \int_0^1 \left|u(s) G\left(s, y(s), D_{0^+}^{p} y(s)\right)\right| ds \\
&\qquad + t\int_0^1 \left|m(s) M\left(s, y(s), D_{0^+}^{p} y(s)\right)\right| ds
\end{aligned}
$$

$$
\begin{aligned}
&+\frac{t}{\Pi}\left|\frac{\Gamma(\alpha)}{\Gamma(\alpha-q)}t_1^{\alpha-q-1}-\frac{\Gamma(\alpha-1)}{\Gamma(\alpha-q-2)}t_1^{\alpha-q-2}\right| \\
&\times\left|I\left(t_1,y(t_1),D_{0^+}^p y(t_1)\right)\right| \\
&+\frac{t\left(t_1^{\alpha-2}-t_1^{\alpha-1}\right)}{\Pi}\left|I_1\left(t_1,y(t_1),D_{0^+}^p y(t_1)\right)\right| \\
\le{}& A_rL_1\frac{\mathbf{B}(\alpha+\delta,k+1)}{\Gamma(\alpha)}+\frac{A_rL_1}{\Gamma(\alpha)}\mathbf{B}(\alpha+\delta,k+1) \\
&+A_r\|u\|_1+A_r\|m\|_1 \\
&+\frac{A_r}{\Pi}\left|\frac{\Gamma(\alpha)}{\Gamma(\alpha-q)}t_1^{\alpha-q-1}-\frac{\Gamma(\alpha-1)}{\Gamma(\alpha-q-2)}t_1^{\alpha-q-2}\right| \\
&+\frac{\left(t_1^{\alpha-2}-t_1^{\alpha-1}\right)}{\Pi}A_r<\infty.
\end{aligned}
\tag{50}
$$

Similarly, we can get for $t\in(t_1,1]$ that

$$
\begin{aligned}
&t^{2-\alpha}\left|(T_1y)(t)\right| \\
&\quad\le A_rL_1\frac{\mathbf{B}(\alpha+\delta,k+1)}{\Gamma(\alpha)}+\frac{A_rL_1}{\Gamma(\alpha)}\mathbf{B}(\alpha+\delta,k+1) \\
&\qquad+A_r\|u\|_1+A_r\|m\|_1+\frac{A_r}{\Pi}\frac{\Gamma(\alpha)}{\Gamma(\alpha-q)}t_1^{\alpha-q-1} \\
&\qquad+\frac{A_r}{\Pi}t_1^{\alpha-1}<\infty.
\end{aligned}
\tag{51}
$$

Furthermore, we have for $t\in(0,t_1]$ that

$$
\begin{aligned}
&t^{2+q-\alpha}\left|D_{0^+}^q(T_1y)(t)\right| \\
&\quad\le A_rL_1\frac{\mathbf{B}(\alpha+\delta-q,k+1)}{\Gamma(\alpha-q)} \\
&\qquad+\frac{A_rL_1}{\Gamma(\alpha-q)}\mathbf{B}(\alpha+\delta,k+1) \\
&\qquad+\frac{A_r\Gamma(\alpha-1)}{\Gamma(\alpha-q-1)}\|u\|_1+\frac{A_r\Gamma(\alpha)}{\Gamma(\alpha-q)}\|m\|_1 \\
&\qquad+\frac{A_r}{\Pi}\frac{\Gamma(\alpha)}{\Gamma(\alpha-q)} \\
&\qquad\times\left|\frac{\Gamma(\alpha)}{\Gamma(\alpha-q)}t_1^{\alpha-q-1}-\frac{\Gamma(\alpha-1)}{\Gamma(\alpha-q-2)}t_1^{\alpha-q-2}\right| \\
&\qquad+\frac{\Gamma(\alpha)}{\Gamma(\alpha-q)}\frac{A_r\left(t_1^{\alpha-2}-t_1^{\alpha-1}\right)}{\Pi}<\infty,
\end{aligned}
\tag{52}
$$

and for $t\in(t_1,1]$ that

$$
\begin{aligned}
&t^{2+q-\alpha}\left|D_{0^+}^q(T_1y)(t)\right| \\
&\quad\le A_rL_1\frac{\mathbf{B}(\alpha+\delta-q,k+1)}{\Gamma(\alpha-q)}+\frac{A_rL_1}{\Gamma(\alpha-q)}\mathbf{B}(\alpha+\delta,k+1) \\
&\qquad+\left(\frac{\Gamma(\alpha-1)}{\Gamma(\alpha-q-1)}+\frac{\Gamma(\alpha)}{\Gamma(\alpha-q)}\right)A_r\|u\|_1 \\
&\qquad+\frac{\Gamma(\alpha)}{\Gamma(\alpha-q)}A_r\|m\|_1 \\
&\qquad+\frac{1}{\Pi}\left(\frac{\Gamma(\alpha)}{\Gamma(\alpha-q)}+\frac{\Gamma(\alpha-1)}{\Gamma(\alpha-q-1)}\right)\frac{\Gamma(\alpha)}{\Gamma(\alpha-q)}t_1^{\alpha-q-1}A_r \\
&\qquad+\frac{1}{\Pi}\left(\frac{\Gamma(\alpha-1)}{\Gamma(\alpha-q-1)}+\frac{\Gamma(\alpha)}{\Gamma(\alpha-q)}\right)t_1^{\alpha-1}A_r<\infty.
\end{aligned}
\tag{53}
$$

Hence,

$$
\begin{aligned}
&\max\left\{\sup_{t\in(0,1)}t^{2-\alpha}\left|(Ty)(t)\right|,\ \sup_{t\in(0,1)}t^{2+q-\alpha}\left|D_{0^+}^q(Ty)(t)\right|\right\} \\
&\quad<+\infty,\quad y\in\overline{\Omega}.
\end{aligned}
\tag{54}
$$

Similarly, we can show that

$$
\begin{aligned}
&\max\left\{\sup_{t\in(0,1)}t^{2-\beta}\left|(Tx)(t)\right|,\ \sup_{t\in(0,1)}t^{2+p-\beta}\left|D_{0^+}^p(Tx)(t)\right|\right\} \\
&\quad<+\infty,\quad y\in\overline{\Omega}.
\end{aligned}
\tag{55}
$$

It is easy to see that $T(\overline{\Omega})$ is uniformly bounded.

Substep 3.2. Prove that $T(\overline{\Omega})$ is equicontinuous on each subinterval $[a,b]\subseteq(t_k,t_{k+1}]$ $(k=0,1)$.

For each $[a,b]\subseteq(t_0,t_1]$, and $s_1,s_2\in[a,b]$ with $s_2<s_1$, we have

$$
\begin{aligned}
&\left|s_1^{2-\alpha}(Ty)(s_1)-s_2^{2-\alpha}(Ty)(s_2)\right| \\
&\quad\le\left|s_1^{2-\alpha}\int_0^{s_1}\frac{(s_1-s)^{\alpha-1}}{\Gamma(\alpha)}\phi(u)f\left(u,y(u),D_{0^+}^p y(u)\right)du\right. \\
&\qquad\left.-s_2^{2-\alpha}\int_0^{s_2}\frac{(s_2-s)^{\alpha-1}}{\Gamma(\alpha)}\phi(u)f\left(u,y(u),D_{0^+}^p y(u)\right)du\right| \\
&\qquad+\left|s_1-s_2\right|A_r \\
&\qquad\times\left[\frac{L_1\mathbf{B}(\alpha+\delta,k+1)}{\Gamma(\alpha)}+\|m\|_1\right. \\
&\qquad+\frac{1}{\Pi}\left|\frac{\Gamma(\alpha)}{\Gamma(\alpha-q)}t_1^{\alpha-q-1}-\frac{\Gamma(\alpha-1)}{\Gamma(\alpha-q-2)}t_1^{\alpha-q-2}\right| \\
&\qquad\left.+\frac{t_1^{\alpha-2}-t_1^{\alpha-1}}{\Pi}\right].
\end{aligned}
\tag{56}
$$

Note that $|\tau_1^\varrho-\tau_2^\varrho|\le|\tau_1-\tau_2|^\varrho$ for all $\tau_1,\tau_2\ge0$ and $\varrho\in(0,1)$.

Since

$$\begin{aligned}
&\left| s_1^{2-\alpha} \int_0^{s_1} \frac{(s_1-s)^{\alpha-1}}{\Gamma(\alpha)} \phi(u) f\left(u, y(u), D_{0^+}^p y(u)\right) du \right. \\
&\left. - s_2^{2-\alpha} \int_0^{s_2} \frac{(s_2-s)^{\alpha-1}}{\Gamma(\alpha)} \phi(u) f\left(u, y(u), D_{0^+}^p y(u)\right) du \right| \\
&\quad \le \left| s_1^{2-\alpha} - s_2^{2-\alpha} \right| A_r L_1 \frac{\mathbf{B}(\alpha+\delta, k+1)}{\Gamma(\alpha)} \\
&\qquad + b^{2-\alpha} A_r L_1 s_1^{\alpha+k+\delta} \int_{s_2/s_1}^1 \frac{(1-w)^{\alpha+\delta-1} w^k dw}{\Gamma(\alpha)} \\
&\qquad + |s_1 - s_2|^{\alpha-1} \frac{A_r L_1 b^{2-\alpha}}{\Gamma(\alpha)} \int_0^b s^k (1-s)^\delta ds \longrightarrow 0 \\
&\qquad\qquad \text{uniformly as } \; s_1 \longrightarrow s_2.
\end{aligned} \tag{57}$$

It follows that

$$\begin{aligned}
&\left| s_1^{2-\alpha} (Ty)(s_1) - s_2^{2-\alpha} (Ty)(s_2) \right| \longrightarrow 0 \\
&\qquad \text{uniformly as } \; s_1 \longrightarrow s_2.
\end{aligned} \tag{58}$$

For $[a,b] \subseteq (t_1, 1]$, and $s_1, s_2 \in [a,b]$ with $s_2 < s_1$, we can prove similarly that

$$\begin{aligned}
&\left| s_1^{2-\alpha} (Ty)(s_1) - s_2^{2-\alpha} (Tyx)(s_2) \right| \longrightarrow 0 \\
&\qquad \text{uniformly as } \; s_1 \longrightarrow s_2.
\end{aligned} \tag{59}$$

On the other hand, for $[a,b] \subseteq (t_0, t_1]$, and $s_1, s_2 \in [a,b]$ with $s_2 < s_1$, we have

$$\begin{aligned}
&\left| s_1^{2+q-\alpha} D_{0^+}^q (T_1 y)(s_1) - s_2^{2+q-\alpha} D_{0^+}^q (T_1 y)(s_2) \right| \\
&\quad \le \left| s_1^{2+q-\alpha} \int_0^{s_1} \frac{(s_1-s)^{\alpha-q-1}}{\Gamma(\alpha-q)} \phi(u) f\left(u, y(u), D_{0^+}^p y(u)\right) du \right. \\
&\qquad \left. - s_2^{2+q-\alpha} \int_0^{s_2} \frac{(s_2-s)^{\alpha-q-1}}{\Gamma(\alpha-q)} \phi(u) f\left(u, y(u), D_{0^+}^p y(u)\right) du \right| \\
&\qquad + |s_2 - s_1| A_r \left[\frac{L_1 B(\alpha+\delta, k+1)}{\Gamma(\alpha-q)} + \frac{\Gamma(\alpha) \|m\|_1}{\Gamma(\alpha-q)} \right. \\
&\qquad\qquad + \frac{1}{\Pi} \frac{\Gamma(\alpha)}{\Gamma(\alpha-q)} \\
&\qquad\qquad \times \left| \frac{\Gamma(\alpha)}{\Gamma(\alpha-q)} t_1^{\alpha-q-1} - \frac{\Gamma(\alpha-1)}{\Gamma(\alpha-q-2)} t_1^{\alpha-q-2} \right| \\
&\qquad\qquad \left. + \frac{\Gamma(\alpha)}{\Gamma(\alpha-q)} \frac{\left| t_1^{\alpha-2} - t_1^{\alpha-1} \right|}{\Pi} \right].
\end{aligned} \tag{60}$$

It is easy to see that

$$\begin{aligned}
&\left| s_1^{2+q-\alpha} - s_2^{2+q-\alpha} \right| A_r L_1 \int_0^1 \frac{(1-w)^{\alpha+\delta-q-1} w^k ds}{\Gamma(\alpha-q)} \longrightarrow 0 \\
&\qquad \text{uniformly as } \; s_1 \longrightarrow s_2,
\end{aligned} \tag{61}$$

$$\begin{aligned}
&b^{2+q-\alpha} A_r L_1 \int_{s_2/s_1}^1 \frac{(1-w)^{\alpha-q-1} w^k dw}{\Gamma(\alpha-q)} \longrightarrow 0 \\
&\qquad \text{uniformly as } \; s_1 \longrightarrow s_2.
\end{aligned} \tag{62}$$

For the third term, if $\alpha - q - 1 \ge 0$, use $|\tau_1^\varrho - \tau_2^\varrho| \le |\tau_1 - \tau_2|^\varrho$, then

$$\begin{aligned}
&\int_0^{s_2} \frac{\left| (s_1-s)^{\alpha-q-1} - (s_2-s)^{\alpha-q-1} \right|}{\Gamma(\alpha-q)} s^k (1-s)^\delta ds \\
&\quad \le |s_1 - s_2|^{\alpha-q-1} \int_0^b \frac{1}{\Gamma(\alpha-q)} s^k (1-s)^\delta ds \longrightarrow 0 \\
&\qquad \text{uniformly as } \; s_1 \longrightarrow s_2.
\end{aligned} \tag{63}$$

If $\alpha - q - 1 < 0$, use $|\tau_1^\varrho - \tau_2^\varrho| \le |\tau_1 - \tau_2|^\varrho$, then

$$\begin{aligned}
&\int_0^{s_2} \frac{\left| (s_1-s)^{\alpha-q-1} - (s_2-s)^{\alpha-q-1} \right|}{\Gamma(\alpha-q)} s^k (1-s)^\delta ds \\
&\quad = \int_0^{s_2} \frac{(s_2-s)^{\alpha-q-1} - (s_1-s)^{\alpha-q-1}}{\Gamma(\alpha-q)} s^k (s_1-s)^\delta ds \\
&\quad \le \left| s_2^{\alpha+\delta+k-q} - s_1^{\alpha+\delta+k-q} \right| \frac{\mathbf{B}(\alpha+\delta+k-q, k+1)}{\gamma(\alpha-q)} \\
&\qquad + b^{\alpha+k+\delta-q} \frac{\mathbf{B}(\alpha+2\delta-q, k+1)}{\Gamma(\alpha-q)} \left| 1 - \frac{s_1}{s_2} \right|^{-\delta} \longrightarrow 0 \\
&\qquad\qquad \text{uniformly as } \; s_1 \longrightarrow s_2.
\end{aligned} \tag{64}$$

For $[a,b] \subseteq (t_1, 1]$, and $s_1, s_2 \in [a,b]$ with $s_2 < s_1$, we can prove similarly that

$$\begin{aligned}
&\left| s_1^{2+q-\alpha} D_{0^+}^q (T_1 y)(s_1) - s_2^{2+q-\alpha} D_{0^+}^q (T_1 y)(s_2) \right| \longrightarrow 0 \\
&\qquad \text{uniformly as } \; s_1 \longrightarrow s_2.
\end{aligned} \tag{65}$$

Similarly, we can show that for each $[a,b] \subseteq (t_0, t_1]$, and $s_1, s_2 \in [a,b]$ with $s_2 < s_1$, we have

$$\begin{aligned}
&\left| s_1^{2-\beta} (Tx)(s_1) - s_2^{2-\beta} (Tx)(s_2) \right| \longrightarrow 0 \\
&\qquad \text{uniformly as } \; s_1 \longrightarrow s_2.
\end{aligned} \tag{66}$$

For $[a,b] \subseteq (t_1, 1]$, and $s_1, s_2 \in [a,b]$ with $s_2 < s_1$, we can prove similarly that

$$\begin{aligned}
&\left| s_1^{2-\beta} (Tx)(s_1) - s_2^{2-\beta} (Tx)(s_2) \right| \longrightarrow 0 \\
&\qquad \text{uniformly as } \; s_1 \longrightarrow s_2.
\end{aligned} \tag{67}$$

For each $[a,b] \subseteq (t_0,t_1]$, and $s_1,s_2 \in [a,b]$ with $s_2 < s_1$, we have

$$\left|s_1^{2+p-\beta}D_{0^+}^p(Tx)(s_1) - s_2^{2+p-\beta}D_{0^+}^p(Tx)(s_2)\right| \longrightarrow 0 \quad \text{uniformly as } s_1 \longrightarrow s_2. \tag{68}$$

For $[a,b] \subseteq (t_1,1]$, and $s_1,s_2 \in [a,b]$ with $s_2 < s_1$, we can prove similarly that

$$\left|s_1^{2+p-\beta}D_{0^+}^p(Tx)(s_1) - s_2^{2+p-\beta}D_{0^+}^p(Tx)(s_2)\right| \longrightarrow 0 \quad \text{uniformly as } s_1 \longrightarrow s_2. \tag{69}$$

So $T(\overline{\Omega})$ is equicontinuous on each subinterval $[a,b] \subseteq (t_k,t_{k+1}](k=0,1)$.

Substep 3.3. Prove that $T(\overline{\Omega})$ is equiconvergent as $t \to 0$, and equiconvergent as $t \to t_1$.

We have

$$\begin{aligned}
&\left|t^{2-\alpha}(Ty)(t) - \int_0^1 u(s)G\left(s,y(s),D_{0^+}^p y(s)\right)ds\right| \\
&\quad \le A_r L_1 t^{2+k+\delta}\frac{\mathbf{B}(\alpha+\delta,k+1)}{\Gamma(\alpha)} \\
&\qquad + \frac{t}{\Gamma(\alpha)}A_r L_1 \mathbf{B}(\alpha+\delta,k+1) \\
&\qquad + tA_r\|m\|_1 \\
&\qquad + \frac{t}{\Pi}\left|\frac{\Gamma(\alpha)}{\Gamma(\alpha-q)}t_1^{\alpha-q-1} - \frac{\Gamma(\alpha-1)}{\Gamma(\alpha-q-2)}t_1^{\alpha-q-2}\right|A_r \\
&\qquad + \frac{t\left|t_1^{\alpha-2}-t_1^{\alpha-1}\right|}{\Pi}A_r.
\end{aligned} \tag{70}$$

It follows that

$$\left|t^{2-\alpha}(Ty)(t) - \int_0^1 u(s)G\left(s,y(s),D_{0^+}^p y(s)\right)ds\right| \longrightarrow 0 \quad \text{uniformly as } t \longrightarrow 0. \tag{71}$$

Similarly, we can show that $t^{2-\alpha}(Ty)(t)$ is equiconvergent at $t = t_1$. On the other hand, we have

$$\begin{aligned}
&\left|t^{2+q-\alpha}D_{0^+}^q(Ty)(t) - \frac{\Gamma(\alpha-1)}{\Gamma(\alpha-q-1)}\right. \\
&\quad \left.\times \int_0^1 u(s)G\left(s,y(s),D_{0^+}^p y(s)\right)ds\right| \\
&\quad \le A_r L_1 t^{2+k+\delta}\frac{\mathbf{B}(\alpha+\delta-q,k+1)}{\Gamma(\alpha-q)} \\
&\qquad + \frac{t}{\Gamma(\alpha-q)}A_r L_1 \mathbf{B}(\alpha+\delta,k+1) \\
&\qquad + t\frac{\Gamma(\alpha)}{\Gamma(\alpha-q)}A_r\|m\|_1 + \frac{t}{\Pi}\frac{\Gamma(\alpha)}{\Gamma(\alpha-q)} \\
&\qquad \times \left|\frac{\Gamma(\alpha)}{\Gamma(\alpha-q)}t_1^{\alpha-q-1} - \frac{\Gamma(\alpha-1)}{\Gamma(\alpha-q-2)}t_1^{\alpha-q-2}\right|A_r \\
&\qquad + \frac{\Gamma(\alpha)}{\Gamma(\alpha-q)}\frac{t\left|t_1^{\alpha-2}-t_1^{\alpha-1}\right|}{\Pi}A_r.
\end{aligned} \tag{72}$$

It follows that

$$\begin{aligned}
&\left|t^{2+q-\alpha}D_{0^+}^q(Ty)(t) - \frac{\Gamma(\alpha-1)}{\Gamma(\alpha-q-1)}\right. \\
&\quad \left.\times \int_0^1 u(s)G\left(s,y(s),D_{0^+}^p y(s)\right)ds\right| \longrightarrow 0 \\
&\qquad \text{uniformly as } t \longrightarrow 0.
\end{aligned} \tag{73}$$

Similarly, we can show that $t^{2+q-\alpha}D_{0^+}^q(Ty)(t)$ is equiconvergent at $t = t_1$.

Similarly we can prove that

$$\left|t^{2-\beta}(Tx)(t) - \int_0^1 v(s)H\left(s,x(s),D_{0^+}^q x(s)\right)ds\right| \longrightarrow 0 \quad \text{uniformly as } t \longrightarrow 0, \tag{74}$$

and $t^{2+p-\beta}D_{0^+}^p(Tx)(t)$ is equiconvergent at $t = 0$, both $t^{2-\beta}(Tx)(t)$ and $t^{2+p-\beta}D_{0^+}^p(Tx)(t)$ are equiconvergent at $t = t_1$.

Hence, $T(\overline{\Omega})$ is equiconvergent as $t \to 0$ and $T(\overline{\Omega})$ is equiconvergent as $t \to t_1$.

So $T(\overline{\Omega})$ is relatively compact. Then T is completely continuous. The proofs are completed. □

3. Main Result

In this section, we will establish the existence of at least one solution of BVP (6)-(7).

Definition 11 (see [26]). An odd homeomorphism Φ of the real line $\mathbb{R}$ onto itself is called a *pseudo-sub-multiplicative function* if there exists a homeomorphism ω of $[0,\infty)$ onto itself which *supports* Φ in the sense that for all $v_1,v_2 \ge 0$ we have $\Phi(v_1v_2) \ge \omega(v_1)\Phi(v_2)$. ω is called the *supporting function* of Φ.

Remark 12. Note that any submultiplicative function is a pseudo-submultiplicative function. Also any function of the form $\Phi(u) := \sum_{j=0}^k c_j|u|^j u,\ u \in \mathbb{R}$ is pseudo-sup-multiplicative, provided that $c_j \ge 0$. Here, a supporting function is defined by $\omega(u) := \min\{u^{k+1},u\}$, $u \ge 0$.

Remark 13. It is clear that a pseudo-submultiplicative function Φ and any corresponding supporting function ω are increasing functions vanishing at zero; moreover, their inverses Φ^{-1} and ν, respectively, are increasing and for all $v_1,v_2 \ge 0$, we have $\Phi^{-1}(v_1v_2) \le \nu(v_1)\Phi^{-1}(v_2)$.

Theorem 14. *Suppose that (a)–(e) and (A)-(B) hold, $\Phi : R \to R$ is a submultiplicative-like function with the supporting function ω, its inverse function is denoted by $\Phi^{-1} : R \to R$ with the supporting function ν. Furthermore, suppose that*

(i) *there exist nonnegative numbers $C_f, B_f, A_f, C_G, B_G, A_G, C_M, B_M$, and A_M such that*

$$\begin{aligned}
&\left|f\left(t, t^{\alpha-2}U, t^{\alpha-q-2}V\right)\right| \\
&\quad \le C_f + B_f\Phi^{-1}(|U|) + A_f\Phi^{-1}(|V|), \\
&\left|G\left(t, t^{\alpha-2}U, t^{\alpha-q-2}V\right)\right| \\
&\quad \le C_G + B_G\Phi^{-1}(|U|) + A_G\Phi^{-1}(|V|), \\
&\left|M\left(t, t^{\alpha-2}U, t^{\alpha-q-2}V\right)\right| \\
&\quad \le C_M + B_M\Phi^{-1}(|U|) + A_M\Phi^{-1}\left(\left|\Phi^{-1}(|U|)\right|\right),
\end{aligned} \tag{75}$$

holds for all $(U, V) \in R^2$, $t \in (0, 1]$.

(ii) *there exist nonnegative numbers $C_g, B_g, A_g, C_H, B_H, A_H, C_N, B_N$, and A_N such that*

$$\begin{aligned}
&\left|g\left(t, t^{\beta-2}U, t^{\beta-p-2}V\right)\right| \le C_g + B_g\Phi(U) + A_g\Phi(V), \\
&\left|H\left(t, t^{\beta-2}U, t^{\beta-p-2}V\right)\right| \le C_H + B_H\Phi(U) + A_H\Phi(V), \\
&\left|N\left(t, t^{\beta-2}U, t^{\beta-p-2}V\right)\right| \le C_N + B_N\Phi(U) + A_N\Phi(V),
\end{aligned} \tag{76}$$

hold for all $(U, V) \in R^2$, $t \in (0, 1]$.

(iii) *there exist the nonnegative numbers $C_I, B_I, A_I, C_{1,I}, B_{1,I}$, and $A_{1,I}$ such that*

$$\begin{aligned}
&\left|I\left(t_1, t_1^{\alpha-2}U, t_1^{\alpha-q-2}V\right)\right| \le C_I + B_I\Phi^{-1}(|U|) + A_I\Phi^{-1}(|V|), \\
&\left|I_1\left(t_1, t_1^{\alpha-2}U, t_1^{\alpha-q-2}V\right)\right| \\
&\quad \le C_{1,I} + B_{1,I}\Phi^{-1}(|U|) + A_{1,I}\Phi^{-1}(|V|),
\end{aligned} \tag{77}$$

hold for all $(U, V) \in R^2$.

(iv) *there exist the nonnegative numbers $C_J, B_J, A_J, C_{1,J}, B_{1,J}$, and $A_{1,J}$ such that*

$$\begin{aligned}
&\left|J\left(t_1, t_1^{\beta-2}U, t_1^{\beta-p-2}V\right)\right| \le C_J + B_J\Phi(U) + A_J\Phi(V), \\
&\left|J_1\left(t_1, t_1^{\beta-2}U, t_1^{\beta-p-2}V\right)\right| \le C_{1,J} + B_{1,J}\Phi(U) + A_{1,J}\Phi(V),
\end{aligned} \tag{78}$$

hold for all $(U, V) \in R^2$.

Then BVP (6)-(7) has at least one solution if

$$\begin{aligned}
&\max\{\Theta_2, \Sigma_2, \Theta_4, \Sigma_4\}\,\nu\left(2\max\{\Upsilon_2, \Lambda_2, \Upsilon_4, \Lambda_4\}\right) < 1 \text{ or} \\
&\frac{\max\{\Upsilon_2, \Lambda_2, \Upsilon_4, \Lambda_4\}}{\omega\left(\left(2\max\{\Theta_2, \Sigma_2, \Theta_4, \Sigma_4\}\right)^{-1}\right)} < 1,
\end{aligned} \tag{79}$$

where

$$\begin{aligned}
\Theta_1 = {} & L_1\frac{\mathbf{B}(\alpha+\delta, k+1)}{\Gamma(\alpha)}C_f + \frac{L_1\mathbf{B}(\alpha+\delta, k+1)}{\Gamma(\alpha)}C_f \\
& + \|u\|_1 C_G + \|m\|_1 C_M \\
& + \frac{1}{\Pi}\left|\frac{\Gamma(\alpha)}{\Gamma(\alpha-q)}t_1^{\alpha-q-1} - \frac{\Gamma(\alpha-1)}{\Gamma(\alpha-q-2)}t_1^{\alpha-q-2}\right|C_I \\
& + \frac{\left|t_1^{\alpha-2} - t_1^{\alpha-1}\right|}{\Pi}C_{1,I}, \\
\Theta_2 = {} & L_1\frac{\mathbf{B}(\alpha+\delta, k+1)}{\Gamma(\alpha)}\left[B_f + A_f\right] \\
& + \frac{L_1\mathbf{B}(\alpha+\delta, k+1)}{\Gamma(\alpha)}\left[B_f + A_f\right] \\
& + \|u\|_1\left[B_G + A_G\right] + \|m\|_1\left[B_M + A_M\right] \\
& + \frac{1}{\Pi}\left|\frac{\Gamma(\alpha)}{\Gamma(\alpha-q)}t_1^{\alpha-q-1} - \frac{\Gamma(\alpha-1)}{\Gamma(\alpha-q-2)}t_1^{\alpha-q-2}\right| \\
& \times\left[B_I + A_I\right] + \frac{\left|t_1^{\alpha-2} - t_1^{\alpha-1}\right|}{\Pi}\left[B_{1,I} + A_{1,I}\right], \\
\Theta_3 = {} & L_1\frac{\mathbf{B}(\alpha+\delta-q, k+1)}{\Gamma(\alpha-q)}C_f \\
& + \frac{L_1}{\Gamma(\alpha-q)}\mathbf{B}(\alpha+\delta, k+1)C_f \\
& + \frac{\Gamma(\alpha-1)}{\Gamma(\alpha-q-1)}\|u\|_1 C_G + \frac{\Gamma(\alpha)}{\Gamma(\alpha-q)}\|m\|_1 C_M \\
& + \frac{1}{\Pi}\frac{\Gamma(\alpha)}{\Gamma(\alpha-q)} \\
& \times\left|\frac{\Gamma(\alpha)}{\Gamma(\alpha-q)}t_1^{\alpha-q-1} - \frac{\Gamma(\alpha-1)}{\Gamma(\alpha-q-2)}t_1^{\alpha-q-2}\right|C_I \\
& + \frac{\Gamma(\alpha)}{\Gamma(\alpha-q)}\frac{\left|t_1^{\alpha-2} - t_1^{\alpha-1}\right|}{\Pi}C_{1,I}, \\
\Theta_4 = {} & L_1\frac{\mathbf{B}(\alpha+\delta-q, k+1)}{\Gamma(\alpha-q)}\left[B_f + A_f\right] \\
& + \frac{L_1}{\Gamma(\alpha-q)}\mathbf{B}(\alpha+\delta, k+1)\left[B_f + A_f\right] \\
& + \frac{\Gamma(\alpha-1)}{\Gamma(\alpha-q-1)}\|u\|_1\left[B_G + A_G\right] \\
& + \frac{\Gamma(\alpha)}{\Gamma(\alpha-q)}\|m\|_1\left[B_M + A_M\right] \\
& + \frac{1}{\Pi}\frac{\Gamma(\alpha)}{\Gamma(\alpha-q)}
\end{aligned}$$

$$
\begin{aligned}
&\times \left| \frac{\Gamma(\alpha)}{\Gamma(\alpha-q)} t_1^{\alpha-q-1} - \frac{\Gamma(\alpha-1)}{\Gamma(\alpha-q-2)} t_1^{\alpha-q-2} \right| \\
&\times [B_I + A_I] \\
&+ \frac{\Gamma(\alpha)}{\Gamma(\alpha-q)} \frac{\left| t_1^{\alpha-2} - t_1^{\alpha-1} \right|}{\Pi} [B_{1,I} + A_{1,I}], \\
\Sigma_1 = {} & L_1 \frac{\mathbf{B}(\alpha+\delta, k+1)}{\Gamma(\alpha)} C_f + \frac{L_1 \mathbf{B}(\alpha+\delta, k+1)}{\Gamma(\alpha)} C_f \\
&+ \|u\|_1 C_G + \frac{1}{\Pi} \frac{\Gamma(\alpha)}{\Gamma(\alpha-q)} t_1^{\alpha-q-1} C_I + \frac{1}{\Pi} t_1^{\alpha-1} C_{1,I}, \\
\Sigma_2 = {} & L_1 \frac{\mathbf{B}(\alpha+\delta, k+1)}{\Gamma(\alpha)} [B_f + A_f] \\
&+ \frac{L_1 \mathbf{B}(\alpha+\delta, k+1)}{\Gamma(\alpha)} [B_f + A_f] + \|u\|_1 [B_G + A_G] \\
&+ \frac{1}{\Pi} \frac{\Gamma(\alpha)}{\Gamma(\alpha-q)} t_1^{\alpha-q-1} [B_I + A_I] + \frac{1}{\Pi} t_1^{\alpha-1} [B_{1,I} + A_{1,I}], \\
\Sigma_3 = {} & L_1 \frac{\mathbf{B}(\alpha+\delta-q, k+1)}{\Gamma(\alpha-q)} C_f \\
&+ \frac{L_1}{\Gamma(\alpha-q)} \mathbf{B}(\alpha+\delta, k+1) C_f \\
&+ \left(\frac{\Gamma(\alpha-1)}{\Gamma(\alpha-q-1)} + \frac{\Gamma(\alpha)}{\Gamma(\alpha-q)} \right) \|u\|_1 C_G \\
&+ \frac{\Gamma(\alpha)}{\Gamma(\alpha-q)} \|m\|_1 C_M \\
&+ \frac{1}{\Pi} \left(\frac{\Gamma(\alpha)}{\Gamma(\alpha-q)} + \frac{\Gamma(\alpha-1)}{\Gamma(\alpha-q-1)} \right) \frac{\Gamma(\alpha)}{\Gamma(\alpha-q)} t_1^{\alpha-q-1} C_I \\
&+ \frac{1}{\Pi} \left(\frac{\Gamma(\alpha-1)}{\Gamma(\alpha-q-1)} + \frac{\Gamma(\alpha)}{\Gamma(\alpha-q)} \right) t_1^{\alpha-1} C_{1,I}, \\
\Sigma_4 = {} & L_1 \frac{\mathbf{B}(\alpha+\delta-q, k+1)}{\Gamma(\alpha-q)} [B_f + A_f] \\
&+ \frac{L_1}{\Gamma(\alpha-q)} \mathbf{B}(\alpha+\delta, k+1) [B_f + A_f] \\
&+ \left(\frac{\Gamma(\alpha-1)}{\Gamma(\alpha-q-1)} + \frac{\Gamma(\alpha)}{\Gamma(\alpha-q)} \right) \|u\|_1 [B_G + A_G] \\
&+ \frac{\Gamma(\alpha)}{\Gamma(\alpha-q)} \|m\|_1 [B_M + A_M] \\
&+ \frac{1}{\Pi} \left(\frac{\Gamma(\alpha)}{\Gamma(\alpha-q)} + \frac{\Gamma(\alpha-1)}{\Gamma(\alpha-q-1)} \right) \\
&\times \frac{\Gamma(\alpha)}{\Gamma(\alpha-q)} t_1^{\alpha-q-1} [B_I + A_I] \\
&+ \frac{1}{\Pi} \left(\frac{\Gamma(\alpha-1)}{\Gamma(\alpha-q-1)} + \frac{\Gamma(\alpha)}{\Gamma(\alpha-q)} \right) \\
&\times t_1^{\alpha-1} [B_{1,I} + A_{1,I}], \\
\Upsilon_1 = {} & L_2 \frac{\mathbf{B}(\beta+\theta, l+1)}{\Gamma(\beta)} C_g \\
&+ \frac{L_2 \mathbf{B}(\beta+\theta, l+1)}{\Gamma(\beta)} C_g + \|v\|_1 C_H + \|n\|_1 C_N \\
&+ \frac{1}{\Xi} \left| \frac{\Gamma(\beta)}{\Gamma(\beta-p)} t_1^{\beta-p-1} - \frac{\Gamma(\beta-1)}{\Gamma(\beta-p-2)} t_1^{\beta-p-2} \right| C_J \\
&+ \frac{\left| t_1^{\beta-2} - t_1^{\beta-1} \right|}{\Xi} C_{1,J}, \\
\Upsilon_2 = {} & L_2 \frac{\mathbf{B}(\beta+\theta, l+1)}{\Gamma(\beta)} [B_g + A_g] \\
&+ \frac{L_2 \mathbf{B}(\beta+\theta, l+1)}{\Gamma(\beta)} [B_g + A_g] \\
&+ \|b\|_1 [B_H + A_H] + \|n\|_1 [B_N + A_N] \\
&+ \frac{1}{\Xi} \left| \frac{\Gamma(\beta)}{\Gamma(\beta-p)} t_1^{\beta-p-1} - \frac{\Gamma(\beta-1)}{\Gamma(\beta-p-2)} t_1^{\beta-p-2} \right| \\
&\times [B_J + A_J] + \frac{\left| t_1^{\beta-2} - t_1^{\beta-1} \right|}{\Xi} [B_{1,J} + A_{1,J}], \\
\Upsilon_3 = {} & L_2 \frac{\mathbf{B}(\beta+\theta-p, l+1)}{\Gamma(\beta-p)} C_g \\
&+ \frac{L_2}{\Gamma(\beta-p)} \mathbf{B}(\beta+\theta, l+1) C_g \\
&+ \frac{\Gamma(\beta-1)}{\Gamma(\beta-p-1)} \|v\|_1 C_H + \frac{\Gamma(\beta)}{\Gamma(\beta-p)} \|n\|_1 C_N \\
&+ \frac{1}{\Xi} \frac{\Gamma(\beta)}{\Gamma(\beta-p)} \\
&\times \left| \frac{\Gamma(\beta)}{\Gamma(\beta-p)} t_1^{\beta-p-1} - \frac{\Gamma(\beta-1)}{\Gamma(\beta-p-2)} t_1^{\beta-p-2} \right| C_J \\
&+ \frac{\Gamma(\beta)}{\Gamma(\beta-p)} \frac{\left| t_1^{\beta-2} - t_1^{\beta-1} \right|}{\Xi} C_{1,J}, \\
\Upsilon_4 = {} & L_2 \frac{\mathbf{B}(\beta+\theta-p, l+1)}{\Gamma(\beta-p)} [B_g + A_g] \\
&+ \frac{L_2}{\Gamma(\beta-p)} \mathbf{B}(\beta+\theta, l+1) [B_g + A_g] \\
&+ \frac{\Gamma(\beta-1)}{\Gamma(\beta-p-1)} \|v\|_1 [B_H + A_H]
\end{aligned}
\tag{80}
$$

$$+\frac{\Gamma(\beta)}{\Gamma(\beta-p)}\|n\|_1\left[B_N+A_N\right]$$
$$+\frac{1}{\Xi}\frac{\Gamma(\beta)}{\Gamma(\beta-p)}$$
$$\times\left|\frac{\Gamma(\beta)}{\Gamma(\beta-p)}t_1^{\beta-p-1}-\frac{\Gamma(\beta-1)}{\Gamma(\beta-p-2)}t_1^{\beta-p-2}\right|\left[B_J+A_J\right]$$
$$+\frac{\Gamma(\beta)}{\Gamma(\beta-p)}\frac{\left|t_1^{\beta-2}-t_1^{\beta-1}\right|}{\Xi}\left[B_{1,J}+A_{1,J}\right],$$

$$\Lambda_1=L_2\frac{\mathbf{B}(\beta+\theta,l+1)}{\Gamma(\beta)}C_g+\frac{L_2\mathbf{B}(\beta+\theta,l+1)}{\Gamma(\beta)}C_g$$
$$+\|v\|_1C_H+\frac{1}{\Xi}\frac{\Gamma(\beta)}{\Gamma(\beta-p)}t_1^{\beta-p-1}C_J+\frac{1}{\Xi}t_1^{\beta-1}C_{1,J},$$

$$\Lambda_2=L_2\frac{\mathbf{B}(\beta+\theta,l+1)}{\Gamma(\beta)}\left[B_g+A_g\right]$$
$$+\frac{L_2\mathbf{B}(\beta+\theta,l+1)}{\Gamma(\beta)}\left[B_g+A_g\right]+\|v\|_1\left[B_H+A_H\right]$$
$$+\frac{1}{\Xi}\frac{\Gamma(\beta)}{\Gamma(\beta-p)}t_1^{\beta-p-1}\left[B_J+A_J\right]+\frac{1}{\Xi}t_1^{\beta-1}\left[B_{1,J}+A_{1,J}\right],$$

$$\Lambda_3=L_2\frac{\mathbf{B}(\beta+\theta-p,l+1)}{\Gamma(\beta-p)}C_g$$
$$+\frac{L_2}{\Gamma(\beta-p)}\mathbf{B}(\beta+\theta,l+1)C_g$$
$$+\left(\frac{\Gamma(\beta-1)}{\Gamma(\beta-p-1)}+\frac{\Gamma(\beta)}{\Gamma(\beta-p)}\right)\|v\|_1C_H$$
$$+\frac{\Gamma(\beta)}{\Gamma(\beta-p)}\|n\|_1C_N$$
$$+\frac{1}{\Xi}\left(\frac{\Gamma(\beta)}{\Gamma(\beta-p)}+\frac{\Gamma(\beta-1)}{\Gamma(\beta-p-1)}\right)\frac{\Gamma(\beta)}{\Gamma(\beta-p)}t_1^{\beta-p-1}C_J$$
$$+\frac{1}{\Xi}\left(\frac{\Gamma(\beta-1)}{\Gamma(\beta-p-1)}+\frac{\Gamma(\beta)}{\Gamma(\beta-p)}\right)t_1^{\beta-1}C_{1,J},$$

$$\Lambda_4=L_2\frac{\mathbf{B}(\beta+\theta-p,l+1)}{\Gamma(\beta-p)}\left[B_g+A_g\right]$$
$$+\frac{L_2}{\Gamma(\beta-p)}\mathbf{B}(\beta+\theta,l+1)\left[B_g+A_g\right]$$
$$+\left(\frac{\Gamma(\beta-1)}{\Gamma(\beta-p-1)}+\frac{\Gamma(\beta)}{\Gamma(\beta-p)}\right)\|v\|_1\left[B_H+A_H\right]$$
$$+\frac{\Gamma(\beta)}{\Gamma(\beta-p)}\|n\|_1\left[B_N+A_N\right]$$
$$+\frac{1}{\Xi}\left(\frac{\Gamma(\beta)}{\Gamma(\beta-p)}+\frac{\Gamma(\beta-1)}{\Gamma(\beta-p-1)}\right)$$
$$\times\frac{\Gamma(\beta)}{\Gamma(\beta-p)}t_1^{\beta-p-1}\left[B_J+A_J\right]$$
$$+\frac{1}{\Xi}\left(\frac{\Gamma(\beta-1)}{\Gamma(\beta-p-1)}+\frac{\Gamma(\beta)}{\Gamma(\beta-p)}\right)t_1^{\beta-1}\left[B_{1,J}+A_{1,J}\right].\tag{81}$$

Proof. To apply Lemma 5, we should define an open bounded subset Ω of $X\times Y$ centered at zero such that assumptions in Lemma 5 hold.

Let $\Omega_1=\{(x,y)\in X\times Y:\ (x,y)=\lambda T(x,y)$ for some $\lambda\in(0,1)\}$. We prove that Ω_1 is bounded. For $(x,y)\in\Omega_1$, we get $(x,y)=\lambda T(x,y)$. It follows that $x=\lambda T_1y$ and $y=\lambda T_2x$.

For $t\in(0,t_1]$, we obtain $t^{2-\alpha}|x(t)|\le t^{2-\alpha}|(T_1y)(t)|\le\Theta_1+\Theta_2\Phi^{-1}(||y||)$.

For $t\in(t_1,1]$,

$$\begin{aligned}
&t^{2-\alpha}|x(t)|\\
&\quad\le t^{2-\alpha}\int_0^t\frac{(t-s)^{\alpha-1}}{\Gamma(\alpha)}\left|\phi(s)f\left(s,y(s),D_{0^+}^py(s)\right)\right|ds\\
&\qquad+\frac{t}{\Gamma(\alpha)}\int_0^1(1-s)^{\alpha-1}\left|\phi(s)f\left(s,y(s),D_{0^+}^py(s)\right)\right|ds\\
&\qquad+(1-t)\int_0^1\left|u(s)G\left(s,y(s),D_{0^+}^py(s)\right)\right|ds\\
&\qquad+t\int_0^1\left|m(s)M\left(s,y(s),D_{0^+}^py(s)\right)\right|ds\\
&\qquad+\frac{1-t}{\Pi}\frac{\Gamma(\alpha)}{\Gamma(\alpha-q)}t_1^{\alpha-q-1}\left|I\left(t_1,y(t_1),D_{0^+}^py(t_1)\right)\right|\\
&\qquad+\frac{1-t}{\Pi}t_1^{\alpha-1}\left|I_1\left(t_1,y(t_1),D_{0^+}^py(t_1)\right)\right|\\
&\quad\le\Sigma_1+\Sigma_2\Phi^{-1}(\|y\|).
\end{aligned}\tag{82}$$

It follows that

$$\sup_{t\in(0,1)}t^{2-\alpha}|x(t)|\le\max\{\Theta_1,\Sigma_1\}+\max\{\Theta_2,\Sigma_2\}\Phi^{-1}(\|y\|).\tag{83}$$

Similarly, we have for $t\in(0,t_1]$ that

$$t^{q+2-\alpha}\left|D_{0^+}^qx(t)\right|\le\Theta_3+\Theta_4\Phi^{-1}(\|y\|)\tag{84}$$

and for $t\in(0,t_1]$

$$t^{q+2-\alpha}\left|D_{0^+}^qx(t)\right|\le\Sigma_3+\Sigma_4\Phi^{-1}(\|y\|).\tag{85}$$

It follows that

$$\begin{aligned}
&\sup_{t\in(0,1)}t^{2+q-\alpha}\left|D_{0^+}^qx(t)\right|\\
&\qquad\le\max\{\Theta_3,\Sigma_3\}+\max\{\Theta_4,\Sigma_4\}\Phi^{-1}(\|y\|).
\end{aligned}\tag{86}$$

Hence,

$$\|x\| \le \max\{\Theta_1, \Sigma_1, \Theta_3, \Sigma_3\} + \max\{\Theta_2, \Sigma_2, \Theta_4, \Sigma_4\}\Phi^{-1}(\|y\|). \tag{87}$$

Similar to the above discussion we can prove that

$$\|y\| \le \max\{\Upsilon_1, \Lambda_1, \Upsilon_3, \Lambda_3\} + \max\{\Upsilon_2, \Lambda_2, \Upsilon_4, \Lambda_4\}\Phi(\|x\|). \tag{88}$$

Case 1. Consider $(\max\{\Theta_2, \Sigma_2, \Theta_4, \Sigma_4\}\nu(2\max\{\Upsilon_2, \Lambda_2, \Upsilon_4, \Lambda_4\}) < 1)$.

With out loss of generality, suppose that

$$\|x\| \ge \Phi^{-1}\left(\frac{\max\{\Upsilon_1, \Lambda_1, \Upsilon_3, \Lambda_3\}}{\max\{\Upsilon_2, \Lambda_2, \Upsilon_4, \Lambda_4\}}\right). \tag{89}$$

Then use Remark 13, and the previous inequalities to get

$$\|x\| \le \max\{\Theta_1, \Sigma_1, \Theta_3, \Sigma_3\} + \max\{\Theta_2, \Sigma_2, \Theta_4, \Sigma_4\}\nu(2\max\{\Upsilon_2, \Lambda_2, \Upsilon_4, \Lambda_4\})\|x\|. \tag{90}$$

It follows that there exists a constant $W > 0$ such that $\|x\| \le W$. Thus

$$\|x\| \le \max\left\{W, \Phi^{-1}\left(\frac{\max\{\Upsilon_1, \Lambda_1, \Upsilon_3, \Lambda_3\}}{\max\{\Upsilon_2, \Lambda_2, \Upsilon_4, \Lambda_4\}}\right)\right\}. \tag{91}$$

Then

$$\|y\| \le \max\{\Upsilon_1, \Lambda_1, \Upsilon_3, \Lambda_3\} + \max\{\Upsilon_2, \Lambda_2, \Upsilon_4, \Lambda_4\}\Phi \times\left(\max\left\{W, \Phi^{-1}\left(\frac{\max\{\Upsilon_1, \Lambda_1, \Upsilon_3, \Lambda_3\}}{\max\{\Upsilon_2, \Lambda_2, \Upsilon_4, \Lambda_4\}}\right)\right\}\right). \tag{92}$$

It follows that Ω_1 is bounded.

Case 2. Consider $((\max\{\Upsilon_2, \Lambda_2, \Upsilon_4, \Lambda_4\}/w((2\max\{\Theta_2, \Sigma_2, \Theta_4, \Sigma_4\})^{-1})) < 1)$.

Without loss of generality, suppose that

$$\|y\| \ge \Phi\left(\frac{\max\{\Theta_1, \Sigma_1, \Theta_3, \Sigma_3\}}{\max\{\Theta_2, \Sigma_2, \Theta_4, \Sigma_4\}}\right). \tag{93}$$

Then using Remark 12 and the previous inequalities, we get

$$\|y\| \le \max\{\Upsilon_1, \Lambda_1, \Upsilon_3, \Lambda_3\} + \frac{\max\{\Upsilon_2, \Lambda_2, \Upsilon_4, \Lambda_4\}}{w\left((2\max\{\Theta_2, \Sigma_2, \Theta_4, \Sigma_4\})^{-1}\right)}\|y\|. \tag{94}$$

It follows that there exists a constant $W > 0$ such that $\|y\| \le W$. We get

$$\|y\| \le \max\left\{W, \Phi\left(\frac{\max\{\Theta_1, \Sigma_1, \Theta_3, \Sigma_3\}}{\max\{\Theta_2, \Sigma_2, \Theta_4, \Sigma_4\}}\right)\right\}. \tag{95}$$

Then

$$\|x\| \le \max\{\Theta_1, \Sigma_1, \Theta_3, \Sigma_3\} + \max\{\Theta_2, \Sigma_2, \Theta_4, \Sigma_4\}\Phi^{-1} \times\left(\max\left\{W, \Phi\left(\frac{\max\{\Theta_1, \Sigma_1, \Theta_3, \Sigma_3\}}{\max\{\Theta_2, \Sigma_2, \Theta_4, \Sigma_4\}}\right)\right\}\right). \tag{96}$$

It follows that Ω_1 is bounded.

To apply Lemma 5, let Ω be a nonempty open bounded subset of X such that $\Omega \supset \overline{\Omega_1}$ centered at zero.

It is easy to see from Lemma 8 that T is a completely continuous operator. One can see that

$$(x, y) \ne \lambda T(x, y) \quad \forall (x, y) \in \partial\Omega, \lambda \in (0, 1). \tag{97}$$

Thus, from Lemma 5, $(x, y) = T(x, y)$ has at least one solution $(x, y) \in \overline{\Omega}$. So (x, y) is a pair of solutions of BVP (3) and BVP (6). The proof of Theorem 14 is complete. □

4. Two Examples

To illustrate the usefulness of our main result, we present two examples that Theorem 14 can readily apply.

Example 15. Consider the following impulsive boundary value problem:

$$\begin{aligned}
&D_{0^+}^{8/5}x(t) = t^{-1/5}(1-t)^{-1} \times\left(c + bt^{6/5}[y(t)]^3 + at^{9/5}\left[D_{0^+}^{1/5}y(t)\right]^3\right), \quad t \in (0,1), \quad t \ne \frac{1}{2},\\
&D_{0^+}^{9/5}y(t) = t^{-1/5}(1-t)^{-1} \times\left(c_0 + b_0t^{1/15}[x(t)]^{1/3} + a_0t^{2/15}\left[D_{0^+}^{1/5}x(t)\right]^{1/3}\right), \quad t \in (0,1), \quad t \ne t_1,\\
&\lim_{t\to 0}t^{2/5}x(t) = G, \qquad \lim_{t\to 0}t^{1/5}y(t) = H,\\
&x(1) = M, \qquad y(1) = N,\\
&\Delta x\left(\frac{1}{2}\right) = c_I, \qquad \Delta y\left(\frac{1}{2}\right) = c_J,\\
&\Delta D_{0^+}^{1}x\left(\frac{1}{2}\right) = c_{1,I}, \qquad \Delta D_{0^+}^{1}y\left(\frac{1}{2}\right) = c_{1,J},
\end{aligned} \tag{98}$$

where c, b, a, c_0, b_0, a_0, G_0, H_0, M_0, N_0, C_I, C_J, $C_{1,I}$, $C_{1,J}$ are constants.

Corresponding to BVP (1), we have

(a) $\alpha = 8/5$, $\beta = 9/5$, $p = q = 1/5$,

(b) $\phi(t) = \psi(t) = t^{-1/5}(1-t)^{-1/5}$, $f(t, U, V) = c + bt^{6/5}U^3 + at^{9/5}V^3$ and $g(t, U, V) = c_0 + b_0t^{1/15}U^{1/3} + a_0t^{2/15}V^{1/3}$ defined on $(0, 1) \times R^2$,

(c) $u(t) = v(t) = m(t) = n(t) \equiv 1$, $G(t,U,V) = G_0$, $H(t,U,V) = H_0$, $M(t,U,V) = M_0$, $N(t,U,V) = N_0$,

(d) $0 = t_0 < t_1 = (1/2) < t_2 = 1$,

(e) $I(t,U,V) = c_I$, $I_1(t,U,V) = c_{1,I}$, $J(t,U,V) = c_J$, $J_1(t,U,V) = c_{1,J}$.

It is easy to show that

(A) ϕ satisfies $\alpha + 2\delta - q > 0$, $\alpha + k + \delta - q \geq 0$, and $|\phi(t)| \leq L_1 t^k (1-t)^\delta$ for all $t \in (0,1)$ with $L_1 = 1$ and $k = -(1/5) = \delta$;

ψ satisfies $\eta + 2\theta - p > 0$, $\beta + l + \theta - p \geq 0$, and $|\psi(t)| \leq L_2 t^l (1-t)^\theta$ for all $t \in (0,1)$ with $L_2 = 1$ and $l = -(1/5) = \theta$;

(B) f, G, M, I, I_1 are β-Caratheodory functions and g, H, N, J, J_1 are α-Caratheodory functions.

Furthermore, we have $\Phi^{-1}(x) = x^3$ and $\Phi(x) = x^{1/3}$ with $w(x) = x^{1/3}$ and $v(x) = x^3$. It is easy to see that

(i) the inequalities

$$\begin{aligned}
&\left|f\left(t, t^{\alpha-2}U, t^{\alpha-q-2}V\right)\right| \leq C_f + B_f\Phi^{-1}(|U|) + A_f\Phi^{-1}(|V|),\\
&\left|G\left(t, t^{\alpha-2}U, t^{\alpha-q-2}V\right)\right| \leq C_G + B_G\Phi^{-1}(|U|) + A_G\Phi^{-1}(|V|),\\
&\left|M\left(t, t^{\alpha-2}U, t^{\alpha-q-2}V\right)\right|\\
&\quad \leq C_M + B_M\Phi^{-1}(|U|) + A_M\Phi^{-1}\left(\left|\Phi^{-1}(|U|)\right|\right)
\end{aligned} \tag{99}$$

hold for all $(U,V) \in R^2$, $t \in (0,1]$ with $C_f = |c|$, $B_f = |b|$, $A_f = |a|$, $C_G = |G_0|$, $B_G = 0$, $A_G = 0$ and $C_M = |M_0|$, $B_M = 0$, $A_M = 0$;

(ii) the inequalities

$$\begin{aligned}
&\left|g\left(t, t^{\beta-2}U, t^{\beta-p-2}V\right)\right| \leq C_g + B_g\Phi(U) + A_g\Phi(V),\\
&\left|H\left(t, t^{\beta-2}U, t^{\beta-p-2}V\right)\right| \leq C_H + B_H\Phi(U) + A_H\Phi(V),\\
&\left|N\left(t, t^{\beta-2}U, t^{\beta-p-2}V\right)\right| \leq C_N + B_N\Phi(U) + A_N\Phi(V)
\end{aligned} \tag{100}$$

hold for all $(U,V) \in R^2$, $t \in (0,1]$ with $C_g = |c_0|$, $B_g = |b_0|$, $A_g = |a_0|$, $C_H = |H_0|$, $B_H = A_H = 0$, $C_N = |N_0|$, $B_N = A_N = 0$;

(iii) the inequalities

$$\begin{aligned}
&\left|I\left(t_1, t_1^{\alpha-2}U, t_1^{\alpha-q-2}V\right)\right| \leq C_I + B_I\Phi^{-1}(|U|) + A_I\Phi^{-1}(|V|),\\
&\left|I_1\left(t_1, t_1^{\alpha-2}U, t_1^{\alpha-q-2}V\right)\right|\\
&\quad \leq C_{1,I} + B_{1,I}\Phi^{-1}(|U|) + A_{1,I}\Phi^{-1}(|V|)
\end{aligned} \tag{101}$$

hold for all $(U,V) \in R^2$ with $C_I = |c_I|$, $B_I = A_I = 0$, $C_{1,I} = |c_{1,I}|$, $B_{1,I} = A_{1,I} = 0$;

(iv) the inequalities

$$\begin{aligned}
&\left|J\left(t_1, t_1^{\beta-2}U, t_1^{\beta-p-2}V\right)\right| \leq C_J + B_J\Phi(U) + A_J\Phi(V),\\
&\left|J_1\left(t_1, t_1^{\beta-2}U, t_1^{\beta-p-2}V\right)\right| \leq C_{1,J} + B_{1,J}\Phi(U) + A_{1,J}\Phi(V)
\end{aligned} \tag{102}$$

hold for all $(U,V) \in R^2$ with $C_J = |c_J|$, $B_J = A_J = 0$, $C_{1,J} = |c_{1,J}|$, $B_{1,J} = A_{1,J} = 0$.

By direct computation, we know that

$$\begin{aligned}
\Theta_2 &= 2\frac{\mathbf{B}(7/5,4/5)}{\Gamma(8/5)}[|b| + |a|],\\
\Sigma_2 &= 2\frac{\mathbf{B}(7/5,4/5)}{\Gamma(8/5)}[|b| + |a|],\\
\Theta_4 &= \left(\frac{\mathbf{B}(6/5,4/5)}{\Gamma(7/5)} + \frac{\mathbf{B}(7/5,4/5)}{\Gamma(7/5)}\right)[|b| + |a|],\\
\Sigma_4 &= \left(\frac{\mathbf{B}(6/5,4/5)}{\Gamma(7/5)} + \frac{\mathbf{B}(7/5,4/5)}{\Gamma(7/5)}\right)[|b| + |a|],\\
\Upsilon_2 &= 2\frac{\mathbf{B}(8/5,4/5)}{\Gamma(9/5)}[|b_0| + |a_0|],\\
\Upsilon_4 &= \left(\frac{\mathbf{B}(7/5,4/5)}{\Gamma(8/5)} + \frac{\mathbf{B}(8/5,4/5)}{\Gamma(8/5)}\right)[|b_0| + |a_0|],\\
\Lambda_2 &= 2\frac{\mathbf{B}(8/5,4/5)}{\Gamma(9/5)}[|b_0| + |a_0|],\\
\Lambda_4 &= \left(\frac{\mathbf{B}(7/5,4/5)}{\Gamma(8/5)} + \frac{\mathbf{B}(8/5,4/5)}{\Gamma(8/5)}\right)[|b_0| + |a_0|].
\end{aligned} \tag{103}$$

Then Theorem 14 implies that the existence of at least one solution if

$$\begin{aligned}
&\max\left\{2\frac{\mathbf{B}(8/5,4/5)}{\Gamma(9/5)}, \frac{\mathbf{B}(7/5,4/5)}{\Gamma(8/5)} + \frac{\mathbf{B}(8/5,4/5)}{\Gamma(8/5)}\right\}\\
&\times\left(\max\left\{2\frac{\mathbf{B}(7/5,4/5)}{\Gamma(8/5)}, \frac{\mathbf{B}(6/5,4/5)}{\Gamma(7/5)} + \frac{\mathbf{B}(7/5,4/5)}{\Gamma(7/5)}\right\}\right)^{1/3}\\
&\times[|b_0| + |a_0|][|b| + |a|]^{1/3} < \frac{1}{\sqrt[3]{2}}.
\end{aligned} \tag{104}$$

Example 16. Consider the following boundary value problem without impulse effects:

$$\begin{aligned}
D_{0^+}^{7/4}x(t) &= t^{-1/4}(1-t)^{-1/4}\\
&\quad\times\left(C + Bt^{3/4}[y(t)]^3 + At^{15/4}\left[D_{0^+}^1 y(t)\right]^3\right),\\
&\qquad t \in (0,1),
\end{aligned}$$

$$D_{0^+}^{5/4} y(t) = t^{-1/8}(1-t)^{-1/8} \times \left(C_0 + B_0 t^{1/4}[x(t)]^{1/3} + A_0 t^{7/12}\left[D_{0^+}^{1/4} x(t)\right]^{1/3}\right), \quad t \in (0,1),$$

$$\lim_{t\to 0} t^{1/4} x(t) = 0, \qquad \lim_{t\to 0} t^{3/4} y(t) = 0, \qquad x(1) = 0, \qquad y(1) = 0, \tag{105}$$

where C, B, A, C_0, B_0, and A_0 are constants.

Corresponding to BVP (1), we have

(a) $\alpha = 7/4$, $\beta = 5/4$, $p = 1$ and $q = 1/4$,

(b) $\phi(t) = t^{-1/4}(1-t)^{-1/4}$, $\psi(t) = t^{-1/8}(1-t)^{-1/8}$, f, g defined on $(0,1) \times R^2$, $f(t,U,V) = C + Bt^{1/12}U^3 + At^{5/12}V^3$ and $g(t,U,V) = C_0 + B_0 t^{1/4}U^{1/3} + A_0 t^{7/12}V^{1/3}$,

(c) $m(t) = n(t) = u(t) = v(t) \equiv 0$, $G(t,U,V) = H(t,U,V) = M(t,U,V) = N(t,U,V) \equiv 0$,

(d) there exists no impulse point,

(e) $I(t,U,V) = I_1(t,U,V) = J(t,U,V) = J_1(t,U,V) \equiv 0$.

It is easy to show that

(A) ϕ satisfies $\alpha + 2\delta - q > 0$, $\alpha + k + \delta - q > 0$, $|\phi(t)| \le L_1 t^k (1-t)^\delta$ for all $t \in (0,1)$ with $L_1 = 1$, $k = -(1/4) = \delta$;

ψ satisfies $\beta + 2\theta - p > 0$, $\beta + l + \theta - p \ge 0$, and $|\psi(t)| \le L_2 t^l (1-t)^\theta$ for all $t \in (0,1)$ with $L_2 = 1$, $l = -(1/8) = \theta$;

(B) f, G, M, I, I_1 are β-Caratheodory functions and g, H, N, J, J_1 are α-Caratheodory functions.

Furthermore, $\Phi(x) = x^{1/3}$ and $\Phi^{-1}(x) = x^3$, we have $w(x) = x^{1/3}$ and $v(x) = x^3$, and

(i) the inequalities

$$\begin{aligned} &\left|f\left(t, t^{\alpha-2}U, t^{\alpha-q-2}V\right)\right| \le C_f + B_f\Phi^{-1}(|U|) + A_f\Phi^{-1}(|V|), \\ &\left|G\left(t, t^{\alpha-2}U, t^{\alpha-q-2}V\right)\right| \le C_G + B_G\Phi^{-1}(|U|) + A_G\Phi^{-1}(|V|), \\ &\left|M\left(t, t^{\alpha-2}U, t^{\alpha-q-2}V\right)\right| \le C_M + B_M\Phi^{-1}(|U|) + A_M\Phi^{-1}\left(\left|\Phi^{-1}(|U|)\right|\right) \end{aligned} \tag{106}$$

hold for all $(U,V) \in R^2$, $t \in (0,1)$ with $C_G = B_G = A_G = C_M = B_M = A_M = 0$, $C_f = |C|$, $B_f = |B|$ and $A_f = |A|$;

(ii) the inequalities

$$\begin{aligned} &\left|g\left(t, t^{\beta-2}U, t^{\beta-p-2}V\right)\right| \le C_g + B_g\Phi(U) + A_g\Phi(V), \\ &\left|H\left(t, t^{\beta-2}U, t^{\beta-p-2}V\right)\right| \le C_H + B_H\Phi(U) + A_H\Phi(V), \\ &\left|N\left(t, t^{\beta-2}U, t^{\beta-p-2}V\right)\right| \le C_N + B_N\Phi(U) + A_N\Phi(V) \end{aligned} \tag{107}$$

hold for all $(U,V) \in R^2$, $t \in (0,1)$ with $C_H = B_H = A_H = C_N = B_N = A_N = 0$, $C_g = |C_0|$, $B_g = |B_0|$ and $A_g = |A_0|$;

(iii) the inequalities

$$\begin{aligned} &\left|I\left(t_1, t_1^{\alpha-2}U, t_1^{\alpha-q-2}V\right)\right| \le C_I + B_I\Phi^{-1}(|U|) + A_I\Phi^{-1}(|V|), \\ &\left|I_1\left(t_1, t_1^{\alpha-2}U, t_1^{\alpha-q-2}V\right)\right| \le C_{1,I} + B_{1,I}\Phi^{-1}(|U|) + A_{1,I}\Phi^{-1}(|V|) \end{aligned} \tag{108}$$

hold for all $(U,V) \in R^2$ with $C_I = B_I = A_I = C_{1,I} = B_{1,I} = A_{1,I} = 0$;

(iv) there exist the nonnegative numbers $A_{i,k}, B_{i,k}, C_{i,k}$ $(i = 1,2)$ such that

$$\begin{aligned} &\left|J\left(t_1, t_1^{\beta-2}U, t_1^{\beta-p-2}V\right)\right| \le C_J + B_J\Phi(U) + A_J\Phi(V), \\ &\left|J_1\left(t_1, t_1^{\beta-2}U, t_1^{\beta-p-2}V\right)\right| \le C_{1,J} + B_{1,J}\Phi(U) + A_{1,J}\Phi(V) \end{aligned} \tag{109}$$

hold for all $(U,V) \in R^2$ with $C_J = B_J = A_J = C_{1,J} = B_{1,J} = A_{1,J} = 0$.

By direct computation, we know that

$$\begin{aligned} \Theta_2 &= 2\frac{\mathbf{B}(3/2,3/4)}{\Gamma(7/4)}[|B| + |A|], \\ \Sigma_2 &= 2\frac{\mathbf{B}(3/2,3/4)}{\Gamma(7/4)}[|B| + |A|], \\ \Theta_4 &= \left(\frac{\mathbf{B}(5/4,3/4)}{\Gamma(3/2)} + \frac{\mathbf{B}(3/2,3/4)}{\Gamma(3/2)}\right)[|B| + |A|], \\ \Sigma_4 &= \left(\frac{\mathbf{B}(5/4,3/4)}{\Gamma(3/2)} + \frac{\mathbf{B}(3/2,3/4)}{\Gamma(3/2)}\right)[|B| + |A|], \\ \Upsilon_2 &= 2\frac{\mathbf{B}(9/8,7/8)}{\Gamma(5/4)}[|B_0| + |A_0|], \\ \Upsilon_4 &= \left(\frac{\mathbf{B}(1/8,7/8)}{\Gamma(\beta-p)} + \frac{\mathbf{B}(9/8,7/8)}{\Gamma(1/4)}\right)[|B_0| + |A_0|], \\ \Lambda_2 &= 2\frac{\mathbf{B}(9/8,7/8)}{\Gamma(5/4)}[|B_0| + |A_0|], \\ \Lambda_4 &= \left(\frac{\mathbf{B}(1/8,7/8)}{\Gamma(1/4)} + \frac{\mathbf{B}(9/8,7/8)}{\Gamma(1/4)}\right)[|B_0| + |A_0|]. \end{aligned} \tag{110}$$

Then Theorem 14 implies the existence of at least one solution if

$$\max\left\{2\frac{\mathbf{B}(3/2,3/4)}{\Gamma(7/4)},\frac{\mathbf{B}(5/4,3/4)}{\Gamma(3/2)}+\frac{\mathbf{B}(3/2,3/4)}{\Gamma(3/2)}\right\}$$
$$\times\left(\max\left\{2\frac{\mathbf{B}(9/8,7/8)}{\Gamma(5/4)},\frac{\mathbf{B}(1/8,7/8)}{\Gamma(\beta-p)}+\frac{\mathbf{B}(9/8,7/8)}{\Gamma(1/4)}\right\}\right)^3$$
$$\times\left[|B_0|+|A_0|\right]^3\left[|B|+|A|\right]<\frac{1}{8}. \tag{111}$$

Remark 17. It is easy to see that the previous boundary value problems have at least one solution for sufficiently small $|B_1|, |B_2|$ and $|A_0|, |B_0|, |a|, |b|, |a_0|$ and $|b_0|$. They cannot be solved by the theorems in [24, 25].

Acknowledgments

This research is partially supported by the Natural Science Foundation of Guangdong province (no. S2011010001900) and the Guangdong Higher Education Foundation for High-Level Talents. This research is partially supported by Ministerio de Economía y Competitividad and EC fund FEDER, Project no. MTM2010-15314, Spain.

References

[1] K. S. Miller and B. Ross, *An Introduction to the Fractional Calculus and Fractional Differential Equations*, Wiley, New York, NY, USA, 1993.

[2] S. G. Samko, A. A. Kilbas, and O. I. Marichev, *Fractional Integral and Derivative. Theory and Applications*, Gordon and Breach, 1993.

[3] A. A. Kilbas, H. M. Srivastava, and J. J. Trujillo, *Theory and Applications of Fractional Differential Equations*, vol. 204 of *North-Holland Mathematics Studies*, Elsevier Science B.V., Amsterdam, The Netherlands, 2006.

[4] B. Ahmad and J. J. Nieto, "Anti-periodic fractional boundary value problems with nonlinear term depending on lower order derivative," *Fractional Calculus and Applied Analysis*, vol. 15, no. 3, pp. 451–462, 2012.

[5] B. Ahmad, J. J. Nieto, A. Alsaedi, and M. El-Shahed, "A study of nonlinear Langevin equation involving two fractional orders in different intervals," *Nonlinear Analysis: Real World Applications*, vol. 13, no. 2, pp. 599–606, 2012.

[6] I. Podlubny and N. Heymans, "Physical interpretation of initial conditions for fractional differential equations with Riemann-Liouville fractional derivatives," *Rheologica Acta*, vol. 45, no. 5, pp. 765–771, 2006.

[7] I. Podlubny, "Geometric and physical interpretation of fractional integration and fractional differentiation," *Fractional Calculus and Applied Analysis*, vol. 5, no. 4, pp. 367–386, 2002.

[8] A. Carpinteri and F. Mainardi, Eds., *Fractals and Fractional Calculus in Continuum Mechanics*, CISM Courses and Lectures, International Center for Mechanical Sciences, no. 378, Springer, New York, NY, USA, 1997.

[9] R. L. Magin, "Fractional calculus in bioengineering, part 1," *Critical Reviews in Biomedical Engineering*, vol. 32, no. 1, pp. 1–104, 2004.

[10] R. L. Magin, "Fractional calculus in bioengineering, part 2," *Critical Reviews in Biomedical Engineering*, vol. 32, no. 1, pp. 105–193, 2004.

[11] R. L. Magin, "Fractional calculus in bioengineering, part 3," *Critical Reviews in Biomedical Engineering*, vol. 32, no. 3-4, pp. 195–377, 2004.

[12] X. Chen, L. Wei, J. Sui, and L. Zheng, "Solving the linear time-fractional wave equation by generalized differential transform method," *Applied Mechanics and Materials*, vol. 204–208, pp. 4476–4480, 2012.

[13] S. Li, B. Fang, T. Yang, Y. Zhang, L. Tan, and W. Huang, "Dynamics of vibration isolation system obeying fractional differentiation," *Aircraft Engineering and Aerospace Technology*, vol. 84, no. 2, pp. 103–108, 2012.

[14] G. S. Priya, P. Prakash, J. J. Nieto, and Z. Kayar, "Higher order numerical scheme for fractional heat equation with Dirichlet and Neumann boundary conditions," *Numerical Heat Transfer B*. In press.

[15] J. Zhao, B. Tang, S. Kumar, and Y. Hou, "The extended fractional subequation method for nonlinear fractional differential equations," *Mathematical Problems in Engineering*, vol. 2012, Article ID 924956, 11 pages, 2012.

[16] V. V. Lakshmikantham, D. D. Baĭnov, and P. S. Simeonov, *Theory of Impulsive Differential Equations*, World Scientific, Singapore, 1989.

[17] V. Kavitha and M. Mallika Arjunan, "Controllability of impulsive quasi-linear fractional mixed Volterra-Fredholm-type integrodifferential equations in Banach spaces," *The Journal of Nonlinear Science and Its Applications*, vol. 4, no. 2, pp. 152–169, 2011.

[18] B. Ahmad and S. Sivasundaram, "Existence results for nonlinear impulsive hybrid boundary value problems involving fractional differential equations," *Nonlinear Analysis: Hybrid Systems*, vol. 3, no. 3, pp. 251–258, 2009.

[19] B. Ahmad and S. Sivasundaram, "Existence of solutions for impulsive integral boundary value problems of fractional order," *Nonlinear Analysis: Hybrid Systems*, vol. 4, no. 1, pp. 134–141, 2010.

[20] B. Ahmad and J. J. Nieto, "Existence of solutions for impulsive anti-periodic boundary value problems of fractional order," *Taiwanese Journal of Mathematics*, vol. 15, no. 3, pp. 981–993, 2011.

[21] Y. Tian and Z. Bai, "Existence results for the three-point impulsive boundary value problem involving fractional differential equations," *Computers & Mathematics with Applications*, vol. 59, no. 8, pp. 2601–2609, 2010.

[22] R. P. Agarwal, M. Benchohra, and S. Hamani, "A survey on existence results for boundary value problems of nonlinear fractional differential equations and inclusions," *Acta Applicandae Mathematicae*, vol. 109, no. 3, pp. 973–1033, 2010.

[23] J. Mawhin, *Topological Degree Methods in Nonlinear Boundary Value Problems*, vol. 40 of *NSFCBMS Regional Conference Series in Mathematics*, American Mathematical Society, Providence, RI, USA, 1979.

[24] B. Ahmad and J. J. Nieto, "Existence results for a coupled system of nonlinear fractional differential equations with three-point boundary conditions," *Computers & Mathematics with Applications*, vol. 58, no. 9, pp. 1838–1843, 2009.

[25] X. Su, "Boundary value problem for a coupled system of nonlinear fractional differential equations," *Applied Mathematics Letters*, vol. 22, no. 1, pp. 64–69, 2009.

[26] G. L. Karakostas, "Positive solutions for the Φ-Laplacian when Φ is a sup-multiplicative-like function," *Electronic Journal of Differential Equations*, vol. 2004, no. 68, pp. 1–12, 2004.

Hindawi Publishing Corporation
Mathematical Problems in Engineering
Volume 2013, Article ID 895640, 10 pages
http://dx.doi.org/10.1155/2013/895640

Research Article

Fractional-Order Generalized Predictive Control: Application for Low-Speed Control of Gasoline-Propelled Cars

M. Romero,[1] A. P. de Madrid,[1] C. Mañoso,[1] V. Milanés,[2] and B. M. Vinagre[3]

[1] *Escuela Técnica Superior de Ingeniería Informática, UNED, Juan del Rosal, 16, 28040 Madrid, Spain*
[2] *California PATH, University of California at Berkeley, Richmond, CA 94804-4698, USA*
[3] *Industrial Engineering School, University of Extremadura, Avenida de Elvas s/n, 06071 Badajoz, Spain*

Correspondence should be addressed to M. Romero; mromero@scc.uned.es

Received 9 November 2012; Accepted 22 January 2013

Academic Editor: Clara Ionescu

There is an increasing interest in using fractional calculus applied to control theory generalizing *classical* control strategies as the PID controller and developing new ones with the intention of taking advantage of characteristics supplied by this mathematical tool for the controller definition. In this work, the fractional generalization of the successful and spread control strategy known as model predictive control is applied to drive autonomously a gasoline-propelled vehicle at low speeds. The vehicle is a Citroën C3 Pluriel that was modified to act over the throttle and brake pedals. Its highly nonlinear dynamics are an excellent test bed for applying beneficial characteristics of fractional predictive formulation to compensate unmodeled dynamics and external disturbances.

1. Introduction

Fractional calculus can be defined as a generalization of derivatives and integrals to noninteger orders, allowing calculations such as deriving a function to real or complex order [1, 2]. Although this branch of mathematical analysis began 300 years ago when Liebniz and L'Hôpital discussed the possibility that n could be a fraction $1/2$ for nth derivative $d^n y/dx^n$, it was really developed at the beginning of the 19th century by Liouville, Riemann, Letnikov, and other mathematicians [3].

Fractional-order operators are commonly represented by D^α that stands for α-th-order derivative. Negative values of α correspond to fractional-order integrals: $D^{-\alpha} \equiv I^\alpha$. These operators can be evaluated using two general fractional definitions, Riemann-Liouville (RL) and Grünwald-Letnikov (GL). Both definitions, continuous and discrete, are equivalent for a wide class of functions which appear in real physical and engineering applications [1]. In this work, discrete domain will be exclusively considered. Hence, in the following the GL definition (1) will be used to implement fractional operators:

$$D^\alpha f(t)_{t=kh} = \lim_{h\to 0} h^{-\alpha} \sum_{j=0}^{\infty} (-1)^j \binom{\alpha}{j} f(kh - jh), \quad \alpha \in \mathbb{R}, \tag{1}$$

where α is the fractional order of the derivative or integral, h is the differential increment—close to zero—, and j varies from 0 to ∞ due to the infinite memory of fractional operators.

In order to describe the dynamical behaviour of systems, the Laplace transform is often used. Expression (2) gives the Laplace transform of the GL definition under zero initial conditions. Nevertheless, the discretization of (2) does not lead to a transfer function with a limited number of coefficients in z [4]. Thus, the so-called *short memory principle* [1] is applied, which means taking into account the behaviour only in the *recent past* that corresponds to a n-term truncated series,

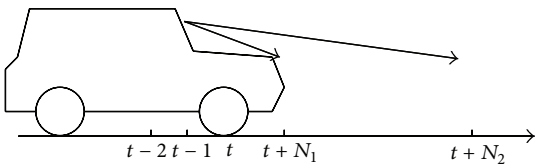

Figure 1: Model-based predictive control analogy.

paying a penalty in the form of some inaccuracy [5]:

$$L\{D^{\pm\alpha} f(t)\} = s^{\pm\alpha} F(s), \quad \forall \alpha \in \mathbb{R}. \tag{2}$$

Nowadays, this mathematical tool is more and more used in control theory to enhance the system performance. Typical fractional-order controllers include the CRONE control [6] and the $\mathrm{PI}^{\lambda}\mathrm{D}^{\mu}$ controller [7, 8]. Advanced control system strategies have also been generalized: fractional optimal control [9–11], fractional fuzzy adaptive control [12], fractional nonlinear control [13], fractional iterative learning control [14], and fractional predictive control, the latter known as fractional-order generalized predictive control (FGPC), which was initially proposed in [15].

Model predictive control (MPC) is an advanced process control methodology in which a dynamical model of the plant is used to predict and optimize the future behaviour of the process over a time interval [16–18]. At each present time t, MPC generates a set of future control signals $u(t+k \mid t)$ based on the prediction of future process outputs $y(t+k \mid t)$ within the time window defined by N_1 (minimum costing horizon), N_2 (maximum costing horizon), and N_u (control horizon). (With this notation, $x(t+k \mid t)$ stands for the value of x at time $t+k$ predicted at time t.) However, only the first element of the control sequence $u(t \mid t)$ is applied to the system input. When the next measurement becomes available (present time equal to $t+1$), the previous procedure is repeated to find new predicted future process outputs $y(t+1+k \mid t+1)$ and calculate the corresponding system input $u(t+1 \mid t+1)$ with prediction time windows moving forward; for this reason this kind of control is also known as receding horizon control (RHC). Figure 1 depicts the analogy between predictive control and a car driver who calculates the car manoeuvre following a receding horizon strategy [16].

MPC has become an industrial standard that has been widely adopted during the last 30 years. With over 2000 industrial installations, this control method is currently the most implemented for process plants [19]. It was originally developed to meet the specialized control needs of petroleum refineries [20, 21]. MPC technology can now be found in a wide variety of application areas such as chemicals [22, 23], solar power plants [24], agriculture [25], or clinical anaesthesia supply [26]. Recent developments related to MPC can be found in [27, 28].

Generalized predictive control (GPC) [29, 30] is one of the most representative MPC formulations. Its fractional-order counterpart, FGPC, uses a real-order fractional cost function to combine the characteristics of fractional calculus and predictive control into a versatile control strategy [31–33].

On the other hand, driver-assistance systems have been a topic of active research during the last decades. They are intended to reduce traffic accidents and traffic congestions [34–37]. Open-loop cruise control (CC) systems are a well-known class of driver-assistance systems, based on controlling the throttle pedal, that reduces driver workload and improve vehicle safety [38].

Nowadays, the tedious task of driving in traffic jams represents an unresolved issue in the automotive sector [39] because commercial vehicles exhibit highly nonlinear dynamics due to the behaviour of the vehicle engine at very low speed. Therefore, it constitutes one of the most important control challenges of the automotive sector [40]. Recently, approaches to resolve this problem have been studied both using experimental scaled-down vehicles [41] and using commercial vehicles [42, 43].

In this paper, an application of FGPC to the velocity control of a mass-produced car at very low speeds is described. The goal is to highlight the beneficial characteristics of FGPC to compensate unmodeled dynamics and external disturbances using the proposed tuning method. These characteristics were shown up in [32], where the lateral control of an autonomous vehicle is carried out by FGPC in the presence of sensor noise and the effect of the communication network.

The remainder of this paper is organized as follows: Section 2 summarizes the fundamentals of fractional predictive control methodology. Section 3 includes the description of the experimental vehicle, presents the design and tuning of the fractional predictive control, and shows the results of the experimental trial, including a comparison with integer-order GPC controllers. Finally, Section 4 draws the main conclusions of this work.

2. Controller Formulation

The GPC control law is obtained by minimizing, possibly subject to a set of constraints, the cost function:

$$J_{\mathrm{GPC}}(\Delta u, t) = \sum_{k=N_1}^{N_2} \gamma_k \left(r(t+k) - y(t+k)\right)^2 + \sum_{k=1}^{N_u} \lambda_k \Delta u(t+k-1)^2, \tag{3}$$

where r is the reference, y is the output, u is the control signal, γ_k and λ_k are nonnegative weighting elements, Δ is the increment operator, and it is assumed that $u(t)$ remains constant from time instant $t+N_u$ $(1 \le N_u \le N_2)$ [29, 30]. For the sake of simplicity in the notation $(\cdot \mid t)$ is omitted, since all expressions are referred to the present time t.

Outputs are predicted making use of a CARIMA model to describe the system dynamics:

$$A\left(z^{-1}\right) y(t) = B\left(z^{-1}\right) u(t) + \frac{T_c\left(z^{-1}\right)}{\Delta} \xi(t), \tag{4}$$

where $B(z^{-1})$ and $A(z^{-1})$ are the numerator and denominator of the model transfer function, respectively, $\xi(t)$ represents uncorrelated zero-mean white noise, and $T_c(z^{-1})$ is a (pre)filter to improve the system robustness rejecting disturbance and noise [44, 45].

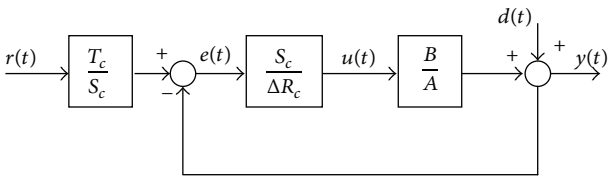

Figure 2: Closed-loop equivalent control schema.

Using model (4), the future system outputs $y(t+k)$ are predicted as $y = y_C + y_F$, where y_C—forced response—is the part of the future output that depends on the future control actions Δu (with $y_C = G \cdot \Delta u$, and G the matrix of the step response coefficients of the model), and y_F—free response—is the part of the future output that does not depend on Δu (i.e., the evolution of the process exclusively due to its present state) [29].

When no constraints are defined, the minimization of (3) leads to a linear time invariant (LTI) control law that can be precomputed in advance.

FGPC generalizes the GPC cost function (3) making use of the so-called fractional-order definite integration operator ${}^{\alpha}I_a^b(\cdot)$ [15, 46, 47] (see the appendix):

$$J_{\mathrm{FGPC}}(\Delta u, t) = {}^{\alpha}I_{N_1}^{N_2}[e(t)]^2 + {}^{\beta}I_1^{N_u}[\Delta u(t-1)]^2, \quad \forall \alpha, \beta \in \mathbb{R}, \tag{5}$$

where $e \equiv r - y$ is the error. This cost function has been discretized with sampling period Δt and evaluated using (A.2).

The FGPC cost function has an equivalent matrix form:

$$J_{\mathrm{FGPC}}(\Delta u, t) \simeq e'\Gamma(\alpha, \Delta t)\, e + \Delta u' \Lambda(\beta, \Delta t)\, \Delta u, \tag{6}$$

where Γ and Λ are infinite-dimensional square real weighting matrices which depend, by construction, on α and β, respectively:

$$\Gamma \equiv \Delta t^{\alpha} \operatorname{diag}\left(\cdots \;\; w_n \;\; w_{n-1} \;\; \cdots \;\; w_1 \;\; w_0\right) \tag{7}$$

with $w_j = \omega_j - \omega_{j-n}$, $n = N_2 - N_1$, $\omega_l = (-1)^l \binom{-\alpha}{l}$, and $\omega_l = 0$, for all $l < 0$;

$$\Lambda \equiv \Delta t^{\beta} \operatorname{diag}\left(\cdots \;\; w_{N_u-1} \;\; w_{N_u-2} \;\; \cdots \;\; w_1 \;\; w_0\right) \tag{8}$$

with $w_j = \omega_j - \omega_{j-n}$, $n = N_u - 1$, $\omega_l = (-1)^l \binom{-\beta}{l}$, and $\omega_l = 0$, for all $l < 0$.

In absence of constraints, the minimization of this cost function leads to a LTI control law similar to the one of GPC whose equivalent closed-loop schema is shown in Figure 2. See [46, 48] and the references therein for details.

R_c and S_c are the controller polynomials obtained from the model polynomials A and B, and the controller parameters N_1, N_u, N_2, α and β, and d stand for disturbance. From schema, it is easy to obtain

$$R_c \Delta u(t) = T_c r(t) - S_c y(t). \tag{9}$$

The value of polynomials R_c and S_c is obtained using the expressions (10). Φ and F are two polynomials obtained from the resolution of two Diophantine equations. See [16–18] for more details:

$$R_c\left(z^{-1}\right) = \frac{T_c\left(z^{-1}\right) + \sum_{i=N_1}^{N_2} k_i \Phi_i}{\sum_{i=N_1}^{N_2} k_i z^{-N_2+i}}, \qquad S_c\left(z^{-1}\right) = \frac{\sum_{i=N_1}^{N_2} k_i F_i}{\sum_{i=N_1}^{N_2} k_i z^{-N_2+i}}. \tag{10}$$

In GPC the weighting sequences γ_k and λ_k are controller parameters defined by the user. However, in FGPC these sequences are obtained from the optimization process itself and depend on the fractional integration orders α (7) and β (8) as well as the controller horizons.

Tuning GPC and FGPC means setting the horizon parameters (N_1, N_u, N_2) together with the weighting sequences γ_k and λ_k for GPC, and α and β for FGPC, respectively. This task is critical because closed-loop stability depends on this choice. In GPC some thumb rules are usually accepted [29]. In FGPC, these thumb rules are also adequate for choosing the horizons [15, 46].

A FGPC-tuning method was proposed in [49]. Based on optimization, the objective is the system to fulfil phase margin, sensitivity functions, and some other robustness specifications. (This tuning method has already been used to tune fractional-order $\mathrm{PI}^{\lambda}\mathrm{D}^{\mu}$ controllers successfully [50–52].) In order to keep the dimension of the optimization problem low, it is assumed that the horizon parameters (N_1, N_u, N_2) are given (for instance, following the thumb-rules previously announced), and only the two unknown parameters, the fractional orders α and β, are used in the optimization process. Thus, the function *FMINCON* of the MATLAB optimization toolbox [53] can be used to solve the corresponding optimization problem.

3. Experimental Application

In this section, we present a practical application of FGPC. We describe its design, tuning, and practical performance on the longitudinal speed control of a commercial vehicle.

3.1. Experimental Vehicle. The vehicle used for the experimental phase is a convertible Citroën C3 Pluriel (Figure 3) which is equipped with automatic driving capabilities by means of hardware modifications to permit autonomous actions on the accelerator and brake pedals. These modifications let the controller's outputs steer the vehicle's actuators.

The car's throttle is handled by an analog signal that represents the pressure on the pedal, generated by an analog card. The action over the throttle pedal is transformed into two analogue values—one of them twice the other—between 0 and 5 V. A switch has been installed on the dashboard to commute between automatic throttle control and original throttle circuit.

The brake's automation has been done taking into account that its action is critical. In case of a failure of any of the autonomous systems, the vehicle can be stopped by human driver intervention. So an electrohydraulic braking system

Figure 3: Commercial Citroën C3 prototype vehicle.

is mounted in parallel with the original one, permitting to coexist the two braking system independently. More details about throttle and brake automation can be found in [54, 55].

Concerning the on-board sensor systems, a real-time kinematic-differential global positioning system (RTK-DGPS) that gives vehicle position with a 1 centimeter precision and an inertial unit (IMU) to improve the positioning when GPS signal fails are used to obtain the vehicle's true position. The car's actual speed and acceleration are obtained from a differential hall effect sensor and a piezoelectric sensor, respectively. These values are acquired via controller area network bus (CAN) and provide the necessary information to the control algorithm, which is running in real-time in the on-board control unit (OCU), generating the control actions to govern the actuators.

For the purpose of this work, the gearbox is always in first gear forcing the car to move at low speed. The sampling interval was fixed by the parameters of GPS at 200 ms. Therefore, the frequency of actions on the pedals is set to 5 Hz. Using these settings, the OCU can approximately perform an action every metre at a maximum speed of 20 km/h.

3.2. Identification of the Longitudinal Dynamics. Due to the gasoline-propelled vehicle dynamics at very low speeds are highly nonlinear, and finding an exact dynamical model for the vehicle is not an easy task. Nevertheless, as we have seen previously, fractional predictive controller needs a CARIMA model of the plant to make the predictions. Therefore, an identification process has to be carried out despite inevitable uncertainties and circuit perturbations.

Since the vehicle always remains in first gear, restricting its speed at less than 20 km/h and acting a high engine brake force, the identification process is only fulfilled for the throttle pedal. Taking the brake pedal effect into account leads us to a hybrid control strategy that is not the purpose of this paper.

The experimental vehicle response is shown in Figure 4 (solid line), where the vehicle has been subjected to several speed changes by means of successive throttle pedal actuations. (In Figure 4, the action of the brake pedal is also depicted but is not taken into consideration in the identification process; it has been used for the purpose of returning to the initial speed, 0 km/h.)

The model of the vehicle is obtained by means of an identification process using the MATLAB Identification Toolbox [56], considering a normalized input—in the interval (0, 1)—for the throttle pedal and the sampling time of GPS fixed at 200 ms:

$$G\left(z^{-1}\right) = \frac{5.1850z^{-4}}{1 - 0.7344z^{-1} - 0.2075z^{-2}}. \tag{11}$$

The time-domain model validation is depicted in Figure 4. It is observable that model (11) captures the vehicle dynamics reasonably good (dash line) in comparison with the experimental data (solid line), despite environment and circuit perturbations.

3.3. Controller Design. This section describes the controller design for the longitudinal speed control of the vehicle described previously. Transfer function (11) constitutes the starting point in the controller tuning, where beneficial characteristics of fractional predictive formulation will be used to compensate unmodeled dynamics and external disturbances.

Other practical requirements have to be taken into account during the design process. (1) The car response has to be smooth to guarantee that its acceleration is less than $\pm 2\,\mathrm{m/s^2}$, the maximum acceptable acceleration for standing passengers [57]. (2) Control action u is normalized and has to be in the interval [0, 1], where negative values are not allowed as they mean brake actions.

Firstly, the horizons are chosen to capture the loop dominant dynamics. We have taken a time window of 2 seconds ahead defined by $N_1 = 1$ and $N_2 = 10$, which is appropriated in a heavy traffic scene (low speed). A wider time window supposes an increment of N_2 that would lead to a system with an excessively slow response. On the other hand, we have also considered the control horizon $N_u = 2$, which represents an agreement between system response speed and comfort of the vehicle's occupants. It is well-known that larger values of N_u produce tighter control actions [16] that could even make the system unstable.

Moreover, we have used a prefilter $T_c(z^{-1})$ to improve the system robustness against the model-process mismatch and the disturbance rejection. In [44] a guideline is given:

$$T_c\left(z^{-1}\right) = \left(1 - \rho z^{-1}\right)^{N_1}, \tag{12}$$

where ρ is recommended to be close to the dominant pole of (11).

Thus, the chosen prefilter has the following expression:

$$T_c\left(z^{-1}\right) = 1 - 0.9z^{-1}. \tag{13}$$

Once the controller horizons and the prefilter are chosen, the objective of the optimization process is finding the pair (α, β) that fulfils some specified robustness criteria. In our case, we shall impose the following.

(i) Maximize the phase margin (no specification is set on the gain margin).

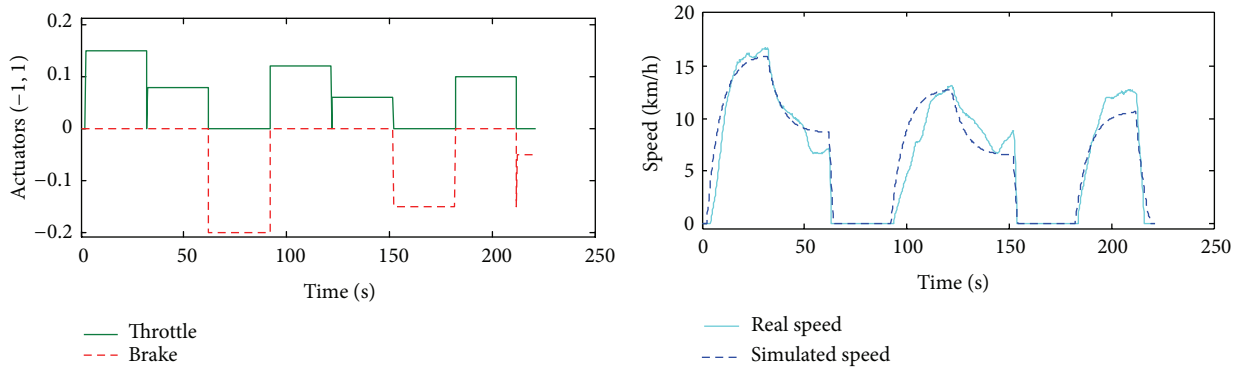

(a) (b)

Figure 4: Experimental vehicle response and time-domain model validation.

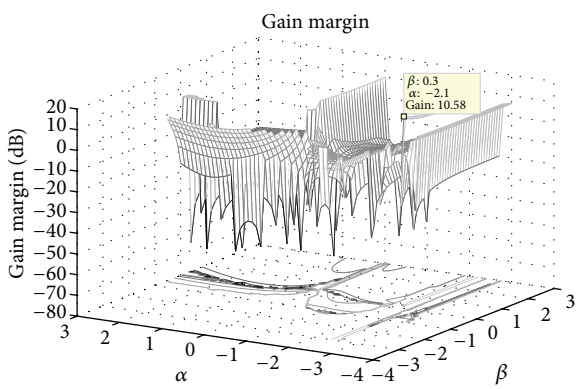

Figure 5: FGPC gain margin versus α and β.

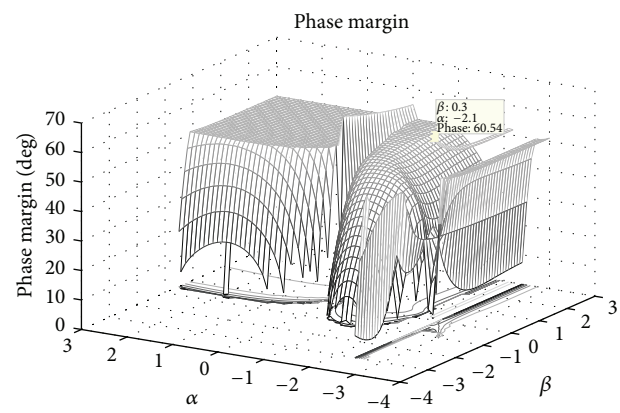

Figure 6: FGPC phase margin versus α and β.

(ii) Sensitivity function $|S(j\omega)| \leq -30$ dB for $\omega \leq 0.01$ rad/s.

(iii) Complementary sensitivity function $|T(j\omega)| \leq 0$ dB for $\omega \geq 0.1$ rad/s.

(Phase margin maximization guarantees smooth system output and robustness; sensitivity functions constraints give good noise and disturbance rejection.)

In order to initialize the optimization algorithm an initial seed (α_0, β_0) is needed. Figures 5 and 6 depict the closed loop magnitude and phase margins, respectively, in the interval $\alpha, \beta \in [-3, 3]$. We select $\alpha_0 = -2.1$ and $\beta_0 = 0.3$ for their corresponding good gain and phase margins.

The optimization process has been carried out in an interval of 20–30 seconds using a PC computer with Intel Core 2 Duo T9300 2.5 GHz running MATLAB 2007a. The solution to the optimization problem is $\alpha^* = -2.2456$ and $\beta^* = 2.9271$, for which the weighting sequences Γ and Λ are given in (14), with a phase margin of 76.76° (and a gain margin of 15.51 dB). The controller sensitivity functions meet the design specifications, as it is depicted in Figure 7:

$$\Gamma = \operatorname{diag}\left(-36.9671 \quad -0.0406 \quad -0.0683 \quad -0.1273 \quad -0.1273 \quad -0.7881 \quad -0.7881 \quad 51.4711 \quad 82.8442 \quad 36.9411\right)$$
$$\Lambda = \operatorname{diag}\left(0.0173 \quad 0.0090\right). \tag{14}$$

3.4. Experimental Results. The experimental trial was accomplished at the Centre for Automation and Robotics (CAR; joint research centre by the Spanish Consejo Superior de Investigaciones Científicas and the Universidad Politécnica de Madrid) private driving circuit using the Citroën C3 Pluriel described previously. The circuit has been designed with scientific purposes and represents an inner-city area with straight-road segments, bends, and so on. Figure 8 shows an aerial sight.

To validate the proposed controller, various target speed changes were set each 25 seconds, trying to keep the speed error close to zero. Moreover, the automatic gearbox was always in first gear, avoiding any effect of gear changes and forcing the car to move at low speed. Figure 9 depicts the responses of the vehicle, both actual—real time—(dot line) and simulated (dash-dot line). The FGPC controller accomplished all practical requirements which were set previously. The vehicle response is stable, smooth, and reasonably good in comparison with its simulation. It is important to remark that the positive reference changes are faster than the negative one. This is mainly due to the fact that the braking manoeuvre has to be achieved by the engine brake force, and it is affected by the slope of the circuit.

With respect to the comfort of the vehicle's occupants, it is observable that vehicle acceleration always remains (in

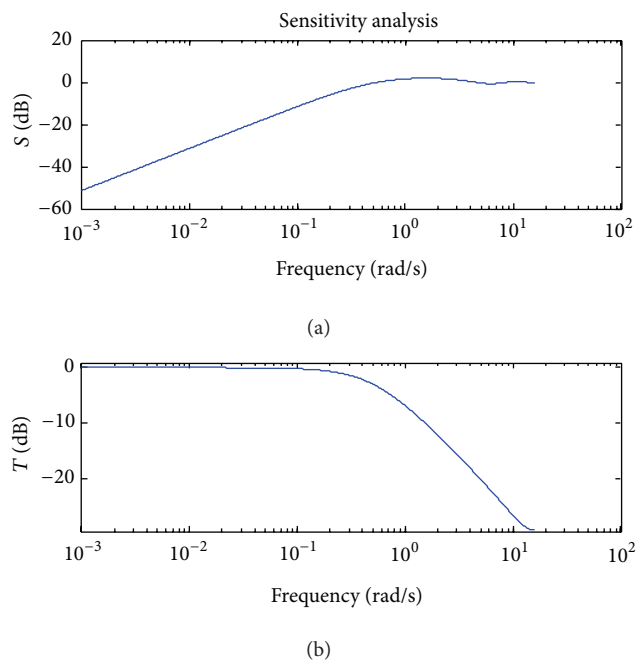

Figure 7: Sensitivity functions.

Figure 8: Private driving circuit at CAR.

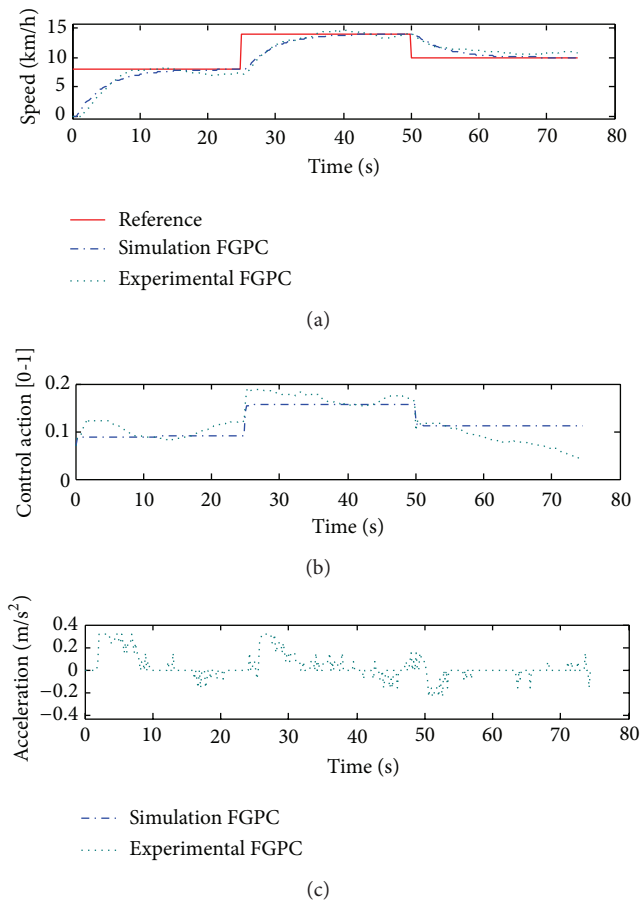

Figure 9: FGPC controller performance.

absolute value) below the maximum acceptable acceleration requirement, 2 m/s^2. It is due to the soft action over the throttle vehicle actuator, satisfying the comfort driving requisites.

For comparison purposes, we have also tested the performance of several GPCs which were tuned using the same horizons ($N_1 = 1$, $N_u = 2$, and $N_2 = 10$) and prefilter T_c (13) as FGPC.

In practice, in GPC it is commonly assumed that the weighting sequences are constant, that is, $\gamma_k = \gamma$ and $\lambda_k = \lambda$. Under this assumption, it has not been possible to find a GPC controller that fulfils the robustness criteria using and equivalent optimization method. (The set of dynamics that can be found with constant weights is much smaller than in the case of FGPC. Furthermore, trying to optimize a GPC controller in the general case (γ_k, λ_k) would lead to an optimization problem with an extremely high dimension. On the other hand, in the case of FGPC one has to optimize only two parameters, α and β, and this automatically leads to nonconstant weighting sequences; recall that GPC and FGPC controllers share a common LTI expression, as was pointed out in Section 2 [49].)

For this reason, we have tuned several GPC controllers with different constant weighting sequences γ and λ. Specifically, $\lambda \in \{10^{-6}, 10^{-1}, 10^{1}, 10^{5}\}$ and $\gamma = 1$ (as the variation of γ does not affect the system dynamics considerably).

Using these settings, we have obtained two GPC controllers that in practice turned out to be unstable although they were stable in simulation. These controllers correspond to $\lambda = 10^{-6}$ and $\lambda = 10^{-1}$ (labelled *Experimental GPC 1* and *Experimental GPC 2* in Figure 10, resp.). Thus, they were not able to compensate unmodeled dynamics and circuit perturbations.

On the other hand, GPC controllers for $\lambda = 10^{1}$ and $\lambda = 10^{5}$ (labelled *Experimental GPC 3* and *Experimental GPC 4* in Figure 11, resp.) were stable in practice. It is well-known that higher values of λ give rise to smooth control actions, increasing the closed loop system robustness [16]. However, an excessively high value of λ could make the system response too slow. It would mean, in practice, that our car could not stop in time, and it would probably crash into the front car.

To quantify these results, we shall compare the principal control quality indicators for the stable realizations (GPC 3, GPC 4, and FGPC) speed error (reference speed—experimental speed), softness of the control action, and acceleration. The last ones require to calculate the fast fourier transform (FFT) to estimate them.

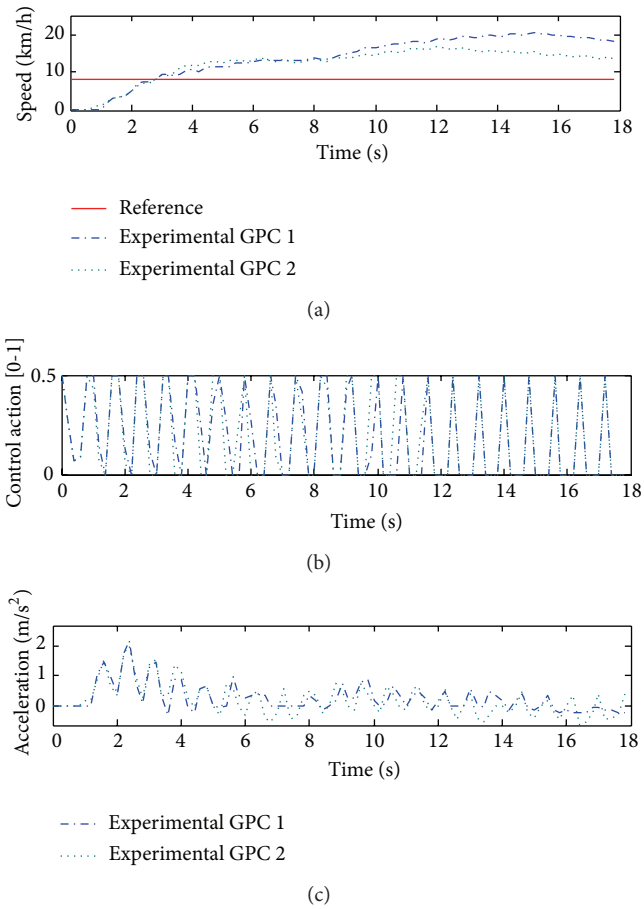

FIGURE 10: Unstable GPC controllers. Action over the throttle has been limited to [0–0.5] for passengers safety during the experimental trial.

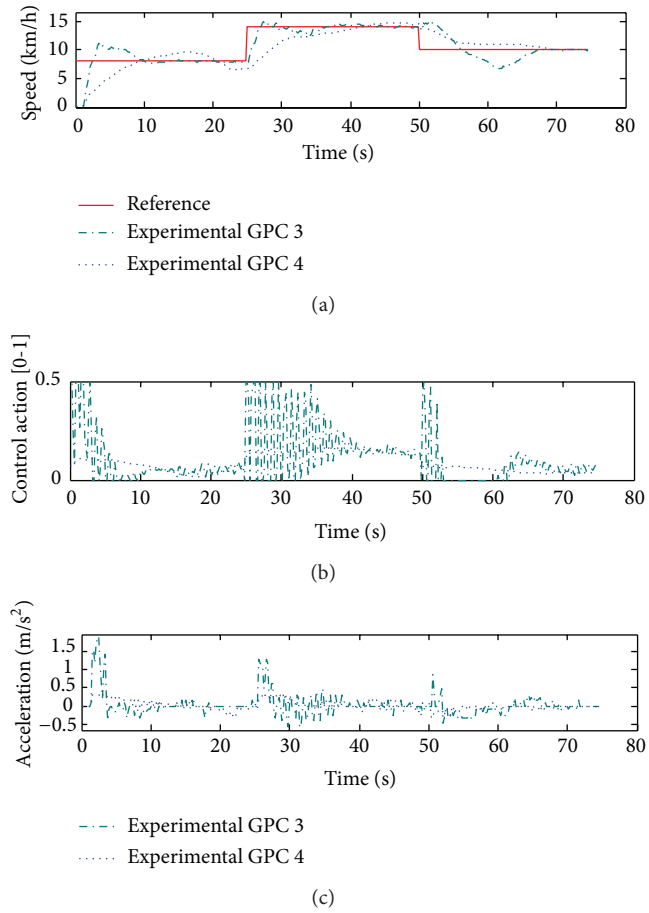

FIGURE 11: Stable GPC controllers.

It is well known that FFT (15) is an efficient algorithm to compute the discrete fourier transform (DFT), $\mathfrak{F}$,

$$U_k = \mathfrak{F}(u_k) = \sum_{i=0}^{N-1} u_k e^{(2\pi N/k_i)}, \quad k = 0, \ldots, N-1, \tag{15}$$

where u_k is the control action or acceleration value at time t_k and N the length of these signals. FFT yields the signal sharpness by means of a frequency spectrum analysis of the sampled signal.

In order to get a good indicator of the overall control action and acceleration signals with robustness to outliers, we have used the median $\tilde{u}$ of sequence U_k.

$$P(U_k \le \tilde{u}) \ge \frac{1}{2} \wedge P(U_k \ge \tilde{u}) \ge \frac{1}{2}. \tag{16}$$

The following widely used statistics parameters have been used to evaluate the speed error:

(i) mean:

$$\bar{e} = \frac{1}{N} \sum_{i=0}^{N-1} e_i, \tag{17}$$

(ii) standard deviation:

$$\sigma = \sqrt{\frac{1}{N} \sum_{i=0}^{N-1} (e_i - \bar{e})^2}, \tag{18}$$

(iii) root mean square error:

$$\mathrm{RMSE} = \sqrt{\frac{1}{N} \sum_{i=0}^{N-1} e_i^2}, \tag{19}$$

where e_k is the speed error at time t_k. Moreover, we have also used the median $\tilde{e}$.

All of these control quality indicators are reflected in Table 1.

One observes (see Figures 9 and 11) that the speed changes of GPC 4 and FGPC are slower than the response of GPC 3, so they need more time to reach the steady state after speed changes. This is reflected in Table 1 where, in terms of speed error, all statistics parameters of GPC 3 are better than the GPC 4 and FGPC ones. However, it presents very poor values in the control action and acceleration indicators due to the very large fluctuations of these signals, as we can see graphically in Figure 11. This undesirable behaviour

Table 1: Comparison of stable controllers.

Contr.	Speed error				Control action	Acceleration
	Mean	St. dev.	Median	RMSE	FFT median	FFT median
GPC 3	0.0474	2.1340	2.5539	2.1317	0.4397	1.9320
GPC 4	0.3955	2.5186	6.3434	2.5461	0.0149	1.0562
FGPC	0.4604	2.4119	5.8174	2.4523	0.0044	0.1652

compromises seriously the comfort of standing passengers, bordering on the maximum acceptable acceleration, $2\,\mathrm{m/s^2}$. Furthermore, it could injurey the throttle actuator due to its continuous and aggressive fluctuations in the control action.

The FGPC controller shows the best behaviour in the steady state without overshoot and presenting the best values in terms of the softness of the control action and acceleration, due to the precise parameters tuning carried out by the optimization method. FGPC takes advantage of its diversity of responses (varying the fractional orders α and β) to meet the design specifications and to improve the system robustness against the model-process mismatch.

4. Conclusions

The longitudinal control of a gasoline-propelled vehicle at low speeds (common situation in traffic jams) constitutes one of the most important topics in the automotive sector due to the highly nonlinear dynamics that the vehicle presents in this situation.

In this paper, the fractional predictive control strategy, FGPC, has been used to solve this problem. Taking advantage of its beneficial characteristics and its tuning method to compensate un-modeled dynamics, a FGPC controller has been designed which has achieved closed loop stability following the changes in the velocity reference. Moreover, practical requirements to guarantee standing passengers comfort have been also achieved by means of the appropriate parameters choice carried out by the optimization-based tuning, in spite of inevitable uncertainties and circuit perturbations.

Finally, the comparison between the fractional predictive control strategy, FGPC, and its integer-order counterpart, GPC, has shown that the task of finding the correct setting for the weighting sequences γ_k and λ_k is crucial. In FGPC, the fractional orders α and β allow us to find them keeping the dimension of the optimization problem low, since only two parameters have been optimized.

Appendix

Fractional-Order Definite Integral Operator

The fractional-order definite integral of function $f(x)$ within interval $[a, b]$ has the following expression [47]:

$$ {}^{\alpha}I_a^b f(x) \equiv \int_a^b \left[D^{1-\alpha} f(x)\right] dx, \quad \alpha, a, b \in \mathbb{R}. \tag{A.1} $$

Using the GL definition (1) assuming that $D^{1-\alpha}[f(x)] \neq 0$, the fractional-order definite integrator operator ${}^{\alpha}I_a^b(\cdot)$ has the following discretized expression with a sampling period Δt:

$$ {}^{\alpha}I_a^b f(x) = \Delta x^{\alpha} \overline{W}' \overline{f}, \tag{A.2} $$

where

$$ \begin{aligned} \overline{W} &= \left(\cdots \ w_b \ \ w_{b-1} \ \cdots \ w_{n+1} \ \ w_n \ \cdots \ w_1 \ \ w_0\right)' \\ \overline{f} &= \left(\cdots \ f(0) \ \ f(\Delta x) \ \cdots \ f(a-\Delta x) \ \ f(a) \right. \\ &\qquad \left. \cdots \ f(b-\Delta x) \ \ f(b)\right)' \end{aligned} \tag{A.3} $$

with $w_j = \omega_j - \omega_{j-n}$, $n = b - a$, $\omega_l = (-1)^l \binom{-\alpha}{l}$, and $\omega_l = 0$, for all $l < 0$.

Conflicts of Interest

The authors report no actual or potential conflict of interests in relation to this manuscript.

Acknowledgments

The authors wish to acknowledge the economical support of the Spanish Distance Education University (UNED), under Project reference PROY29 (Proyectos Investigación 2012), and the AUTOPIA Program of the Center for Automation and Robotics UPM-CSIC.

References

[1] I. Podlubny, *Fractional Differential Equations*, vol. 198 of *Mathematics in Science and Engineering*, Academic Press, San Diego, Calif, USA, 1999.

[2] K. B. Oldham and J. Spanier, *The Fractional Calculus*, vol. 111 of *Mathematics in Science and Engineering*, Academic Press, New York, NY, USA, 1974.

[3] K. S. Miller and B. Ross, *An Introduction to the Fractional Calculus and Fractional Differential Equations*, John Wiley & Sons, New York, NY, USA, 1993.

[4] B. M. Vinagre, C. A. Monje, and A. J. Calderón, "Fractional order systems and fractional order control actions," in *Proceedings of the 41st Conference on Decision and Control. Tutorial Workshop 2: Fractional Calculus Applications in Automatic Control and Robotics*, Las Vegas, Nev, USA, 2002.

[5] I. Podlubny, "Numerical solution of ordinary fractional differential equations by the fractional difference method," in *Advances in Difference Equations (Veszprém, 1995)*, pp. 507–515, Gordon and Breach, Amsterdam, The Netherlands, 1997.

[6] A. Oustaloup, B. Mathieu, and P. Lanusse, "The CRONE control of resonant plants: application to a flexible transmission," *European Journal of Control*, vol. 1, pp. 113–121, 1995.

[7] I. Podlubny, "Fractional-order systems and $PI^{\lambda}D^{\mu}$-controllers," *IEEE Transactions on Automatic Control*, vol. 44, no. 1, pp. 208–214, 1999.

[8] I. Petráš, "The fractional-order controllers," *Journal of Electrical Engineering*, vol. 50, pp. 284–288, 1999.

[9] O. P. Agrawal, "A general formulation and solution scheme for fractional optimal control problems," *Nonlinear Dynamics*, vol. 38, no. 1–4, pp. 323–337, 2004.

[10] O. P. Agrawal and D. Baleanu, "A Hamiltonian formulation and a direct numerical scheme for fractional optimal control problems," *Journal of Vibration and Control*, vol. 13, no. 9-10, pp. 1269–1281, 2007.

[11] C. Tricaud and Y. Q. Chen, "Solving fractional order optimal control problms in RIOTS_95—a general purpose optimal control problems solver," in *Proceedings of the 3rd IFAC Workshop on Fractional Differentiation and Its Applications*, Ankara, Turkey, 2008.

[12] M. O. Efe, "Fractional fuzzy adaptive sliding-mode control of a 2-DOF direct-drive robot arm," *IEEE Transactions on Systems, Man, and Cybernetics, Part B*, vol. 38, no. 6, pp. 1561–1570, 2008.

[13] I. S. Jesus, J. T. Machado, and R. S. Barbosa, "Fractional order nonlinear control of heat system," in *Proceedings of the 3rd IFAC Workshop on Fractional Differentiation and Its Applications*, Ankara, Turkey, 2008.

[14] Y. Li, Y. Chen, and H.-S. Ahn, "Fractional-order iterative learning control for fractional-order linear systems," *Asian Journal of Control*, vol. 13, no. 1, pp. 54–63, 2011.

[15] M. Romero, A. P. de Madrid, C. Mañoso, and R. Hernandez, "Generalized predictive control of arbitrary real order," in *New Trends in Nanotechnology and Fractional Calculus Applications*, D. Baleanu, Z. B. Guvenc, and J. A. T. Machado, Eds., pp. 411–418, Springer, Dordrecht, The Netherlands, 2009.

[16] E. F. Camacho and C. Bordons, *Model Predictive Control*, Springer, New York, NY, USA, 2nd edition, 2004.

[17] J. A. Rossiter, *Model Based Predictive Control. A Practical Approach*, CRC Press, New York, NY, USA, 2003.

[18] J. M. Maciejowski, *Predictive Control with Constraints*, Prentice Hall, New York, NY, USA, 2002.

[19] J. Qin and T. Badgwell, "An overview of industrial model predictive control technology," in *Proceedings of the International Conference on Chemical Process*, J. C. Kantor, C. E. Garcia, and B. Carnahan, Eds., vol. 93 of *AIChE Symposium Series*, pp. 232–256, 1997.

[20] C. R. Cutler and B. L. Ramaker, "Dynamic matrix control—a computer control algorithm," in *Proceedings of Joint Automatic Control Conference*, San Francisco, Calif, USA, 1980.

[21] W. L. Luyben, Ed., *Practical Distillation Control*, Van Nostrand Reinhold, New York, NY, USA, 1992.

[22] T. Alvarez, M. Sanzo, and C. de Prada, "Identification and constrained multivariable predictive control of chemical reactors," in *Proceedings of the IEEE Conference on Control Applications*, pp. 663–664, Albany, NY, USA, September 1995.

[23] J. M. Martín Sánchez and J. Rodellar, *Adaptive Predictive Control. From the Concepts to Plant Optimization*, Prentice Hall, Upper Saddle River, NJ, USA, 1996.

[24] E. F. Camacho and M. Berenguel, "Application of generalized predictive control to a solar power plant," in *Proceedings of the IEEE Conference on Control Applications*, pp. 1657–1662, Glasgow, UK, August 1994.

[25] F. Han, C. Zuo, W. Wu, J. Li, and Z. Liu, "Model predictive control of the grain drying process," *Mathematical Problems in Engineering*, vol. 2012, Article ID 584376, 12 pages, 2012.

[26] D. A. Linkens and M. Mahfouf, "Generalized predictive control (GPC) in clinical anaesthesia," in *Advances in Model-Based Predictive Control*, D. W. Clarke, Ed., pp. 429–445, Oxford University Press, Oxford, UK, 1994.

[27] H. Yang and S. Li, "A data-driven bilinear predictive controller design based on subspace method," *Asian Journal of Control*, vol. 13, no. 2, pp. 345–349, 2011.

[28] X.-H. Chang and G.-H. Yang, "Fuzzy robust constrained model predictive control for nonlinear systems," *Asian Journal of Control*, vol. 13, no. 6, pp. 947–955, 2011.

[29] D. W. Clarke, C. Mohtadi, and P. S. Tuffs, "Generalized predictive control. Part I. The basic algorithm," *Automatica*, vol. 23, no. 2, pp. 137–148, 1987.

[30] D. W. Clarke, C. Mohtadi, and P. S. Tuffs, "Generalized predictive control. Part II. Extensions and interpretations," *Automatica*, vol. 23, no. 2, pp. 149–160, 1987.

[31] M. Romero, I. Tejado, B. M. Vinagre, and A. P. de Madrid, "Position and velocity control of a servo by using GPC of arbitrary real order," in *New Trends in Nanotechnology and Fractional Calculus Applications*, D. Baleanu, Z. B. Guvenc, and J. A. T. Machado, Eds., pp. 369–376, Springer, Dordrecht, The Netherlands, 2009.

[32] M. Romero, I. Tejado, J. I. Suárez, B. M. Vinagre, and A. P. De Madrid, "GPC strategies for the lateral control of a networked AGV," in *Proceedings of the 5th International Conference on Mechatronics (ICM '09)*, Málaga, Spain, April 2009.

[33] I. Tejado, M. Romero, B. M. Vinagre, A. P. de Madrid, and Y. Q. Chen, "Experiences on an internet link characterization and networked control of a smart wheel," *International Journal of Bifurcation and Chaos*, vol. 22, no. 4, 2012.

[34] R. Bishop, "A survey of intelligent vehicle applications worldwide," in *Proceedings of the IEEE Intelligent Vehicles Symposium*, pp. 25–30, Dearborn, Mich, USA, 2000.

[35] G. Marsden, M. McDonald, and M. Brackstone, "Towards an understanding of adaptive cruise control," *Transportation Research Part C*, vol. 9, no. 1, pp. 33–51, 2001.

[36] A. Vahidi and A. Eskandarian, "Research advances in intelligent collision avoidance and adaptive cruise control," *IEEE Transactions on Intelligent Transportation Systems*, vol. 4, no. 3, pp. 132–153, 2003.

[37] B. Van Arem, C. J. G. Van Driel, and R. Visser, "The impact of cooperative adaptive cruise control on traffic-flow characteristics," *IEEE Transactions on Intelligent Transportation Systems*, vol. 7, no. 4, pp. 429–436, 2006.

[38] T. Aono and T. Kowatari, "Throttle-control algorithm for improving engine response based on air-intake model and throttle-response model," *IEEE Transactions on Industrial Electronics*, vol. 53, no. 3, pp. 915–921, 2006.

[39] N. B. Hounsell, B. P. Shrestha, J. Piao, and M. McDonald, "Review of urban traffic management and the impacts of new vehicle technologies," *IET Intelligent Transport Systems*, vol. 3, no. 4, pp. 419–428, 2009.

[40] S. Moon, I. Moon, and K. Yi, "Design, tuning, and evaluation of a full-range adaptive cruise control system with collision avoidance," *Control Engineering Practice*, vol. 17, no. 4, pp. 442–455, 2009.

[41] L. Cai, A. B. Rad, and W. L. Chan, "An intelligent longitudinal controller for application in semiautonomous vehicles," *IEEE Transactions on Industrial Electronics*, vol. 57, no. 4, pp. 1487–1497, 2010.

[42] V. Milanés, J. Villagrá, J. Godoy, and C. González, "Comparing fuzzy and intelligent PI controllers in stop-and-go manoeuvres," *IEEE Transactions on Control Systems Technology*, vol. 20, no. 3, pp. 770–778, 2011.

[43] I. Tejado, V. Milanés, J. Villagrá, J. Godoy, H. HosseinNia, and B. M. Vinagre, "Low speed control of an autonomous vehicle by using a fractional PI," in *Proceedings of the 18th World Congress International Federation Automatic Control*, pp. 15025–15030, Milano, Italy, 2011.

[44] T.-W. Yoon and D. W. Clarke, "Observer design in receding-horizon predictive control," *International Journal of Control*, vol. 61, no. 1, pp. 171–191, 1995.

[45] C. Mañoso, A. P. de Madrid, M. Romero, and R. Hernández, "GPC with structured perturbations: the influence of prefiltering and terminal equality constraints," *ISRN Applied Mathematics*, vol. 2012, Article ID 623484, 12 pages, 2012.

[46] M. Romero, A. P. de Madrid, C. Mañoso, and B. M. Vinagre, "Fractional-order generalized predictive control: formulation and some properties," in *proceedings of the 11th International Conference on Control, Automation, Robotics and Vision (ICARCV '10)*, pp. 1495–1500, Singapore, December 2010.

[47] M. Romero, A. P. de Madrid, and B. M. Vinagre, "Arbitrary real-order cost functions for signals and systems," *Signal Processing*, vol. 91, no. 3, pp. 372–378, 2011.

[48] M. Romero, A. P. de Madrid, C. Mañoso, and B. M. Vinagre, "A survey of fractional-order generalized predictive control," in *Proceedings of the 51st Conference on Decision and Control*, pp. 6867–6872, Maui, Hawaii, USA, 2012.

[49] M. Romero, I. Tejado, A. P. de Madrid, and B. M. Vinagre, "Tuning predictive controllers with optimization: application to GPC and FGPC," in *Proceedings of the 18th World World Congress International Federation Automatic Control*, pp. 10824–10829, Milano, Italy, 2011.

[50] C. A. Monje, A. J. Calderón, B. M. Vinagre, Y. Chen, and V. Feliu, "On fractional PI^{λ} controllers: some tuning rules for robustness to plant uncertainties," *Nonlinear Dynamics*, vol. 38, no. 1–4, pp. 369–381, 2004.

[51] Y. Q. Chen, H. Dou, B. M. Vinagre, and C. A. Monje, "A robust tuning method for fractional order PI controllers," in *Proceedings of the 2nd IFAC Workshop on Fractional Differentiation and Its Applications*, Porto, Portugal, 2006.

[52] C. A. Monje, B. M. Vinagre, V. Feliu, and Y. Chen, "Tuning and auto-tuning of fractional order controllers for industry applications," *Control Engineering Practice*, vol. 16, no. 7, pp. 798–812, 2008.

[53] Mathworks Inc., "Matlab optimization toolbox user's guide," 2007.

[54] V. Milanés, C. González, J. E. Naranjo, E. Onieva, and T. de Pedro, "Electro-hydraulic braking system for autonomous vehicles," *International Journal of Automotive Technology*, vol. 11, no. 1, pp. 89–95, 2010.

[55] V. Milanés, D. F. Llorca, B. M. Vinagre, C. González, and M. A. Sotelo, "Clavileno: evolution of an autonomous car," in *Proceedings of the 13th IEEE International Intelligent Transportation Systems*, Madeira, Portugal, 2010.

[56] Mathworks Inc., "Matlab identification toolbox user's guide," 2007.

[57] BECHTEL, "Compendium of executive summaries from the maglev system concept definition final reports," Tech. Rep., U.S. Department of Transportation, 1993, http://ntl.bts.gov/DOCS/CES.html.

Hindawi Publishing Corporation
Mathematical Problems in Engineering
Volume 2013, Article ID 890157, 22 pages
http://dx.doi.org/10.1155/2013/890157

Research Article

Image Denoising via Nonlinear Hybrid Diffusion

Xiaoping Ji, Dazhi Zhang, Zhichang Guo, and Boying Wu

Department of Mathematics, Harbin Institute of Technology, Harbin 150001, China

Correspondence should be addressed to Dazhi Zhang; zhang-d-z@163.com

Received 3 December 2012; Accepted 15 February 2013

Academic Editor: Jocelyn Sabatier

A nonlinear anisotropic hybrid diffusion equation is discussed for image denoising, which is a combination of mean curvature smoothing and Gaussian heat diffusion. First, we propose a new edge detection indicator, that is, the diffusivity function. Based on this diffusivity function, the new diffusion is nonlinear anisotropic and forward-backward. Unlike the Perona-Malik (PM) diffusion, the new forward-backward diffusion is adjustable and under control. Then, the existence, uniqueness, and long-time behavior of the new regularization equation of the model are established. Finally, using the explicit difference scheme (PM scheme) and implicit difference scheme (AOS scheme), we do numerical experiments for different images, respectively. Experimental results illustrate the effectiveness of the new model with respect to other known models.

1. Introduction

Image restoration and smoothing are important in problems ranging from medical diagnostic tests to defense applications such as target recognition. Over the past 20 years, the use of variational methods and nonlinear partial differential equations (PDEs) has significantly grown and evolved to address the image restoration problem. Let u_0 be the intensity of an image obtained from a noiseless image by adding Gaussian noise with zero mean, defined on a rectangle $\Omega \subset \mathbb{R}^2$, and let u represent the reconstructed image. The problem is to recover the restoration image u, from the observed, noisy image u_0, where the two are related by $u_0 = u + \text{noise}$.

1.1. Nonlinear Diffusion. A large number of image restoration techniques are conveniently formulated using some nonlinear partial differential equations (PDEs) approach. The review article [1] provides a historical description of the use of PDEs in image processing. In [2], Perona and Malik developed an anisotropic diffusion scheme for image denoising. The basic idea of this nonlinear smoothing scheme was to smooth the image while preserving the edges in it. This was done by using equation

$$\begin{aligned} u_t &= \operatorname{div}\left(c\left(|\nabla u|\right)\nabla u\right), \\ u(0,x) &= f, \end{aligned} \tag{1}$$

where f is the noisy image and u is the image to be smoothed and u_t describes its evolution over time. The diffusivity $c(|\nabla u|)$ controls the amount of diffusion. $c(s)$ is also an edge indicator and a smooth nonincreasing function and has such properties as $c(0) = 1$, $c(s) \geq 0$, and $c(s) \to 0$, as $s \to \infty$. This ensures that strong edges are less blurred by the diffusion filter than noise and low-contrast details.

In [3], Iijima employs the following linear diffusivity function:

$$c\left(|x|\right) = 1. \tag{2}$$

Because the model is linear isotropic diffusion, it cannot preserve the edge and some features. The PM diffusivity function [2] is usually

$$c_{\mathrm{PM}}\left(|x|\right) = \frac{1}{1 + |x|^2/K^2}. \tag{3}$$

The PM diffusion is nonlinear anisotropic diffusion and can preserve the most features, especially edges in the image. Here are some of the previously employed diffusivity functions.

Charbonnier diffusivity [4]:

$$c\left(|x|\right) = \frac{1}{\sqrt{1 + |x|^2/K^2}}. \tag{4}$$

TV diffusivity [5]:

$$c(|x|) = \frac{1}{|x|}. \tag{5}$$

Weickert diffusivity [6]:

$$c(|x|) = \begin{cases} 1, & |x| = 0 \\ 1 - \exp\left(\dfrac{-3.31488}{|x|^8/k^8}\right), & |x| > 0. \end{cases} \tag{6}$$

Except the diffusivity functions, there are other diffusivity functions, such as BFB diffusivity [7] and FAB diffusivity [8, 9]. Well-posedness results are available for linear diffusivity, Charbonnier diffusivity, and TV diffusivity, since they result from convex potentials. For PM diffusivity, Weickert diffusivity, and BFB diffusivity, which can be related to nonconvex potentials, some well-posedness questions are open in the continuous setting [10, 11], while already a space-discretisation creates well-posed processes [12]. In practice, the ill-posedness results in a mild instability in the discrete problem. Regions of high gradients develop a "staircase" instability that involves dynamic coarsening of the steps as time evolves [13, 14].

To make the images more pleasing to the eye, it would be useful to reduce staircasing effect. Many models to reduce this effect have been proposed in the literature. A simple adjustment with practical applications is to include a short range mollifier in the nonlinear diffusion [15]. The new well-posed equation is given by

$$\begin{gathered} \frac{\partial u}{\partial t} = \operatorname{div}\left(c\left(\left|\nabla G_\sigma * u\right|\right)\nabla u\right), \quad \text{in } \Omega \times (0,T), \\ u(0,x) = u_0, \quad \text{in } \Omega, \\ \frac{\partial u}{\partial \vec{n}} = 0, \quad \text{on } \partial\Omega \times (0,T), \end{gathered} \tag{7}$$

where G_σ is the Gaussian kernel, as described in Section 2. Existence and uniqueness of solutions to this modified Perona-Malik equation have been proved for initial data $u_0 \in L^2(\Omega)$. Another way is to use a higher-order version of the Perona-Malik equation, examples of which are given in [16–18].

Some authors consider a new class of fractional-order anisotropic diffusion equations to remove the noise [19–27]. These proposed equations can be seen as generalizations of second-order and fourth-order anisotropic diffusion equations. Numerical results show that these methods can not only remove noise and eliminate the staircase effect efficiently in the nontextured region but also preserve the small details such as textures well in the textured region.

1.2. The TV Framework. The famous total variation method first proposed by Rudin et al. [28] consists in solving the following constrained minimization problem:

$$\begin{gathered} \min \int_\Omega |\nabla u|, \\ \int_\Omega u\,dx = \int_\Omega u_0, \qquad \int_\Omega |u - u_0|_2^2 dx = \eta^2. \end{gathered} \tag{8}$$

Here, the first constrain indicates that the noise has zero mean, and the second one uses a priori information that the standard deviation of the noise is η. This problem is naturally linked to the unconstrained problem

$$\min_{u \in \mathrm{BV}(\Omega)} E(u) = \int_\Omega |\nabla u| + \lambda \|u - u_0\|_{L^2(\Omega)}^2. \tag{9}$$

Mathematically, this is reasonable, since it is natural to study solutions of this problem in the space of functions of bounded variation, $\mathrm{BV}(\Omega)$, allowing for discontinuities which are necessary for edge reconstruction. The TV model has been studied extensively (see [29–32], et al.) and has proved to be an invaluable tool for preserving edges in image restoration problem. Given the success of TV-based diffusion, various modifications have been introduced. For instance, in [33], Strongand and Chan propose the Adaptive Total Variation model

$$\min_{u \in \mathrm{BV}(\Omega)} E_g(u) = \int_\Omega g(x)|\nabla u| + \lambda \|u - u_0\|_{L^2(\Omega)}^2, \tag{10}$$

in which they introduce a control factor, $g(x)$, which slows the diffusion at likely edges. The factor $g(x)$ controls the speed of the diffusion and has demonstrated good results as it aids in noise reduction. It is also good at reconstructing edges, since the type of diffusion is the same as that of the original TV model.

The TV model is well posed, but TV-based denoising favors the piecewise constant solutions. Sometimes, this also causes "staircasing effect" [34–41], in which noisy smooth regions are processed into piecewise constant regions (see Figures 3–5). The blocky solution fails to satisfy visual impression and can develop false edges, which can mislead a human or computer into identifying erroneous features, not present in the true image.

Some authors consider another regularizing term to remove the noise [34], which is as follows:

$$\inf_u E(u) = \int_\Omega |\nabla u|^{p(|\nabla u|)} dx + \lambda \|f - u\|_{L^2(\Omega)}^2, \tag{11}$$

where $\lim_{s\to 0} p(s) \to 2$, $\lim_{s\to\infty} p(s) \to 1$, and p is monotonically decreasing. This model should reap the benefits of both isotropic and TV-based diffusions, as well as a combination of the two. However, it is difficult to study mathematically, since the lower semicontinuity of the functional is not readily evident. In [35], Chen et al. modify the model and propose a functional with variable exponent, $1 \le p(x) \le 2$, which is a combination of total variation based regularization and Gaussian smoothing.

From the models mentioned above, we can see that based on the PDE framework, the diffusivity functions affect the quality of the reconstructed image. In this paper, based on a new diffusivity function, we propose a new image denoising model which generalizes the approaches due to Perona and Malik [2], Chen et al. [35], and El-Fallah and Ford [42]. In the next section, we will describe this model more precisely. In Section 3, we prove the existence and uniqueness of the proposed model. The theorem can be proved by a similar argument developed in [15], but due to the presence of high degeneration and nonlinearity, more careful estimates are needed. We will give a modified proof in the sections. In the next two section, we first obtain some properties of the weak solution for the new model, and then using these properties, the long-time behavior of the proposed model is established. In Section 6, we describe an iterative scheme which converges to the solution. In the final section, we will give the numerical results which indicate the new model is able to preserve edges and denoise better than the existing methods, for instance, the TV model and PM model.

2. Nonlinear Hybrid Diffusion Model

2.1. The New Model. In this paper, we propose the following model:

$$\frac{\partial u}{\partial t} = \operatorname{div}\left(\frac{\nabla u}{\left(|\nabla u|^2+1\right)^{(2-p(|\nabla u|^2))/2}}\right), \quad \text{in } \Omega\times(0,T), \tag{12}$$

$$u(0,x) = f, \quad \text{in } \Omega, \tag{13}$$

$$\frac{\partial u}{\partial \vec{n}} = 0, \quad \text{on } \partial\Omega\times(0,T), \tag{14}$$

where

$$p\left(|\nabla u|^2\right) = 1 + \frac{1}{1+k|\nabla u|^2}, \quad k>0,\ \sigma>0, \tag{15}$$

f is the original image, $k>0$, σ and $T>0$ are fixed constants, Ω is a bounded open domain of $\mathbb{R}^N$ with the appropriate smooth boundary, and $\vec{n}$ denotes the unit outward normal to the boundary $\partial\Omega$.

2.2. Hybrid Diffusion. As $s\to+\infty$, $p(s)\to 1$, the new divergence operator is changed as follows:

$$\operatorname{div}\left(\frac{\nabla u}{\left(|\nabla u|^2+1\right)^{(2-p(|\nabla u|))/2}}\right) \longrightarrow \operatorname{div}\left(\frac{\nabla u}{\sqrt{|\nabla u|^2+1}}\right), \tag{16}$$

where the last term is the divergence operator of the mean curvature diffusion equation [42]. However, when $s=0$, $p(s)=2$, the original divergence operator is changed as follows:

$$\operatorname{div}\left(\frac{\nabla u}{\left(|\nabla u|^2+1\right)^{(2-p(|\nabla u|))/2}}\right) \longrightarrow \Delta u, \tag{17}$$

where the last term is the diffusion term of the heat equation.

Hence, the new model has a hybrid diffusion type which combined the mean curvature diffusion with the heat diffusion and has the following advantages.

(i) Inside the regions where the magnitude of the gradient of u is weak, the new model acts like the heat equation, resulting in isotropic smoothing.

(ii) Near the region's boundaries where the magnitude of the gradient is large, the new model acts like the mean curvature equation, resulting in anisotropic smoothing; the regularization is little and the edges are preserved.

2.3. The New Diffusivity Function. Let

$$C(s) = (1+s)^{(p(s)-2)/2}, \tag{18}$$

where

$$p(s) = 1 + \frac{1}{1+ks}. \tag{19}$$

Now, we discuss the properties of $C(s)$ as follows.

Proposition 1. *One has the following:*

(a) $C:[0,+\infty)\to(0,+\infty)$ *is a strict decreasing function, and* $0\le C(s)\le 1$, *for* $s\in\overline{\mathbb{R}}_+$ *(see Figure 1(a));*

(b) $C(0)=1$, *and* $\lim_{s\to\infty}C(s)=0$ *(see Figure 1(a));*

(c) $\lim_{s\to+\infty}\dfrac{sC'(s)}{C(s)} = -1/2$;

(d) $\lim_{s\to+\infty}\sqrt{1+s}\,C(s)=1$ *and* $\lim_{s\to+\infty}sC(s^2)=1$;

(e) $\lim_{s\to+\infty}s\,C'(s^2)=k/2$.

Proof. By a direct calculation, we have

$$\begin{gathered} C(s) = \exp\left\{-\frac{ks\ln(1+s)}{2(1+ks)}\right\}, \\ C'(s) = -kC(s)\,\frac{s(ks+1)+(1+s)\ln(1+s)}{2(1+s)(1+ks)^2} < 0, \end{gathered} \tag{20}$$

which implies (a)–(e). □

Remark 2. In terms of the image processing, it is easy to see the following.

(1) From (a) and (b), the edge detection function $C(s)$ is like that of the original Perona-Malik diffusion.

(2) (c) implies that $C(s)\approx 1/\sqrt{s}$ or $C(s)\approx 1/\sqrt{1+s}$ as $s\to+\infty$.

(3) The diffusion coefficient $C(s)$ is dependent on the exponent $p(s)$, which have the similar function with the fractional operator [19–27].

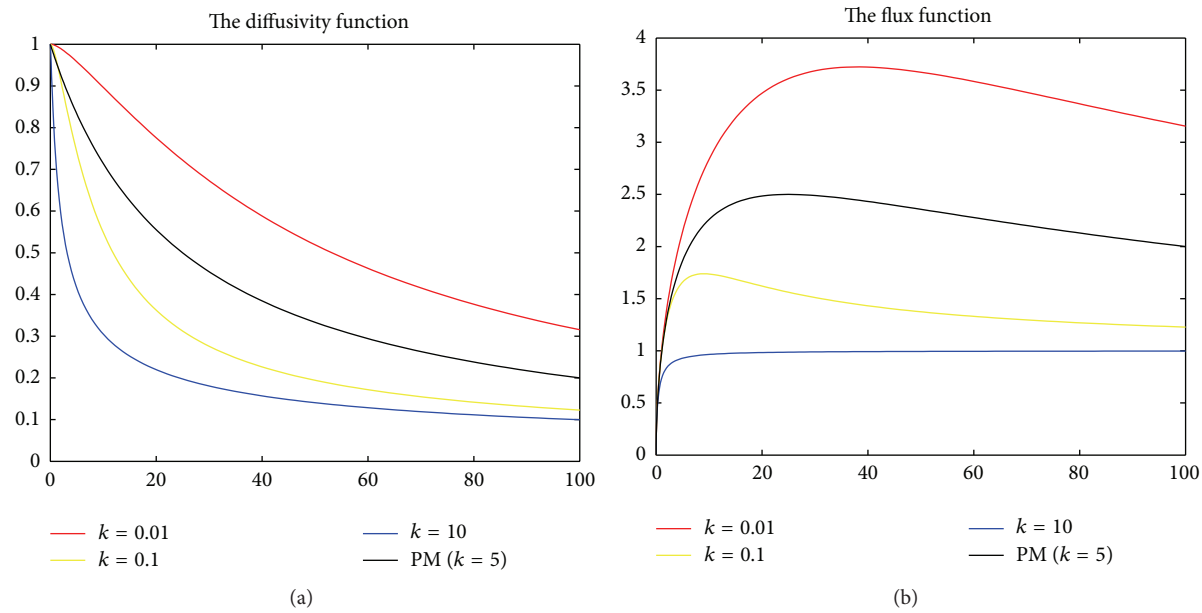

FIGURE 1: (a) Diffusivity function $C(s)$, for $k = 0.01, 0.1, 10$ and the PM diffusivity for $k = 5$. (b) The Flux function $\mathscr{F}(s)$ for $k = 0.01, 0.1, 10$ and PM flux function for $k = 5$.

2.4. Forward-Backward Diffusion. For the diffusivity function $C(s)$ it follows the new flux function $\mathscr{F}(s)$ which is defined by

$$\mathscr{F}(s) := sC\left(s^2\right), \tag{21}$$

where the variable s stands for the norm of the gradient $|\nabla u|$.

In the two-dimensional case, (32) can be replaced by [43]

$$\begin{aligned} \partial_t u &= \operatorname{div}\left(C\left(|\nabla u|^2\right)\nabla u\right) \\ &= C\left(|\nabla u|^2\right)u_{TT} + \mathscr{F}'(\nabla u)\,u_{NN}, \end{aligned} \tag{22}$$

where we have denoted by u_{NN} and u_{TT} the second derivatives of u in the direction $N(x, y) = \nabla u/|\nabla u|$ which is parallel to ∇u and $T(x, y)$ in the orthogonal direction to $N(x, y)$, respectively:

$$\begin{aligned} u_{NN} &= \frac{u_x^2 u_{xx} + u_y^2 u_y y + 2u_x u_y u_{xy}}{|\nabla u|^2}, \\ u_{TT} &= \frac{u_x^2 u_{yy} + u_y^2 u_x x - 2u_x u_y u_{xy}}{|\nabla u|^2}. \end{aligned} \tag{23}$$

Remark 3. From Proposition 1(d), we impose

$$\lim_{s\to\infty}\frac{\mathscr{F}'(s)}{C\left(s^2\right)} = 0, \tag{24}$$

which implies that it is preferable to smooth more in the T-direction than in the N-direction.

Proposition 4. *There exists $s_0 \in (0, +\infty)$ such that $\mathscr{F}'(s) \geq 0$ for $|s| \leq s_0$, and $\mathscr{F}'(s) < 0$ for $|s| > s_0$ (see Figure 1(b)). Moreover,*

$$s_0 > e^k - 1. \tag{25}$$

Proof. By a direct calculation, we have

$$\begin{aligned} \mathscr{F}'(s) &= C\left(s^2\right) + 2s^2 C'\left(s^2\right) \\ &= C\left(s^2\right)\frac{h\left(s^2\right)}{\left(1+s^2\right)\left(1+ks^2\right)^2}, \end{aligned} \tag{26}$$

where

$$h(s) = \left(k^2+k\right)s^2 + (2k+1)s + 1 - ks(1+s)\ln(1+s), \tag{27}$$

for $s > 0$. Then

$$\begin{aligned} h'(s) &= \left(2k^2+k\right)s + (2k+1) - k(2s+1)\ln(1+s), \\ h''(s) &= k\left((2k-1) - 2\ln(1+s) + \frac{1}{1+s}\right) \\ &< 2k(k - \ln(1+s)) \\ &< 0, \end{aligned} \tag{28}$$

for $k < \ln(1+s)$; that is, $s > e^k - 1$. It is noticed that, for $s = e^k - 1$,

$$\begin{aligned} h(s) &= ks^2 + \left(2k+1-k^2\right)s + 1 > 0, \\ \lim_{s\to+\infty} h(s) &= -\infty. \end{aligned} \tag{29}$$

□

Because of the continuousness of $g(s)$, there exists a unique point $s_0 \in (0, +\infty)$ such that $h(s_0) = 0$, and $h(s) \geq 0$ for $e^k - 1 < s \leq s_0$, and $h(s) < 0$ for $s > s_0$. For $k > \ln(1+s)$, that is, $0 < s < e^k - 1$,

$$\begin{aligned} h(s) &= \left(k^2 + k\right) s^2 + (2k+1) s + 1 - ks(1+s)\ln(1+s) \\ &> ks^2 + \left(2k + 1 - k^2\right) s + 1 \\ &> 0. \end{aligned} \tag{30}$$

From Proposition 4, the new model is of forward diffusion along isophotes (i.e., lines of constant grey value) and of forward-backward diffusion along flow lines (i.e., lines of maximal grey value variation).

Remark 5. (1) From Proposition 4, the threshold value s_0 about forward and backward diffusion is estimated as follows:

$$s_0 > e^k - 1. \tag{31}$$

Therefore, k plays the role of a control parameter separating forward from backward diffusion areas.

(2) From Figure 2, we can see, for $k \geq 1$, the part of the backward diffusion ($F'(s) < 0$) is not evident; for $k = 0.02$, the flux function is similar to the PM flux.

2.5. The Modified Regularization Equation. Using the similar skill in [15], the new model can be regularized by

$$\frac{\partial u}{\partial t} = \operatorname{div}\left(C\left(\left|\nabla G_\sigma * u\right|^2\right)\nabla u\right), \quad \text{in } \Omega \times (0,T), \tag{32}$$

$$u(0,x) = f, \quad \text{in } \Omega, \tag{33}$$

$$\frac{\partial u}{\partial \vec{n}} = 0, \quad \text{on } \partial\Omega \times (0,T), \tag{34}$$

where $G_\sigma(x)$ is the Gaussian kernel, namely,

$$G_\sigma(x) = \frac{1}{(4\pi\sigma)^{N/2}} \exp\left(-\frac{|x|^2}{4\sigma}\right). \tag{35}$$

This small amount of linear filtering allows $C(|\nabla G_\sigma * u|^2)$ to measure edges of u in a more "global" sense, so that it is not easily affected by local discretization. It is noticed that equation (32)–(34) is forward diffusion. In [15], while use of the mollifier may seem to be counterproductive, since the original intention was to avoid the blurring caused by linear filtering, the results can be quite impressive and are in fact a great improvement over linear filtering. In the new model, the forward-backward diffusion under control by the factor k, and therefore, we do not use this skill in numerical Experiments.

3. Existence and Uniqueness of Weak Solutions

In this section, we establish the existence and uniqueness of weak solutions of the proposed model (32)–(34) following the arguments in [15, 43, 44].

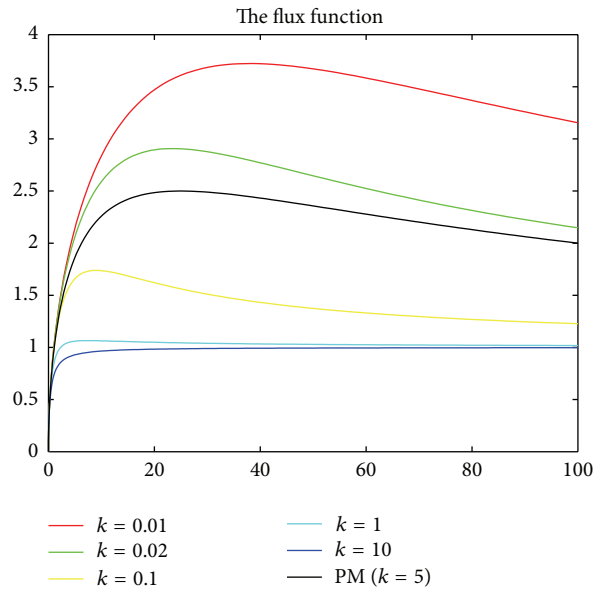

Figure 2: Flux function $\mathcal{F}(s)$ for $k = 0.01, 0.02, 0.1, 1, 10$ and PM flux function for $k = 5$.

The standard notations are used throughout. We denote by $H^k(\Omega)$, k a positive integer, the set of all functions u defined in Ω such that u and its distributional derivatives $\partial^m u/\partial x^m$ of order $|m| = \sum_{j=1}^N m_j \leq k$ all belong to $L^2(\Omega)$. $H^k(\Omega)$ is a Hilbert space with the norm

$$\|u\|_{H^k(\Omega)} = \left(\sum_{|m|\leq k} \int_\Omega \left|\frac{\partial^m u}{\partial x^m}\right|^2 dx\right)^{1/2}. \tag{36}$$

The space $L^\infty(0,T;X)$ consists of all functions u such that, for almost every t in $(0,T)$, u belongs to X. $L^\infty(0,T;X)$ is a normed space with the norm

$$\|u\|_{L^\infty(0,T;X)} = \operatorname*{ess\,sup}_{0\leq t\leq T} \|u(\cdot,t)\|_X. \tag{37}$$

We denote by $H^1(\Omega)'$ the dual of $H^1(\Omega)$.

We introduce the solution space W of the problem (32)–(34) as follows:

$$W(0,T) = \left\{w \in L^\infty\left(0,T;H^1(\Omega)\right); \frac{dw}{dt} \in L^2\left(Q_T\right)\right\}. \tag{38}$$

Obviously, W is a Banach space with the norm

$$\|w\|_W = \|w\|_{L^\infty(0,T;H^1(\Omega))} + \left\|\frac{\partial w}{\partial t}\right\|_{L^2(Q_T)}. \tag{39}$$

The solutions considered here are in the following weak sense.

Definition 6. A function u is called a weak solution of the problem (32)–(34), if $u \in W$ satisfies (32) and conditions (33) and (34) a.e. with derivatives of u in the sense of distributions.

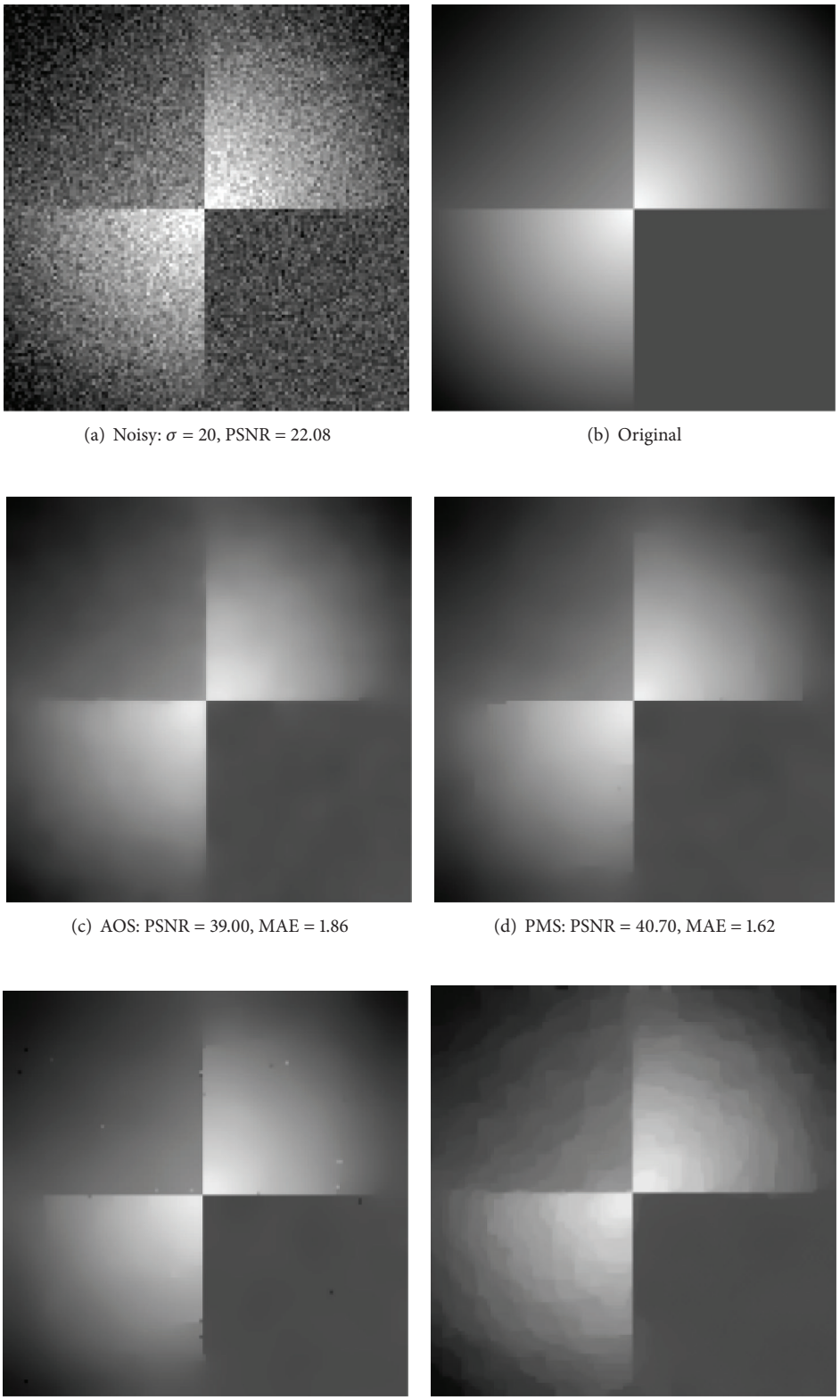

(a) Noisy: $\sigma = 20$, PSNR = 22.08

(b) Original

(c) AOS: PSNR = 39.00, MAE = 1.86

(d) PMS: PSNR = 40.70, MAE = 1.62

(e) PM: PSNR = 39.74, MAE = 1.78

(f) TV: PSNR = 37.08, MAE = 2.52

Figure 3: Synthetic image (128×128) (a) Noisy image corrupted by Gaussian noise for $\sigma = 20$. (b) Original image. (c) Our algorithm by AOS, $k = 0.02$, $\tau = 2$ (11 steps). (d) Our algorithm by PMS, $\tau = 0.25$ (62 steps). (e) PM algorithm, $K = 5$, $\tau = 0.25$ (90 steps). (f) TV algorithm, $\tau = 0.1$ (360 steps).

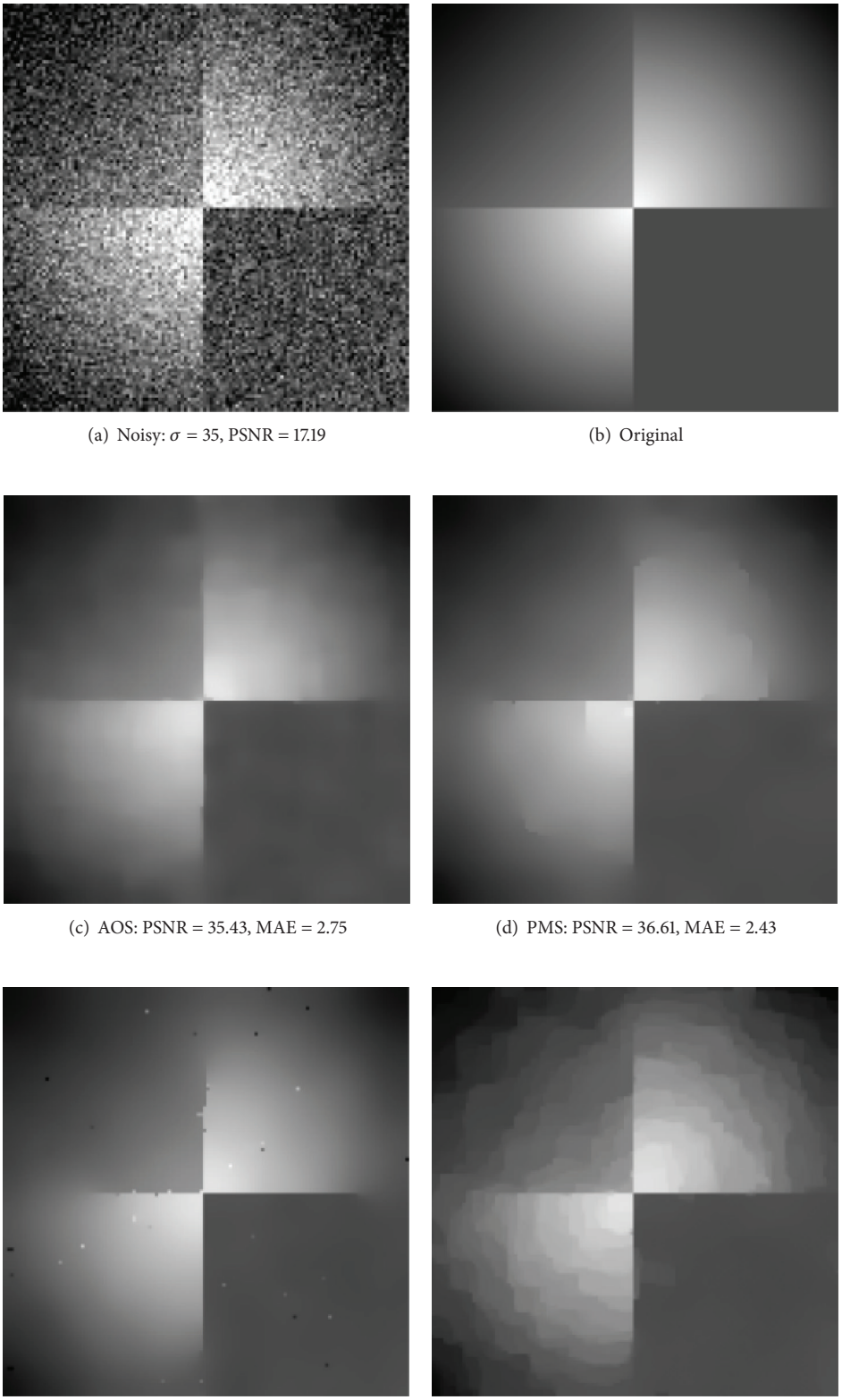

(a) Noisy: $\sigma = 35$, PSNR = 17.19

(b) Original

(c) AOS: PSNR = 35.43, MAE = 2.75

(d) PMS: PSNR = 36.61, MAE = 2.43

(e) PM: PSNR = 34.81, MAE = 2.76

(f) TV: PSNR = 34.05, MAE = 3.65

Figure 4: Synthetic image (128×128). (a) Noisy image corrupted by Gaussian noise for $\sigma = 35$. (b) Original image. (c) Our algorithm by AOS, $k = 0.02$, $\tau = 2$ (11 steps). (d) Our algorithm by PMS, $\tau = 0.25$ (115 steps). (e) PM algorithm, $K = 7$, $\tau = 0.25$ (130 steps). (f) TV algorithm, $\tau = 0.1$ (600 steps).

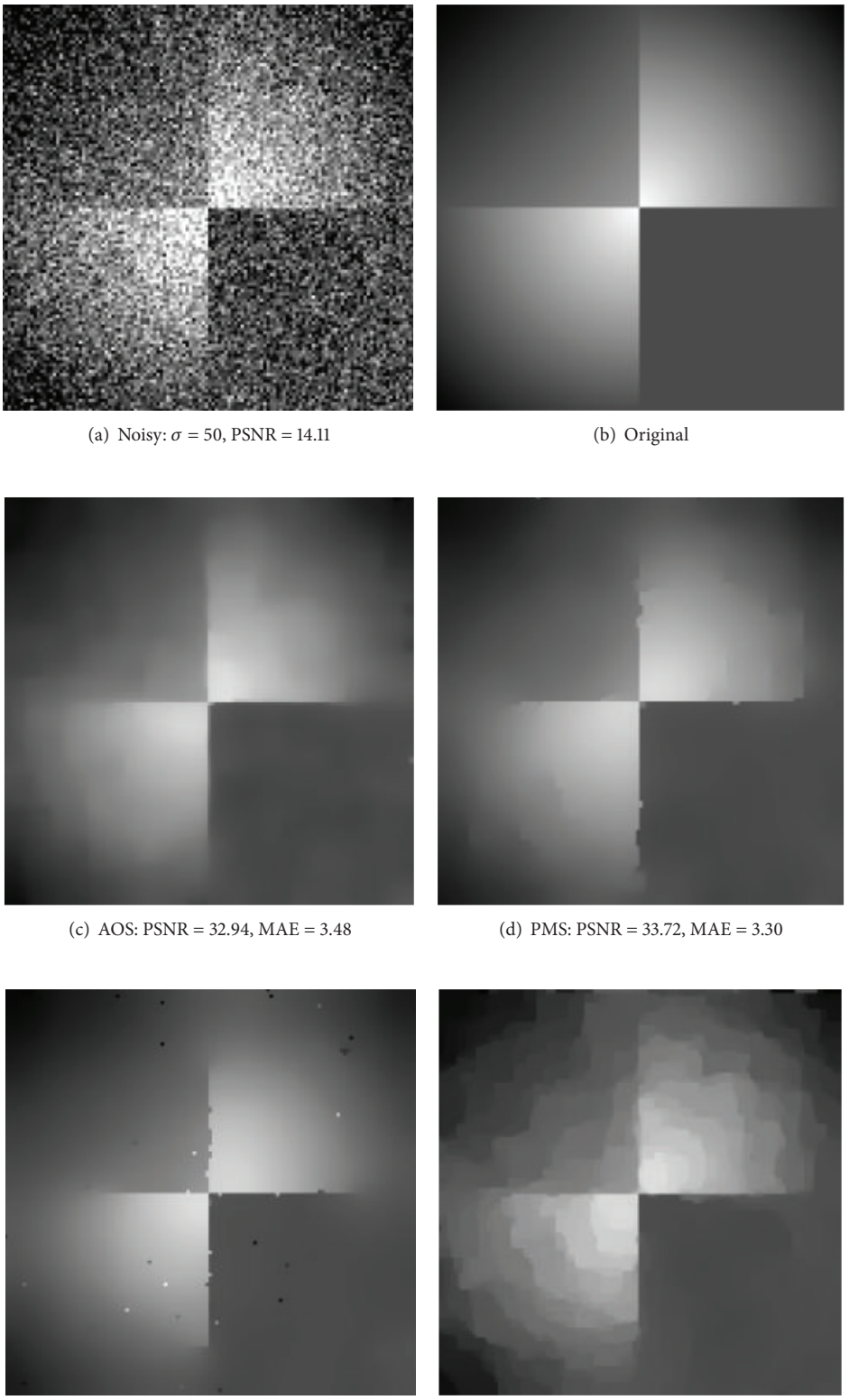

(a) Noisy: $\sigma = 50$, PSNR = 14.11

(b) Original

(c) AOS: PSNR = 32.94, MAE = 3.48

(d) PMS: PSNR = 33.72, MAE = 3.30

(e) PM: PSNR = 31.90, MAE = 3.66

(f) TV: PSNR = 31.36, MAE = 4.88

Figure 5: Synthetic image (128×128). (a) Noisy image corrupted by Gaussian noise for $\sigma = 50$. (b) Original image. (c) Our algorithm by AOS, $k = 0.02$, $\tau = 2$ (11 steps). (d) Our algorithm by PMS, $\tau = 0.25$ (115 steps). (e) PM algorithm, $K = 7$, $\tau = 0.25$ (130 steps). (f) TV algorithm, $\tau = 0.1$ (600 steps).

We will show the existence of weak solutions by the Schauder fixed point theorem. For this purpose, we need to discuss the corresponding linearized problem

$$\frac{\partial u}{\partial t} = \operatorname{div}\left(C\left(\left|\nabla G_\sigma * w\right|^2\right)\nabla u\right), \quad \text{in } \Omega \times (0,T), \tag{40}$$

$$u(0,x) = f, \quad \text{in } \Omega, \tag{41}$$

$$\frac{\partial u}{\partial \vec{n}} = 0, \quad \text{on } \partial\Omega \times (0,T). \tag{42}$$

Proposition 7. *For any $f \in L^2(\Omega)$, the problem* (40)–(42) *admits a unique weak solution $u \in W$.*

By classical theory, Proposition 7 can be proved by the Galerkin method (see [29, 31] for details).

Now, the theorem for the existence and uniqueness of weak solutions is stated as follow.

Theorem 8. *Let $f \in H^1(\Omega)$ and $\| f\|_{H^1(\Omega)}$ is appropriately small. Then the problem* (32)–(34) *admits one and only one weak solution $u(x,t)$ such that $\partial u/\partial t \in L^2(Q_T)$, $u \in L^\infty(0,T;H^1(\Omega) \cap u \in C([0,T],L^2(\Omega))$.*

Proof. Firstly, we consider the proof of the existence, which is based on the Schauder fixed point argument. Let $w \in W$ such that

$$\|w\|_{L^\infty(0,T;L^2(\Omega))} \le \|f\|_{L^2(\Omega)}, \qquad \left\|\frac{\partial w}{\partial t}\right\|_{L^2(Q_T)} \le \|f\|_{H^1(\Omega)}. \tag{43}$$

We consider the following linear problem (P_w):

$$\left\langle \frac{du(t)}{dt}, v\right\rangle_{H^1(\Omega)' \times H^1(\Omega)} + \int_\Omega C\left(\left|\nabla G_\sigma * w\right|^2\right)\nabla u(t)\,\nabla v(t)\,dx = 0 \tag{P_w}$$

for all $v \in H^1(\Omega)$, a.e. $t \in [0,T]$. Since w and $\partial w/\partial t$ satisfy (43), then $|\nabla G_\sigma * w|$ and $|\nabla G_\sigma * (\partial w/\partial t)|$ belong to $L^\infty((0,T);C^\infty(\Omega))$ and there exists a constant $M = M(G_\sigma, \| f\|_{H^1(\Omega)})$ such that $|\nabla G_\sigma * w| \le M$ and $|\nabla G_\sigma * (\partial w/\partial t)| \le M$ a.e. t, for all $x \in \Omega$. Since $C(s)$ is decreasing and positive, it follows that a.e. in $(0,T) \times \Omega$:

$$1 \ge C\left(\left|\nabla G_\sigma * w\right|^2\right) \ge C\left(M^2\right) = \nu. \tag{44}$$

Then by applying Proposition 7 on the linearized problem, we will prove that the problem (P_w) has a unique solution $u_w \in W$ satisfying the estimates

$$\|u_w\|_{L^\infty(0,T;H^1(\Omega))} \le c_1, \tag{45}$$

$$\|u_w\|_{L^\infty(0,T;L^2(\Omega))} \le \|f\|_{L^2(\Omega)}, \tag{46}$$

$$\left\|\frac{\partial u_w}{\partial t}\right\|_{L^2(Q_T)} \le \|f\|_{H^1(\Omega)}, \tag{47}$$

where c_1 is the constant depending only on the constant ν, G_σ, and $\| f\|_{H^1(\Omega)}$. Choosing $v = u_w$ in (P_w), integrating over the interval $(0,t)$, we arrive to the inequality

$$\frac{1}{2}\int_\Omega u_w^2\,dx + \nu\int_0^t\int_\Omega \left|\nabla u_w\right|^2 dx\,ds \le \frac{1}{2}\int_\Omega f^2\,dx, \tag{48}$$

which implies (46). Choosing $v = \partial u_w/\partial t$ in (P_w), integrating by parts yields

$$\int_\Omega \left(\frac{\partial u_w}{\partial t}\right)^2 dx + \frac{1}{2}\int_\Omega C\left(\left|\nabla G_\sigma * w\right|^2\right)\frac{\partial\left|\nabla u_w\right|^2}{\partial t}dx = 0. \tag{49}$$

Integrating over the interval $(0,t)$ we arrive to that

$$\begin{aligned}\int_0^t\int_\Omega \left(\frac{\partial u_w}{\partial s}\right)^2 dx\,ds &+ \frac{1}{2}\int_\Omega C\left(\left|\nabla G_\sigma * w\right|^2\right)\left|\nabla u_w\right|^2 dx \\ &= \frac{1}{2}\int_\Omega C\left(\left|\nabla G_\sigma * w\right|^2\right)\left|\nabla f\right|^2 dx \\ &\quad + \frac{1}{2}\int_0^t\int_\Omega C'\left(\left|\nabla G_\sigma * w\right|^2\right) \\ &\qquad \times \nabla\left(G_\sigma * w\right)\nabla\left(G_\sigma * \frac{\partial w}{\partial s}\right)\left|\nabla u_w\right|^2 dx\,ds.\end{aligned} \tag{50}$$

From Proposition 1 and (48), noticing that $|C'(s^2)s| \le k$, we can deduce that

$$\begin{aligned}\int_0^t\int_\Omega \left(\frac{\partial u_w}{\partial s}\right)^2 dx\,ds &+ \frac{\nu}{2}\int_\Omega |\nabla u|^2 dx \\ &\le \int_\Omega \left|\nabla f\right|^2 dx + \frac{Mk}{4\nu}\int_\Omega f^2\,dx\,ds.\end{aligned} \tag{51}$$

Since $\| f\|_{H^1(\Omega)}$ is small, letting $Mk/(8\nu) \le 1$ yields (45) and (47). From (45)–(47), we introduce the subspace W_0 of W defined by

$$\begin{aligned}W_0 = \Big\{ & w \in W(0,T), w(0) = f \\ & \|w\|_{L^\infty(0,T;H^1(\Omega))} \le c_1, \\ & \|w\|_{L^\infty(0,T;L^2(\Omega))} \le \|f\|_{L^2(\Omega)}, \\ & \left\|\frac{dw}{dt}\right\|_{L^2(Q_T)} \le \|f\|_{H^1(\Omega)}\Big\}.\end{aligned} \tag{52}$$

By construction, $w \to S(w) \equiv u_w$ is a mapping from W_0 into W_0. Moreover, one can prove that W_0 is not empty, convex, and weakly compact in $W(0,T)$.

In order to use the Schauder fixed point theorem, we need to prove that the mapping $S : w \to u_w$ is weakly continuous from W_0 into W_0. Let w_j be a sequence that converges weakly to some w in W_0 and let $u_j = u_{w_j}$. We have to prove that $S(w_j) = u_j$ converges weakly to $S(w) = u_w$. From (45)–(47), and classical results of compact inclusion in Sobolev

spaces [45], we can extract from w_j, respectively, from u_j, a subsequence such that, for some u, we have

$$\begin{gathered}
\frac{du_j}{dt} \rightharpoonup \frac{du}{dt}, \quad \text{weakly in } L^2(Q_T), \\
u_j \to u, \quad \text{in } L^\infty\left(0,T;L^2(\Omega)\right), \\
\frac{\partial u_j}{\partial x_k} \rightharpoonup \frac{\partial u}{\partial x_k}, \quad \text{weakly} * \text{ in } L^\infty\left(0,T;L^2(\Omega)\right), \\
w_j \longrightarrow w, \quad \text{in } L^\infty\left(0,T;L^2(\Omega)\right), \\
\frac{\partial G_\sigma}{\partial x_k} * w_j \longrightarrow \frac{\partial G_\sigma}{\partial x_k} * w, \\
\text{in } L^2(\Omega), \quad \text{a.e. on } (0,T)\times\Omega, \\
C\left(\left|\nabla G_\sigma * w_j\right|^2\right) \longrightarrow C\left(\left|\nabla G_\sigma * w\right|^2\right), \\
\text{in } L^2\left(0,T;L^2(\Omega)\right), \\
u_j(0) \longrightarrow u(0), \quad \text{in } L^2(\Omega).
\end{gathered} \tag{53}$$

The above convergence allows us to pass to the limit in the problem (P_{w_j}) and obtain $u = u_w = S(w)$. Moreover, since the solution is unique, the whole sequence $u_j = S(w_j)$ converges weakly in W_0 to $u = S(w)$; that is, S is weakly continuous. Consequently, thanks to Schauder's fixed-point theorem, there exists $w \in W_0$ such that $w = S(w) = u_w$. The function u_w solves (32)–(34).

Now, we turn to the proof of the uniqueness, following the idea in [44]. Let u_1 and u_2 be two weak solutions of (32)–(34). For almost every t in $[0,T]$ and $i = 1,2$, we have

$$\begin{gathered}
\frac{d}{dt}(u_1-u_2)(t) - \operatorname{div}\left(\alpha_1(t)\nabla(u_1-u_2)(t)\right) \\
= \operatorname{div}\left((\alpha_1-\alpha_2)(t)\nabla u_2(t)\right), \\
(u_1-u_2)(0,x) = 0, \quad \text{in } \Omega, \\
\frac{\partial(u_1-u_2)}{\partial\vec{n}} = 0, \quad \text{on } \partial\Omega\times(0,T),
\end{gathered} \tag{54}$$

in the distribution sense, where

$$\alpha_i = C\left(\left|\nabla G_\sigma * u_i\right|^2\right). \tag{55}$$

Then multiplying the above equality by (u_1-u_2), integrating over Ω, and using the Neumann boundary condition, we get a.e. $t \in [0,T]$,

$$\begin{aligned}
&\frac{1}{2}\frac{d}{dt}\int_\Omega (u_1(t)-u_2(t))^2 dx + \int_\Omega \alpha_1\left|\nabla u_1(t)-\nabla u_2(t)\right|^2 dx \\
&\quad = -\int_\Omega (\alpha_1-\alpha_2)\nabla u_2(t)\cdot(\nabla u_1(t)-\nabla u_2(t))\,dx.
\end{aligned} \tag{56}$$

Since $C(s)$ is decreasing and positive, it follows that a.e. in $(0,T)\times\Omega$, $\alpha_i \geq \nu$, which implies from (56),

$$\begin{aligned}
&\frac{1}{2}\frac{d}{dt}\int_\Omega (u_1(t)-u_2(t))^2 dx + \nu\int_\Omega \left|\nabla u_1(t)-\nabla u_2(t)\right|^2 dx \\
&\quad \leq \int_\Omega \left|\alpha_1-\alpha_2\right|\left|\nabla u_2(t)\cdot(\nabla u_1(t)-\nabla u_2(t))\right| dx.
\end{aligned} \tag{57}$$

Moveover, since $C(s)$, G_{σ_1}, and G_σ are smooth, we have

$$\left|\alpha_1(t)-\alpha_2(t)\right|_{L^\infty(\Omega)} \leq C_4\left|u_1(t)-u_2(t)\right|_{L^2(\Omega)}, \tag{58}$$

where C_4 is a constant that depends only on g_1, ν, and G_σ. From (58) and by using Young's inequality, we obtain

$$\begin{aligned}
&\frac{1}{2}\frac{d}{dt}\int_\Omega (u_1(t)-u_2(t))^2 dx + \nu\int_\Omega \left|\nabla u_1(t)-\nabla u_2(t)\right|^2 dx \\
&\quad \leq \frac{1}{2\nu}C_4^2\int_\Omega (u_1(t)-u_2(t))^2 dx\int_\Omega \left|\nabla u_2(t)\right|^2 dx \\
&\qquad + \frac{\nu}{2}\int \left|\nabla(u_1-u_2)(t)\right|^2 dx,
\end{aligned} \tag{59}$$

from which we deduce

$$\begin{aligned}
&\frac{d}{dt}\int_\Omega (u_1(t)-u_2(t))^2 dx \\
&\quad \leq \frac{1}{\nu}C_4^2\int_\Omega (u_1(t)-u_2(t))^2 dx\int_\Omega \left|\nabla u_2(t)\right|^2 dx.
\end{aligned} \tag{60}$$

Since $u_1(0) = u_2(0) = f$, using Gronwall's inequality yields

$$\int_\Omega (u_1(t)-u_2(t))^2 dx \leq 0; \tag{61}$$

that is, $u_1 = u_2$. □

Remark 9. Let u be the weak solution of problem (32)–(34) obtained in the proof of Theorem 8. Then from the proof we get that $u \in L^\infty(\mathbb{R}^+;H^1(\Omega))$, $\partial u/\partial t \in L^2(Q_\infty)$, where $Q_\infty = \Omega\times\mathbb{R}^+$.

4. Some Properties of Weak Solution

In this section, we first investigate the continuity with respect to initial data of the weak solution for (32)–(34), and then investigate the stability of the weak solution and the maximum principle. According to the uniqueness proof in Theorem 8, we obtain the following theorem.

Theorem 10. *Assume u is the weak solutions of problem* (32)–(34) *with the initial data f. Then*

$$\begin{gathered}
\int_\Omega (u-f)\,dx = 0, \\
\left\|u(\cdot,t)-f_\Omega\right\|_{L^2(\Omega)} \leq e^{-\nu t/\mu}\left\|f-f_\Omega\right\|_{L^2(\Omega)},
\end{gathered} \tag{62}$$

a.e. $t \in [0,+\infty)$, where $f_\Omega = \left(\frac{1}{|\Omega|}\right)\int_\Omega f\,dx$, and $|\Omega|$ is Lebesgue measure of Ω.

Proof. Let u be the solutions for problem (32)–(34) with the initial data f. For almost every t in $[0,T]$, we have

$$\frac{\partial u}{\partial t} = \operatorname{div}\left(C\left(\left|\nabla G_\sigma * u\right|^2\right)\nabla u\right), \quad \text{in } \Omega\times(0,T), \tag{63}$$

$$u(0,x) = f, \quad \text{in } \Omega, \tag{64}$$

$$\frac{\partial u}{\partial \vec{n}} = 0, \quad \text{on } \partial\Omega\times(0,T), \tag{65}$$

in the distribution sense. Integrating over the interval $(0,t)$ and using the Neumann boundary condition yield

$$\int_\Omega (u-f)\,dx = 0. \tag{66}$$

Then, multiplying the above equality (63) by $(u-f_\Omega)$, and integrating over Ω, and integrating by parts yield

$$\frac{1}{2}\frac{d}{dt}\int_\Omega (u-f_\Omega)^2 dx + \int_\Omega C\left(\left|\nabla G_\sigma * u\right|^2\right)|\nabla u|^2 dx = 0. \tag{67}$$

Using the following Poincaré-Wirtinger inequality [46, page 148], we have

$$\left\|u - \frac{1}{|\Omega|}\int_\Omega u dx\right\|^2_{L^2(\Omega)} = \left\|u-f_\Omega\right\|^2_{L^2(\Omega)} \le \mu\int_\Omega |\nabla u|^2 dx, \tag{68}$$

with the constant $\mu \equiv \mu(\Omega)$. Substituting (68) to (67) yields

$$\frac{d}{dt}\int_\Omega (u-f_\Omega)^2 dx \le -\frac{2\nu}{\mu}\int_\Omega (u-f_\Omega)^2 dx. \tag{69}$$

Multiplying this inequality by $e^{2\nu t/\mu}$ and integrating over the interval $(0,t)$ we arrive to the inequality

$$\int_\Omega (u-f_\Omega)^2 dx \le e^{-2\nu t/\mu}\int_\Omega (f-f_\Omega)^2 dx. \tag{70}$$

Hence, we obtain the assertion of the theorem. □

Next, let us build upon the maximum principle as follows.

Theorem 11. *Let u be the weak solutions of problem* (32)–(34) *with the initial data f and $f \in L^\infty(\Omega)$. Then*

$$\inf_{x\in\Omega} f \le u \le \sup_{x\in\Omega} f. \tag{71}$$

Proof. Let $I := \sup_{x\in\Omega} f$, and $J := \inf_{x\in\Omega} f$. Multiply (32) by $(u-I)_+$, where

$$(u-I)_+ = \begin{cases} u-I, & \text{if } u-M>0, \\ 0, & \text{otherwise}, \end{cases} \tag{72}$$

and integrate over Ω to get

$$\begin{aligned} &\frac{1}{2}\frac{d}{dt}\int_\Omega (u(t)-I)_+^2 dx \\ &\quad + \int_\Omega C\left(\left|\nabla G_\sigma * u_i\right|^2\right)\left|\nabla(u(t)-I)_+\right|^2 dx = 0. \end{aligned} \tag{73}$$

Then

$$\frac{1}{2}\frac{d}{dt}\int_\Omega (u(t)-I)_+^2 dx \le 0. \tag{74}$$

Therefore, $(1/2)(d/dt)\int_\Omega (u(t)-I)_+^2 dx$ is decreasing in t, and since

$$\int_\Omega (u(t)-I)_+^2 dx \ge 0, \quad \int_\Omega (u(t)-I)_+^2 dx\Big|_{t=0} = 0, \tag{75}$$

we have that

$$\int_\Omega (u(t)-I)_+^2 dx = 0, \quad \forall t\in[0,+\infty), \tag{76}$$

and so

$$u(t) \le \sup_{x\in\Omega} f \quad \text{a.e. on } \Omega, \forall t>0. \tag{77}$$

Multiplying (32) by $(u-J)_-$, a similar argument yields that $u \ge J$ for all $t\in[0,+\infty)$. Equation (71) is followed directly. □

5. Behavior as $t \to \infty$

In this section, we investigate the asymptotic behavior of the weak solution as time tends to infinity and obtain the equilibrium weak solution.

Lemma 12. *Let u be the weak solutions of problem* (32)–(34) *with the initial data $f \in L^\infty(\Omega)\cap H^1(\Omega)$, and $\lim_{n\to\infty} t_n = +\infty$. Then*

(i) *for all $\tau \ge 0$, $\{u(t_n+\tau,\cdot)\}_{n=1}^\infty \to f_\Omega$ in $L^2(\Omega)$,*

(ii) *there exists a subsequence of $\{t_n\}_{n=1}^\infty$, denoted also by itself, such that for all $T\ge 0$, $\{u(\cdot,t_n+\cdot)\}_{n=1}^\infty$ converges to f_Ω weakly in $L^2((0,T),H^1(\Omega))$ and strongly in $L^2(Q_T)$, and $\{(\partial u(\cdot,t_n+\cdot))/\partial t\}_{n=1}^\infty$ converges to 0 weakly in $L^2(Q_T)$.*

Proof. For all $T\ge 0$, since $\{u(t_n+\cdot,\cdot)\}_{n=1}^\infty$ are uniform bounded in $L^\infty((0,T);H^1(\Omega)) \cap L^\infty(Q_T)$, and $\partial u/\partial t$ is bounded in $L^2(Q_T)$, and then there exist $g(t,x)$ and the subsequence of $\{t_n\}_{n=1}^\infty$ which is independent on T, and denoted by $\{t_{n_j}\}_{j=1}^\infty$, such that

$$\begin{aligned} &u\left(t_{n_j}+\cdot,\cdot\right) \rightharpoonup g \quad \text{weakly in} \\ &\quad L^\infty\left((0,T);H^1(\Omega)\right)\cap L^\infty(Q_T), \\ &u\left(t_{n_j}+\cdot,\cdot\right) \longrightarrow g \quad \text{strongly in } L^2(Q_T), \\ &\frac{\partial u\left(t_{n_j}+\cdot,\cdot\right)}{\partial t} \rightharpoonup \frac{\partial g}{\partial t} \quad \text{weakly in } L^2(Q_T), \end{aligned} \tag{78}$$

where $g \in L^\infty((0,T);H^1(\Omega)) \cap L^\infty(Q_T)$. From Theorem 10, we have

$$\int_\Omega \left(u\left(t_{n_j}+t,x\right)-f_\Omega\right)^2 dx \le e^{-2\nu(t_{n_j}+t)}\int_\Omega (f-f_\Omega)^2 dx. \tag{79}$$

Letting $j \to \infty$, we can obtain the first part of Lemma 12. For (79), integrate over $(0,T)$ to get

$$\int_0^T \int_\Omega \left(u\left(t_{n_j}+t,x\right)-f_\Omega\right)^2 dx \le 2\nu e^{-2\nu t_{n_j}}\left(1-e^{-2\nu T}\right)\int_\Omega (f-f_\Omega)^2 dx. \tag{80}$$

Letting $j \to \infty$, we can obtain that

$$u\left(t_{n_j}+\cdot,\cdot\right) \longrightarrow f_\Omega \quad \text{strongly in } L^2\left(Q_T\right). \tag{81}$$

Noticing that $u(t_{n_j}+\cdot,\cdot) \to g$ strongly in $L^2(Q_T)$, we have

$$g(t,x) = f_\Omega, \quad \text{a.e. } (x,t) \in Q_T. \tag{82}$$

Since $(\partial u(t_{n_j}+\cdot,\cdot))/\partial t \rightharpoonup \partial g/\partial t$ weakly in $L^2(Q_T)$, and therefore, we have

$$\frac{\partial u\left(t_{n_j}+\cdot,\cdot\right)}{\partial t} \rightharpoonup 0 \quad \text{weakly in } L^2\left(Q_T\right). \tag{83}$$

Hence, we obtain the remaining part of the lemma. □

Now let us consider the following problem:

$$\operatorname{div}\left(C\left(\left|\nabla G_\sigma * u\right|^2\right)\nabla u\right) = 0, \quad \text{in } \Omega, \tag{84}$$

$$\frac{\partial u}{\partial \vec{n}} = 0, \quad \text{on } \partial\Omega, \tag{85}$$

$$\int_\Omega (u-f) = 0. \tag{86}$$

Theorem 13. *Assume $f \in L^1(\Omega)$. Then the problem* (84)–(86) *admits one and only one weak solution $u \in H^1(\Omega)$ such that*

$$\int_\Omega C\left(\left|\nabla G_\sigma * u\right|^2\right)\nabla u \nabla v = 0, \quad \forall v \in C^\infty\left(\overline{\Omega}\right), \qquad \int_\Omega (u-f) = 0. \tag{87}$$

Proof. It is clearly that $u = f_\Omega$ is one solution for the problem (84)–(86).

Next we we turn to the proof of the uniqueness of the solution for the problem (84)–(86). Let u_1 and u_2 be two weak solutions of (84)–(86). Multiplying (84) by u, integrating over Ω, and using the Neumann boundary condition, we get

$$\int_\Omega C\left(\left|\nabla G_\sigma * u\right|^2\right)|\nabla u|^2 = 0. \tag{88}$$

Using the following Poincaré-Wirtinger inequality, we have

$$\left\|u - \frac{1}{|\Omega|}\int_\Omega u\,dx\right\|_{L^2(\Omega)}^2 = \|u-f_\Omega\|_{L^2(\Omega)}^2 \le \mu \int_\Omega |\nabla u|^2 dx, \tag{89}$$

with the constant $\mu \equiv \mu(\Omega)$. Substituting (86) and (89) to (88) yields

$$\int_\Omega (u-f_\Omega)^2 dx = 0. \tag{90}$$

Then

$$\int_\Omega (u_1-u_2)^2 dx \le \int_\Omega (u_1-f_\Omega)^2 dx + \int_\Omega (u_2-f_\Omega)^2 dx = 0. \tag{91}$$

That is, $u_1 = u_2$. □

Theorem 14. *let u be the weak solution of problem* (32)–(34), *Then when $t \to \infty$, u tends to be steady-state solution f_Ω, that is, the solution for Problem* (84)–(86).

Proof. Let

$$u^n(\cdot,\cdot) = u\left(t_n+\cdot,\cdot\right). \tag{92}$$

Then u^n is the weak solutions of problem (32)–(34) with the initial data $u(t_n,\cdot)$. From Lemma 12, we obtain there exists a subsequence of $\{u^n\}_{n=1}^\infty$, denoted also by itself, such that, for all $T \ge 0$,

$$u^n \rightharpoonup f_\Omega \quad \text{weakly in } L^\infty\left((0,T);H^1(\Omega)\right) \cap L^\infty\left(Q_T\right), \qquad u^n \longrightarrow f_\Omega \quad \text{strongly in } L^2\left(Q_T\right), \qquad \frac{\partial u^n}{\partial t} \rightharpoonup 0 \quad \text{weakly in } L^2\left(Q_T\right), \tag{93}$$

which implies that as $t \to \infty$, u tends to be steady-state solution f_Ω, which is the unique solution for problem (84)–(86). □

Remark 15. From Theorems 10, 11, and 14, we can observe the following:

(i) $\inf_{x\in\Omega} f \le u \le \sup_{x\in\Omega} f$, which means that no new features are introduced in the image in process.

(ii) u_Ω, the mean of u, is constant f_Ω.

(iii) $\int_\Omega (u-f_\Omega)^2 dx$ tends to zero, which means that u converges in the $L^2(\Omega)$-strong topology to the average of the initial data.

6. Convergent Iterative Scheme

A convergent iterative scheme for (32) is given in this section.

Theorem 16. *Let $f \in H^1(\Omega)$. The sequence $\{u^n\}_{n=1}$ defined by solving the iterative scheme*

$$\frac{\partial u^{n+1}}{\partial t} = \operatorname{div}\left(C\left(\left|\nabla G_\sigma * u^n\right|^2\right)\nabla u^{n+1}\right), \quad \text{in } (0,T)\times\Omega, \qquad u^{n+1}(0,x) = f, \quad \text{in } \Omega, \qquad \frac{\partial u^{n+1}}{\partial \vec{n}} = 0, \quad \text{on } \partial(0,T)\times\Omega \tag{94}$$

converges in $C([0,T],L^2(\Omega))$ *to the strong solution of* (32)–(34).

Proof. We denote by $\alpha^n = C(|\nabla G_\sigma * u^n|^2)$. By Proposition 7, problem (94) has a unique solution u^{n+1}. It is clear that

$$\alpha^n \geq C\left(\left|\nabla G_\sigma * f\right|^2_{L^\infty(\Omega)}\right) \quad \text{a.e. in } (0,T)\times\Omega. \tag{95}$$

Now we verify that the sequence $\{u\}_{n=1}^\infty$ converges in $C([0,T],L^2(\Omega))$ to u, the strong solution of (32)–(34).

As in Section 3, from the estimate (60), we have

$$\begin{aligned}\frac{d}{dt}\int_\Omega \left(u^{n+1}(t)-u(t)\right)^2 dx \\ \leq \frac{1}{\nu}C_4^2\int_\Omega \left(u^n(t)-u(t)\right)^2 dx \int_\Omega |\nabla u(t)|^2 dx.\end{aligned} \tag{96}$$

Moreover, we have

$$\int_\Omega (f-u)^2 dx \leq C_0 \quad \forall t\in[0,T], \tag{97}$$

where C_0 is a constant which only depends on $\|f\|_{H^1(\Omega)}$. Then Gronwall's inequality yields, for any $t\in[0,T]$:

$$\int_\Omega \left(u^1(t)-u(t)\right)^2 dx \leq C_0\int_0^t a(s)\,ds, \tag{98}$$

where

$$a(s) = C_4^2\int_\Omega |\nabla u(s)|^2 dx. \tag{99}$$

By (96) and (98), we can deduce

$$\frac{d}{dt}\left(\left\|u^2(t)-u(t)\right\|^2_{L^2(\Omega)}\right) \leq C_0 a(t)\int_0^t a(s)\,ds, \tag{100}$$

and thus,

$$\left\|u^2(t)-u(t)\right\|^2_{L^2(\Omega)} \leq C_0\frac{1}{2}\left(\int_0^t a(s)\,ds\right)^2. \tag{101}$$

Finally, we obtain by iterating

$$\left\|u^{n+1}(t)-u(t)\right\|^2_{L^2(\Omega)} \leq C_0\frac{1}{(n+1)!}\left(\int_0^T a(s)\,ds\right)^{n+1}, \tag{102}$$

which implies that the sequence $\{u\}_{n=1}^\infty$ converges in $C([0,T],L^2(\Omega))$ to the strong solution of (32)–(34). □

7. Numerical Implementation

We present in this section some numerical examples illustrating the capability of our model. We also compare it with the known models (PM and TV). In the next two sections, two numerical discrete schemes, the PM scheme (PMS) and the AOS scheme, will be proposed.

7.1. The PM Scheme. To discretize (12), the finite difference scheme in [2] is used. Denote the space step by $h=1$ and the time step by τ. Thus, we have

$$\begin{aligned}\nabla_N\left(u_{i,j}\right) &= u_{i-1,j}-u_{i,j}, & \nabla_S\left(u_{i,j}\right) &= u_{i+1,j}-u_{i,j},\\ \nabla_E\left(u_{i,j}\right) &= u_{i,j+1}-u_{i,j}, & \nabla_W\left(u_{i,j}\right) &= u_{i,j-1}-u_{i,j}.\end{aligned} \tag{103}$$

The numerical algorithms for problems (12)–(14) are given in the following:

$$\begin{aligned}u_{i,j}^{n+1} = u_{i,j}^n + \tau\Big(&C\left(\left|\nabla_N\left(u_{i,j}^n\right)\right|^2\right)\cdot\nabla_N\left(u_{i,j}^n\right)\\ &+C\left(\left|\nabla_S\left(u_{i,j}^n\right)\right|^2\right)\cdot\nabla_S\left(u_{i,j}^n\right)\\ &+C\left(\left|\nabla_E\left(u_{i,j}^n\right)\right|^2\right)\cdot\nabla_E\left(u_{i,j}^n\right)\\ &+C\left(\left|\nabla_W\left(u_{i,j}^n\right)\right|^2\right)\cdot\nabla_W\left(u_{i,j}^n\right)\Big),\end{aligned} \tag{104}$$

where $0\leq\tau\leq 1/4$ for the numerical scheme to be stable.

7.2. The AOS Scheme. Using the scheme in [47], (12) can be discretized as

$$u^{n+1} = \frac{1}{m}\sum_{l=1}^m\left[I-m\tau A_l\left(u^k\right)\right]^{-1}u^n, \tag{105}$$

where $A(u^n)=[a_{ij}(u^n)]$,

$$\begin{aligned}a_{ij}\left(u^n\right) &:= \begin{cases}\dfrac{C_i^n+C_j^n}{2h^2} & [j\in\mathcal{N}(i)]\\ -\displaystyle\sum_{n\in\mathcal{N}(i)}\dfrac{C_i^n+C_N^n}{2h^2} & (j=i),\\ 0 & (\text{else}),\end{cases}\\ C_i^n &:= C\left[\frac{1}{2}\sum_{p,q\in\mathcal{N}(i)}\left(\frac{u_p^n-u_q^n}{2h}\right)\right],\end{aligned} \tag{106}$$

where $\mathcal{N}(i)$ is the set of the two neighbors of pixel i (boundary pixels have only one neighbor).

AOS schemes with large time steps still reveal average grey value invariance, stability based on extremum principle, Lyapunov functionals, and convergence to a constant steady-state.

7.3. Comparison with Other Methods. For comparison purposes, some very classical noise removal algorithms from the literature are considered, such as the PM Algorithm [2] (see (1)–(3)) and the TV algorithm [28] (see (9)).

The denoising algorithms were tested on three images: a synthetic image (128 × 128 pixels), a Lena image (300 × 300 pixels), and a boat image (512 × 512 pixels). For each image, a noisy observation is generated by adding the original image by Gaussian noise, standard deviation $\sigma\in\{20,35,50\}$.

(a) Noisy: $\sigma = 20$, PSNR = 22.09

(b) Original

(c) AOS: PSNR = 29.72, MAE = 6.08

(d) PMS: PSNR = 29.58, MAE = 6.15

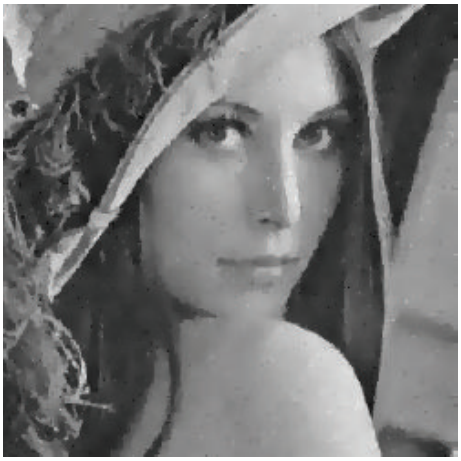

(e) PM: PSNR = 28.81, MAE = 6.46

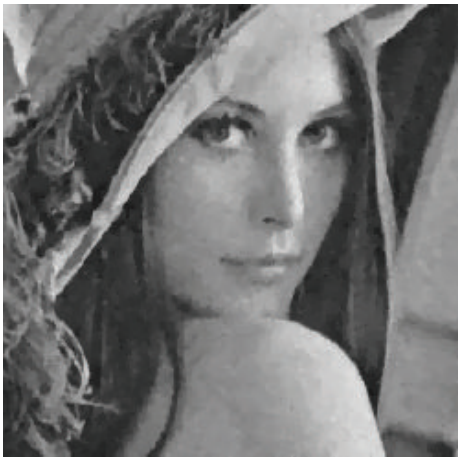

(f) TV: PSNR = 29.15, MAE = 6.38

Figure 6: Lenna image (300×300). (a) Noisy image corrupted by Gaussian noise for $\sigma = 20$. (b) Original image. (c) Our algorithm by AOS, $k = 1$, $\tau = 2$ (4 steps). (d) Our algorithm by PMS, $\tau = 0.25$ (47 steps). (e) PM algorithm, $K = 5$, $\tau = 0.25$ (55 steps). (f) TV algorithm, $\tau = 0.1$ (182 steps).

(a) Noisy: $\sigma = 35$, PSNR = 17.21

(b) Original

(c) AOS: PSNR = 27.45, MAE = 7.77

(d) PMS: PSNR = 27.03, MAE = 8.08

(e) PM: PSNR = 25.55, MAE = 8.98

(f) TV: PSNR = 26.87, MAE = 8.23

Figure 7: Lenna image (300×300). (a) Noisy image corrupted by Gaussian noise for $\sigma = 35$. (b) Original image. (c) Our algorithm by AOS, $k = 0.02$, $\tau = 2$ (8 steps). (d) Our algorithm by PMS, $\tau = 0.25$ (96 steps). (e) PM algorithm, $K = 7$, $\tau = 0.25$ (84 steps). (f) TV algorithm, $\tau = 0.1$ (400 steps).

(a) Noisy: $\sigma = 50$, PSNR = 14.12

(b) Original

(c) AOS: PSNR = 26.03, MAE = 9.11

(d) PMS: PSNR = 25.60, MAE = 9.46

(e) PM: PSNR = 23.81, MAE = 10.77

(f) TV: PSNR = 24.43, MAE = 9.93

Figure 8: Lenna image (300×300). (a) Noisy image corrupted by Gaussian noise for $\sigma = 50$. (b) Original image. (c) Our algorithm by AOS, $k = 0.02$, $\tau = 2$ (12 steps). (d) Our algorithm by PMS, $\tau = 0.25$ (154 steps). (e) PM algorithm, $K = 9$, $\tau = 0.25$ (108 steps). (f) TV algorithm, $\tau = 0.1$ (650 steps).

(a) Noisy: $\sigma = 20$, PSNR = 22.11

(b) Original

(c) AOS: PSNR = 29.93, MAE = 5.73

(d) PMS: PSNR = 29.75, MAE = 5.76

(e) PM: PSNR = 28.64, MAE = 6.22

(f) TV: PSNR = 29.13, MAE = 5.97

Figure 9: Boat image (512×512). (a) Noisy image corrupted by Gaussian noise for $\sigma = 20$. (b) Original image. (c) Our algorithm by AOS, $k = 0.2$, $\tau = 2$ (4 steps). (d) Our algorithm by PMS, $\tau = 0.25$ (47 steps). (e) PM algorithm, $K = 5$, $\tau = 0.25$ (55 steps). (f) TV algorithm, $\tau = 0.1$ (194 steps).

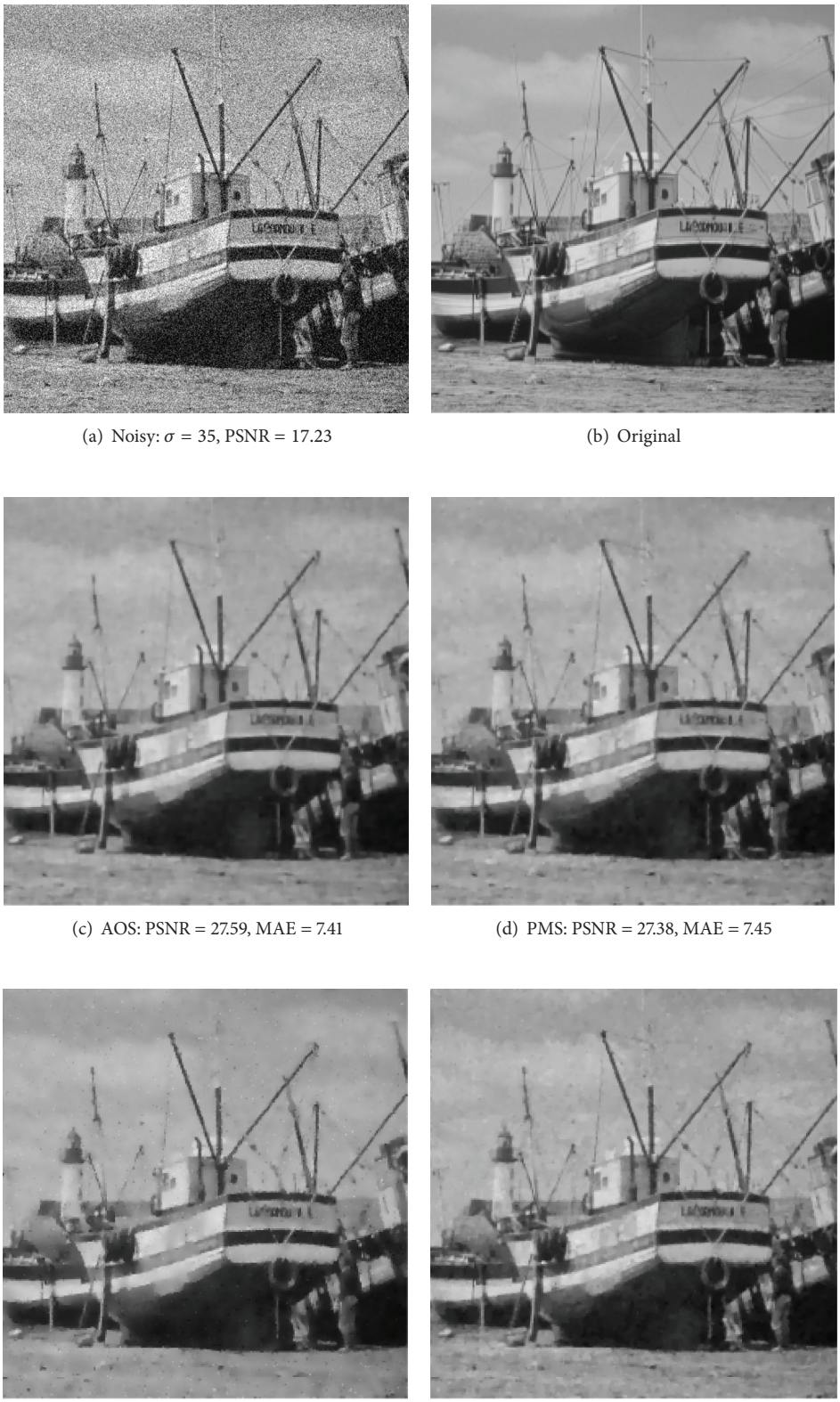

(a) Noisy: $\sigma = 35$, PSNR = 17.23

(b) Original

(c) AOS: PSNR = 27.59, MAE = 7.41

(d) PMS: PSNR = 27.38, MAE = 7.45

(e) PM: PSNR = 25.85, MAE = 8.22

(f) TV: PSNR = 26.50, MAE = 7.98

Figure 10: Boat image (512×512). (a) Noisy image corrupted by Gaussian noise for $\sigma = 35$. (b) Original image. (c) Our algorithm by AOS, $k = 0.2$, $\tau = 2$ (9 steps). (d) Our algorithm by PMS, $\tau = 0.25$ (110 steps). (e) PM algorithm, $K = 7$, $\tau = 0.25$ (90 steps). (f) TV algorithm, $\tau = 0.1$ (450 steps).

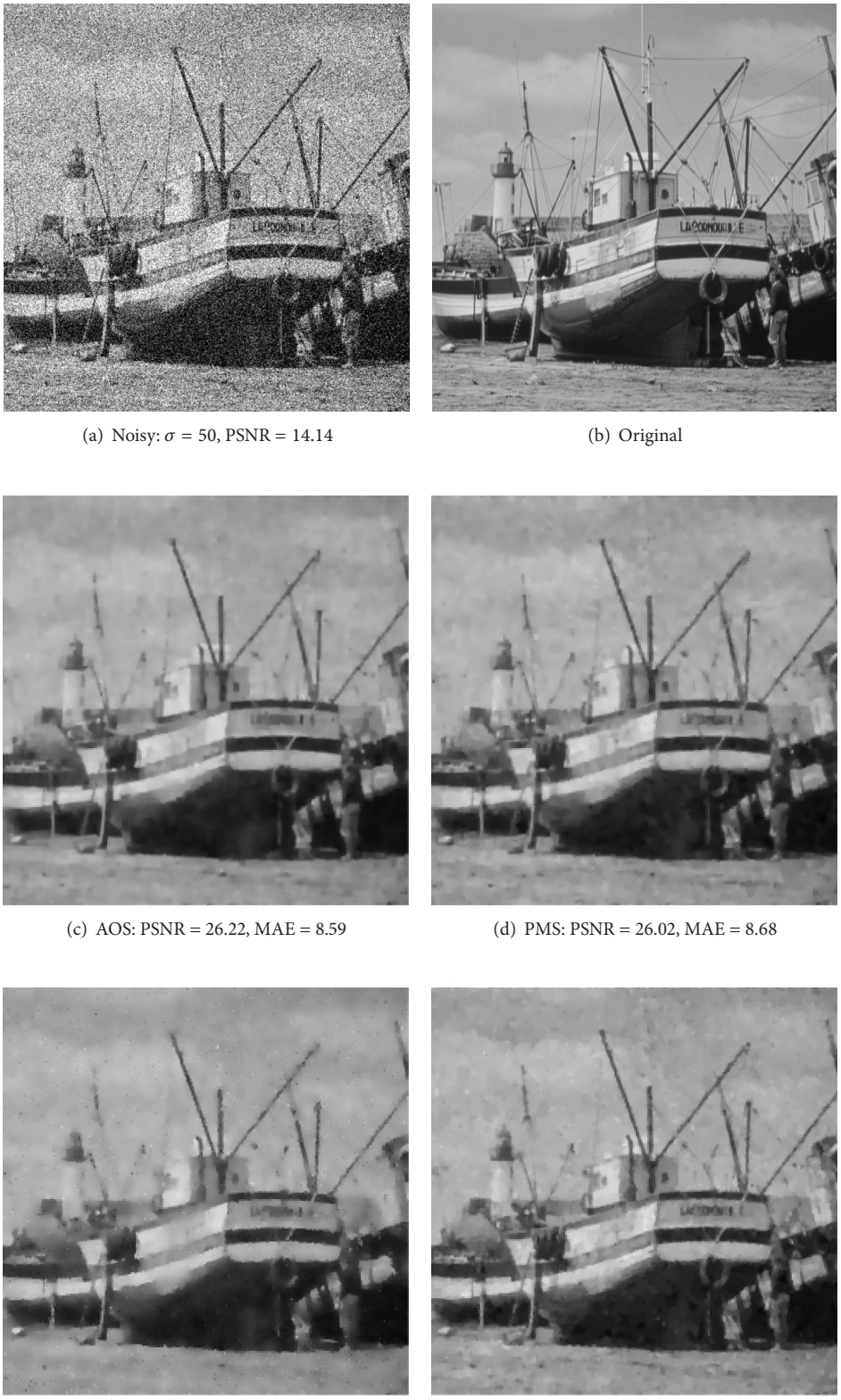

(a) Noisy: $\sigma = 50$, PSNR = 14.14

(b) Original

(c) AOS: PSNR = 26.22, MAE = 8.59

(d) PMS: PSNR = 26.02, MAE = 8.68

(e) PM: PSNR = 24.17, MAE = 9.93

(f) TV: PSNR = 25.63, MAE = 8.98

Figure 11: Boat image (512×512). (a) Noisy image corrupted by Gaussian noise for $\sigma = 50$. (b) Original image. (c) Our algorithm by AOS, $k = 0.2$, $\tau = 2$ (15 steps). (d) Our algorithm by PMS, $\tau = 0.25$ (170 steps). (e) PM algorithm, $K = 9$, $\tau = 0.25$ (115 steps). (f) TV algorithm, $\tau = 0.1$ (710 steps).

Table 1: PSNR, MAE, and CPU time (seconds) of all methods.

PSNR				MAE				CPU time(s)			
The synthetic image (128 × 128)											
σ	20	35	50	σ	20	35	55	σ	20	35	55
AOS	39.00	**35.43**	**32.94**	AOS	1.86	**2.75**	**3.48**	AOS	**0.43**	**0.41**	**0.54**
PMS	**40.70**	**36.61**	**33.72**	PMS	**1.65**	**2.43**	**3.30**	PMS	1.33	2.65	3.91
PM	**39.74**	34.81	31.90	PM	**1.78**	2.76	3.66	PM	**0.70**	**1.04**	**1.82**
TV	37.08	34.05	31.36	TV	2.52	3.65	4.88	TV	4.41	7.57	11.15
The Lena image (300 × 300)											
σ	20	35	50	σ	20	35	50	σ	20	35	50
AOS	**29.72**	**27.44**	**26.03**	AOS	**6.08**	**7.77**	**9.11**	AOS	**0.96**	**1.94**	**2.13**
PMS	**29.58**	**27.03**	**25.60**	PMS	**6.15**	**8.08**	**9.46**	PMS	5.05	14.80	18.77
PM	28.81	25.55	23.81	PM	6.46	8.98	10.77	PM	**2.30**	**4.78**	**12.24**
TV	29.15	26.87	24.43	TV	6.38	8.23	9.93	TV	14.32	32.68	49.26
The boat image (512 × 512)											
σ	20	35	50	σ	20	35	50	σ	20	35	50
AOS	**29.93**	**27.59**	**26.22**	AOS	**5.73**	**7.41**	**8.59**	AOS	**4.02**	**6.19**	**9.58**
PMS	**29.75**	**27.38**	**26.02**	PMS	**5.76**	**7.45**	**8.68**	PMS	19.76	39.00	60.44
PM	28.64	25.85	24.17	PM	6.22	8.22	9.93	PM	**9.24**	**14.90**	**18.90**
TV	29.13	26.50	25.63	TV	5.97	7.98	8.98	TV	49.51	109.15	172.17

Peak-signal-to-noise-ratio (PSNR) and the mean absolute-deviation error (MAE) are used to measure the quality of the restoration results. They are defined as

$$\mathrm{PSNR} = 10 \log_{10}\left(\frac{255^2 \mathrm{MN}}{\|u_O - u\|_2^2}\right), \qquad \mathrm{MAE} = \frac{\|u_O - u\|_1}{\mathrm{MN}}, \tag{107}$$

where u_O and u are the original image and the restored image, respectively. The stopping criterion of all methods is set to achieve the maximal PSNR or the best MAE.

For fair comparison, the parameters of PM and TV were tweaked manually to reach their best performance level. In the PM scheme, there are two parameters: the influencing factor k and the time step $\tau = 0.25$. In the AOS scheme, besides the same influencing factor k with PM scheme, the time step τ can be very large (in general, $\tau = 2$ for the maximal PSNR). Notice that the parameters of our method are very stable with respect to the image. From these experiments, we also observe that the PSNR reaches a maximum rapidly and decreases rapidly. So the steady-state solution is arrived when $t \to \infty$, but the time evolution may be stopped earlier to achieve an optimal tradeoff between noise removal and edge preservation (the time when the largest PSNR achieves).

The results are depicted in Figures 3–5 for the synthetic image, Figures 6–8 for the Lena image, and Figures 9–11 for the boat image. Our methods do a good job at restoring faint geometrical structures of the images even for high values of σ; see for instance the results on the boat image for $\sigma = 50$. Our algorithm performs among the best and even outperforms its competitors most of the time both visually and quantitatively as revealed by the PSNR and MAE values. For TV method, the number of iterations necessary to satisfy the stopping rule rapidly increases when σ increases. For PM method, the appropriate parameter K is necessary.

Figures 3, 4, and 5 illustrate the proposed model is able to reconstruct sharp edges and nonuniform regions while avoiding staircasing. TV-based diffusion reconstructs sharp edges, but the staircasing effect is clear evidence. PM-based diffusion also reconstructs sharp edges but creates isolated black and white speckles in the denoise image. The proposed model reconstructs sharp edges as effectively as PM-based diffusion and recovers smooth regions as effectively as pure isotropic diffusion (in particular, without staircasing). The denoising performance results are tabulated in Table 1 where the best PSNR and MAE value is shown in boldface. The PSNR improvement brought by our approach can be quite high particularly for $\sigma = 50$ (see, e.g., Figures 5, 8, and 11) and the visual resolution is quite respectable. But even for $\sigma = 20$, the PSNR of our algorithm can be higher than that of PM and TV methods.

Table 1 summarizes the computational times for all algorithms. From [47], we know the AOS is a high efficient algorithm. It is less than twice the typical effort needed for an explicit scheme, a rather low price for gaining absolute stability. Moreover, the new algorithm by AOS scheme performs high PSNRs on real images (Figures 6, 7, 8, 9, 10 and 11).

8. Conclusions

This work proposes quite an original, efficient method for noise removal. Noise removal is a difficult problem that arises in various applications relevant to active imaging system.

The main ingredients of our method are as follows. (1) Dependent on the diffusivity function $C(s)$, the new model

is hybrid diffusion which is combination of mean curvature smoothing and Gaussian heat diffusion. (2) The new diffusion is forward-backward diffusion, but the backward diffusion is under control and the restored image does not create new features. (3) There are less parameters in the new model and the resultant algorithm is insensitive to these parameters. (4) The new model can be performed by AOS scheme, which is very efficient.

Our experimental results demonstrate that the new algorithm is very efficient and the quality of restored images by our method is quite well.

Acknowledgments

The authors would like to express their sincere thanks to the referees for their valuable suggestions in the revision of the paper which contributed greatly to this work. This work was partially supported by the Fundamental Research Funds for the Central Universities (Grants HIT.NSRIF.2011003 and HIT.NSRIF.2012065), the National Science Foundation of China (Grant no. 11271100), the Aerospace Supported Fund, China, under Contract no. 2011-HT-HGD-06, China Postdoctoral Science Foundation funded project, Grant no. 2012M510933, and also the 985 project of Harbin Institute of Technology.

References

[1] V. Caselles, J.-M. Morel, G. Sapiro, and A. Tannenbaum, "Introduction to the special issue on partial differential equations and geometry-driven diffusion in image processing and analysis," *IEEE Transactions on Image Processing*, vol. 7, no. 3, pp. 269–273, 1998.

[2] P. Perona and J. Malik, "Scale-space and edge detection using anisotropic diffusion," *IEEE Transactions on Pattern Analysis and Machine Intelligence*, vol. 12, no. 7, pp. 629–639, 1990.

[3] T. Iijima, "Basic theory on normalization of pattern (in case of typical onedimensional pattern)," *Bulletin of the Electrotechnical Laboratory*, vol. 26, pp. 368–388, 1962 (Japanese).

[4] P. Charbonnier, L. Blanc-Feraud, G. Aubert, and M. Barlaud, "Two deterministic half-quadratic regularization algorithms for computed imaging," in *Proceedings of IEEE International Conference on Image Processing*, vol. 2, pp. 168–172, IEEE Computer Society Press, Austin, Tex, USA, November 1994.

[5] J. Weickert, *Anisotropic Diffusion in Image Processing*, European Consortium for Mathematics in Industry, B. G. Teubner, Stuttgart, Germany, 1998.

[6] F. Andreu, C. Ballester, V. Caselles, and J. M. Mazón, "Minimizing total variation flow," *Differential and Integral Equations*, vol. 14, no. 3, pp. 321–360, 2001.

[7] S. L. Keeling and R. Stollberger, "Nonlinear anisotropic diffusion filtering for multiscale edge enhancement," *Inverse Problems*, vol. 18, no. 1, pp. 175–190, 2002.

[8] G. Gilboa, N. Sochen, and Y. Y. Zeevi, "Forward-and-backward diffusion processes for adaptive image enhancement and denoising," *IEEE Transactions on Image Processing*, vol. 11, no. 7, pp. 689–703, 2002.

[9] B. Smolka, "Combined forward and backward anisotropic diffusion filtering of color images," in *Pattern Recognition*, L. van Gool, Ed., vol. 2449 of *Lecture Notes in Computer Science*, pp. 314–320, Springer, Berlin, Germany, 2002.

[10] S. Kichenassamy, "The Perona-Malik paradox," *SIAM Journal on Applied Mathematics*, vol. 57, no. 5, pp. 1328–1342, 1997.

[11] B. Kawohl and N. Kutev, "Maximum and comparison principle for one-dimensional anisotropic diffusion," *Mathematische Annalen*, vol. 311, no. 1, pp. 107–123, 1998.

[12] J. Weickert and B. Benhamouda, "A semidiscrete nonlinear scale-space theory and its relation to the Perona-Malik paradox," in *Advances in Computer Vision*, F. Solina, W. G. Kropatsch, R. Klette, and R. Bajcsy, Eds., pp. 1–10, Springer, Wien, Austria, 1997.

[13] S. Esedoglu, *An analysis of the Perona-Malik Scheme [Ph.D. thesis]*, Courant Institute of Mathematical Sciences, New York, NY, USA, 2000.

[14] S. Kichenassamy, "The Perona-Malik paradox," *SIAM Journal on Applied Mathematics*, vol. 57, no. 5, pp. 1328–1342, 1997.

[15] L. Alvarez, P.-L. Lions, and J.-M. Morel, "Image selective smoothing and edge detection by nonlinear diffusion. II," *SIAM Journal on Numerical Analysis*, vol. 29, no. 3, pp. 845–866, 1992.

[16] J. Tumblin and G. Turk, "LCIS: a boundary hierarchy for detail-preserving contrast reduction," in *Proceedings of the SIGGRAPH Annual Conference on Computer Graphics*, pp. 83–90, Los Angeles, Calif, USA, August 1999.

[17] G. W. Wei, "Generalized Perona-Malik equation for image restoration," *IEEE Signal Processing Letters*, vol. 6, no. 7, pp. 165–167, 1999.

[18] Y. L. You and M. Kaveh, "Fourth-order partial differential equations for noise removal," *IEEE Transactions on Image Processing*, vol. 9, no. 10, pp. 1723–1730, 2000.

[19] B. Mathieu, P. Melchior, A. Oustaloup, and C. Ceyral, "Fractional differentiation for edge detection," *Signal Processing*, vol. 83, no. 11, pp. 2421–2432, 2003.

[20] R. W. Ibrahim, "On generalized Srivastava-Owa fractional operators in the unit disk," *Advances in Difference Equations*, vol. 2011, pp. 1–12, 2011.

[21] Y. Pu, "Fractional calculus approach to texture of digital image," in *Proceedings of the 8th International Conference on Signal Processing (ICSP '06)*, vol. 2, pp. 15–20, November 2006.

[22] Y. Zhang, Y. Pu, and J. Zhou, "Construction of fractional differential masks based on Riemann-Liouville definition," *Journal of Computational Information Systems*, vol. 6, no. 10, pp. 3191–3200, 2010.

[23] D. Chen, Y. Chen, and D. Xue, "Digital fractional order Savitzky-Golay differentiator," *IEEE Transaction on Circuits and Systems*, vol. 11, no. 58, pp. 758–762, 2011.

[24] J. Hu, Y. Pu, and J. Zhou, "Fractional integral denoising algorithm and implementation of fractional integral filter," *Journal of Computational Information Systems*, vol. 7, no. 3, pp. 729–736, 2011.

[25] Y. Liu, Y. Pu, and J. Zhou, "Design of image denoising filter based on fractional integral," *Journal of Computational Information Systems*, vol. 6, no. 9, pp. 2839–2847, 2010.

[26] J. Hu, Y. Pu, and J. Zhou, "A novel image denoising algorithm based on Riemann-Liouville definition," *Journal of Computers*, vol. 6, no. 7, pp. 1332–1338, 2011.

[27] H. A. Jalab and R. W. Ibrahim, "Denoising algorithm based on generalized fractional integral operator with two parameters," *Discrete Dynamics in Nature and Society*, vol. 2012, Article ID 529849, 14 pages, 2012.

[28] L. I. Rudin, S. Osher, and E. Fatemi, "Nonlinear total variation based noise removal algorithms," *Physica D: Nonlinear Phenomena*, vol. 60, no. 1–4, pp. 259–268, 1992.

[29] R. Acar and C. R. Vogel, "Analysis of bounded variation penalty methods for ill-posed problems," *Inverse Problems*, vol. 10, no. 6, pp. 1217–1229, 1994.

[30] P. Blomgren, T. F. Chan, P. Mulet, and C. K. Wong, "Total variation image restoration: numerical methods and extensions," in *Proceedings of the International Conference on Image Processing*, pp. 384–387, October 1997.

[31] V. Caselles, J.-M. Morel, and C. Sbert, "An axiomatic approach to image interpolation," *IEEE Transactions on Image Processing*, vol. 7, no. 3, pp. 376–386, 1998.

[32] A. Chambolle and P.-L. Lions, "Image recovery via total variation minimization and related problems," *Numerische Mathematik*, vol. 76, no. 2, pp. 167–188, 1997.

[33] D. M. Strongand and T. F. Chan, "Spatially and scale adaptive total variation based regularization and anisotropic diffusion in image processing," Tech. Rep. CAM96-46(UCLA), University of California, Los Angeles, Calif, USA, 1996.

[34] P. Blomgren, T. F. Chan, P. Mulet, and C. K. Wong, "Total variation image restoration: numerical methods and extensions," in *Proceedings of the International Conference on Image Processing*, pp. 384–387, October 1997.

[35] Y. Chen, S. Levine, and M. Rao, "Variable exponent, linear growth functionals in image restoration," *SIAM Journal on Applied Mathematics*, vol. 66, no. 4, pp. 1383–1406, 2006.

[36] A. Chambolle and P.-L. Lions, "Image recovery via total variation minimization and related problems," *Numerische Mathematik*, vol. 76, no. 2, pp. 167–188, 1997.

[37] D. C. Dobson and F. Santosa, "Recovery of blocky images from noisy and blurred data," *SIAM Journal on Applied Mathematics*, vol. 56, no. 4, pp. 1181–1198, 1996.

[38] M. Nikolova, "Weakly constrained minimization: application to the estimation of images and signals involving constant regions," *Journal of Mathematical Imaging and Vision*, vol. 21, no. 2, pp. 155–175, 2004.

[39] W. Ring, "Structural properties of solutions to total variation regularization problems," *Mathematical Modelling and Numerical Analysis*, vol. 34, no. 4, pp. 799–810, 2000.

[40] R. T. Whitaker and S. M. Pizer, "A mulit-scale approach to nonuniform diffusion," *Computer Vision, Graphics, and Image Processing: Image Understand*, vol. 57, no. 1, pp. 99–110, 1993.

[41] Y. L. You, W. Xu, A. Tannenbaum, and M. Kaveh, "Behavioral analysis of anisotropic diffusion in image processing," *IEEE Transactions on Image Processing*, vol. 5, no. 11, pp. 1539–1553, 1996.

[42] A. I. El-Fallah and G. E. Ford, "On mean curvature diffusion in nonlinear image filtering," *Pattern Recognition Letters*, vol. 19, no. 5-6, pp. 433–437, 1998.

[43] G. Aubert and P. Kornprobst, *Mathematical Problems in Image Processing: PDEs and the Calculus of Variations*, vol. 147 of *Applied Mathematical Sciences*, Springer, New York, NY, USA, 2002.

[44] L. C. Evans, *Partial Differential Equations*, vol. 19 of *Graduate Studies in Mathematics*, American Mathematical Society, Providence, RI, USA, 1998.

[45] R. A. Adams, *Sobolev Spaces*, vol. 65 of *Pure and Applied Mathematics Series of Monographs and Textbooks*, Academic Press, New York, NY, USA, 1975.

[46] L. Ambrosio, N. Fusco, and D. Pallara, *Functions of Bounded Variation and Free Discontinuity Problems*, Oxford Mathematical Monographs, Oxford University Press, Oxford, UK, 2000.

[47] J. Weickert, B. M. Ter Haar Romeny, and M. A. Viergever, "Efficient and reliable schemes for nonlinear diffusion filtering," *IEEE Transactions on Image Processing*, vol. 7, no. 3, pp. 398–410, 1998.

Hindawi Publishing Corporation
Mathematical Problems in Engineering
Volume 2013, Article ID 795651, 7 pages
http://dx.doi.org/10.1155/2013/795651

Research Article

An Implementation Solution for Fractional Partial Differential Equations

Nicolas Bertrand, Jocelyn Sabatier, Olivier Briat, and Jean-Michel Vinassa

Bordeaux 1 University, CNRS UMR 5218, IMS Laboratory, 351 cours de la Libération, 33405 Talence Cedex, France

Correspondence should be addressed to Jocelyn Sabatier; jocelyn.sabatier@u-bordeaux1.fr

Received 9 November 2012; Accepted 3 December 2012

Academic Editor: José Tenreiro Machado

The link between fractional differentiation and diffusion equation is used in this paper to propose a solution for the implementation of fractional diffusion equations. These equations permit us to take into account species anomalous diffusion at electrochemical interfaces, thus permitting an accurate modeling of batteries, ultracapacitors, and fuel cells. However, fractional diffusion equations are not addressed in most commercial software dedicated to partial differential equations simulation. The proposed solution is evaluated in an example.

1. Introduction

For an electrochemical system, species diffusion is often modeled by Fick's laws [1]. However, in almost all systems, the transport mechanism is different from the classical diffusion characterized by Fick's laws. This kind of diffusion is denoted by anomalous diffusion [2]. Anomalous diffusion is characterized by a mean squared displacement of the diffusing particles that has a power law dependence on time $\langle r^2 \rangle \sim t^{\gamma}$ with γ between 0 and 2 (for classical diffusion $\langle r^2 \rangle \sim t$).

The theoretical approach of this type of diffusion is strongly related to fractional calculus [3]. It was indeed demonstrated that stochastic processes of random walks can be represented by fractional diffusion equations [4].

Among all existing anomalous diffusion equations, three diffusion modes, respectively, called "anomalous diffusion Ia" (ADIA), "anomalous diffusion Ib" (ADIB), and "anomalous diffusion II" (ADII) are characterized by a Fick's equations adaptation for phenomena considered [5].

In this paper, the authors have only considered ADIB type diffusion equations but the proposed contribution can be extended to others classes of equation. In the sequel, the link between fractional differentiation and diffusion is used to propose a solution for the implementation of a fractional diffusion equation in software such as COMSOL Multiphysics. These software applications are now powerful tools for engineers to simulate complex systems combining several physical domains such as electrochemistry and thermal. However they are not adapted to take into account anomalous diffusion and thus to model diffusion interfaces as in batteries, ultracapacitors, or fuel cells.

The link between fractional differentiation and diffusion equation is reminded in the second section of the paper. This link should be used to implement fractional differentiation in software dedicated to numerical solving of partial differential equation such as COMSOL Multiphysics software. However, as shown in Section 2, the diffusion equation form of a fractional system requires the computation of an inverse Fourier transform that is in most cases impossible to get analytically. This is why this paper proposes alternative partial differential equations approximation that exhibits a fractional behavior in a given frequency band. These differential equations can be easily implemented to simulate a fractional differentiator and thus a fractional diffusion equation.

2. Link between Fractional Systems and Partial Differential Equations

2.1. Partial Differential Equation Representation and Approximation of a Fractional System. For presentation simplicity,

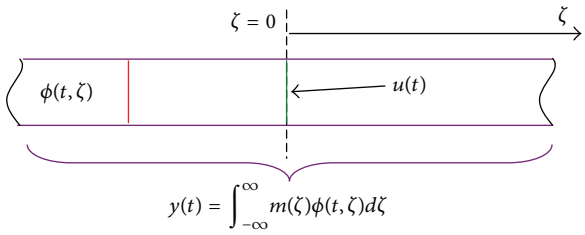

Figure 1: Representation of system (12) and thus system (1).

the following fractional system (fractional integrator) is considered

$$H(s) = s^{-\gamma}, \tag{1}$$

with $0 < \gamma < 1$. Its link with diffusion equation can be demonstrated using the system impulse response [6] defined by the Mellin-Fourier integral of (1):

$$h(t) = L^{-1}\{s^{-\gamma}\} = \lim_{\omega\to\infty} \frac{1}{2j\pi} \int_{c-j\infty}^{c+j\infty} e^{st} s^{-\gamma} ds, \tag{2}$$

where c is greater than the abscissa of the singular points of $H(s)$. Using poles definition that can be found in [6, 7], this system does not generate poles and its impulse response is thus given by

$$h(t) = \frac{\sin(\gamma\pi)}{\pi} \int_0^{\infty} x^{-\gamma} e^{-tx} dx. \tag{3}$$

Response of system (1) to an input $u(t)$ is defined as the convolution product of the impulse response $h(t)$ with the input $u(t)$:

$$y(t) = \int_0^t h(t-\tau)\, u(\tau)\, d\tau, \tag{4}$$

and thus using relation (3) and through an integral permutation

$$y(t) = \int_0^{\infty} \frac{\sin(\gamma\pi)}{\pi} x^{-\gamma} \left(\int_0^t e^{-(t-\tau)x} u(\tau)\, d\tau \right) dx. \tag{5}$$

Let

$$w(t,x) = \int_0^t e^{-(t-\tau)x} u(\tau)\, d\tau \tag{6}$$

the following state space representation can be obtained for system (1):

$$\begin{aligned} \frac{\partial w(t,x)}{\partial t} &= -xw(t,x) + u(t), \\ y(t) &= \frac{\sin(\gamma\pi)}{\pi} \int_0^{\infty} x^{-\gamma} w(t,x)\, dx. \end{aligned} \quad x \in \mathbb{R}^+. \tag{7}$$

Such a representation can be generalised to a large class of fractional systems as demonstrated in [8, 9]. In these works, second relation in (7) is rewritten as

$$y(t) = \int_0^{\infty} \mu(x)\, w(t,x)\, dx, \tag{8}$$

and representations (7) and (8) are denoted by diffusive representation. For a fractional transfer function defined by

$$F(p) = \frac{B(p)}{A(p)} \tag{9}$$

with $B(p) = \sum_{l=0}^{r} q_l p^{\beta_l}$ and $A(p) = \sum_{k=0}^{m} r_k p^{\alpha_k}$ where $\beta_{l+1} \geq \beta_l \geq 0$, function $\mu(x)$ is defined by [9]

$$\begin{aligned} \mu(x) &= \frac{1}{2i\pi} \left[F((-x)^-) - F((-x)^+) \right] \\ &= \frac{1}{\pi} \frac{\sum_{k=0}^{m} \sum_{l=0}^{q} a_k q_l \sin((\alpha_k - \beta_l)\pi)\, x^{\alpha_k+\beta_l}}{\sum_{k=0}^{m} \alpha_k^2 x^{2\alpha_k} + \sum_{0\leq k<l<m} 2a_k a_l \cos((\alpha_k-\alpha_l)\pi)\, x^{\alpha_k+\alpha_l}}. \end{aligned} \tag{10}$$

Initial conditions are defined for system (7) by $w(0,x) = \rho(x)$ and thus permits giving the exact expression of the system response with initial conditions [7]

$$y(t) = \int_0^{\infty} \mu(x) \left(w(0,x) e^{-xt} + \int_0^t e^{-x(t-\tau)} u(\tau)\, d\tau \right) dx. \tag{11}$$

Through several changes of variables described in [7], system (1), (but also a large number of fractional systems) can be described by

$$\begin{aligned} \frac{\partial \phi(t,\zeta)}{\partial t} &= \frac{\partial^2 \phi(t,\zeta)}{\partial \zeta^2} + u(t)\,\delta(\zeta), \\ y(t) &= \int_{-\infty}^{\infty} m(\zeta)\, \phi(t,\zeta)\, d\zeta. \end{aligned} \tag{12}$$

Relation (10) shows that a fractional integrator can thus be seen as an infinite dimensional system described by a diffusion equation. This interpretation is represented by Figure 1 [7] in which

(i) the input $u(t)$ applied at the abscissa $\zeta = 0$,

(ii) the real distributed state $\phi(t,\zeta)$,

(iii) the output (weighed sum on the state) appears. This remark can be generalized to a large number of fractional systems and thus demonstrates their link with diffusion equations.

Implementation of relation (10) requires the integral truncation that can be done as follows:

$$y(t) = \int_{-\zeta_2}^{\zeta_1} m(\zeta)\, \phi(t,\zeta)\, d\zeta. \tag{13}$$

In (13) $m(\zeta) = \mathfrak{F}^{-1}\{4\pi^2 x \mu(4\pi^2 x^2)\}$ where $\mathfrak{F}^{-1}$ denotes the inverse Fourier transform. This relation is in practice impossible to compute analytically in most cases. To solve this problem, another partial differential equation is now proposed.

2.2. Another Partial Differential Equation Approximation. Using Laplace transform and introducing $\mu(x)$ function ($\mu(x) = \sin(\gamma\pi)x^{-\gamma}/\pi$ for a fractional integrator such as (1)), relation (3) becomes

$$H(s) = \int_0^{+\infty} \frac{\mu(x)}{(s+x)} dx. \tag{14}$$

Using change of variable $x = e^{-z}$, relation (15) becomes

$$H(s) = \int_{-\infty}^{+\infty} \frac{\mu(e^{-z}) e^{-z}}{(s+e^{-z})} dz. \tag{15}$$

Implementation of such a transfer function requires the integral truncation, namely,

$$H(s) \approx \int_{Z_i}^{Z_f} \frac{\mu(e^{-z})}{(s/e^{-z}+1)} dz. \tag{16}$$

Note that $Z_i \in \mathbb{R}$, $Z_f \in \mathbb{R}$ are homogenous to the logarithm of a frequency. Now Let $x(z,t)$ be a function of the space variable z of finite dimension ($z \in \lfloor Z_i \cdots Z_f \rfloor$) and of the time variable t. This function satisfies the class of partial differential equations

$$\beta(z) \frac{\partial w(z,t)}{\partial z} + \gamma(z) \frac{\partial^2 w(z,t)}{\partial t \, \partial z} = u(t). \tag{17}$$

Also, let the system output $y(t)$ be given by

$$y(t) = w(Z_f, t) - w(Z_i, t) = \int_{Z_i}^{Z_f} \frac{\partial w(z,t)}{\partial z} dz. \tag{18}$$

This partial differential equation class has been studied in [10]. Transfer function that links the system input and output is defined by

$$G(s) = \frac{Y(s)}{U(s)} = \int_0^{Z} \frac{\beta^{-1}(z)}{1+\gamma(z)\beta^{-1}(z)s} dz. \tag{19}$$

Now if

$$\begin{gathered} \beta^{-1}(z) = \mu(e^{-z}), \\ \gamma^{-1}(z)\beta(z) = e^{-z} \text{ and thus } \gamma(z) = \frac{e^{z}}{\mu(e^{-z})}. \end{gathered} \tag{20}$$

It turns out that the solution of the partial differential equation defined by (15) and (16) is an approximation of the response of the system whose transfer is defined by (14) (and thus by (1) for a fractional integrator). Such a representation can thus be used to approximate a fractional system or a fractional integrator. It is now used to implement a fractional diffusion equation.

3. Application to Fractional Partial Differential Equations Implementation

Implementation problem of a fractional partial differential equation using simulation software such as Comsol Multiphysics is now addressed and the followingclass of equation is considered:

$$\frac{\partial^{1-\gamma} C_1(t,x)}{\partial t^{1-\gamma}} = -D \frac{\partial^2 C_1(t,x)}{\partial x^2}, \tag{21}$$

with the following boundary and initial conditions:

$$\frac{\partial C_1(t,0)}{\partial x} = \frac{\partial C_1(t,L)}{\partial x} = 0, \qquad C_1(0,x) = g(x). \tag{22}$$

It is an *ADIb* type anomalous diffusion equation that can also be rewritten as

$$Y(t,x) = -D \frac{\partial^2 C_1(t,x)}{\partial x^2}, \tag{23}$$

with

$$Y(t,x) = \frac{\partial^{1-\gamma} C_1(t,x)}{\partial t^{1-\gamma}}, \tag{24}$$

$$\frac{\partial C_1(t,0)}{\partial x} = \frac{\partial C_1(t,L)}{\partial x} = 0, \qquad C_1(0,x) = f(x). \tag{25}$$

According to the demonstration in Section 2 and in [11], $(1-\gamma)$ fractional derivative of $C_1(t,x)$ can be approximated by

$$U(t,x) = \frac{\partial C_1(t,x)}{\partial t}, \tag{26}$$

$$U(t,x) = \frac{\partial w(z,x,t)}{\partial z} \frac{1}{R(z)} + C(z) \frac{\partial^2 w(z,x,t)}{\partial z \, \partial t}, \tag{27}$$

$$Y(t,x) = w(Z_f, x, t) - w(Z_i, x, t) = \int_{Z_i}^{Z_f} \frac{\partial w(z,x,t)}{\partial z} dz, \tag{28}$$

where functions $C(z)$ and $R(z)$ are, respectively, defined by

$$C(z) = C(0) e^{-Az}, \qquad R(z) = R(0) e^{Bz}. \tag{29}$$

Implementation of (24) using approximations from (26) to (29) thus requires 2 geometries. In a first 1D-type geometry, (23) is implemented. To take into account relation (24), a second 2D-type geometry is created.

Values Z_i and Z_f for the 2D geometry along the z axis are used to define the range of frequency $[\omega_i, \omega_f]$ for which the approximation of the fractional differentiation is expected using the relations

$$\omega_i = e^{Z_i}, \qquad \omega_f = e^{Z_f}. \tag{30}$$

Note that frequencies ω_i and ω_f depend, respectively, on the simulation duration T_d and the sampling time T_s. These frequencies can be defined using the following rules: $\omega_i \ll 2\pi/T_d$ and $\omega_f \gg 2\pi/T_s$.

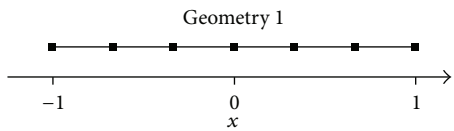

Figure 2: 1D geometry representation.

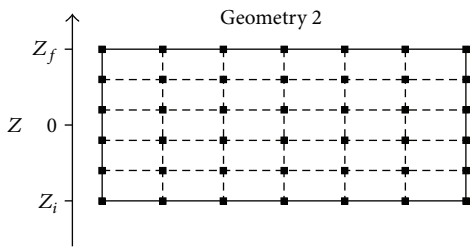

Figure 3: 2D geometry representation.

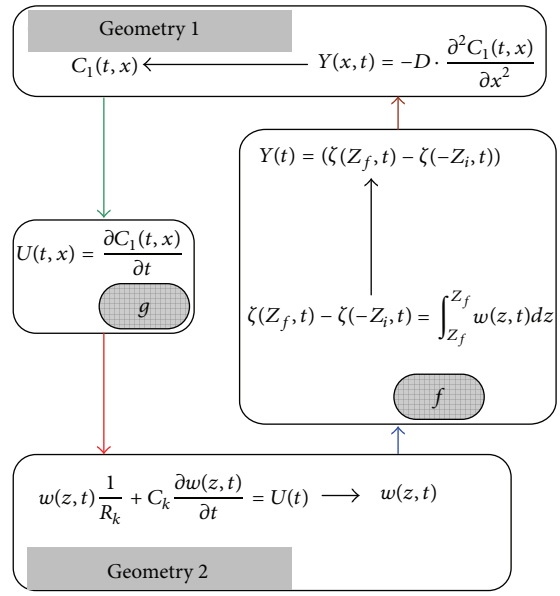

Figure 4: Information exchanged between the two geometries.

Information produced in the two geometries are then exchanged as described in Figure 4.

4. Example

The following diffusion system with $x \in [0 \cdots L]$ is considered:

$$\frac{\partial^{1-\gamma} C_1(t,x)}{\partial t^{1-\gamma}} = -D \frac{\partial^2 C_1(t,x)}{\partial x^2}, \tag{31}$$

with the following initial and boundaries conditions:

$$C_1(t,0) = h(t), \qquad C_1(t,L) = j(t), \qquad C_1(0,x) = 0. \tag{32}$$

For $\gamma = 0.5$, $D = 0.1$ m/s, $j(t) = 0$ and

$$\begin{aligned} h(t) &= K \cdot (t - t_0) \text{ heaviside } (t - t_0) \\ &\quad - K(t - t_1) \text{ heaviside } (t - t_1) \\ &= h_1(t) - h_2(t) \quad t \geq 0. \end{aligned} \tag{33}$$

As shown in the appendix, system (31) and (32) solution is defined by

$$C_1(x,t) = 0 \quad \text{for } t \leq t_0, \tag{34}$$

$$\begin{aligned} C_1(x,t) &= \sum_0^\infty \left(2 \cdot \frac{\left(1 - e^{(n\pi)^4 D^2 (t-t_0)} \operatorname{erfc}\left((n\pi)^2 D \sqrt{(t-t_0)}\right)\right)}{(n\pi)^5 D^2} - \frac{4 \cdot (t-t_0)^{0.5}}{(n\pi)^3 D \cdot \Gamma(0.5)} \right) \\ &\quad \times \sin(n\pi x) + (1-x) \cdot h_1(t) \quad \text{for } t_0 \leq t \leq t_1, \end{aligned} \tag{35}$$

$$\begin{aligned} C_1(x,t) &= \sum_0^\infty \left(2 \cdot \frac{\left(1 - e^{(n\pi)^4 D^2 (t-t_0)} \operatorname{erfc}\left((n\pi)^2 D \sqrt{(t-t_0)}\right)\right)}{(n\pi)^5 D^2} - \frac{4 \cdot (t-t_0)^{0.5}}{(n\pi)^3 D \cdot \Gamma(0.5)} \right. \\ &\quad \left. - 2 \cdot \frac{\left(1 - e^{(n\pi)^4 D^2 (t-t_1)} \operatorname{erfc}\left((n\pi)^2 D \sqrt{(t-t_1)}\right)\right)}{(n\pi)^5 D^2} + \frac{4 \cdot (t-t_1)^{0.5}}{(n\pi)^3 D \cdot \Gamma(0.5)} \right) \\ &\quad \times \sin(n\pi x) + (1-x) \cdot (h_1(t) - h_2(t)) \quad \text{for } t \geq t_1. \end{aligned} \tag{36}$$

For $t_1 = 5$ s and $t_2 = 10$ s, this solution is represented by Figure 5.

The analytical solution is compared with the results produced by COMSOL Multiphysics for function $C_1(x,t)$ using the implementation and geometries described in Figures 2–4. For the implementation, $\omega_i = 0.01$ rd/s and $\omega_f = 1000$ rd/s.

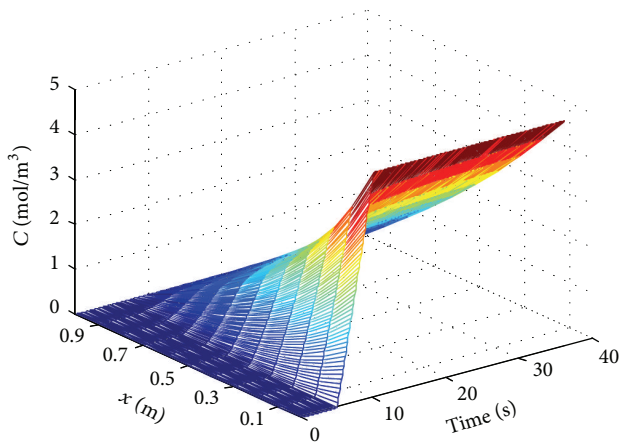

FIGURE 5: Function $C_1(x,t)$ produced by COMSOL Multiphysics.

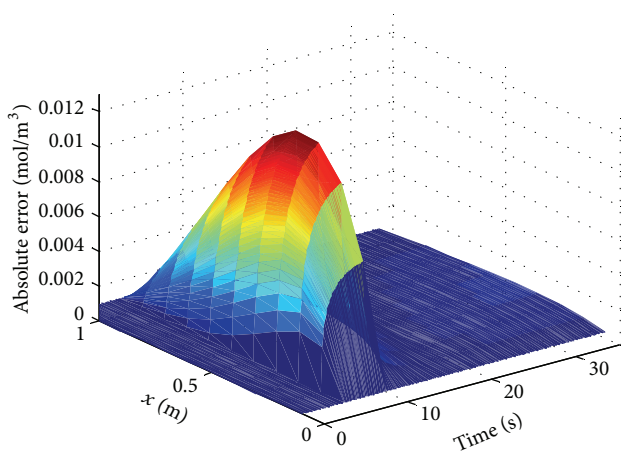

FIGURE 6: Absolute error between function $C_1(x,t)$ and the solution computed with COMSOL Multiphysics.

Figure 6 is a representation of the absolute error between function $C_1(x,t)$ and the solution computed with COMSOL Multiphysics. This really small error permits us to validate the method we used for the implementation of a fractional diffusion equation using a partial differential equation for the approximation of a fractional derivative.

5. Conclusion

This paper proposes a method for the implementation of a fractional diffusion equation into simulation softwares such as COMSOL Multiphysics. These software applications are now powerful tools for engineers to simulate complex systems combining several physical domains such as electrochemical and thermal. However they are not adapted to take into account anomalous diffusion and thus to model diffusion interfaces as in batteries, ultracapacitors, or fuel cells. To permit the implementation, the link between fractional systems and diffusion equation is used. The fractional diffusion equation considered is splitted into two parts and the remaining fractional equation is approximated by a partial differential equation. For the implementation of this partial differential equation, an additional geometry is created (a 1D system is transformed into a 2D system). The efficiency of the proposed method is evaluated in an example. The results obtained showed the efficiency of the proposed method.

Appendix

This appendix demonstrates how, using material provided in [12], the analytical solution of the following fractional diffusion equation:

$$\frac{\partial^{1-\gamma} C_1(t,x)}{\partial t^{1-\gamma}} = -D\frac{\partial^2 C_1(t,x)}{\partial x^2}, \quad x \in [0 \cdots L] \tag{A.1}$$

with the following initial and boundaries conditions

$$C_1(t,0) = h(t), \qquad C_1(t,L) = j(t), \qquad C_1(0,x) = 0, \tag{A.2}$$

is obtained. To obtain homogenous conditions at $x = 0$ and $x = 1$, the following change of variable is used:

$$V(x,t) = C_1(x,t) + U(x,t) \tag{A.3}$$

with

$$U(x,t) = \left(1 - \frac{x}{L}\right) h(t) + \frac{x}{L} j(t). \tag{A.4}$$

System (A.1) thus becomes

$$\begin{gathered} \frac{\partial^{1-\gamma} V(t,x)}{\partial t^{1-\gamma}} = -D\frac{\partial^2 V(t,x)}{\partial x^2} + f(x,t), \\ V(t,0) = 0, \qquad V(L) = 0, \qquad V(0,x) = g(x), \end{gathered} \tag{A.5}$$

with

$$\begin{gathered} f(x,t) = -\left(1 - \frac{x}{L}\right) \frac{\partial^{1-\gamma} h(t)}{\partial t^{1-\gamma}} - \frac{x}{L} \frac{\partial^{1-\gamma} j(t)}{\partial t^{1-\gamma}}, \\ g(x) = -\left(1 - \frac{x}{L}\right) h(0) - \frac{x}{L} j(0). \end{gathered} \tag{A.7}$$

Separation variable method leads to writing $V(x,t)$ as:

$$V(x,t) = \sum_{1}^{\infty} T_n(t) \sin(n\pi x) \tag{A.9}$$

with

$$\frac{\partial^{1-\gamma} T_n(t)}{\partial t^{1-\gamma}} + (n\pi)^2 D T_n(t) = f_n(t), \tag{A.10}$$

$$T_n(0) = 2\int_0^1 g(\zeta) \sin(n\pi\zeta)\, d\zeta, \tag{A.11}$$

$$f_n(t) = 2\int_0^1 f(x,t) \sin(n\pi x)\, dx. \tag{A.12}$$

Now let $\gamma = 0.5$, $j(t) = 0$, and

$$h(t) = 0, \quad t \le t_0,$$
$$h(t) = K(t - t_0), \quad t \le t \le t_1, \tag{A.13}$$
$$h(t) = K(t_1 - t_0), \quad x \ge t_1.$$

Solution of system (A.1) is given, according to (A.9), (A.10), and (A.11)

$$V(x,t) = \sum_1^\infty T_n(t) \sin(n\pi x), \tag{A.16}$$

$$\frac{\partial^{1-\gamma} T_n(t)}{\partial t^{1-\gamma}} + (n\pi)^2 D T_n(t) = f_n(t), \tag{A.17}$$

$$T_n(0) = 0 \tag{A.18}$$

with

$$f_n(t) = 2\int_0^1 f(x,t)\sin(n\pi x)\,dx, \tag{A.19}$$

$$f(x,t) = -(1-x)\frac{\partial^{1-\gamma} h(t)}{\partial t^{1-\gamma}}, \tag{A.20}$$

$$g(x) = -(1-x)h(0) = 0, \tag{A.21}$$

$$V(x,t) = C_1(x,t) + U(x,t), \tag{A.22}$$

$$U(x,t) = (1-x)h(t). \tag{A.23}$$

Combining relations (A.19) and (A.20) leads to

$$f_n(t) = -2\frac{\partial^{1-\gamma} h(t)}{\partial t^{1-\gamma}} \int_0^1 (1-x)\sin(n\pi x)\,dx, \tag{A.24}$$

and thus

$$f_n(t) = -\frac{4}{n\pi}\frac{\partial^{1-\gamma} h(t)}{\partial t^{1-\gamma}}. \tag{A.25}$$

Laplace transform applied to (A.17) leads to

$$p^{0.5} T_n(p) + (n\pi)^2 D T_n(p) = \frac{4}{n\pi} p^{0.5} h(p), \tag{A.26}$$

and thus

$$T_n(p) = \frac{(4/n\pi)\, p^{0.5} h(p)}{p^{0.5} + (n\pi)^2 D}. \tag{A.27}$$

If $h(t)$ is written as

$$\begin{aligned} h(t) &= K(t - t_0)\ \text{heaviside}\ (t - t_0) \\ &\quad - K(t - t_1)\ \text{heaviside}\ (t - t_1) \\ &= h_1(t) - h_2(t), \quad t \ge 0, \end{aligned} \tag{A.28}$$

relation (A.27) becomes

$$\begin{aligned} T_n(p) &= \frac{(4/n\pi)\, p^{0.5} h_1(p)}{p^{0.5} + (n\pi)^2 D} - \frac{(4/n\pi)\, p^{0.5} h_2(p)}{p^{0.5} + (n\pi)^2 D} \\ &= T_{n1}(p) - T_{n2}(p). \end{aligned} \tag{A.29}$$

Within the interval $0 < t < t_0$, $h_1(t) = 0$ and thus using (A.27) $T_{n1}(t) = 0$.

If $t > t_0$, function $h(t)$ is a ramp and thus

$$T_{n1}(p) = \frac{(4/n\pi)\, p^{0.5}\left(K/p^2\right)}{p^{0.5} + (n\pi)^2 D}. \tag{A.30}$$

Inverse Laplace transform then permits

$$\begin{aligned} T_{n1}(t) &= 2 \cdot \frac{\left(1 - e^{(n\pi)^4 D^2 (t - t_0)} \operatorname{erfc}\left((n\pi)^2 D \sqrt{(t - t_0)}\right)\right)}{(n\pi)^5 D^2} \\ &\quad - \frac{4 \cdot (t - t_0)^{0.5}}{(n\pi)^3 D \cdot \Gamma(0.5)}. \end{aligned} \tag{A.31}$$

Within the interval $0 < t < t_1$, $h_2(t) = 0$, and thus $T_{n2}(t) = 0$.

Using a similar method, $T_{n2}(t)$ where $t > t_1$ is given by

$$\begin{aligned} T_{n2}(t) &= 2 \cdot \frac{\left(1 - e^{(n\pi)^4 D^2 (t - t_1)} \operatorname{erfc}\left((n\pi)^2 D \sqrt{(t - t_1)}\right)\right)}{(n\pi)^5 D^2} \\ &\quad - \frac{4 \cdot (t - t_1)^{0.5}}{(n\pi)^3 D \cdot \Gamma(0.5)}. \end{aligned} \tag{A.32}$$

Finally, using (A.3), system (A.1) and (A.2) solution is defined by, using (34), (35), and (36).

Conflict of Interests

The authors declare no conflict of interests.

References

[1] R. B. Bird, W. E. Stewart, and E. N. Lightfoot, *Transport Phenomena*, John Wiley & Sons, New York, NY, USA, 2nd edition, 2002.

[2] A. Compte and R. Metzler, "The generalized Cattaneo equation for the description of anomalous transport processes," *Journal of Physics A*, vol. 30, no. 21, pp. 7277–7289, 1997.

[3] A. Compte, "Stochastic foundations of fractional dynamics," *Physical Review E*, vol. 53, no. 4, pp. 4191–4193, 1996.

[4] R. Gorenflo and F. Mainardi, "Some recent advances in theory and simulation of fractional diffusion processes," *Journal of Computational and Applied Mathematics*, vol. 229, no. 2, pp. 400–415, 2009.

[5] J. Bisquert and A. Compte, "Theory of the electrochemical impedance of anomalous diffusion," *Journal of Electroanalytical Chemistry*, vol. 499, no. 1, pp. 112–120, 2001.

[6] A. Oustaloup, *Systèmes Asservis Linéaires D'ordre Fractionnaire*, Masson, Paris, France, 1983.

[7] J. Sabatier, M. Merveillaut, R. Malti, and A. Oustaloup, "How to impose physically coherent initial conditions to a fractional system?" *Communications in Nonlinear Science and Numerical Simulation*, vol. 15, no. 5, pp. 1318–1326, 2010.

[8] G. Montseny, "Diffusive representation of pseudo-differential time-operators," *Esaim*, vol. 5, pp. 159–175, 1998.

[9] D. Matignon, "Stability properties for generalized fractional differential systems," *Esaim*, vol. 5, pp. 145–158, 1998.

[10] F. Levron, J. Sabatier, A. Oustaloup, and L. Habsieger, "From partial differential equations of propagative recursive systems to non-integer differentiation," *Fractional Calculus & Applied Analysis*, vol. 2, no. 3, pp. 245–264, 1999.

[11] J. Sabatier, H. C. Nguyen, X. Moreau, and A. Oustaloup, "Fractional behaviour of partial differential equations whose coefficients are exponential functions of the space variable," *Mathematical and Computer Modelling of Dynamical Systems*, 2013.

[12] Y. Lin and C. Xu, "Finite difference/spectral approximations for the time-fractional diffusion equation," *Journal of Computational Physics*, vol. 225, no. 2, pp. 1533–1552, 2007.

Hindawi Publishing Corporation
Mathematical Problems in Engineering
Volume 2013, Article ID 508543, 16 pages
http://dx.doi.org/10.1155/2013/508543

Research Article

Fast Image Segmentation Based on Efficient Implementation of the Chan-Vese Model with Discrete Gray Level Sets

Songsong Li and Qingpu Zhang

School of Management, Harbin Institute of Technology, Harbin 150001, China

Correspondence should be addressed to Songsong Li; lisongsong@hit.edu.cn

Received 3 December 2012; Accepted 28 January 2013

Academic Editor: Clara Ionescu

A new image segmentation based on fast implementation of the Chan-Vese model is proposed. This approach differs from previous methods in that we do not need to solve the Euler-Lagrange equation of the underlying variational problem. First, through experiments, we observe that for the smooth image segmentation, Chan-Vese model (CVM) can be simplified. Utilizing the Gaussian low pass filter, we pretreat the original image and regularize the level curves. Then, we calculate the energy directly on discrete gray level sets, find the minimizer of the energy, and obtain the segmentation results. We analyze the algorithm and prove that under discrete gray level sets, the global minimum of the energy is same as the one obtained by the previous methods. Another advantage of this method is that the reinitialization is not needed. Since there are at most 255 discrete gray level sets, the algorithm improves the computational speed dramatically. And the complexity of the algorithm is $O(N)$, where N is the number of pixels in the image. So even for the large images, it is also very efficient. We apply our segmentation algorithm to synthetic and real world images to emphasize the performances of our model compared with other segmentation models.

1. Introduction

Images are the proper 2D projections of the 3D world containing various objects. To successfully reconstruct the 3D world, at least approximately, the first crucial step is to identify the regions in images that correspond to individual objects. This is the well-known problem of image segmentation. It has broad applications in variety of important fields such as computer vision and medical image processing.

Variational methods [1–16] have been extensively used and studied in image segmentation in the past decade because of their flexibility modeling and various advantages in the numerical implementation. These methods drive one or more initial curve(s), based on gradient and/or region information in the image, to the boundaries of objects in that image. The basic idea of variational methods is to minimize an energy. This functional generally depends on the features of the image. The classical way to solve the minimization problem is to solve the corresponding Euler-Lagrange equation. For instance, relatively early, Mumford and Shah [1] introduced a celebrated segmentation model by minimizing an energy functional that penalizes smoothness within regions and the length of their discontinuity contours. Recently, Chan and Vese [4] developed an active contour without edge model to deal with the problem of image segmentation by using the level-set framework introduced by Osher and Paragios [17]. Tsai et al. [5] also independently developed a segmentation method which is similar to it. The active contour methods [4–8, 10, 13] based on level-set framework have several advantages. First, they can deal with topological changes such as break and merger. Second, intrinsic geometric elements such as the normal vector and the curvature can be easily expressed with respect to the level-set function. Third, this level-set framework can be extended and applied in any dimension.

However, the active contour methods based on level-set framework have some limitations. First, these methods are usually implemented by solving the partial differential equations (PDEs) and thus computational efficiency sharply decline because of numerical stability constraints. Particularly, the signed distance reinitialization procedure is necessary. It severely limits the efficiency of Chan-Vese model. Second, most methods have the initialization problem [6]: different initial curves produce different segmentations because of

the nonconvexity of Chan-Vese model. More recently, some of the researchers develop fast algorithms [14–16, 18–20] for the Chan-Vese image segmentation model. In [14, 15, 18], the authors develop fast algorithms based on calculating the variational energy of the Chan-Vese model directly without the length term, that is, solving PDEs. In [14], the authors develop a fast method for image segmentation without solving the Euler-Lagrange equation of the underlying variational problem proposed by Chan and Vese [4]. Instead, they calculate the energy directly and check if the energy is decreased when they change a point inside the level-set to outside or vice versa. Later, various modifications of Chan-Vese model, related to different aspects of the image analysis, have been proposed, such as adaptive segmentation of vector images [7, 8, 19, 20] knowledge-based segmentation [13].

An efficient implementation method for the Chan-Vese model is proposed in this paper. Since the simplified Chan-Vese model is without the length term, the new method does not have to solve PDEs. Our method is the hybrid of the discrete simplified Chan-Vese model and the discrete gray level-set framework. First, we decouple the Chan-Vese model into two stages: in the first stage, utilizing Gaussian low pass filter to pretreat the original image and obtaining some appropriate smooth versions of the original image; in the second stage, segmenting the smooth image by Chan-Vese model without the length term. Second, we implement the previous algorithm based on the discrete gray level-set framework. Our segmentation method is also divided into two stages: in the first stage, we smooth the image into required scale; in the second stage, we calculate the energy directly on discrete gray level sets and find the minimizer of the energy. Each stage is independent and at each stage the method is flexible. The new method bears some similarities to [14, 15, 18], but we calculate the energy directly on discrete gray level sets, which is a new framework. More complicated issues which are not considered in [14], such as sensitivity to noise, are discussed. The segmentation method can also deal with complicated image, and the CPU time of large size/complicated images is not too long. First, we do not need to solve the Euler-Lagrange equation of the underlying variational problem, so the initial conditions and the procedure of reinitiation are not needed. Second, in the second stage of our algorithm, the main computation process is adding operators and logical operators, which costs little CPU time, so the complexity of the algorithm is $O(N)$.

This paper is organized as follows. In Section 2, we present the Chan-Vese piecewise smooth active contours model [4] (also the algorithm of Tsai et al. [5]) for image segmentation. In Section 3, we give a full account of our model. Experimental results are presented in Section 4, and the final section is our conclusion.

2. The Main Idea of the Chan-Vese Active Contours Model

In this section, we present the main idea of the Chan-Vese active contours model in order to develop the idea of the new fast hybrid level-set algorithm.

The active contour model proposed by Chan and Vese [4] is a particular case of the Mumford-Shah model [1]. Consider an image u^0 with the domain $\Omega \subset \mathbb{R}^2$. Let the segmenting closed curve C (active contour) divide Ω into two partitions Ω_1 and Ω_2, which is corresponding to the image subdomains inside and outside the curve C, respectively. It minimizes the following energy functional:

$$F(c_1, c_2, C) = \nu \cdot \text{Length}(C) + \sum_{i=1}^{2} \int_{\Omega_1} \left(u^0(x,y) - c_i\right)^2 dxdy, \quad i = 1, 2, \tag{1}$$

where c_i is the average value of $u^0(x, y)$ in each region Ω_i and ν is a positive constant.

Using the level-set method in [17], the authors replace the unknown curve C by the level-set function $\phi(x, y)$ defined by

$$\begin{aligned} C &= \{(x,y) \mid \phi(x,y) = 0\}, \\ \Omega_1 &= \text{inside}(C) = \{(x,y) \mid \phi(x,y) > 0\}, \\ \Omega_2 &= \text{outside}(C) = \{(x,y) \mid \phi(x,y) < 0\}. \end{aligned} \tag{2}$$

Denote the Heaviside function H

$$H(z) = \begin{cases} 1, & \text{if } z \geq 0, \\ 0, & \text{if } z < 0. \end{cases} \tag{3}$$

Then the energy functional (1) can be written in terms of the level-set formulation as

$$F(c_1, c_2, \phi) = \nu \int_\Omega |\nabla H(\phi)| \, dxdy + \int_\Omega \left(u^0 - c_1\right)^2 H(\phi) \, dxdy + \int_\Omega \left(u^0 - c_2\right)^2 (1 - H(\phi)) \, dxdy. \tag{4}$$

The finial segmentation curve could be obtained from the minimizer of the energy functional (4) with respect to ϕ. Using a gradient descent method, minimizing (4) yields the following problem:

$$\frac{\partial \phi}{\partial t} = \delta(\phi) \left[\nu \cdot div\left(\frac{\nabla \phi}{|\nabla \phi|}\right) - \left(u^0 - c_1\right)^2 + \left(u^0 - c_2\right)^2 \right], \tag{5}$$

where $\delta(\phi) = H'(\phi)$ in the distribution sense and

$$c_1 = \frac{\int_\Omega u^0 H(\phi) \, dx}{\int_\Omega H(\phi) \, dx}, \qquad c_2 = \frac{\int_\Omega u^0 (1 - H(\phi)) \, dx}{\int_\Omega (1 - H(\phi)) \, dx}. \tag{6}$$

From the solution of the problems (5) and (6), we obtain the evolution of $C(t)$, defined by $\{(x, y) \mid \phi(x, y, t) = 0\}$, which is the boundary between the sets $\{(x, y) \mid u^0 \approx c_1\}$ and $\{(x, y) \mid u^0 \approx c_2\}$. Therefore, the original image is segmented u^0 into two parts.

It is noticed that (5) is a nonlinear parabolic partial differential equation. So it requires expensive computation

since the solution is on a large time domain (i.e., from the initial curve location to the finally achieved steady state). In particular, we need to reinitialize the level-set function ϕ to a signed distance function in each iteration. If we do not do it, when the level-set function ϕ becomes very sharp or flat during the evolution, it makes computation highly inaccurate. Although some semi-implicit methods in [21, 22] could be used to partially alleviate the computational burden, the process of reinitialization is very important and may not be avoided by using some level-set methods. All in all, the Chan and Vese algorithm works very well for image segmentation, but solving the Euler-Lagrange equations (5) and (6) and reinitializing the level-set function cost a lot of CPU time.

In Section 3, we will propose a fast hybrid gray level-set algorithm in order to overcome the previous shortcomings of the Chan-Vese model.

3. Our Method

In this section, we show a two-stage scheme for implementation of the piecewise constant segmentation model. More precisely, the smooth version of the original image is first obtained by some smooth filters, and then minimizing the modified Chan-Vese energy functional on the gray level sets, the image is divided into two subregions.

3.1. Segmentation for the Smooth Image. In the Chan-Vese segmentation model, the parameter ν in (4) is a weight of the regularizing term, which controls the length of the zero level-set. When the noise level is high, the parameter ν should be large and only large objects are detected. When the noise level is low, the parameter ν could be small and objects of small size are detected. Because the Chan-Vese model is independent of the gradient of the image, the input image can be smooth enough [4]. So the segmentation method for the smooth image should be different from the method for the noise image. In Figure 1, we present results of the noise image and some smooth versions of the noise image by the Chan-Vese model with the same parameter $\nu = 0$, respectively. It is noticed that for the smooth image, the parameter ν could vanish in Chan-Vese model, and the good segmentation is also obtained.

Now, based on the previous facts, we assume that the input image is reasonably smooth, and then the parameter ν could vanish in (4). Hence the following simplified Chan-Vese model without the length term is considered:

$$F(c_1, c_2, \phi) = \int_\Omega (u - c_1)^2 H(\phi)\, dxdy + \int_\Omega (u - c_2)^2 (1 - H(\phi))\, dxdy. \tag{7}$$

Using the gradient descent method, minimizing (7) can solve the following problem:

$$\frac{\partial \phi}{\partial t} = \delta(\phi)\left(-(u - c_1)^2 + (u - c_2)^2\right), \tag{8}$$

where $\delta(\phi) = H'(\phi)$ in the distribution sense and

$$c_1 = \frac{\int_\Omega uH(\phi)\, dx}{\int_\Omega H(\phi)\, dx}, \qquad c_2 = \frac{\int_\Omega u(1 - H(\phi))\, dx}{\int_\Omega (1 - H(\phi))\, dx}. \tag{9}$$

The simplified Chan-Vese algorithm is sketched in the following.

Algorithm 1. The simplified Chan-Vese algorithm is the following two-stage scheme.

(1) By the smooth filter obtain some appropriate smooth versions u of the noise image u^0.

(2) Calculate the minimum of the simplified Chan-Vese energy (7).

(i) Initialize ϕ^0, $n = 0$.
(ii) Compute $c_1(\phi^n)$ and $c_2(\phi^n)$ by (9).
(iii) Solve the equation in ϕ from (8), to obtain ϕ^{n+1}.
(iv) Reinitialize ϕ locally (this step is optional).
(v) Check whether the solution is stationary. If not, $n = n + 1$ and repeat (ii)–(v).

The main difference between Algorithm 1 and the original Chan-Vese model is whether the input image requires smooth pretreatment. In Algorithm 1, there are a lot of methods to smooth image, such as Gaussian low pass filter, averaging filter, Laplacian filter, and enhancing filter based on PDEs. In this paper, we choose the simplest and possibly one of the most popular ways, Gaussian low pass filter. Though all image information, such as the noise and edges, will be indistinguishably destroyed by this filter, it tampers with the segmentation result little, since the Chan-Vese model makes use of a stopping edge function based on the density of the image instead of the gradient. It is notice that if the images are noisy, we do a preprocessing step to smooth or enhance the images firstly, or else this step is needless. In Figures 2 and 3, we present the other two experiments by Algorithm 1. In the two experiments, Figure 3(a) is smoother than Figure 2(a), so Figure 3(a) needs to be smoothed more. For the level-set method, it is inevitable to reinitialize the level-set function for the stability of algorithms. However, for Algorithm 1, we need not reinitialize the level-set function ϕ to a signed distance function in each iteration, which is different from the Chan-Vese model. In Section 4, from the numerical experiments, we show the interesting phenomenon.

Now, let us observe the following facts: for the noise image, the gray level lines are disorderly and irregular, while for the smooth image, the gray level lines are smooth and regular. These basic remarks are illustrated in Figure 4. In Figure 4(j), the contour line is very approximate to the real edges of the original image. Hence, we think the best segmentation result is one of the contour lines. How can the best segmentation result, that is, the most appropriate contour line, be obtained? In the next subsection, we will answer the question and then propose the new algorithm.

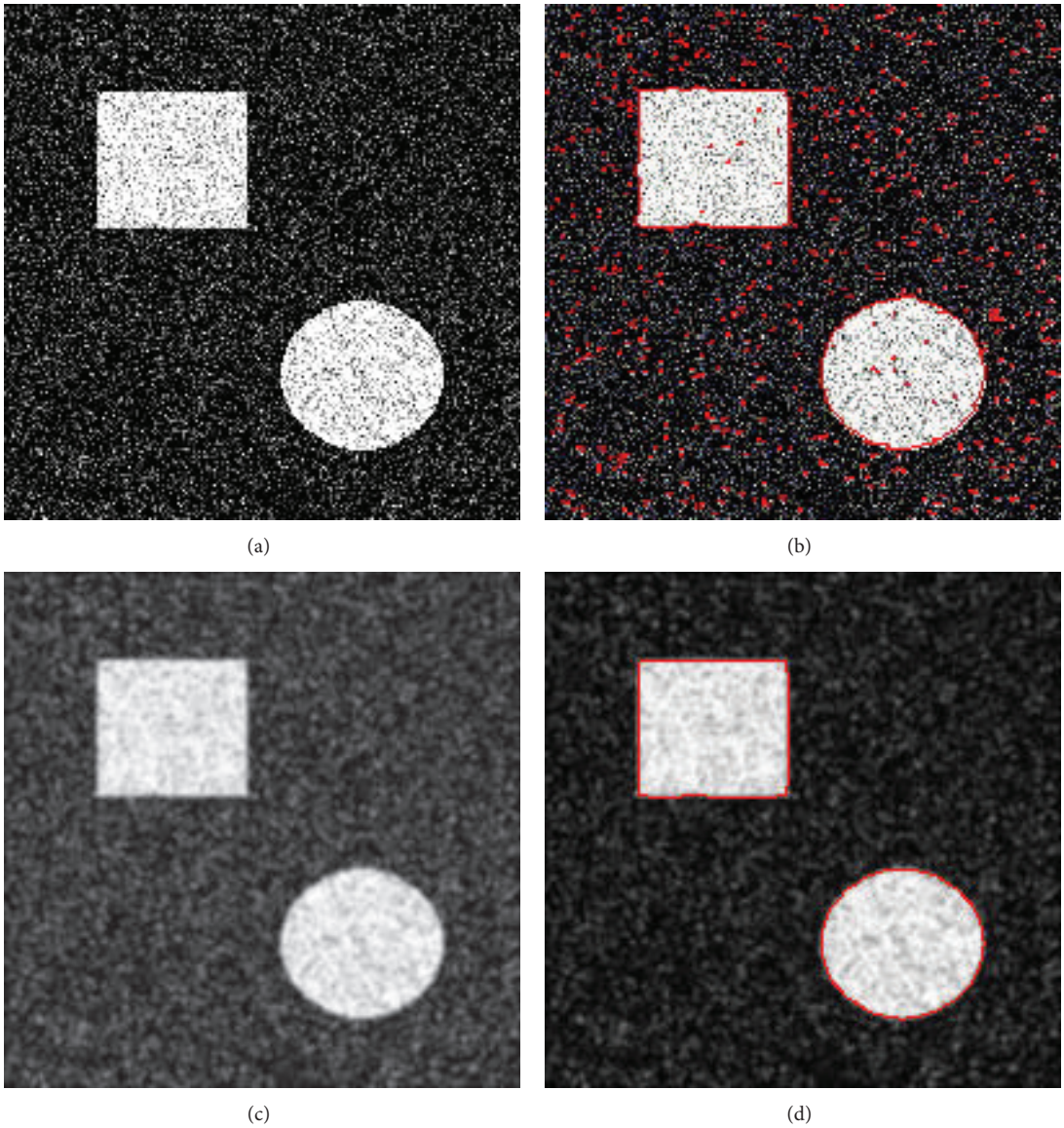

Figure 1: Segmentation results of the CV model. (a) The noise image with Gaussian white noise of mean 0 and variance 0.1. (b) The segmentation result of the noise image. (c) The smooth image by Gaussian low pass filter with $\sigma = 0.9$. (d) The segmentation result of the smooth image.

3.2. The Discrete Simplified Chan-Vese Energy Functional on the Discrete Gray Level Sets. Let $u_{i,j}$, for $(i,j) \in D \equiv \{1,\ldots,M\} \times \{1,\ldots,N\}$, be the gray level of a true M-by-N image $\mathbf{u}$ at pixel location (i,j), and let $[s_{\min}, s_{\max}]$ be the range of $\mathbf{u}$, that is, $s_{\min} \le u_{i,j} \le s_{\max}$. Let $D_1 \subset D$ and $D_2 = D \setminus D_1$, and then the image $\mathbf{u}$ is divided into two regions by the pixel location. Instead u^0 by $\mathbf{u}$, $H(\phi)$ by D_1, and $(1 - H(\phi))$ by D_2, respectively. Then minimizing the energy (7) is changed into minimizing

$$F_1(c_1, c_2, D_1, D_2) = \sum_{(i,j)\in D_1} (u_{i,j} - c_1)^2 + \sum_{(i,j)\in D_2} (u_{i,j} - c_2)^2, \tag{10}$$

with

$$c_1 = \frac{\sum_{(i,j)\in D_1} u_{i,j}}{|D_1|}, \qquad c_2 = \frac{\sum_{(i,j)\in D_2} u_{i,j}}{|D_2|}, \tag{11}$$

where $|D_1| = \sum_{(i,j)\in D_1} 1$ is the number of pixels in D_1 and $|D_2| = \sum_{(i,j)\in D_2} 1$ is the number of pixels in D_2. When the energy F_1 reaches a minimum, the best segmentation results are obtained, that is, the subregion D_1 and subregion D_2. It is noticed that since the selection of D_1 and D_2 is arbitrary, there are lots of combinations (D_1, D_2), so minimizing the energy F_1 is difficult. Now, we try to narrow the scope of the probable combinations. For any $K \in [s_{\min}, s_{\max}]$, the image $\mathbf{u}$ is divided into two subregions, that is, $D_1^K \equiv \{(k,l) : u_{k,l} < K\}$ and $D_2^K \equiv \{(k,l) : u_{k,l} \ge K\}$.

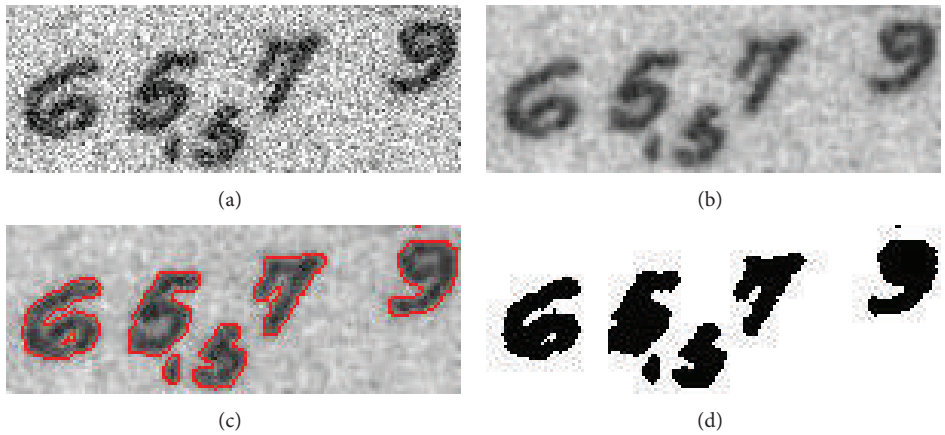

(a) (b) (c) (d)

Figure 2: Segmentation results by Algorithm 1. (a) The noise image. (b) The smooth image by Gaussian low pass filter with $\sigma = 0.8$. (c) The segmentation contour line. (d) The segmentation result.

Definition 2 (discrete gray level-set). The K-discrete gray level-set D^K which is the set of pixel location (i, j) is defined as follows:

$$D^K \equiv \left\{(i, j) : u_{i,j} < K\right\}, \tag{12}$$

where $u_{i,j}$ is the gray level of the image $\mathbf{u}$ at pixel location (i, j).

Then $D_2^K = D \setminus D_1$, for $D_1^K \equiv \{(k, l) : u_{k,l} < K\}$. Let $\mathscr{A} \equiv \{(D_1^K, D_2^K), K \in [s_{\min}, s_{\max}]\}$, and then the element number of the set $\mathscr{A}$ is $s_{\max} - s_{\min} + 1$. For every level K, the image $\mathbf{u}$ is always divided into two disjointed subregions by D_1^K and D_2^K. In Figure 4, the boundary of $D_1^K(D_2^K)$ is displayed at the different levels K, for the image u.

Theorem 3. *Minimizing the energy functional F_1 is equivalent to*

$$\begin{aligned}\min_{(D_1,D_2)\in\mathscr{A}} & F_2(c_1, c_2, D_1, D_2) \\ &= \sum_{(i,j)\in D_1} \left(u_{i,j} - c_1\right)^2 + \sum_{(i,j)\in D_2} \left(u_{i,j} - c_2\right)^2,\end{aligned} \tag{13}$$

where c_1 and c_2 are defined as (11).

Proof. If $(D_1, D_2) \in \mathscr{A}$, then for any $(i, j) \in D_1$, $(i', j') \in D_2$, we have $u_{i,j} \le u_{i',j'}$ and $c_1 \le c_2$, where c_1 and c_2 are defined as (11). It is obvious that $\min F_1 \le F_2$. We only need to prove $F_2 \le F_1$.

Assume there exist two subdomains D_1 and D_2 such that F_1 attains its minimizer. If there exist $(i_1, j_1) \in D_1$ and $(i_2, j_2) \in D_2$ such that $u_{i_1,j_1} > u_{i_2,j_2}$, then we denote $D_1' = D_1 - (i_1, j_1) + (i_2, j_2)$ and $D_2' = D_2 - (i_2, j_2) + (i_1, j_1)$.

Comparing the energy $F_1(c_1, c_2, D_1, D_2)$ and $F_1'(c_1', c_2', D_1', D_2')$, we get

$$\begin{aligned}F_1 - F_1' &= \sum_{(i,j)\in D_1} \left(u_{i,j} - c_1\right)^2 + \sum_{(i,j)\in D_2} \left(u_{i,j} - c_2\right)^2 \\ &\quad - \sum_{(i,j)\in D_1'} \left(u_{i,j} - c_1\right)^2 - \sum_{(i,j)\in D_2'} \left(u_{i,j} - c_2\right)^2 \\ &= -\left|D_1\right| c_1^2 - \left|D_2\right| c_2^2 + \left|D_1'\right| c_1'^2 + \left|D_2'\right| c_2'^2 \\ &= \left|D_1\right| \left(c_1' + c_1\right)\left(c_1' - c_1\right) + \left|D_2\right| \left(c_2' + c_2\right)\left(c_2' - c_2\right) \\ &= \left(c_1' + c_1\right)\left(u_{i_2,j_2} - u_{i_1,j_1}\right) \\ &\quad + \left(c_2' + c_2\right)\left(u_{i_1,j_1} - u_{i_2,j_2}\right) \\ &= \left(c_1' + c_1 - c_2' - c_2\right)\left(u_{i_2,j_2} - u_{i_1,j_1}\right).\end{aligned} \tag{14}$$

Since $c_1 \le c_2$, we have

$$\begin{aligned}&c_1' + c_1 - c_2' - c_2 \\ &\quad = 2c_1 - \frac{u_{i_1,j_1} - u_{i_2,j_2}}{\left|D_1\right|} - 2c_2 + \frac{u_{i_2,j_2} - u_{i_1,j_1}}{\left|D_2\right|} < 0.\end{aligned} \tag{15}$$

So we get

$$F_1' < F_1. \tag{16}$$

Since the energy F_1 obtains its minimizer, it is a contradiction. We complete the proof of the theorem. □

By the proof mentioned previously, we can easily see that

$$\begin{aligned}F_1 &= \sum_{(i,j)\in D_1} \left(u_{i,j} - c_1\right)^2 + \sum_{(i,j)\in D_2} \left(u_{i,j} - c_2\right)^2 \\ &= \sum_{(i,j)\in D} u_{i,j}^2 - \left|D_1\right| c_1^2 - \left|D_2\right| c_2^2.\end{aligned} \tag{17}$$

Hence we have the following.

Theorem 4. *Minimizing the energy functional F_1 is equivalent to*

$$\max_{(D_1^K, D_2^K)\in\mathscr{A}} E(K) \equiv \left\{\left|D_1^K\right| c_1^2 + \left|D_2^K\right| c_2^2\right\}, \tag{18}$$

where $K \in [s_{\min}, s_{\max}]$ and c_1 and c_2 are defined as (11).

FIGURE 3: Segmentation results of Algorithm 1. (a) The noise image. (b) The smooth image by Gaussian low pass filter with $\sigma = 0.1$. (c) The segmentation contour line. (d) The segmentation result.

Now, if the energy functional E reaches a maximum, the best segmentation results are obtained, that is, the subregion D_1^K and subregion D_2^K. Since $K = s_{\min}, s_{\min} + 1, \ldots, s_{\max}$, the energy functional E has $s_{\max} - s_{\min} + 1$ cases, and then the maximum of E is easily found. The algorithm is sketched here in the following.

Algorithm 5. The method of maximizing the following functional E.

(1) Sweep the image $\mathbf{u}$ once, record the number of all pixels at every gray level of the image $\mathbf{u}$ which range from $s_{\min}$ to $s_{\max}$.

(2) Calculate the energy $E(K)$ by (18), for $K \in [s_{\min}, s_{\max}]$, and find the maximizer $\mathscr{K}$.

(3) The image $\mathbf{u}$ is divided into two subregions, that is, $D_1^{\mathscr{K}} = \{(i, j) : \mathbf{u} < \mathscr{K}\}$ and $D_2^{\mathscr{K}} = \{(i, j) : \mathbf{u} \geq \mathscr{K}\}$.

Remark 6. In fact, we restrict $D_1^K = \{(i, j) : \mathbf{u} < K, (i, j) \in D\}$, $D_2^K = \{(i, j) : \mathbf{u} \geq K, (i, j) \in D\}$, since if two pixels with the same value K belong to both D_1^K and D_2^K, it will be ambiguous to determinant. However, the pixel number of $\mathbf{u}$ at K gray level is a little and cannot influence the maximizer of the energy $E(K)$. The experiment result shows that our approximated method is still efficient.

3.3. The Final Method. Based on Algorithm 5, the following is the new two-phase scheme for image segmentation.

Algorithm 7. (i) (*Smooth the original image*): For the input noise image $\mathbf{u}^0$, use the Gaussian smooth filter to obtain the smooth image u_S (If the input image is noiseless, this step is optional).

(ii) (*Segmentation*): Use Algorithm 5 to obtain the segmentation results for the smooth image u_S, that is.

(1) Sweep the image u_S once, record the number of all pixels at every gray level of the image u_S which range from $s_{\min}$ to $s_{\max}$.

(2) Calculate the energy $E(K)$ by (18), for $K \in [s_{\min}, s_{\max}]$, and find the maximizer $\mathscr{K}$.

(3) The image $\mathbf{u}^0$ is divided into two subregions, that is, $D_1^{\mathscr{K}} = \{(i, j) : u_S(i, j) < \mathscr{K}\}$ and $D_2^{\mathscr{K}} = \{(i, j) : u_S(i, j) \geq \mathscr{K}\}$, and this completes a segmentation.

Remark 8 (segmentation for various types of noisy image). There are lots of methods to obtain the smooth image in the first phase of the new method.

(i) If the type of noise is "salt and pepper," for example, the AMF (adaptive median filter) can be selected.

(ii) If the noise is "addition gauss noise," for example, the gaussian lower-pass filter, the TV method [23], the PM method [24], and the other anisotropic diffusion method can be used to smooth the original image.

(iii) If the noise is "Poisson noise," for example, the Variational method [25] can be used to denoise the original image.

In the new algorithm, the segmentation is only dependent on the smooth image but not sensitive to the smoothing scale. In Figure 5, using the new algorithm, we deal with the image with different types of noise.

Remark 9. In the new algorithm, we select the Gauss low pass filter to obtain the smooth image. However the filter is not necessary. If the image is corrupted by the different way, we will select the different filters, such as average filter, Laplacian filter, and unsharp filter. For the addition Gaussian noise, the gaussian lower-pass filter may be the best tradeoff between time and segmentation.

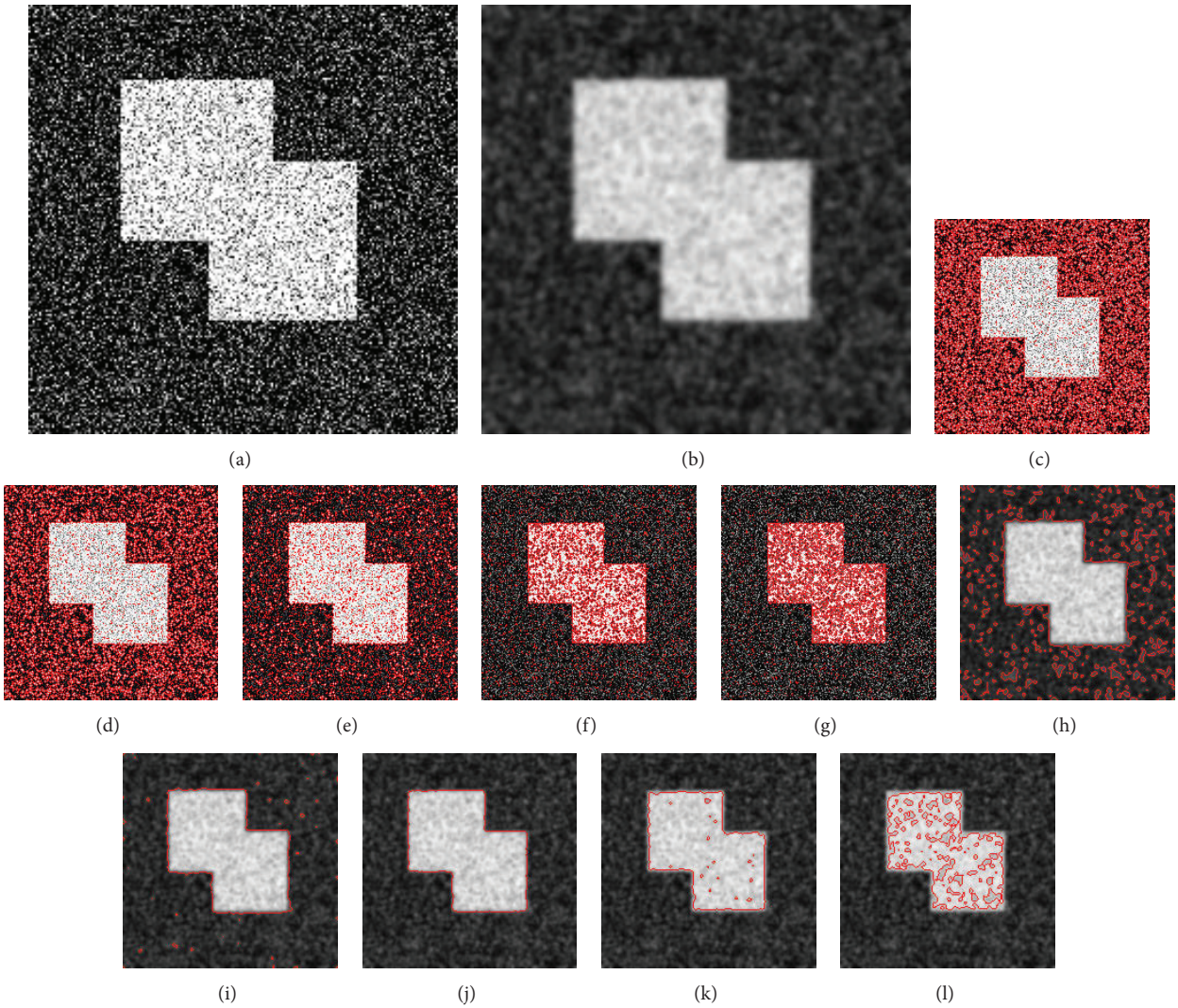

Figure 4: The level lines at different gray levels. (a) The noise image with Gaussian white noise of mean 0 and variance 0.2. (b) The smooth image by Gaussian low pass filter with $\sigma = 1.5$. (c)–(g) The level lines of the noise image at the gray level, 60, 80, 120, 180, and 200. (h)–(l) The level lines of the smooth image at the gray level, 60, 80, 120, 180, and 200.

4. Simulations

In this section, numerical examples on some synthetic and real world images are presented to illustrate the effectiveness of the new two-phase scheme in Section 4 by comparing it with Chan-Vese model.

4.1. Configuration. In the new algorithm, the first stage is smoothing the original image by low pass filter. The low pass filter is generally made by convolution with Gaussian of increasing variance, which is as follows:

$$u = G_\sigma * u^0, \tag{19}$$

where $G_\sigma = (1/\sigma)\exp\{-|x|^2/4\sigma^2\}$ and $*$ denotes the convolution operation. Koenderink [26] noticed that the convolution of signal with Gaussian at each scale is equivalent to the solution of the heat equation with the signal as initial datum u^0; that is,

$$\begin{aligned} \frac{\partial u}{\partial t} &= \Delta u, \\ u(x,0) &= u^0. \end{aligned} \tag{20}$$

Assuming a time step size of Δt and a space grid size of h, we quantize the time and space coordinates as follows:

$$\begin{aligned} t &= n\Delta t, \quad n = 0,1,2,\ldots, \\ x &= ih, \quad i = 0,1,2,\ldots,I, \\ y &= jh, \quad j = 0,1,2,\ldots,J, \end{aligned} \tag{21}$$

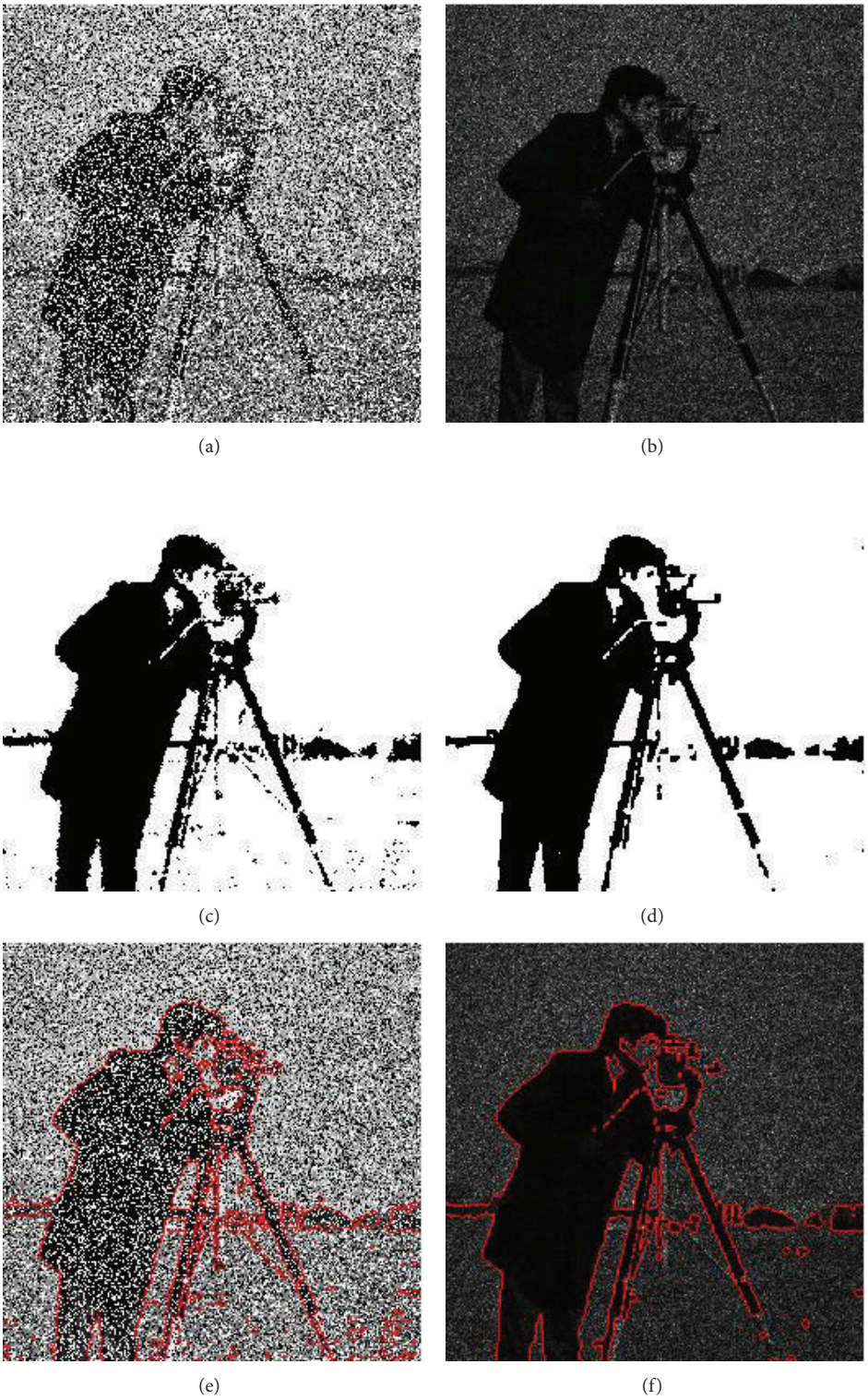

Figure 5: Segmentations for the *Cameraman* image with different types of noise. (a) The noise image corrupted by 50% salt and pepper noise. (b) The noise image corrupted by Poisson noise with the variance 4. (c)-(d) The segmentation results of the new algorithm. (e)-(f) The segmentation counter of the new algorithm.

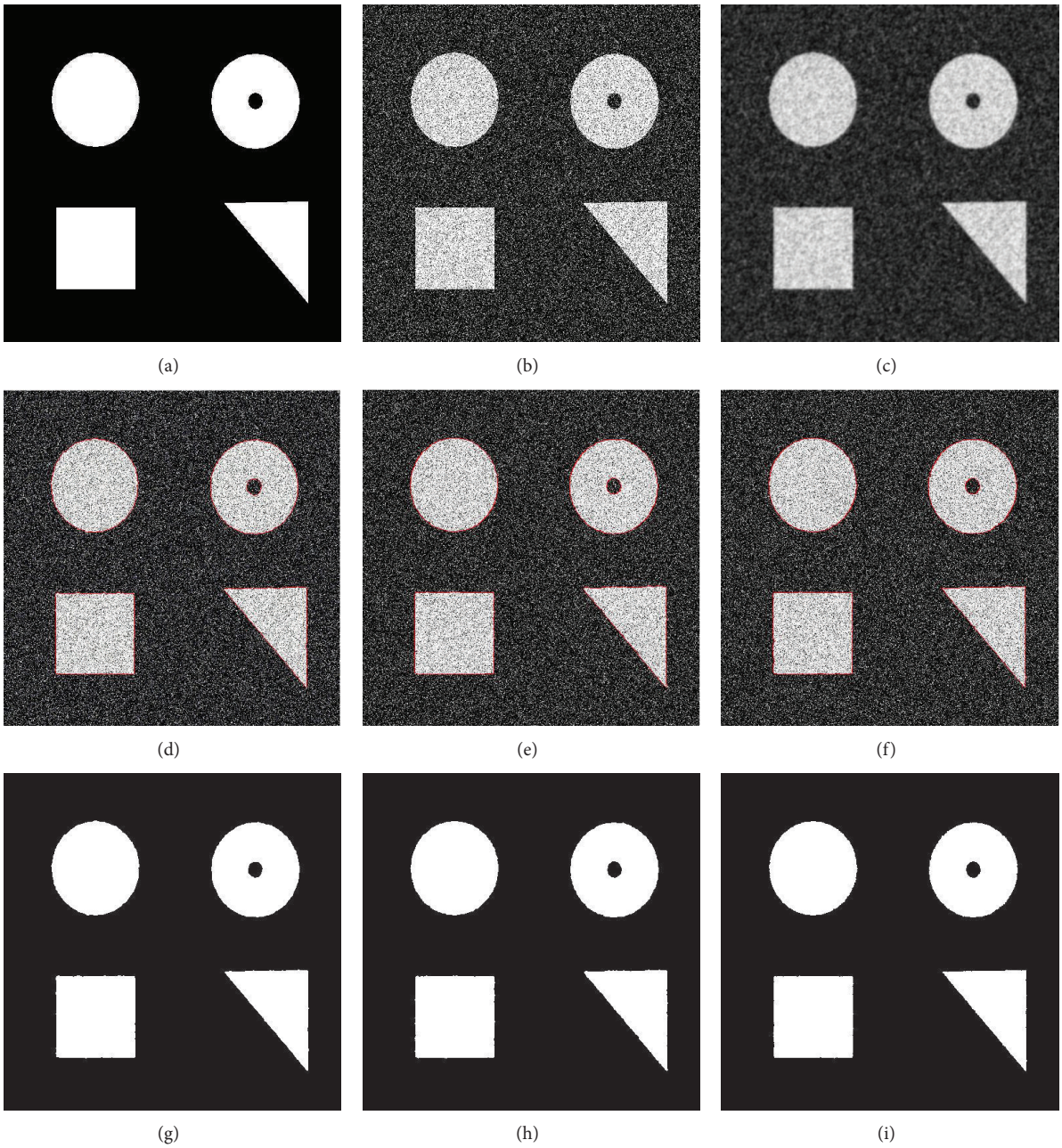

Figure 6: Segmentations for the noise *Test01* image. (a) The original image. (b) Corrupted *Test01* image with Gaussian noise (1.93 dB). (c) Smoothed *Test01* image with the numerical scheme (23) ($\lambda = 0.2$). (d) Algorithm 7. (e) Algorithm 1. (f) CVM. (g)–(i) The segmentation counter of Algorithm 7, Algorithm 1, and CVM, respectively.

where $Ih \times Jh$ is the size of image support. The classical five-point explicit numerical schemes of the heat equation (20) are as follows:

$$\frac{u_{i,j}^{n+1} - u_{i,j}^{n}}{\Delta t} = \frac{u_{i+1,j}^{n} + u_{i-1,j}^{n} + u_{i,j+1}^{n} + u_{i,j-1}^{n} - 4u_{i,j}^{n}}{h^2}, \quad (22)$$

or equivalently

$$u_{i,j}^{n+1} = u_{i,j}^{n} + \lambda \left(u_{i+1,j}^{n} + u_{i-1,j}^{n} + u_{i,j+1}^{n} + u_{i,j-1}^{n} - 4u_{i,j}^{n} \right), \quad (23)$$

where $\lambda = \Delta t / h^2 < 1/4$ is for the stable of numerical scheme.

The simulations are performed in Matlab R2007b on a 2.8 GHz Pentium 4 processor. For comparison purpose, the Chan-Vese method (CVM) [4] is also tested. We utilize a locally one-dimensional (LOD) scheme for CVM, which is an unconditional scheme [10].

4.2. Segmentation Performance. In Figures 6 and 7, we illustrate the performance of CVM, Algorithms 1 and 7 on synthetic noise *Test01* and *Test02* images. Among the segmentations, all algorithms give similar and good performances. For CVM (the Chan-Vese method), utilizing the

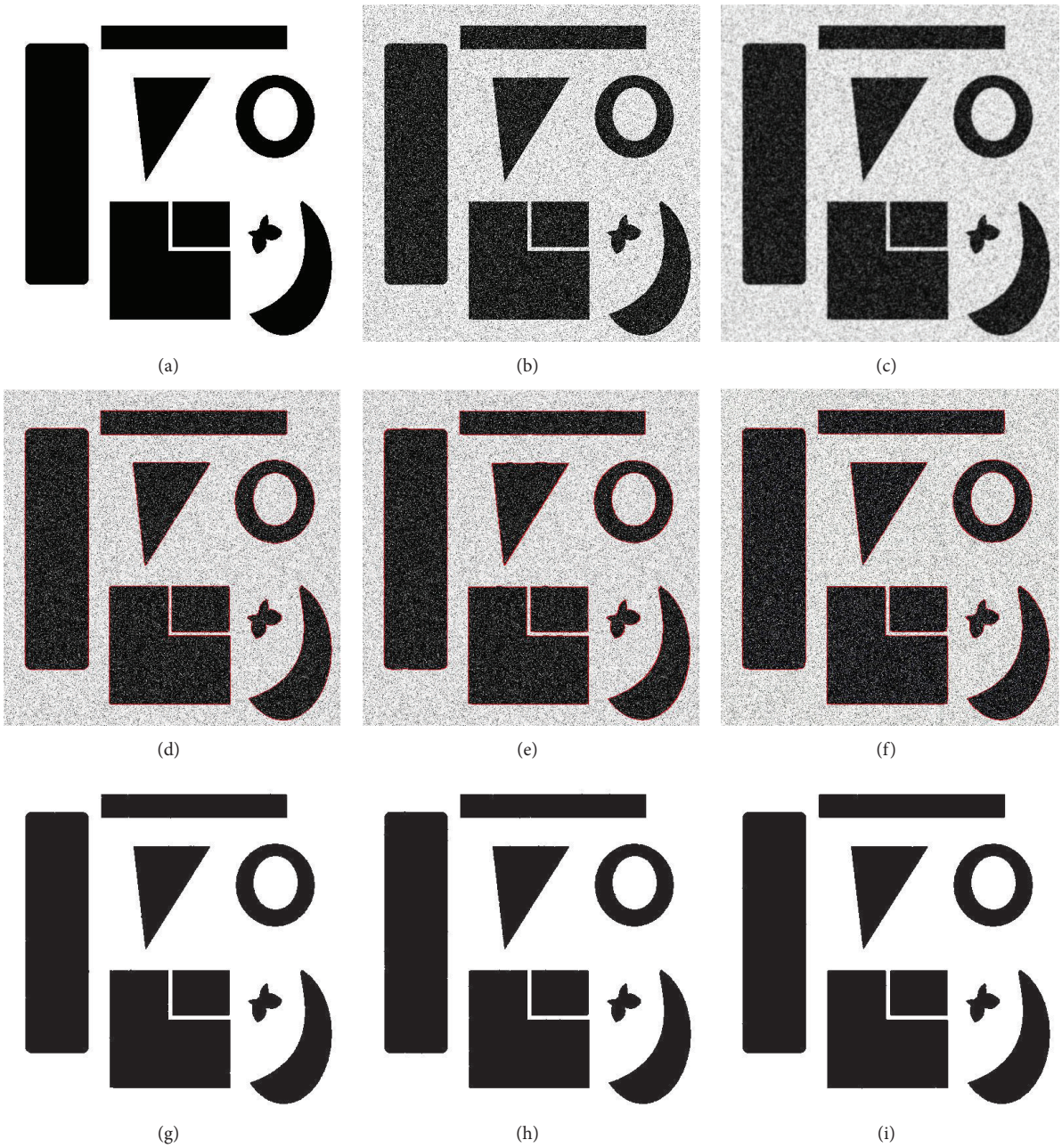

Figure 7: Segmentations for the noise *Test02* image. (a) The original image. (b) Corrupted *Test02* image with Gaussian noise (5.34 dB). (c) Smoothed *Test02* image with the numerical scheme (23) ($\lambda = 0.1$). (d) Algorithm 7. (e) Algorithm 1. (f) CVM. (g)–(i) The segmentation counter of Algorithms 7, 1, and CVM, respectively.

unconditionally LOD scheme, the time step size can be sufficiently large to reduce the iteration steps (only 6/7 steps in Table 1). However, re-initializing the level-set function costs a lot of CPU time (in Table 1).

In Figure 8, on the synthetic noise *Test03* image, we illustrate the results of Algorithm 1 with reinitialization and without reinitialization, respectively. One can see that in the segmentation process, reinitializing the level-set function or not influences the results of Algorithm 1 little (Figures 8(d)–8(g)). In CVM, reinitialization lets the level-set function ϕ not be very sharp, and $|\nabla\phi| = 1$ in mathematics. Algorithm 1 does not need $\nabla\phi$, so reinitialization is not necessary.

In Figures 9 and 10, we illustrate the results of Algorithm 1 without reinitialization and Algorithm 7 about a real *CT* and *Stone* image. Few differences between the segmented images are observed, but our method works much more faster than CVM (in Table 1).

4.3. Robustness with the Smooth Scale σ. Instead of the low pass filter, we use the scheme (23) to smooth the image. Hence, the smooth scale σ depends on the parameter λ and the iteration step. The smoother of the original image, the more regular of the optimal gray level line. But if we regularize

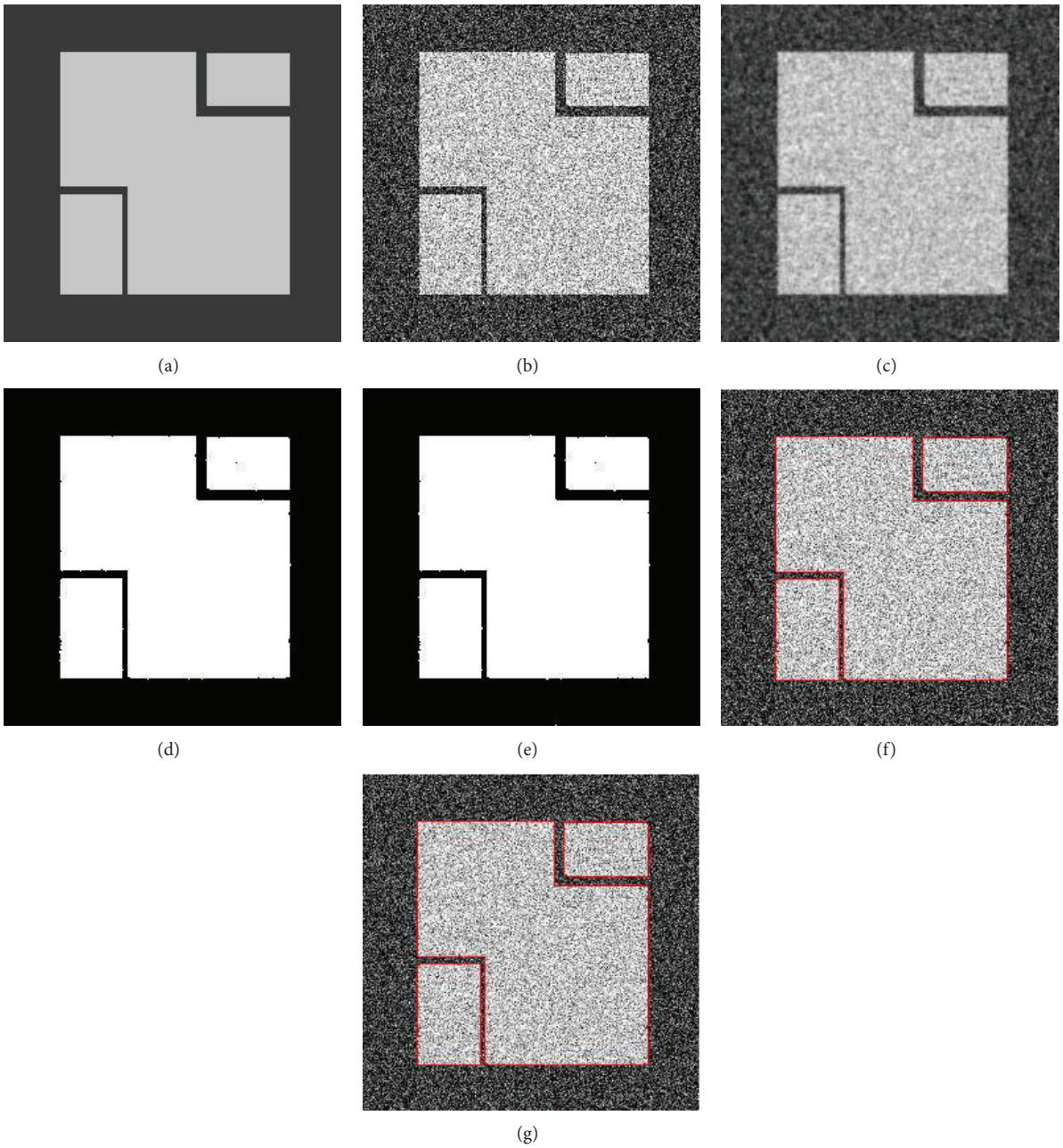

Figure 8: Segmentations for the noise *Test03* image. (a) The original image (size 256 × 256). (b) Corrupted *Test02* image with Gaussian noise (4.47 dB). (c) Smoothed *Stone* image with the numerical scheme (23) ($\lambda = 0.1$ and 4 steps). (d) Algorithm 1 without re-initializing the level-set function. (e) Algorithm 1 with re-initializing the level-set function. (f)-(g) The segmentation counter of (d) and (e), respectively.

too much, we will remove details from the image (in figures, the corner information is lost). In Figure 11, we illustrate how our model works on a real nebula image with $\lambda = 0.1$ and different iteration steps. In Figure 11, we can see that in different smooth scales σ, the gray level lines are different and evolved into the more regular ones. Compared with CVM, Algorithm 1 need not the initial level-set function ϕ_0 and reinitialization. In Algorithm 1, we just adjust the parameter λ and the iteration step, and always obtain the global minimum of the energy functional.

4.4. Computational Complexity. We end this section by considering the complexity of our algorithm. Our algorithm requires two phases: smoothing the original image and segmenting. The first phase is done by the scheme (23). Similar to other low pass filters, it is fast. It is also worth mentioning that one of the efficient implementations of the scheme (23) is FFT (Fast Fourier Transform Algorithm) and the complexity of this stage is $O(N)$, where N is the number of pixels in the image. In the second segmentation phase, our algorithm only sweeps the image once, so the complexity of

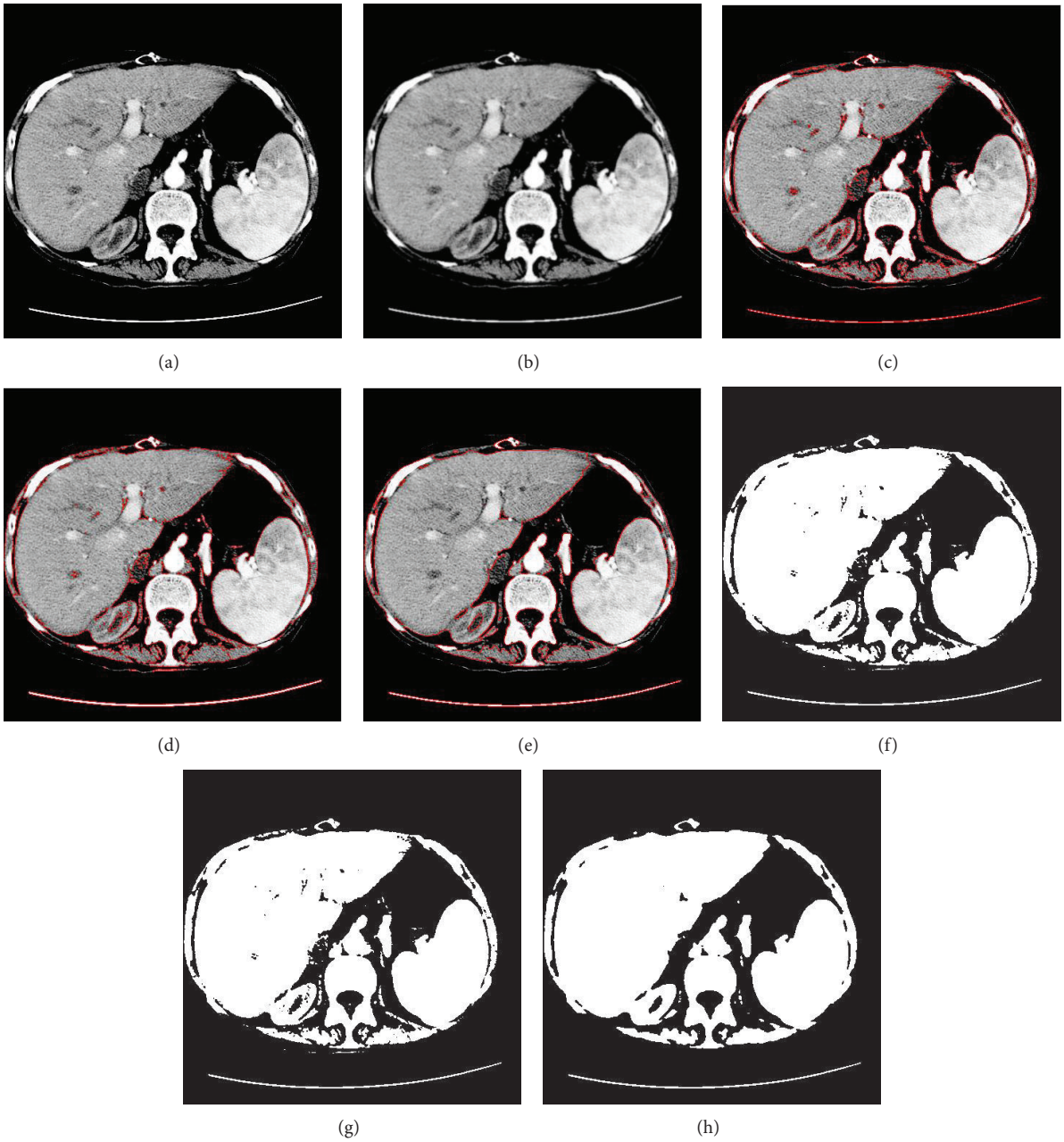

Figure 9: Segmentations for the noise CT image. (a) The original image. (b) Smoothed CT image with the numerical scheme (23) ($\lambda = 0.1$). (c) Algorithm 7. (d) Algorithm 1. (e) CVM. (f)–(h) The segmentation counter of Algorithms 7, 1, and CVM, respectively.

the stage is no more than $O(N)$. In Table 1, we compare the CPU time needed of all three algorithms. We summarize that the CPU time of our Algorithm 7 is about 0.01–0.08 seconds which is the fastest in three algorithms.

4.5. Comparison with Some Other Segmentation Methods. There are some classical segmentation methods, such as the watershed algorithm [27], the Canny filter [28], and the Sobel filter. In Figure 12, the smooth versions of the images mentioned previously are processed by these algorithms. Watershed algorithm provides the advantages of stabilization and speediness, but is prone to oversegmentation in Figures 12(a)–12(c). In Figures 12(d)–12(f), the segmentation result of the Sobel operator is sensitive to the threshold: if the threshold is too small, the redundant edges will be detected; if the threshold is too big, the detected edges will be broken. The Canny filter is sensitive to noise in Figures 12(h)–12(i).

5. Summary and Further Research Directions

In this paper, we have proposed and implemented a new image segmentation algorithm based on the Chan-Vese

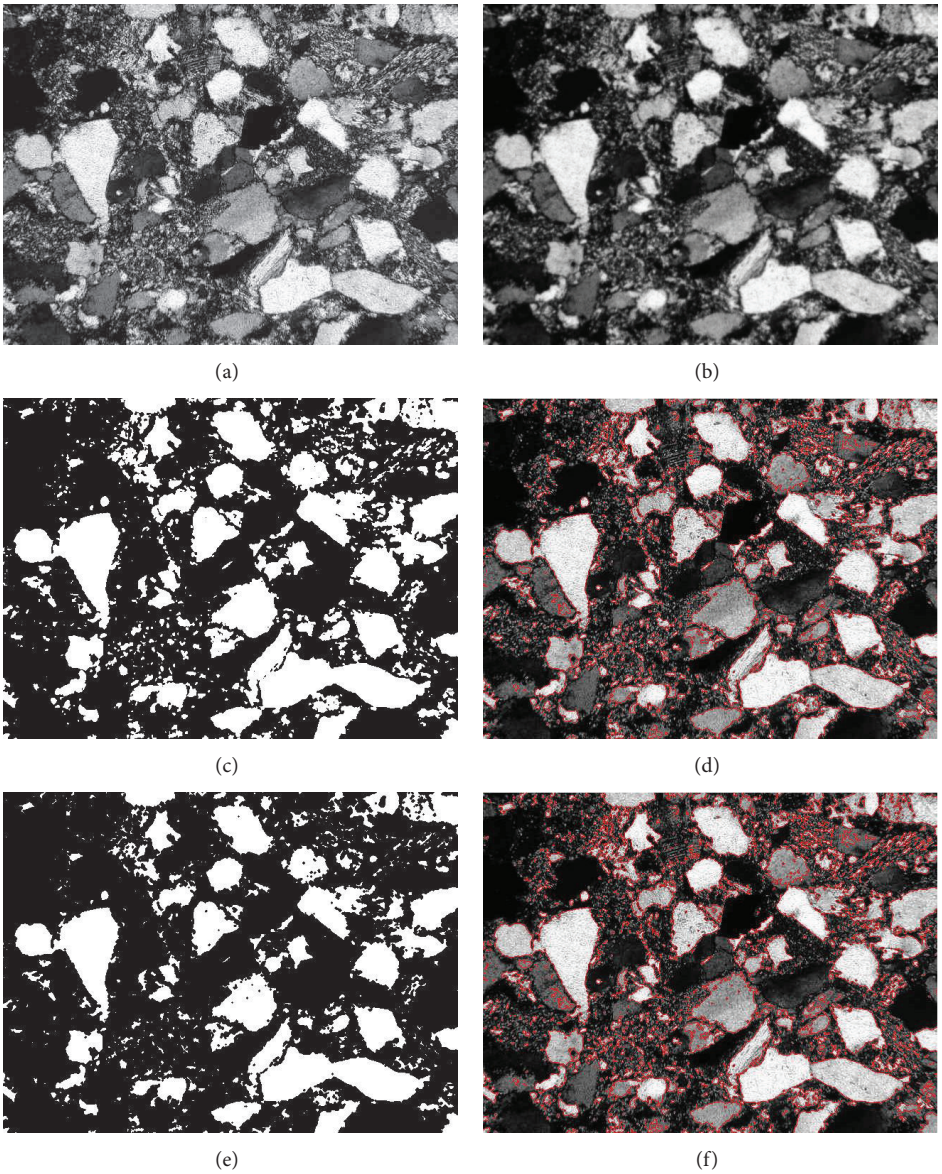

Figure 10: Segmentations for the noise *Stone* image. (a) The original image. (b) Smoothed *Stone* image with the numerical scheme (23) ($\lambda = 0.1$). (c) Algorithm 7. (d) Algorithm 1. (e)–(f) The segmentation counter of Algorithms 7 and 1, respectively.

active contour model. The discrete gray level-set method is employed in our numerical implementation. This algorithm works in two steps, smoothing the noisy image by using the heat equation filter method and then using the new discrete gray level-set method to segment the region of the original image.

In the Chan-Vese segmentation algorithm, the initialization of the level-set functions is a difficult problem. In the proposed new segmentation algorithm, the initialization is not required. And each step is simple and easily achieved. In the first step, there are a lot of algorithms to get the smooth version of the original image, and in the second step, we sweep the image only once and calculate (18) at every gray level (in fact, only 256 gray level sets) and then find the optimal gray level. In Table 1, we show the CPU time of the Chan-Vese method and our proposed method. Obviously, our method is more efficient than the Chan-Vese method.

Table 1: Comparison of CPU time in seconds and iterative step.

Image	CVM		Algorithm 1		Algorithm 7	
	CPU (s)	Steps	CPU (s)	Steps	CPU (s)	Steps
Test01	482.3674	7	130.0337	5	0.0554	4
Test02	277.7851	6	126.7503	6	0.0540	4
CT	437.8700	8	1.9336	36	0.0406	3
Stone			6.7793	81	0.0798	5

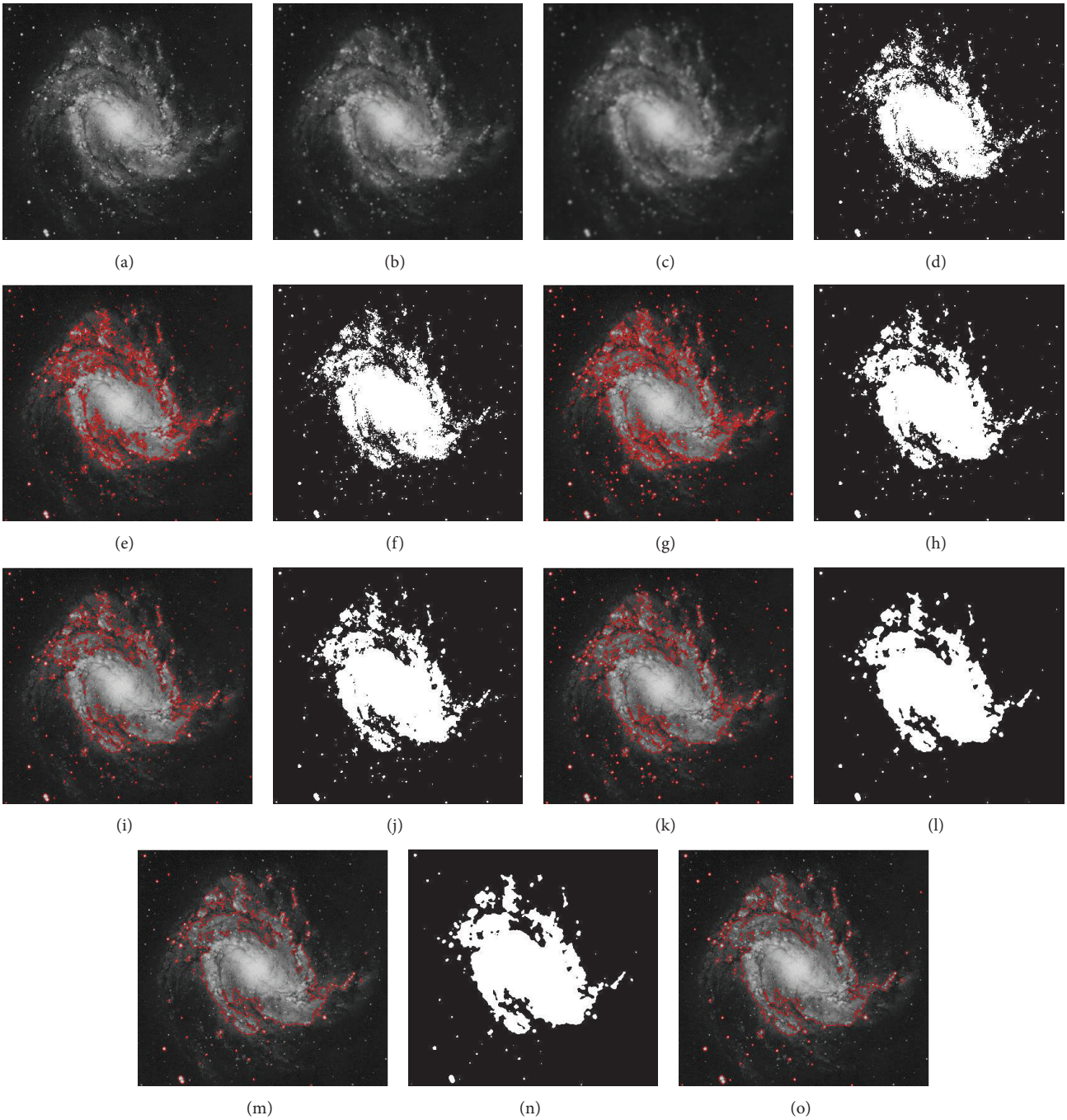

Figure 11: Segmentations for the noise *Star* image. (a) The original image. (b) Smoothed *Star* image with the numerical scheme (23) ($\lambda = 0.1$ and 3 steps). (c) Smoothed *Star* image ($\lambda = 0.1$ and 10 steps). (d)–(g) Segmentation for the original image by Algorithms 7 and 1, respectively. (h)–(k) The segmentation for the smooth image (b). (l)–(o) The segmentation for the smooth image (c).

Compared with the previous simultaneous segmentation methods [4, 5, 10], the proposed method is more simple, efficient, and flexible. First, we separate the segmentation processes into smoothing the original image and segmenting the smooth image into two regions, and in the second step, the mass of the computation process is adding operators and logical operators. Therefore, the CPU time of the second step is only a little (Tables 1 and 2). Second, the first step is just to get some smooth versions of the original image, so in some sense the second step is independent of the result of the first step, and the second step must have a result (of course, it is not always good).

While we have not pursued it in this paper, one of the potential advantages of our method is that we can also use it

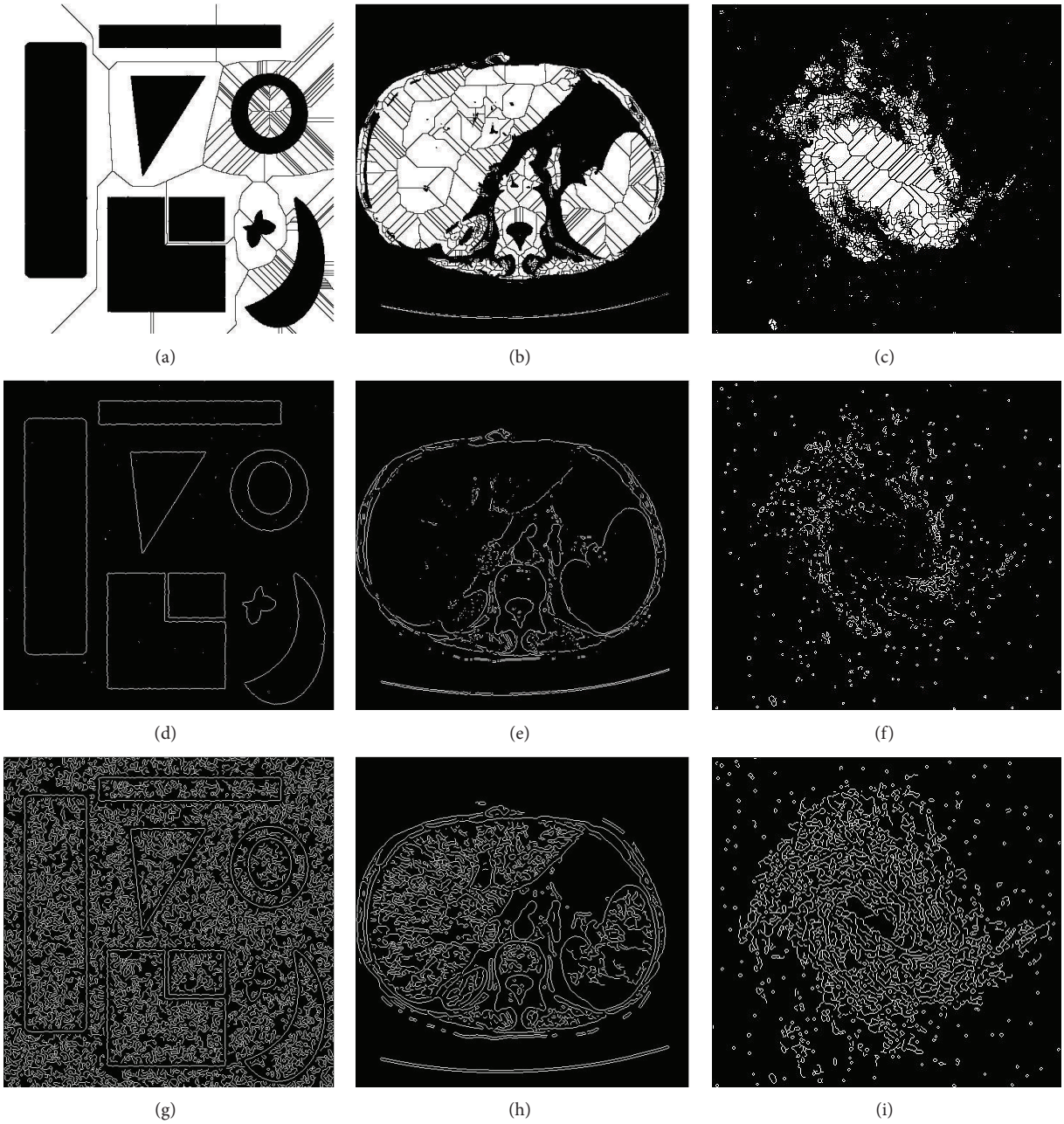

Figure 12: Some classical segmentation methods for the smooth images. (a)–(c) The segmentations based on the watershed Algorithm. (d)–(f) The segmentations from the Sobel operator. (g)–(i) The segmentations from the Canny filter.

Table 2: The CPU time in seconds and iterative step.

λ	Algorithm 1		Algorithm 5	
	CPU (s)	Steps	CPU (s)	Steps
	0.4154	4	0.0202	0
0.1	1.7060	20	0.0323	3
0.1	1.7703	26	0.0640	10

to color image. For example, one method for the color image segmentation is that we replace (1) by the new energy function proposed by Chan et al. [8], and other processes are similar to this paper.

Acknowledgments

This work is supported by the Heilongjiang Postdoctoral Fund (Grant No. LBH-Z12102), the Fundamental Research Funds for the Central Universities (Grant No. HIT.HSS.201201), the National Natural Science Foundation of China (Grant No. 71173060, 70773028, and 71031003), and

the Natural Science Foundation of Heilongjiang Province of China (Grant No. G201006).

References

[1] D. Mumford and J. Shah, "Optimal approximations by piecewise smooth functions and associated variational problems," *Communications on Pure and Applied Mathematics*, vol. 42, no. 5, pp. 577–685, 1989.

[2] M. Kass, A. Witkin, and D. Terzopoulos, "Snakes: active contour models," *International Journal of Computer Vision*, vol. 1, no. 4, pp. 321–331, 1988.

[3] V. Caselles, F. Catté, T. Coll, and F. Dibos, "A geometric model for active contours in image processing," *Numerische Mathematik*, vol. 66, no. 1, pp. 1–31, 1993.

[4] T. F. Chan and L. A. Vese, "Active contours without edges," *IEEE Transactions on Image Processing*, vol. 10, no. 2, pp. 266–277, 2001.

[5] A. Tsai, A. Yezzi, and A. S. Willsky, "Curve evolution implementation of the Mumford-Shah functional for image segmentation, denoising, interpolation, and magnification," *IEEE Transactions on Image Processing*, vol. 10, no. 8, pp. 1169–1186, 2001.

[6] S. Gao and T. D. Bui, "Image segmentation and selective smoothing by using Mumford-Shah model," *IEEE Transactions on Image Processing*, vol. 14, no. 10, pp. 1537–1549, 2005.

[7] L. A. Vese and T. F. Chan, "A multiphase level set framework for image segmentation using the Mumford and Shah model," *International Journal of Computer Vision*, vol. 50, no. 3, pp. 271–293, 2002.

[8] T. F. Chan, B. Y. Sandberg, and L. A. Vese, "Active contours without edges for vector-valued images," *Journal of Visual Communication and Image Representation*, vol. 11, no. 2, pp. 130–141, 2000.

[9] S. Kichenassamy, A. Kumar, P. Olver, A. Tannenbaum, and A. Yezzi, "Gradient flows and geometric active contour models," in *Proceedings of the 5th International Conference on Computer Vision*, pp. 810–815, June 1995.

[10] R. Kimmel, "Fast edge integration," in *Geometric Level Set Methods in Imaging, Vision, and Graphics*, chpater 3, pp. 59–77, Springer, New York, NY, USA, 2003.

[11] R. Malladi, J. Sethian, and B. Vemuri, "Evolutionary fronts for topology independent shape modeling and recovery," in *Proceedings of the 3rd European Conference on Computer Vision (ECCV '94)*, vol. 1, pp. 3–13, Stockholm, Sweden, 1994.

[12] S. C. Zhu, "Region competition: unifying snakes, region growing, and bayes/mdl for multiband image segmentation," *IEEE Transactions on Pattern Analysis and Machine Intelligence*, vol. 18, no. 9, pp. 884–900, 1996.

[13] N. Paragios and R. Deriche, "Coupled geodesic active regions for image segmentation: a level set approach," in *Proceedings of the European Conference in Computer Vision (ECCV '00)*, vol. 2, pp. 224–240, Dublin, UK, 2000.

[14] Y. Shi and W. C. Karl, "A fast level set method without solving PDEs," in *Proceedings of the IEEE International Conference on Acoustics, Speech, and Signal Processing (ICASSP '05)*, pp. II97–II100, Philadelphia, Pa, USA, March 2005.

[15] B. Song and T. Chan, "A fast algorithm for level set based optimization," Tech. Rep. CAM02-68, UCLA Department of Mathematics, 2002.

[16] L. He and S. J. Osher, "Solving the Chan-Vese model by a multiphase level set algorithm based on the topological derivative," in *Proceedings of the 1st International Conference on ScaleSpace Variational Methods in Computer Vision (SSVM'07)*, pp. 777–788, 2007.

[17] S. Osher and N. Paragios, *Geometric Level Set Methods in Imaging, Vision, and Graphics*, Springer, New York, NY, USA, 2003.

[18] Y. Pan, J. D. Birdwell, and S. M. Djouadi, "Efficient Implementation of the Chan-Vese models without solving PDEs," in *Proceedings of the International Workshop On Multimedia Signal Processing (MMSP '06)*, pp. 350–353, Victoria, Canada, October 2006.

[19] Y. Pan, J. D. Birdwell, and S. M. Djouadi, "An efficient bottom-up image segmentation method based on region growing, region competition and the mumford shah functional," in *Proceedings of the IEEE 8th Workshop on Multimedia Signal Processing, (MMSP '06)*, pp. 344–349, Victoria, Canada, October 2006.

[20] X. F. Wang, D. S. Huang, and H. Xu, "An efficient local Chan-Vese model for image segmentation," *Pattern Recognition*, vol. 43, no. 3, pp. 603–618, 2010.

[21] J. Weickert, B. Romeny, and M. A. Viergever, "Efficient and reliable schemes for nonlinear diffusion filtering," *IEEE Transactions on Image Processing*, vol. 7, no. 3, pp. 398–410, 1998.

[22] J. Weickert, "Applications of nonlinear diffusion in image processing and computer vision," *Acta Mathematica Universitatis Comenianae*, vol. 70, no. 1, pp. 33–50, 2000.

[23] L. I. Rudin, S. Osher, and E. Fatemi, "Nonlinear total variation based noise removal algorithms," *Physica D*, vol. 60, no. 1-4, pp. 259–268, 1992.

[24] P. Perona and J. Malik, "Scale-space and edge detection using anisotropic diffusion," *IEEE Transactions on Pattern Analysis and Machine Intelligence*, vol. 12, no. 7, pp. 629–639, 1990.

[25] T. Le, R. Chartrand, and T. J. Asaki, "A variational approach to reconstructing images corrupted by Poisson noise," *Journal of Mathematical Imaging and Vision*, vol. 27, no. 3, pp. 257–263, 2007.

[26] J. J. Koenderink, "The structure of images," *Biological Cybernetics*, vol. 50, no. 5, pp. 363–370, 1984.

[27] F. Meyer, "Topographic distance and watershed lines," *Signal Processing*, vol. 38, no. 1, pp. 113–125, 1994.

[28] J. Canny, "A computational approach to edge detection," *IEEE Transactions on Pattern Analysis and Machine Intelligence*, vol. 8, no. 6, pp. 679–698, 1986.

Hindawi Publishing Corporation
Mathematical Problems in Engineering
Volume 2013, Article ID 569286, 7 pages
http://dx.doi.org/10.1155/2013/569286

Research Article

On a Generalized Laguerre Operational Matrix of Fractional Integration

A. H. Bhrawy,[1,2] D. Baleanu,[3,4,5] L. M. Assas,[1,6] and J. A. Tenreiro Machado[7]

[1] *Department of Mathematics, Faculty of Science, King Abdulaziz University, Jeddah 21589, Saudi Arabia*
[2] *Department of Mathematics, Faculty of Science, Beni-Suef University, Beni-Suef 62511, Egypt*
[3] *Department of Mathematics and Computer Sciences, Faculty of Arts and Sciences, Cankaya University, Eskisehir Yolu 29.km, 06810 Yenimahalle Ankara, Turkey*
[4] *Department of Chemical and Materials Engineering, Faculty of Engineering, King Abdulaziz University, Jeddah 21589, Saudi Arabia*
[5] *Institute of Space Sciences, RO 76900, Magurele-Bucharest, Romania*
[6] *Department of Mathematics, Faculty of Science, Umm Al-Qura University, Mecca 21955, Saudi Arabia*
[7] *Department of Electrical Engineering, Polytechnic of Porto, Institute of Engineering, 4314200-072 Porto, Portugal*

Correspondence should be addressed to D. Baleanu; dumitru@cankaya.edu.tr

Received 18 December 2012; Accepted 18 January 2013

Academic Editor: József Kázmér Tar

A new operational matrix of fractional integration of arbitrary order for generalized Laguerre polynomials is derived. The fractional integration is described in the Riemann-Liouville sense. This operational matrix is applied together with generalized Laguerre tau method for solving general linear multiterm fractional differential equations (FDEs). The method has the advantage of obtaining the solution in terms of the generalized Laguerre parameter. In addition, only a small dimension of generalized Laguerre operational matrix is needed to obtain a satisfactory result. Illustrative examples reveal that the proposed method is very effective and convenient for linear multiterm FDEs on a semi-infinite interval.

1. Introduction

The problems of FDEs arise in various areas of science and engineering. In particular, multiterm fractional differential equations have been used to model various types of viscoelastic damping (see, e.g., [1–13] and the references therein). In the last few decades both theory and numerical analysis of FDEs have received an increasing attention (see, e.g., [1–4, 14–17] and references therein).

Spectral methods are a class of techniques used in applied mathematics and scientific computing to numerically solve some differential equations. The main idea is to write the solution of the differential equation as a sum of certain orthogonal polynomial and then obtain the coefficients in the sum in order to satisfy the differential equation. Due to high-order accuracy, spectral methods have gained increasing popularity for several decades, particularly in the field of computational fluid dynamics (see, e.g., [18–24] and the references therein).

The usual spectral methods are only available for bounded domains for solving FDEs; see [25–28]. However, it is also interesting to consider spectral methods for FDEs on the half line. Several authors developed the generalized Laguerre spectral method for the half line for ordinary, partial, and delay differential equations; see [29–31]. Recently, Saadatmandi and Dehghan [25] have proposed an operational Legendre-tau technique for the numerical solution of multiterm FDEs. The same technique based on operational matrix of Chebyshev polynomials has been used for the same problem (see [32]). In [33], Doha et al. derived the Jacobi operational matrix of fractional derivatives which applied together with spectral tau method for numerical solution of general linear multiterm fractional differential equations. Bhrawy et al. [27] used a quadrature shifted Legendre-tau method for treating multiterm linear FDEs with variable coefficients. More recently, Bhrawy and Alofi [34] proposed the operational

Chebyshev matrix of fractional integration in the Riemann-Liouville sense which was applied together with spectral tau method for solving linear FDEs.

The operational matrix of integer integration has been determined for several types of orthogonal polynomials, such as Chebyshev polynomials [35], Legendre polynomials [36], and Laguerre and Hermite [37]. Recently, Singh et al. [38] derived the Bernstein operational matrix of integration. Till now, and to the best of our knowledge, most of formulae corresponding to those mentioned previously are unknown and are traceless in the literature for fractional integration for generalized Laguerre polynomials in the Riemann-Liouville sense. This partially motivates our interest in operational matrix of fractional integration for generalized Laguerre polynomials. Another motivation is concerned with the direct solution techniques for solving the integrated forms of FDEs on the half line using generalized Laguerre tau method based on operational matrix of fractional integration in the Riemann-Liouville sense. Finally, the accuracy of the proposed algorithm is demonstrated by test problems.

The paper is organized as follows. In the next section, we introduce some necessary definitions. In Section 3 the generalized Laguerre operational matrix of fractional integration is derived. In Section 4 we develop the generalized Laguerre operational matrix of fractional integration for solving linear multiorder FDEs. In Section 5 the proposed method is applied to two examples.

2. Some Basic Preliminaries

The most used definition of fractional integration is due to Riemann-Liouville, which is defined as

$$J^{\nu} f(x) = \frac{1}{\Gamma(\nu)} \int_0^x (x-t)^{\nu-1} f(t)\, dt, \qquad \nu > 0, \quad x > 0, \quad \text{and } J^0 f(x) = f(x). \tag{1}$$

The operator J^{ν} has the property:

$$J^{\nu} x^{\beta} = \frac{\Gamma(\beta+1)}{\Gamma(\beta+1+\nu)}\, x^{\beta+\nu}. \tag{2}$$

The next equation defines the Riemann-Liouville fractional derivative of order ν:

$$D^{\nu} f(x) = \frac{d^m}{dx^m}\left(J^{m-\nu} f(x)\right), \tag{3}$$

where $m-1 < \nu \le m$, $m \in N$, and m is the smallest integer greater than ν.

If $m-1 < \nu \le m$, $m \in N$, then

$$\begin{aligned} D^{\nu} J^{\nu} f(x) &= f(x), \\ J^{\nu} D^{\nu} f(x) &= f(x) - \sum_{i=0}^{m-1} f^{(i)}(0^+)\frac{x^i}{i!}, \quad x > 0. \end{aligned} \tag{4}$$

Now, let $\Lambda = (0,\infty)$ and $w^{(\alpha)}(x) = x^{\alpha} e^{-x}$ be a weight function on Λ in the usual sense. Define the following:

$$L^2_{w^{(\alpha)}}(\Lambda) = \{v \mid v \text{ is measurable on } \Lambda \text{ and } \|v\|_{w^{(\alpha)}} < \infty\}, \tag{5}$$

equipped with the following inner product and norm:

$$\begin{aligned} (u,v)_{w^{(\alpha)}} &= \int_{\Lambda} u(x)\, v(x)\, w^{(\alpha)}(x)\, dx, \\ \|v\|_{w^{(\alpha)}} &= (u,v)^{1/2}_{w^{(\alpha)}}. \end{aligned} \tag{6}$$

Next, let $L_i^{(\alpha)}(x)$ be the generalized Laguerre polynomials of degree i. We know from [39] that, for $\alpha > -1$,

$$L_{i+1}^{(\alpha)}(x) = \frac{1}{i+1}\left[(2i+\alpha+1-x)\, L_i^{(\alpha)}(x) - (i+\alpha)\, L_{i-1}^{(\alpha)}(x)\right], \qquad i = 1, 2, \ldots, \tag{7}$$

where $L_0^{(\alpha)}(x) = 1$ and $L_1^{(\alpha)}(x) = 1+\alpha-x$. The set of generalized Laguerre polynomials is the $L^2_{w^{(\alpha)}}(\Lambda)$-orthogonal system, namely,

$$\int_0^{\infty} L_j^{(\alpha)}(x)\, L_k^{(\alpha)}(x)\, w^{(\alpha)}(x)\, dx = h_k \delta_{jk}, \tag{8}$$

where δ_{jk} is the Kronecher function and $h_k = (\Gamma(i+\alpha+1))/i!$.

The generalized Laguerre polynomials of degree i, on the interval Λ, are given by

$$L_i^{(\alpha)}(x) = \sum_{k=0}^{i} (-1)^k \frac{\Gamma(i+\alpha+1)}{\Gamma(k+\alpha+1)(i-k)!k!} x^k, \qquad i = 0, 1, \ldots. \tag{9}$$

The special value

$$D^q L_i^{(\alpha)}(0) = (-1)^q \sum_{j=0}^{i-q} \frac{(i-j-1)!}{(q-1)!\,(i-j-q)!} L_j^{(\alpha)}(0), \quad i \ge q, \tag{10}$$

where $L_j^{(\alpha)}(0) = (\Gamma(j+\alpha+1))/(\Gamma(\alpha+1)\, j!)$, will be of important use later.

A function $u(x) \in L^2_{w^{(\alpha)}}(\Lambda)$ may be expressed in terms of generalized Laguerre polynomials as

$$\begin{aligned} u(x) &= \sum_{j=0}^{\infty} a_j L_j^{(\alpha)}(x), \\ a_j &= \frac{1}{h_k}\int_0^{\infty} u(x)\, L_j^{(\alpha)}(x)\, w^{(\alpha)}(x)\, dx, \quad j = 0, 1, 2, \ldots. \end{aligned} \tag{11}$$

In practice, only the first $(N+1)$ terms of generalized Laguerre polynomials are considered. Then we have

$$u_N(x) = \sum_{j=0}^{N} a_j L_j^{(\alpha)}(x) = C^T \phi(x), \tag{12}$$

where the generalized Laguerre coefficient vector C and the generalized Laguerre vector $\phi(x)$ are given by

$$C^T = [c_0, c_1, \ldots, c_N],$$
$$\phi(x) = \left[L_0^{(\alpha)}(x), L_1^{(\alpha)}(x), \ldots, L_N^{(\alpha)}(x)\right]^T. \tag{13}$$

If we define the q times repeated integration of generalized Laguerre vector $\phi(x)$ by $J^q\phi(x)$, then (cf. Paraskevopoulos [36])

$$J^q\phi(x) \simeq P^{(q)}\phi(x), \tag{14}$$

where q is an integer value and $\mathbf{P}^{(q)}$ is the operational matrix of integration of $\phi(x)$. For more details see [36].

3. Generalized Laguerre Operational Matrix of Fractional Integration

The main objective of this section is to derive an operational matrix of fractional integration for generalized Laguerre vector.

Theorem 1. *Let $\phi(x)$ be the generalized Laguerre vector and $\nu > 0$, then*

$$J^\nu\phi(x) \simeq \mathbf{P}^{(\nu)}\phi(x), \tag{15}$$

where $\mathbf{P}^{(\nu)}$ is the $(N+1)\times(N+1)$ operational matrix of fractional integration of order ν in the Riemann-Liouville sense and is defined as follows:

$$\mathbf{P}^{(\nu)} = \begin{pmatrix} \Theta_\nu(0,0) & \Omega_\nu(0,1) & \Theta_\nu(0,2) & \cdots & \Theta_\nu(0,N) \\ \Theta_\nu(1,0) & \Theta_\nu(1,1) & \Theta_\nu(1,2) & \cdots & \Theta_\nu(1,N) \\ \vdots & \vdots & \vdots & \cdots & \vdots \\ \Theta_\nu(i,0) & \Theta_\nu(i,1) & \Theta_\nu(i,2) & \cdots & \Theta_\nu(i,N) \\ \vdots & \vdots & \vdots & \cdots & \vdots \\ \Theta_\nu(N,0) & \Theta_\nu(N,1) & \Theta_\nu(N,2) & \cdots & \Theta_\nu(N,N) \end{pmatrix}, \tag{16}$$

where

$$\Theta_\nu(i,j) = \sum_{k=0}^{i}\sum_{r=0}^{j}\frac{(-1)^{k+r}j!\Gamma(i+\alpha+1)\Gamma(k+\nu+\alpha+r+1)}{(i-k)!(j-r)!r!\Gamma(k+\nu+1)\Gamma(k+\alpha+1)\Gamma(\alpha+r+1)}. \tag{17}$$

Proof. Using the analytic form of the generalized Laguerre polynomials $L_i^{(\alpha)}(x)$ of degree i (9) and (2), then

$$\begin{aligned} J^\nu L_i^{(\alpha)}(x) &= \sum_{k=0}^{i}(-1)^k\frac{\Gamma(i+\alpha+1)}{(i-k)!k!\Gamma(k+\alpha+1)}J^\nu x^k \\ &= \sum_{k=0}^{i}(-1)^k\frac{\Gamma(i+\alpha+1)}{(i-k)!\Gamma(k+\nu+1)\Gamma(k+\alpha+1)} \\ &\quad\times x^{k+\nu}, \quad i = 0, 1, \cdots, N. \end{aligned} \tag{18}$$

Now, approximate $x^{k+\nu}$ by $N+1$ terms of generalized Laguerre series, we have

$$x^{k+\nu} = \sum_{j=0}^{N}c_jL_j^{(\alpha)}(x), \tag{19}$$

where c_j is given from (11) with $u(x) = x^{k+\nu}$; that is,

$$c_j = \sum_{r=0}^{j}(-1)^r\frac{j!\Gamma(k+\nu+\alpha+r+1)}{(j-r)!r!\Gamma(r+\alpha+1)}, \quad j = 1, 2, \ldots, N. \tag{20}$$

In virtue of (18) and (19), we get

$$J^\nu L_i^{(\alpha)}(x) = \sum_{j=0}^{N}\Theta_\nu(i,j)L_j^{(\alpha)}(x), \quad i = 0, 1, \ldots, N, \tag{21}$$

where

$$\Theta_\nu(i,j) = \sum_{k=0}^{i}\sum_{r=0}^{j}\frac{(-1)^{k+r}j!\Gamma(i+\alpha+1)\Gamma(k+\nu+\alpha+r+1)}{(i-k)!(j-r)!r!\Gamma(k+\nu+1)\Gamma(k+\alpha+1)\Gamma(\alpha+r+1)} \quad j = 1, 2, \ldots N. \tag{22}$$

Accordingly, (21) can be written in a vector form as follows:

$$J^\nu L_i(x) \simeq [\Theta_\nu(i,0), \Theta_\nu(i,1), \Theta_\nu(i,2), \cdots, \Theta_\nu(i,N)]\phi(x), \quad i = 0, 1, \ldots, N. \tag{23}$$

Equation (23) leads to the desired result. □

4. Generalized Laguerre Tau Method Based on Operational Matrix

In this section, the generalized Laguerre tau method based on operational matrix is proposed to numerically solve FDEs. In order to show the fundamental importance of generalized Laguerre operational matrix of fractional integration, we adopt it for solving the following multiorder FDE:

$$D^\nu u(x) = \sum_{i=1}^{k}\gamma_jD^{\beta_i}u(x) + \gamma_{k+1}u(x) + f(x), \quad \text{in } \Lambda = (0, \infty), \tag{24}$$

with initial conditions

$$u^{(i)}(0) = d_i, \quad i = 0, \ldots, m-1, \tag{25}$$

where γ_i $(i = 1, \ldots, k+1)$ are real constant coefficients, $m-1 < \nu \le m$, $0 < \beta_1 < \beta_2 < \ldots < \beta_k < \nu$, and $g(x)$ is a given source function.

The proposed technique, based on the FDE (24), is converted to a fully integrated form via fractional integration

in the Riemann-Liouville sense. Subsequently, the integrated form equations are approximated by representing them as linear combinations of generalized Laguerre polynomials. Finally, the integrated form equation is converted to an algebraic equation by introducing the operational matrix of fractional integration of the generalized Laguerre polynomials.

If we apply the Riemann-Liouville integral of order ν on (24), after making use of (4), we get the integrated form of (24), namely,

$$\begin{aligned} u(x) - \sum_{j=0}^{m-1} u^{(j)}(0^+)\frac{x^j}{j!} &= \sum_{i=1}^{k}\gamma_i J^{\nu-\beta_i}\left[u(x) - \sum_{j=0}^{m_i-1} u^{(j)}(0^+)\frac{x^j}{j!}\right] \\ &\quad + \gamma_{k+1}J^{\nu}u(x) + J^{\nu}f(x), \\ u^{(i)}(0) &= d_i, \quad i = 0,\ldots,m-1, \end{aligned} \tag{26}$$

where $m_i - 1 < \beta_i \le m_i$, $m_i \in N$, implies that

$$\begin{aligned} u(x) &= \sum_{i=1}^{k}\gamma_i J^{\nu-\beta_i}u(x) + \gamma_{k+1}J^{\nu}u(x) + g(x), \\ u^{(i)}(0) &= d_i, \quad i = 0,\ldots,m-1, \end{aligned} \tag{27}$$

where

$$g(x) = J^{\nu}f(x) + \sum_{j=0}^{m-1} d_j\frac{x^j}{j!} + \sum_{i=1}^{k}\gamma_i J^{\nu-\beta_i}\left(\sum_{j=0}^{m_i-1} d_j\frac{x^j}{j!}\right). \tag{28}$$

In order to use the tau method with Laquerre operational matrix for solving the fully integrated problem (27) with initial conditions (25), we approximate $u(x)$ and $g(x)$ by the Laguerre polynomials:

$$u_N(x) \simeq \sum_{i=0}^{N} c_i L_i^{(\alpha)}(x) = C^T\phi(x), \tag{29}$$

$$g(x) \simeq \sum_{i=0}^{N} g_i L_i^{(\alpha)}(x) = G^T\phi(x), \tag{30}$$

where the vector $G = [g_0,\ldots,g_N]^T$ is given but $C = [c_0,\ldots,c_N]^T$ is an unknown vector.

After making use of Theorem 1 (relation (15)) the Riemann-Liouville integral of orders ν and $(\nu - \beta_j)$ of the approximate solution (29) can be written as

$$J^{\nu}u_N(x) \simeq C^T J^{\nu}\phi(x) \simeq C^T\mathbf{P}^{(\nu)}\phi(x), \tag{31}$$

$$J^{\nu-\beta_j}u_N(x) \simeq C^T J^{\nu-\beta_j}\phi(x) \simeq C^T\mathbf{P}^{(\nu-\beta_j)}\phi(x), \quad j = 1,\ldots,k, \tag{32}$$

respectively, where $\mathbf{P}^{(\nu)}$ is the $(N+1)\times(N+1)$ operational matrix of fractional integration of order ν. Employing (29)-(32) the residual $R_N(x)$ for (27) can be written as

$$R_N(x) = \left(C^T - C^T\sum_{j=1}^{k}\gamma_j\mathbf{P}^{(\nu-\beta_j)} - \gamma_{k+1}C^T\mathbf{P}^{(\nu)} - G^T\right)\phi(x). \tag{33}$$

As in a typical tau method, we generate $N - m + 1$ linear algebraic equations by applying

$$\left\langle R_N(x), L_j^{(\alpha)}(x)\right\rangle = \int_0^{\infty} R_N(x)\,w^{(\alpha)}(x)\,L_j^{(\alpha)}(x)\,dx = 0, \quad j = 0,1,\ldots,N-m. \tag{34}$$

Also by substituting Eqs. (11) and (29) in Eq (25), we get

$$u^{(i)}(0) = C^T\mathbf{D}^{(i)}\phi(0) = d_i, \quad i = 0,1,\ldots,m-1. \tag{35}$$

Equations (34) and (35) generate $N-m+1$ and m set of linear equations, respectively.

These linear equations can be solved for unknown coefficients of the vector C. Consequently, $u_N(x)$ given in (29) can be calculated, which leads to the solution of (24) with the initial conditions (25).

5. Illustrative Examples

To illustrate the effectiveness of the proposed method in the present paper, two test examples are carried out in this section. The results obtained by the present methods reveal that the present method is very effective and convenient for linear FDEs on the half line.

Example 2. Consider the FDE

$$\begin{aligned} D^2u(x) + D^{1/2}u(x) + u(x) &= x^2 + 2 + \frac{2.6666666667}{\Gamma(0.5)}x^{1.5}, \\ u(0) = 0, \quad u'(0) &= 0, \quad x \in \Lambda, \end{aligned} \tag{36}$$

whose exact solution is given by $u(x) = x^2$.

If we apply the technique described in Section 4 with $N = 2$, then the approximate solution can be written as

$$\begin{aligned} u_N(x) &= \sum_{i=0}^{2} c_i L_i^{(\alpha)}(x) = C^T\phi(x), \\ P^{(2)} &= \begin{pmatrix} \Theta_2(0,0) & \Theta_2(0,1) & \Theta_2(0,2) \\ \Theta_2(1,0) & \Theta_2(1,1) & \Theta_2(1,2) \\ \Theta_2(2,0) & \Theta_2(2,1) & \Theta_2(2,2) \end{pmatrix}, \\ P^{(3/2)} &= \begin{pmatrix} \Theta_{3/2}(0,0) & \Theta_{3/2}(0,1) & \Theta_{3/2}(0,2) \\ \Theta_{3/2}(1,0) & \Theta_{3/2}(1,1) & \Theta_{3/2}(1,2) \\ \Theta_{3/2}(2,0) & \Theta_{3/2}(2,1) & \Theta_{3/2}(2,2) \end{pmatrix}, \\ G &= \begin{pmatrix} g_0 \\ g_1 \\ g_2 \end{pmatrix}. \end{aligned} \tag{37}$$

Table 1: c_0, c_1, and c_2 for different values of α for Example 2.

α	c_0	c_1	c_2
−0.5	0.75	−3	2
0	2	−4	2
0.5	3.75	−5	2
1	6	−6	2
2	12	−8	2
3	20	−10	2

Table 2: c_0, c_1, c_2, and c_3 for different values of α for Example 3.

α	c_0	c_1	c_2	c_3
−0.5	15/8	−45/4	15	−6
0	6	−18	18	−6
0.5	105/8	−105/4	21	−6
1	24	−36	24	−6
2	60	−60	30	−6
3	120	−90	36	−6

Using (34) we obtain

$$\begin{aligned}&\left(\Theta_{3/2}(0,2)+\Theta_2(0,2)\right)c_0+\left(\Theta_{3/2}(1,2)+\Theta_2(1,2)\right)c_1\\&\quad+\left(1+\Theta_{3/2}(2,2)+\Theta_2(2,2)\right)c_2+g_2=0.\end{aligned}\tag{38}$$

Now, by applying (35), we have

$$c_0+(\alpha+1)c_1+\frac{(\alpha+1)(\alpha+2)}{2}c_2=0.\tag{39}$$

$$-c_1-(\alpha+2)c_2=0.\tag{40}$$

Finally by solving (38)–(40), we have the 3 unknown coefficients with various choices of α given in Table 1. Then, we get

$$c_0=\alpha^2+3\alpha+2,\qquad c_1=-2\alpha-4,\qquad c_2=2.\tag{41}$$

Thus we can write

$$u(x)=\left(c_0,\ c_1,\ c_2\right)\begin{pmatrix}L_0^{(\alpha)}(x)\\L_1^{(\alpha)}(x)\\L_2^{(\alpha)}(x)\end{pmatrix}=x^2,\tag{42}$$

which is the exact solution.

Example 3. As the first example, we consider the following fractional initial value problem:

$$\begin{aligned}&D^{3/2}u(x)+3u(x)=3x^3+\frac{8}{\Gamma(0.5)}x^{1.5},\\&u(0)=0,\quad u'(0)=0,\quad x\in\Lambda,\end{aligned}\tag{43}$$

whose exact solution is given by $u(x)=x^3$.

If we apply the technique described in Section 4 with $N=3$, then the approximate solution can be written as

$$\begin{aligned}&u_N(x)=\sum_{i=0}^{3}c_iL_i^{(\alpha)}(x)=C^T\phi(x),\\&P^{(3/2)}=\begin{pmatrix}\Theta_{3/2}(0,0)&\Theta_{3/2}(0,1)&\Theta_{3/2}(0,2)&\Theta_{3/2}(0,3)\\\Theta_{3/2}(1,0)&\Theta_{3/2}(1,1)&\Theta_{3/2}(1,2)&\Theta_{3/2}(1,3)\\\Theta_{3/2}(2,0)&\Theta_{3/2}(2,1)&\Theta_{3/2}(2,2)&\Theta_{3/2}(2,3)\\\Theta_{3/2}(3,0)&\Theta_{3/2}(3,1)&\Theta_{3/2}(3,2)&\Theta_{3/2}(3,3)\end{pmatrix},\\&G=\begin{pmatrix}g_0\\g_1\\g_2\\g_3\end{pmatrix}.\end{aligned}\tag{44}$$

Using (34) we obtain

$$\begin{aligned}&3\Theta_{3/2}(0,2)c_0+3\Theta_{3/2}(1,2)c_1\\&\quad+\left(1+3\Theta_{3/2}(2,2)\right)c_2+3\Theta_{3/2}(3,2)c_3+g_2=0,\\&3\Theta_{3/2}(0,3)c_0+3\Theta_{3/2}(1,3)c_1\\&\quad+3\Theta_{3/2}(2,3)c_2+\left(1+3\Theta_{3/2}(3,3)\right)c_3+g_3=0.\end{aligned}\tag{45}$$

Now, applying (35) we get

$$\begin{aligned}&C^T\phi(0)=c_0+(\alpha+1)c_1\\&\quad+\frac{(\alpha+1)(\alpha+2)}{2}c_2+\frac{(\alpha+1)(\alpha+2)(\alpha+3)}{6}c_3=0,\\&C^TD^{(1)}\phi(0)\\&\quad=-c_1-(\alpha+2)c_2-\frac{(\alpha+3)(\alpha+2)}{2}c_3=0.\end{aligned}\tag{46}$$

By solving the linear system (45)–(49) we have the 4 unknown coefficients with various choices of α in Table 2, and we get

$$\begin{aligned}c_0&=\alpha^3+6\alpha+11\alpha+6,\\c_1&=-3\alpha^2-15\alpha-18,\\c_2&=6\alpha+18,\\c_3&=-6.\end{aligned}\tag{47}$$

Thereby we can write

$$u_N(x)=\sum_{i=0}^{3}c_iL_i^{(\alpha)}(x)=x^3.\tag{48}$$

Numerical results will not be presented since the exact solution is obtained.

Example 4. Consider the following equation:

$$\begin{aligned}&D^2u(x)-2Du(x)+D^{1/2}u(x)+u(x)\\&=x^7+\frac{2048}{429\sqrt{\pi}}x^{6.5}-14x^6+42x^5-x^2-\frac{8}{3\sqrt{\pi}}x^{1.5}+4x-2,\\&u(0)=0,\quad u'(0)=0,\quad x\in\Lambda,\end{aligned}\tag{49}$$

whose exact solution is given by $u(x)=x^7-x^2$.

Now, we can apply the technique described in Examples 2 and 3, with $\alpha = 0$ and $N = 7$, then we have

$$\begin{aligned} c_0 &= 5038, & c_1 &= -35276, \\ c_2 &= 105838, & c_3 &= -176400, \\ c_4 &= 176400, & c_5 &= -105840, \\ c_6 &= 35280, & c_7 &= -5040. \end{aligned} \tag{50}$$

Thus we can write

$$u_N(x) = \sum_{i=0}^{7} c_i L_i(x) = x^7 - x^2, \tag{51}$$

which is the exact solution.

6. Conclusions

In this paper, we have presented the operational matrix of fractional integration of the generalized Laguerre polynomials, and, as an important application, we describe how to use the operational tau technique to numerically solve the FDEs. The basic idea of this technique is as follows.

(i) The FDE is converted to a fully integrated form via multiple integration in the Riemann-Liouville sense.

(ii) Subsequently, the various signals involved in the integrated form equation are approximated by representing them as linear combinations of generalized Laguerre polynomials.

(iii) Finally, the integrated form equation is converted into an algebraic equation by introducing the operational matrix of fractional integration of the generalized Laguerre polynomials.

To the best of our knowledge, the presented theoretical formula for generalized Laguerre is completely new, and we do believe that this formula may be used to solve some other kinds of fractional-order initial value problems on a semi-infinite interval.

References

[1] I. Podlubny, *Fractional Differential Equations*, vol. 198 of *Mathematics in Science and Engineering*, Academic Press, San Diego, Calif, USA, 1999.

[2] S. Das, *Functional Fractional Calculus for System Identification and Controls*, Springer, Berlin, Germany, 2008.

[3] A. A. Kilbas, H. M. Srivastava, and J. J. Trujillo, *Theory and Applications of Fractional Differential Equations*, vol. 204 of *North-Holland Mathematics Studies*, Elsevier Science B.V., Amsterdam, The Netherlands, 2006.

[4] S. Das, K. Vishal, P. K. Gupta, and A. Yildirim, "An approximate analytical solution of time-fractional telegraph equation," *Applied Mathematics and Computation*, vol. 217, no. 18, pp. 7405–7411, 2011.

[5] D. Baleanu, K. Diethelm, E. Scalas, and J. J. Trujillo, *Fractional Calculus Models and Numerical Methods*, vol. 3 of *Series on Complexity, Nonlinearity and Chaos*, World Scientific, Hackensack, NJ, USA, 2012.

[6] R. Hilfer, Ed., *Applications of Fractional Calculus in Physics*, World Scientific, River Edge, NJ, USA, 2000.

[7] D. Baleanu, J. A. T. Machado, and A. C. J. Luo, Eds., *Fractional Dynamics and Control*, Springer, New York, NY, USA, 2012.

[8] J. T. Machado, V. Kiryakova, and F. Mainardi, "Recent history of fractional calculus," *Communications in Nonlinear Science and Numerical Simulation*, vol. 16, no. 3, pp. 1140–1153, 2011.

[9] C. M. A. Pinto, "Stability of quadruped robots' trajectories subjected to discrete perturbations," *Nonlinear Dynamics*, vol. 70, no. 3, pp. 2089–2094, 2012.

[10] H. Jafari, H. Tajadodi, and D. Baleanu, "A modified variational iteration method for solving fractional Riccati differential equation by Adomian polynomials," *Fractional Calculus and Applied Analysis*, vol. 16, no. 1, pp. 109–122, 2013.

[11] C. M. Ionescu and R. De Keyser, "Relations between fractional-order model parameters and lung pathology in chronic obstructive pulmonary disease," *IEEE Transactions on Biomedical Engineering*, vol. 56, no. 4, pp. 978–987, 2009.

[12] C. M. Ionescu, P. Segers, and R. De Keyser, "Mechanical properties of the respiratory system derived from morphologic insight," *IEEE Transactions on Biomedical Engineering*, vol. 56, no. 4, pp. 949–959, 2009.

[13] S. Bhalekar, V. Daftardar-Gejji, D. Baleanu, and R. Magin, "Transient chaos in fractional Bloch equations," *Computers & Mathematics with Applications*, vol. 64, no. 10, pp. 3367–3376, 2012.

[14] S. Esmaeili, M. Shamsi, and Y. Luchko, "Numerical solution of fractional differential equations with a collocation method based on Müntz polynomials," *Computers & Mathematics with Applications*, vol. 62, no. 3, pp. 918–929, 2011.

[15] Z. Odibat, S. Momani, and V. S. Erturk, "Generalized differential transform method: application to differential equations of fractional order," *Applied Mathematics and Computation*, vol. 197, no. 2, pp. 467–477, 2008.

[16] D. Băleanu, O. G. Mustafa, and R. P. Agarwal, "An existence result for a superlinear fractional differential equation," *Applied Mathematics Letters*, vol. 23, no. 9, pp. 1129–1132, 2010.

[17] D. Băleanu, O. G. Mustafa, and R. P. Agarwal, "On the solution set for a class of sequential fractional differential equations," *Journal of Physics A*, vol. 43, no. 38, p. 385209, 7, 2010.

[18] E. H. Doha and W. M. Abd-Elhameed, "Efficient solutions of multidimensional sixth-order boundary value problems using symmetric generalized Jacobi-Galerkin method," *Abstract and Applied Analysis*, vol. 2012, Article ID 749370, 19 pages, 2012.

[19] A. H. Bhrawy and Al-Shomrani, "A Jacobi dual-Petrov Galerkin-Jacobi collocation method for solving Korteweg-de Vries equations," *Abstract and Applied Analysis*, vol. 2012, Article ID 418943, 16 pages, 2012.

[20] A. H. Bhrawy and M. A. Alghamdi, "Numerical solutions of odd order linear and nonlinear initial value problems using shifted Jacobi spectral approximations," *Abstract and Applied Analysis*, vol. 2012, Article ID 364360, 25 pages, 2012.

[21] E. H. Doha, A. H. Bhrawy, and R. M. Hafez, "On shifted Jacobi spectral method for high-order multi-point boundary value problems," *Communications in Nonlinear Science and Numerical Simulation*, vol. 17, no. 10, pp. 3802–3810, 2012.

[22] A. H. Bhrawy, A. S. Alofi, and S. I. El-Soubhy, "Spectral shifted Jacobi tau and collocation methods for solving fifth-order boundary value problems," *Abstract and Applied Analysis*, vol. 2011, Article ID 823273, 14 pages, 2011.

[23] E. H. Doha, A. H. Bhrawy, and R. M. Hafez, "A Jacobi dual-Petrov-Galerkin method for solving some odd-order ordinary differential equations," *Abstract and Applied Analysis*, vol. 2011, Article ID 947230, 21 pages, 2011.

[24] A. H. Bhrawy and W. M. Abd-Elhameed, "New algorithm for the numerical solutions of nonlinear third-order differential equations using Jacobi-Gauss collocation method," *Mathematical Problems in Engineering*, vol. 2011, Article ID 837218, 14 pages, 2011.

[25] A. Saadatmandi and M. Dehghan, "A new operational matrix for solving fractional-order differential equations," *Computers & Mathematics with Applications*, vol. 59, no. 3, pp. 1326–1336, 2010.

[26] E. H. Doha, A. H. Bhrawy, and S. S. Ezz-Eldien, "Efficient Chebyshev spectral methods for solving multi-term fractional orders differential equations," *Applied Mathematical Modelling*, vol. 35, no. 12, pp. 5662–5672, 2011.

[27] A. H. Bhrawy, A. S. Alofi, and S. S. Ezz-Eldien, "A quadrature tau method for fractional differential equations with variable coefficients," *Applied Mathematics Letters*, vol. 24, no. 12, pp. 2146–2152, 2011.

[28] A. H. Bhrawy and M. M. Al-Shomrani, "A shifted Legendre spectral method for fractional-order multi-point boundary value problems," *Advances in Differential Equations*, 2012.

[29] B.-Y. Guo and L.-L. Wang, "Modified Laguerre pseudospectral method refined by multidomain Legendre pseudospectral approximation," *Journal of Computational and Applied Mathematics*, vol. 190, no. 1-2, pp. 304–324, 2006.

[30] D. Funaro, "Estimates of Laguerre spectral projectors in Sobolev spaces," in *Orthogonal Polynomials and Their Applications (Erice, 1990)*, C. Brezinski, L. Gori, and A. Ronveaux, Eds., vol. 9 of *IMACS Ann. Comput. Appl. Math.*, pp. 263–266, Baltzer, Basel, Switzerland, 1991.

[31] M. Gülsu, B. Gürbüz, Y. Öztürk, and M. Sezer, "Laguerre polynomial approach for solving linear delay difference equations," *Applied Mathematics and Computation*, vol. 217, no. 15, pp. 6765–6776, 2011.

[32] E. H. Doha, A. H. Bhrawy, and S. S. Ezz-Eldien, "A Chebyshev spectral method based on operational matrix for initial and boundary value problems of fractional order," *Computers & Mathematics with Applications*, vol. 62, no. 5, pp. 2364–2373, 2011.

[33] E. H. Doha, A. H. Bhrawy, and S. S. Ezz-Eldien, "A new Jacobi operational matrix: an application for solving fractional differential equations," *Applied Mathematical Modelling*, vol. 36, no. 10, pp. 4931–4943, 2012.

[34] A. H. Bhrawy and A. S. Alofi, "The operational matrix of fractional integration for shifted Chebyshev polynomials," *Applied Mathematics Letters*, vol. 26, no. 1, pp. 25–31, 2013.

[35] P. N. Paraskevopoulos, "Chebyshev series approach to system identification, analysis and optimal control," *Journal of the Franklin Institute*, vol. 316, no. 2, pp. 135–157, 1983.

[36] P. N. Paraskevopoulos, "Legendre series approach to identification and analysis of linear systems," *IEEE Transactions on Automatic Control*, vol. 30, no. 6, pp. 585–589, 1985.

[37] E. H. Doha, H. M. Ahmed, and S. I. El-Soubhy, "Explicit formulae for the coefficients of integrated expansions of Laguerre and Hermite polynomials and their integrals," *Integral Transforms and Special Functions*, vol. 20, no. 7-8, pp. 491–503, 2009.

[38] A. K. Singh, V. K. Singh, and O. P. Singh, "The Bernstein operational matrix of integration," *Applied Mathematical Sciences*, vol. 3, no. 49–52, pp. 2427–2436, 2009.

[39] G. Szegö, *Orthogonal Polynomials*, American Mathematical Society, Providence, RI, USA, 1959.

Hindawi Publishing Corporation
Mathematical Problems in Engineering
Volume 2013, Article ID 878097, 10 pages
http://dx.doi.org/10.1155/2013/878097

Research Article

Challenges in the Application of Fractional Derivative Models in Capturing Solute Transport in Porous Media: Darcy-Scale Fractional Dispersion and the Influence of Medium Properties

Yong Zhang,[1] Charalambos Papelis,[2] Michael H. Young,[3] and Markus Berli[1]

[1] *Division of Hydrologic Sciences, Desert Research Institute, Las Vegas, NV 89119, USA*
[2] *Department of Civil Engineering, New Mexico State University, Las Cruces, NM 88003, USA*
[3] *Bureau of Economic Geology, Jackson School of Geosciences, University of Texas at Austin, Austin, TX 78712, USA*

Correspondence should be addressed to Yong Zhang; yong.zhang@dri.edu

Received 28 October 2012; Accepted 18 January 2013

Academic Editor: József Kázmér Tar

Heterogeneous media consisting of segregated flow regions are fractional-order systems, where the regional-scale anomalous diffusion can be described by the fractional derivative model (FDM). The standard FDM, however, first, cannot characterize the Darcy-scale dispersion through repacked sand columns, and second, the link between medium properties and model parameters remains unknown. To fill these two knowledge gaps, this study applies a tempered fractional derivative model (TFDM) to capture bromide transport through laboratory repacked sand. Column transport experiments are conducted first, where glass beads and silica sand with different diameters are repacked individually. Late-time tails are observed in the breakthrough curves (BTC) of bromide even in relatively homogeneous glass beads. The TFDM can capture the observed subdiffusion, especially the late-time BTC with a transient declining rate. Results also show that both the size distribution of repacked sand and the magnitude of fluid velocity can affect subdiffusion. In particular, a wider sand size distribution or a smaller flow rate can enhance the subdiffusion, leading to a smaller time index and a higher truncation parameter in the TFDM. Therefore, the Darcy-scale dispersion follows the tempered stable law, and the model parameters might be related to the soil size and flow conditions.

1. Introduction

Geological formations usually exhibit multiscale physical and/or chemical heterogeneity, which can lead to the space and/or time nonlocal dependency for solute transport (see the extensive review by Zhang et al. [1]). For example, the existence of preferential flow paths can force the fast movement of dissolved contaminants, resulting in superdiffusion. The mass flux at any position therefore depends on the flux not only at adjacent neighbors but also at a wide range of upstream zones. Such spatial nonlocal dependency can be efficiently characterized by the space fractional derivative, which is a generalization of its integer-order counterpart [2, 3]. In addition, the sorption-desorption mechanism can cause non-Markovian evolution of tracer mass in time, a typical subdiffusion that has been described by the time fractional derivative model (FDM) [1].

Two major knowledge gaps, however, remain for the FDM. First, while the FDM has been applied by hydrologists to simulate contaminant transport through regional-scale heterogeneous porous and fractured media for more than a decade [4], its applicability for Darcy-scale dispersion remains obscure. Indeed, some studies implied that the standard FDM may not be applicable for small-scale dispersion [5], due to the discrepancy between the finite medium size and the infinite distribution of particle dynamics (i.e., jump sizes and waiting times) assumed by the standard FDM. Second, the link between medium properties and FDM parameters has not been evaluated systematically. This unknown relationship, as commented by Neuman and Tartakovsky [6], suggests a failure of the physical model itself at the Darcy-scale.

This study attempts to fill the above knowledge gaps. We apply a tempered fractional derivative model (TFDM),

which is a generalization of the standard FDM, to capture bromide transport through laboratory repacked sand. This way, the applicability of the fractional-order partial differential equation on Darcy-scale dispersion can be tested reliably. Hence the first knowledge gap can be filled. The combined study of laboratory experiments and stochastic analysis may also reveal the trend of major transport parameters varying with sand properties. Such trend might lead to the answer regarding the second knowledge gap.

Laboratory experiments of solute transport through sand columns were conducted extensively by the hydrology community to explore the dynamics of dissolved solutes. For example, recent experiments [7, 8] identified non-Fickian diffusion for passive tracer transport through repacked laboratory columns of macroscopically homogeneous sand. Curve-fitting applications further show that the non-Fickian diffusion characterized by the nonsymmetric plume cannot be explained efficiently by the 2nd-order advection-dispersion equation (ADE) model based on Fickian diffusion [6, 9]. Well-designed laboratory experiments and alternative conceptual models are needed to explore the nature of transport through sand columns that may have been missed or misinterpreted previously, and then, to build the link between medium properties (measurable in the laboratory) and model parameters (controlling diffusion).

The rest of the paper is organized as follows. In Section 2, we introduce the laboratory experiments conducted to explore the Darcy-scale dispersion in repacked sand columns with different filling materials and to evaluate the influence of soil properties and fluid velocity on the transport of bromide. In Section 3, a fractional derivative-based, nonlocal transport model is developed and compared with the other nonlocal models. In Section 4, the proposed model is used to capture the observed Darcy-scale transport. In Section 5, we discuss the factors that affect bromide transport. Subdiffusion dominated by either slow advection or diffusion is also discussed to further explore the physical nature of the observed anomalous transport. Conclusions are summarized in Section 6.

2. Laboratory Experiments

2.1. Experimental Setup. We conducted laboratory experiments to measure the breakthrough curve (BTC) of one conservative tracer (bromide, as NaBr) in various sand packs. A glass column with internal dimensions of 150 mm (length) × 15.9 mm (diameter) was packed with glass beads or silica sand (Figure 1(a)).

Three different types of column experiments were conducted. For the first type of experiment (denoted by Run 1 in the following), the column was filled with uniform glass beads with an average diameter of 0.4 mm (Figure 1(b)) to represent a "homogeneous" porous medium microstructure.

For the second type of experiments (denoted by Run 2), two different sizes of glass beads were well mixed and packed, forming networks with mobile and relatively immobile domains. The first group of these experiments included glass beads with average diameters of 1 and 0.2 mm, while the second group included glass beads with average diameters of 0.4 and 0.2 mm.

For the third type of experiments (denoted by Run 3), silica sand with a specific particle size distribution was used to represent "natural" soil, where the irregular shape of the sand may affect the interconnected pores and the corresponding tracer dynamics. The overall particle size distribution was obtained by combining the following size fractions obtained by sieving: 0.85~1.0 mm (representing the coarse sand), 0.35~0.425 mm (medium sand), and 0.15~0.25 mm (fine sand), respectively. For description simplicity, in the following we denote the three size fractions by 1, 0.4, and 0.2 mm size silica sand, respectively, corresponding to the glass beads with similar diameters used in the second type of experiment. The sand was then cleaned with acid before packing.

After the column was packed, the following steps were performed to obtain BTCs. A five-point calibration of the bromide ion selective electrode (ISE) (Orion) was performed. The potential of standard solutions was measured from the lowest to the highest bromide concentration. Deionized water (DI) was run through the column for at least 2 hours prior to tracer injection to establish the flow domain. The pulse of bromide (of volume 10 mL) was then injected into the column (oriented horizontally) at a concentration of 1 mol/L, and discrete samples were collected from the outlet using a fraction collector (Teledyne ISCO). The sampling interval at early and late times was shortened to better record the tails of the BTC, known to be critical signals of non-Fickian transport. The bromide concentration was measured in all collected samples using the calibrated ISE probe with a detection limit of 10^{-5} mol/L.

The flow velocity was adjusted during the experiment using a rotary peristaltic pump and controller (Cole Palmer Masterflex) (Figure 1(a)) to evaluate the potential influence of flow rate on bromide dispersion. The average flow rate, and, hence, linear velocity were larger than those in real aquifers, to shorten the experimental periods and to provide advection-dominated transport systems.

2.2. Experiment Results

2.2.1. Run 1: Homogeneous Glass Beads. Figure 2 shows the measured BTC for this run. The BTC is symmetric for most of the times (Figure 2(a)), which can be explained by the classical Fickian diffusive model:

$$\frac{\partial P}{\partial t} = -V\frac{\partial P}{\partial x} + D\frac{\partial^2 P}{\partial x^2}, \tag{1}$$

where P is the density (or the tracer concentration in this case), V is the average linear velocity, and D is the macroscopic dispersion coefficient.

A slight late-time tail in the BTC (Figure 2(b)) close to the detection limit implies that transport can be subdiffusive even in homogeneous media, although the subdiffusive portion can only be detected at low concentrations.

2.2.2. Run 2: Heterogeneous Glass Beads. The BTC measured in Run 2 contains a much heavier late-time BTC tail than the

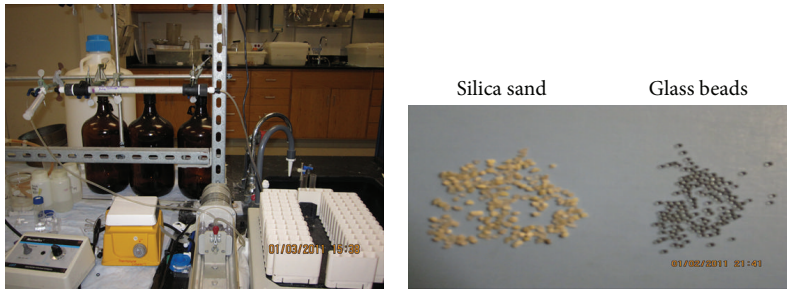

(a) (b)

Figure 1: (a) Photograph of the experimental setup. (b) The medium: silica sand (left) and glass beads (right).

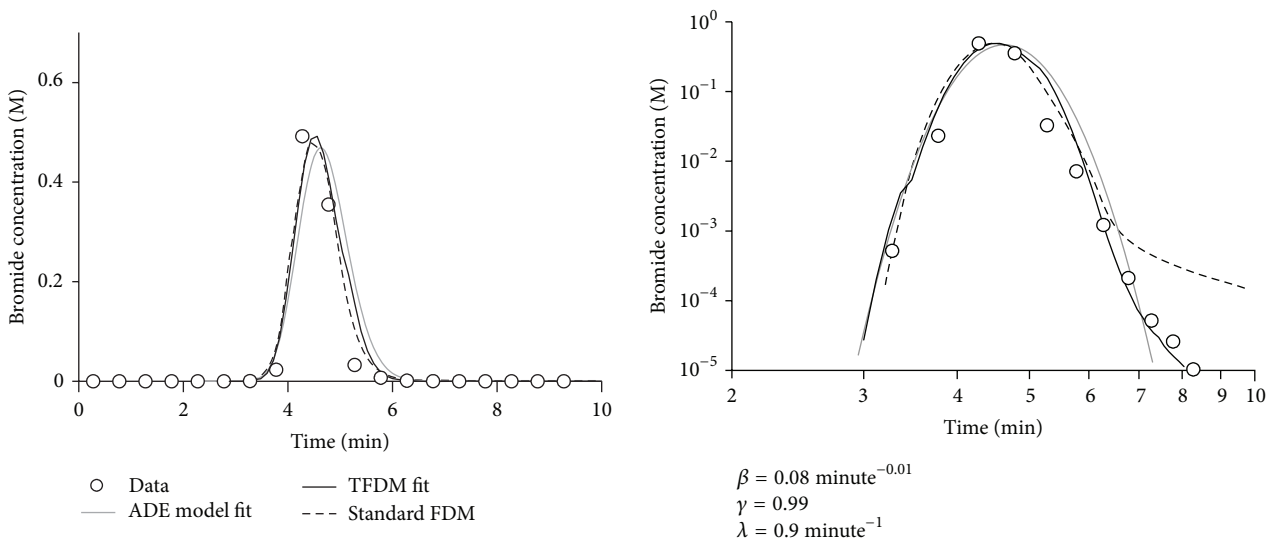

(a) (b)

Figure 2: BTC for the first type of experiment (i.e., Run 1 where the column filled with homogeneous glass beads) (a). (b) is the log-log plot of (a). The parameters shown in (b) are those fitted by the tempered fractional derivative model (2a) and (2b).

"homogeneous" case (Figure 3(a)) used in Run 1. The mixture of glass beads in this run has a wider size distribution of glass beads (i.e., more "heterogeneous" than the one used in Run 1). In addition, the late-time BTC tail for the larger diameter (1 + 0.2 mm) mixture is also heavier than that for the smaller diameter (0.4 + 0.2 mm) mixture (Figure 3(a)).

Note that the BTC tail declines faster for a higher fluid velocity, as shown by the glass beads with a 0.4 + 0.2 mm mixture (Figure 3(a)). The late-time BTC tail for the larger diameter (1 + 0.2 mm) mixture, however, seems less sensitive to fluid velocity (Figure 3(a)), probably due to the short duration of the experimental time. Thus, the experimental time for this specific case is apparently not long enough to capture any response of BTC to the variation of fluid velocity. Note that a dimensionless time scale is used in Figure 3. In Section 4, we will simulate the measured BTC using stochastic models, where the subtle discrepancy for BTCs with different fluid velocity might be gleaned.

2.2.3. Run 3: Heterogeneous Silica Sand. The observed BTC for Run 3 also contains an apparent late-time tail (Figure 3(b)), showing the strong subdiffusive process. The discrepancy between different mixtures, however, is not as apparent as that for glass beads.

The late-time tail in the BTC shrinks with the increase of fluid velocity (Figure 3(b)), similar to the behavior found in Run 2. The influence of fluid velocity on BTC will be viewed further using a numerical model (see Section 3.2) and a dimensional time scale (shown in Figure 4).

3. The Tempered Fractional Derivative Model

3.1. Review of Nonlocal Transport Methods. Nonlocal transport theories were developed recently to capture non-Fickian diffusion, as reviewed extensively by Haggerty et al. [10], Berkowitz et al. [9], Neuman and Tartakovsky [6], and

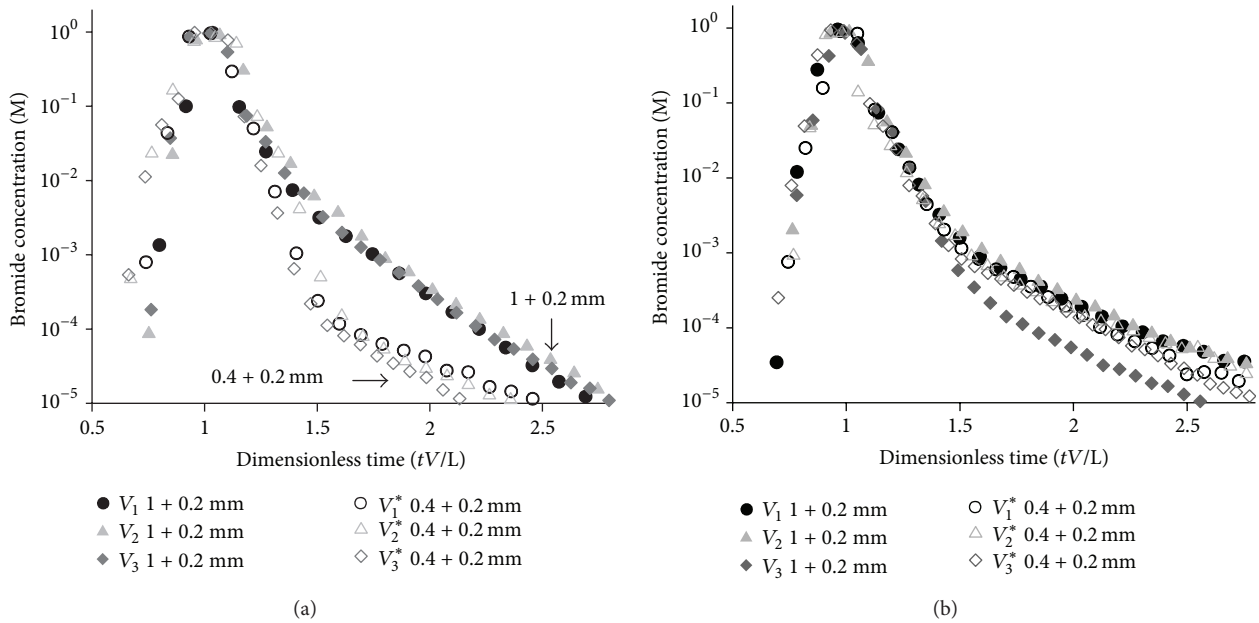

Figure 3: The measured BTCs for the laboratory experiment Run 2 (i.e., the column filled with glass beads) (a) and Run 3 (i.e., the column filled with silica sand) (b). In the legend shown in (a), "V" denotes the flow velocity: $V_1^* < V_2^* < V_3^*$ (see the text for details).

Zhang et al. [1]. The most efficient model for laboratory-scale transport was found to be the continuous time random walk (CTRW) framework by Berkowitz and Scher [11]. The CTRW framework defines empirical distributions for the transition time $\psi(t)$ of solute particles after experiencing enough variations of local velocity. Levy and Berkowitz [7] found that, if the transition time has a power law tail $\psi(t) \sim t^{-1-\xi}$ (where $0 < \xi < 2$), the CTRW captures the observed non-Fickian diffusion in sandboxes filled with homogeneous or heterogeneous sand, where the exponent ξ decreases with increasing fluid velocity. Berkowitz and Scher [11] extended the CTRW model used by Levy and Berkowitz [7] by assigning a truncated power law for the transition time $\psi(t) \sim (t_1 + t)^{-1-\xi}\exp(-t/t_2)$ (see also Table 1), where t_1 is a median time for transitions between sites and t_2 is the cut-off time of the power law spectrum. From the point of view of random walks [1], the transition time also represents the time for each particle to move. Hence the standard CTRW model actually assumes that all solute particles are in motion all the time. In other words, the subdiffusion is assumed to be the result of slow advection, as also shown by Berkowitz and Scher [11].

Molecular diffusion, however, may also cause the subdiffusive effect, as suggested by the physical process of multiple rate mass transfer [10]. After solutes whose transport is controlled by advection are flushed out, diffusion out of the relatively immobile domains causes later arrivals and the apparent late-time tail of a breakthrough curve. Repacked soils in the laboratory can contain immobile or stagnant regions, where the effect of diffusion on subdiffusion should not be neglected. In this study, we check this mechanism and compare it with the slow advection-related subdiffusion.

3.2. The TFDM for Diffusion-Dominated Subdiffusion. The tempered stable model proposed by Meerschaert et al. [5] is a concise version of the multirate mass transfer model with a finite number of rate coefficients. It contains the least number of parameters and can be computationally efficient, if solved appropriately. Hence we choose it as the appropriate model for the diffusion-dominated subdiffusion (i.e., subdiffusion due to the effect of slow diffusion of solute particles).

In our representation, we propose the following tempered fractional derivative model, or TFDM, by generalizing the current time fractional derivative models [1] and the tempered stable model [5]

$$\frac{\partial C_{\text{tot}}}{\partial t} + \beta^* e^{-\lambda t}\frac{\partial^\gamma}{\partial t^\gamma}\left[e^{\lambda t}C_{\text{tot}}\right] - \beta^*\lambda^\gamma C_{\text{tot}} = -\frac{\partial}{\partial x}\left[VC_{\text{tot}} - D\frac{\partial^{\alpha-1}C_{\text{tot}}}{\partial x^{\alpha-1}}\right] + IC_{\text{tot}}, \tag{2a}$$

$$\frac{\partial C_m}{\partial t} + \beta^* e^{-\lambda t}\frac{\partial^\gamma}{\partial t^\gamma}\left[e^{\lambda t}C_m\right] - \beta^*\lambda^\gamma C_m = -\frac{\partial}{\partial x}\left[VC_m - D\frac{\partial^{\alpha-1}C_m}{\partial x^{\alpha-1}}\right], \tag{2b}$$

where C_{tot} and C_m denote the resident concentration in the total and mobile phase, respectively, β^* denotes the capacity coefficient, λ is the truncation parameter, γ ($0 < \gamma \leq 1$ in this study) is the scale index in time characterizing the power-law slope of waiting times, α ($1 < \alpha \leq 2$) is the space index characterizing the displacement of the plume front, and $IC = \beta^*\delta(t)[\delta(t) - \int_t^\infty e^{-\lambda\tau}\tau^{-\gamma-1}/\Gamma(-\gamma)\, d\tau]$ accounts for the initial condition. When $\alpha = 1$, the TFDM (2a) and (2b) reduces

Table 1: Comparison of the TFDM (2) and the standard CTRW model reviewed by Berkowitz et al. [9]. Note that the standard CTRW defines various empirical memory functions, and the memory function listed below is the most commonly used one (which is a truncated power law similar to the memory function used in the TFDM (2a) and (2b)). In the CTRW model, the parameter $\tau_2 = t_2/t_1$ denotes the ratio of the two characteristic times t_2 and t_1, and $\Gamma[-\xi, (\tau_2)^{-1}]$ is the incomplete Gamma function.

Comparison	TFDM (2a) and (2b)	The standard CTRW [9]
Physical theory behind the model	Scaling limit of CTRW	The general master equation
Form of the memory function	$\int_t^\infty e^{-\lambda r} \frac{\gamma r^{-\gamma-1}}{\Gamma(1-\gamma)} dr$	$\frac{(\tau_2)^{\xi} \exp(-t/t_2)(1+t/t_1)^{-1-\xi}}{t_1 \exp[(\tau_2)^{-1}]\Gamma[-\xi,(\tau_2)^{-1}]}$
Number and value of parameters to capture sub-diffusion	3 $(\beta^*, \lambda, \gamma)$, with $0 < \gamma < 1$	4 (β^*, ξ, t_1, t_2), with $0 < \xi < 2$
Mechanism for sub-diffusion	Diffusion	Slow advection
Modeling super-diffusion	Applicable with $1 < \alpha < 2$	N/A
Modeling the mixed diffusion	Applicable with $0 < \gamma < 1$ and $1 < \alpha < 2$	N/A
Multidimensional extension	Multiscaling index [12]	No multiscaling index
Spatial variability of transport	V and D can vary in space	V and D are spatial averages

to the tempered stable model proposed by Meerschaert et al. [5]. In addition, the Riemann-Liouville fractional derivative is used for both the space and time fractional derivatives. This type of fractional derivative is selected because the corresponding Langevin method is known [12] and used for numerical approximations in this study.

Model (2a) and (2b) can be derived using either the fractal mobile/immobile (FMI) approach [4] or the subordination approach [5]. In the FMI approach, the generalized transport equations for the total and mobile concentrations are

$$\begin{gathered}\frac{\partial C_{\text{tot}}}{\partial t} + \beta^* \frac{\partial C_{\text{tot}}}{\partial t} * g(t) = L_x C_{\text{tot}}, \\ C_{\text{tot}}(x, t = 0) = m_0 \delta(x), \\ \frac{\partial C_m}{\partial t} + \beta^* \frac{\partial C_m}{\partial t} * g(t) = L_x C_m - \beta^* g(t) m_0 \delta(x),\end{gathered} \tag{3}$$

where the symbol $*$ denotes convolution, $g(t)$ represents a generalized memory function, m_0 denotes the initial mass (which can be normalized to 1), and the operator L_x describes the flux due to advection and dispersion. When the memory function $g(t) = \int_t^\infty e^{-\lambda r}(\gamma r^{-\gamma-1}/\Gamma(1-\gamma))dr$ and the nonlocal dispersive flux $L_x = -VC + D(\partial^{\alpha-1}C/\partial x^{\alpha-1})$ are used, the above model reduces to (2a) and (2b). In the 2nd approach (subordination), the total concentration can be expressed as $C_{\text{tot}}(x,t) = \int_0^\infty p(x,u) \cdot q(u,t)du$, where u denotes the operational time and $p(x,u)$ and $q(u,t)$ are densities of random walking particles in the mobile and immobile phases, respectively [12]. The governing equation for the total concentration C_{tot} therefore is model (2a), if the first density $p(x,u)$ is governed by the motion process $\partial p/\partial u = -\partial[Vp - D\partial^{\alpha-1}p/\partial x^{\alpha-1}]/\partial x$ and the second density $q(u,t)$ is governed by the waiting time process $\partial q/\partial u = \partial q/\partial t + \beta^* e^{-\lambda t}\partial^\gamma[e^{\lambda t}q]/\partial t^\gamma - \beta^*\lambda^\gamma q$ [12]. Similar arguments (see [5]) lead to the governing equation for the mobile concentration, which is (2b) in this case.

The two fractional derivative terms in model (2a) and (2b) have specific physical meanings that may help to explain the experimental data. First, the time fractional term is used to distinguish solute particle status (i.e., mobile versus immobile). In particular, the time drift term $(\partial/\partial t)$ is assigned to mobile particles, with the waiting time (represented by the two remaining terms on the left hand side of (2a) and (2b)) for immobile particles. The physical time therefore increases linearly when particles are in motion, and then it has a positive dispersive component (because $0 < \gamma \leq 1$) for each immobile particle. The evolution of physical time due to drift and dispersion in time is analogous to the advective and dispersive displacement for solute particles in space—the advective term accounts for the mean solute displacement, while the dispersive term adds random noise (either positive or negative) caused by the deviation of local velocities. The distinction for solute particle status is required for field applications, where the mobile concentration or mass can differ significantly from that in the immobile or total phase [13], especially at early or late times. Second, the space fractional derivative term on the right hand side of (2a) and (2b) describes the possible fast motion through preferential flow paths. In practical applications, both the early and late arrivals can be critical [1]. Heavy leading edges of tracer plumes have been observed for regional-scale transport (see, e.g., Adams and Gelhar [14]). These observations lead to a specific question: will any small-scale preferential flow path in saturated repacked sand generate the leading edge of a plume? The BTCs observed above provide the first hand material to answer this question. It is also noteworthy that the CTRW framework used by Levy and Berkowitz [7] and Berkowitz and Scher [11] does not have the above two properties. Further comparison of the TFDM (2a) and (2b) and the standard CTRW framework can be seen in Table 1.

The model in (2a) and (2b) can be approximated by a spatiotemporal Lagrangian solver proposed by Zhang et al. [12]. The approximation for the classical fractional derivative models is combined with the exponential rejection method proposed by Baeumer and Meerschaert [15] (that can generate the tempered stable random variables) to form

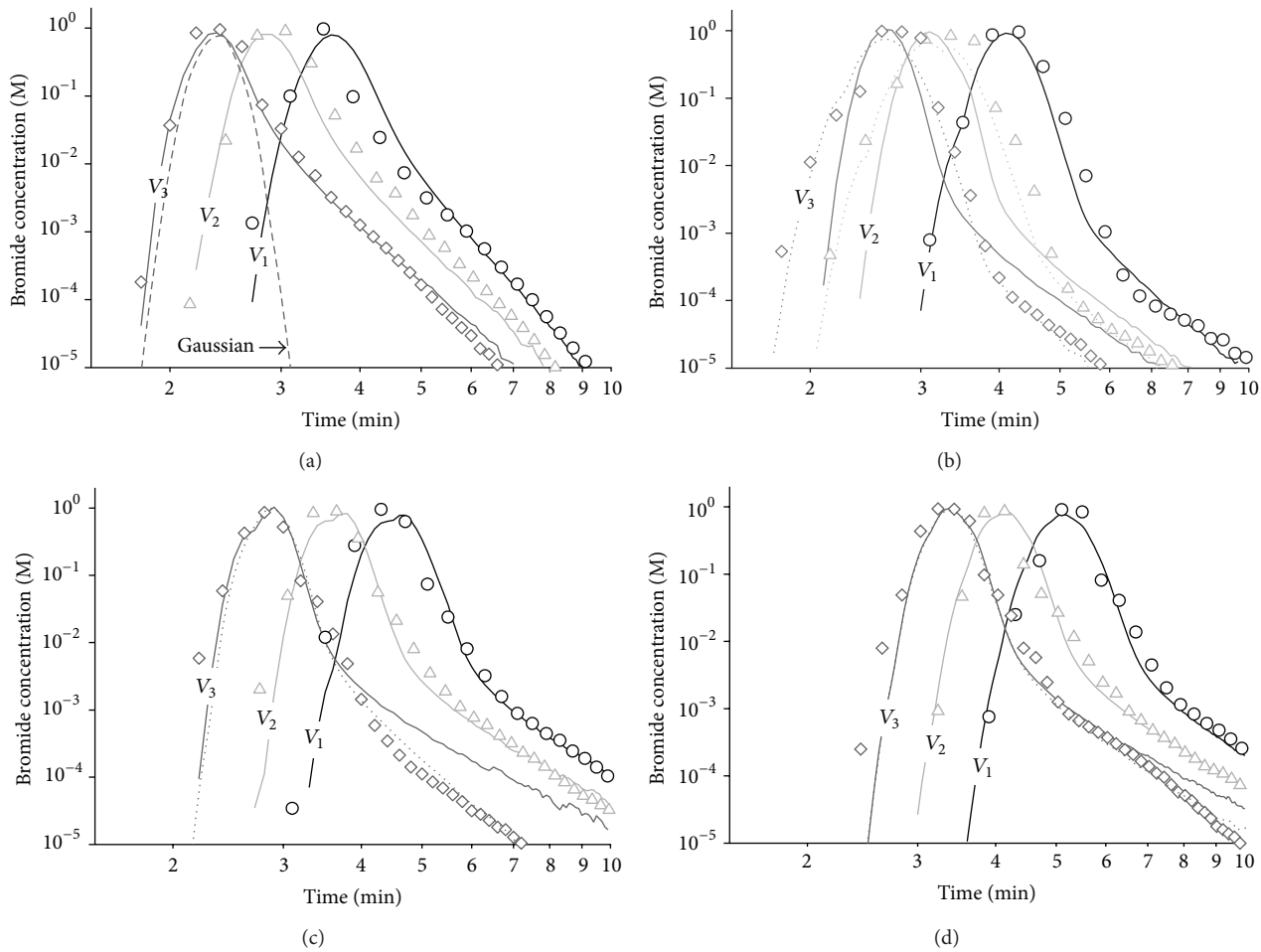

Figure 4: The laboratory observed bromide BTCs (symbols) versus the best-fit or predicted solutions using the TFDM model (2a) and (2b) (solid lines) for glass beads with sizes 1 + 0.2 mm (a) and 0.4 + 0.2 mm (b) and silica sand with sizes 1 + 0.2 mm (c) and 0.4 + 0.2 mm (d). The dashed line in (a) is the best-fit Gaussian solution, shown for comparison. The dots in (b), (c), and (d) are the updated, best-fit results using the TFDM model (2a) and (2b) for each individual BTC.

a fully Lagrangian solver for (2a) and (2b). The resultant particle tracking scheme is similar to the one proposed by Zhang and Papelis [16], where the time and space fractional terms were separated (in different models).

4. Applications

Model (2a) and (2b) now can be used to capture the BTCs described in Section 2. Note that the resident concentration (i.e., solution of (2a) and (2b)) needs to be transformed to its flux counterpart (i.e., the BTC). We first fit Run 1 (with homogeneous glass beads) by adjusting the dispersion coefficient D, capacity coefficient β^*, truncation parameter λ, and the two scale indexes γ and α. Note that the five parameters have different impacts on the BTC. For example, D affects the peak concentration, α dominates the early tail, γ controls the slope of the late-time tail, β^* affects the mass partition for particles at different phases, and λ controls the transition time from the power law tail to the exponential one. This helps us find quickly the best-fit value for each parameter. The average linear velocity V (3.56 cm/min) was measured in the laboratory. Results (Figure 2) show that TFDM (2a) and (2b) can fit the observed BTC, with the best-fit parameters $D = 0.23\,\text{cm}^2/\text{min}$, $\beta^* = 0.08\,\text{min}^{-0.01}$, $\lambda = 0.9\,\text{min}^{-1}$, $\gamma = 0.99$, and $\alpha = 2.0$. The standard FDM, however, slightly overestimates the late-time BTC tail (Figure 2).

For Run 2 using 1 + 0.2 mm glass beads, we first fit the BTC using the TFDM (2a) and (2b) with the slowest flow velocity ($V_1 = 4.66$ cm/min, see the black line in Figure 4(a)). The best-fit parameters, including $D = 0.13\,\text{cm}^2/\text{min}$, $\beta^* = 0.16\,\text{min}^{-0.1}$, $\lambda = 0.9\,\text{min}^{-1}$, $\gamma = 0.90$, and $\alpha = 2.0$, were then used to predict the BTC for the other two cases with larger velocities. Predictions of model (2a) and (2b) generally match the measured BTCs, while the classical second-order ADE (shown by the dashed line in Figure 4(a)) underestimates the BTC late-time tail.

For Run 2 using 0.4 + 0.2 mm glass beads, the best-fit parameters for the BTC with the slowest flow velocity V_1 (3.89 cm/min) are $D = 0.13\,\text{cm}^2/\text{min}$, $\beta^* = 0.07\,\text{min}^{-0.02}$, $\lambda = 0.45\,\text{min}^{-1}$, $\gamma = 0.98$, and $\alpha = 2.0$. Model prediction,

however, overestimates the late-time tail for BTC with velocities V_2 and V_3 (shown by the solid lines in Figure 4(b)). The relatively lighter BTC tail due to a larger velocity can be captured by a slightly larger truncation parameter λ and/or a smaller capacity coefficient β^* (see the dotted lines in Figure 4(b)). For example, the best-fit parameters for the BTC with a larger velocity V_2 (5.09 cm/min) are $\beta^* = 0.07\,\text{min}^{-0.02}$, $\lambda = 0.50\,\text{min}^{-1}$, and $\gamma = 0.98$.

The same conclusion is found for Run 3 with silica sand (Figures 4(c) and 4(d)), where a higher velocity corresponds to a larger λ and/or a smaller β^*. Note, however, that model parameters are not sensitive to the size distribution for this run, which is consistent to the measurements described in Section 2.

5. Discussion

5.1. Factors Affecting the Subdiffusion of Bromide and the Model Parameters. Laboratory experiments show that the subdiffusion increases by increasing the range of the sand size distribution, especially when the column is filled with glass beads. A wider sand size distribution tends to enhance subdiffusion, because broader distributions of particle diameter more readily form immobile regions. Bromide transport through silica sand is not as sensitive to the size distribution as the glass beads, which might be due to either the strong influence of the irregular shape of silica sand on the mass exchange between mobile and relatively immobile regions and/or the relatively large flow rate required for the laboratory experiments that counterbalances the size effect. Future studies are needed to explore further the influence of sand shape and low flow rate on subdiffusion.

Water flow rates across the sand column also affect subdiffusion. As the flow rate in nonaggregated material increases, the percentage of the total domain dominated by diffusive transport decreases. Hence the increase of fluid velocity likely decreases the contribution of diffusion to the arrival times of solute particles. In particular, if the observation period is short, the late-time subdiffusive behavior affected by the flow rate may not be detected. Hence the total experimental period should be as long as possible, to identify the full behavior of subdiffusion at late times.

The TFDM parameters can efficiently capture the subtle variation of subdiffusion. For example, the temporal scale index γ increases (representing the decrease of subdiffusion) with the decrease of the size range of mixed glass beads, given the relatively declining contribution of immobile regions to subdiffusion. Meanwhile, the capacity coefficient decreases, also illustrating the decline of subdiffusion. Though our results are compelling, they are not sufficient to build a quantitative relationship between the TFDM parameters and medium heterogeneity. To establish a purely predictive physical model, substantial effort involving laboratory experiments, analytical analysis, and numerical evaluations is still needed.

In addition, the standard FDM tends to overestimate the late-time BTC tail (see, e.g., the dashed line in Figure 2), since it assumes an infinite waiting time distribution. In a typical sand column at the Darcy-scale, the maximum trapping period (also known as the residence time) of solute particles may be finite. In other words, the waiting time distribution may have an upper limit. Such limit can be captured efficiently by the TFDM using the truncation parameter.

Finally, the best-fit space scale index α in model (2a) and (2b) is limited to 2.0 for all the observed BTCs in this study, implying that the dynamics for solute particles in *mobile time* are limited to Brownian motion (with a drift). As shown in Figure 4, the early tail of the BTC is as steep as an exponential function. The lack of an apparent leading edge confirms the difference between the repacked sand and real-world soils; clearly, simulating the real-world fast motion paths using repacked sand is difficult, if not impossible. In contrast, the real-world subdiffusive behavior can be captured by laboratory experiments, most likely due to the insensitivity of subdiffusion to the exact location of immobile regions [1].

5.2. The Slow Advection Dominated Subdiffusive Model and Its Limitations in Capturing Real-World Transport. To further understand the subdiffusive process, we simulate again the measured BTCs by assuming that the observed subdiffusion is driven by slow advection. A time fractional derivative model can be built to describe an advection-dominated subdiffusion. Assuming a CTRW with independent jump sizes and waiting times (or the elapsed time during two subsequent jumps), the corresponding scaling limit is

$$e^{-\lambda t}\frac{\partial^{\gamma}}{\partial t^{\gamma}}\left[e^{\lambda t}C\right]-\lambda^{\gamma}C=-\frac{\partial}{\partial x}\left[VC-D\frac{\partial^{\alpha-1}C}{\partial x^{\alpha-1}}\right]+IC, \tag{4}$$

which is the reduced form of the TFDM (2a) and (2b) without the time drift term and capacity coefficient. Model (4) can also be derived directly by assuming that the drift in time is zero in the TFDM model (2a) and (2b).

Applications show that model (4) captures most BTCs for Run 2 with 1 + 0.2 mm glass beads (Figure 5(a)). The best-fit parameters are $V = 3.81$ cm/min, $D = 0.13\,\text{cm}^2$/min, $\lambda = 1.4\,\text{min}^{-1}$, $\gamma = 0.98$, and $\alpha = 2.0$, for the BTC with the smallest fluid velocity V_1 (4.66 cm/min). Theoretically, the space scale index α (capturing superdiffusion) and the time scale index γ (representing the degree of subdiffusion) are independent. The truncation parameter λ however might be related to γ, since both of them describe the waiting time distribution of tracer particles and they all depend on properties of relatively immobile domains. A future study with extensive laboratory experiments is needed to reveal the quantitative relationship among model parameters. It is also noteworthy that both the time scale index γ and the truncation parameter λ are larger than those for model (2a) and (2b). The relatively large γ and λ in model (4) have to be used to capture the relatively steep power law late-time tail of the BTC (with a slope ~ -6.5 in a log-log plot). In model (2a) and (2b), the steep late-time BTC is explained by the relatively small time ratio that particles spend in the immobile and mobile phases (so that particles exit the immobile phase quickly and form the steep late-time tail of BTC), which can be captured conveniently by a small value of capacity coefficient β^*. Therefore, model (2a) and (2b) can describe

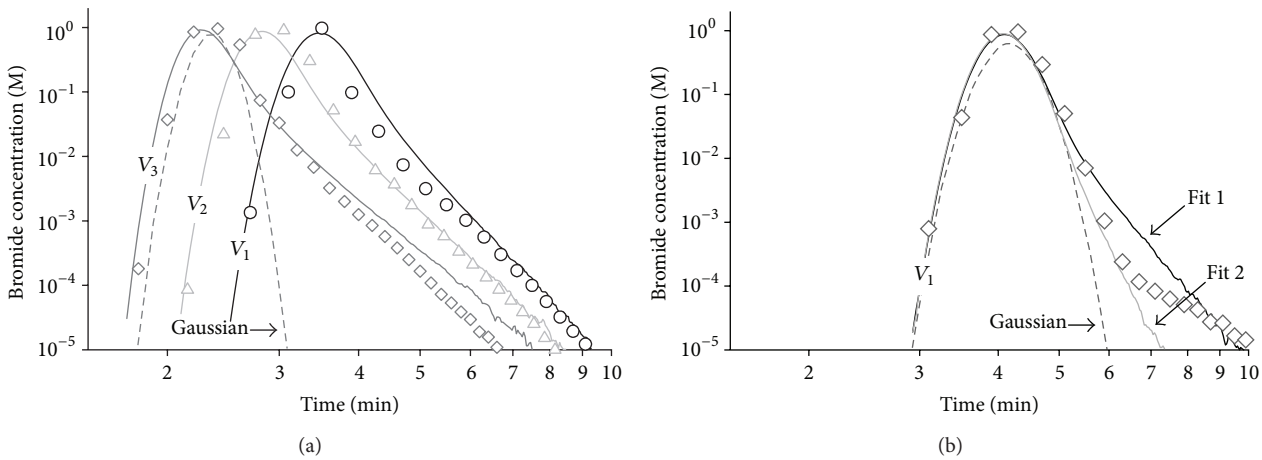

Figure 5: Best-fit of BTCs (solid lines) using model (4) versus the laboratory measurement (symbols), assuming that the subdiffusion is advection dominated, for glass beads with sizes 1 + 0.2 mm (a) and 0.4 + 0.2 mm (b). The dashed line is the best-fit Gaussian solution, shown for comparison. See text for the meaning and model parameters for "fit 1" and "fit 2."

a wide range of BTCs with various late-time tails, while model (4) has limited capability due to the lack of the controlling parameter β^*. In addition, the best-fit velocity in model (4) is smaller than the measured average linear velocity, an artificial effect due to more jumps than that in model (2a) and (2b) (because model (4) misses the actual *mobile time*; see also Zhang et al. [1]).

Further applications show that model (4) cannot fit any other BTCs. For example, model (4) misses the BTC tail for Run 2 with 0.4 + 0.2 mm glass beads (Figure 5(b)). Fit 1 and fit 2 shown in Figure 5(b) represent two fitting results using (4). The parameters used are $\lambda = 2.0\,\text{min}^{-1}$ and $\gamma = 0.99$ for fit 2 and $\lambda = 0.9\,\text{min}^{-1}$ and $\gamma = 0.99$ for fit 1. The scale index γ approaches the maximum limit 1, and the truncation parameter λ cannot improve the fit at all.

It is possible to extend model (4) to capture BTCs similar to the one shown in Figure 5(b), by using the time fractional derivative model with two time scales proposed by Meerschaert et al. [17] (so that γ can be larger than 1). This extension, however, still has two serious limitations. First, the CTRW model differs significantly for different ranges of index γ and it represents different physical processes [17]. Second, model (4) cannot capture the mobile mass decline, no matter the range of γ. Therefore, the TFDM model (2a) and (2b) is superior to its simplified version (such as model (4)) in capturing real-world subdiffusion.

5.3. Applicability and Limitation of the TFDM (2a) *and* (2b). The TFDM model (2a) and (2b) may also be used to capture open channel flow and transport, such as the transport of dye in rivers [1, 4, 10]. Although advection is the dominant factor for transport in surface systems, the observed late-time tail of the BTC for a dye is caused by the molecular diffusion during the mass exchange between open channel and hyporheic zone [4] or the many relatively immobile domains in natural rivers [1]. The mechanism for the diffusion-related subdiffusion is therefore similar to that discussed above for porous media. We will check the applicability of the model (2a) and (2b) in surface dynamic processes in a future study.

The TFDM (2a) and (2b) may be applied to dynamic processes observed in the other fractional-order systems in multiple disciplines, such as sedimentation engineering and chemical engineering. For example, quantifying anomalous dynamics of suspended and bedload sediment transport in natural rivers remains a significant challenge in river morphology studies, due to the stochastic nature of sediment transport in a complex system with multiscale intrinsic heterogeneity. The TFDM (2a) and (2b) may capture the random process of sediment transport, especially the intermittent mobile and immobile dynamics. In addition, anomalous kinetics is well documented for chemical reactions, where the non-Fickian motion of reactant molecules (the main reason why the diffusion-limited anomalous kinetics deviate significantly from the thermodynamic law) may be efficiently simulated by the TFDM (2a) and (2b) with a particle-based scheme.

One of the major limitations of the TFDM (2a) and (2b) is the representative scale of model parameters. Nonlocal transport models are upscaling tools that replace detailed medium heterogeneity information with memory kernels in space and/or time. How to define the representative scale and how to delineate the effective range for the model index in nonstationary systems remain to be shown. This study shows that the representative scale for the tempered fractional diffusion is no less than the laboratory scale. Will the variable-order or the distributed-order fractional derivatives (where the order of the fractional derivative is no longer a constant) capture the evolution of heterogeneity, and should the nonlocal transport models be conditioning on local system properties measured at each representative scale? These remain open questions. In addition, the TFDM (2a) and (2b) differs significantly from the standard fractional derivative models because the former is scale dependent. Can the TFDM (2a) and (2b) capture the scaling behavior for

transport observed in practical engineering processes? We will focus on these questions in a future study.

6. Conclusions

The fractional engine is a promising tool to capture anomalous dispersion in heterogeneous media, but major challenges do exist, including the Darcy-scale fractional dispersion and the influence of medium heterogeneity. In this study, laboratory experiments were combined with stochastic model analysis to explore the applicability of the fractional engine in capturing Darcy-scale dispersion in sand columns filled with various materials and to explore the potential link between medium properties and model parameters. The following four main conclusions are drawn.

(1) The tempered fractional derivative model can capture subdiffusion at the Darcy-scale. The physical model distinguishes solute status, contains the least number of parameters, and can be extended conveniently to capture advanced transport processes. Most importantly, the TFDM can characterize the transient decline rate of the late-time BTC, probably due to the finite distribution of particle waiting times, while the standard FDM tends to overestimate the late-time tail of BTC.

(2) Both the sand particle size distribution and the fluid velocity can affect the Darcy-scale subdiffusion. All of the measured BTCs of bromide contain an apparent late-time tail, which is heavier for a wider particle size distribution of sand or a smaller fluid velocity. These two properties can enhance the relative contribution of diffusion to the late-time arrivals of solute particles. Hence both medium properties and flow conditions can affect subdiffusion, which is consistent with the conclusion of Berkowitz and Scher [11]. However, to build a quantitative relationship between the two properties and model parameters, additional laboratory and numerical experiments are needed.

(3) Diffusion-controlled subdiffusion is possible. In heterogeneous or even homogeneous sand columns, subdiffusive transport due to molecular diffusion occurs even for a large Peclet number. The relatively immobile regions formed during soil repacking cause diffusion-controlled subdiffusion, following the physical process of multirate mass transfer. The diffusion-controlled subdiffusion can be apparent in undisturbed soils, where the immobile zones are almost inevitable and the corresponding mass transfer rate varies significantly in space.

(4) There are serious limitations in applying the slow-advection-dominated subdiffusive model, such as model (4), to capture real-world subdiffusion due to mass exchange. In the slow advection-dominated subdiffusive model, the transient anomalous mass decline cannot be captured. The best-fit velocity differs from the measurement, and the time scale index has a wider range and represents different physical processes. These limitations cause high uncertainty in predicting non-Fickian transport.

Acknowledgments

This work was supported by the Desert Research Institute (DRI) and the National Science Foundation (NSF) under Grant no. DMS-1025417. Part of the experiments was conducted by Wallace Atterberry supported by the first author. This paper does not necessary reflect the views of NSF or DRI. The authors thank three anonymous reviewers for helpful comments that improved the paper.

References

[1] Y. Zhang, D. A. Benson, and D. M. Reeves, "Time and space nonlocalities underlying fractional-derivative models: distinction and literature review of field applications," *Advances in Water Resources*, vol. 32, no. 4, pp. 561–581, 2009.

[2] R. Metzler and J. Klafter, "The random walk's guide to anomalous diffusion: a fractional dynamics approach," *Physics Reports*, vol. 339, no. 1, pp. 1–77, 2000.

[3] R. Metzler and J. Klafter, "The restaurant at the end of the random walk: recent developments in the description of anomalous transport by fractional dynamics," *Journal of Physics A*, vol. 37, no. 31, pp. R161–R208, 2004.

[4] R. Schumer, D. A. Benson, M. M. Meerschaert, and B. Baeumer, "Fractal mobile/immobile solute transport," *Water Resources Research*, vol. 39, no. 10, Article ID W1296, 2003.

[5] M. M. Meerschaert, Y. Zhang, and B. Baeumer, "Tempered anomalous diffusion in heterogeneous systems," *Geophysical Research Letters*, vol. 35, no. 17, Article ID L17403, 2008.

[6] S. P. Neuman and D. M. Tartakovsky, "Perspective on theories of non-Fickian transport in heterogeneous media," *Advances in Water Resources*, vol. 32, no. 5, pp. 670–680, 2009.

[7] M. Levy and B. Berkowitz, "Measurement and analysis of non-Fickian dispersion in heterogeneous porous media," *Journal of Contaminant Hydrology*, vol. 64, no. 3-4, pp. 203–226, 2003.

[8] M. Bromly and C. Hinz, "Non-Fickian transport in homogeneous unsaturated repacked sand," *Water Resources Research*, vol. 40, no. 7, Article ID W07402, 2004.

[9] B. Berkowitz, A. Cortis, M. Dentz, and H. Scher, "Modeling Non-fickian transport in geological formations as a continuous time random walk," *Reviews of Geophysics*, vol. 44, no. 2, Article ID RG2003, 2006.

[10] R. Haggerty, S. A. McKenna, and L. C. Meigs, "On the late-time behavior of tracer test breakthrough curves," *Water Resources Research*, vol. 36, no. 12, pp. 3467–3479, 2000.

[11] B. Berkowitz and H. Scher, "Exploring the nature of non-Fickian transport in laboratory experiments," *Advances in Water Resources*, vol. 32, no. 5, pp. 750–755, 2009.

[12] Y. Zhang, M. M. Meerschaert, and B. Baeumer, "Particle tracking for time-fractional diffusion," *Physical Review E*, vol. 78, no. 3, Article ID 036705.

[13] C. Harvey and S. M. Gorelick, "Rate-limited mass transfer or macrodispersion: which dominates plume evolution at the Macrodispersion Experiment (MADE) site?" *Water Resources Research*, vol. 36, no. 3, pp. 637–650, 2000.

[14] E. E. Adams and L. W. Gelhar, "Field study of dispersion in a heterogeneous aquifer, 2. Spatial moments analysis," *Water Resources Research*, vol. 28, no. 12, pp. 3293–3307, 1992.

[15] B. Baeumer and M. M. Meerschaert, "Tempered stable Lévy motion and transient super-diffusion," *Journal of Computational and Applied Mathematics*, vol. 233, no. 10, pp. 2438–2448, 2010.

[16] Y. Zhang and C. Papelis, "Particle-tracking simulation of fractional diffusion-reaction processes," *Physical Review E*, vol. 84, no. 6, Article ID 066704, 2011.

[17] M. M. Meerschaert, Y. Zhang, and B. Baeumer, "Particle tracking for fractional diffusion with two time scales," *Computers & Mathematics with Applications*, vol. 59, no. 3, pp. 1078–1086, 2010.

Hindawi Publishing Corporation
Mathematical Problems in Engineering
Volume 2013, Article ID 320415, 9 pages
http://dx.doi.org/10.1155/2013/320415

Research Article

A Study of Nonlinear Fractional Differential Equations of Arbitrary Order with Riemann-Liouville Type Multistrip Boundary Conditions

Bashir Ahmad,[1] Sotiris K. Ntouyas,[2] and Ahmed Alsaedi[1]

[1] *Department of Mathematics, Faculty of Science, King Abdulaziz University, P.O. Box 80203, Jeddah 21589, Saudi Arabia*
[2] *Department of Mathematics, University of Ioannina, 451 10 Ioannina, Greece*

Correspondence should be addressed to Bashir Ahmad; bashirahmad_qau@yahoo.com

Received 28 November 2012; Accepted 19 January 2013

Academic Editor: José Tenreiro Machado

We develop the existence theory for nonlinear fractional differential equations of arbitrary order with Riemann-Liouville type boundary conditions involving nonintersecting finite many strips of arbitrary length. Our results are based on some standard tools of fixed point theory. For the illustration of the results, some examples are also discussed.

1. Introduction

The subject of fractional calculus has recently developed into a hot topic for the researchers in view of its numerous applications in the field of physics, mechanics, chemistry, engineering, and so forth. One can find the systematic progress of the topic in the books ([1–6]). A significant characteristic of a fractional-order differential operator distinguishing it from the integer-order differential operator is that it is nonlocal in nature, that is, the future state of a dynamical system or process involving fractional derivative depends on its current state as well its past states. In fact, this feature of fractional-order operators has contributed towards the popularity of fractional-order models, which are recognized as more realistic and practical than the classical integer-order models. In other words, we can say that the memory and hereditary properties of various materials and processes can be described by differential equations of arbitrary order. There has been a rapid development in the theoretical aspects such as periodicity, asymptotic behavior, and numerical methods for fractional equations. For some recent work on the topic, see ([7–23]) and the references therein. In particular, Ahmad et al. [22] studied nonlinear fractional differential equations and inclusions of arbitrary order with multistrip boundary conditions.

In this paper, we continue the study initiated in [22] and consider a boundary value problem of fractional differential equations of arbitrary order $q \in (n-1, n]$, $n \geq 2$ with finite many multistrip Riemann-Liouville type integral boundary conditions:

$$\begin{gathered} {}^{c}D^{q}x(t) = f(t, x(t)), \quad t \in [0, T], \\ x(0) = 0, \qquad x'(0) = 0, \ldots, x^{(n-2)}(0) = 0, \\ x(T) = \sum_{i=1}^{m} \gamma_i \left[I^{\beta_i} x(\eta_i) - I^{\beta_i} x(\zeta_i) \right], \end{gathered} \tag{1}$$

where ${}^{c}D^{q}$ denotes the Caputo fractional derivative of order q, f is a given continuous function, I^{β_i} is the Riemann-Liouville fractional integral of order $\beta_i > 0$, $i = 1, 2, \ldots, m$, $0 < \zeta_1 < \eta_1 < \zeta_2 < \eta_2 < \ldots < \zeta_m < \eta_m < T$, and $\gamma_i \in \mathbb{R}$ are suitable chosen constants.

Regarding the motivation of the problem, we know that the strip conditions appear in the mathematical modeling of

certain real world problems, for instance, see [24, 25]. In [22], the authors considered the nonlocal strip conditions of the form:

$$x(1) = \sum_{i=1}^{n-2} \alpha_i \int_{\zeta_i}^{\eta_i} x(s)\, ds, \quad 0 < \zeta_i < \eta_i, < 1, \quad i = 1, 2, \ldots, (n-2). \tag{2}$$

In the problem (1), we have introduced Riemann-Liouville type multistrip integral boundary conditions which can be interpreted as the controller at the right-end of the interval under consideration is influenced by a discrete distribution of finite many nonintersecting sensors (strips) of arbitrary length expressed in terms of Riemann-Liouville type integral boundary conditions. For some engineering applications of strip conditions, see ([26–32]).

The main objective of the present study is to develop some existence results for the problem (1) by using standard techniques of fixed point theory. The paper is organized as follows. In Section 2 we discuss a linear variant of the problem (1), which plays a key role in developing the main results presented in Section 3. For the illustration of the theory, we have also included some examples.

2. Preliminary Result

Let us begin this section with some basic definitions of fractional calculus [2–4].

Definition 1. If $g(t) \in AC^n[a,b]$, then the Caputo derivative of fractional order q is defined as

$$\begin{aligned} {}^cD^q_{a^+} g(t) &= \frac{1}{\Gamma(n-q)} \int_a^t (t-s)^{n-q-1} g^{(n)}(s)\, ds \\ &= I^{n-q}_{a^+} D^n g(x), \quad n-1 < q < n, \ n = [q]+1, \end{aligned} \tag{3}$$

where $[q]$ denotes the integer part of the real number q. For details, see Theorem 2.1 ([4, page 92]). Here $AC^n[a,b]$ denote the space of real valued functions $g(t)$ which have continuous derivatives up to order $n-1$ on $[a,b]$ such that $g^{n-1}(t) \in AC[a,b]$.

Definition 2. The Riemann-Liouville fractional integral of order q is defined as

$$I^q g(t) = \frac{1}{\Gamma(q)} \int_0^t \frac{g(s)}{(t-s)^{1-q}} ds, \quad q > 0, \tag{4}$$

provided the integral exists.

The following result associated with a linear variant of problem (1) plays a pivotal role in establishing the main results.

Lemma 3. *For $h \in C[0,T]$, the fractional boundary value problem*

$$\begin{aligned} &{}^cD^q x(t) = h(t), \quad t \in [0,T], \ q \in (n-1, n] \\ &x(0) = 0, \qquad x'(0) = 0, \ldots, x^{(n-2)}(0) = 0, \\ &x(T) = \sum_{i=1}^{m} \gamma_i \left[I^{\beta_i} x(\eta_i) - I^{\beta_i} x(\zeta_i) \right], \end{aligned} \tag{5}$$

has a unique solution $x(t) \in AC^n[0,T]$ given by

$$\begin{aligned} x(t) = {} & \frac{1}{\Gamma(q)} \int_0^t (t-s)^{q-1} h(s)\, ds \\ & - \frac{t^{n-1}}{\lambda \Gamma(q)} \int_0^T (T-s)^{q-1} h(s)\, ds \\ & + \frac{t^{n-1}}{\lambda \Gamma(q)} \sum_{i=1}^{m} \frac{\gamma_i}{\Gamma(\beta_i)} \\ & \times \left[\int_0^{\eta_i} \int_0^s (\eta_i - s)^{\beta_i - 1} \right. \\ & \times (s-u)^{q-1} h(u)\, du\, ds \\ & - \int_0^{\zeta_i} \int_0^s (\zeta_i - s)^{\beta_i - 1} (s-u)^{q-1} \\ & \left. \times h(u)\, du\, ds \right], \end{aligned} \tag{6}$$

where

$$\lambda = \left(T^{n-1} - \sum_{i=1}^{m} \gamma_i \frac{\left(\eta_i^{\beta_i + n - 1} - \zeta_i^{\beta_i + n - 1} \right) \Gamma(n)}{\Gamma(\beta_i + n)} \right) \neq 0. \tag{7}$$

Proof. The general solution of fractional differential equations in (5) can be written as

$$x(t) = \frac{1}{\Gamma(q)} \int_0^t (t-s)^{q-1} h(s)\, ds - c_0 - c_1 t - \cdots - c_{n-1} t^{n-1}. \tag{8}$$

Using the given boundary conditions, it is found that $c_0 = 0$, $c_1 = 0, \ldots, c_{n-2} = 0$. Applying the Riemann-Liouville integral operator I^{β_i} on (8), we get

$$\begin{aligned} I^{\beta_i} x(t) &= \frac{1}{\Gamma(\beta_i)} \int_0^t (t-s)^{\beta_i - 1} \\ &\quad \times \left(\frac{1}{\Gamma(q)} \int_0^s (s-u)^{q-1} h(u)\, du - c_{n-1} s^{n-1} \right) ds \\ &= \frac{1}{\Gamma(\beta_i)\Gamma(q)} \int_0^t \int_0^s (t-s)^{\beta_i - 1} (s-u)^{q-1} h(u)\, du\, ds \\ &\quad - c_{n-1} \frac{1}{\Gamma(\beta_i)} \int_0^t (t-s)^{\beta_i - 1} s^{n-1} ds. \end{aligned} \tag{9}$$

Using the condition $x(T) = \sum_{i=1}^m \gamma_i [I^{\beta_i} x(\eta_i) - I^{\beta_i} x(\zeta_i)]$, together with the fact that

$$\frac{1}{\Gamma(\beta_i)} \int_0^t (t-s)^{\beta_i - 1} s^{n-1} ds = \frac{t^{\beta_i + n - 1} \Gamma(n)}{\Gamma(\beta_i + n)}, \tag{10}$$

we obtain

$$\begin{aligned} &\frac{1}{\Gamma(q)} \int_0^T (T-s)^{q-1} h(s)\, ds - c_{n-1} T^{n-1} \\ &\quad = \sum_{i=1}^m \frac{\gamma_i}{\Gamma(q)\Gamma(\beta_i)} \\ &\qquad \times \left[\int_0^{\eta_i} \int_0^s (\eta_i - s)^{\beta_i - 1} (s-u)^{q-1} h(u)\, du\, ds \right. \\ &\qquad \left. - \int_0^{\zeta_i} \int_0^s (\zeta_i - s)^{\beta_i - 1} (s-u)^{q-1} h(u)\, du\, ds \right] \\ &\quad - c_{n-1} \sum_{i=1}^m \gamma_i \frac{\left(\eta_i^{\beta_i + n - 1} - \zeta_i^{\beta_i + n - 1}\right) \Gamma(n)}{\Gamma(\beta_i + n)}, \end{aligned} \tag{11}$$

which yields

$$\begin{aligned} c_{n-1} &= \frac{1}{\lambda \Gamma(q)} \int_0^T (T-s)^{q-1} h(s)\, ds \\ &\quad - \frac{1}{\lambda \Gamma(q)} \sum_{i=1}^m \frac{\gamma_i}{\Gamma(\beta_i)} \\ &\qquad \times \left[\int_0^{\eta_i} \int_0^s (\eta_i - s)^{\beta_i - 1} \right. \\ &\qquad \times (s-u)^{q-1} h(u)\, du\, ds \\ &\qquad \left. - \int_0^{\zeta_i} \int_0^s (\zeta_i - s)^{\beta_i - 1} (s-u)^{q-1} \right. \\ &\qquad \left. \times h(u)\, du\, ds \right], \end{aligned} \tag{12}$$

where λ is given by (7). Substituting the values of c_0, $c_1, \ldots, c_{n-2}, c_{n-1}$ in (8), we obtain (6). This completes the proof. □

3. Main Results

Let $\mathscr{C} := C([0,T], \mathbb{R})$ denotes the Banach space of all continuous functions defined on $[0,T] \times \mathbb{R}$ endowed with a topology of uniform convergence with the norm $\|x\| = \sup_{t \in [0,T]} |x(t)|$.

By Lemma 3, we define an operator $\mathscr{P} : \mathscr{C} \to \mathscr{C}$ as

$$\begin{aligned} (\mathscr{P}x)(t) &= \frac{1}{\Gamma(q)} \int_0^t (t-s)^{q-1} f(s, x(s))\, ds \\ &\quad - \frac{t^{n-1}}{\lambda \Gamma(q)} \int_0^T (T-s)^{q-1} f(s, x(s))\, ds \\ &\quad + \frac{t^{n-1}}{\lambda \Gamma(q)} \sum_{i=1}^m \frac{\gamma_i}{\Gamma(\beta_i)} \\ &\qquad \times \left[\int_0^{\eta_i} \int_0^s (\eta_i - s)^{\beta_i - 1} (s-u)^{q-1} \right. \\ &\qquad \times f(u, x(u))\, du\, ds \\ &\qquad - \int_0^{\zeta_i} \int_0^s (\zeta_i - s)^{\beta_i - 1} (s-u)^{q-1} \\ &\qquad \left. \times f(u, x(u))\, du\, ds \right], \\ &\qquad t \in [0,T]. \end{aligned} \tag{13}$$

Observe that the problem (1) has a solution if and only if the associated fixed point problem $\mathscr{P}x = x$ has a fixed point.

In the first result we prove an existence and uniqueness result by means of Banach's contraction mapping principle. For the sake of convenience, we set

$$\begin{aligned} \Lambda &= \frac{T^q}{\Gamma(q+1)} + \frac{T^{q+n-1}}{|\lambda| \Gamma(q+1)} \\ &\quad + \frac{T^{n-1}}{|\lambda|} \sum_{i=1}^m \gamma_i \frac{\eta_i^{q+\beta_i} - \zeta_i^{q+\beta_i}}{\Gamma(q+\beta_i+1)}. \end{aligned} \tag{14}$$

Theorem 4. *Suppose that $f : [0,T] \times \mathbb{R} \to \mathbb{R}$ is a continuous function and satisfies the following assumption:*

(A_3)

$$\begin{aligned} &|f(t,x) - f(t,y)| \le L |x - y|, \\ &\forall t \in [0,1],\ L > 0,\ x, y \in \mathbb{R}. \end{aligned} \tag{15}$$

Then the boundary value problem (1) *has a unique solution provided*

$$L < \frac{1}{\Lambda}, \tag{16}$$

where Λ is given by (14).

Proof. With $r \geq M\Lambda/(1-L\Lambda)$, we define $B_r = \{x \in \mathscr{C} : \|x\| \leq r\}$, where $M = \sup_{t\in[0,T]}|f(t,0)| < \infty$ and Λ is given by (14). Then we show that $\mathscr{P}B_r \subset B_r$. For $x \in B_r$, by means of the inequality $|f(s,x(s))| \leq |f(s,x(s)) - f(s,0)| + |f(s,0)| \leq L\|x\| + M \leq Lr + M$, it can easily be shown that

$$\|\mathscr{P}x\| = (Lr + M)\Lambda \leq r. \tag{17}$$

Now, for $x, y \in \mathscr{C}$ and for each $t \in [0,T]$, we obtain

$$\begin{aligned}
&\|(\mathscr{P}x) - (\mathscr{P}y)\| \\
&\leq \sup_{t\in[0,T]} \left\{ \frac{1}{\Gamma(q)} \int_0^t (t-s)^{q-1} \left|f(s,x(s)) - f(s,y(s))\right| ds \right. \\
&\quad + \frac{t^{n-1}}{\lambda\Gamma(q)} \int_0^T (T-s)^{q-1} \\
&\qquad \times \left|f(s,x(s)) - f(s,y(s))\right| ds \\
&\quad + \frac{t^{n-1}}{\lambda\Gamma(q)} \\
&\quad \times \sum_{i=1}^m \frac{\gamma_i}{\Gamma(\beta_i)} \\
&\qquad \times \left[\int_0^{\eta_i} \int_0^s (\eta_i - s)^{\beta_i - 1} \right. \\
&\qquad\quad \times (s-u)^{q-1} du \\
&\qquad\quad \times \left|f(u,x(u)) - f(u,y(u))\right| ds \\
&\qquad - \int_0^{\zeta_i} \int_0^s (\zeta_i - s)^{\beta_i - 1} (s-u)^{q-1} \\
&\qquad\quad \times \left|f(u,x(u)) \right. \\
&\qquad\quad \left. \left. - f(u,y(u))\right| du\, ds \right] \Bigg\} \\
&\leq L\Lambda \|x - y\|.
\end{aligned} \tag{18}$$

Note that Λ depends only on the parameters involved in the problem. As $L\Lambda < 1$, therefore $\mathscr{P}$ is a contraction. Hence, by Banach's contraction mapping principle, the problem (1) has a unique solution on $[0,T]$. □

Example 5. Let us consider the following 4-strip nonlocal boundary value problem:

$$\begin{gathered}
{}^cD^{9/2}x(t) = f(t,x(t)), \quad t \in [0,2], \\
x(0) = 0, \qquad x'(0) = 0, \qquad x''(0) = 0, \qquad x'''(0) = 0, \\
x(T) = \sum_{i=1}^4 \gamma_i \left[I^{\beta_i} x(\eta_i) - I^{\beta_i} x(\zeta_i) \right],
\end{gathered} \tag{19}$$

where $q = 9/2$, $n = 5$, $\zeta_1 = 1/4$, $\eta_1 = 1/2$, $\zeta_2 = 2/3$, $\eta_2 = 1$, $\zeta_3 = 5/4$, $\eta_3 = 4/3$, $\zeta_4 = 3/2$, $\eta_4 = 7/4$, $\gamma_1 = 5$, $\gamma_2 = 10$, $\gamma_3 = 15$, $\gamma_4 = 25$, $\beta_1 = 5/4$, $\beta_2 = 7/4$, $\beta_3 = 9/4$, $\beta_4 = 11/4$.

With the given values of the parameters involved, we find that

$$\begin{aligned}
\lambda &= \left(T^{n-1} - \sum_{i=1}^m \gamma_i \frac{\left(\eta_i^{\beta_i+n-1} - \zeta_i^{\beta_i+n-1}\right)\Gamma(n)}{\Gamma(\beta_i+n)} \right) \\
&\simeq 9.334784, \\
\Lambda &= \frac{T^q}{\Gamma(q+1)} + \frac{T^{q+n-1}}{|\lambda|\,\Gamma(q+1)} + \frac{T^{n-1}}{|\lambda|} \sum_{i=1}^m \gamma_i \frac{\eta_i^{q+\beta_i} - \zeta_i^{q+\beta_i}}{\Gamma(q+\beta_i+1)} \\
&\simeq 1.406972.
\end{aligned} \tag{20}$$

Let us choose

$$f(t,x(t)) = \frac{1}{\sqrt[3]{(t+8)}} \left(\tan^{-1} x\right) + \sqrt{4 + 3\sin 2t}. \tag{21}$$

Clearly $L = 1/2$ as $|f(t,x) - f(t,y)| \leq (1/2)|x-y|$ and $L < 1/\Lambda$, where $\Lambda \simeq 1.406972$. Therefore all the conditions of Theorem 4 hold and consequently there exists a unique solution for the problem (19) with $f(t,x(t))$ given by (21).

In case of the following unbounded nonlinear function:

$$f(t,x(t)) = \frac{x}{7} + \frac{1}{\sqrt[3]{(t+8)}} \left(\tan^{-1} x\right) + \sqrt{4 + 3\sin 2t}, \tag{22}$$

we have $L = 9/14$ and $L < 1/\Lambda$ ($\Lambda \simeq 1.406972$). As before, the problem (19) with $f(t,x(t))$ given by (22) has a unique solution.

In the second result we use the Leray-Schauder alternative.

Theorem 6 ((Leray-Schauder alternative) [33, page 4]). *Let X be a Banach space. Assume that $T : X \to X$ is completely continuous operator and the set*

$$V = \{u \in X \mid u = \mu T u,\ 0 < \mu < 1\} \tag{23}$$

is bounded. Then T has a fixed point in X.

Theorem 7. *Assume that there exists a positive constant L_1 such that $|f(t,x)| \leq L_1$ for $t \in [0,T]$, $x \in \mathbb{R}$. Then the problem* (1) *has at least one solution.*

Proof. First of all, we show that the operator $\mathscr{P}$ is completely continuous. Note that the operator $\mathscr{P}$ is continuous in view

of the continuity of f. Let $\mathscr{B} \subset \mathscr{C}$ be a bounded set. By the assumption that $|f(t,x)| \le L_1$, for $x \in \mathscr{B}$, we have

$$\begin{aligned}
&|(\mathscr{P}x)(t)| \\
&\le \frac{1}{\Gamma(q)}\int_0^t (t-s)^{q-1}\left|f(s,x(s))\right| ds \\
&\quad + \frac{t^{n-1}}{|\lambda|\Gamma(q)}\int_0^T (T-s)^{q-1}\left|f(s,x(s))\right| ds \\
&\quad + \frac{t^{n-1}}{|\lambda|\Gamma(q)}\sum_{i=1}^m \frac{\gamma_i}{\Gamma(\beta_i)} \\
&\qquad \times \left[\int_0^{\eta_i}\int_0^s (\eta_i - s)^{\beta_i-1}(s-u)^{q-1} \right. \\
&\qquad\qquad \times \left|f(u,x(u))\right| du\, ds \\
&\qquad - \int_0^{\zeta_i}\int_0^s (\zeta_i - s)^{\beta_i-1}(s-u)^{q-1} \\
&\qquad\qquad \left. \times \left|f(u,x(u))\right| du\, ds\right] \\
&\le L_1\left[\frac{1}{\Gamma(q)}\int_0^t (t-s)^{q-1}ds + \frac{t^{n-1}}{|\lambda|\Gamma(q)}\int_0^t (T-s)^{q-1}ds \right. \\
&\quad + \frac{t^{n-1}}{|\lambda|\Gamma(q)}\sum_{i=1}^m \frac{\gamma_i}{\Gamma(\beta_i)} \\
&\qquad \times \left[\int_0^{\eta_i}\int_0^s (\eta_i - s)^{\beta_i-1} \right. \\
&\qquad\qquad \times (s-u)^{q-1} du\, ds \\
&\qquad - \int_0^{\zeta_i}\int_0^s (\zeta_i - s)^{\beta_i-1} \\
&\qquad\qquad \left.\left. \times (s-u)^{q-1} du\, ds\right]\right] \\
&\le L_1\left\{\frac{T^q}{\Gamma(q+1)} + \frac{T^{q+n-1}}{|\lambda|\Gamma(q+1)} \right. \\
&\quad \left. + \frac{T^{n-1}}{|\lambda|}\sum_{i=1}^m \gamma_i \frac{\eta_i^{q+\beta_i} - \zeta_i^{q+\beta_i}}{\Gamma(q+\beta_i+1)}\right\} = L_2,
\end{aligned} \tag{24}$$

which implies that $\|(\mathscr{P}x)\| \le L_2$. Further, we find that

$$\begin{aligned}
&\left|(\mathscr{P}x)'(t)\right| \\
&= \frac{1}{\Gamma(q-1)}\int_0^t (t-s)^{q-2}\left|f(s,x(s))\right| ds \\
&\quad + \frac{(n-1)t^{n-2}}{|\lambda|\Gamma(q)}\int_0^T (T-s)^{q-1}\left|f(s,x(s))\right| ds \\
&\quad + \frac{(n-1)t^{n-2}}{|\lambda|\Gamma(q)} \\
&\quad \times \sum_{i=1}^m \frac{\gamma_i}{\Gamma(\beta_i)}\left[\int_0^{\eta_i}\int_0^s (\eta_i - s)^{\beta_i-1}(s-u)^{q-1} \right. \\
&\qquad\qquad \times \left|f(u,x(u))\right| du\, ds \\
&\qquad - \int_0^{\zeta_i}\int_0^s (\zeta_i - s)^{\beta_i-1}(s-u)^{q-1} \\
&\qquad\qquad \left. \times \left|f(u,x(u))\right| du\, ds\right] \\
&\le L_1\left[\frac{1}{\Gamma(q-1)}\int_0^t (t-s)^{q-2}ds \right. \\
&\quad + \frac{(n-1)t^{n-2}}{|\lambda|\Gamma(q)}\int_0^T (T-s)^{q-1}ds \\
&\quad + \frac{(n-1)t^{n-2}}{|\lambda|\Gamma(q)} \\
&\quad \times \sum_{i=1}^m \frac{\gamma_i}{\Gamma(\beta_i)}\left(\int_0^{\eta_i}\int_0^s (\eta_i - s)^{\beta_i-1} \right. \\
&\qquad\qquad \times (s-u)^{q-1} \\
&\qquad\qquad \times \left|f(u,x(u))\right| du\, ds \\
&\qquad - \int_0^{\zeta_i}\int_0^s (\zeta_i - s)^{\beta_i-1} \\
&\qquad\qquad \times (s-u)^{q-1} \\
&\qquad\qquad \times \left|f(u,x(u))\right| \\
&\qquad\qquad \left.\left. \times\ du\, ds\right)\right] \\
&\le L_1\left\{\frac{T^{q-1}}{\Gamma(q)} + \frac{(n-1)T^{q+n-2}}{|\lambda|\Gamma(q+1)} \right. \\
&\quad \left. + \frac{(n-1)T^{n-2}}{|\lambda|}\sum_{i=1}^m \gamma_j \frac{\eta_i^{q+\beta_i} - \zeta_i^{q+\beta_i}}{\Gamma(q+\beta_i+1)}\right\} = L_3.
\end{aligned} \tag{25}$$

Hence, for $t_1, t_2 \in [0,T]$, we have

$$\left|(\mathscr{P}x)(t_2) - (\mathscr{P}x)(t_1)\right| \le \int_{t_1}^{t_2}\left|(\mathscr{P}x)'(s)\right| ds \le L_3(t_2 - t_1). \tag{26}$$

This implies that $\mathscr{P}$ is equicontinuous on $[0,T]$. Thus, by the Arzelá-Ascoli theorem, the operator $\mathscr{P} : \mathscr{C} \to \mathscr{C}$ is completely continuous.

Next, we consider the set

$$V = \{x \in \mathscr{C} \mid x = \mu\mathscr{P}x,\ 0 < \mu < 1\}, \tag{27}$$

and show that the set V is bounded. Let $x \in V$, then $x = \mu\mathscr{P}x, 0 < \mu < 1$. For any $t \in [0,T]$, we have

$$\begin{aligned}
|x(t)| &= \mu\left|(\mathscr{P}x)(t)\right| \\
&\le \frac{1}{\Gamma(q)}\int_0^t (t-s)^{q-1}\left|f(s,x(s))\right| ds \\
&\quad + \frac{t^{n-1}}{|\lambda|\Gamma(q)}\int_0^T (T-s)^{q-1}\left|f(s,x(s))\right| ds \\
&\quad + \frac{t^{n-1}}{|\lambda|\Gamma(q)}\sum_{i=1}^m \frac{\gamma_i}{\Gamma(\beta_i)} \\
&\qquad \times\left[\int_0^{\eta_i}\int_0^s (\eta_i - s)^{\beta_i-1}(s-u)^{q-1}\right. \\
&\qquad\qquad \times\left|f(u,x(u))\right| du\, ds \\
&\qquad - \int_0^{\zeta_i}\int_0^s (\zeta_i - s)^{\beta_i-1}(s-u)^{q-1} \\
&\qquad\qquad \left.\times\left|f(u,x(u))\right| du\, ds\right] \\
&\le L_1\left\{\frac{T^q}{\Gamma(q+1)} + \frac{T^{q+n-1}}{|\lambda|\Gamma(q+1)}\right. \\
&\qquad \left. + \frac{T^{n-1}}{|\lambda|}\sum_{i=1}^m \gamma_i \frac{\eta_i^{q+\beta_i} - \zeta_i^{q+\beta_i}}{\Gamma(q+\beta_i+1)}\right\} = M_1.
\end{aligned} \tag{28}$$

Thus, $\|x\| \le M_1$ for any $t \in [0,T]$. So, the set V is bounded. Thus, by the conclusion of Theorem 6, the operator $\mathscr{P}$ has at least one fixed point, which implies that (1) has at least one solution. □

Example 8. Consider the boundary value problem of Example 5 with

$$f(t,x(t)) = \frac{3e^{\sqrt{(2-|x(t)|)^3}}\left[\cos 4t + 2\ln\left(1 + 4\sin^2 x(t)\right)\right]}{\sqrt{(10+\cos x(t))}}. \tag{29}$$

Observe that $|f(t,x)| \le L_1$ with $L_1 = e^{2\sqrt{2}}(1+\ln 25)$. Thus the hypothesis of Theorem 7 is satisfied. Hence by the conclusion of Theorem 7, the problem (19) with $f(t,x(t))$ given by (29) has at least one solution.

In the next we prove one more existence result for problem (1), based on the following known result.

Theorem 9 (see [34]). *Let X be a Banach space. Assume that Ω is an open bounded subset of X with $\theta \in \Omega$ and let $T : \overline{\Omega} \to X$ be a completely continuous operator such that*

$$\|Tu\| \le \|u\|, \quad \forall u \in \partial\Omega. \tag{30}$$

Then T has a fixed point in $\overline{\Omega}$.

Theorem 10. *Let there exist a small positive number τ such that $|f(t,x)| \le \nu|x|$ for $0 < |x| < \tau$, with $0 < \nu \le 1/\Lambda$, where Λ is given by* (14). *Then the problem* (1) *has at least one solution.*

Proof. Let us define $\mathscr{B}_\tau = \{x \in \mathscr{C} \mid \|x\| < \tau\}$ and take $x \in \mathscr{C}$ such that $\|x\| = \tau$, that is, $x \in \partial\mathscr{B}_\tau$. As before, it can be shown that $\mathscr{P}$ is completely continuous and

$$\begin{aligned}
\|\mathscr{P}x\| &\le \sup_{t\in[0,t]}\left\{\frac{1}{\Gamma(q)}\int_0^t (t-s)^{q-1}\left|f(s,x(s))\right| ds\right. \\
&\qquad + \frac{t^{n-1}}{|\lambda|\Gamma(q)} \\
&\qquad \times\int_0^T (T-s)^{q-1}\left|f(s,x(s))\right| ds \\
&\qquad + \frac{t^{n-1}}{|\lambda|\Gamma(q)} \\
&\qquad \times\sum_{i=1}^m \frac{\gamma_i}{\Gamma(\beta_i)} \\
&\qquad\quad \times\left[\int_0^{\eta_i}\int_0^s (\eta_i - s)^{\beta_i-1}(s-u)^{q-1}\right. \\
&\qquad\qquad \times\left|f(u,x(u))\right| du\, ds \\
&\qquad\quad - \int_0^{\zeta_i}\int_0^s (\zeta_i - s)^{\beta_i-1}(s-u)^{q-1} \\
&\qquad\qquad \left.\left.\times\left|f(u,x(u))\right| du\, ds\right]\right\} \\
&\le \Lambda\nu\|x\|,
\end{aligned} \tag{31}$$

which in view of the given condition ($\nu\Lambda \le 1$), gives $\|\mathscr{P}x\| \le \|x\|$, $x \in \partial\mathscr{B}_\tau$. Therefore, by Theorem 9, the operator $\mathscr{P}$ has at least one fixed point, which in turn implies that the problem (1) has at least one solution. □

Example 11. Consider the boundary value problem of Example 5 and let us consider

$$\begin{aligned}
f(t,x(t)) &= x\left(b^5 + x^4(t)\right)^{1/5} + 2\left(1+\cos\left(t^4+3\right)\right)^5 \\
&\quad \times(1-\cos x(t)), \quad x \ne 0,\ b > 0.
\end{aligned} \tag{32}$$

For sufficiently small x (ignoring x^2 and higher powers of x), we have

$$\begin{aligned}
&\left|x\left(b^5 + x^4(t)\right)^{1/5} + 2\left(1+\cos\left(t^4+3\right)\right)^5(1-\cos x(t))\right| \\
&\quad \le b|x|.
\end{aligned} \tag{33}$$

Choosing $b \le 1/\Lambda$, all the assumptions of Theorem 10 hold. Therefore, the conclusion of Theorem 10 implies that the

problem (19) with $f(t,x(t))$ given by (32) has at least one solution.

Our final existence result is based on Leray-Schauder nonlinear alternative.

Lemma 12 ((Nonlinear alternative for single valued maps) [33, page 135]). *Let E be a Banach space, C a closed, convex subset of E, U an open subset of C and $0 \in U$. Suppose that $F : \overline{U} \to C$ is a continuous, compact (i.e., $F(\overline{U})$ is a relatively compact subset of C) map. Then either*

(i) *F has a fixed point in $\overline{U}$, or*

(ii) *there is a $u \in \partial U$ (the boundary of U in C) and $\lambda \in (0,1)$ with $u = \lambda F(u)$.*

Theorem 13. *Assume that*

(A_1) *there exist a function $\sigma \in C([0,1],\mathbb{R}^+)$, and a nondecreasing function $\psi : \mathbb{R}^+ \to \mathbb{R}^+$ such that $|f(t,x)| \le \sigma(t)\psi(\|x\|)$, for all $(t,x) \in [0,T] \times \mathbb{R}$;*

(A_2) *there exists a constant $M > 0$ such that*

$$\frac{M}{\psi(M)\Lambda\|\sigma\|} > 1. \tag{34}$$

Then the boundary value problem (1) *has at least one solution on* $[0,T]$.

Proof. Consider the operator $\mathscr{P} : \mathscr{C} \to \mathscr{C}$ defined by (13). We show that $\mathscr{P}$ *maps bounded sets into bounded sets in* $C([0,T],\mathbb{R})$. For a positive number r, let $B_r = \{x \in C([0,T],\mathbb{R}) : \|x\| \le r\}$ be a bounded set in $C([0,T],\mathbb{R})$. Then

$$\begin{aligned}
\|\mathscr{P}x\| \le \sup_{t\in[0,T]} \Bigg\{ & \frac{1}{\Gamma(q)} \int_0^t (t-s)^{q-1} \left|f(s,x(s))\right| ds \\
& + \frac{t^{n-1}}{|\lambda|\Gamma(q)} \int_0^T (T-s)^{q-1} \left|f(s,x(s))\right| ds \\
& + \frac{t^{n-1}}{|\lambda|\Gamma(q)} \times \sum_{i=1}^m \frac{\gamma_i}{\Gamma(\beta_i)} \\
& \times \Bigg[\int_0^{\eta_i} \int_0^s (\eta_i - s)^{\beta_i - 1} \times (s-u)^{q-1} \times \left|f(u,x(u))\right| du\, ds \\
& - \int_0^{\zeta_i} \int_0^s (\zeta_i - s)^{\beta_i - 1} \times (s-u)^{q-1} \times \left|f(u,x(u))\right| \times du\, ds \Bigg] \Bigg\} \\
\le \psi(r) \Bigg\{ & \frac{T^q}{\Gamma(q+1)} + \frac{T^{q+n-1}}{|\lambda|\Gamma(q+1)} \\
& + \frac{T^{n-1}}{|\lambda|} \sum_{i=1}^m \gamma_i \frac{\eta_i^{q+\beta_i} - \zeta_i^{q+\beta_i}}{\Gamma(q+\beta_i+1)} \Bigg\} \|\sigma\|.
\end{aligned} \tag{35}$$

Next we show that F *maps bounded sets into equicontinuous sets of* $C([0,1],\mathbb{R})$. Let $t', t'' \in [0,1]$ with $t' < t''$ and $x \in B_r$, where B_r is a bounded set of $C([0,1],\mathbb{R})$. Then we obtain

$$\begin{aligned}
& \left|(\mathscr{P}x)(t'') - (\mathscr{P}x)(t')\right| \\
& = \Bigg| \frac{1}{\Gamma(q)} \int_0^{t''} (t''-s)^{q-1} f(s,x(s))\, ds \\
& \quad - \frac{1}{\Gamma(q)} \int_0^{t'} (t'-s)^{q-1} f(s,x(s))\, ds \\
& \quad - \frac{\left[(t'')^{n-1} - (t')^{n-1}\right]}{\lambda\Gamma(q)} \int_0^T (T-s)^{q-1} f(s,x(s))\, ds \\
& \quad + \frac{\left[(t'')^{n-1} - (t'')^{n-1}\right]}{\lambda\Gamma(q)} \\
& \quad \times \sum_{i=1}^m \frac{\gamma_i}{\Gamma(\beta_i)} \Bigg[\int_0^{\eta_i} \int_0^s (\eta_i - s)^{\beta_i - 1} (s-u)^{q-1} \times \left|f(u,x(u))\right| du\, ds \\
& \qquad - \int_0^{\zeta_i} \int_0^s (\zeta_i - s)^{\beta_i - 1} (s-u)^{q-1} \times \left|f(u,x(u))\right| du\, ds \Bigg] \Bigg| \\
& \le \frac{1}{\Gamma(q)} \int_0^{t'} \left|(t''-s)^{q-1} - (t'-s)^{q-1}\right| \psi(r)\sigma(s)\, ds \\
& \quad + \frac{1}{\Gamma(q)} \int_{t'}^{t''} \left|t''-s\right|^{q-1} \psi(r)\sigma(s)\, ds \\
& \quad + \frac{\left|(t'')^{n-1} - (t')^{n-1}\right|}{|\lambda|\Gamma(q)} \int_0^T |T-s|^{q-1} \psi(r)\sigma(s)\, ds \\
& \quad + \frac{\left|(t'')^{n-1} - (t')^{n-1}\right|}{|\lambda|\Gamma(q)} \\
& \quad \times \sum_{i=1}^m \frac{\gamma_i}{\Gamma(\beta_i)} \Bigg[\int_0^{\eta_i} \int_0^s (\eta_i - s)^{\beta_i - 1} (s-u)^{q-1} du\, \psi(r)\sigma(s)\, ds \\
& \qquad - \int_0^{\zeta_i} \int_0^s (\zeta_i - s)^{\beta_i - 1} (s-u)^{q-1} \psi(r)\sigma(s)\, du\, ds \Bigg].
\end{aligned} \tag{36}$$

Obviously the right hand side of the above inequality tends to zero independently of $x \in B_r$ as $t'' - t' \to 0$. As $\mathscr{P} : C([0,T],\mathbb{R}) \to C([0,T],\mathbb{R})$ satisfies the above assumptions, therefore it follows by the Arzelá-Ascoli theorem that $\mathscr{P}$ is completely continuous.

Let x be a solution. Then, for $t \in [0,T]$, and following the similar computations as before, we find that

$$\begin{aligned} |x(t)| &= |\mu(\mathscr{P}x)(t)| \\ &\le \psi(r)\left\{\frac{T^q}{\Gamma(q+1)} + \frac{T^{q+n-1}}{|\lambda|\Gamma(q+1)}\right. \\ &\quad \left. + \frac{T^{n-1}}{|\lambda|}\sum_{i=1}^{m}\gamma_i\frac{\eta_i^{q+\beta_i} - \zeta_i^{q+\beta_i}}{\Gamma(q+\beta_i+1)}\right\}\|\sigma\|. \end{aligned} \tag{37}$$

In consequence, we have

$$\frac{\|x\|}{\psi(\|x\|)\Lambda\|\sigma\|} \le 1. \tag{38}$$

Thus, by (A_2), there exists M such that $\|x\| \ne M$. Let us set

$$V = \{x \in C([0,T],\mathbb{R}) : \|x\| < M+1\}. \tag{39}$$

Note that the operator $\mathscr{P} : \overline{V} \to C([0,T],\mathbb{R})$ is continuous and completely continuous. From the choice of V, there is no $x \in \partial V$ such that $x = \mu\mathscr{P}(x)$ for some $\mu \in (0,1)$. Consequently, by the nonlinear alternative of Leray-Schauder type (Lemma 12), we deduce that $\mathscr{P}$ has a fixed point $x \in \overline{V}$ which is a solution of the problem (1). This completes the proof. □

Example 14. Consider the boundary value problem of Example 5 with

$$f(t,x(t)) = \frac{1}{\sqrt{t+4}}\left(1 + \frac{|x|}{1+|x|}\right) \le \sigma(t)\psi(\|x\|). \tag{40}$$

Then $\sigma(t) = 1/\sqrt{t+4}$ and $\psi(\|x\|) = 2$. Using $\|\sigma\| = 1/2$, $\Lambda \simeq 1.406972$, we find by the condition (A_2) that $M > \Lambda$. Thus all the assumptions of Theorem 13 are satisfied. Hence, it follows by Theorem 13 that the problem (19) with $f(t,x(t))$ defined by (40) has at least one solution.

If we choose an unbounded nonlinearity as follows:

$$f(t,x(t)) = \frac{1}{\sqrt{t+4}}\left(1 + \frac{|x|}{1+|x|} + \frac{|x|}{2}\right). \tag{41}$$

Then $f(t,x(t)) \le \sigma(t)\psi(\|x\|)$ with $\sigma(t) = 1/\sqrt{t+4}$ and $\psi(\|x\|) = 2 + \|x\|/2$. Using the earlier arguments, with $\|\sigma\| = 1/2$, $\Lambda \simeq 1.406972$, we find that $M > M_1$, $M_1 \approx 2.170392$. Hence the problem (19) with $f(t,x(t))$ given by (41) has at least one solution.

Acknowledgment

The authors are grateful to the anonymous referees for their valuable comments.

References

[1] K. S. Miller and B. Ross, *An Introduction to the Fractional Calculus and Differential Equations*, A Wiley-Interscience Publication, John Wiley & Sons, New York, NY, USA, 1993.

[2] S. G. Samko, A. A. Kilbas, and O. I. Marichev, *Fractional Integrals and Derivatives*, Gordon and Breach Science Publishers, Yverdon, Switzerland, 1993.

[3] I. Podlubny, *Fractional Differential Equations*, vol. 198 of *Mathematics in Science and Engineering*, Academic Press, San Diego, Calif, USA, 1999.

[4] A. A. Kilbas, H. M. Srivastava, and J. J. Trujillo, *Theory and Applications of Fractional Differential Equations*, vol. 204 of *North-Holland Mathematics Studies*, Elsevier Science B.V., Amsterdam, The Netherlands, 2006.

[5] V. Lakshmikantham, S. Leela, and J. V. Devi, *Theory of Fractional Dynamic Systems*, Cambridge Academic, Cambridge, UK, 2009.

[6] D. Baleanu, K. Diethelm, E. Scalas, and J. J. Trujillo, *Fractional Calculus Models and Numerical Methods*, vol. 3 of *Series on Complexity, Nonlinearity and Chaos*, World Scientific, Boston, Mass, USA, 2012.

[7] M. Benchohra, S. Hamani, and S. K. Ntouyas, "Boundary value problems for differential equations with fractional order and nonlocal conditions," *Nonlinear Analysis: Theory, Methods & Applications*, vol. 71, no. 7-8, pp. 2391–2396, 2009.

[8] R. P. Agarwal, M. Benchohra, and S. Hamani, "A survey on existence results for boundary value problems of nonlinear fractional differential equations and inclusions," *Acta Applicandae Mathematicae*, vol. 109, no. 3, pp. 973–1033, 2010.

[9] K. Balachandran and J. J. Trujillo, "The nonlocal Cauchy problem for nonlinear fractional integrodifferential equations in Banach spaces," *Nonlinear Analysis: Theory, Methods & Applications*, vol. 72, no. 12, pp. 4587–4593, 2010.

[10] D. Băleanu and O. G. Mustafa, "On the global existence of solutions to a class of fractional differential equations," *Computers & Mathematics with Applications*, vol. 59, no. 5, pp. 1835–1841, 2010.

[11] W. Zhong and W. Lin, "Nonlocal and multiple-point boundary value problem for fractional differential equations," *Computers & Mathematics with Applications*, vol. 59, no. 3, pp. 1345–1351, 2010.

[12] V. Gafiychuk and B. Datsko, "Mathematical modeling of different types of instabilities in time fractional reaction-diffusion systems," *Computers & Mathematics with Applications*, vol. 59, no. 3, pp. 1101–1107, 2010.

[13] B. Ahmad and J. J. Nieto, "Riemann-Liouville fractional integro-differential equations with fractional nonlocal integral boundary conditions," *Boundary Value Problems*, vol. 2011, article 36, 9 pages, 2011.

[14] B. Ahmad and S. K. Ntouyas, "A four-point nonlocal integral boundary value problem for fractional differential equations of arbitrary order," *Electronic Journal of Qualitative Theory of Differential Equations*, vol. 2011, no. 22, 15 pages, 2011.

[15] C. Cuevas, H. Soto, and A. Sepúlveda, "Almost periodic and pseudo-almost periodic solutions to fractional differential and integro-differential equations," *Applied Mathematics and Computation*, vol. 218, no. 5, pp. 1735–1745, 2011.

[16] N. J. Ford and M. L. Morgado, "Fractional boundary value problems: analysis and numerical methods," *Fractional Calculus and Applied Analysis*, vol. 14, no. 4, pp. 554–567, 2011.

[17] B. Ahmad and S. K. Ntouyas, "A note on fractional differential equations with fractional separated boundary conditions,"

Abstract and Applied Analysis, vol. 2012, Article ID 818703, 11 pages, 2012.

[18] A. Aghajani, Y. Jalilian, and J. J. Trujillo, "On the existence of solutions of fractional integro-differential equations," *Fractional Calculus and Applied Analysis*, vol. 15, no. 1, pp. 44–69, 2012.

[19] W. Sudsutad and J. Tariboon, "Existence results of fractional integro-differential equations with m-point multi-term fractional order integral boundary conditions," *Boundary Value Problems*, vol. 2012, article 94, 2012.

[20] B. Ahmad and S. K. Ntouyas, "Existence results for nonlocal boundary value problems of fractional differential equations and inclusions with strip conditions," *Boundary Value Problems*, vol. 2012, article 55, 2012.

[21] B. Ahmad and J. J. Nieto, "Riemann-liouville fractional differential equations with fractional boundary conditions," *Fixed Point Theory*, vol. 13, pp. 329–336, 2012.

[22] B. Ahmad, J. J. Nieto, A. Alsaedi, and M. El-Shahed, "A study of nonlinear Langevin equation involving two fractional orders in different intervals," *Nonlinear Analysis: Real World Applications*, vol. 13, no. 2, pp. 599–606, 2012.

[23] A. Cabada and G. Wang, "Positive solutions of nonlinear fractional differential equations with integral boundary value conditions," *Journal of Mathematical Analysis and Applications*, vol. 389, no. 1, pp. 403–411, 2012.

[24] B. Ahmad, T. Hayat, and S. Asghar, "Diffraction of a plane wave by an elastic knife-edge adjacent to a rigid strip," *The Canadian Applied Mathematics Quarterly*, vol. 9, no. 4, pp. 303–316, 2001.

[25] S. Asghar, B. Ahmad, and M. Ayub, "Diffraction from an absorbing half plane due to a finite cylindrical source," *Acustica-Acta Acustica*, vol. 82, pp. 365–367, 1996.

[26] G. S. Wang and A. F. Blom, "A strip model for fatigue crack growth predictions under general load conditions," *Engineering Fracture Mechanics*, vol. 40, no. 3, pp. 507–533, 1991.

[27] H. Jiang, F. Liu, I. Turner, and K. Burrage, "Analytical solutions for the multi-term time-space Caputo-Riesz fractional advection-diffusion equations on a finite domain," *Journal of Mathematical Analysis and Applications*, vol. 389, no. 2, pp. 1117–1127, 2012.

[28] E. Yusufoglu and I. Turhan, "A mixed boundary value problem in orthotropic strip containing a crack," *Journal of the Franklin Institute*, vol. 349, no. 9, pp. 2750–2769, 2012.

[29] Dh. Chang and A. Kotousov, "A strip yield model for two collinear cracks," *Engineering Fracture Mechanics*, vol. 90, pp. 121–128, 2012.

[30] B. Lebental and F. Bourquin, "Visco-acoustic modelling of a vibrating plate interacting with water confined in a domain of micrometric size," *Journal of Sound and Vibration*, vol. 331, no. 8, pp. 1870–1886, 2012.

[31] T. V. Renterghem, D. Botteldooren, and K. Verheyen, "Road traffic noise shielding by vegetation belts of limited depth," *Journal of Sound and Vibration*, vol. 331, no. 10, pp. 2404–2425, 2012.

[32] J. Poblet-Puig and A. Rodrguez-Ferran, "Modal-based prediction of sound transmission through slits and openings between rooms," *Journal of Sound and Vibration*, vol. 332, pp. 1265–1287, 2012.

[33] A. Granas and J. Dugundji, *Fixed Point Theory*, Springer Monographs in Mathematics, Springer, New York, NY, USA, 2005.

[34] D. R. Smart, *Fixed Point Theorems*, Cambridge University Press, Cambridge, UK, 1980.

Hindawi Publishing Corporation
Mathematical Problems in Engineering
Volume 2013, Article ID 408232, 9 pages
http://dx.doi.org/10.1155/2013/408232

Research Article

A Novel Image Fusion Method Based on FRFT-NSCT

Peiguang Wang, Hua Tian, and Wei Zheng

College of Electronic and Information Engineering, Hebei University, Baoding 071002, China

Correspondence should be addressed to Hua Tian; h_h_tian5@163.com

Received 9 November 2012; Accepted 12 January 2013

Academic Editor: József Kázmér Tar

Nonsubsampled Contourlet transform (NSCT) has properties such as multiscale, localization, multidirection, and shift invariance, but only limits the signal analysis to the time frequency domain. Fractional Fourier transform (FRFT) develops the signal analysis to fractional domain, has many super performances, but is unable to attribute the signal partial characteristic. A novel image fusion algorithm based on FRFT and NSCT is proposed and demonstrated in this paper. Firstly, take FRFT on the two source images to obtain fractional domain matrices. Secondly, the NSCT is performed on the aforementioned matrices to acquire multiscale and multidirection images. Thirdly, take fusion rule for low-frequency subband coefficients and directional bandpass subband coefficients to get the fused coefficients. Finally, the fused image is obtained by performing the inverse NSCT and inverse FRFT on the combined coefficients. Three modes images and three fusion rules are demonstrated in the proposed algorithm test. The simulation results show that the proposed fusion approach is better than the methods based on NSCT at the same parameters.

1. Introduction

Image fusion is synthesizing two or more images of the same object, which come from different sensors, into a new image. The new image can describe the object more accurately and more comprehensively. Image fusion has been widely used in military, remote sensing, robot vision, medical image processing, and other areas. Along with the developing of mathematical tools and fusion rules, the image fusion methods are continually renewing. Recently, various fusion methods based on multiscale transforms (MSTs) have been proposed and some satisfactory results have been obtained (i.e., Pyramid, Wavelet, etc.). These multiscale methods can decompose the image into low-frequency subbands and high-frequency subbands, detailed and coarse features remain in the two types of subbands; and then process separately in different subbands for different demands [1, 2]. MST-based image fusion methods provide much better performance than the previous simple methods. At present the discrete wavelet transform becomes the most popular multiscale method in image fusion because of its good local characteristics at the spatial domain and frequency domain [3, 4]. However, the wavelet transform has limitations such as limited directions (only three directions, horizontal, vertical, diagonal) and nonoptimal-sparse representation of images. In order to solve these limitations, the new multiscale transforms (i.e., Curvelet, Contourlet, etc.) are introduced in image fusion [5, 6].

Do and Vetterli proposed a multidirection and multiresolution image expression method, namely, Contourlet transform in 2002 [7]. This transformation has good direction sensitivity, the anisotropy, and can catch accurately the image edge information. In comparison with the wavelet transform, Contourlet transform has stronger power of expression image geometry characteristic. Therefore the Contourlet transform suits two-dimensional image processing, such as image enhancement, image denoising, and so forth. It can obtain better effect than the wavelet transform; Miao and Wang applied the Contourlet transform in the image fusion [8]. However, because of the need for up sampler and down sampler, the Contourlet transform lacks the shift invariance, which usually causes the Gibbs effect. A. L. da Cunha et al. proposed a new Contourlet transform with the shift invariance, called Nonsubsampled Contourlet transform (NSCT) in 2006 [9]. In NSCT nonsubsample filter banks replace the up sampler and down sampler as filter banks to obtain the shift invariance. Because of these advantages such as multiscale, multi-directions, good spatial and frequency

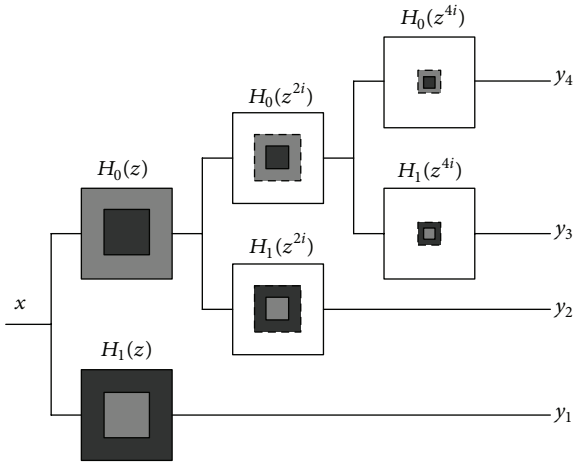

Figure 1: NSP framework.

localization, and shift invariance, many image fusion methods based on NSCT have been proposed and provided with high performance [10, 11].

The fractional Fourier transform (FRFT) is a new transformation which develops the signal analysis into fractional time-frequency domain. It is a revolving operation of the signal Wigner distribution, and it revolves the Fourier transform or the angle Fourier transform. The introduction of the parameter p, the order of the FRFT, strengthens the transform's flexibility. The parameter p varies from 0 to 1, and the signal is moved from time domain to frequency domain. FRFT can reflect the signal information in the time domain and the frequency domain simultaneously, so essentially it is a kind of unified time frequency transformation [12–15]. FRFT retains all characteristics of Fourier transform and also has some important properties which the traditional Fourier transform does not have. FRFT has been used in the field of communication, the SAR data processing, and the image processing. Furthermore new algorithms based on FRFT, such as fractional wavelet transform (FRWT), have been employed in signal processing field [16–18].

Nonsubsampled Contourlet transform (NSCT) has properties such as multiscale, localization, multi-direction, and shift invariance, which, however, only limits the signal analysis to the time frequency domain. Fractional Fourier transform (FRFT) develops the signal analysis to fractional domain and has many super performances but is unable to attribute the signal partial characteristic. Combining the merits of NSCT and FRFT to meet the high demands, a novel kind of image fusion algorithm based on FRFT-NSCT is proposed in this paper. The related theories and the flow charts of the fusion algorithm are introduced in Section 2. The experimental results and analyses for three modes images and three fusion rules are presented in Section 3 and the conclusions are given in Section 4.

2. Image Fusion Based on FRFT-NSCT

2.1. Nonsubsampled Contourlet Transform (NSCT). The NSCT is a shift invariant version of the Contourlet transform.

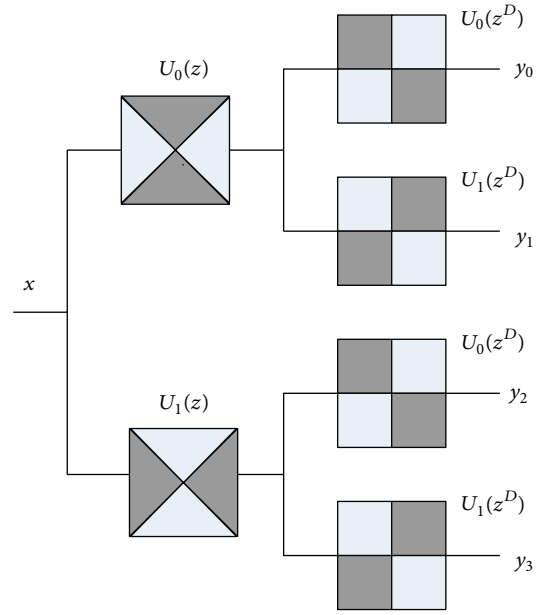

Figure 2: NSDFB framework.

The Contourlet transform employs Laplacian pyramids (LPs) for multiscale decomposition and directional filter banks (DFBs) for directional decomposition. To achieve shift invariance, the NSCT is built upon nonsubsampled pyramids (NSPs) and nonsubsampled directional filter banks (NSDFBs). The NSP is a two-channel nonsubsampled filter bank and has no downsampling or upsampling, and hence it is shift invariant. The multiscale decomposition is achieved by iterating using the nonsubsampled filter banks. Such expansion has $J+1$ redundancy, where J denotes the number of decomposition levels. For the next level, all filters are upsampled by 2 in both dimensions. The cascading of the analysis part is shown in Figure 1 [19, 20].

The equivalent filters of a kth level cascading NSP are given by

$$H_n^{\mathrm{eq}}(z) = \begin{cases} H_1\left(z^{2^{n-1}I}\right)\prod_{j=0}^{n-2} H_0\left(z^{2^j I}\right) & 1 \le n < k, \\ \prod_{j=0}^{n-2} H_0\left(z^{2^j I}\right) & n = k+1. \end{cases} \tag{1}$$

The NSDFB is a shift-invariant version of the critically sampled DFB in the Contourlet transform. The building block of a NSDFB is also a two-channel nonsubsampled filter bank. To obtain finer directional decomposition, the NSDFBs are iterated. For the next level, all filters are upsampled by a quincunx matrix given by $D = \left[\begin{smallmatrix} 1 & 1 \\ 1 & -1 \end{smallmatrix}\right]$. Figure 2 illustrates four-channel ecomposition with two-channel fan filter banks.

The equivalent filter in each channel is given by

$$U_k^{\mathrm{eq}}(z) = U_i(z)\, U_j\left(z^D\right). \tag{2}$$

The NSCT is obtained by combining the 2D NSP and the NSDFB as shown in Figure 3. If the building blocks of NSP

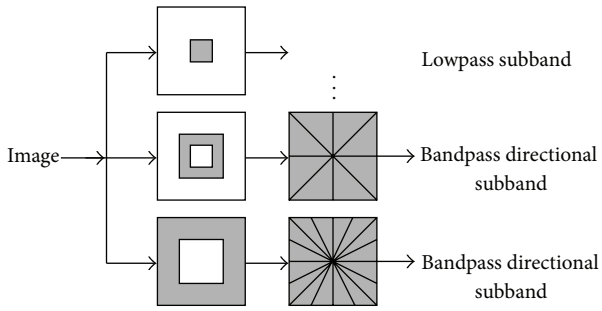

Figure 3: Decomposition framwork of the NSCT.

and the NSDFB are invertible, then the NSCT is invertible. The NSCT allows any number of 2^l directions in each scale, and then the NSCT has redundancy given by $1 + \sum_{j=1}^{J} 2^{lj}$, where lj denotes the number of levels in the NSDFB at the jth scale [20].

The NSCT is very suitable for image fusion because it has such important properties as multiresolution, localization, shift invariance, and multi-direction. Usually the process of image fusion based on NSCT includes the following: first, get the low-frequency and high-frequency components of all scales by using multiscale and multi-direction NSCT decomposition to the image A and image B separately, and then fuse them via different fusion rules to get the combined coefficients of the fused image, finally, the fused image can be obtained by using inverse NSCT.

2.2. Fractional Fourier Transform (FRFT). If $f(x) \in L^2(R)$, its p order FRFT is defined as

$$F_p(u) = \{F^p[f(x)]\}(u) = \int_{-\infty}^{\infty} K_p(u,x) f(x)\, dx, \quad (3)$$

where $K_p(u,x)$ is FRFT kernel function as follows:

$$K_p(u,x) = \begin{cases} \sqrt{\dfrac{1 - j\cot\alpha}{2\pi}} \\ \quad \times \exp\left[j\left(\dfrac{x^2+u^2}{2\tan\alpha} - \dfrac{xu}{\sin\alpha} \right)\right], & \alpha \neq n\pi \\ \delta(x-u), & \alpha = 2n\pi \\ \delta(x+u), & \alpha = (2n \pm 1)\pi, \end{cases} \quad (4)$$

where $a = p\pi/2$ is rotating angle, p is the order of the fractional Fourier transform, when $p \in [0,1]$, $a \in [0, \pi/2]$, $p \neq 2n$. If $p = 0$, FRFT is $f(x)$. If $p = 1$, FRFT is the conventional Fourier transform. The p order inverse fractional Fourier transform (IFRFT) is the FRFT with $-p$ order [21–24].

The data after performing FRFT contains both the time domain information and the frequency domain information. When p varies from 0 to 1 the signal FRFT result varies from the input function continuous transformation to the Fourier transformation. That indicates the process characteristic of signal changing from the time domain to frequency domain. FRFT introduces p into analysis processing, so it has some characteristics which the traditional Fourier transformation does not have, and develops the signal analysis scope. But from the above definition, we know FRFT is a kind of global transformation, so it is unable to give the signal local characteristics which are very important in the nonsteady signal processing.

2.3. FRFT-NSCT Fusion Method. Mendlovic et al. define the fractional wavelet transform (FRWT): performing a FRFT with the fractional order p over the entire input signal and then performing the conventional wavelet decomposition. For reconstruction, one should use the conventional inverse wavelet transform and then carry out a FRFT with the fractional order of $-p$ to return back to the plane of the input function [25].

According to this idea a new image fusion method based on FRFT-NSCT is proposed. First perform fractional Fourier transformation on two source images to obtain the fractional field transformation result, and then take nonsubsampled Contourlet transform (NSCT) on it to decompose to different frequency bands and directions, obtain the fused coefficients according to some fusion rules, and finally obtain the fused image through inverse nonsubsampled Contourlet transform (INSCT) and inverse fractional Fourier transform (IFRFT). The flowchart of the image fusion method based on FRFT-NSCT is illustrated in Figure 4. The final fused image qualities vary with the choice of the order p of FRFT, NSCT decomposition layer, pyramidal filter, directional filter, and fusion rules.

2.4. Objective Performance Evaluation. Human visual perception can help judge the effects of fusion results. However, it is easily influenced by visual psychological factors. The effect of image fusion should be based on subjective vision and objective quantitative evaluation criteria. Some objective evaluation merits, such as entropy, average gradient, and standard deviation, and so forth, are employed to describe the information contained in the fused images [26, 27].

(1) Information entropy (IE): the IE of the image is an important index to measure the abound degree of the image information. Based on the principle of Shannon information theory, the IE of the image is defined as

$$E = -\sum_{i=1}^{m} P_i \log_2 P_i, \quad (5)$$

where p_i is the ratio of the number of pixels with gray value equal to i over the total number of the pixels. IE reflects the capacity of the information carried by images. The larger the IE is, the more information the image carries.

(2) Average gradient (AG): AG is the index to reflect the expression ability of the little detail contrast and texture

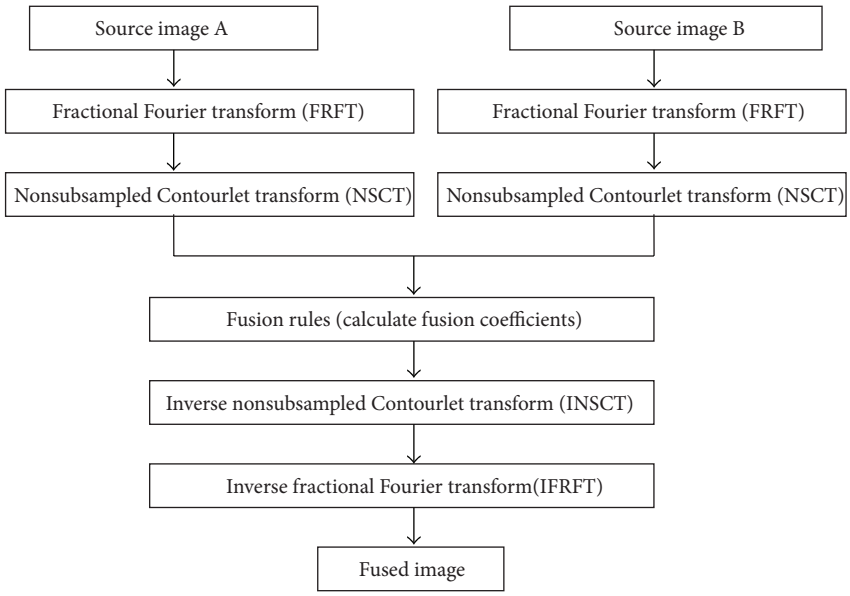

Figure 4: Flowchart of the FRFT-NSCT image fusion.

variation, and the definition of the image. It can be expressed as

$$\overline{G} = \frac{1}{(M-1)(N-1)} \times \sum_{i=1}^{M-1}\sum_{j=1}^{N-1}\sqrt{\frac{(F(i,j)-F(i+1,j))^2+(F(i,j)-F(i,j+1))^2}{2}}, \quad (6)$$

where $F(i, j)$ is the gray value of the pixel (i, j). Generally, the larger the average gradient, the clearer fusion image is.

3. Experiments and Results

3.1. Experimental Source Images. Without loss of generality, three groups of different pattern images, with the same size of 512×512, are employed in the following experiments.

(1) *Multifocus images.* Figures 5(a) and 5(b) illustrate a pair of test images with different focuses, the right focusing image and the left focusing image of two clocks.

(2) *Multispectrum images*. Figures 6(a) and 6(b) are the visible image and the infrared image of the same scene. In visible image, a person is very difficult to be recognized, but path, bush, square table, and stockade can be distinguished. In the infrared image, a person can be seen clearly, but other sceneries are quite hazy.

(3) *Multimode medicine images*. Figures 7(a) and 7(b) show two different mode medicine images, CT image and the SPECT image of the thyroid gland. The resolution of CT image is high; the imaging of the bone is very clear, but the imaging of the soft tissue lesions is poor. The SPECT image is conducive to identify the scope of the focal lesions, because its image of the soft tissue is clear. However, the SPECT image lacks the rigid bone tissue as a positioning reference.

Supplementary information exists separately in the two images of every group; therefore image fusion is very suitable for processing these images.

3.2. Fusion Rules. In the process of image fusion, the choice of fusion rules is very important because it can influence the fusion results. The common fusion rules include weighted average, max select, gradient, regional energy and regional variance, and so forth. In this paper our purpose is to compare the FRFT-NSCT fusion method with NSCT fusion method under the same parameters condition, so three simple fusion rules are chosen in the experiment here.

(1) Fusion rule $1^{\#}$: both the low-frequency and the high-frequency coefficients follow the average value rule.

(2) Fusion rule $2^{\#}$: the low-frequency coefficients follow the average value and the high-frequency coefficients follow the largest absolute value rule.

(3) Fusion rule $3^{\#}$: both the low-frequency and the high-frequency coefficients follow the largest absolute value rule.

3.3. Experimental Results. In this section the proposed fusion algorithm based on FRFT-NSCT is compared with NSCT fusion algorithm. The parameters are set the same in the experiments. According to Section 2.1, the NSCT decomposition layer is chosen 3, the nonsubsampled pyramid (NSP) is adopted the pyramidal filter "maxflat," and the nonsubsampled directional filter bank (NSDFB) is employed

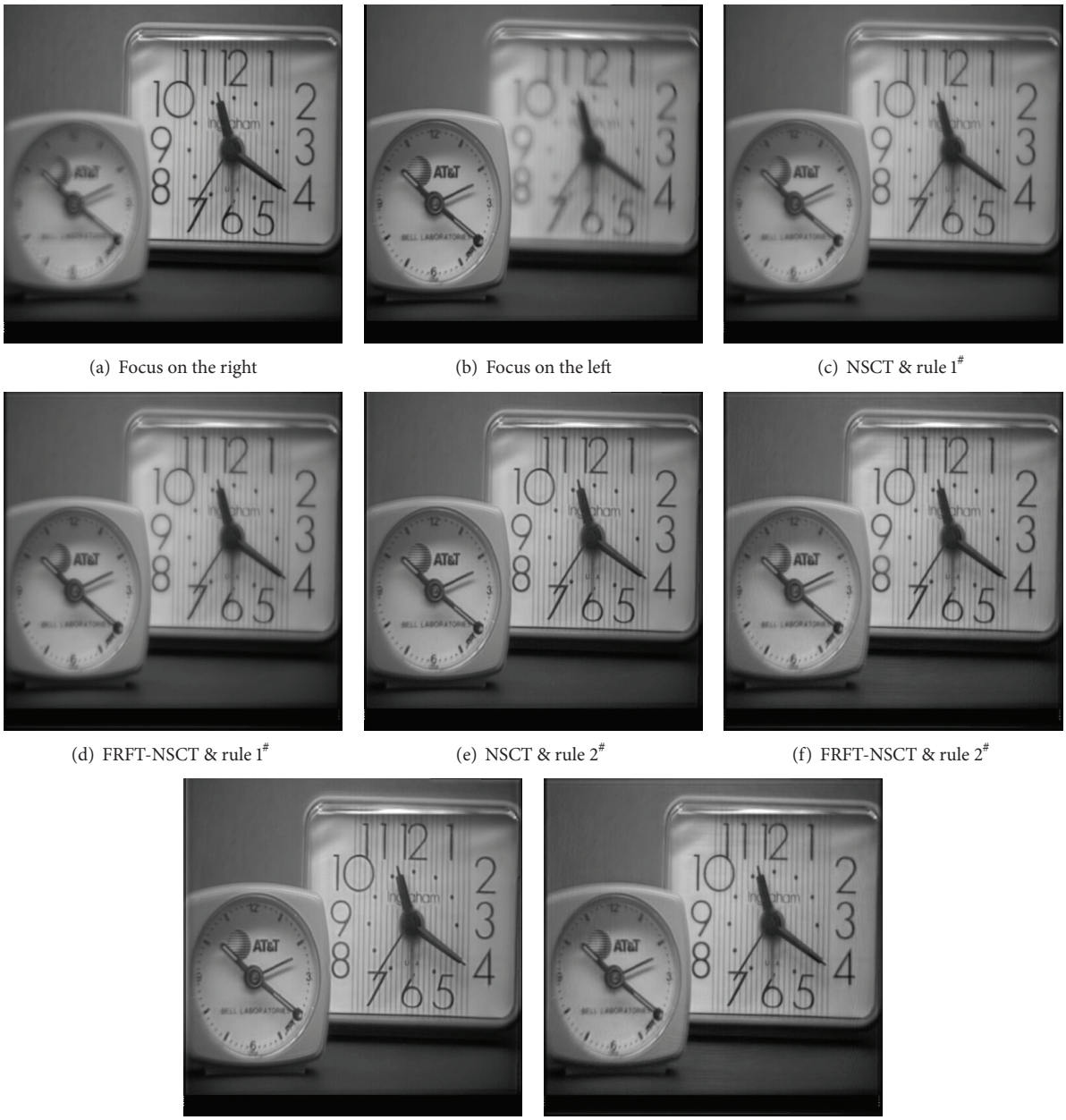

(a) Focus on the right (b) Focus on the left (c) NSCT & rule $1^{\#}$

(d) FRFT-NSCT & rule $1^{\#}$ (e) NSCT & rule $2^{\#}$ (f) FRFT-NSCT & rule $2^{\#}$

(g) NSCT & rule $3^{\#}$ (h) FRFT-NSCT & rule $3^{\#}$

Figure 5: Fusion results of the multifocus images.

"dmaxflat7." The order of the FRFT, p, is 0.9. The simulation software is MATLAB V7.1. The computer configuration is Intel Core i3-2100 CPU, 3.10 GHz CPU clock speed and 2.99 GB memory.

Figures 5(c)–5(h) illustrate the multifocus images fusion results based on two fusion methods and three fusion rules. Compared with the source images, all of the fused images eliminate the effects resulting from the different focuses of the camera and can make all the objects in the fused images clear. Among three fusion rules, the fusion rules $2^{\#}$ and $3^{\#}$ are better than fusion rule $1^{\#}$, especially the fusion rule $2^{\#}$ obtains more outline information and the detail information of the source images. Observe subjectively, the difference between the fused images based on NSCT and based on FRFT-NSCT are not very obvious by the same fusion rules.

Figures 6(c)–6(h) show the infrared and visible image fusion results. Compared with the source images, all of the fused images contain the visible information and infrared information simultaneously. FRFT-NSCT outperforms NSCT on the rule $1^{\#}$and rule $2^{\#}$. Especially on the fusion rule $2^{\#}$, FRFT-NSCT attains more outline information and detail information of the source images. Comparing

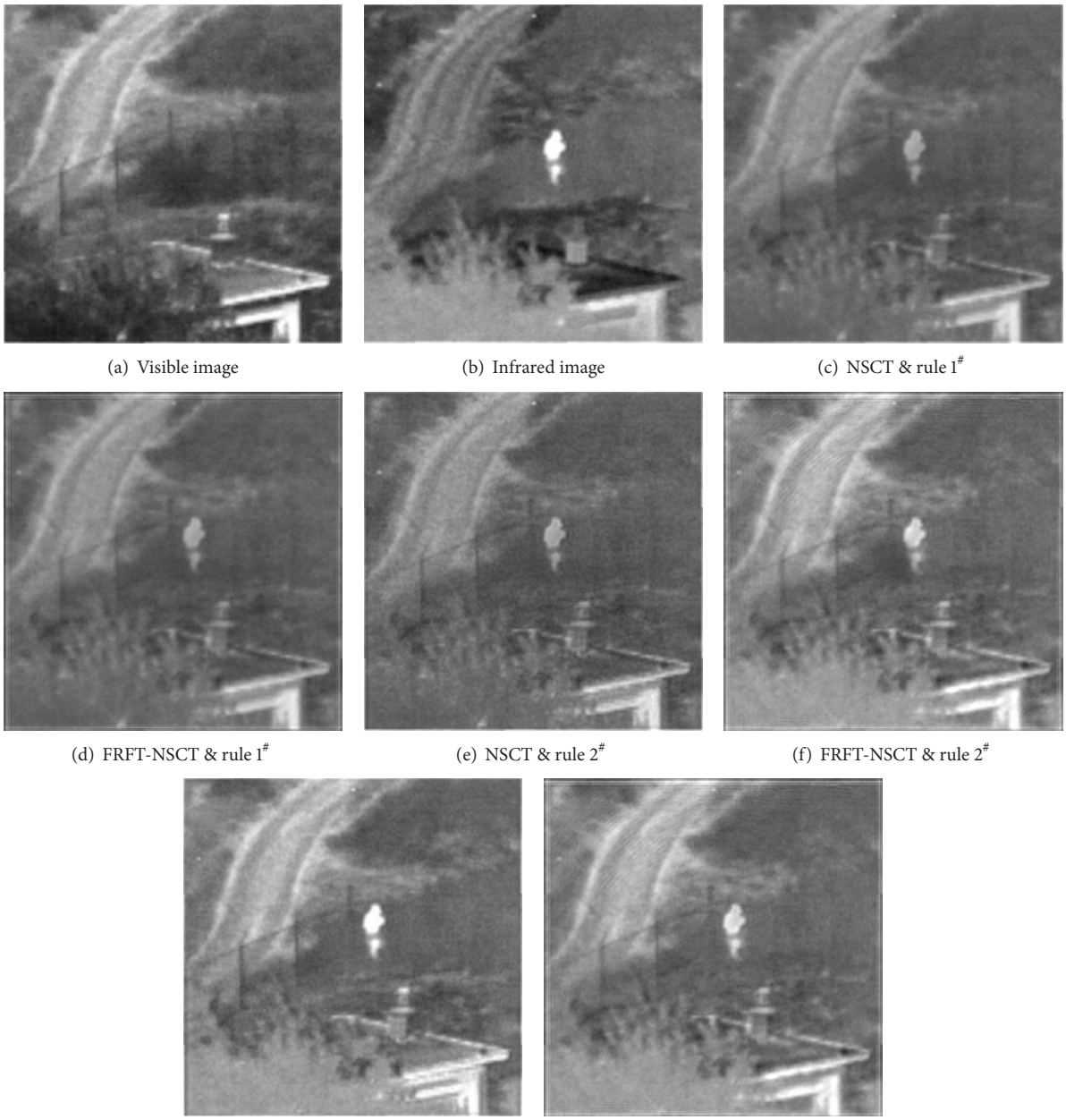

(a) Visible image (b) Infrared image (c) NSCT & rule $1^{\#}$

(d) FRFT-NSCT & rule $1^{\#}$ (e) NSCT & rule $2^{\#}$ (f) FRFT-NSCT & rule $2^{\#}$

(g) NSCT & rule $3^{\#}$ (h) FRFT-NSCT & rule $3^{\#}$

Figure 6: Fusion results of multispectrum images.

Figure 6(g) with Figure 6(h), we can see that on the rule $3^{\#}$, NSCT is lighter than FRFT-NSCT, but FRFT-NSCT is clearer than NSCT.

Figures 7(c)–7(h) illustrate the multimodality medical images fusion results. Compared with the source images, all of the fused images synthesize the bone information and the soft tissue lesions information. FRFT-NSCT gets more outline information and detail information of the source images than NSCT, especially on the fusion rule $3^{\#}$. Because of the great difference of the source images background, the fused image background varies with the fusion rules.

The above is human visual perception. However, it is easily influenced by visual psychological factors. The objective evaluation criteria such as entropy, mean value and average gradient, and so forth can also judge the fusion results. Table 1 gives the quantitative fusion results of the three style images, based on the two methods and the three fusion rules.

Entropy can weigh image information abundance; the larger entropy is, the more image information contained in the fused image. Average gradient may indicate the distinct degree of an image. The larger the average gradient, the clearer fusion image is. The fusion time can measure the

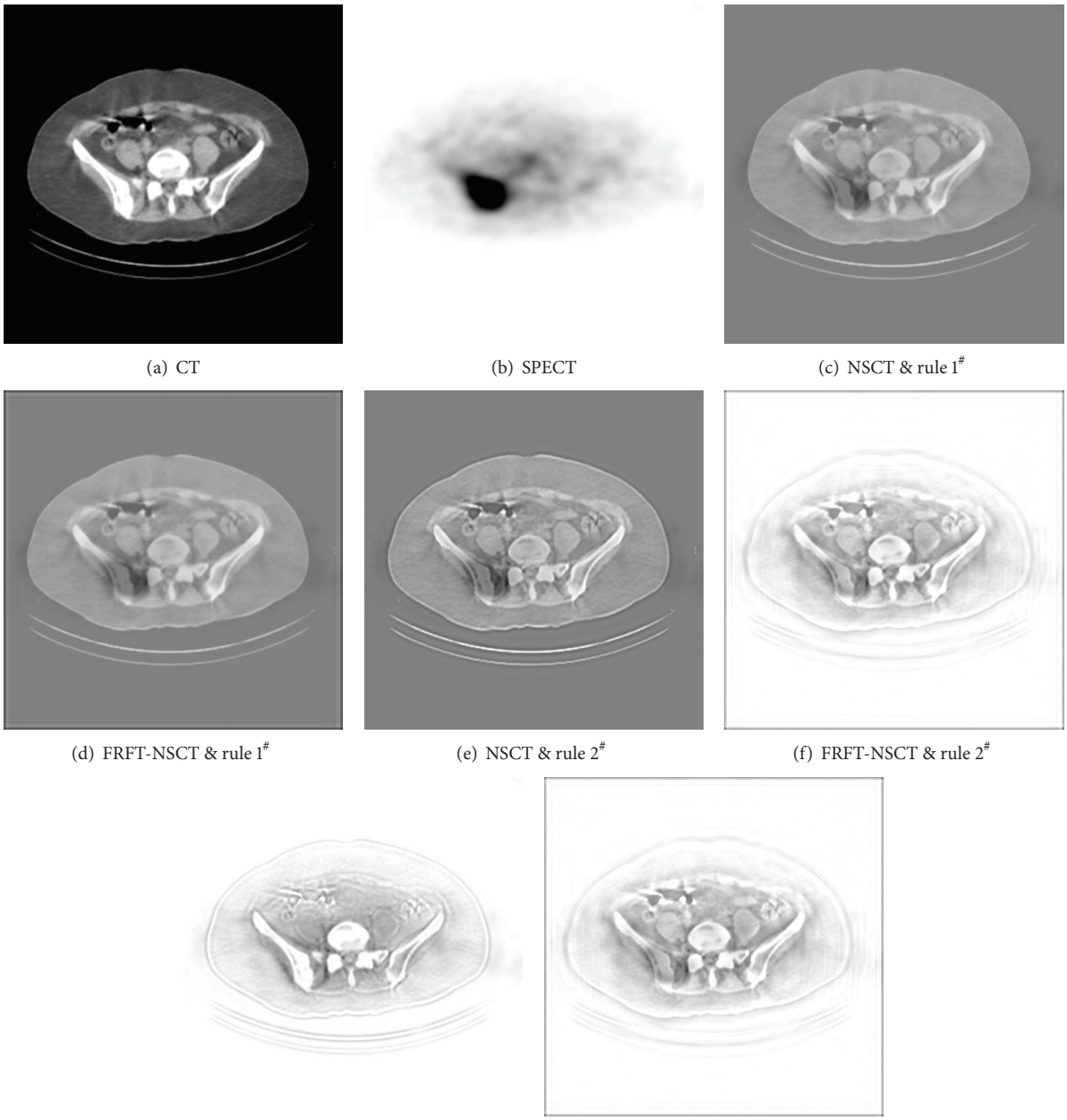

(a) CT (b) SPECT (c) NSCT & rule 1#

(d) FRFT-NSCT & rule 1# (e) NSCT & rule 2# (f) FRFT-NSCT & rule 2#

(g) NSCT & rule 3# (h) FRFT-NSCT & rule 3#

Figure 7: Fusion results of multimodality medical images.

complexity of the algorithm. From Table 1, we can see that the quantitative evaluation criteria are in accordance with the visual effect in principle. Table 1 shows that the value of the entropy and average gradient of the FRFT-NSCT are larger than those of NSCT, except the value underlined. That means the fused image based on the FRFT-NSCT usually has more detail information and higher spatial resolution than that of the NSCT, because FRFT-NSCT combines the multiscale, multi-direction, and shift invariance of NSCT with the fractional domain analysis of FRFT, but the fusion time of the FRFT-NSCT is almost twice as bigger as the time of the NSCT. That indicates the complexity of the FRFT-NSCT is higher than NSCT, so the FRFT-NSCT method is more suitable for the situation that demands high precision rather than speed.

4. Conclusions

In image fusion study, the multiscale algorithm has been the main trend. In this paper, a novel fusion method based on FRFT-NSCT is proposed. The nonsubsampled Contourlet transform (NSCT) has properties such as multiscale, multi-direction, and shift invariance. The fractional Fourier transform (FRFT) develops the signal analysis into fractional domain and can reflect the signal information in the time domain and the frequency domain simultaneously.

Table 1: Evaluation criteria of NSCT-based fusion method and FRFT-NSCT-based fusion method.

Image	Fusion method	Fusion rules	Entropy	Average gradient	Fusion time (s)
Multifocus images	NSCT	1#	7.2875	2.8112	200.274324
	FRFR-NSCT	1#	7.4792	2.9483	431.291303
	NSCT	2#	7.3651	4.0919	201.992649
	FRFR-NSCT	2#	7.5294	4.1447	435.006276
	NSCT	3#	7.3654	4.1382	201.088658
	FRFR-NSCT	3#	7.5316	4.1912	424.331975
Visible light & infrared images	NSCT	1#	6.4158	2.0073	202.955161
	FRFR-NSCT	1#	6.4222	2.5573	413.585567
	NSCT	2#	6.4608	2.7797	200.966261
	FRFR-NSCT	2#	6.8802	3.3953	413.735101
	NSCT	3#	6.9314	3.0062	202.404612
	FRFR-NSCT	3#	**6.8475**	3.4081	416.433884
CT&SPECT medical images	NSCT	1#	3.6556	1.1601	207.066354
	FRFR-NSCT	1#	4.8169	2.2516	431.697082
	NSCT	2#	4.5866	2.0947	208.800631
	FRFR-NSCT	2#	4.6902	2.4386	431.882050
	NSCT	3#	3.7528	1.6275	208.549554
	FRFR-NSCT	3#	4.6902	2.4386	436.366335

FRFT-NSCT combines the merits of the FRFT with that of the NSCT. For testing the effect of the proposed method, three groups of different pattern images are introduced as the source images, and three fusion rules are chosen. Fused images based on FRFT-NSCT can get more outline information and detail information of the source images than NSCT. The fused results demonstrate that the proposed algorithm has validity and feasibility. Further problems, such as parameter optimization, fusion rules improving, color image processing, and quick-algorithm will be discussed in the follow-up research.

Acknowledgments

This work is supported by National Natural Science Foundation of China (no. 11271106), the Plan of Scientific Research of Hebei Education Department (no. 2010218), and Open Foundation of Biomedical Multidisciplinary Research Center of Hebei University (no. BM201103).

References

[1] K. Song and J. W. Ji, "An image fusion algorithm based on the wavelet transform," *Journal of Shen Yang Agricultural University*, vol. 38, pp. 845–848, 2007.

[2] C. Gargour, M. Gabrea, V. Ramachandran, and J. M. Lina, "A short introduction to wavelets and their applications," *IEEE Circuits and Systems Magazine*, vol. 9, no. 2, pp. 57–68, 2009.

[3] G. Pajares and J. M. de la Cruz, "A wavelet-based image fusion tutorial," *Pattern Recognition*, vol. 37, no. 9, pp. 1855–1872, 2004.

[4] D. Y. Qin, J. D. Wang, and P. Li, "Wavelet base selection and evaluation for image fusion," *Optoelectronic Technology*, vol. 26, pp. 203–207, 2006.

[5] F. Nencini, A. Garzelli, S. Baronti, and L. Alparone, "Remote sensing image fusion using the curvelet transform," *Information Fusion*, vol. 8, no. 2, pp. 143–156, 2007.

[6] Q. Xiao-Bo, Y. Jing-Wen, X. Hong-Zhi, and Z. Zi-Qian, "Image fusion algorithm based on spatial frequency-motivated pulse coupled neural networks in nonsubsampled contourlet transform domain," *Acta Automatica Sinica*, vol. 34, no. 12, pp. 1508–1514, 2008.

[7] M. N. Do and M. Vetterli, "The contourlet transform: an efficient directional multiresolution image representation," *IEEE Transactions on Image Processing*, vol. 14, no. 12, pp. 2091–2106, 2005.

[8] Q. Miao and B. Wang, "A novel image fusion method using contourlet transform," *IEEE Transactions on Image Processing*, vol. 6, pp. 548–552, 2006.

[9] A. L. da Cunha, J. Zhou, and M. N. Do, "The nonsubsampled contourlet transform: Theory, design, and applications," *IEEE Transactions on Image Processing*, vol. 15, no. 10, pp. 3089–3101, 2006.

[10] W. Kong, Y. Lei, and X. Ni, "Fusion technique for grey-scale visible light and infrared images based on non-subsampled contourlet transform and intensity-hue-saturation transform," *IET Signal Processing*, vol. 5, no. 1, pp. 75–80, 2011.

[11] Y. Xiao-Hui and J. Li-Cheng, "Fusion algorithm for remote sensing images based on nonsubsampled contourlet transform," *Acta Automatica Sinica*, vol. 34, no. 3, pp. 274–281, 2008.

[12] L. B. Almeida, "The fractional Fourier transform and time-frequency representations," *IEEE Transactions on Signal Processing*, vol. 42, no. 11, pp. 3084–3091, 1994.

[13] R. Saxena and K. Singh, "Fractional Fourier transform: a novel tool for signal processing," *Journal of the Indian Institute of Science*, vol. 85, no. 1, pp. 11–26, 2005.

[14] T. Alieva, M. J. Bastiaans, and M. L. Calvo, "Fractional transforms in optical information processing," *EURASIP Journal on Applied Signal Processing*, vol. 2005, no. 10, pp. 1498–1519, 2005.

[15] R. Tao, Y. L. Li, and Y. Wang, "Short-time fractional fourier transform and its applications," *IEEE Transactions on Signal Processing*, vol. 58, no. 5, pp. 2568–2580, 2010.

[16] E. Dinç, F. Demirkaya, D. Baleanu, Y. Kadioğlu, and E. Kadioğlu, "New approach for simultaneous spectral analysis of a complex mixture using the fractional wavelet transform," *Communications in Nonlinear Science and Numerical Simulation*, vol. 15, no. 4, pp. 812–818, 2010.

[17] J. Shi, N. Zhang, and X. P. Liu, "A novel fractional wavelet transform and its applications," *Science China Information Sciences*, vol. 55, no. 6, pp. 1270–1279, 2012.

[18] N. Taneja, B. Raman, and I. Gupta, "Selective image encryption in fractional wavelet domain," *International Journal of Electronics and Communications*, vol. 65, no. 4, pp. 338–344, 2011.

[19] T. Lei, Z. Feng, and Z. Zong-gui, "Multi-resolutioan image fusion based on the nonsubsampled Contourlet transform," *Information and Control*, vol. 37, no. 3, pp. 291–297, 2008.

[20] Z. Qiang and G. Baolong, "Fusion of multifocus images based on the nonsubsampled contourlet transform," *Acta Photonica Sinica*, vol. 37, no. 4, pp. 838–843, 2008.

[21] C. Candan, M. Alper Kutay, and H. M. Ozaktas, "The discrete fractional fourier transform," *IEEE Transactions on Signal Processing*, vol. 48, no. 5, pp. 1329–1337, 2000.

[22] R. Tao, B. Deng, and Y. Wang, "Research progress of the fractional Fourier transform in signal processing," *Science in China Information Sciences*, vol. 49, no. 1, pp. 1–25, 2006.

[23] J. Shi, Y. Chi, and N. Zhang, "Multichannel sampling and reconstruction of bandlimited signals in fractional Fourier domain," *IEEE Signal Processing Letters*, vol. 17, no. 11, pp. 909–912, 2010.

[24] H. Yi, C. Y. Fan, J. G. Yang, and X. T. Huang, "Imaging and locating multiple ground moving targets based on keystone transform and FrFT for single channel SAR system," in *Proceedings of the Asia-Pacific Conference on Synthetic Aperture Radar (APSAR '09)*, pp. 771–774, October 2009.

[25] D. Mendlovic, Z. Zalevsky, D. Mas, J. García, and C. Ferreira, "Fractional wavelet transform," *Applied Optics*, vol. 36, no. 20, pp. 4801–4806, 1997.

[26] T. Guanqun, L. Dapeng, and L. Guanghua, "On image fusion based on different rules of wavelet transform," *Acta Photonica Sinica*, vol. 33, no. 2, pp. 221–224, 2004.

[27] W. Huang and Z. Jing, "Evaluation of focus measures in multi-focus image fusion," *Pattern Recognition Letters*, vol. 28, no. 4, pp. 493–500, 2007.

Hindawi Publishing Corporation
Mathematical Problems in Engineering
Volume 2013, Article ID 149289, 8 pages
http://dx.doi.org/10.1155/2013/149289

Research Article

Texture Enhancement Based on the Savitzky-Golay Fractional Differential Operator

Hamid A. Jalab[1] and Rabha W. Ibrahim[2]

[1] *Faculty of Computer Science & Information Technology, University of Malaya, 50603 Kuala Lumpur, Malaysia*
[2] *Institute of Mathematical Sciences, University of Malaya, 50603 Kuala Lumpur, Malaysia*

Correspondence should be addressed to Rabha W. Ibrahim; rabhaibrahim@yahoo.com

Received 13 August 2012; Revised 5 January 2013; Accepted 5 January 2013

Academic Editor: José Tenreiro Machado

Texture enhancement for digital images is the most important technique in image processing. The purpose of this paper is to design a texture enhancement technique using fractional order Savitzky-Golay differentiator, which leads to generalizing the Savitzky-Golay filter in the sense of the Srivastava-Owa fractional operators. By employing this generalized fractional filter, texture enhancement is introduced. Consequently, it calculates the generalized fractional order derivative of the given image using the sliding weight window over the image. Experimental results show that the operator can extract more subtle information and make the edges more prominent. In general, the capability of the generalized fractional differential will be high because it is sensitive to the subtle fluctuations of values of pixels.

1. Introduction

Texture is an important feature of natural images; hence, a variety of image texture applications has been intensively studied by many researchers [1]. Image texture is defined as a function of the spatial variation in pixel intensities (gray values). Smith and Chang [2] have defined texture as visual patterns, which have properties of homogeneity and not resulting from only a single color or intensity.

In the image, texture features capture information about repeating patterns. Texture analysis can be classified into three models: structural, statistical, and signal theoretic methods [3]. Therefore, the analysis of texture parameters is a useful approach for increasing the information accessible from images. In texture enhancement technique, which is based on mask operation, each pixel is modified according to value of the neighbourhood around the pixel of interest. One important aspect of an image, which enables us to perform this, is the notion of frequencies. Fundamentally, the frequencies of an image are the amount, by which the gray values change with distance. High-frequency components are characterized by huge changes in gray values over small distances; examples of high frequency components are edges and noise. On the other hand, low-frequency components are parts of the image, which are characterized by little change in the gray values [4]. Fractional differential mask can further preserve the low-frequency contour feature in those smooth areas, and nonlinearly keep the high-frequency marginal feature in those areas, where the gray-level changes heavily, and also enhances texture details in those areas, where the gray-level does not change evidently.

Fractional integration and fractional differentiation are generalizations of notions of integer-order integration and differentiation and include nth derivatives and *n-fold* integrals as particular cases [5, 6]. Many applications of fractional calculus in physics have replaced the time derivative in an evolution equation with a derivative of fractional order [7–11]. Fractional calculus has been applied to a variety of physical phenomena, including anomalous diffusion, transmission line theory, problems involving oscillations, nanoplasmonics, solid mechanics, astrophysics, and viscoelasticity. Currently, fractional calculus (integral and differential operators) is heavily used in control design [12, 13], Furthermore, in image processing [14–19], all results that are based on the fractional

calculus operators (differential and integral) show that this method not only is effective, but also has good immunity.

The digital fractional order differentiator is an important topic in fractional calculus that can estimate the fractional order derivative of any given digital signals, without known function. The Savitzky-Golay filter is a simplified digital differentiator that is implemented by a local polynomial regression technique [20, 21]. Now, Savitzky-Golay digital differentiator has been one of the most popular numerical differentiation methods, due to its high computing speed and strong antinoise ability.

Recently, the interest in using texture enhancement technique based on mask operation has grown in the field of image processing. Pu and Zhou [22] have implemented multiscale texture segmentation by fractional differential. They have proposed two fractional differential masks and presented the structures and parameters of each mask, respectively. Then they have discussed the multi-scale texture segmentation based on the fractional mask. Pu [23] has proposed a fractional calculus approach to enhance the texture of digital image. He has found that the textural detail enhancing capability of fractional derivative-based texture operator is much better than integer derivative. Zhang et al. [24] have used the fractional differential masks based on the classical Riemann-Liouville definition. They have concluded that the fractional order between 1 and 2 can enhance the texture and edges in multiscale, by controlling the fractional order.

In this paper, we have used a generalized fractional differential based on the generalized Savitzky-Golay filter in sense of Srivastava-Owa fractional operators for image texture enhancement. The Savitzky-Golay filter has become a powerful signal and image processing tool, which has found application in many scientific areas. Moreover, the Savitzky-Golay filter method is considered to be a good approach in image texture enhancement, which is used as an alternative to classical techniques. The rest of the paper is organized as follows: Sections 2 and 3 explain the fractional calculus and the generalized fractional integral operator, respectively, Section 4 describes the construction of fractional differential Savitzky-Golay filter, Section 5 elucidates the experimental results, and Section 6 concludes the paper.

2. Fractional Calculus

The idea of the fractional calculus (i.e., calculus of integrals and derivatives of any arbitrary real or complex order) was found over 300 years ago. Abel in 1823 scrutinized the generalized tautochrone problem and for the first time applied fractional calculus techniques in a physical problem.

2.1. The Riemann-Liouville Operators. The Riemann-Liouville fractional derivative strongly poses the physical interpretation of the initial conditions required for the initial value problems involving fractional differential equations. Moreover, this operator possesses advantages of fast convergence, high stability, and higher accuracy to derive different types of numerical algorithms [6].

The fractional (arbitrary) order integral of the function f of order $\alpha > 0$ is defined by

$$I_a^\alpha f(t) = \int_a^t \frac{(t-\tau)^{\alpha-1}}{\Gamma(\alpha)} f(\tau)\, d\tau. \tag{1}$$

When $a = 0$, we write $I_a^\alpha f(t) = f(t) * \phi_\alpha(t)$, where $(*)$ denoted the convolution product, $\phi_\alpha(t) = t^{\alpha-1}/\Gamma(\alpha)$, $t > 0$ and $\phi_\alpha(t) = 0$, $t \le 0$, and $\phi_\alpha \to \delta(t)$ as $\alpha \to 0$, where $\delta(t)$ is the delta function.

The fractional (arbitrary) order derivative of the function f of order $0 \le \alpha < 1$ is defined by

$$D_a^\alpha f(t) = \frac{d}{dt}\int_a^t \frac{(t-\tau)^{-\alpha}}{\Gamma(1-\alpha)} f(\tau)\, d\tau = \frac{d}{dt} I_a^{1-\alpha} f(t). \tag{2}$$

When $a = 0$, we have

$$\begin{aligned} D^\alpha t^\mu &= \frac{\Gamma(\mu+1)}{\Gamma(\mu-\alpha+1)} t^{\mu-\alpha}, \quad \mu > -1,\ 0 < \alpha < 1, \\ I^\alpha t^\mu &= \frac{\Gamma(\mu+1)}{\Gamma(\mu+\alpha+1)} t^{\mu+\alpha}, \quad \mu > -1,\ \alpha > 0. \end{aligned} \tag{3}$$

The Caputo fractional derivative of order $\mu > 0$ is defined, for a smooth function f, by

$${}^cD_a^\mu f(t) = \int_a^t \frac{(t-\tau)^{n-\mu-1}}{\Gamma(n-\mu)} f^{(n)}(\tau)\, d\tau, \tag{4}$$

where $n = [\mu] + 1$ (the notation $[\mu]$ stands for the largest integer not greater than μ). Note that there is a relationship between the Riemann-Liouville differential operator and the Caputo operator:

$$D_a^\mu f(t) = {}^cD_a^\mu f(t) + \frac{1}{\Gamma(1-\mu)} \frac{f(a)}{(t-a)^\mu}, \tag{5}$$

and they are equivalent in a physical problem (i.e., a problem which specifies the initial conditions).

2.2. The Srivastava-Owa Operators. In [25], Srivastava and Owa defined and studied fractional operators (derivative and integral) in the complex z-plane $\mathbb{C}$ for analytic functions.

The fractional derivative of order β is defined, for a function $f(z)$ by

$$D_z^\beta f(z) := \frac{1}{\Gamma(1-\beta)} \frac{d}{dz} \int_0^z \frac{f(\zeta)}{(z-\zeta)^\beta} d\zeta, \quad 0 \le \beta < 1, \tag{6}$$

where the function $f(z)$ is analytic in simply-connected region of the complex z-plane $\mathbb{C}$ containing the origin and the multiplicity of $(z-\zeta)^{-\beta}$ is removed by requiring $\log(z-\zeta)$ to be real when $(z-\zeta) > 0$. Furthermore, for $n \le \beta < n+1$, the fractional differential operator is defined as

$$D_z^\beta f(z) = \frac{d^n}{dz^n} D_z^{\beta-n} f(z), \quad n \in \mathbb{N}. \tag{7}$$

The fractional integral of order β is defined, for a function $f(z)$, by

$$I_z^{\beta} f(z) := \frac{1}{\Gamma(\beta)} \int_0^z f(\zeta)(z-\zeta)^{\beta-1} d\zeta, \quad \beta > 0, \tag{8}$$

where the function $f(z)$ is analytic in simply connected region of the complex z-plane ($\mathbb{C}$) containing the origin and the multiplicity of $(z-\zeta)^{\beta-1}$ is removed by requiring $\log(z-\zeta)$ to be real when $(z-\zeta) > 0$:

$$\begin{aligned} D_z^{\beta} z^{\mu} &= \frac{\Gamma(\mu+1)}{\Gamma(\mu-\beta+1)} z^{\mu-\beta}, \quad \mu > -1,\ 0 \le \beta < 1 \\ I_z^{\beta} z^{\mu} &= \frac{\Gamma(\mu+1)}{\Gamma(\mu+\beta+1)} z^{\mu+\beta}, \quad \mu > -1,\ \beta > 0. \end{aligned} \tag{9}$$

Note that the real case of the Srivastava-Owa operators is equivalence to the Riemann-Liouville operators.

3. Generalized Fractional Integral Operator

This section briefly describes the mathematical background for the fractional integral operator that has been used by the proposed algorithm. The usual way of representing the fractional derivatives is by the Riemann-Liouville formula D_t^{α}. Another way to represent the fractional derivatives is by the Grünwald-Letnikov formula [23]. The discrete approximations derived from the Grünwald-Letnikov fractional derivatives present some limitations, such as the following[26]:

(i) they frequently originate unstable numerical methods;

(ii) the order of accuracy of such approaches is never higher than one.

To implement the generalized fractional integral method, Ibrahim in [27] has imposed a formula for the generalized fractional integral. Consider, for natural $n \in \mathbb{N} = \{1, 2, \ldots\}$ and real μ, the n-fold integral of the form

$$I_z^{\alpha,\mu} f(z) = \int_0^z \zeta_1^{\mu} d\zeta_1 \int_0^{\zeta_1} \zeta_2^{\mu} d\zeta_2 \cdots \int_0^{\zeta_{n-1}} \zeta_n^{\mu} f(\zeta_n)\, d\zeta_n. \tag{10}$$

Applying the Cauchy formula for iterated integrals implies

$$\begin{aligned} \int_0^z \zeta_1^{\mu} d\zeta_1 \int_0^{\zeta_1} \zeta^{\mu} f(\zeta)\, d\zeta &= \int_0^z \zeta^{\mu} f(\zeta)\, d\zeta \int_{\zeta}^z \zeta_1^{\mu} d\zeta_1 \\ &= \frac{1}{\mu+1} \int_0^z \left(z^{\mu+1} - \zeta^{\mu+1}\right) \zeta^{\mu} f(\zeta)\, d\zeta. \end{aligned} \tag{11}$$

Repeating the above step $n-1$ times we obtain

$$\begin{aligned} &\int_0^z \zeta_1^{\mu} d\zeta_1 \int_0^{\zeta_1} \zeta_2^{\mu} d\zeta_2 \cdots \int_0^{\zeta_{n-1}} \zeta_n^{\mu} f(\zeta_n)\, d\zeta_n \\ &\quad = \frac{(\mu+1)^{1-n}}{(n-1)!} \int_0^z \left(z^{\mu+1} - \zeta^{\mu+1}\right)^{n-1} \zeta^{\mu} f(\zeta)\, d\zeta, \end{aligned} \tag{12}$$

which yields the fractional operator type

$$I_z^{\alpha,\mu} f(z) = \frac{(\mu+1)^{1-\alpha}}{\Gamma(\alpha)} \int_0^z \left(z^{\mu+1} - \zeta^{\mu+1}\right)^{\alpha-1} \zeta^{\mu} f(\zeta)\, d\zeta, \tag{13}$$

where α and $\mu \neq -1$ are real numbers and the function $f(z)$ is analytic in the simply connected region of the complex z-plane $\mathbb{C}$ containing the origin, and the multiplicity of $(z^{\mu+1} - \zeta^{\mu+1})^{-\alpha}$ is removed by requiring $\log(z^{\mu+1} - \zeta^{\mu+1})$ to be real when $(z^{\mu+1} - \zeta^{\mu+1}) > 0$. When $\mu = 0$, we arrive at the standard Srivastava-Owa fractional integral, which is used to define the Srivastava-Owa fractional derivatives.

Corresponding to the generalized fractional integrals (13), we define the generalized differential operator of order α by

$$D_z^{\alpha,\mu} f(z) := \frac{(\mu+1)^{\alpha}}{\Gamma(1-\alpha)} \frac{d}{dz} \int_0^z \frac{\zeta^{\mu} f(\zeta)}{\left(z^{\mu+1} - \zeta^{\mu+1}\right)^{\alpha}} d\zeta, \quad 0 < \alpha \le 1, \tag{14}$$

where the function $f(z)$ is analytic in the simply connected region of the complex z-plane $\mathbb{C}$ containing the origin and the multiplicity of $(z^{\mu+1} - \zeta^{\mu+1})^{-\alpha}$ is removed by requiring $\log(z^{\mu+1} - \zeta^{\mu+1})$ to be real when $(z^{\mu+1} - \zeta^{\mu+1}) > 0$.

Proposition 1 (see [27]). *The generalized derivative of the function $f(z) = z^{\nu}$, $\nu \in \mathbb{R}$ is given by the following:*

$$D_z^{\alpha,\mu} f(z) = \frac{(\mu+1)^{\alpha-1} \Gamma(\nu/(\mu+1)+1)}{\Gamma(\nu/(\mu+1)+1-\alpha)} z^{(1-\alpha)(\mu+1)+\nu-1}, \tag{15}$$

which is later used to compute the coefficient matrix $W^{(\alpha,\mu)}$.

4. Construction of the Fractional Differential Savitzky-Golay Filter

The Savitzky-Golay filter has been introduced for computing the numerical derivatives and is also called a digital smoothing polynomial filter. The Savitzky-Golay method is often used to preserve higher moments in the data, thus reducing the distortion of essential features of the data.

In this section, we will generalize this filter for calculating the fraction derivatives which will be utilized by the proposed algorithm.

Assume a uniformly sampled signal, our aim is to estimate its nth order derivative using I-point filtering window and an n-degree polynomial [21]:

$$f_n(i) = \sum_{k=0}^{n} a_k i^k, \tag{16}$$

which is used to fit the given signal $i = 1, 2, \ldots, I$. In matrix notation, (16) is reduced to the system

$$Y = XA + \varepsilon, \tag{17}$$

where ε is the estimate error, A is the $n+1\times 1$ coefficient matrix and X is the $I\times(n+1)$ Vandermonde matrix defined by

$$X=\begin{pmatrix}1 & 1^1 & \cdots & 1^n\\ 1 & 2^1 & \cdots & 2^n\\ \vdots & \vdots & \cdots & \vdots\\ 1 & I^1 & \cdots & I^n\end{pmatrix}. \tag{18}$$

The coefficients of the best-fit polynomial can be obtained by minimizing the sum of the squared errors between the actual data and fitting points. Thus,

$$B=\left(X^TX\right)^{-1}X^TY \tag{19}$$

implies

$$\widehat{Y}=WY, \tag{20}$$

where W denotes the moving window's coefficients matrix. Consequently, the nth order derivative can be estimate by

$$\widehat{Y}^{(dn)}=W^{(dn)}Y. \tag{21}$$

Now, in view of Proposition 1, we have

$$\widehat{Y}^{(\alpha,\mu)}=W^{(\alpha,\mu)}Y=A\left(X^TX\right)^{-1}X^TY, \tag{22}$$

where

$$\begin{aligned}A=\Bigg[&\frac{(\mu+1)^{\alpha-1}}{\Gamma(1-\alpha)}i^{(1-\alpha)(\mu+1)-1},\\ &\frac{(\mu+1)^{\alpha-1}\Gamma(1/(\mu+1)+1)}{\Gamma(1/(\mu+1)+1-\alpha)}i^{(1-\alpha)(\mu+1)},\ldots,\\ &\frac{(\mu+1)^{\alpha-1}\Gamma(n/(\mu+1)+1)}{\Gamma(n/(\mu+1)+1-\alpha)}i^{(1-\alpha)(\mu+1)+n-1}\Bigg].\end{aligned} \tag{23}$$

Note that when $\mu=0$, we have the Riemann-Liouville differential operator. Moreover, when $I=n+1$, the Vandermonde matrix X is a square matrix. The purpose of the Savitzky-Golay filter is to estimate $W^{(\alpha,\mu)}$, which can be used to calculate the nth order derivative of any given signal [21]. The coefficient matrix $W^{(\alpha,\mu)}$ can be computed by

$$W^{(\alpha,\mu)}=AX^{-1}, \tag{24}$$

where

$$X=\begin{pmatrix}1 & 1^1 & \cdots & 1^n\\ 1 & (1+\phi)^1 & \cdots & (1+\phi)^n\\ 1 & (1+2\phi)^1 & \cdots & (1+2\phi)^n\\ \vdots & \vdots & \cdots & \vdots\\ 1 & I^1 & \cdots & I^n\end{pmatrix}, \tag{25}$$

where ϕ is the sampling interval.

Table 1: Moving window of fractional differential weights with 3×3 dimension.

1	1^1	1^2
1	$(1+\phi)^1$	$(1+\phi)^2$
1	I^1	I^2

Table 2: Moving window of fractional differential weights with 3×3 dimension for $\varphi=1$, $\alpha=0.4$, and $\mu=0.5$.

0.2268	0.3057	−0.0060
−0.8687	1.2983	0.0420
−1.0277	1.2742	0.2016

Table 3: Moving window of fractional differential weights with 3×3 dimension for $\varphi=1$, $\alpha=0.5$, and $\mu=0.5$.

0.0732	0.3951	−0.0076
−0.8192	1.126	0.0416
−0.7999	0.9307	0.1772

The matrix X can be assumed as the formula of computation time; therefore, the generalized Savitzky-Golay filter can be viewed as the generalization of the differentiator. However, digital image is a function of two variables, so, we can generalize these definitions to include both the x and y values.

The mask is designed into $r\times r$ size matrix M which has r layers (r is odd). The window's size can be an arbitrary odd number, and a larger window can improve the accuracy of fractional differential, but increases the computational time. Therefore, we proceed to use moving window $W^{(\alpha,\mu)}$ with 3×3 size as shown in Table 1.

The fractional differential operator can enhance edges and contours as well as reserve the texture details. The nine values output of each fractional differential window $h(x,y)$ is performed by sliding the mask window $w(s,t)$ over the image f. Generally one can start at the top left corner of the image block through all the pixels, where the fractional differential mask fits entirely within the boundaries of the image. The output of each image block is nine values, which represent the texture information in each image block, that takes the following formula:

$$h(x,y)=w(s,t)\,f(x+s,y+t), \tag{26}$$

where f is the value of an image pixel and w is the value of filter mask.

5. Experimental Results and Discussion

The reason of this experiment is to validate the correctness of the proposed algorithm.

Performance tests for the algorithm proposed by this paper were implemented using Matlab 2010a on Intel (R) Core i7 at 2.2 GHz, 4 GB DDR3 Memory, and system type 64-bit, Window 7. The computation time per image differs for each image and depends mainly on the window's size as well as image size.

Table 4: Performance evaluation of the proposed algorithm compared to four statistical measures for image (a).

Images	Entropy	Homogeneity	Contrast	Energy
Original image (a)	0.036	0.999	0.025	0.998
Proposed algorithm with ($\mu = 0.5, \alpha = 0.4$)	0.224	0.949	2.767	0.881
Proposed algorithm with ($\mu = 0.5, \alpha = 0.5$)	0.260	0.941	3.219	0.860

Table 5: Performance evaluation of the proposed algorithm compared to four statistical measures for image (b).

Images	Entropy	Homogeneity	Contrast	Energy
Original image (b)	0	1	0	1
Proposed algorithm with ($\mu = 0.5, \alpha = 0.4$)	0.017	0.997	0.112	0.994
Proposed algorithm with ($\mu = 0.5, \alpha = 0.5$)	0.032	0.995	0.214	0.989

The proposed texture features enhancement algorithm includes the following steps:

(i) read the original gray-scale image;

(ii) set the value of n and I (≥ 1);

(iii) set the value of the image sampling interval ϕ;

(iv) set the values of the fractional power parameters ($\alpha, \mu \in (0, 1)$);

(v) compute Savitzky-Golay moving window $W^{(\alpha,\mu)}$ as in (24);

(vi) compute the Vandermonde matrix X as in (25);

(vii) apply the Savitzky-Golay fractional differential mask with the corresponding image pixels by sliding the window over the image.

By varying both the fractional powers α and μ, keeping I, and n fixed ($I = 9$, $n = 2$), the elements of the Savitzky-Golay moving window $W^{(\alpha,\mu)}$ have been computed as shown in Tables 2 and 3.

Tables 2 and 3. show the coefficients of the fractional differential moving window for different values of α. All coefficient values are not equal to zero, which implies that the magnitude response of Savitzky-Golay filter is not also zero in the image region. This will likely improve the texture detail. However, the qualities of texture is defined by the spatial distribution of gray values for this reason, we have used gray-scale images for testing, which are shown in Figures 1(a) and 1(b).

In order to illustrate the efficiency of the proposed algorithm in Figure 2, we have presented an illustration of the obtained results for the texture enhancement of the original images of Figure 1.

The proposed enhancement algorithm shows good enhancement performance for both, testing images by different degrees of fractional power values α and μ which are experimentally fixed at $\alpha = 0.4$, 0.5 and $\mu = 0.5$, and the value of the image sampling interval $\varphi = 1$. It is seen that, the proposed enhancement algorithm using fractional differential masks, can extract more texture information and sharpen edges more efficiently. The eye's qualitative analysis of the proposed algorithm acts as one of the important parameters to judge its performance.

Other metrics used to judge the algorithm performance are the statistical measures. In this paper, among the statistical features, the following second-order statistics are used as texture features in representing images. The gray-level co-occurrence matrix (GLCM) is a statistical method used to describe textures in an image, by modeling texture as a two-dimensional gray level variation [28]. Four statistical measures are extracted to evaluate the images texture enhancement; these are entropy, homogeneity, contrast, and energy.

(1) Entropy measures the amount of information, and the larger value of entropy is the greater amount of information carried by image, but inversely correlated to energy. Entropy feature of gray-scale cooccurrence matrix is one of the features having the best discriminatory power, which is given in following equation:

$$\text{Entropy} = \sum_{i,j} p(i,j) \log p(i,j), \tag{27}$$

where $p(i, j)$ is the probability for gray-scale i and j and occurs at two pixels.

(2) Homogeneity measures the closeness of the distribution of elements in the GLCM to the GLCM diagonal:

$$\text{Homogeneity} = \sum_{i,j} \frac{p(i,j)}{1 + |i - j|}. \tag{28}$$

(3) Contrast measures the intensity contrast between a pixel and its neighbour over the whole image:

$$\text{Contrast} = \sum_{i,j} p(i - j)^2. \tag{29}$$

(4) Energy measures the sum of squared elements in the gray-level cooccurrence matrix (GLCM):

$$\text{Energy} = \sum_{i,j} p(i,j)^2. \tag{30}$$

Figure 2 shows the results of the proposed enhancement algorithm for $\mu = 0.5$ with (a) $\alpha = 0.4$, and (b) $\alpha = 0.5$.

(a) (b)

Figure 1: Original images.

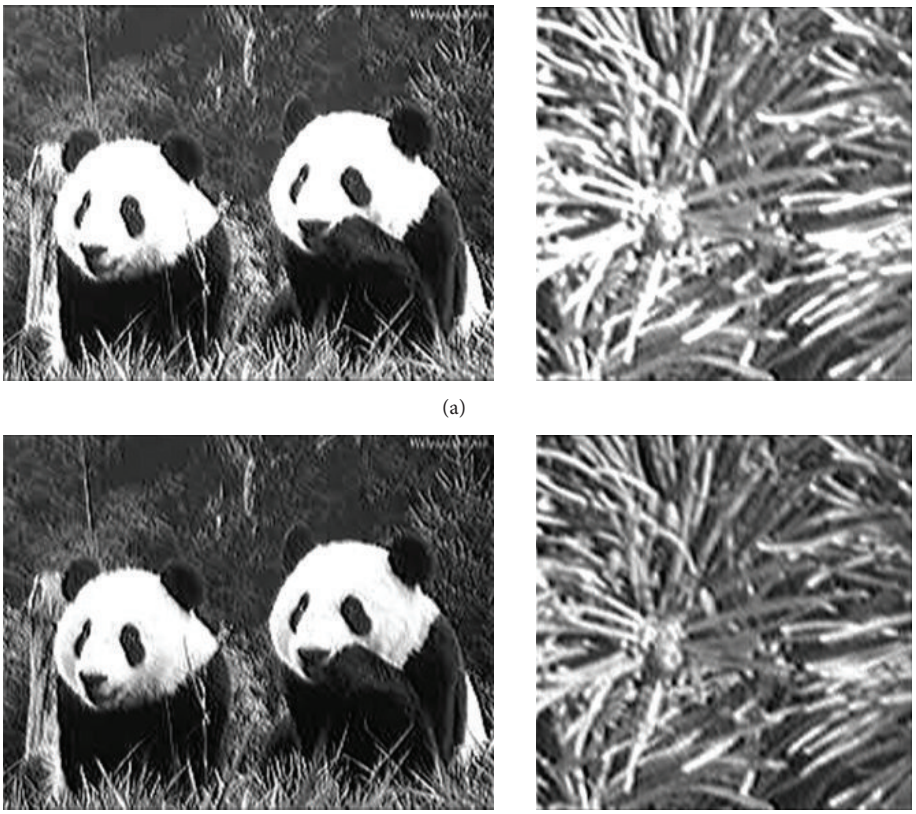

(a)

(b)

Figure 2: The results of the proposed algorithm for $\mu = 0.5$ and; (a) $\alpha = 0.4$, (b) $\alpha = 0.5$.

The variation of the image texture is observed when α is increased from 0.4 to 0.5. So, the selection of differential order is important.

Tables 4 and 5 and Figures 3 and 4 show the performance evaluation of the proposed algorithm for image (a) and image (b) according to those four statistical measures of gray-level cooccurrence matrix (GLCM). It can be clearly seen that there has been a large increase in the value of entropy, which means the greater amount of information is carried by image due to texture enhancement. The entropy values for image (a) climbed to approximately 0.224 for $\alpha = 0.4$ and to 0.26 for $\alpha = 0.5$ for all texture enhancement cases. Moreover, for image (a), it inversely correlated to energy, which decreases to approximately 0.881 for $\alpha = 0.4$ and to 0.860 for $\alpha = 0.5$ and from its value of the original testing image. The homogeneity steadiness is reduced with the increase of texture enhancement, which means more divergence of the distribution of elements of information carried by image due to texture enhancement process. While the contrast showed diverse tendencies for all texture enhancement cases, it is conclude that the intensity contrast between a pixel and its neighbour over the whole image are changed too. This variation in the

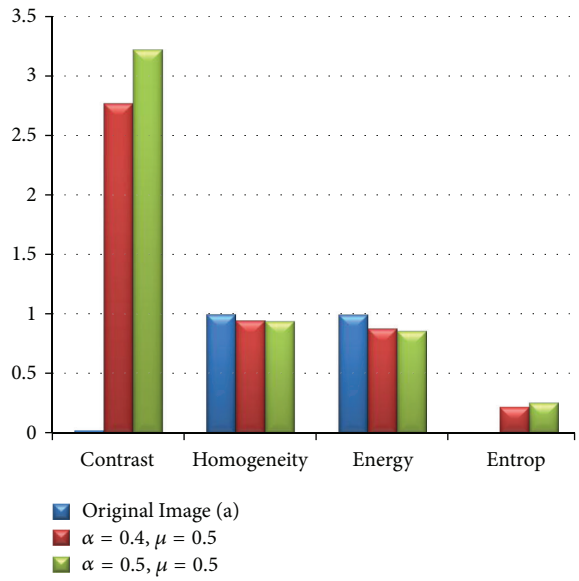

Figure 3: The evaluation performance of the proposed algorithm compared to four statistical measures for image (a).

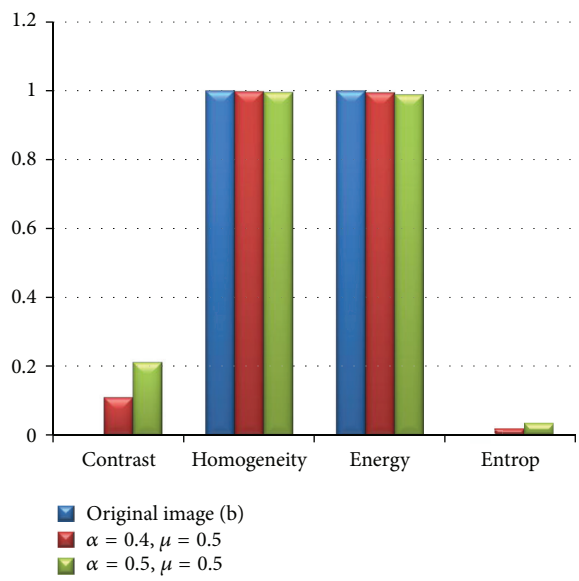

Figure 4: The evaluation performance of the proposed algorithm compared to four statistical measures for image (b).

statistical measures makes the proposed algorithm capable to control the degree of texture enhancement of the image by controlling the fractional order parameters α, μ and φ.

6. Conclusion

In this paper, a texture enhancement technique using fractional order Savitzky-Golay differentiator, which leads to generalize Savitzky-Golay filter in sense of Srivastava-Owa fractional operators, have been introduced. The new algorithm presented in this paper can control the degree of texture enhancement of the image with the fractional power values. The new approach can control the degree of texture enhancement of the image with fractional order of the parameters α, μ, and φ. However, the technique is by no means limited only to images, instead, it can be applied in the setting of different image applications, taking into consideration the limitations of each imaging method. Furthermore, our goal is to keep away from the effect of the noise that caused in the texture enhancement of the image and to control the degree of texture enhancement of the image with the filter mask parameters. The experiment results had demonstrated the efficacy of this algorithm according to the metrics used to judge the algorithm performance.

Acknowledgments

The authors would like to thank the reviewers for their comments on earlier versions of this paper. This research has been funded by university of Malaya, under Grant no. UMRG 104-12ICT.

References

[1] H. A. Jalab, "Image retrieval system based on color layout descriptor and Gabor filters," in *Proceedings of the IEEE Conference on Open Systems (ICOS '11)*, pp. 32–36, 2011.

[2] J. R. Smith and S. F. Chang, "Automated binary texture feature sets for image retrieval," in *Proceedings of the IEEE International Conference on Acoustics, Speech, and Signal Processing (ICASSP '96)*, pp. 2239–2242, May 1996.

[3] N. Bouguila and R. I. Hammoud, "Color texture classification by a discrete statistical model and feature selection," in *Proceedings of the IEEE International Conference on Image Processing (ICIP '09)*, pp. 1381–1384, November 2009.

[4] A. McAndrew, "An introduction to digital image processing with matlab notes for SCM2511 image processing," in *School of Computer Science and Mathematics*, pp. 1–264, Victoria University of Technology, 2004.

[5] S. G. Samko, A. A. Kilbas, and O. I. Marichev, *Fractional Integrals and Derivatives*, Gordon and Breach Science Publishers, Yverdon, Switzerland, 1993.

[6] K. S. Miller and B. Ross, *An Introduction to the Fractional Calculus and Fractional Differential Equations*, A Wiley-Interscience Publication, John Wiley & Sons, New York, NY, USA, 1993.

[7] A. Oustaloup, F. Levron, B. Mathieu, and F. M. Nanot, "Frequency-band complex noninteger differentiator: characterization and synthesis," *IEEE Transactions on Circuits and Systems I*, vol. 47, no. 1, pp. 25–39, 2000.

[8] R. Malti, M. Aoun, F. Levron, and A. Oustaloup, "Analytical computation of the H_2-norm of fractional commensurate transfer functions," *Automatica*, vol. 47, no. 11, pp. 2425–2432, 2011.

[9] R. Malti, X. Moreau, F. Khemane, and A. Oustaloup, "Stability and resonance conditions of elementary fractional transfer functions," *Automatica*, vol. 47, no. 11, pp. 2462–2467, 2011.

[10] S. Victor, P. Melchior, and A. Oustaloup, "Robust path tracking using flatness for fractional linear MIMO systems: a thermal

application," *Computers & Mathematics with Applications*, vol. 59, no. 5, pp. 1667–1678, 2010.

[11] L. Sommacal, P. Melchior, A. Dossat et al., "Improvement of the muscle fractional multimodel for low-rate stimulation," *Biomedical Signal Processing and Control*, vol. 2, no. 3, pp. 226–233, 2007.

[12] D. N. Gruel, P. Lanusse, and A. Oustaloup, "Robust control design for multivariable plants with time-delays," *Chemical Engineering Journal*, vol. 146, no. 3, pp. 414–427, 2009.

[13] P. Lanusse, A. Oustaloup, and J. Sabatier, "Robust design of an anti-windup compensated 3rd-generation CRONE controller," in *Advances in Fractional Calculus*, pp. 527–542, Springer, Dordrecht, The Netherlands, 2007.

[14] J. Hu, Y. Pu, and J. Zhou, "A novel image denoising algorithm based on riemann-liouville definition," *Journal of Computers*, vol. 6, no. 7, pp. 1332–1338, 2011.

[15] H. A. Jalab and R. W. Ibrahim, "Denoising algorithm based on generalized fractional integral operator with two parameters," *Discrete Dynamics in Nature and Society*, vol. 2012, Article ID 529849, 14 pages, 2012.

[16] H. Jalab and R. Ibrahim, "Texture feature extraction based on fractional mask convolution with cesáro means for content-based image retrieval," in *Proceedings of the 12th Pacific Rim Conference on Artificial Intelligence*, pp. 170–179, 2012.

[17] Y. Liu, Y. Pu, and J. Zhou, "Design of image denoising filter based on fractional integral," *Journal of Computational Information Systems*, vol. 6, no. 9, pp. 2839–2847, 2010.

[18] J. Hu, Y. Pu, and J. Zhou, "Fractional integral denoising algorithm and implementation of fractional integral filter," *Journal of Computational Information Systems*, vol. 7, no. 3, pp. 729–736, 2011.

[19] B. Mathieu, P. Melchior, A. Oustaloup, and C. Ceyral, "Fractional differentiation for edge detection," *Signal Processing*, vol. 83, no. 11, pp. 2421–2432, 2003.

[20] R. W. Schafer, "What is a savitzky-golay filter?" *IEEE Signal Processing Magazine*, vol. 28, no. 4, pp. 111–117, 2011.

[21] D. Chen, D. Xue, and F. Pan, "Digital fractional order Savitzky-Golay differentiator," in *IEEE Transactions on Circuits and Systems II*, vol. 58, pp. 758–762, 2011.

[22] Y.-F. Pu and J.-L. Zhou, "A novel approach for multi-scale texture segmentation based on fractional differential," *International Journal of Computer Mathematics*, vol. 88, no. 1, pp. 58–78, 2011.

[23] Y. Pu, "Fractional calculus approach to texture of digital image," in *Proceedings of the 8th International Conference on Signal Processing (ICSP '06)*, November 2006.

[24] Y. Zhang, Y. Pu, and J. Zhou, "Construction of fractional differential masks based on Riemann-Liouville definition," *Journal of Computational Information Systems*, vol. 6, no. 10, pp. 3191–3200, 2010.

[25] H. M. Srivastava and S. Owa, *Univalent Functions, Fractional Calculus, and Their Applications*, Ellis Horwood, Chichester, UK, 1989.

[26] E. Sousa, "How to approximate the fractional derivative of order $1 < \alpha \leq 2$," *International Journal of Bifurcation and Chaos in Applied Sciences and Engineering*, vol. 22, no. 4, 13 pages, 2012.

[27] R. W. Ibrahim, "On generalized Srivastava-Owa fractional operators in the unit disk," *Advances in Difference Equations*, vol. 2011, pp. 1–10, 2011.

[28] S. Selvarajah and S. Kodituwakku, "Analysis and comparison of texture features for content based image retrieval," *International Journal of Latest Trends in Computing*, vol. 108, 2011.

Hindawi Publishing Corporation
Mathematical Problems in Engineering
Volume 2013, Article ID 287040, 5 pages
http://dx.doi.org/10.1155/2013/287040

Research Article

Fractional Describing Function Analysis of PWPF Modulator

Xinsheng Wang,[1,2] Danwei Wang,[2] Senqiang Zhu,[2] and Eng Kee Poh[3]

[1] *Department of Control Science and Engineering, Harbin Institute of Technology at Weihai, Weihai 264209, China*
[2] *EXQUISITUS, Centre for E-City, School of Electrical and Electronic Engineering, Nanyang Technological University, Singapore 639798*
[3] *DSO National Laboratories, Singapore 117510*

Correspondence should be addressed to Xinsheng Wang; wangxswh@126.com

Received 9 November 2012; Accepted 8 January 2013

Academic Editor: Clara Ionescu

Pulse-width pulse-frequency (PWPF) modulators are widely used in spacecraft thruster control. Their dynamic characteristic is still lack of effective analysis tools. This paper presents a fractional describing function method to describe the frequency characteristics of PWPF. A frequency-dependent gain and phase shift are clearly described by fractional-order expression, and the fractional-order behaviors depict the nonlinear properties of PWPF modulators. This fractional describing function method can also be applied to other kinds of modulators.

1. Introduction

Spacecrafts commonly deploy thrusters as actuators for attitude control [1]. As thrusters work on on/off switching, there is a conversion from continuous desired torque control command to an on/off signal for spacecraft thrusters. There are two common approaches for thruster activation. The simplest converter is a bang-bang controller which is, however, vulnerable to noise. Several improved controllers have been proposed, such as bang-bang controller with dead zone or time-optimal bang-bang controller [2]. Another kind of the converter is pulse modulators, which produce a pulse command sequence to the thruster valves by adjusting pulse width and/or pulse frequency according to the level of input [3]. Among the known pulse modulators, the pulse-width pulse-frequency (PWPF) modulators are the most common and enjoy advantages over bang-bang control systems [4]. But the inherent nonlinearity of PWPF has inhibited the dynamic analysis of attitude control system.

Describing function method is a well-known analysis tool for a kind of nonlinear system with certain structure. If the output signal of a nonlinear device can be approximated by the fundamental harmonics, the fundamental harmonics can be used to define the frequency characteristics of the nonlinear element and is called a describing function [5]. The describing function method is primarily used to analyze the stability and limit cycle of nonlinear control systems and is inherently approximate. In the last decades, many new criteria were established to improve the accuracy. These new types of describing function methods include area-matching method, root-mean-square method, and corrected RMS method [3].

Recently, fractional calculus has been increasingly applied to mechanical systems, electricity, and bioengineering [6, 7]. Fractional calculus studies derivatives and integrals of fractional order. It is shown that fractional-order system works more accurately than integer-order system [8, 9]. With the development of computational tools, more and more fractional-order models and controllers are studied [10, 11]. Noticeably, the describing function method is also considered in the framework of nonlinear fractional-order systems [12, 13]. In this paper, fractional describing function will be introduced to describe the dynamics of PWPF actuators.

2. Pulse-Width Pulse-Frequency Modulator

Pulse modulators are commonly used in thruster control of fuel valves. There are various kinds of pulse modulators, such as pulse-width modulator, pulse-frequency modulator,

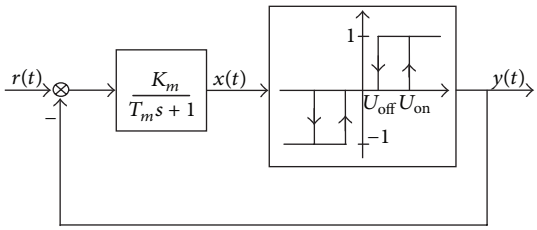

Figure 1: Structure of PWPF modulator.

Table 1: Static characteristic variables of PWPF modulator.

On time	$T_{on} = -T_m \ln\left(1 - \frac{h}{U_{on} - K_m(C-U)}\right)$
Off time	$T_{off} = -T_m \ln\left(1 - \frac{h}{K_m C - U_{off}}\right)$
Modulator frequency	$f = \frac{1}{T_{on} + T_{off}}$
Duty cycle	$\mathrm{DC} = \frac{T_{on}}{T_{on} + T_{off}}$
Equivalent internal deadband	$C_d = \frac{U_{on}}{K_m}$
Equivalent internal saturation level	$C_s = 1 + \frac{U_{off}}{K_m}$

pseudo-rate modulator, and pulse-width pulse-frequency (PWPF) modulator [14, 15]. PWPF modulator is preferred for its operation has almost linear input/output relationship [16, 17]. A PWPF modulator mainly comprises two components: a first-order lag filter and a Schmitt trigger inside a feedback loop, as shown in Figure 1. A Schmitt trigger is an on-off relay with a dead zone and hysteresis. It differs from bang-bang controller in that there are two thresholds: one on-value U_{on} and one off-value U_{off}. These values define a hysteresis as $h = U_{on} - U_{off}$. The output of the Schmitt trigger is compared with the reference signal, and the error is fed to the first-order filter whose output is the input of the Schmitt trigger. PWPF modulator operates in a quasilinear mode by modulating the width of the output pulses and the distance between them simultaneously. And it can produce pulses in two directions: positive and negative pulses.

With a constant input C, the PWPF modulator drives the thruster valve with an on-off pulse sequence having a nearly linear duty cycle. The time interval in which the modulator has a nonzero output is denoted T_{on}, and the time interval with a zero output is denoted T_{off}. Static characteristics variables of PWPF are collected in Table 1. These variables are considered in the modulator design. Paper [18] shows the relationship between the static characteristics of PWPF modulator and selection of its parameters.

The static analysis of PWPF modulator shows that it operates near linear to the constant input over a large range between the deadband C_d and saturation level C_s. The modulator's operations are independent from the spacecraft's parameters and allow easy parameter tuning, especially when there are different requirements through different phases of operation. In addition, this modulator has the superiority in fuel consumption and pointing accuracy in the presence of vibrations. However, attitude control systems usually operate on dynamic mode, and PWPF modulators will introduce phase lag to the attitude control systems, which can cause instability. Dynamic analysis is necessary for the attitude control system design. But as to this nonlinear device, effective tools are limited. This work will propose the use of fractional-order describing function method and develops some useful techniques.

3. Derivation of Fractional Describing Function

Describing function method is an approximation method for analyzing nonlinear dynamics, because only the first harmonic of the output of a nonlinear element is considered. But here describing function method is beneficial for PWPF modulator analysis for the following reasons. Firstly, the first-order filter which is in series with the nonlinear element serves as a low-pass filter in PWPF modulator. Secondly, the attitude control system is a high-order system, where high harmonics are attenuated substantially. In this section, the PWPF modulator is considered as a single device and its fractional describing function is developed.

3.1. Describing Function of Hysteresis. A nonlinear element to a sinusoidal input $x(t) = X\sin(\omega t)$ in general does not generate a sinusoidal output, but the output $y(t)$ is periodic. If the nonlinearity is symmetrical with respect to the variation around zero, the output signal can be decomposed to the Fourier series:

$$\begin{aligned} y(t) &= \sum_{n=1}^{\infty} \left(A_n \cos n\omega t + B_n \sin n\omega t\right) \\ &= \sum_{n=1}^{\infty} Y_n \sin\left(n\omega t + \varphi_n\right), \end{aligned} \tag{1}$$

where

$$\begin{aligned} A_n &= \frac{1}{\pi}\int_0^{2\pi} y(t)\cos n\omega t d(\omega t), \\ B_n &= \frac{1}{\pi}\int_0^{2\pi} y(t)\sin n\omega t d(\omega t), \\ Y_n &= \sqrt{A_n^2 + B_n^2}, \\ \varphi_n &= \tan^{-1}\frac{A_n}{B_n}, \end{aligned} \tag{2}$$

and the frequency of the fundamental harmonic is the same frequency as the input with amplitude Y_1 and phase shift φ_1:

$$\begin{aligned} y_1(t) &= A_1 \cos\omega t + B_1 \sin\omega t \\ &= Y_1 \sin\left(\omega t + \varphi_1\right). \end{aligned} \tag{3}$$

With the assumption that the amplitude of fundamental harmonic is much larger than the amplitude of other harmonics, the describing function is defined as the complex ratio of

the fundamental harmonic component of the output and the input, that is,

$$N(X,\omega) = \frac{Y_1}{X} e^{j\varphi_1}, \tag{4}$$

where $N(X,\omega)$ is the describing function of the nonlinear element, X is the sinusoidal input amplitude, ω is the frequency of input sinusoid, Y_1 is the amplitude of the fundamental harmonic, Y_1/X is the describing function gain, and φ_1 is the describing function phase.

Imposing this harmonic balance principle, $N(X,\omega)$ can be used as frequency characteristic of nonlinear element to analyze the dynamics of a linear closed-loop system. The Schmitt trigger in PWPF modulator exhibits hysteresis nonlinearity, whose describing function of hysteresis can be deduced as shown above directly:

$$N(X) = \frac{4}{\pi X}\sqrt{1-\left(\frac{h}{X}\right)^2} - j\frac{4h}{\pi X^2}. \tag{5}$$

Remark 1. The describing function defined above is based on fundamental harmonic equivalence. The influence of high order harmonics can be considered as system uncertainty.

3.2. Frequency Characteristics of PWPF. The PWPF modulator is a unit in the attitude control system. Considering, the frequency characteristics of PWPF as a whole is convenient for analysis and design of the attitude control system. In the structure of Figure 1, the frequency characteristic of the first-order filter is

$$L(j\omega) = \frac{K_m}{1+j\omega T_m}. \tag{6}$$

Then the frequency characteristic of the PWPF closed-loop system is

$$NN(X,\omega) = \left(\frac{4K_m}{\pi X}\sqrt{1-\left(\frac{h}{X}\right)^2} - j\frac{4hK_m}{\pi X^2}\right) \times\left(\left(1+\frac{4K_m}{\pi X}\sqrt{1-\left(\frac{h}{X}\right)^2}\right)+j\left(\omega T_m-\frac{4hK_m}{\pi X^2}\right)\right)^{-1}. \tag{7}$$

If the describing function is independent of frequency ω, it is plotted with varying nonlinear input X. But when it is a function of both amplitude X and frequency ω, certain ω values are selected to view the plot of frequency characteristics. Consequently, this kind of plot lacks frequency dependent information. For control system dynamic analysis, information about how the amplitude and phase of a nonlinear element change with frequency is important because the nonlinear part usually adds phase lag to control system, which would destroy close-loop stability of the control system.

Now, a fractional describing function is introduced to give a direct relationship between the nonlinear characteristic and frequency. For illustration purpose, set the parameters of PWPF as follows: $K_m = 7.46$, $T_m = 1.33$, $U_{\text{on}} = 0.45$, and $U_{\text{off}} = 0.25$. Figure 2 shows the Nichols plot of the closed-loop describing function $NN(X,\omega)$. It can be seen that with the amplitude X changing from 0.5 to 10 the magnitude of $NN(X,\omega)$ decreases, and the phase lag increases. To show the characteristic with frequency, several curves corresponding with different frequencies are plotted. Though it is clear that higher frequency induces larger phase lag, but the curves are separated and cannot show continuous information about frequency.

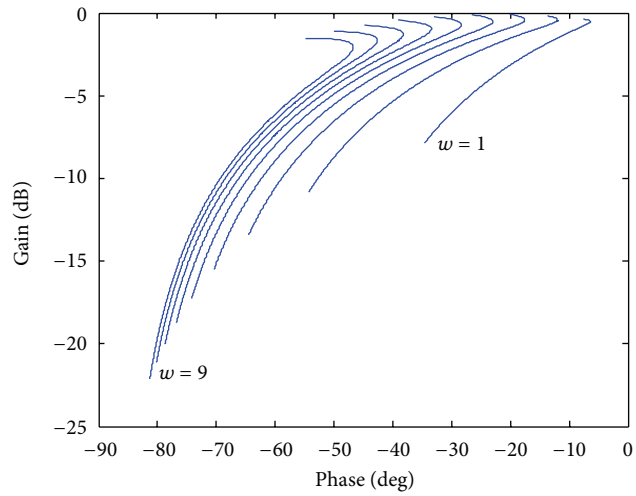

Figure 2: Nichols plot of $NN(X,\omega)$.

To reveal the relationship between the describing function and the frequency of interest, the real part and imaginary part of $NN(X,\omega)$ are studied, respectively. For attitude control, the interested frequency is relatively low. Figures 3 and 4 show the log-log plots of the real part and imaginary part of $NN(X,\omega)$ versus the exciting frequency ω, respectively, where the nonlinear input X is from 0.5 to 1. Approximately, the curves can be considered as straight lines. Then a fractional-order behavior is investigated.

The fractional-order behavior is described by power functions, so it is called fractional describing function. The new function can be written as

$$FNN(X,\omega) = -a\omega^{-b} - jc\omega^{-d}, \quad \{a,b,c,d\} \in \mathrm{R}^+. \tag{8}$$

Figure 3 shows that the real part of $NN(X,\omega)$ can be considered as a constant, that is, $b = 0$ and $-0.9 < a < -0.88$. Figure 4 shows that the imaginary part of $NN(X,\omega)$ is fractional with $-0.75 < d < -0.7$ and $0.11 < c < 0.13$. These values will vary with system parameters, but the fractional property remains the same. It can be seen that the range of parameters $\{a,b,c,d\}$ does not vary much. We can choose one set of values to simulate the frequency characteristic of the PWPF modulator. Here, we set the values $\{a,b,c,d\} = \{-0.9, 0, 0.12, -0.74\}$. With the help of available fractional calculator software [19, 20], frequency characteristic diagrams can be plotted. Figure 5 shows the Bode diagram of $FNN(X,\omega)$. It predicts a phase lag of

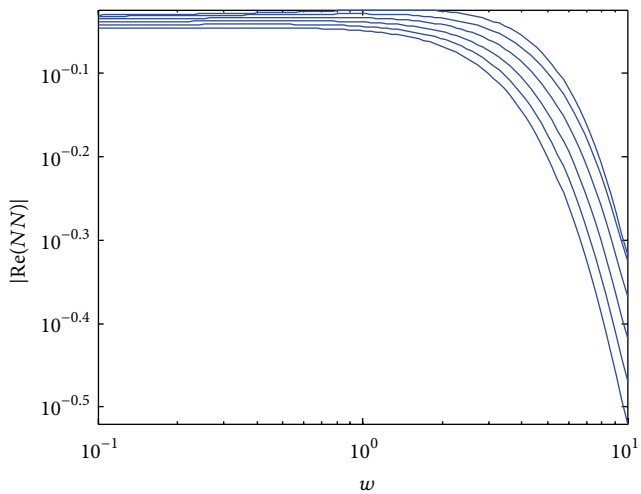

Figure 3: Log-log plots of $|\operatorname{Re}(NN)|$.

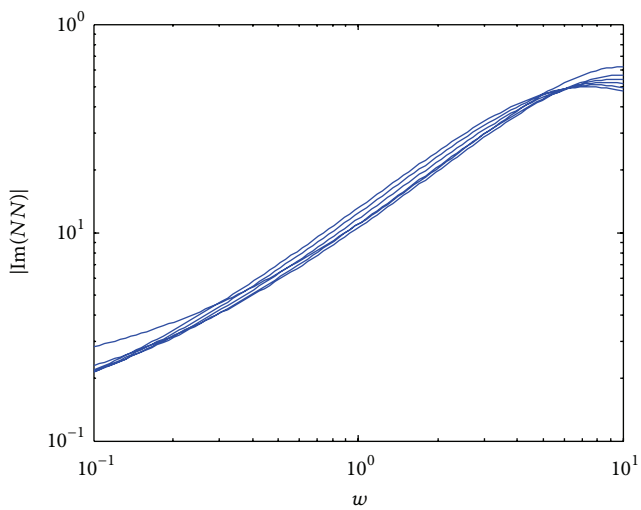

Figure 4: Log-log plots of $|\operatorname{Im}(NN)|$.

about 10 degrees to 25 degrees between frequency 1 rad/s to 5 rad/s, which relates well with the analysis result in [3]. This information is crucial to the stability analysis of attitude control system.

Remark 2. The deduced fractional describing function is useful for system stability analysis for it is considered around the crossover frequency.

4. Conclusions

PWPF modulator is a nonlinear actuator in spacecraft attitude control system. The nonlinear dynamic behavior of PWPF modulator is investigated by the fractional describing function in this paper. The nonlinear element of PWPF is a Schmitt trigger, and its frequency characteristic can be described by describing function, and the fractional behaviors are caused by nonlinear element in PWPF. The frequency

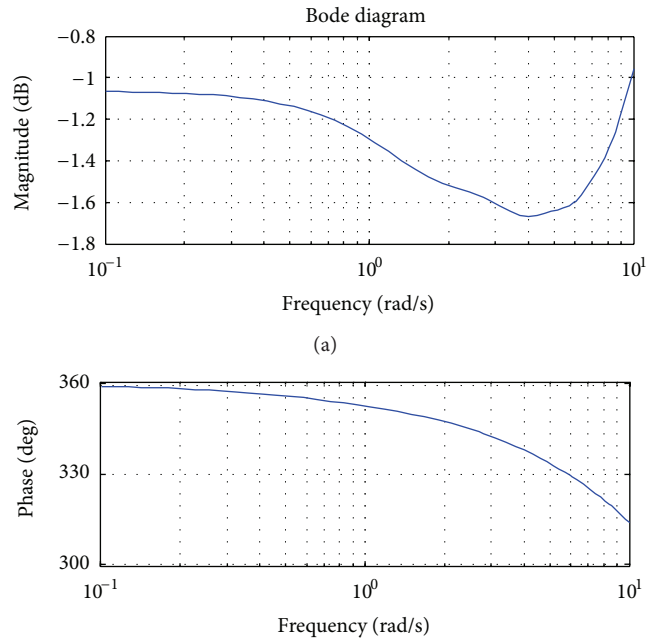

Figure 5: Bode diagram of $FNN(X, \omega)$.

characteristic of the actuator is frequency dependent. The log-log plots of the real part and imaginary part of a modulator clearly reveal the fractional-order behavior. The imaginary component is described by fractional-order power function over a certain frequency range. With fractional calculus, these frequency-dependent gain and phase information can be plotted in Bode diagram and used for control system design. Furthermore, the fractional describing function method should be an effective tool for other kinds of modulators.

Acknowledgments

This work is funded in part by the China Scholarship Council (CSC) and in part under Project Agreement no. DSOCL10004 with DSO National Laboratories, Singapore.

References

[1] M. J. Sidi, *Spacecraft Dynamics and Control: A Practical Engineering Approach*, Cambridge Aerospace Series, Cambridge university press, New York, NY, USA, 1997.

[2] B. Wie and C. T. Plescia, "Attitude stabilization of flexible spacecraft during station-keeping maneuvers," *Journal of Guidance, Control, and Dynamics*, vol. 7, no. 4, pp. 430–436, 1984.

[3] T. C. Anthony, B. Wie, and S. Carroll, "Pulse-modulated control synthesis for a flexible spacecraft," *Journal of Guidance, Control, and Dynamics*, vol. 13, no. 6, pp. 1014–1022, 1990.

[4] B. N. Agrawal, "Spacecraft vibration suppression using smart structure," in *Proceedings of the 4th International Congress on Sound and Vibration*, pp. 563–570, St. Petersburg, Russia, 1996.

[5] H. Khalil, *Nonlinear System*, Prentice Hall, Upper Saddle River, NJ, USA, 2002.

[6] R. L. Bagley and R. A. Calico, "Fractional order state equations for the control of viscoelastically damped structures," *Journal of Guidance, Control, and Dynamics*, vol. 14, no. 2, pp. 304–311, 1991.

[7] C. M. Ionescu, J. A. T. Machado, and R. De Keyser, "Modeling of the lung impedance using a fractional-order ladder network with constant phase elements," *IEEE Transactions on Biomedical Circuits and Systems*, vol. 5, no. 1, pp. 83–89, 2011.

[8] I. Podlubny, "Fractional-order systems and $PI^{\lambda}D^{\mu}$-controllers," *Institute of Electrical and Electronics Engineers. Transactions on Automatic Control*, vol. 44, no. 1, pp. 208–214, 1999.

[9] A. Oustaloup, J. Sabatier, and P. Lanusse, "From fractal robustness to the CRONE control," *Fractional Calculus & Applied Analysis*, vol. 2, no. 1, pp. 1–30, 1999.

[10] C. A. Monje, Y. Chen, B. M. Vinagre, D. Xue, and V. Feliu, *Fractional-Order Systems and Controls*, Springer, New York, NY, USA, 2010.

[11] Y. Luo and Y. Chen, "Fractional order [proportional derivative] controller for a class of fractional order systems," *Automatica*, vol. 45, no. 10, pp. 2446–2450, 2009.

[12] M. S. Tavazoei and M. Haeri, "Describing function based methods for predicting chaos in a class of fractional order differential equations," *Nonlinear Dynamics*, vol. 57, no. 3, pp. 363–373, 2009.

[13] F. B. Duarte and J. T. MacHado, "Fractional describing function of systems with Coulomb friction," *Nonlinear Dynamics*, vol. 56, no. 4, pp. 381–387, 2009.

[14] B. Wie, *Space Vehicle Dynamics and Control*, AIAA Educational Series, Washington, DC, USA, 1998.

[15] Q. Hu and G. Ma, "Variable structure control and active vibration suppression of flexible spacecraft during attitude maneuver," *Aerospace Science and Technology*, vol. 9, no. 4, pp. 307–317, 2005.

[16] G. Song, N. V. Buck, and B. N. Agrawal, "Spacecraft vibration reduction using pulse-width pulse-frequency modulated input shaper," *Journal of Guidance, Control, and Dynamics*, vol. 22, no. 3, pp. 433–440, 1999.

[17] K. H. Kienitz and J. Bals, "Pulse modulation for attitude control with thrusters subject to switching restrictions," *Aerospace Science and Technology*, vol. 9, no. 7, pp. 635–640, 2005.

[18] T. D. Krovel, *Optimal tuning of PWPF modulator for attitude control [M.S. thesis]*, Norwegian University of Science and Technology, 2005.

[19] Y. Q. Chen, I. Petráš, and D. Xue, "Fractional order control—a tutorial," in *Proceedings of the American Control Conference (ACC '09)*, pp. 1397–1411, St. Louis, Mo, USA, June 2009.

[20] I. Petráš, "Fractional-order memristor-based Chua's circuit," *IEEE Transactions on Circuits and Systems II: Express Briefs*, vol. 57, no. 12, pp. 975–979, 2010.

Hindawi Publishing Corporation
Mathematical Problems in Engineering
Volume 2013, Article ID 654759, 6 pages
http://dx.doi.org/10.1155/2013/654759

Research Article

Study on Space-Time Fractional Nonlinear Biological Equation in Radial Symmetry

Yanqin Liu[1,2]

[1] *Department of Mathematics, Dezhou University, Dezhou 253023, China*
[2] *Nonlinear Dynamics and Chaos Group, School of Management, Tianjin University, Tianjin 30072, China*

Correspondence should be addressed to Yanqin Liu; yqlin8801@yahoo.cn

Received 1 September 2012; Revised 24 December 2012; Accepted 25 December 2012

Academic Editor: Clara Ionescu

We consider the initial stage of space-time fractional generalized biological equation in radial symmetry. Dimensionless multiorder fractional nonlinear equation was first given, and approximate solutions were derived in the form of series using the homotopy perturbation method with a new modification. And the influence of fractional derivative is also discussed.

1. Introduction

The problem of biological diffusion is an issue of increasing significance in contemporary ecology [1, 2]. In case of favourable environmental conditions, the alien population may begin to grow and spread over the area and thus the local initial structural perturbation of the native biological community may lead to large-scale dramatic changes in the community structure. Recently, it has turned out that many phenomena in engineering, physics, chemistry, and other sciences [3–5] can be described very successfully by models using mathematical tools fractional calculus [6, 7], such as anomalous transport in disordered systems [8–10], some percolations in porous media, and the diffusion biological population. Mathematical aspects of the biological problem have been considered in many papers [11–13]. El-Sayed et al. [14] studied the fractional-order biological population model in the form $\partial^\alpha u/\partial t^\alpha = \partial^2(u^2)/\partial x^2 + \partial^2(u^2)/\partial y^2 + f(u)$ using the Adomian decomposition method. Wazwaz and Gorguis [15] gave a detailed study of integer Fisher's diffusion equation by using Adomian decomposition method. Najeeb et al. [16] studied the time fractional Fisher's equation and approximate analytical solutions were obtained by using homotopy analysis method. Petrovskii et al. [17] obtained an exact solution of the spatiotemporal dynamics of a predator-prey community by using an approximate change of variables, and the properties of the solution exhibit biologically reasonable dependence on the parameter values. Liu and Xin [18] studied the fractional Lotka-Volterra equations using the homotopy perturbation method.

This paper is devoted to investigating approximate solutions of a generalized fractional nonlinear population diffusion equation in radical symmetry. The structure of the paper is as follows. In Section 2, a brief review of the theory of fractional calculus will be given to fix notation and provide a convenient reference. In Section 3, a mathematical formulation of the generalized multifractional population diffusion model in radical symmetry is given. In Section 4, we extend the homotopy perturbation method and a new reliable modification to the fractional nonlinear population diffusion system and give some properties of this model. Conclusions and prospects will be presented in Section 5.

2. Fractional Calculus

There are several approaches to define the fractional calculus; the Riemann-Liouville and Caputo fractional operators are defined as follows.

Definition 1. The Riemann-Liouville fractional integral operator $J^\alpha(\alpha \geq 0)$ of a function $f(t)$ is defined as

$$J^\alpha f(t) = \frac{1}{\Gamma(\alpha)} \int_0^t (t-\tau)^{\alpha-1} f(\tau)\, d\tau, \quad (\alpha \geq 0), \tag{1}$$

where $\Gamma(\cdot)$ is the well-known gamma function, and some properties of the operator J^α are as follows:

$$J^\alpha J^\beta f(t) = J^{\alpha+\beta} f(t), \quad (\alpha \geq 0, \beta \geq 0),$$
$$J^\alpha t^\gamma = \frac{\Gamma(1+\gamma)}{\Gamma(1+\gamma+\alpha)} t^{\alpha+\gamma}, \quad (\gamma \geq -1). \tag{2}$$

Definition 2. The Caputo fractional derivative D^α of a function $f(t)$ is defined as

$$ {}_0D_t^\alpha f(t) = \frac{1}{\Gamma(n-\alpha)} \int_0^t \frac{f^{(n)}(t)\, d\tau}{(t-\tau)^{\alpha+1-n}}, \quad (n-1 < \operatorname{Re}(\alpha) \leq n, n \in N). \tag{3}$$

The following are two basic properties of the Caputo fractional derivative:

$$ {}_0D_t^\alpha t^\beta = \frac{\Gamma(1+\beta)}{\Gamma(1+\beta-\alpha)} t^{\beta-\alpha},$$
$$ {}_0D_t^\alpha \left({}_0D_t^m f(t)\right) = {}_0D_t^{\alpha+m} f(t), \quad (m = 0, 1, 2, \ldots;\ n-1 < \alpha \leq n),$$
$$\left(J^\alpha D^\alpha\right) f(t) = f(t) - \sum_{k=0}^{n-1} f^{(k)}(0^+) \frac{t^k}{k!}. \tag{4}$$

We have chosen the Caputo fractional derivative because it allows traditional initial and boundary conditions to be included in the formulation of the problem. And some other properties of fractional derivative can be found in [3, 5].

3. Main Equations

It is widely accepted that the spatiotemporal dynamics of a biological community can be qualitatively described by diffusion-reaction equations [2, 19]. A remarkable point is that, in some cases, relatively simple single-species models provide not only qualitative but also quantitative descriptions of the dynamics of a population. In this paper, we first consider a single-species parabolic nonlinear equation arising in the spatial diffusion of biological populations [11, 14]

$$\frac{\partial u(x,y,t)}{\partial t} = D\left(\frac{\partial^2}{\partial x^2}\left(u^2\right) + \frac{\partial^2 u}{\partial y^2}\left(u^2\right)\right) + f(u), \tag{5}$$

where $u(x,y,t) \geq 0$ is the population density at position x, y, and time t, coefficient D describes the intensity of mixing due to animals self-motion, the term $f(u)$ describes multiplication and mortality of a given population, $f(0) = f(K) = 0$, and parameter K is being treated as the carrying capacity for the given population. Let us assume that the initial distribution of the species is symmetrical, with the density of the species depending only on the distance from the origin. Assuming also that the environment is homogeneous, that is, both D and $f(u)$ not depends explicitly on the position in space, we arrive at the following problem:

$$\frac{\partial u(r,t)}{\partial t} = D\left(\frac{\partial^2}{\partial r^2}\left(u^2\right) + \frac{1}{r}\frac{\partial}{\partial r}\left(u^2\right)\right) + f(u), \quad u(r,0) = \varphi(r,l), \tag{6}$$

where $0 < r < l$ and l is the typical size of the domain and initial condition $\varphi(r,l)$ promptly approaches zero when $r/l \gg 1$. It has turned out that the diffusion of biological population can be described very successfully by fractional calculus. In this paper, we discuss the corresponding fractional equation and the main aim is to solve the nonlinear fractional biological population model in the following form:

$$\frac{\partial^\alpha u(r,t)}{\partial t^\alpha} = D\left(\frac{\partial^{1+\beta}}{\partial r^{1+\beta}}\left(u^2\right) + \frac{1}{r}\frac{\partial^\beta}{\partial r^\beta}\left(u^2\right)\right) + f(u), \quad u(r,0) = \varphi(r,l), \tag{7}$$

where $0 < \alpha \leq 1$, $0 < \beta \leq 1$ is the Caputo derivative. A proper choice of the dimensionless variables, that is, in our case, the choice of scales for the variables u, r, and t, is an important point. Coming with the property ${}_0D_t^\alpha f(t) = a_0^{-\alpha} D_t^\alpha f(at)$ of the Caputo derivative and using reduced dimensionless variables defined as

$$\tilde{u} = \frac{u}{K}, \qquad \tilde{r} = \frac{r}{l}, \qquad \tilde{t} = \left(\frac{KD}{l^{1+\beta}}\right)^{1/\alpha} t \tag{8}$$

(8) can be reduced to the respective dimensionless forms (tildes will be omitted hereafter):

$$\frac{\partial^\alpha u}{\partial t^\alpha} = \frac{\partial^{1+\beta}}{\partial r^{1+\beta}}\left(u^2\right) + \frac{1}{r}\frac{\partial^\beta}{\partial r^\beta}\left(u^2\right) + F(u), \quad u(r,0) = \varphi(r,1), \tag{9}$$

where $F(u) = (l^{1+\beta}/KD) f(u)$.

4. Approximate Solution to the Equation

We now proceed to derive approximate solution to fractional nonlinear population diffusion equation (9).

Case 1. In this case, we will examine the following time-space fractional nonlinear population model:

$$\frac{\partial^\alpha u}{\partial t^\alpha} = \frac{\partial^{1+\beta}}{\partial r^{1+\beta}}\left(u^2\right) + \frac{1}{r}\frac{\partial^\beta}{\partial r^\beta}\left(u^2\right) + hu, \tag{10}$$

$$u(r,0) = r, \tag{11}$$

where $F(u) = hu$, $h =$ constant, corresponding to the *Malthusian* law. According to the homotopy perturbation method, we construct the following simple homotopy:

$$\frac{\partial^\alpha u}{\partial t^\alpha} = p\left[\frac{\partial^{1+\beta}}{\partial r^{1+\beta}}\left(u^2\right) + \frac{1}{r}\frac{\partial^\beta}{\partial r^\beta}\left(u^2\right) + hu\right], \tag{12}$$

where $p \in [0,1]$ is an embedding parameter. In case $p = 0$, (12) is a fractional differential equation, $D_t^\alpha u = 0$, which is easy to solve, and when $p = 1$, (12) turns out to be the original one (10). The basic assumption is that the solutions can be written as a power series in p:

$$u = \sum_{n=0}^{\infty} p^n u_n = u_0 + pu_1 + p^2 u_2 + p^3 u_3 + \cdots, \tag{13}$$

u_0 is an initial approximation of (10). The approximate solutions of the original equations can be obtained by setting $p = 1$, that is,

$$u(x,t) = \lim_{p \to 1} \sum_{n=0}^{\infty} p^n u_n = u_0 + u_1 + u_2 + u_3 + \cdots. \tag{14}$$

Instituting (13) into (12) and comparing coefficients of terms with identical powers of p then applying J^α on both sides of equations yield

$$\begin{aligned}
u_0 &= r, \\
u_1 &= J^\beta \left[\frac{\partial^{1+\beta}}{\partial r^{1+\beta}} \left(u_0^2\right) + \frac{1}{r} \frac{\partial^\beta}{\partial r^\beta} \left(u_0^2\right) + hu_0 \right] \\
&= \frac{hrt^\alpha}{\Gamma(1+\alpha)} + \frac{2r^{1-\beta}t^\alpha}{\Gamma(1+\alpha)\Gamma(2-\beta)} \\
&\quad + \frac{2r^{1-\beta}t^\alpha}{\Gamma(1+\alpha)\Gamma(3-\beta)}, \\
u_2 &= J^\beta \left[\frac{\partial^{1+\beta}}{\partial r^{1+\beta}} \left(2u_0u_1\right) + \frac{1}{r} \frac{\partial^\beta}{\partial r^\beta} \left(2u_0u_1\right) + hu_1 \right] \\
&= \frac{h^2rt^{2\alpha}}{\Gamma(1+2\alpha)} + \frac{8r^{1-2\beta}t^{2\alpha}}{\Gamma(1+2\alpha)\Gamma(2-2\beta)} \\
&\quad - \frac{4r^{1-2\beta}t^{2\alpha}\beta}{\Gamma(1+2\alpha)\Gamma(2-2\beta)} + \frac{4r^{1-2\beta}t^{2\alpha}}{\Gamma(1+2\alpha)\Gamma(3-2\beta)} \\
&\quad + \frac{6hr^{1-\beta}t^{2\alpha}}{\Gamma(1+2\alpha)\Gamma(2-\beta)} + \frac{6hr^{1-\beta}t^{2\alpha}}{\Gamma(1+2\alpha)\Gamma(3-\beta)} \\
&\quad + \frac{8r^{1-2\beta}t^{2\alpha}\Gamma(2-\beta)}{\Gamma(1+2\alpha)\Gamma(2-2\beta)\Gamma(3-\beta)} \\
&\quad - \frac{4r^{1-2\beta}t^{2\alpha}\beta\Gamma(2-\beta)}{\Gamma(1+2\alpha)\Gamma(2-2\beta)\Gamma(3-\beta)} \\
&\quad + \frac{4r^{1-2\beta}t^{2\alpha}\Gamma(3-\beta)}{\Gamma(1+2\alpha)\Gamma(3-2\beta)\Gamma(2-\beta)}, \\
u_3 &= J^\beta \left[\frac{\partial^{1+\beta}}{\partial r^{1+\beta}} \left(2u_0u_2 + u_1^2\right) + \frac{1}{r} \frac{\partial^\beta}{\partial r^\beta} \left(2u_0u_2 + u_1^2\right) + hu_2 \right] \\
&\quad \vdots
\end{aligned} \tag{15}$$

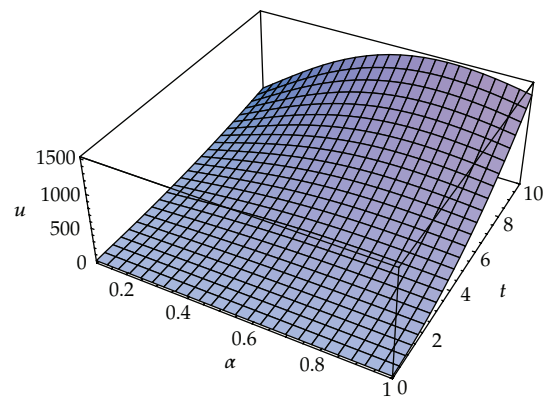

Figure 1: The surface of second-order approximate solution of (10) when $r = 0.6$, $\beta = 1$.

and so on, in this manner the rest of components of the solution can be obtained. The solution of (10) in series form is given by

$$\begin{aligned}
u(r,t) &= r + \frac{hrt^\alpha}{\Gamma(1+\alpha)} + \frac{2r^{1-\beta}t^\alpha}{\Gamma(1+\alpha)\Gamma(2-\beta)} \\
&\quad + \frac{2r^{1-\beta}t^\alpha}{\Gamma(1+\alpha)\Gamma(3-\beta)} + \cdots.
\end{aligned} \tag{16}$$

Figure 1 shows the approximate solution for (10) and (11) by using the homotopy perturbation method when choosing $r = 0.6$, $\beta = 1$. From the figure, it is clear to see the time evolution of nonlinear population diffusion density and we also know that the approximate solution of fractional population model is continuous with the fractional parameter α. Figure 2 shows the approximate solution for (10) and (11) when $r = 0.6$, $\alpha = 1$, and the approximate solution of fractional population model is continuous with the fractional parameter β. Figures 3 and 4 show the approximate solution for (10) and (11) when the time $t = 10$, from the figures, we also know that the population density changes with the parameters $\alpha, \beta,$ and r.

Case 2. In this case, we will examine the following time-space fractional nonlinear population model:

$$\frac{\partial^\alpha u}{\partial t^\alpha} = \frac{\partial^{1+\beta}}{\partial r^{1+\beta}} \left(u^2\right) + \frac{1}{r} \frac{\partial^\beta}{\partial r^\beta} \left(u^2\right) + hu(1-gu), \tag{17}$$

$$u(r,0) = e^r, \tag{18}$$

$F(u) = hu(1-gu)$, h, g are constant, corresponding to the *Verhulst* law. According to the homotopy perturbation method, we construct the following simple homotopy:

$$\frac{\partial^\alpha u}{\partial t^\alpha} = p \left[\frac{\partial^{1+\beta}}{\partial r^{1+\beta}} \left(u^2\right) + \frac{1}{r} \frac{\partial^\beta}{\partial r^\beta} \left(u^2\right) + hu(1-gu) \right]. \tag{19}$$

For this case, it is difficult to solve the multifractional equation. We give a new modification of the homotopy perturbation method; the modified form of the homotopy

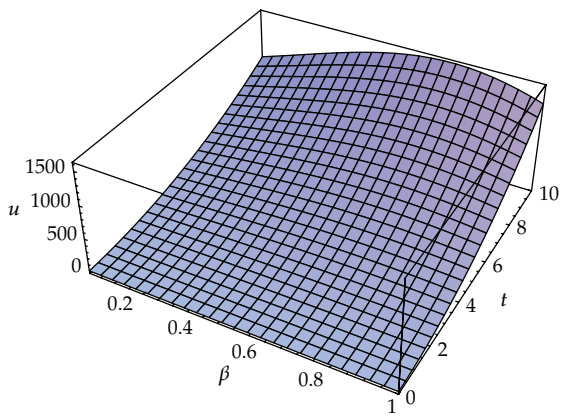

Figure 2: The surface of second-order approximate solution of (10) when $r = 0.6$, $\alpha = 1$.

perturbation method can be established based on the initial condition expressed in the Taylor series. We suggest that $u(r,0)$ be expressed in the Taylor series

$$e^r = 1 + r + \frac{r^2}{2} + \frac{r^3}{6} + \cdots. \tag{20}$$

Instituting (13) into (19) and comparing coefficients of terms with identical powers of p then applying J^α on both sides of equations yield

$$\begin{aligned}
u_0 &= 1,\\
u_1 &= r + J^\beta\left[\frac{\partial^{1+\beta}}{\partial r^{1+\beta}}\left(u_0^2\right) + \frac{1}{r}\frac{\partial^\beta}{\partial r^\beta}\left(u_0^2\right) + hu_0 - hgu_0^2\right]\\
&= r + \frac{(h-hg)\,t^\alpha}{\Gamma(1+\alpha)},\\
u_2 &= \frac{r^2}{2} + J^\beta\left[\frac{\partial^{1+\beta}}{\partial r^{1+\beta}}(2u_0u_1)\right.\\
&\qquad\left. + \frac{1}{r}\frac{\partial^\beta}{\partial r^\beta}(2u_0u_1) + hu_1 - 2hgu_0u_1\right]\\
&= \frac{r^2}{2} + \frac{(hr-2ghr)\,t^\alpha}{\Gamma(1+\alpha)} + \frac{h^2t^\alpha}{\Gamma(1+2\alpha)}\\
&\qquad - \frac{3gh^2t^{2\alpha}}{\Gamma(1+2\alpha)} + \frac{2g^2h^2t^{2\alpha}}{\Gamma(1+2\alpha)} + \frac{2r^{-\beta}t^\alpha}{\Gamma(2-\beta)\Gamma(1+\alpha)},\\
u_3 &= J^\beta\left[\frac{\partial^{1+\beta}}{\partial r^{1+\beta}}\left(2u_0u_2 + u_1^2\right) + \frac{1}{r}\frac{\partial^\beta}{\partial r^\beta}\right.\\
&\qquad\left. \times\left(2u_0u_2 + u_1^2\right) + hu_2 - hg\left(2u_0u_2 + u_1^2\right)\right]\\
&= \frac{r^3}{6} + \frac{hrt^\alpha}{\Gamma(1+\alpha)} - \frac{2hgr^2t^\alpha}{\Gamma(1+\alpha)}\\
&\qquad - \frac{h^3gt^{3\alpha}\Gamma(1+2\alpha)}{\Gamma^2(1+\alpha)\Gamma(1+3\alpha)} + \frac{2h^3g^2t^{3\alpha}\Gamma(1+2\alpha)}{\Gamma^2(1+\alpha)\Gamma(1+3\alpha)}\\
&\qquad - \frac{h^3g^3t^{3\alpha}\Gamma(1+2\alpha)}{\Gamma^2(1+\alpha)\Gamma(1+3\alpha)} + \frac{h^2t^{2\alpha}}{\Gamma(1+2\alpha)}\\
&\qquad - \frac{gh^2t^{2\alpha}}{\Gamma(1+2\alpha)} - \frac{4h^2grt^{2\alpha}}{\Gamma(1+2\alpha)} + \frac{6g^2h^2t^{2\alpha}}{\Gamma(1+2\alpha)}\\
&\qquad - \frac{2h^3gt^{3\alpha}}{\Gamma(1+3\alpha)} + \frac{6g^2h^3t^{3\alpha}}{\Gamma(1+3\alpha)}\\
&\qquad - \frac{4g^3h^3t^{3\alpha}}{\Gamma(1+3\alpha)} + \frac{4r^{1-\beta}t^\alpha}{\Gamma(2-\beta)\Gamma(1+\alpha)}\\
&\qquad + \frac{4hr^{-\beta}t^{2\alpha}}{\Gamma(2-\beta)\Gamma(1+2\alpha)}\\
&\qquad - \frac{6ghr^{-\beta}t^{2\alpha}}{\Gamma(2-\beta)\Gamma(1+2\alpha)} - \frac{4hgr^{-\beta}t^{2\alpha}}{\Gamma(2-\beta)\Gamma(1+2\alpha)}\\
&\qquad + \frac{4r^{1-2\beta}t^{2\alpha}\Gamma(1-\beta)}{\Gamma(1-2\beta)\Gamma(2-\beta)\Gamma(1+2\alpha)}\\
&\qquad + \frac{4r^{1-\beta}t^\alpha}{\Gamma(3-\beta)\Gamma(1+\alpha)} - \frac{4r^{-1-2\beta}t^{2\alpha}\beta\Gamma(-\beta)}{\Gamma(1+2\alpha)\Gamma(2-\beta)\Gamma(-2\beta)}\\
&\qquad \vdots
\end{aligned} \tag{21}$$

and so on, in this manner the rest of components of the solution can be obtained. The solution of (17) in series form is given by

$$\begin{aligned}
u(r,t) = e^r &+ \frac{(h-hg)\,t^\alpha}{\Gamma(1+\alpha)} + \frac{(hr-2ghr)\,t^\alpha}{\Gamma(1+\alpha)}\\
&+ \frac{h^2t^\alpha}{\Gamma(1+2\alpha)} - \frac{3gh^2t^{2\alpha}}{\Gamma(1+2\alpha)} + \cdots.
\end{aligned} \tag{22}$$

Case 3. We will consider the following initial value problem of time-space fractional nonlinear diffusion equation:

$$\frac{\partial^\alpha u}{\partial t^\alpha} = \frac{\partial^{1+\beta}}{\partial r^{1+\beta}}\left(u^2\right) + \frac{1}{r}\frac{\partial^\beta}{\partial r^\beta}\left(u^2\right) + F(u), \tag{23}$$

$$u(r,0) = \varphi(r). \tag{24}$$

According to the homotopy perturbation method, we construct the following simple homotopy:

$$\frac{\partial^\alpha u}{\partial t^\alpha} = p\left[\frac{\partial^{1+\beta}}{\partial r^{1+\beta}}\left(u^2\right) + \frac{1}{r}\frac{\partial^\beta}{\partial r^\beta}\left(u^2\right) + F(u)\right]. \tag{25}$$

The modified form of the homotopy perturbation method can be established based on the initial condition expressed in the Taylor series; the initial condition $u(r,0)$ is expressed in the Taylor series

$$u(r,0) = \varphi(r) = \sum_{n=0}^{\infty}\varphi_n(r). \tag{26}$$

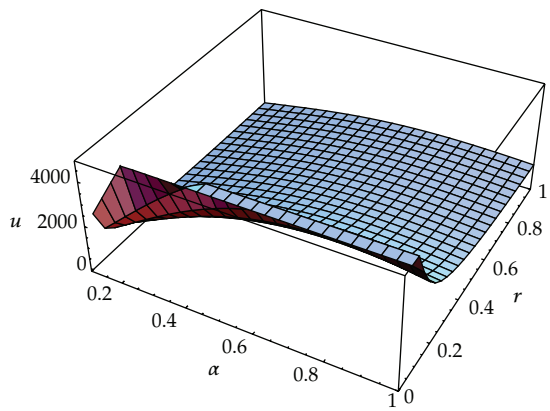

Figure 3: The surface of second-order approximate solution of (10) when $t = 10$, $\beta = 1$.

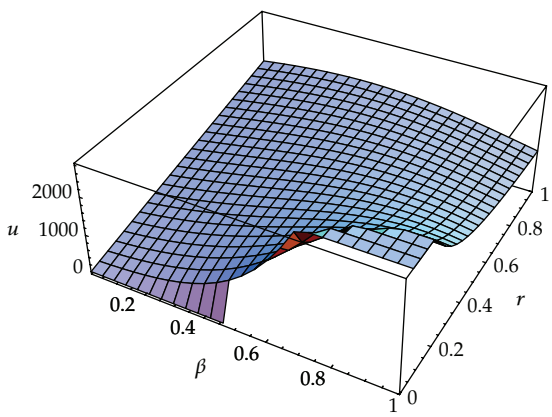

Figure 4: The surface of second-order approximate solution of (10) when $t = 10$, $\alpha = 1$.

Instituting (12) into (23) and equating coefficients of terms with identical powers of p

$$\begin{aligned} p^0 &: D_t^\alpha u_0 = 0, \quad u_0(r,0) = \varphi_0(r), \\ &\vdots \\ p^n &: D_t^\alpha u_n = \frac{\partial^{1+\beta}}{\partial r^{1+\beta}}(v_{n-1}) + \frac{1}{r}\frac{\partial^\beta}{\partial r^\beta}(v_{n-1}) + F_{n-1}, \\ &\qquad u_n(r,0) = \varphi_n(r), \end{aligned} \tag{27}$$

where v_{n-1} is the coefficient of p^{n-1} in u^2 and F_{n-1} is the coefficient of p^{n-1} in $F(u)$, then applying J^α, the inverse operator of D_t^α, on both sides of equations, it is obvious that (27) are easy to solve, the components u_n, $n \geq 0$ of the homotopy perturbation method can be completely determined, and series solutions are thus entirely determined.

5. Conclusion

Approximate solutions of the multifractional nonlinear diffusion population equations in radial symmetry were derived using the homotopy perturbation method and the new modification of homotopy perturbation method. The solutions are given in the form of series with easily computable terms. The results reveal that the new modified method is very effective for solving nonlinear diffusion equation of multifractional order. This is the first step to study the multifractional nonlinear population diffusion in radical symmetry, and we will make subsequent research, for example, exact solution and self-similar exact solution of these fractional nonlinear system. And we hope that this work is a step in this direction.

Acknowledgments

The author expresses thanks to the referees for their fruitful advices and comments. This work was supported by the National Science Foundation of Shandong Province (Grants no. Y2007A06 and ZR2010Al019) and the China Postdoctoral Science Foundation (Grant no. 20100470783.)

References

[1] N. Shigesada and K. Kawasaki, *Biological Invasions: Theory and Practice*, Oxford University, Oxford, UK, 1997.

[2] S. Petrovskii and N. Shigesada, "Some exact solutions of a generalized Fisher equation related to the problem of biological invasion," *Mathematical Biosciences*, vol. 172, no. 2, pp. 73–94, 2001.

[3] I. Podlubny, *Fractional Differential Equations*, Academic Press, New York, NY, USA, 1999.

[4] J. Sabatier, O. P. Agrawal, and J. A. T. Machado, *Advances in Fractional Calculus: Theoretical Developments and Applications in Physics and Engineering*, Springer, Dordrecht, The Netherlands, 2007.

[5] R. Hilfer, *Applications of Fractional Calculus in Physics*, World Scientific, Singapore, 2000.

[6] J. T. Machado, V. Kiryakova, and F. Mainardi, "Recent history of fractional calculus," *Communications in Nonlinear Science and Numerical Simulation*, vol. 16, no. 3, pp. 1140–1153, 2011.

[7] E. K. Lenzi, G. A. Mendes, R. S. Mendes, L. R. Da Silva, and . L. S. Lucena, "Exact solutions to nonlinear nonautonomous space-fractional diffusion equations with absorption," *Physical Review E*, vol. 67, no. 51, Article ID 051109, 2003.

[8] E. K. Lenzi, L. C. Malacarne, R. S. Mendes, and I. T. Pedron, "Anomalous diffsion, nonlinear fractional Fokker-Planck equation and solutions," *Physica A*, vol. 319, pp. 245–252, 2003.

[9] M. Bologna, C. Tsallis, and P. Grigolini, "Anomalous diffusion associated with nonlinear fractional derivative Fokker-Planck-like equation: exact time-dependent solutions," *Physical Review E*, vol. 62, no. 2, pp. 2213–2218, 2000.

[10] C. Tsallis and E. K. Lenzi, "Anomalous diffusion: nonlinear fractional Fokker-Planck equation," *Chemical Physics*, vol. 284, pp. 341–347, 2002.

[11] F. Shakeri and M. Dehghan, "Numerical solution of a biological population model using He's variational iteration method," *Computers & Mathematics with Applications*, vol. 54, no. 7-8, pp. 1197–1209, 2007.

[12] Y. Tan, H. Xu, and S.-J. Liao, "Explicit series solution of travelling waves with a front of Fisher equation," *Chaos, Solitons and Fractals*, vol. 31, no. 2, pp. 462–472, 2007.

[13] A. Kadem and D. Baleanu, "Homotopy perturbation method for the coupled fractional Lotka-Volterra equations," *Romanian Journal of Physics*, vol. 56, no. 3-4, pp. 332–338, 2011.

[14] A. M. A. El-Sayed, S. Z. Rida, and A. A. M. Arafa, "Exact solutions of fractional-order biological population model," *Communications in Theoretical Physics*, vol. 52, no. 6, pp. 992–996, 2009.

[15] A.-M. Wazwaz and A. Gorguis, "An analytic study of Fisher's equation by using Adomian decomposition method," *Applied Mathematics and Computation*, vol. 154, no. 3, pp. 609–620, 2004.

[16] A. K. Najeeb, K. Nasir-Uddin, A. Asmat, and J. Muhammad, "Approximate analytical solutions of fractional reaction-diffusion equations," *Journal of King Saud University*, vol. 24, no. 2, pp. 111–118, 2012.

[17] S. Petrovskii, H. Malchow, and B.-L. Li, "An exact solution of a diffusive predator-prey system," *Proceedings of The Royal Society of London A*, vol. 461, no. 2056, pp. 1029–1053, 2005.

[18] Y. Liu and B. Xin, "Numerical solutions of a fractional predator-prey system," *Advances in Difference Equations*, vol. 2011, Article ID 190475, 11 pages, 2011.

[19] N. A. Khan, M. Ayaz, L. Jin, and A. Yildirim, "On the approximate solutions for the time-fractional reaction-diffusion equation of Fisher type," *International Journal of the Physical Science*, vol. 6, pp. 2483–2496, 2011.

Hindawi Publishing Corporation
Mathematical Problems in Engineering
Volume 2013, Article ID 726721, 10 pages
http://dx.doi.org/10.1155/2013/726721

Research Article

Fractional Resonance-Based $RL_\beta C_\alpha$ Filters

Todd J. Freeborn,[1] Brent Maundy,[1] and Ahmed Elwakil[2]

[1] *Department of Electrical and Computer Engineering, University of Calgary, 2500 University Drive NW, Calgary, AB, Canada T2N 1N4*
[2] *Department of Electrical and Computer Engineering, University of Sharjah, P.O. Box 27272, Sharjah, UAE*

Correspondence should be addressed to Todd J. Freeborn; todd.freeborn@gmail.com

Received 17 September 2012; Accepted 20 December 2012

Academic Editor: József Kázmér Tar

We propose the use of a fractional order capacitor and fractional order inductor with orders $0 \leq \alpha, \beta \leq 1$, respectively, in a fractional $RL_\beta C_\alpha$ series circuit to realize fractional-step lowpass, highpass, bandpass, and bandreject filters. MATLAB simulations of lowpass and highpass responses having orders of $(\alpha + \beta) = 1.1$, 1.5, and 1.9 and bandpass and bandreject responses having orders of 1.5 and 1.9 are given as examples. PSPICE simulations of 1.1, 1.5, and 1.9 order lowpass and 1.0 and 1.4 order bandreject filters using approximated fractional order capacitors and fractional order inductors verify the implementations.

1. Introduction

Fractional calculus, the branch of mathematics concerning differentiations and integrations to noninteger order, has been steadily migrating from the theoretical realms of mathematicians into many applied and interdisciplinary branches of engineering [1]. These concepts have been imported into many broad fields of signal processing having many diverse applications, which include electromagnetics [2], wave propagation in human cancellous bone [3], state-of-charge estimation in batteries [4], thermal systems [5], and more. From the import of these concepts into electronics for analog signal processing has emerged the field of fractional order filters. This import into filter design has yielded much recent progress in theory [6–9], noise analysis [10], stability analysis [11], and implementation [12–14]. These filter circuits have all been designed using the fractional Laplacian operator, s^α, because the algebraic design of transfer functions are much simpler than solving the difficult time domain representations of fractional derivatives. A fractional derivative of order α is given by the Caputo derivative [15] as

$$ {}_a^C D_t^\alpha f(t) = \frac{1}{\Gamma(\alpha - n)} \int_a^t \frac{f^{(n)}(\tau)\, d\tau}{(t-\tau)^{\alpha+1-n}}, \tag{1} $$

where $\Gamma(\cdot)$ is the gamma function and $n - 1 \leq \alpha \leq n$. We use the Caputo definition of a fractional derivative over other approaches because the initial conditions for this definition take the same form as the more familiar integer-order differential equations. Applying the Laplace transform to the fractional derivative of (1) with lower terminal $a = 0$ yields

$$ \mathscr{L}\left\{ {}_0^C D_t^\alpha f(t) \right\} = s^\alpha F(s) - \sum_{k=0}^{n-1} s^{\alpha-k-1} f^{(k)}(0), \tag{2} $$

where s^α is also referred to as the fractional Laplacian operator. With zero initial conditions, (2) can be simplified to

$$ \mathscr{L}\left\{ {}_0^C D_t^\alpha f(t) \right\} = s^\alpha F(s). \tag{3} $$

Therefore it becomes possible to define a general fractance device with impedance proportional to s^α [16], where the traditional circuit elements are special cases of the general device when the order is −1, 0, and 1 for a capacitor, resistor, and inductor, respectively. The expressions of the voltage across a traditional capacitor and inductor are defined by integer order integration and differentiation, respectively, of the current through them. We can expand these devices to

the fractional domain using integrations and differentiations of non-integer order. Then the time domain expressions for the voltage across the fractional order capacitor and fractional order inductor become

$$v_C^{\alpha}(t) = \frac{1}{C\Gamma(\alpha)} \int_0^t \frac{i(\tau)}{(t-\tau)^{1-\alpha}} d\tau, \qquad v_L^{\beta}(t) = L\frac{d^{\beta} i(t)}{dt^{\beta}}, \tag{4}$$

where $0 \le \alpha, \beta \le 1$ are the fractional orders of the capacitor and inductor, respectively, $i(t)$ is the current through the devices, C is the capacitance with units $\mathrm{F/s}^{1-\alpha}$, L is the inductance with units $\mathrm{H/s}^{1-\beta}$, and [s] is a unit of time not to be mistaken with the Laplacian operator. Note that we will refer to the units of these devices as [F] and [H] for simplicity.

By applying the Laplace transform to (4), with zero initial conditions, the impedances of these fractional order elements are given as $Z_C^{\alpha}(s) = 1/s^{\alpha}C$ and $Z_L^{\beta}(s) = s^{\beta}L$ for the fractional order capacitor and fractional order inductor, respectively. Using these fractional elements in circuits increases the range of responses that can be realized, expanding them from the narrow integer subset to the more general fractional domain. While these devices are not yet commercially available, recent research regarding their manufacture and production shows very promising results [17, 18]. Therefore, it is becoming increasingly important to develop the theory behind using these fractional elements so that when they are available their unique characteristics can be fully taken advantage of.

While a thorough stability analysis of the fractional $RL_{\beta}C_{\alpha}$ circuit has been presented in [11], the full range of filter responses possible with this topology have not. In this paper we examine the responses possible using a fractional order capacitor and fractional order inductor with orders of $0 \le \alpha, \beta \le 1$ in a series $RL_{\beta}C_{\alpha}$ circuit to realize fractional step filters. With this topology, fractional lowpass, highpass, bandpass, and bandreject filters of order $(\alpha + \beta)$ are realized. MATLAB simulations of lowpass and highpass responses having orders of $(\alpha + \beta) = 1.1$, 1.5, and 1.9 and bandpass and bandreject having orders of 1.5 and 1.9 are presented. PSPICE simulations of 1.1, 1.5, and 1.9 order lowpass and 1.0 and 1.4 order bandreject filters are presented using approximations of both fractional order capacitors and fractional order inductors to verify the $RL_{\beta}C_{\alpha}$ circuit and its implementation.

2. Fractional Responses

The traditional RLC circuit uses standard capacitors and inductors with which only 2nd order filter responses can be realized. We can further generalize this filter to the fractional domain by introducing fractional orders for both frequency-dependent elements. This approach of replacing traditional components with fractional components has previously been investigated for fractional order capacitors in the Sallen-Key filter, Kerwin-Huelsman-Newcomb biquad [7], and Tow-Thomas biquad [14]. The addition of the two fractional parameters allows the $RL_{\beta}C_{\alpha}$ circuit to realize any order $0 \le \alpha + \beta \le 2$. With this modification fractional lowpass, highpass, bandpass, and bandreject filter responses requiring only rearrangement of the series components are realizable. The topologies to realize these four fractional order filter responses are shown in Figure 1.

2.1. Fractional Lowpass Filter (FLPF). The circuit shown in Figure 1(a) can be used to realize a lowpass filter response with a transfer function given by

$$T_{\mathrm{FLPF}}(s) = \frac{V_o(s)}{V_{\mathrm{in}}(s)} = \frac{1/LC}{s^{\alpha+\beta} + s^{\alpha}(R/L) + 1/LC}. \tag{5}$$

This transfer function realizes an FLPF response with DC gain of 1, high frequency gain of zero, and fractional attenuation of $-20(\alpha + \beta)$ dB/decade in the stopband. With the magnitude of (5) given as

$$\begin{aligned} \left|T_{\mathrm{FLPF}}(\omega)\right| &= \Big(2RLC^2\omega^{2\alpha+\beta}\cos(0.5\pi\beta) + 2RC\omega^{\alpha}\cos(0.5\alpha\pi) \\ &\quad + 2LC\omega^{\beta+\alpha}\cos(0.5(\beta+\alpha)\pi) \\ &\quad + R^2C^2\omega^{2\alpha} + L^2C^2\omega^{2\beta+2\alpha} + 1\Big)^{-1/2}. \end{aligned} \tag{6}$$

The MATLAB simulated magnitude responses of (5) with fractional orders of $\alpha + \beta = 1.1$, 1.5, and 1.9 with $\beta = 1$, $R = 1\,\Omega$, $L = 1$ H, and $C = 1$ F are illustrated in Figure 2, respectively. From the magnitude responses of Figure 2 we see stopband attenuations and $\omega_{3_{\mathrm{dB}}}$ frequencies of -22, -30, and -38 dB/decade and 1.623×10^{-4}, 0.3995, and 1.209 rad/s for the 1.1, 1.5, and 1.9 order FLPFs, respectively. This confirms the decreasing fractional step of the stopband attenuation as the order, $(\alpha + \beta)$, increases.

The half power frequency, $\omega_{3_{\mathrm{dB}}}$, can be found by numerically solving the following equation:

$$\left|T_{\mathrm{FLPF}}\left(\omega_{3_{\mathrm{dB}}}\right)\right| = \frac{1}{\sqrt{2}} \tag{7}$$

for $\omega_{3_{\mathrm{dB}}}$. Solving (7) for fixed values of β when α is varied from 0.1 to 1 in steps of 0.01 and $R = L = C = 1$ yields the values given in Figure 3. These values show a general trend that as both α and β increase, the half power frequency increases. It should be noted that all subsequent MATLAB simulations are performed for fixed values of β when α is varied in steps of 0.01 from 0.1 to 1.0 with all components fixed with values of $R = 1\,\Omega$, $L = 1$ H, and $C = 1$ F.

2.2. Fractional Highpass Filter (FHPF). The circuit shown in Figure 1(b) can be used to realize a highpass filter response with a transfer function given by

$$T_{\mathrm{FHPF}}(s) = \frac{V_o(s)}{V_{\mathrm{in}}(s)} = \frac{s^{\alpha+\beta}}{s^{\alpha+\beta} + s^{\alpha}(R/L) + 1/LC} \tag{8}$$

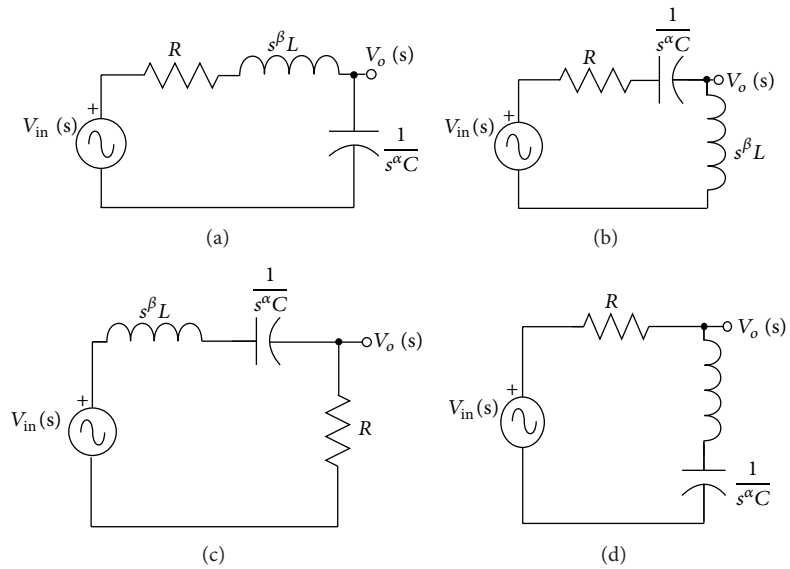

FIGURE 1: Fractional $RL_{\beta}C_{\alpha}$ topologies to realize $(\alpha + \beta)$ order (a) FLPF, (b) FHPF, (c) FBPF, and (d) FBRF responses.

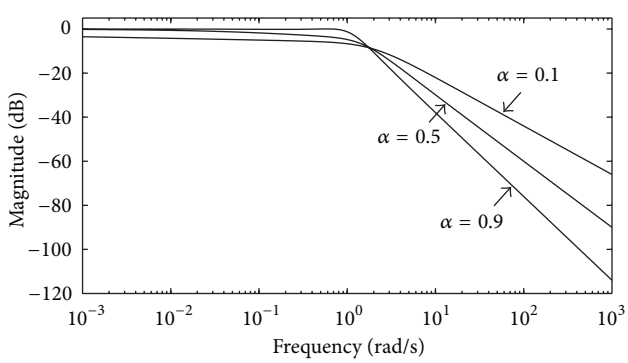

FIGURE 2: Simulated magnitude response of (5) when $\beta = 1$, $\alpha = 0.1$, 0.5, and 0.9 for $R = 1\,\Omega$, $L = 1$ H, and $C = 1$ F.

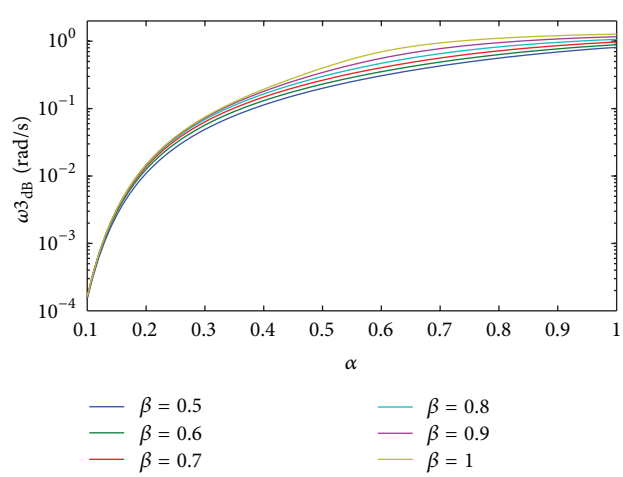

FIGURE 3: Half power frequencies of (5) for fixed values of β when α is varied from 0.1 to 1 in steps of 0.01 and $R = 1\,\Omega$, $L = 1$ H, and $C = 1$ F.

with DC gain of zero, high frequency gain of 1, and fractional attenuation of $20(\alpha + \beta)$ dB/decade in the stopband. The magnitude of (8) is given as

$$\begin{aligned} &\left|T_{\text{FHPF}}(\omega)\right| \\ &\quad = LC\omega^{\beta+\alpha}\left(2RLC^2\omega^{2\alpha+\beta}\cos(0.5\pi\beta)\right. \\ &\qquad + 2CR\omega^{\alpha}\cos(0.5\alpha\pi) \\ &\qquad + 2LC\omega^{\beta+\alpha}\cos(0.5(\beta+\alpha)\pi) \\ &\qquad \left. + R^2C^2\omega^{2\alpha} + L^2C^2\omega^{2\beta+2\alpha} + 1\right)^{-1/2}. \end{aligned} \tag{9}$$

The MATLAB simulated magnitude response of (8) with fractional orders of $\alpha + \beta = 1.1$, 1.5, and 1.9 when $R = 1\,\Omega$, $L = 1$ H, and $C = 1$ F are illustrated in Figure 4. From the magnitude responses of Figure 4 we see stopband attenuations and $\omega_{3_{\text{dB}}}$ frequencies of of 22, 30, and 38 dB/decade and 1.795, 1.232, and 0.8570 rad/s for the 1.1, 1.5, and 1.9 order FHPFs, respectively.

The half power frequency, $\omega_{3_{\text{dB}}}$, can be found by numerically solving the equation $|T_{\text{FHPF}}(\omega_{3_{\text{dB}}})| = 1/\sqrt{2}$ for $\omega_{3_{\text{dB}}}$. The values calculated with fixed β and varied α are shown in Figure 5. These values show a general trend that as both α and β increase, the half power frequency decreases.

2.3. Fractional Bandpass Filter (FBPF). The circuit shown in Figure 1(c) can be used to realize a bandpass filter response with a transfer function given by

$$T_{\text{FBPF}}(s) = \frac{V_o(s)}{V_{\text{in}}(s)} = \frac{s^{\alpha}(R/L)}{s^{\alpha+\beta} + s^{\alpha}(R/L) + 1/LC}. \tag{10}$$

This transfer function realizes an asymmetric FBPF response with DC and high frequency gains of zero and fractional

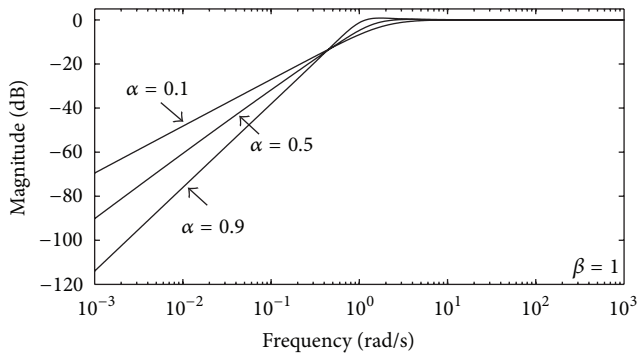

Figure 4: Simulated magnitude response of (8) when $\beta = 1, \alpha = 0.1$, 0.5, and 0.9 for $R = 1\,\Omega$, $L = 1$ H, and $C = 1$ F.

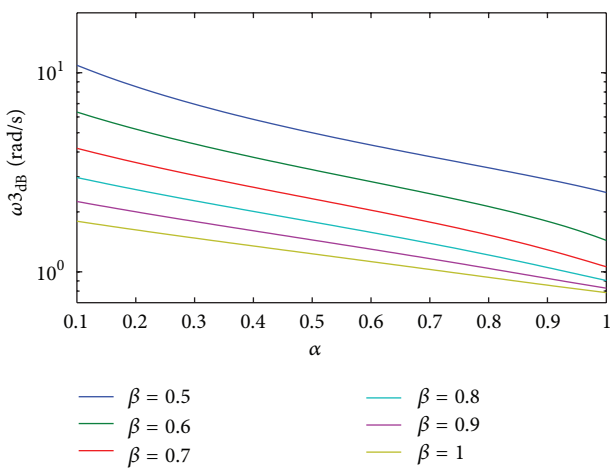

Figure 5: Half power frequencies of (8) for fixed values of β when α is varied from 0.1 to 1 in steps of 0.01 and $R = 1\,\Omega$, $L = 1$ H, and $C = 1$ F.

attenuations of 20α and -20β dB/decade for frequencies lower and higher, respectively, than the maxima frequency (ω_M). With the magnitude of (10) given as

$$\begin{aligned}\left|T_{\text{FBPF}}(\omega)\right| &= RC\omega^{\alpha}\left(2RLC^2\omega^{2\alpha+\beta}\cos(0.5\pi\beta)\right.\\ &\quad + 2RC\omega^{\alpha}\cos(0.5\alpha\pi)\\ &\quad + 2LC\omega^{\beta+\alpha}\cos(0.5(\beta+\alpha)\pi)\\ &\quad \left.+R^2\omega^{2\alpha}C^2 + L^2C^2\omega^{2\beta+2\alpha} + 1\right)^{-1/2}.\end{aligned} \tag{11}$$

The MATLAB simulated magnitude response of (10) with fractional orders of $\alpha + \beta = 1.5$, and 1.9 when $\beta = 1$, $R = 1\,\Omega$, $L = 1$ H, and $C = 1$ F are illustrated in Figure 6. From the simulated magnitude responses, we see that the low frequency stopband has attenuations of 10 and 18 dB/decade while the high frequency stopband maintains an attenuation of −20 dB/decade. The stopband attenuations closely match those predicted and confirm that the low and high frequency stopband attenuations are independent of

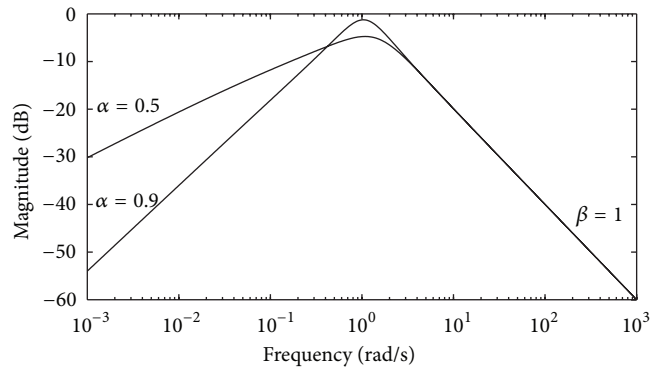

Figure 6: Simulated magnitude response of (10) when $\beta = 1$, $\alpha = 0.5$ and 0.9 for $R = 1\,\Omega$, $L = 1$ H, and $C = 1$ F.

Table 1: Maxima frequency and corresponding magnitude, half power frequencies, and quality factors of FBPFs given in Figure 6.

α	ω_M (rad/s)	$\lvert T(\omega_M)\rvert$ (dB)	ω_1, ω_2 (rad/s)	Q
0.5	1.082	−4.747	0.3173, 2.4171	0.5151
0.9	1.038	−1.246	0.5773, 1.7961	0.8516

Table 2: Minima frequency and corresponding magnitude, half power frequencies, and quality factors of FBRFs given in Figure 10.

α	ω_m (rad/s)	$\lvert T(\omega_m)\rvert$ (dB)	ω_1, ω_2 (rad/s)	Q
0.5	0.8974	−7.241	0.2145, 1.850	0.5486
0.9	0.9989	−17.35	0.5309, 1.701	0.8539

each other (which is unique for fractional-order bandpass filters), with low frequency stopband attenuations dependent only on the order of the fractional capacitor, α, and the high frequency stopband only on the order of the fractional inductor, β.

The maxima frequency can be found by numerically solving the following equation:

$$\frac{d\left|T_{\text{FBPF}}(\omega)\right|}{d\omega} = 0 \tag{12}$$

for ω. Solving (12) for varying α and fixed values of β yields the maxima frequencies given in Figure 7(a). The quality factor, Q, can be found by numerically solving

$$\left|T_{\text{FBPF}}(\omega)\right| = \frac{\left|T_{\text{FBPF}}(\omega_M)\right|}{\sqrt{2}} \tag{13}$$

for its two real roots, ω_1 and ω_2, and then evaluating $Q = \omega_M/|\omega_1 - \omega_2|$. Solving these equations numerically for varying α and fixed values of β yields the quality factors given in Figure 7(b). While there is no clear trend for ω_M, Q shows an increase with increasing order for fixed β when $R = 1\,\Omega$, $L = 1$ H, and $C = 1$ F. The maxima frequency (ω_M), maximum magnitude ($|T(\omega_M)|$), half power frequencies, ($\omega_{1,2}$), and quality factors (Q) of the FBPF responses shown in Figure 6, solved numerically as described previously, are given in Table 1.

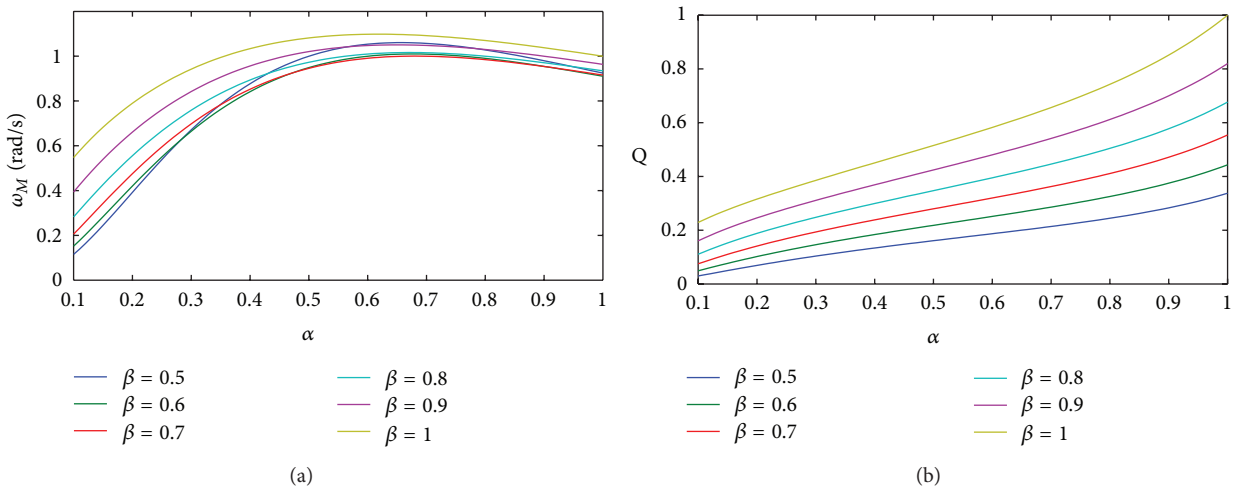

Figure 7: (a) Maxima frequencies and (b) quality factors of (10) for fixed values of β when α is varied from 0.1 to 1 in steps of 0.01 and $R = 1\,\Omega$, $L = 1$ H, $C = 1$ F.

It is possible to increase the quality factor of these circuits by decreasing the value of R for fixed order and values of L and C. The quality factors of the FBPF when $\beta = 1$, $L = 1$ H, and $C = 1$ F for α and R varied from 0.1 to 1 in steps of 0.01 are given in Figure 8. From this figure, we can see that the increasing Q is more pronounced with higher orders.

2.4. Fractional Bandreject Filter (FBRF). The circuit shown in Figure 1(d) is able to realize a bandreject filter response with a transfer function given by

$$T_{\text{FBRF}}(s) = \frac{V_o(s)}{V_{\text{in}}(s)} = \frac{s^{\alpha+\beta} + 1/LC}{s^{\alpha+\beta} + s^{\alpha}(R/L) + 1/LC}. \tag{14}$$

This transfer function realizes an asymmetric FBRF response with DC and high frequency gains of 1. With the magnitude of (14) given as

$$\begin{aligned} &\left|T_{\text{FBRF}}(\omega)\right| \\ &= \left(L^2C^2\omega^{2\beta+2\alpha} + 2LC\omega^{\beta+\alpha}\cos\left(0.5(\alpha+\beta)\pi\right) + 1\right)^{1/2} \\ &\quad / \left(2RC\omega^{\alpha}\cos(0.5\alpha\pi) + 2LC\omega^{\beta+\alpha}\cos\left(0.5(\alpha+\beta)\pi\right)\right. \\ &\quad \left. + C^2R^2\omega^{2\alpha} + 2RLC^2\omega^{2\alpha+\beta}\cos(0.5\pi\beta) + L^2C\omega^{2\beta+2\alpha} + 1\right)^{1/2}. \end{aligned} \tag{15}$$

The minima frequency, ω_m, can be found by numerically solving $d|T_{\text{FBRF}}(\omega)|/d\omega = 0$ for ω. Solving this equation when $R = 1\,\Omega$, $L = 1$ H, and $C = 1$ F for fixed values of β when α is varied from 0.1 to 1 yields the values given in Figure 9(a), while Q, can be found by numerically solving $|T_{\text{FBRF}}(\omega)| = 1/\sqrt{2}$ for its two real roots, ω_1 and ω_2, and then evaluating $Q = \omega_m/|\omega_1 - \omega_2|$. The quality factor calculated for FBRFs while α is varied for fixed β is given in Figure 9(b), respectively, again, with the general trend showing that Q increases with increasing order.

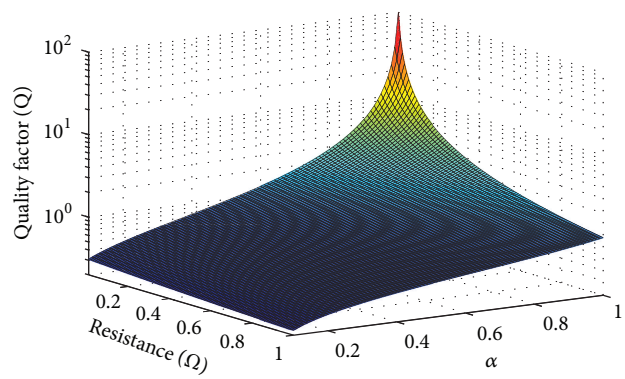

Figure 8: Quality factors of (10) for $\beta = 1$, $L = 1$ H, $C = 1$ F when α and R are varied from 0.1 and 0.01, respectively, to 1 in steps of 0.01.

The MATLAB simulated magnitude responses of (14) with fractional orders of $\alpha + \beta = 1.5$ and 1.9 when $\beta = 1$, $R = 1\,\Omega$, $L = 1$ H, and $C = 1$ F are illustrated in Figure 10. From this figure, we can clearly observe the asymmetric nature of this FBRF, with the attenuation of the low and high frequency stop bands dependent on the element orders of α and β, respectively. The minima frequency (ω_m), minimum magnitude ($|T(\omega_m)|$), half power frequencies ($\omega_{1,2}$), and quality factors (Q) of these responses are given in Table 2. It is possible to increase the quality factor of the FBRF by decreasing the value of R for fixed order and values of L and C. The quality factors of the FBRF when $\beta = 1$, $L = 1$ H, and $C = 1$ F for α varied from 0.1 to 1 and R varied from 0.5 to 1 in steps of 0.01 are given in Figure 11. From this figure, we can see that like the FBPF the increasing Q is more pronounced with higher orders. It should be noted, though, that it is not possible to calculate a quality factor for FBRFs with both low order and resistance. The minima peak of these filters increases with decreasing order and resistance and when the minima increases above $1/\sqrt{(2)}$ it is not possible to calculate the quality factor using the previous definition.

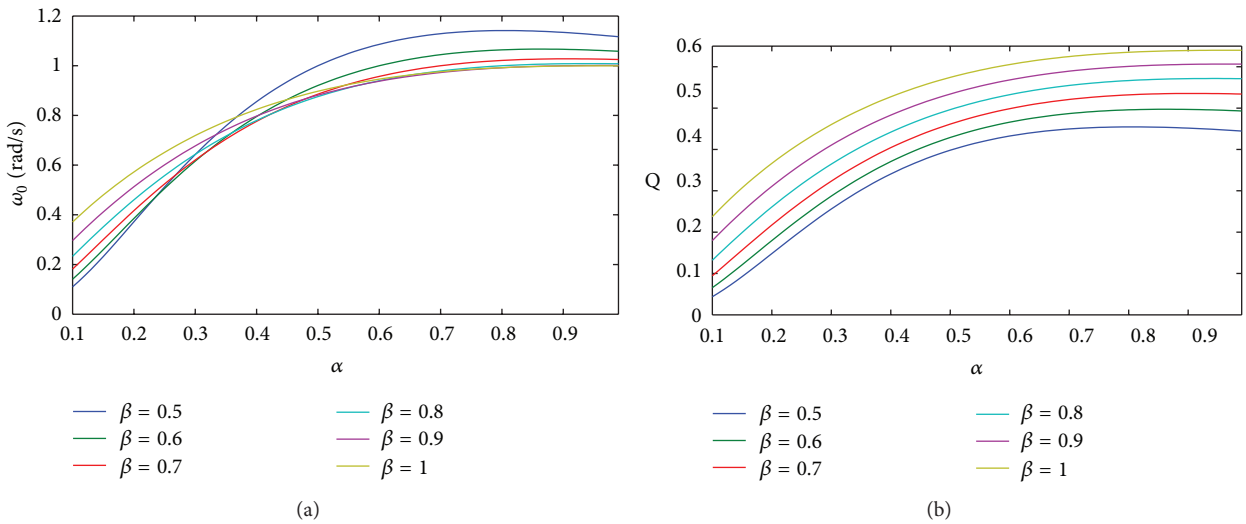

Figure 9: (a) Minima frequencies and (b) quality factors of FBRFs for fixed values of β when α is varied from 0.1 to 1 in steps of 0.01 and $R = 1\,\Omega$, $L = 1$ H, and $C = 1$ F.

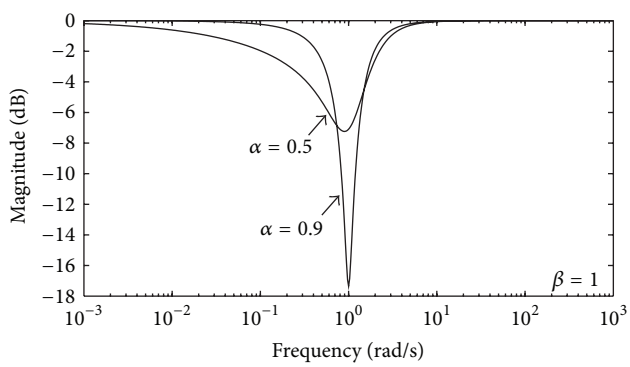

Figure 10: Simulated magnitude response of (14) when $\beta = 1$, $\alpha = 0.5$ and 0.9 for $R = 1\,\Omega$, $L = 1$ H, and $C = 1$ F.

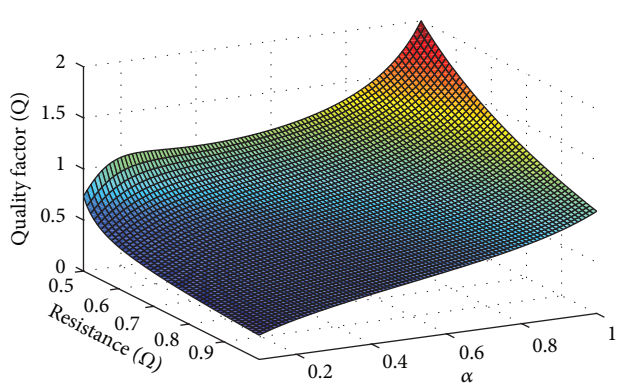

Figure 11: Quality factors of (14) for $\beta = 1$, $L = 1$ H, $C = 1$ F when α and R are varied from 0.1 and 0.5, respectively, to 1 in steps of 0.01.

3. Circuit Simulation Results

Although there is currently much progress regarding the realization of fractional order capacitors [17, 18], there are no commercial devices using these processes available to implement these circuits. As well, even though supercapacitors have been shown to exhibit fractional impedances [19, 20], their high capacitance and limited order ($0.5 \leq \alpha \leq 0.6$) limit their usefulness in signal processing circuits. Until commercial devices with the desired characteristics become available, integer order approximations must be used to realize fractional circuits. There are many methods to create an approximation of s^{α} that include continued fraction expansions (CFEs) as well as rational approximation methods [21]. These methods present a large array of approximations with the accuracy and approximated frequency band increasing as the order of the approximation increases. Here, a CFE method [22] was selected to model the fractional order capacitors for PSPICE simulations. Collecting eight terms of the CFE yields a 4th order approximation of the fractional capacitor that can be physically realized using the RC ladder network in Figure 12.

Now, while an RC ladder can be used to approximate a fractional order capacitor, this same topology cannot realize a fractional order inductor as it would require negative component values. However, we can use a fractional order capacitor as a component in a general impedance converter circuit (GIC), shown in Figure 13, which is used to simulate a grounded impedance [23]. Figure 13 realizes the impedance

$$Z = \frac{s^{\beta} C R_1 R_3 R_5}{R_2} \tag{16}$$

simulating a fractional inductor of order β with inductance $L = CR_1R_3R_5/R_2$.

Using both the approximated fractional order capacitor and fractional order inductor, we can realize the FBRF shown in Figure 1(d) with orders $\alpha + \beta = 1.0$ and $\alpha + \beta = 1.4$ when $\alpha = 0.5$. The realized circuit is given in Figure 14 with the RC ladder shown as the inset for the fractional order capacitor and the GIC circuit as the inset for the fractional order inductor. The R, L, and C values

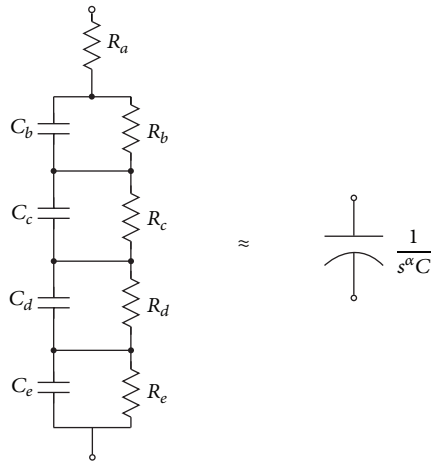

Figure 12: RC ladder structure to realize a 4th order integer approximation of a fractional order capacitor.

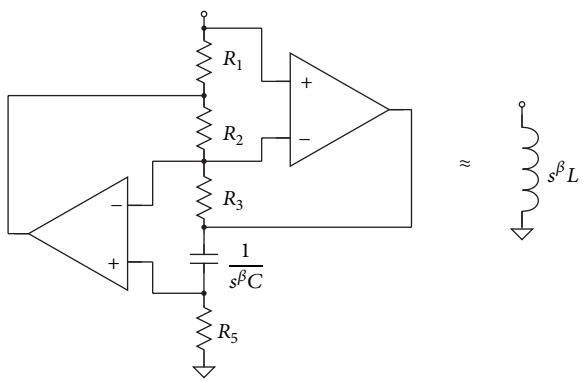

Figure 13: GIC topology to simulate a grounded fractional order inductor using a fractional order capacitor as a component.

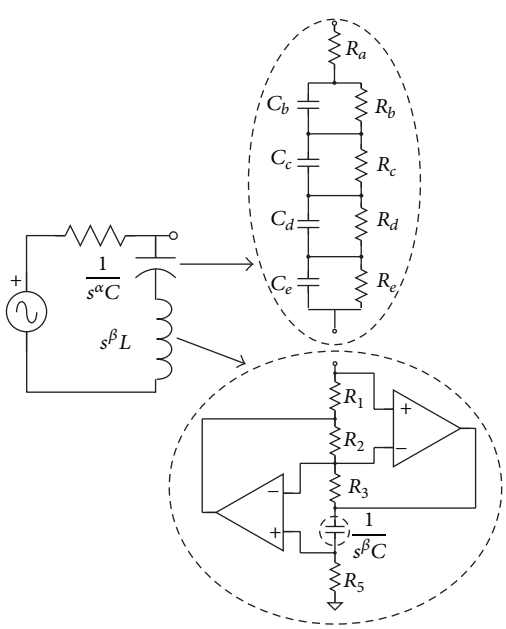

Figure 14: Approximated FBRF circuit realized with RC ladder approximation of fractional order capacitors and GIC approximation of a fractional order inductor.

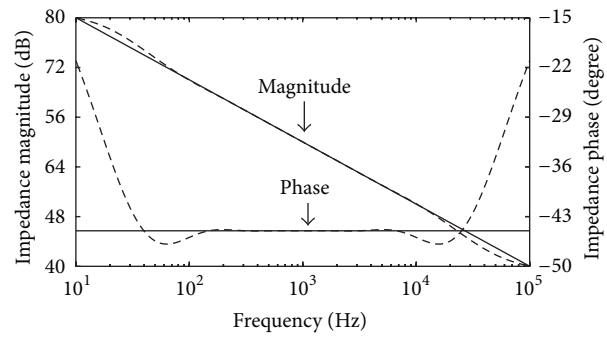

Figure 15: Magnitude and phase response of the approximated fractional order capacitor (dashed) compared to the ideal (solid) with capacitance of 12.6 μF and order 0.5 after scaling to a center frequency of 1 kHz.

Table 3: Component values to realize 1.0 and 1.4 order FBRFs for $\alpha = 0.5$ and $\beta = 0.5$ and 0.9, respectively, after magnitude scaled by a factor of 1000 and frequency shifted to 1 kHz.

Component	Values	
	$\beta = 0.5$	$\beta = 0.9$
R (Ω)	1000	1000
L (H)	12.6	0.382
C (μF)	12.6	12.6

required to realize these circuits after applying a magnitude scaling of 1000 and frequency scaling to 1 kHz are given in Table 3. The component values required for the 4th order approximation of the fractional capacitances with values of 12.6 and 0.382 μF and orders of 0.5 and 0.9, respectively, using the RC ladder network in Figure 12, shifted to a center frequency of 1 kHz, are given in Table 4. The magnitude and phase of the ideal (solid line) and 4th order approximated (dashed) fractional order capacitor with capacitance 12.6 μF and order $\alpha = 0.5$, shifted to a center frequency of 1 kHz, are presented in Figure 15. From this figure we observe that the approximation is very good over almost 4 decades, from 200 Hz to 70 kHz, for the magnitude and almost 2 decades, from 200 Hz to 6 kHz, for the phase. In these regions, the deviation of the approximation from ideal does not exceed 1.23 dB and 0.23° for the magnitude and phase, respectively. The simulated fractional order inductors of 12.6 and 0.382 H can be realized using fractional capacitances of 12.6 and 0.382 μF, respectively, when $R_1 = R_2 = R_3 = R_5 = 1000\,\Omega$.

Using the component values in Tables 3 and 4, the approximated FBRF, shown in Figure 14, was simulated in PSPICE using MC1458 op amps to realize responses of order $(\alpha + \beta) = 1.0$ and 1.4 when $\alpha = 0.5$ and $\beta = 0.5$ and 0.9. The PSPICE simulated magnitude responses (dashed lines) compared to the ideal responses (solid lines) are shown in Figure 16. We can clearly see from the magnitude response of both the MATLAB and PSPICE simulated responses that this filter does realize a fractional band reject response and that the simulation shows good agreement with the ideal response observing both symmetric and asymmetric characteristics for the 1.0 and 1.4 order filters, respectively. Note, though,

Table 4: Component values to realize 4th order approximations of fractional order capacitors with a center frequency of 1 kHz.

Component	Values				
	$C = 1\,\mu$F $\alpha = 0.1$	$C = 1\,\mu$F $\alpha = 0.5$	$C = 12.6\,\mu$F $\alpha = 0.5$	$C = 0.382\,\mu$F $\alpha = 0.9$	$C = 1\,\mu$F $\alpha = 0.9$
R_a (Ω)	274.7 k	1.402 k	111.1	6.8	2.6
R_b (Ω)	81.9 k	3.17 k	251.7	43.3	16.5
R_c (Ω)	56.1 k	4.78 k	378.7	130.7	49.9
R_d (Ω)	66.3 k	11.2 k	888.9	670.4	255.9
R_e (Ω)	154.1 k	92.9 k	7369.7	146189.7	55789.8
C_b (nF)	0.165	6.64	68.9	705	1846
C_c (μF)	0.0015	0.023	0.296	1.13	2.97
C_d (μF)	0.0052	0.043	0.537	1.03	2.69
C_e (μF)	0.015	0.055	0.695	0.207	0.544

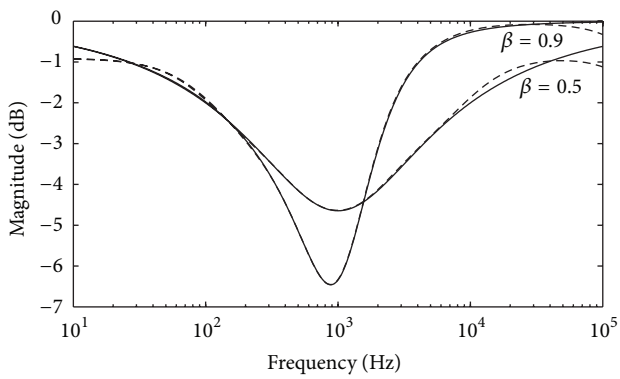

Figure 16: PSPICE simulations using Figure 14 compared to ideal simulations of (14) as dashed and solid lines, respectively, to realize approximated FBRFs of orders $\alpha + \beta = 1.0$ and 1.4 when $\alpha = 0.5$.

that the PSPICE simulations deviate from the MATLAB simulated transfer function at low and high frequencies, which is a result of using the 4th order approximation of the fractional order capacitors. We highlight that this filter presents two characteristics not possible using integer order filters: (a) bandreject responses have not been possible from integer order filters with order less than 2 and (b) asymmetric responses with independent control of stopband attenuation have never been presented.

3.1. Fractional Bruton Transformation. The Bruton transformation applies an impedance transformation to each element of a passive ladder circuit to create an active circuit realization using the concept of frequency-dependent negative resistance that does not require the use of inductors [24]. This method can be expanded to the fractional-order domain to remove the fractional order inductor from the $RL_\beta C_\alpha$ circuit. Where the integer order transformation scales each element by $1/s$, the fractional Bruton transformation scales each element by $1/s^\beta$. Applying this scaling to a resistor transforms it to a fractional order capacitor, a fractional order inductor to a resistor, and a fractional order capacitor to a new fractional element of order $0 \le \alpha + \beta \le 1$. This new fractional element can be a resistor, capacitor, or frequency-dependent negative resistor (FDNR) when $\alpha + \beta = 0$, 1, and 2, respectively. Note that we will use the units of [Ω] when referring to this fractional element in order to remain consistent with the FDNR, whose symbol we are also using to represent this element. The FLPF of Figure 1(a) after applying the fractional Bruton transformation is shown in Figure 17. The transfer function of this transformed circuit is given by

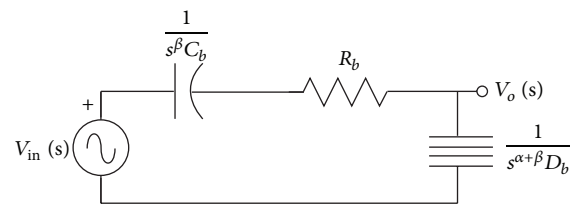

Figure 17: FLPF of Figure 1(a) after applying the fractional Bruton transformation.

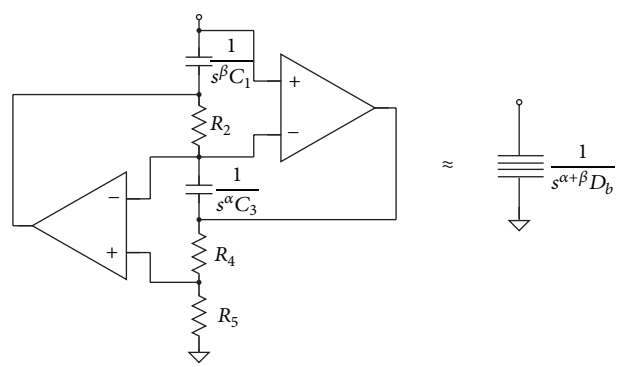

Figure 18: GIC topology to simulate a grounded fractional element of order $0 \le \alpha + \beta \le 2$ using two fractional order capacitors components.

$$T_{\text{FLPF}}(s) = \frac{V_o(s)}{V_{\text{in}}(s)} = \frac{1/R_b D_b}{s^{\alpha+\beta} + s^\alpha/R_b C_b + 1/R_b D_b}, \qquad (17)$$

where $C_b = 1/R$, $R_b = L$, and $D_b = C$ for the transfer function to be equivalent to (5).

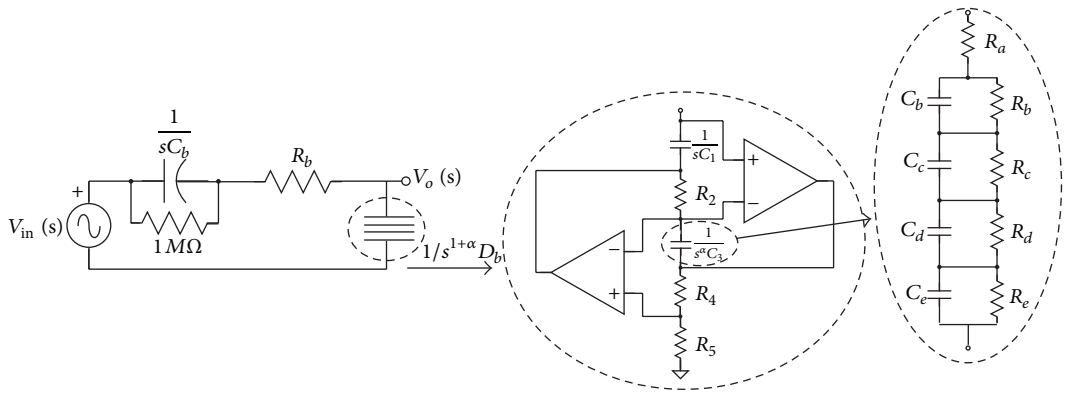

Figure 19: Approximated FLPF of Figure 17 realized with RC ladder approximations of fractional order capacitors and GIC approximation of a fractional element of order $(\alpha + \beta)$.

Table 5: Component values to realize fractional elements with GIC topology of Figure 18.

Component	Values		
	D_b = 66.38 nΩ Order = 1.1	D_b = 2.01 nΩ Order = 1.5	D_b = 60.74 pΩ Order = 1.9
C_1 (μF), β	1, 1	1, 1	1, 1
C_3 (μF), α	1, 0.1	1, 0.5	1, 0.9
R_2 (Ω)	66.38 k	2.01 k	60.74
R_4 (Ω)	1000	1000	1000
R_5 (Ω)	1000	1000	1000

This new fractional element can be realized using a GIC with two fractional order capacitors, this topology is shown in Figure 18 and has an impedance

$$Z_D = \frac{R_5}{s^{\alpha+\beta}C_1C_3R_2R_4} \tag{18}$$

simulating a fractional element with impedance $D_b = C_1C_3R_2R_4/R_5$. A GIC has also previously been employed to realize a fractional order capacitor of 36 μF and $\alpha = 1.6$ in [7]. Using the topology of Figure 17 to simulate the FLPFs of Figure 2, magnitude scaled by 1000 and frequency shifted to 1 kHz, requires $C_b = 0.1592\,\mu$F, $R_b = 1000\,\Omega$, and D_b = (66.38 n, 2.01 n, 60.74 p)Ω for the $(\alpha + \beta) = 1.1$, 1.5, and 1.9 order filters, respectively, when $\beta = 1$. The components required to simulate the impedance of the fractional element using the GIC topology are given in Table 5, with the values of the fractional order capacitor C_3 approximated with the RC ladder of Figure 12 given in Table 4.

The approximated FLPF, shown in Figure 19, was simulated in PSPICE using MC1458 op amps to realize a $(\alpha + \beta) = 1.9$ order filter when $\beta = 1$. The PSPICE simulated magnitude responses (dashed lines) compared to the ideal responses (solid lines) are shown in Figure 20. Note that a 1 MΩ resistor has been added to bypass the capacitor and provide a DC path to the noninverting input terminal of the upper op amp in the fractional element realization for its bias current [23].

The PSPICE simulated magnitude responses of the FLPFs show very good agreement with the MATLAB simulated ideal

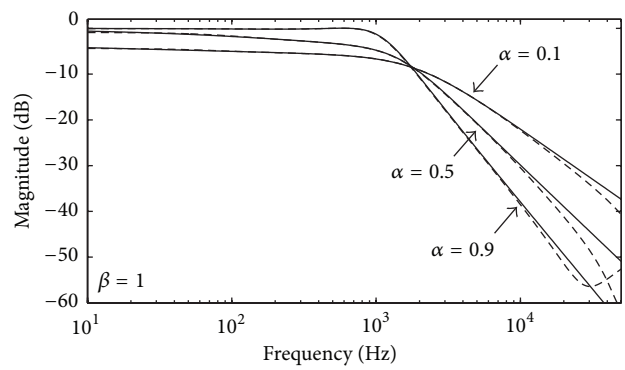

Figure 20: PSPICE simulation using Figure 19 compared to ideal simulations of (17) as dashed and solid lines, respectively, to realize approximated FLPF of order $\alpha + \beta = 1.9$ when $\beta = 1$.

response. Verifying the fractional Bruton transformed FLPFs as well as the GIC realizations of a fractional element of order $(\alpha + \beta)$ using approximated fractional order capacitors. The deviations above 20 kHz can be attributed to the approximations of the fractional order capacitors and nonidealities of the op amps used to realize the fractional order inductors.

4. Conclusion

We have proposed modifying the traditional series RLC circuit to use a fractional order capacitor and fractional order inductor to realize a fractional $RL_\beta C_\alpha$ circuit that is capable of realizing fractional lowpass, highpass, bandpass, and bandreject filter responses of order $0 < \alpha + \beta \leq 2$ requiring only modification of the element arrangement. This topology can realize bandpass or bandreject responses with order less than 2 which are not possible using an integer order circuit. In addition, these proposed bandpass and bandreject filters show asymmetric bandpass characteristics with independent control of the stopband attenuations through manipulation of the fractional elements orders, which is not easily accomplished using integer order filters. We have also shown how to realize a new fractional element of order $(\alpha +$

$\beta) \leq 2$ and a fractional order inductor using fractional order capacitors in a GIC circuit. PSPICE simulations of FBRFs and FLPFs verify the fractional characteristics of these circuits as well as the proposed realizations using approximated fractional elements.

Acknowledgments

T. J. Freeborn would like to acknowledge Canada's National Sciences and Engineering Research Council (NSERC), Alberta Innovates-Technology Futures, and Alberta Advanced Education and Technology for their financial support of this research through their graduate student scholarships.

References

[1] A. S. Elwakil, "Fractional-order circuits and systems: an emerging interdisciplinary research area," *IEEE Circuits and Systems Magazine*, vol. 10, no. 4, pp. 40–50, 2010.

[2] J. A. Tenreiro Machado, I. S. Jesus, A. Galhano, and J. Boaventura Cunha, "Fractional order electromagnetics," *Signal Processing*, vol. 86, no. 10, pp. 2637–2644, 2006.

[3] N. Sebaa, Z. E. A. Fellah, W. Lauriks, and C. Depollier, "Application of fractional calculus to ultrasonic wave propagation in human cancellous bone," *Signal Processing*, vol. 86, no. 10, pp. 2668–2677, 2006.

[4] J. Sabatier, M. Aoun, A. Oustaloup, G. Grégoire, F. Ragot, and P. Roy, "Fractional system identification for lead acid battery state of charge estimation," *Signal Processing*, vol. 86, no. 10, pp. 2645–2657, 2006.

[5] J. D. Gabano and T. Poinot, "Fractional modelling and identification of thermal systems," *Signal Processing*, vol. 91, no. 3, pp. 531–541, 2011.

[6] A. G. Radwan, A. S. Elwakil, and A. M. Soliman, "Fractional-order sinusoidal oscillators: design procedure and practical examples," *IEEE Transactions on Circuits and Systems*, vol. 55, no. 7, pp. 2051–2063, 2008.

[7] A. G. Radwan, A. S. Elwakil, and A. M. Soliman, "On the generalization of second-order filters to the fractional-order domain," *Journal of Circuits, Systems and Computers*, vol. 18, no. 2, pp. 361–386, 2009.

[8] A. Soltan, A. G. Radwan, and A. M. Soliman, "Butterworth passive filter in the fractional order," in *Proceedings of the International Conference on Microelectronics (ICM '11)*, pp. 1–5, Hammamet, Tunisia, 2011.

[9] P. Ahmadi, B. Maundy, A. S. Elwakil, and L. Belostostski, "High-quality factor asymmetric-slope band-pass filters: a fractional-order capacitor approach," *IET Circuits, Devices & Systems*, vol. 6, no. 3, pp. 187–197, 2012.

[10] A. Lahiri and T. K. Rawat, "Noise analysis of single stage fractional-order low pass filter using stochastic and fractional calculus," *ECTI Transactions on Electronics and Communications*, vol. 7, no. 2, pp. 136–143, 2009.

[11] A. Radwan, "Stability analysis of the fractional-order $RL_{\beta}C_{\alpha}$ circuit," *Journal of Fractional Calculus and Applications*, vol. 3, no. 1, pp. 1–15, 2012.

[12] T. J. Freeborn, B. Maundy, and A. S. Elwakil, "Field programmable analogue array implementations of fractional step filters," *IET Circuits, Devices & Systems*, vol. 4, no. 6, pp. 514–524, 2010.

[13] B. Maundy, A. S. Elwakil, and T. J. Freeborn, "On the practical realization of higher-order filters with fractional stepping," *Signal Processing*, vol. 91, no. 3, pp. 484–491, 2011.

[14] T. J. Freeborn, B. Maundy, and A. S. Elwakil, "Fractional-step Tow-Thomas biquad filters," *Nonlinear Theory and Its Applications, IEICE (NOLTA)*, vol. 3, no. 3, pp. 357–374, 2012.

[15] I. Podlubny, *Fractional Differential Equations: An Introduction to Fractional Derivatives, Fractional Differential Equations, to Methods of Their Solution and some of Their Applications*, vol. 198, Academic Press, San Diego, Calif, USA, 1999.

[16] M. Nakagawa and K. Sorimachi, "Basic characteristics of a fractance device," *IEICE—Transactions on Fundamentals of Electronics, Communications and Computer Sciences E*, vol. 75, pp. 1814–1819, 1992.

[17] M. Sivarama Krishna, S. Das, K. Biswas, and B. Goswami, "Fabrication of a fractional order capacitor with desired specifications: a study on process identification and characterization," *IEEE Transactions on Electron Devices*, vol. 58, no. 11, pp. 4067–4073, 2011.

[18] T. Haba, G. Ablart, T. Camps, and F. Olivie, "Influence of the electrical parameters on the input impedance of a fractal structure realised on silicon," *Chaos, Solitons Fractals*, vol. 24, no. 2, pp. 479–490, 2005.

[19] J. J. Quintana, A. Ramos, and I. Nuez, "Identification of the fractional impedance of ultracapacitors," in *Proceedings of the 2nd Workshop on Fractional Differentiation and Its Applications (IFAC '06)*, pp. 289–293, 2006.

[20] A. Dzieliński, G. Sarwas, and D. Sierociuk, "Comparison and validation of integer and fractional order ultracapacitor models," *Advances in Difference Equations*, vol. 2011, article 11, 2011.

[21] I. Podlubny, I. Petráš, B. M. Vinagre, P. O'Leary, and Ľ. Dorčák, "Analogue realizations of fractional-order controllers," *Nonlinear Dynamics: An International Journal of Nonlinear Dynamics and Chaos in Engineering Systems*, vol. 29, no. 1–4, pp. 281–296, 2002.

[22] B. Krishna and K. Reddy, "Active and passive realization of fractance device of order 1/2," *Active and Passive Electronic Components*, vol. 2008, Article ID 369421, 5 pages, 2008.

[23] R. Schaumann and M. E. Van Valkenburg, *Design of Analog Filters*, Oxford University Press, 2001.

[24] L. T. Bruton, "Network transfer functions using the concept of frequency-dependent negative resistance," *IEEE Transactions on Circuit Theory*, vol. CT-16, no. 3, pp. 406–408, 1969.

Hindawi Publishing Corporation
Mathematical Problems in Engineering
Volume 2013, Article ID 562320, 10 pages
http://dx.doi.org/10.1155/2013/562320

Review Article

Power Law and Entropy Analysis of Catastrophic Phenomena

J. A. Tenreiro Machado,[1] Carla M. A. Pinto,[2] and A. Mendes Lopes[3]

[1] *Department of Electrical Engineering, Institute of Engineering, Polytechnic of Porto (ISEP), Rua Dr. António Bernardino de Almeida, 431, 4200-072 Porto, Portugal*
[2] *Institute of Engineering, Polytechnic of Porto (ISEP) and Center of Mathematics of the University of Porto, Rua Dr. António Bernardino de Almeida, 431, 4200-072 Porto, Portugal*
[3] *UISPA, IDMEC-Polo FEUP, Faculty of Engineering, University of Porto, Rua Dr. Roberto Frias, 4200-465 Porto, Portugal*

Correspondence should be addressed to J. A. Tenreiro Machado; jtm@isep.ipp.pt

Received 17 September 2012; Accepted 13 December 2012

Academic Editor: József Kázmér Tar

Catastrophic events, such as wars and terrorist attacks, tornadoes and hurricanes, earthquakes, tsunamis, floods and landslides, are always accompanied by a large number of casualties. The size distribution of these casualties has separately been shown to follow approximate power law (PL) distributions. In this paper, we analyze the statistical distributions of the number of victims of catastrophic phenomena, in particular, terrorism, and find double PL behavior. This means that the data sets are better approximated by two PLs instead of a single one. We plot the PL parameters, corresponding to several events, and observe an interesting pattern in the charts, where the lines that connect each pair of points defining the double PLs are almost parallel to each other. A complementary data analysis is performed by means of the computation of the entropy. The results reveal relationships hidden in the data that may trigger a future comprehensive explanation of this type of phenomena.

1. Introduction

Power laws (PLs) have been widely reported in the modeling of distinct phenomena and have been associated with long memory behavior, self-similarity, fractal structures and fractional calculus. In [1], for example, PLs are interpreted as a manifestation of the long memory property of systems with fractional dynamics and, in [2], several complex systems exhibiting PL behavior are analysed in the perspective of fractional dynamics. Fractional calculus and PLs are used in [3, 4] to model the dynamics of financial markets. In [5] the complexity of the human body is characterized through fractal measures and its dynamics described by means of fractional calculus.

Catastrophic events are characterized by a huge severity, usually defined by a large number of casualties. By catastrophic events, we mean wars, terrorist attacks, tornadoes, earthquakes, floods, and landslides. The distribution of the number of casualties in these events is proved to be a PL [6–12].

PL distributions were first mentioned in 1896, when Pareto described the distribution of income [13]. Pareto proved that the relative number of individuals with an annual income larger than a certain value x was proportional to a power of x. This has been known by Pareto distribution. After this work, Auerbach [14] demonstrated an analogous result for city size distributions. Ranking cities from 1 to n, with the city with bigger population ranked as 1, Auerbach demonstrated that the product of cities populations by their ranks was approximately constant, for a given territory. Estoup [15] and Zipf [16, 17] applied PLs to words frequencies in texts. They found that there are words that are used more often than others and the distribution of word frequencies follows a PL. Zipf [17] described the distribution of city sizes by a Pareto distribution.

Often, to show that a certain data set follows a PL distribution, researchers depict a plot of the size versus frequency of the event studied. In logarithmic scales, they obtain a straight line with negative slope. In the case of

the Pareto distribution, the behavior is exactly linear, and is given by

$$\ln(P[X \geq x]) = \ln C - \ln \widetilde{\alpha} - \widetilde{\alpha} \ln x, \quad (1)$$

where X is a random variable following a PL distribution, $\widetilde{\alpha} > 0$, $\widetilde{C} = C/\widetilde{\alpha} > 0$. In these distributions, the tail falls asymptotically according to the value of $\widetilde{\alpha}$, translating in heavy tails, comparatively to other distributions. Zipf's law is a special case of the Pareto's law, with coefficient $\widetilde{\alpha} = 1$. Relevant reviews on PL distributions can be found in [18–20].

In many cases a single PL holds for the entire range of the random variable that represents the system. In other cases, the statistical distribution is better described by multiple PLs [21]. In such cases, different PLs, characterized by distinct PL parameters, fit, more adequately, the real data. Double PL behaviors have been pointed out by others in different phenomena. For example, in [22] many instances are shown of two PLs expressed by means of a generalized beta distribution function and, in [23], the double PL behavior is explicitly studied in the frequency of words in texts. Moreover, beyond the ranking problem, two PLs are manifested in other type of problems such as in turbulence, earth magnetic pole fluctuations, paleolake sedimentation density subject to volcanism, and avalanche distributions, to mention a few [24].

In this paper, we analyze the statistical distributions of the number of victims caused by catastrophic phenomena and find double PL behavior. Moreover, we plot the PL parameters, corresponding to several events, and observe an interesting pattern in the charts, where the lines that connect each pair of points defining the double PLs are roughly parallel to each other. Then, a complementary data analysis is performed by means of the computation of the Shannon entropy. The results reveal relationships hidden in the data that may trigger a future comprehensive explanation of this type of phenomena.

Bearing these ideas in mind, this paper is organized as follows. In Section 2, the results found in the literature concerning PLs and casualties in natural and human-made disasters are summarized. Section 3 analyses the PL behavior of catastrophic phenomena using data from real disasters. In Section 4 several entropy measures are used to characterize the data. Finally, in Section 5, the main results and conclusions of this paper are discussed.

2. Brief Review of PLs in Catastrophic Occurrences

Patterns seen in wars, terrorist attacks, tornadoes, earthquakes, landslides, floods, and other severe occurrences have been at close attention by various researchers [6–12, 25–28]. Many attentive explanations have arisen in the literature. Nevertheless, a complete understanding of these patterns is a complex task. Important and intricate political, geographical, historical, and, even cultural, factors oppose to a better understanding. Predicting the number of casualties in natural or human-made disasters is extremely important in developing predisaster strategies. Aspects like rationalization of medical supplies and food, gathering emergency teams, organize shelter spaces, amongst others, have to be dealt with, in order to minimize the damage.

A PL behavior is indicative of a particular property of a system, it indicates that the size of an event is inversely proportional to its frequency. In this sense, large casualties are associated with low frequency phenomena, and more frequent events are less harmful in terms of preserving human lives [7, 25]. Examples of phenomena with low probability and huge casualties are the two world wars (WWs), high magnitude earthquakes, strong tornadoes, huge tsunamis, and amongst others.

In 1948, Richardson [7], analyzed domestic and international cases of violence, in the period from 1820 to 1945. He distributed the cases, according to casualties measured in powers of 10, into five categories. The two WWs were classified in the highest category. In a later work [25], the same author showed that if the frequency of an occurrence decreased by a factor close to three, then the number of casualties increased by a power of 10.

Guzzetti [26] considers landslide events in specific periods in different countries, such as Italy, Canada, Alps, Hong Kong, Japan, and China. He shows that the plot of the cumulative distribution function of the number of landslide events versus the number of casualties is well approximated by a straight line. This result suggests a PL distribution of the data.

Cederman [11] followed Richardson's work [7, 25]. He used data from the Correlates of War (COW) Project [29], focusing on interstate wars. He computed the cumulative relative frequency of war size and showed that it obeyed a PL. The author proposed a self-organized critical dynamical system, that replicated the PL behavior seen in real data. Its model allowed conflict to spread and diffuse, potentially over long periods of time, due to the quasi-parallel execution.

In 2005, Jonkman [27] studied the distribution of killings in global events, focusing on the number of human deaths caused by three types of floods (river floods, flash floods, and drainage issues), between January 1975 and June 2002. The author plotted the global frequency of events with N or more deaths versus N. He observed a PL behavior for earthquakes but not for flood data. Becerra et al. [30] use the same data set as Jonkman [27], but consider all disasters combined, both globally and disaggregated by continent. They obtained straight-line log-log plots for all disasters combined. The slopes of the casualties PL distributions were smaller than those for modern wars and terrorism. The explanation for this remained an open question. Another unsolved issue was the existence of PL behavior in combined disasters and not in individual disasters, such as floods. Here it is worth mentioning that casualties in earthquakes verified a PL distribution [6, 27, 30].

Johnson et al. [28] suggested a microscopic theory to explain similarity in patterns of violence, such as war and global terrorism. The similarity was observed regardless of

underlying ideologies, motivations, and the terrain in which events occurred. The authors introduced a model where the insurgent force behaved as a self-organizing system, which evolved dynamically through the continual coalescence and fragmentation of its constituent groups. They analyzed casualties' patterns arising within a given war, unlike previous studies that focused on the total casualty figure for one particular war [7, 11, 25, 31]. A PL behavior fitted well the data not only from Iraq, Colombia, and non-G7 terrorism, but also with data obtained from the war in Afghanistan. The PL parameter for Iraq, Colombia, and Afghanistan was (close to) $\widetilde{\alpha} = 2.5$. This value of the coefficient equalized the coefficient value characterizing non-G7 terrorism. In the literature, the PL parameter value was $\widetilde{\alpha} = 2.51$ for non-G7 countries [32] and $\widetilde{\alpha} = 1.713$ for G7 countries. This result suggested that PL patterns would emerge within any modern asymmetric war, fought by loosely-organized insurgent groups.

In 2006, Bogen and Jones [33] treated the severity of terrorist attacks in terms of deaths and injured. They applied a PL distribution to victim/event rates and used the PL to predict mortality due to terrorism, through the year 2080. Authors claimed that these PL models could be used to improve strategies "to assess, prevent and manage terror-related risks and consequences".

Clauset et al. [34] studied the frequency and the number of casualties (deaths and injuries) of terrorist attacks, since 1968. They observed a scale-invariance behavior, with the frequency being an inverse power of the casualties. This behavior was independent of the type of weapon, economic development, and distinct time scales. The authors presented a new model to fit the frequency of severe terrorist attacks, since previous models in the literature failed to produce the heavy tail in the PL distribution. Their model assumed that the severity of an occurrence was a function of the execution plan, and that selection tools were better suited to model competition between states and nonstate actors. Finally, researchers claimed that periodicity was a common feature in global terrorism, with period close to roughly 13 years.

Bohorquez et al. [12] studied the quantitative relation between human insurgency, global terrorism and ecology. They introduced a new model to explain the size distribution of casualties or the timing of within-conflict events. They considered insurgent populations as self-organized groups that dynamically evolved through decision-making processes. The main assumptions of the model were (i) being consistent with work on human group dynamics in everyday environments, (ii) having a new perception of modern insurgencies, as fragmented, transient, and evolving, and (iii) using a decision-making process about when to attack based on competition for media attention. Authors applied a PL distribution to Iraq and Colombia wars, with parameter value close to $\widetilde{\alpha} = 2.5$. A coefficient value of $\widetilde{\alpha} = 2.5$ was in concordance with the coefficient value of $\widetilde{\alpha} = 2.48 \pm 0.07$ obtained by Clauset et al. [34] on global terrorism. A PL fit to Spanish and American Civil wars revealed a PL parameter value smaller (around $\widetilde{\alpha} = 1.7$). Authors claimed that their model suggested a remarkable link between violent and nonviolent human actions, due to its similarity to financial market models.

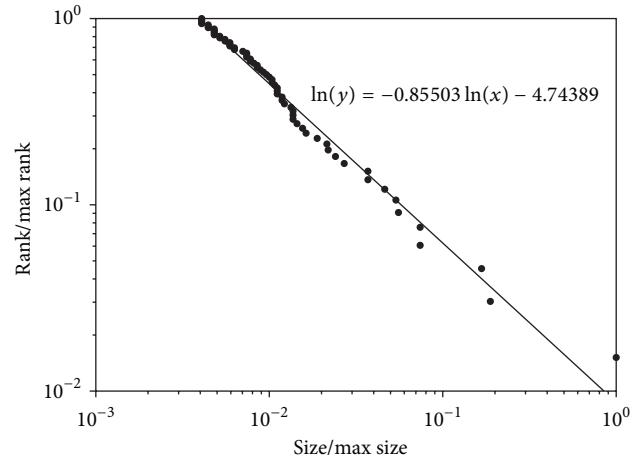

Figure 1: Rank/frequency log-log plot corresponding to the distribution of casualties caused by industrial accidents in Central/South America over the period 1900–2011 (min size = 10; max size = 2700; max rank = 66).

3. Power Law Behavior in Catastrophic Phenomena

In this section we investigate the statistical distributions of random variables that represent the number of human casualties in several human-made and natural hazards.

Data from the EM-DAT International Disaster Database (http://www.emdat.be/) and the Global Terrorism Database (GTD) (http://www.start.umd.edu/gtd/) are analyzed. The EM-DAT database contains information on over than 18000 worldwide natural and technological disasters, from 1900 to present. The EM-DAT is maintained by the Centre for Research on the Epidemiology of Disasters (CRED) at the School of Public Health of the Université Catholique de Louvain, located in Brussels, Belgium [35]. The GTD database is an open-source database that includes information on more than 98000 worldwide terrorist attacks, from 1970 up to 2010 [31].

PLs are observed in several natural and man-made systems. Examples of single and double PLs in real data are given in Figures 1 and 2, respectively. The former represents the complementary cumulative distribution of the severity of industrial accidents in Central/South America over the period 1900–2011. The adopted measure to quantify the severity of an event is the total number of fatalities. The depicted graph corresponds to a rank/frequency log-log plot. To construct the graph, we first sort the data (i.e., the accidents) in decreasing order according to their severity, and number them, consecutively, starting from one [36]. Then a normalization of the values is carried out, meaning that the number of fatalities (x-axis) is divided by the corresponding highest value, and the rank (y-axis) is divided by the rank of the smallest event. Finally, PLs are adjusted to the data using a least squares algorithm. All the log-log plots presented in this paper are made following this procedure.

Figure 2 corresponds to the distribution of casualties caused by earthquakes in Central/South America in

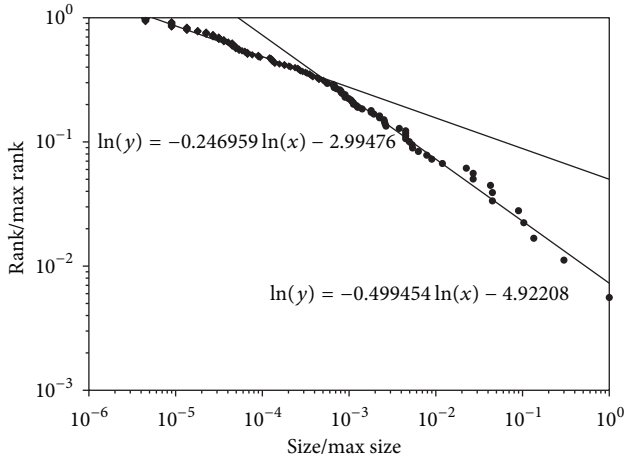

FIGURE 2: Rank/frequency log-log plot corresponding to the distribution of casualties caused by earthquakes in Central/South America over the period 1900–2011 (min size = 1; max size = 222570; max rank = 179).

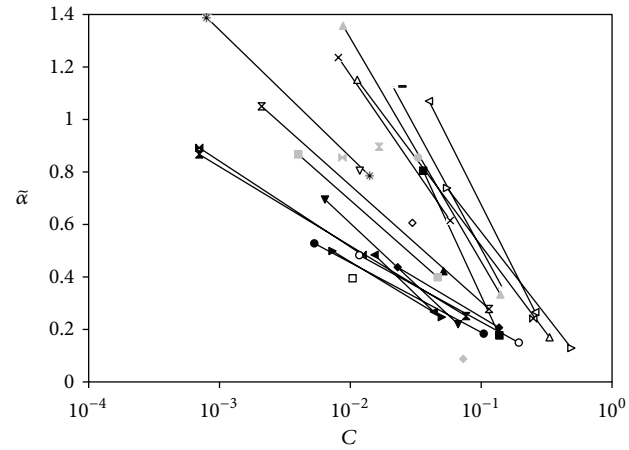

FIGURE 3: Locus of the parameters $(\widetilde{C}_i, \widetilde{\alpha}_i)$, $i = 1, 2$, that characterize the PLs corresponding to the number of casualties in certain combinations of disaster type/location, $\mathrm{DT}_j/\mathrm{DL}_k$.

the period 1900–2011, representing one event that can be approximated by a double PL.

As can be seen in Figure 1, a single PL (SPL) with parameters $(\widetilde{C}, \widetilde{\alpha}) = (0.0087, 0.8550)$ fits to the data. The distribution depicted in Figure 2 is better approximated by a double PL (DPL) with parameters $(\widetilde{C}_1, \widetilde{\alpha}_1) = (0.0500, 0.2470)$ and $(\widetilde{C}_2, \widetilde{\alpha}_2) = (0.0073, 0.4995)$. The change in the behavior occurs at the relative value of $x = 0.000539$, approximately.

We analyzed the data available at the EM-DAT database in terms of disaster type (DT_j) and disaster location (DL_k), $j = 1, \ldots, 11$ and $k = 1, \ldots, 6$ categories, respectively: $\mathrm{DT}_j = \{$Drought, Earthquake, Epidemic, Extreme temperature, Flood, Industrial accident, Mass movement wet, Storm, Transport accident, Volcano, Wildfire$\}$; $\mathrm{DL}_k = \{$Africa, North America, Central & South America, Europe (including Russia), Asia (not including SE Asia), Oceania (including SE Asia)$\}$. The period of analysis was 1900–2011 for every case. The total number of combinations (location/type) is 11×6. Nevertheless, for 14 cases, there is insufficient data to compute reliable statistical distributions. For all cases, taking the number of casualties as the variable of interest, we obtain statistical distributions that can be approximated by either a SPL (16 cases) or a DPL (36 cases), similar to the ones depicted in Figures 1 and 2.

In Figure 3 we depict the locus of the parameters $(\widetilde{C}_i, \widetilde{\alpha}_i)$, $i = 1, 2$, corresponding to the analyzed cases. As can be seen, an interesting pattern emerges, where the lines that connect the pairs of points that characterize the DPLs have identical orientation. This geometrical pattern reflects a relationship between the two parts of the DPL distributions (DPL1—part closer to the head; and DPL2—part closer to the tail). Besides the observation that $\widetilde{\alpha}_2 > \widetilde{\alpha}_1$, in all cases, further investigation on the reason for this behavior is needed.

We pursued our study with the analysis of the GTD database. First, the events associated to human casualties were grouped by year (Y_r) starting in 1980 up to 2010 (except 1993, because there is no data available): $Y_r = \{1980, \ldots, 2010\} \setminus \{1993\}$, $r = 1, \ldots, 30$. We found that all the statistical distributions can be approximated by DPLs. In Figures 4 and 5, the time evolution of the parameters of the DPLs $(\widetilde{C}_i, \widetilde{\alpha}_i)$, $i = 1, 2$, is shown. Regarding the parameters $\widetilde{C}_i$, it can be seen that they have identical behavior, although $\widetilde{C}_2$ varies more than $\widetilde{C}_1$ and is always smaller than it.

With respect to $\widetilde{\alpha}_i$, we have a similar evolution but, in this case, the parameter $\widetilde{\alpha}_2$ is always greater than $\widetilde{\alpha}_1$. As severe terrorist attacks correspond to points closer to the tail of the distribution, DPL2, which is characterized by a larger $\widetilde{\alpha}$, this means that those events are more similar between each other than the smaller events (that correspond to DPL1).

To complement the analysis with respect to the date of the occurrences, the parameters $(\widetilde{C}_i, \widetilde{\alpha}_i)$ of the PLs, corresponding to Y_r, were plotted (Figure 6). As can be seen, a pattern similar to the described previously (Figure 3) is observed.

We have also studied the distributions of the casualties in terrorist attacks, occurred in the period 1970–2010, but with respect to other criteria, namely, the type of used weapon (W_i), region where the event took place (R_j), target (T_k), and type of attack (A_l). Each criterion was then divided into $i = 1, \ldots, 6$, $j = 1, \ldots, 13$, $k = 1, \ldots, 19$, and $l = 1, \ldots, 8$ categories, respectively: $W_i = \{$Chemical, Explosives, Firearms, Incendiary, Melee, Vehicle$\}$; $R_j = \{$Australasia & Oceania, Central America & Caribbean, Central Asia, East Asia, Eastern Europe, Middle East & North Africa, North America, South America, South Asia, Southeast Asia, Sub-Saharan Africa, USSR & Newly Independent States (NIS), Western Europe$\}$; $T_k = \{$Airports & Airlines, Business, Educational Institution, Food or Water Supply, Government (Diplomatic), Government (General), Journalists & Media, Maritime, Military, NGO, Police, Private Citizens & Property, Religious Figures/Institutions, Telecommunication, Terrorists, Tourists, Transportation, Utilities, Violent Political Party$\}$; $A_l = \{$Armed Assault, Assassination,

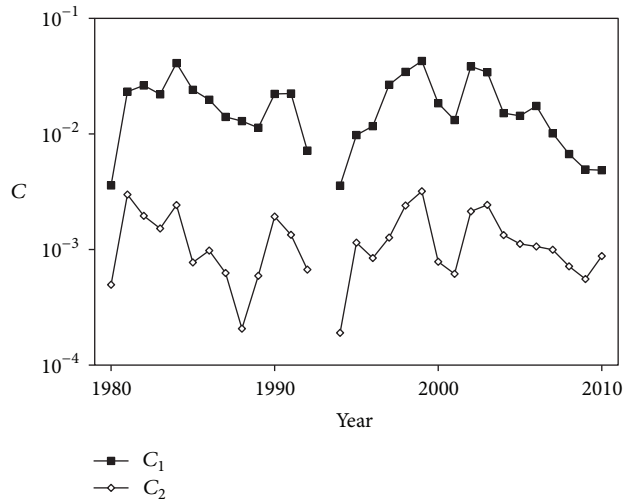

Figure 4: Time evolution of parameters $\widetilde{C}_i$, $i = 1, 2$, of the DPLs corresponding to terrorist attacks over the period 1980–2010, Y_r.

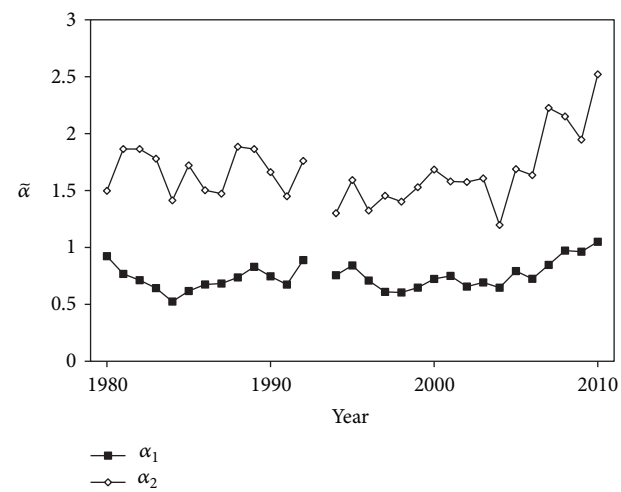

Figure 5: Time evolution of parameters $\widetilde{\alpha}_i$, $i = 1, 2$, of the DPLs corresponding to terrorist attacks over the period 1980–2010, Y_r.

Bombing/Explosion, Facility/Infrastructure Attack, Hijacking, Hostage Taking (Barricade Incident), Hostage Taking (Kidnapping), and Unarmed Assault}.

Most cases are characterized by DPLs. However, in a few situations a SPL fits better to the data. The main results are summarized in Table 1. Moreover, we observed that the parameters corresponding to all distributions characterized by DPLs display a pattern similar to the ones mentioned previously (Figures 3 and 6), where the lines connecting the slopes and intercepts of DPL1 $(\widetilde{\alpha}_1, \widetilde{C}_1)$ to its companion DPL2 $(\widetilde{\alpha}_2, \widetilde{C}_2)$, for the same data set, have identical orientation in the $(\widetilde{C}, \widetilde{\alpha})$ Cartesian space.

4. Entropy of Catastrophic Phenomena

In this section we analyse the entropy of data collected from the GTD database, that is, data related to terrorism. To

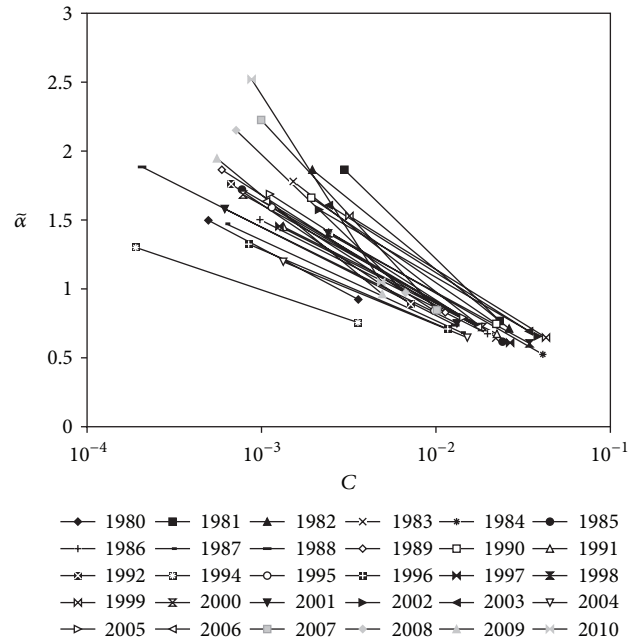

Figure 6: Locus of the parameters $(\widetilde{C}_i, \widetilde{\alpha})$, $i = 1, 2$ that characterize the distributions of terrorist attacks over the period 1980–2010, Y_r.

calculate the entropies we construct histograms of relative frequencies, using bins of width one (one casualty), and approximate the probabilities p_i by the relative frequencies. We present results obtained for terrorist events grouped by year (Y_r), as defined in the previous section. Nevertheless, it should be noticed that similar results are obtained for all other human-made and natural hazards.

Clausius [37] and Boltzmann [38] were the first authors to define entropy in the field of thermodynamics. Later on, Shannon [39] and Jaynes [40] applied their results to information theory [41].

The most celebrated entropy is the so-called Shannon entropy S defined by

$$S = -\sum_{i=1}^{W} p_i \ln p_i. \tag{2}$$

The Shannon entropy represents the expected value of the information $-\ln p_i$. Therefore, for the uniform probability distribution we have $p_i = W^{-1}$ and the Shannon entropy takes its maximum value $S = \ln W$, yielding the Boltzmann's famous formula, up to a multiplicative factor k denoting the Boltzmann constant. Thus, in thermodynamic equilibrium, the Shannon entropy can be identified as the "physical entropy" of the system.

Rényi and Tsallis entropies are generalizations of Shannon's entropy and are given by, respectively,

$$\begin{aligned} S_q^{(R)} &= \frac{1}{1-q} \ln\left(\sum_{i=1}^{W} p_i^q\right), \qquad q > 0, \\ S_q^{(T)} &= \frac{1}{q-1}\left(1 - \sum_{i=1}^{W} p_i^q\right). \end{aligned} \tag{3}$$

Table 1: PL fit to the distributions of casualties in terrorist attacks.

Criterion	Category	SPL $(\widetilde{C}, \widetilde{\alpha})$	DPL1 $(\widetilde{C}_1, \widetilde{\alpha}_1)$	DPL2 $(\widetilde{C}_2, \widetilde{\alpha}_2)$
Weapon (W_i)	W_1	0.0391 0.5849		
	W_2		0.0082 0.7514	0.0002 1.7198
	W_3		0.0017 0.8660	0.0000 1.9624
	W_4		0.0236 0.6877	0.0021 1.4890
	W_5		0.0057 0.6909	0.0003 1.3579
	W_6	0.0249 0.7801		
Region (R_i)	R_1	0.0438 1.0147		
	R_2		0.0214 0.6412	0.0009 1.6905
	R_3	0.0174 1.1905		
	R_4	0.0065 0.9073		
	R_5	0.0012 1.2141		
	R_6		0.0091 0.8051	0.0006 1.7088
	R_7	0.0009 1.1415		
	R_8		0.0193 0.7814	0.0008 2.0675
	R_9		0.0036 0.8742	0.0001 2.0552
	R_{10}		0.0128 0.8561	0.0012 1.6578
	R_{11}		0.0091 0.6454	0.0004 1.3132
	R_{12}	0.0023 0.9956		
	R_{13}	0.0001 1.5523		
Target (T_i)	T_1		0.0438 0.5144	0.0092 1.2488
	T_2		0.0057 0.8884	0.0003 1.7180
	T_3		0.0002 1.3589	0.0012 0.8458
	T_4	0.0452 0.7923		
	T_5	0.0015 1.1259		
	T_6		0.0006 1.1152	0.0001 1.5162
	T_7	0.0014 1.6106		
	T_8		0.0576 0.4694	0.0094 0.9070
	T_9		0.0353 0.5669	0.0009 1.6291
	T_{10}		0.0090 0.9645	0.0031 1.2573
	T_{11}		0.0047 0.8991	0.0001 1.8354
	T_{12}		0.0036 0.7778	0.0000 1.8667
	T_{13}		0.0158 0.7353	0.0018 1.6106
	T_{14}	0.0462 0.9774		
	T_{15}		0.0168 0.8610	0.0026 1.6824
	T_{16}	0.0234 0.7635		
	T_{17}		0.0340 0.5892	0.0014 1.5178
	T_{18}		0.0225 0.7389	0.0074 1.0708
	T_{19}		0.0108 0.7918	0.0025 1.1650
Type (A_i)	A_1		0.0049 0.7346	0.0000 1.7982
	A_2		0.0014 1.5201	0.0001 2.6555
	A_3		0.0059 0.8116	0.0001 2.0621
	A_4		0.0261 0.6339	0.0016 1.4880
	A_5	0.0305 0.7186		
	A_6	0.0116 0.7316		
	A_7		0.0072 0.9689	0.0014 1.6214
	A_8		0.0471 0.7006	0.0034 2.0186

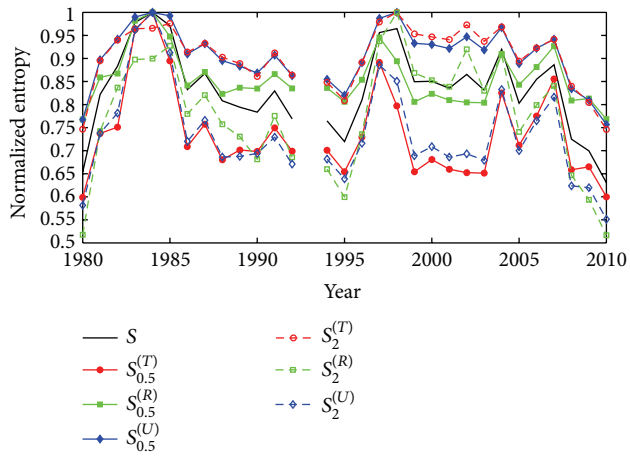

FIGURE 7: Total Shannon, Tsallis, Rényi, and Ubriaco normalized entropies, as a function of the year of the events, Y_r; $q = 0.5$ and $q = 2$.

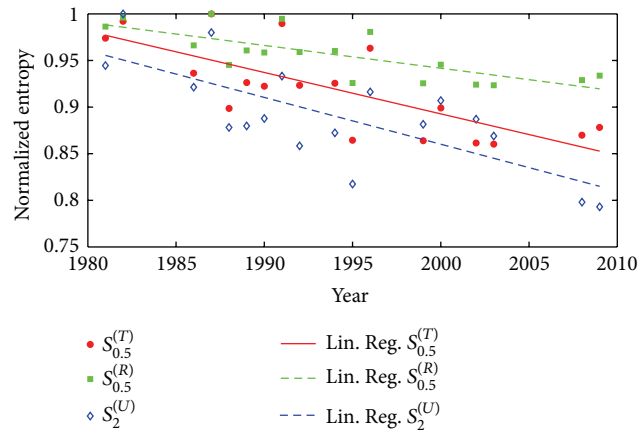

FIGURE 8: Total Tsallis and Rényi normalized entropies ($q = 0.5$) and Ubriaco's ($q = 2$), as a function of the events in years {1981, 1982, 1986–1992, 1994–1996, 1999, 2000, 2002, 2003, 2008, 2009}.

Tsallis entropy reduces to Rényi entropy when $q \to 1$. Tsallis entropy was applied to diffusion equations [42] and Fokker-Planck systems [43]. Rényi entropy has an inverse power law equilibrium distribution [44] and satisfies the zeroth law of thermodynamics [45]. The two parameters Sharma-Mittal entropy [46] is accepted as a generalization of Tsallis, Rényi, and Boltzmann-Gibbs entropies, for limiting cases of the parameters [47].

Recently, more general entropy measures have been proposed in the literature, where the additivity axiom has been relaxed. For instance, Ubriaco [48] proposed the following formula for the fractional entropy:

$$S_q^{(U)} = \sum_{i=1}^{W} (-\ln p_i)^q p_i \tag{4}$$

that has the same properties as the Shannon entropy except additivity.

Applications of entropy in distinct complex systems can be found in [49–57].

In Figure 7 the total Shannon normalized entropy (S) is depicted, as well as Tsallis' ($S_q^{(T)}$), Rényi's ($S_q^{(R)}$) and Ubriaco's ($S_q^{(U)}$), for $q = 0.5$, and $q = 2$, as a function of the year of the events, Y_r. Figures 9, 10, and 11 show $S_q^{(T)}$, $S_q^{(R)}$ and $S_q^{(U)}$ normalized entropies, as a function of the year, Y_r, and entropy parameter $0.1 \le q \le 10$.

In Figure 7 we observe two types of behavior, namely, short- and long-term phenomena. In what concerns short time behavior, we verify peaks during 1983–1985, 1997-1998, 2004–2007, and minima at 1980, 1995, and 2010. In what concerns long-time relationships a smooth decreasing is observed for $S_{0.5}^{(T)}$, $S_{0.5}^{(R)}$, and $S_2^{(U)}$. Removing the maxima and minima we get a time series for years 1981, 1982, 1986–1992, 1994–1996, 1999, 2000, 2002, 2003, 2008, and 2009 (Figure 8). Larger/smaller entropies correspond to charts closer/afar uniform distributions; therefore, seemingly, we have less/more organized terrorist events in global terms.

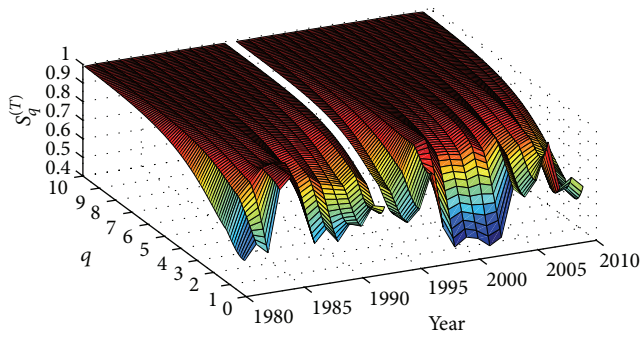

FIGURE 9: Total Tsallis normalized entropy, $S_q^{(T)}$, as a function of the year of the events, Y_r, and parameter q.

These conclusions remain invariant for Figures 9 to 11, where we vary both the entropy definition and the parameter tuning. Therefore, we conclude that such results are robust against such type of variations.

As discussed in the previous section, the statistical distributions of real data can be approximated by either single or double PLs. In the latter case, we study, not only the total entropy, but also the entropy associated to each part of the distributions. Therefore, we compute the entropy associated to DPL1 and DPL2, that approximate the first and second part of the distributions, respectively. When adopting this procedure we are restricted to the Shannon and Ubriaco entropies, as Tsallis' and Rényi's do not admit the associativity described above.

In the sequel we present several results of the analysis, taking into account the grouping criteria Y_r, W_i, R_j, T_k, and A_l. Figure 12 depicts the Shannon entropy versus parameter $\tilde{\alpha}$ for all statistical distributions. The black squares (denoted "SPL") correspond to the plot of $\tilde{\alpha}$ versus the total entropy of the respective distributions, S. The black circles (denoted "DPL1") are the plot of $\tilde{\alpha}_1$ versus the entropy associated to the first parts of the distributions, S_1. The white circles (denoted "DPL2") represent the plot of $\tilde{\alpha}_2$ versus the entropy associated

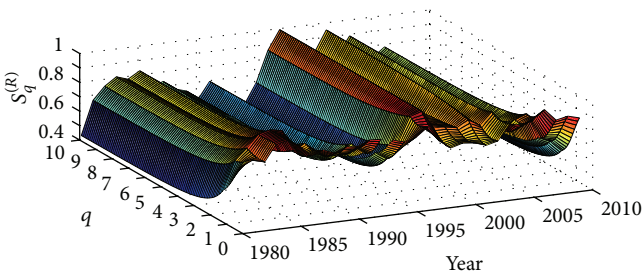

FIGURE 10: Total Rényi normalized entropy, $S_q^{(R)}$, as a function of the year of the events, Y_r, and parameter q.

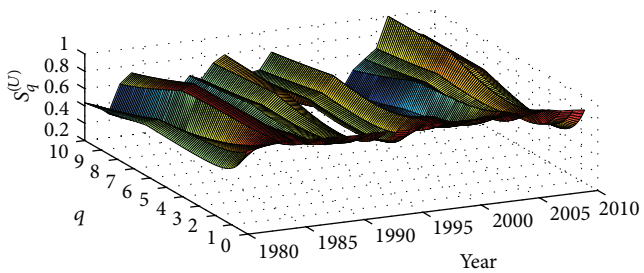

FIGURE 11: Total Ubriaco normalized entropy, $S_q^{(U)}$, as a function of the year of the events, Y_r, and parameter q.

to the second parts of the distributions, S_2. As can be seen, for the distributions that behave as single PLs, higher entropies correspond to the lower values of the parameter $\widetilde{\alpha}$ and the two parameters are linearly related. A similar pattern is observed for the parameters corresponding to DPL1. For DPL2 the parameter $\widetilde{\alpha}_2$ increases with entropy, but the almost linear relation between both parameters remains.

Figure 13 shows identical results for the Ubriaco entropy. The plot corresponds to $q = 0.5$, nevertheless, identical results are obtained for other values.

For all DPLs related to terrorist events, n ($n = 1, \ldots, 60$), we find that the parameters $(\widetilde{C}_i, \widetilde{\alpha}_i)$, $i = 1, 2$ obey the following relation:

$$\widetilde{\alpha}_{1n} \left|\log \widetilde{C}_{1n}\right|^p = \widetilde{\alpha}_{2n} \left|\log C_{2n}\right|^p + \epsilon_n, \tag{5}$$

where $p = -1.612$. The mean value of ϵ_n is $\overline{\epsilon} = 0.002$, and the corresponding standard deviation is $\sigma_\epsilon = 0.036$. Moreover, for the analyzed data, we find $\widetilde{\alpha}_{in} |\log \widetilde{C}_{in}|^p = k_{in}$. Parameters k_{in} are approximately constant, with mean value $\overline{k} = 0.277$ and standard deviation $\sigma_k = 0.06$.

It is worth noticing that (5) is similar to Poisson's law of an adiabatic reversible process, involving ideal gases, given by

$$P_1 V_1^\gamma = P_2 V_2^\gamma, \tag{6}$$

where variables P_i and V_i represent pressure and specific volume, respectively. Equation (6) implies that $PV^\gamma = \text{const}$. Parameter γ is called Poisson's coefficient, taking values $\gamma = 5/3 \simeq 1.67$ and $\gamma = 7/5 = 1.40$ for monoatomic and diatomic gases, respectively. Additionally, it should be noticed that the absolute value of the exponent p is very similar to the one observed for an ideal gas undergoing a reversible adiabatic process.

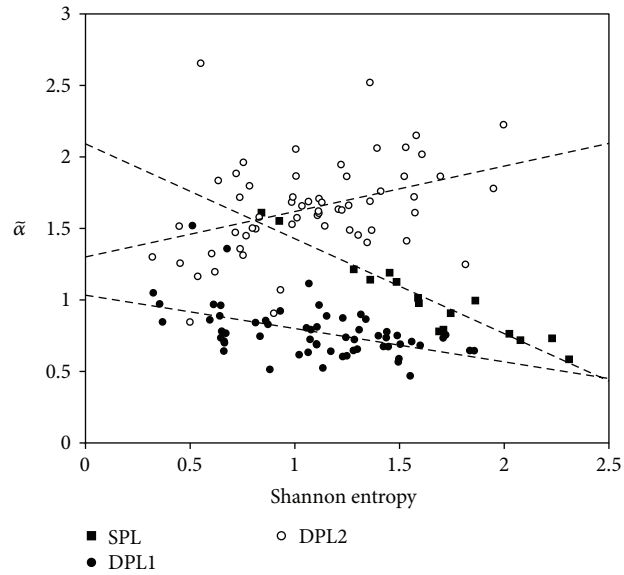

FIGURE 12: Parameters $\widetilde{\alpha}$ versus Shannon entropies for the distributions corresponding to the criteria Y_r, W_i, R_j, T_k, and A_l; "SPL" corresponds to $(S, \widetilde{\alpha})$; "DPL1" corresponds to $(S_1, \widetilde{\alpha}_1)$; "DPL2" corresponds to $(S_2, \widetilde{\alpha}_2)$.

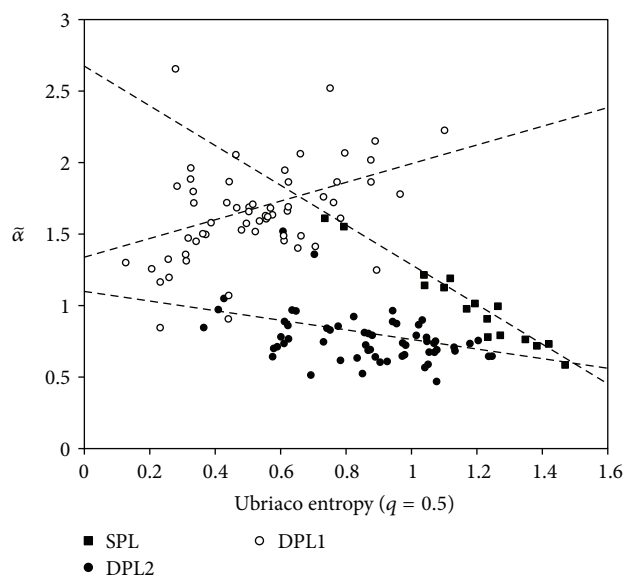

FIGURE 13: Parameters $\widetilde{\alpha}$ versus Ubriaco entropies for the distributions corresponding to the criteria Y_r, W_i, R_j, T_k, and A_l; "SPL" corresponds to $(S_q^{(U)}, \widetilde{\alpha})$; "DPL1" corresponds to $(S_{q1}^{(U)}, \widetilde{\alpha}_1)$; "DPL2" corresponds to $(S_{q2}^{(U)}, \widetilde{\alpha}_2)$; $q = 0.5$.

5. Conclusions

PLs have been widely reported in the modeling of distinct phenomena and have been associated with long memory behavior, self-similarity, fractal structures, and fractional calculus.

In this paper we reviewed interesting and important results on PLs distributions and their applications to the

modeling of the number of victims in catastrophic events. We found double PL behavior in real data of catastrophic occurrences, in particular, terrorism. We have plotted the two PLs parameters, $(\widetilde{C}_i, \widetilde{\alpha}_i)$, $i = 1, 2$, corresponding to certain events, and observed an interesting pattern in the chart, where the lines that connect each pair of points defining the double PLs are almost aligned to each other. We have also computed the entropy of the data sets. This complementary analysis of the numerical data revealed extra relationships but the fact is that these phenomena have a dense and rich volume of characteristics and further research efforts are needed to a deeper understanding.

References

[1] J. Tenreiro Machado, F. B. Duarte, and G. M. Duarte, "Power law analysis of financial index dynamics," *Discrete Dynamics in Nature and Society*, vol. 2012, Article ID 120518, 12 pages, 2012.

[2] J. Tenreiro Machado, "And I say to myself: 'What a fractional worl'," *Fractional Calculus and Applied Analysis*, vol. 14, no. 4, pp. 635–654, 2011.

[3] E. Scalas, R. Gorenflo, and F. Mainardi, "Fractional calculus and continuous-time finance," *Physica A*, vol. 284, no. 1–4, pp. 376–384, 2000.

[4] F. Mainardi, M. Raberto, R. Gorenflo, and E. Scalas, "Fractional calculus and continuous-time finance. II: the waiting-time distribution," *Physica A*, vol. 287, no. 3-4, pp. 468–481, 2000.

[5] B. J. West, "Fractal physiology and the fractional calculus: a perspective," *Frontiers in Physiology*, vol. 1, p. 12, 2010.

[6] B. Gutenberg and R. F. Richter, "Frequency of earthquakes in california," *Bulletin of the Seismological Society of America*, vol. 34, pp. 185–188, 1944.

[7] L. F. Richardson, "Variation of the Frequency of Fatal Quarrels with Magnitude," *Journal of the American Statistical Association*, vol. 43, pp. 523–546, 1948.

[8] J. M. Carlson and J. S. Langer, "Mechanical model of an earthquake fault," *Physical Review A*, vol. 40, no. 11, pp. 6470–6484, 1989.

[9] D. C. Roberts and D. L. Turcotte, "Fractality and self-organized criticality of wars," *Fractals*, vol. 6, no. 4, pp. 351–357, 1998.

[10] D. R. Davis and D. E. Weinstein, "Bones, bombs, and break points: the geography of economic activity," *The American Economic Review*, vol. 92, no. 5, pp. 1269–1289, 2002.

[11] L. E. Cederman, "Modeling the size of wars: from billiard balls to sandpiles," *American Political Science Review*, vol. 97, no. 1, pp. 135–150, 2003.

[12] J. C. Bohorquez, S. Gourley, A. R. Dixon, M. Spagat, and N. F. Johnson, "Common ecology quantifies human insurgency," *Nature*, vol. 462, no. 7275, pp. 911–914, 2009.

[13] V. Pareto, *Cours d'Economie Politique*, Droz, Geneva, Switzerland, 1896.

[14] F. Auerbach, "Das Gesetz der Belvolkerungskoncentration," *Petermanns Geographische Mitteilungen*, vol. 59, pp. 74–76, 1913.

[15] J. B. Estoup, *Gammes Stenographiques*, Institut de France, 1916.

[16] G. Zipf, *Selective Studies and the Principle of Relative Frequency in Language*, Harvard University Press, Cambridge, Mass, USA, 1932.

[17] G. Zipf, *Human Behavior and the Priciple of Least Effort*, Addison-Wesley, Cambridge, Mass, USA, 1949.

[18] W. Li, "References on Zipf's law," http://www.sorinsolomon.net/~sorin/ccs/zipf/references%20on%20zipf%27s%20law.htm.

[19] D. Sornette, *Critical Phenomena in Natural Sciences*, chapter 14, Springer, Heidelberg, Germany, 2nd edition, 2003.

[20] C. M. A. Pinto, A. M. Lopes, and J. A. Tenreiro Machado, "A review of power laws in real life phenomena," *Communications in Nonlinear Science and Numerical Simulations*, vol. 17, no. 9, pp. 3558–3578, 2012.

[21] J. Tuldava, "The frequency spectrum of text and vocabulary," *Journal of Quantitative Linguistics*, vol. 3, no. 1, pp. 38–50, 1996.

[22] G. Martínez-Mekler, R. Alvarez Martínez, M. Beltrán del Río, R. Mansilla, P. Miramontes, and G. Cocho, "Universality of rank-ordering distributions in the arts and sciences," *PLoS One*, vol. 4, no. 3, Article ID e4791, 2009.

[23] R. F. I. Cancho and R. V. Solé, "Two regimes in the frequency of words and the origins of complex lexicons: Zipf's law revisited," *Journal of Quantitative Linguistics*, vol. 8, no. 3, pp. 165–173, 2001.

[24] R. Alvarez-Martinez, G. Martinez-Mekler, and G. Cochoa, "Order-disorder transition in conflicting dynamics leading to rank-frequency generalized beta distributions," *Physica A*, vol. 390, no. 1, pp. 120–130, 2011.

[25] L. F. Richardson, *Statistics of Deadly Quarrels*, Quadrangle Books, Chicago, Ill, USA, 1960.

[26] F. Guzzetti, "Landslide fatalities and the evaluation of landslide risk in Italy," *Engineering Geology*, vol. 58, no. 2, pp. 89–107, 2000.

[27] S. N. Jonkman, "Global perspectives on loss of human life caused by floods," *Natural Hazards*, vol. 34, no. 2, pp. 151–175, 2005.

[28] N. F. Johnson, M. Spagat, J. A. Restrepo et al., "Universal patterns underlying ongoingwars and terrorism," http://arxiv.org/abs/physics/0605035.

[29] D. S. Geller and J. David Singer, *Nations at War: A Scientific Study of International Conflict*, Cambridge Studies in International Relations, Cambridge University Press, Cambridge, UK, 1998.

[30] O. Becerra, N. Johnson, P. Meier, J. Restrepo, and M. Spagat, "Natural disasters, casualties and power laws: a comparative analysis with armed conflict," in *Proceedings of the Annual Meeting of the American Political Science Association*, Loews Philadelphia, and the Pennsylvania Convention Center, Philadelphia, Pa, USA, 2006, http://www.allacademic.com/meta/p151714_index.html.

[31] M. E. J. Newman, "Power laws Pareto distributions and Zipf's law," *Contemporary Physics*, vol. 46, pp. 323–351, 2005.

[32] A. Clauset and M. Young, "Scale invariance in global terrorism," http://arxiv.org/abs/physics/0502014.

[33] K. T. Bogen and E. D. Jones, "Risks of mortality and morbidity from worldwide terrorism: 1968–2004," *Risk Analysis*, vol. 26, no. 1, pp. 45–59, 2006.

[34] A. Clauset, M. Young, and K. S. Gleditsch, "On the frequency of severe terrorist events," *Journal of Conflict Resolution*, vol. 51, no. 1, pp. 58–87, 2007.

[35] EM-DAT, "The OFDA/CRED International Disaster Database," Université catholique de Louvain, Brussels, Belgium, http://www.emdat.net/.

[36] National Consortium for the Study of Terrorism and Responses to Terrorism (START), "Global Terrorism Database," 2011, http://www.start.umd.edu/gtd/.

[37] R. Clausius, *The Mechanical Theory of Heat with Its Applications to the Steam Engine and to Physical Properties of Bodies*, John van Voorst, London, UK, 1865.

[38] L. Boltzmann, *Vorlesungen ber Gastheorie*, J. A. Barth, Leipzig, Germany, 1896.

[39] C. E. Shannon, "A mathematical theory of communication," *The Bell System Technical Journal*, vol. 27, pp. 379–423, 623–656, 1948.

[40] E. T. Jaynes, "Information theory and statistical mechanics," vol. 106, pp. 620–630, 1957.

[41] A. I. Khinchin, *Mathematical Foundations of Information Theory*, Dover, New York, NY, USA, 1957.

[42] A. R. Plastino, M. Casas, and A. Plastino, "A nonextensive maximum entropy approach to a family of nonlinear reaction-diffusion equations," *Physica A*, vol. 280, no. 3, pp. 289–303, 2000.

[43] T. D. Frank and A. Daffertshofer, "H-theorem for nonlinear Fokker-Planck equations related to generalized thermostatistics," *Physica A*, vol. 295, no. 3-4, pp. 455–474, 2001.

[44] E. K. Lenzi, R. S. Mendes, and L. R. da Silva, "Statistical mechanics based on Renyi entropy," *Physica A*, vol. 280, no. 3-4, pp. 337–345, 2000.

[45] A. S. Parvan and T. S. Biró, "Extensive Rényi statistics from non-extensive entropy," *Physics Letters A*, vol. 340, no. 5-6, pp. 375–387, 2005.

[46] B. D. Sharma and D. P. Mittal, "New nonadditive measures of entropy for discrete probability distributions," *Journal of Mathematical Sciences*, vol. 10, pp. 28–40, 1975.

[47] T. D. Frank and A. Daffertshofer, "Exact time-dependent solutions of the Renyi Fokker-Planck equation and the Fokker-Planck equations related to the entropies proposed by Sharma and Mittal," *Physica A*, vol. 285, no. 3, pp. 351–366, 2000.

[48] M. R. Ubriaco, "Entropies based on fractional calculus," *Physics Letters A*, vol. 373, no. 30, pp. 2516–2519, 2009.

[49] P. T. Landsberg and V. Vedral, "Distributions and channel capacities in generalized statistical mechanics," *Physics Letters A*, vol. 247, no. 3, pp. 211–217, 1998.

[50] A. Plastino and A. R. Plastino, "Tsallis Entropy and Jaynes' information theory formalism," *Brazilian Journal of Physics*, vol. 29, no. 1, pp. 50–60, 1999.

[51] X. Li, C. Essex, M. Davison, K. H. Hoffmann, and C. Schulzky, "Fractional diffusion, irreversibility and entropy," *Journal of Non-Equilibrium Thermodynamics*, vol. 28, no. 3, pp. 279–291, 2003.

[52] H. J. Haubold, A. M. Mathai, and R. K. Saxena, "Boltzmann-Gibbs entropy versus Tsallis entropy: recent contributions to resolving the argument of Einstein concerning "neither Herr Boltzmann nor Herr Planck has given a definition of W"? Essay review," *Astrophysics and Space Science*, vol. 290, no. 3-4, pp. 241–245, 2004.

[53] P. N. Rathie and S. da Silva, "Shannon, Lévy, and Tsallis: a note," *Applied Mathematical Sciences*, vol. 2, no. 28, pp. 1359–1363, 2008.

[54] R. M. Gray, *Entropy and Information Theory*, Springer, New York, NY, USA, 2009.

[55] J. A. Tenreiro Machado, A. C. Costa, and M. F. M. Lima, "Dynamical analysis of compositions," *Nonlinear Dynamics*, vol. 65, no. 4, pp. 339–412, 2011.

[56] J. A. T. Machado, A. C. Costa, and M. D. Quelhas, "Entropy analysis of the DNA code dynamics in human chromosomes," *Computers & Mathematics with Applications*, vol. 62, no. 3, pp. 1612–1617, 2011.

[57] J. A. Tenreiro Machado, A. C. Costa, and M. D. Quelhas, "Shannon, Rényie and Tsallis entropy analysis of DNA using phase plane," *Nonlinear Analysis: Real World Applications*, vol. 12, no. 6, pp. 3135–3144, 2011.

Hindawi Publishing Corporation
Mathematical Problems in Engineering
Volume 2013, Article ID 358473, 3 pages
http://dx.doi.org/10.1155/2013/358473

Research Article

One-Phase Problems for Discontinuous Heat Transfer in Fractal Media

Ming-Sheng Hu,[1] Dumitru Baleanu,[2,3,4] and Xiao-Jun Yang[1,5]

[1] *Institute of Software Science, Zhengzhou Normal University, Zhengzhou 450044, China*
[2] *Department of Mathematics and Computer Sciences, Faculty of Arts and Sciences, Cankaya University, 06530 Ankara, Turkey*
[3] *Department of Chemical and Materials Engineering, Faculty of Engineering, King Abdulaziz University, P.O. Box 80204, Jeddah 21589, Saudi Arabia*
[4] *Institute of Space Sciences, Magurele, RO-077125 Bucharest, Romania*
[5] *Department of Mathematics and Mechanics, China University of Mining and Technology, Xuzhou, Jiangsu 221008, China*

Correspondence should be addressed to Xiao-Jun Yang; dyangxiaojun@163.com

Received 7 November 2012; Accepted 20 December 2012

Academic Editor: József Kázmér Tar

We first propose the fractal models for the one-phase problems of discontinuous transient heat transfer. The models are taken in sense of local fractional differential operator and used to describe the (dimensionless) melting of fractal solid semi-infinite materials initially at their melt temperatures.

1. Introduction

We know that the local fractional calculus is set up on fractals. Fractal media is complex, and it appears in different fields of engineering and physics. Fractal physical parameters are considered as local fractional continuous functions, which is fractal characteristics of local fractional functional analysis from fractal geometry point of view. Moreover, the local fractional calculus is a powerful tool to model Fourier law of heat conductions in discontinuous heat transfer in fractal media. Local fractional heat-conduction equations may be applied to describe the fractal behaviors of discontinuous heat transfer in fractal media.

As it is known the Goodman's heat balance integral method represents an approximate technique for generating functional solutions to thermal problems that were described by differential equations [1–3]. Based on theory of fractional calculus [4, 5], both the Stefan problem and the heat-balance integral method governed by a fractional diffusion equation were investigated [6–8]. However, we mention that the above problems are considered in the smooth condition.

On the other hand the heat transfer with nonsmooth condition (fractal space) is an interesting topic. The various phenomena in nanoscale heat (e.g., a charged jet in electrospinning process) can produce both continuous nanofibers and discontinuous nanoporous material. For continuous case, the classical Fourier law is valid. However, for nanoporous material, the fractal Fourier law should be used. For examples, the generalized transfer equation in a medium with fractal geometry was considered in [9], the Fourier's law heat conduction in the discontinuous media was investigated in [10], and the heat transfer from discontinuous media was discussed in [11, 12].

Maybe, there are one-phase problems of fractal heat transfer in nanoporous materials. The aim of this paper is to study the fractal models for one-phase problems. The organization of the paper is organized as follows. In Section 2, we introduce the concept of local fractional derivative and give some results on local fractional chain rule and the fractal complex transform. Section 3 is devoted to the fractal models for the one-phase problems of discontinuous transient heat transfer. Finally, conclusions are given in Section 4.

2. Preliminaries

In this section, we give some basic definitions and properties of the local fractional differential operator theory which are

used further in this paper. In order to discuss the fractal behaviors of materials, we start with the fractal result derived from the fractal geometry.

Lemma 1 (see [11, 12]). *Let F be a subset of the real line and be a fractal. If $f:(F,d)\to(\Omega',d')$ is a bi-Lipschitz mapping, then there is for constants $\rho,\tau>0$ and $F\subset R$,*

$$\rho^s H^s(F)\le H^s(f(F))\le \tau^s H^s(F) \tag{1}$$

such that for all $x_1, x_2\in F$,

$$\rho^\alpha|x_1-x_2|^\alpha\le|f(x_1)-f(x_2)|\le\tau^\alpha|x_1-x_2|^\alpha. \tag{2}$$

For the convenience of the reader, we represent here the following results.

Following Lemma 1, we have [11]

$$|f(x_1)-f(x_2)|\le\tau^\alpha|x_1-x_2|^\alpha \tag{3}$$

such that

$$|f(x_1)-f(x_2)|<\varepsilon^\alpha, \tag{4}$$

where α is fractal dimension of F.

Definition 2. If

$$|f(x)-f(x_0)|<\varepsilon^\alpha \tag{5}$$

with $|x-x_0|<\delta$, for $\varepsilon,\delta>0$ and $\varepsilon,\delta\in R$, then $f(x)$ is called local fractional continuous at $x=x_0$, and it is denoted by

$$\lim_{x\to x_0} f(x)=f(x_0). \tag{6}$$

$f(x)$ is local fractional continuous on the interval (a,b), denoted through [11–14]

$$f(x)\in C_\alpha(a,b) \tag{7}$$

if (5) is valid for $x\in(a,b)$.

Definition 3. Let $f(x)\in C_\alpha(a,b)$. Local fractional derivative of $f(x)$ of order α at $x=x_0$ is defined as [11–14]

$$f^{(\alpha)}(x_0)=\left.\frac{d^\alpha f(x)}{dx^\alpha}\right|_{x=x_0}=\lim_{x\to x_0}\frac{\Delta^\alpha(f(x)-f(x_0))}{(x-x_0)^\alpha}, \tag{8}$$

where $\Delta^\alpha(f(x)-f(x_0))\cong\Gamma(1+\alpha)\Delta(f(x)-f(x_0))$.

If $y(x)=(f\circ u)(x)$ where $u(x)=g(x)$, then we have [11, 14]

$$\frac{d^\alpha y(x)}{dx^\alpha}=f^{(\alpha)}(g(x))\left(g^{(1)}(x)\right)^\alpha, \tag{9}$$

where $f^{(\alpha)}(g(x))$ and $g^{(1)}(x)$ exist.

If $y(x)=(f\circ u)(x)$ where $u(x)=g(x)$, then we have [11, 14]

$$\frac{d^\alpha y(x)}{dx^\alpha}=f^{(1)}(g(x))\,g^{(\alpha)}(x), \tag{10}$$

where we assume that $f^{(1)}(g(x))$ and $g^{(\alpha)}(x)$ exist.

Let us suppose that there is a relation as given below [14]

$$X=\frac{(px)^\alpha}{\Gamma(1+\alpha)},\qquad Y=\frac{(qy)^\alpha}{\Gamma(1+\alpha)}, \tag{11}$$

where q and p are constants and $0<\alpha\le1$, then there exists an equation transformation pair, namely,

$$p^\alpha\frac{dU_1(X)}{dX}+q^\alpha\frac{dU_2(Y)}{dY}=0\Longleftrightarrow\frac{d^\alpha U_1(x)}{dx^\alpha}+\frac{d^\alpha U_2(y)}{dy^\alpha}=0. \tag{12}$$

We stress on the fact that the above method is different from fractional complex transform method discussed in [15, 16]. The fractional complex transform method is proposed in [15, 16], while fractal complex transform method is based on the local fractional calculus theory [14].

3. Fractal Models for One-Phase Problems

We propose a one-phase fractal problem that describes the (dimensionless) melting of a fractal solid semi-infinite material initially at its melt temperature. The corresponding equations are given by the following expressions:

$$\frac{\partial^\alpha u}{\partial t^\alpha}=\frac{\partial^{2\alpha}u}{\partial x^{2\alpha}},\quad 0<x<s,\ t>0, \tag{13}$$

$$\frac{\partial^\alpha u}{\partial x^\alpha}=\beta^\alpha\frac{d^\alpha s}{dt^\alpha},\quad x=s(t),\ t>0, \tag{14}$$

$$u=0,\qquad x>0,\qquad t=0, \tag{15}$$

$$u=0,\qquad x=s(t),\quad t>0, \tag{16}$$

$$u=1,\qquad x=0,\qquad t\ge0. \tag{17}$$

We mention that (13) governs the flow of heat in the fractal liquid region [11, 12], the fractal Stefan condition (14) describes the absorption of heat at the melt front where the fractal Stefan number β^α [11] (it is also derived from fractal complex transform [14]). Equations (15) and (16) prescribe the temperature at the fractal fixed boundary $x=0$ and on the moving melt front $x=s(t)$, and (16) gives the initial temperature of the fractal semi-infinite solution domain. We notice that (13) is derived from the local fractional one-dimensional heat conduction equation with fractal media, which can be written in the form [11]

$$\rho^\alpha c^\alpha\frac{\partial^\alpha u}{\partial t^\alpha}=K^{2\alpha}\frac{\partial^{2\alpha}u}{\partial x^{2\alpha}}, \tag{18}$$

where $K^{2\alpha}$ denotes the thermal conductivity of the fractal material, which is related to fractal dimensions of materials. It is shown that the fractal dimensions of materials are an important characteristic value. Here, we consider the fractal Fourier flow, which is discontinuous; however, it is found that it is local fractional continuous. Like classical Fourier flow, its thermal conductivity is an approximate value for fractal one when $\alpha=1$ [11].

The alternative form of the condition (14) can be derived from the fact that the total local fractional derivative of the temperature at $x = s(t)$ is zero, that is, $D^{\alpha}u(s(t),t)/Dt^{\alpha} = 0$, which leads us to the following expression:

$$\frac{\partial u}{\partial x}\frac{d^{\alpha}s}{dt^{\alpha}} + \frac{d^{\alpha}u}{dt^{\alpha}} = 0. \tag{19}$$

Then, by using (13) and (19) we conclude that

$$\frac{d^{\alpha}s}{dt^{\alpha}} = -\frac{d^{\alpha}u/dt^{\alpha}}{\partial u/\partial x} = -\frac{\partial^{2\alpha}u/\partial x^{2\alpha}}{\partial u/\partial x}. \tag{20}$$

As a result, it leads us to the following final equation:

$$\left(\frac{\partial^{\alpha}u}{\partial x^{\alpha}}\right)\left(\frac{\partial u}{\partial x}\right) = \beta^{\alpha}\frac{\partial^{2\alpha}u}{\partial x^{2\alpha}}, \quad x = s(t), \ t > 0. \tag{21}$$

This result is no sense because fractal flow is local fractional continuous at x. If u is local fractional continuous, and u is continuous, we deduce that fractal dimension is $\alpha = 1$. Hence, we can obtain the classical results [2, 3].

Another alternative form of the condition (14) is derived from the fact that the total local fractional derivative of the temperature at $x = s(t)$ is zero, that is,

$$\frac{D^{\alpha}u(s(t),t)}{Dt^{\alpha}} = 0, \tag{22}$$

which implies in our case that

$$\frac{\partial^{\alpha}u}{\partial x^{\alpha}}\left(\frac{ds}{dt}\right)^{\alpha} + \frac{d^{\alpha}u}{dt^{\alpha}} = 0. \tag{23}$$

By using (13) and (23), we finally obtain

$$\left(\frac{ds}{dt}\right)^{\alpha} = -\frac{1}{\Gamma(1-\alpha)}\frac{d^{\alpha}s}{dt^{\alpha}} = -\frac{1}{\Gamma(1-\alpha)}\frac{\partial^{2\alpha}u/\partial x^{2\alpha}}{\partial^{\alpha}u/\partial x^{\alpha}}, \tag{24}$$

which leads us to the final form as given below

$$\left(\frac{\partial^{\alpha}u}{\partial x^{\alpha}}\right)^{2} = \frac{\beta^{\alpha}}{\Gamma(1-\alpha)}\frac{\partial^{2\alpha}u}{\partial x^{2\alpha}}, \quad x = s(t), \ t > 0. \tag{25}$$

4. Conclusions

In this paper we have proposed alternative fractal models for the one-phase problems of discontinuous transient heat transfer in fractal media. By applying the fractal complex transform and the chain rule within local fractional derivative, we have derived the one-phase problems of discontinuous transient heat transfer in fractal media, which describe the (dimensionless) melting of fractal solid semi-infinite materials initially at their melt temperatures. We consider the fractal models for the one-phase problems of discontinuous transient heat transfer. The fractal models for one-phase problems are classical examples when the fractional dimension is equal to 1. The discontinuous transient heat transfer in fractal media can serve as a good starting point for experimental investigations and further discussions.

Acknowledgments

This paper is sponsored by the National Natural Science Foundation of China (NSFC, Grant U1204703), the Key Scientific and Technological Project of Henan Province (122102310004), the Fundamental Research Funds for the Central Universities (HUST: 2012QN087, 2012QN088), and the Innovation Scientists and Technicians Troop Construction Projects of Zhengzhou City (10LJRC190, 121PRKXF658-4).

References

[1] T. R. Goodman, "The heat-balance integral and its application to problems involving a change of phase," *Transactions of the ASME*, vol. 80, pp. 335–342, 1958.

[2] G. E. Bell, "A refinement of the heat balance integral method applied to a melting problem," *International Journal of Heat and Mass Transfer*, vol. 21, no. 11, pp. 1357–1362, 1978.

[3] A. S. Wood, "A new look at the heat balance integral method," *Applied Mathematical Modelling*, vol. 25, no. 10, pp. 815–824, 2001.

[4] A. A. Kilbas, H. M. Srivastava, and J. J. Trujillo, *Theory and Applications of Fractional Differential Equations*, vol. 204, Elsevier Science, Amsterdam, The Netherlands, 2006.

[5] J. Sabatier, O. P. Agrawal, and J. A. Tenreiro Machado, *Advances in Fractional Calculus: Theoretical Developments and Applications in Physics and Engineering*, Springer, New York, NY, USA, 2007.

[6] V. R. Voller, "An exact solution of a limit case Stefan problem governed by a fractional diffusion equation," *International Journal of Heat and Mass Transfer*, vol. 53, no. 23-24, pp. 5622–5625, 2010.

[7] J. Hristov, "Heat-balance integral to fractional (half-time) heat diffusion sub-model," *Thermal Science*, vol. 14, no. 2, pp. 291–316, 2010.

[8] J. Hristov, "Approximate solutions to fractional sub-diffusion equations: the heat-balance integral method," *The European Physical Journal-Special Topics*, vol. 193, pp. 229–243, 2011.

[9] R. R. Nigmatullin, "The realization of the generalized transfer equation in a medium with fractal geometry," *Physica Status Solidi*, vol. 133, no. 1, pp. 425–430, 1986.

[10] J. H. He, "A new fractal derivation," *Thermal Science*, vol. 15, pp. S145–S147, 2011.

[11] X. J. Yang, *Advanced Local Fractional Calculus and Its Applications*, World Science Publisher, New York, NY, USA, 2012.

[12] X. J. Yang, "Heat transfer in discontinuous media," *Advances in Mechanical Engineering and Its Applications*, vol. 1, no. 3, pp. 47–53, 2012.

[13] X. J. Yang, *Local Fractional Functional Analysis and Its Applications*, Asian Academic Publisher Limited, Hong Kong, 2011.

[14] X. J. Yang, "The zero-mass renormalization group differential equations and limit cycles in non-smooth initial value problems," *Prespacetime Journal*, vol. 3, no. 9, pp. 913–923, 2012.

[15] Z. B. Li and J. H. He, "Application of the fractional complex transform to fractional differential equations," *Nonlinear Science Letters A*, vol. 2, no. 3, pp. 121–126, 2011.

[16] Z. B. Li and J. H. He, "Fractional complex transform for fractional differential equations," *Mathematical and Computational Applications*, vol. 15, no. 5, pp. 970–973, 2010.

Hindawi Publishing Corporation
Mathematical Problems in Engineering
Volume 2012, Article ID 971641, 12 pages
doi:10.1155/2012/971641

Research Article

Dynamical Analysis of the Global Warming

J. A. Tenreiro Machado[1] and António M. Lopes[2]

[1] *Department of Electrical Engineering, Institute of Engineering of Porto, Rua Dr. António Bernardino de Almeida 431, 4200-072 Porto, Portugal*
[2] *IDMEC-Pólo FEUP, Faculdade de Engenharia, Universidade do Porto, Rua Dr. Roberto Frias, 4200-465 Porto, Portugal*

Correspondence should be addressed to J. A. Tenreiro Machado, jtm@isep.ipp.pt

Received 17 September 2012; Accepted 31 October 2012

Academic Editor: Clara Lonescu

Global warming is a major concern nowadays. Weather conditions are changing, and it seems that human activity is one of the main causes. In fact, since the beginning of the industrial revolution, the burning of fossil fuels has increased the nonnatural emissions of carbon dioxide to the atmosphere. Carbon dioxide is a greenhouse gas that absorbs the infrared radiation produced by the reflection of the sunlight on the Earth's surface, trapping the heat in the atmosphere. Global warming and the associated climate changes are being the subject of intensive research due to their major impact on social, economic, and health aspects of human life. This paper studies the global warming trend in the perspective of dynamical systems and fractional calculus, which is a new standpoint in this context. Worldwide distributed meteorological stations and temperature records for the last 100 years are analysed. It is shown that the application of Fourier transforms and power law trend lines leads to an assertive representation of the global warming dynamics and a simpler analysis of its characteristics.

1. Introduction

The standard approach for modelling natural and artificial phenomena in the perspective of dynamical systems is to adopt the tools of mathematics and, in particular, the classical integral and differential calculus.

Fractional calculus (FC) is a common expression that is used to denote the branch of calculus that extends the concepts of integrals and derivatives to noninteger and complex orders [1–9]. During the last decade FC was found to play a fundamental role in the modelling of a considerable number of phenomena [10–15] and emerged as an important tool for the study of dynamical systems where classical methods reveal strong limitations. As a consequence, nowadays, the application of FC concepts encompasses a wide spectrum

of studies [16–19], ranging from dynamics of financial markets [20, 21], biological systems, [22, 23] and DNA sequencing [24] up to mechanical [13, 25–28] and electrical systems [29–31].

The generalization of the concept of derivative and integral to noninteger orders, α, has been addressed by many mathematicians. The Riemann-Liouville, Grünwald-Letnikov, and Caputo definitions of fractional derivative, given by (1.1)–(1.3), are the most used [32]:

$$ {}_{a}^{\mathrm{RL}}D_{t}^{\alpha} f(t) = \frac{1}{\Gamma(n-\alpha)} \frac{d^n}{dt^n} \int_a^t \frac{f(\tau)}{(t-\tau)^{\alpha-n+1}} d\tau, \quad n-1 < \alpha < n, \tag{1.1} $$

$$ {}_{a}^{\mathrm{GL}}D_{t}^{\alpha} f(t) = \lim_{h\to 0} \frac{1}{h^{\alpha}} \sum_{k=0}^{[(t-a)/h]} (-1)^k \binom{\alpha}{k} f(t-kh), \tag{1.2} $$

$$ {}_{a}^{C}D_{t}^{\alpha} f(t) = \frac{1}{\Gamma(n-\alpha)} \int_a^t \frac{f^{(n)}(\tau)}{(t-\tau)^{\alpha-n+1}} d\tau, \quad n-1 < \alpha < n, \tag{1.3} $$

where $\Gamma(\cdot)$ represents the Euler's gamma function, the operator $[x]$ is the integer part of x, and h is a time step.

The Laplace transform applied to (1.1) yields

$$ L\left\{ {}_{a}^{\mathrm{RL}}D_{t}^{\alpha} f(t) \right\} = s^{\alpha} L\{f(t)\} - \sum_{k=0}^{n-1} s^k \, {}_{0}^{\mathrm{RL}}D_{t}^{\alpha-k-1} f(0^+), \tag{1.4} $$

where L and s denote the Laplace operator and variable, respectively.

The Mittag-Leffler (M-L) function, $E_{\alpha}(t)$, plays an important role in the context of FC, being defined by

$$ E_{\alpha}(t) = \sum_{k=0}^{\infty} \frac{t^k}{\Gamma(\alpha k + 1)}. \tag{1.5} $$

This function establishes a connection between purely exponential and power law behaviours that characterize integer and fractional order phenomena, respectively. In particular, if $\alpha = 1$, then $E_1(t) = e^t$. For large values of t, $E_{\alpha}(t)$ has the asymptotic behaviour:

$$ E_{\alpha}(-t) \approx \frac{1}{\Gamma(1-\alpha)} \frac{1}{t}, \quad \alpha \neq 1, \ 0 < \alpha < 2. \tag{1.6} $$

The Laplace transform (1.7) permits a natural extension of transform pairs from exponential function and integer powers of s towards M-L function and fractional powers of s:

$$ L\{E_{\alpha}(-at^{\alpha})\} = \frac{s^{\alpha-1}}{s^{\alpha} + a}. \tag{1.7} $$

The generalization promoted by FC leads directly to fractional dynamical models, but the fact is that neither their limits of application nor the methods and tools for capturing them seem to be well defined at the present stage of scientific knowledge.

This paper studies the complex dynamics characteristics of the global warming. It is believed that human activity is the main cause of such a phenomenon, and dramatic consequences to the planet are expected if the warming trend observed in the last century persists. The main goal is to analyse and discuss the characteristics of the global warming in the perspective of dynamical systems, which is a new standpoint in this context. It is shown that the application of Fourier transforms and power law trend lines leads to an assertive representation of the global warming dynamics and a simpler analysis of its characteristics.

The paper is organized as follows. Section 2 contextualizes the main subject. A heuristic approach to analyse the data from the meteorological stations in the time domain is proposed, and several characteristics of the global warming are exposed. Section 3 formulates the framework of the analysis in the perspective of FC and analyses the fractional dynamics of the system. Finally, Section 4 outlines the main conclusions.

2. Characteristics of the Global Warming

Earth is warming, and it seems that human activity and solar effects are the main probable causes [33–35]. Some impacts such as the record of high temperatures, the melting glaciers, and severe flooding are becoming increasingly common across the countries and around the world [36, 37]. Aside from the effect on temperature, warming leads to the modification of wind patterns, the development of humidity, and the alteration of the rates of precipitation. These phenomena are being the subject of intensive research due to major impact on social, economic, and health aspects of human life [38–40].

Figures 1 and 2 show average temperatures computed for two decades separated by almost one hundred years. The white marks on the maps represent meteorological stations. Figure 1 is the contour plot of the worldwide temperatures corresponding to the period 1910–1919, and Figure 2 corresponds to the period 2000–2009. The temperature difference between the two decades is presented in Figure 3, showing that the northern hemisphere has been more affected by warming.

In our study, the Global Historical Climatology Network-Monthly (GHCN-M), version 3 dataset of monthly mean temperature [41], available at the National Oceanic and Atmospheric Administration, National Climatic Data Center (NOAA-NCDC) (http://www.ncdc.noaa.gov/ghcnm/v3.php), is used. The current archive contains temperature records from 7280 meteorological stations located on land areas. However, few stations have long records, and these are essentially restricted to the northern hemisphere (the United States and Western Europe). As the computation of the Fourier transform requires quite long time series, a sample of 210 worldwide meteorological stations, distributed as uniformly as possible, and having 100 years length records, was selected. Most stations of Africa, Alaska, Canada and the northern and southern regions of the globe do not meet the previous condition, which means that the results for these regions (and also for sea areas), plotted on the maps, may be less accurate.

Each data record consists of the average temperatures per month. Some occasional gaps of one month in the data (represented on the original data by the value −9999) are substituted by a linear interpolation between the two adjacent values. Moreover, although of minor influence, the distinct number of days of each month and the leap years are also taken into account. For the whole sample of meteorological stations, as the data is available for slightly different periods of time, depending on the station, the period from January 1910 up to December 2010 is considered for all cases.

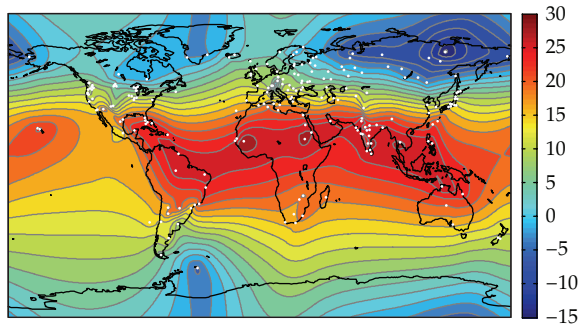

Figure 1: Global average temperatures: decade 1910–1919.

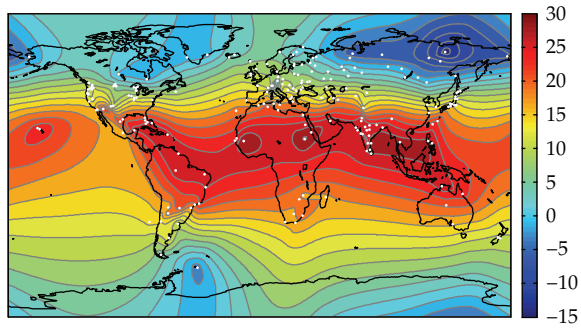

Figure 2: Global average temperatures: decade 2000–2009.

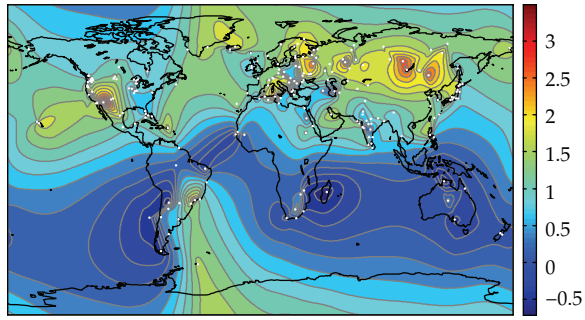

Figure 3: Temperature difference between decades 2000–2009 and 1910–1919.

Figure 4 depicts the time evolution of the monthly average temperature of one typical station (Tokyo, Japan, Lat 35.67 N, Lon 139.75 W), where three processes are visible, namely, (i) a continuous, almost linear, temperature increase, (ii) an annual periodic variation, and (iii) a "random" temperature variation that may be the symptom of a fractional dynamical behaviour.

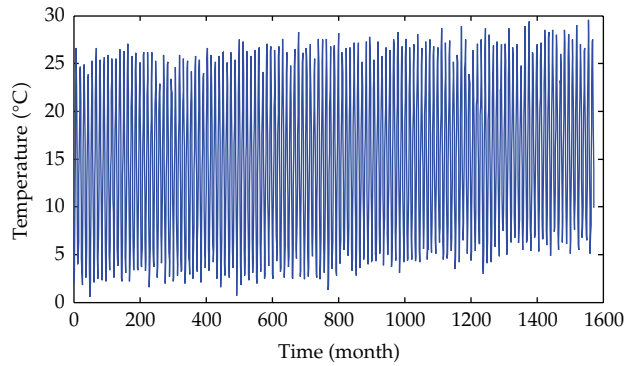

Figure 4: Monthly average temperatures for Tokyo, Japan, meteorological station (January 1881–August 2011).

In this study, a heuristic decomposition of the time series is first proposed. The temperature signal from the ith meteorological station, $T_i(t)$, $i = 1, \ldots, 210$, is approximated by the sum given in the following:

$$T_i(t) \approx a_0 + a_1 \cdot t + a_2 \cdot \sin(\omega \cdot t + a_3) + a_4 \cdot \sin(2\omega \cdot t + a_5), \tag{2.1}$$

where t is time, $\omega = 2\pi/T$ represents the angular frequency, and T is one year.

The coefficients a_0 and a_1 are the parameters of a trend line adjusted to the original data, $T_i(t)$, using the least squares algorithm. This trend line is then subtracted from the signal $T_i(t)$, and, for the result, the two first harmonics of the Fourier series are calculated. The corresponding coefficients are (a_2, a_3) and (a_4, a_5), respectively.

Figures 5–11 show the mapping of the coefficients. Coefficient a_0 is closely related to the average temperature and highlights the warmer regions of the globe (Figure 5), whereas coefficient a_1 (Figure 6) emphasizes the gradient of temperature increase. Consequently, Figure 6 is highly correlated with Figure 3.

The parameters of the first harmonic, namely, a_2 and a_3, are depicted in Figures 7 and 8, respectively. The amplitude of the sinusoid (Figure 7) unveils a strong mark centred in Siberia and a weaker, but also clear, mark in North America, respectively. Figure 8 represents the map of coefficient a_3, corresponding to the phase of the sine function. As expected, northern and southern hemispheres are in phase opposition. The analysis and physical meaning of the coefficients a_4 and a_5 that correspond to the second harmonic of the heuristic approximation are more difficult and seem to point to a less significant meaning (Figures 9 and 10). Nevertheless, those parameters might also reveal relationships hidden in the data that can trigger a future comprehensive explanation of these phenomena.

It is important to notice that the heuristic approximation given by (2.1) captures most of the energy of the original signals. Moreover, the energy contained in the second harmonic is almost negligible. This is illustrated in Figures 11 and 12. Figure 11 represents the percentage of energy captured by the heuristic approximation with reference to the total energy of the original signals, revealing a percentage in the interval [86% 99%]. Figure 12 represents the case of not including the second harmonic. We verify that it exhibits only slight differences when compared to the previous one.

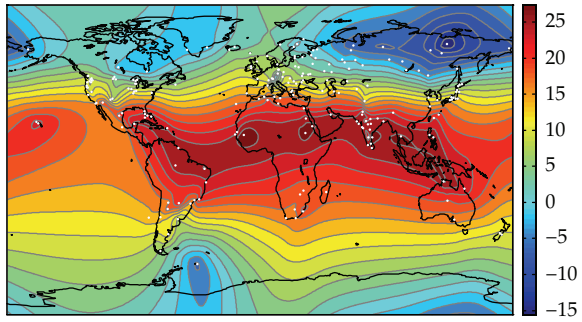

Figure 5: Map of coefficient a_0 of expression (2.1).

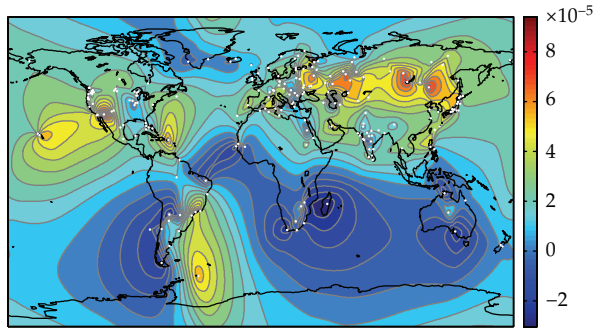

Figure 6: Map of coefficient a_1 of expression (2.1).

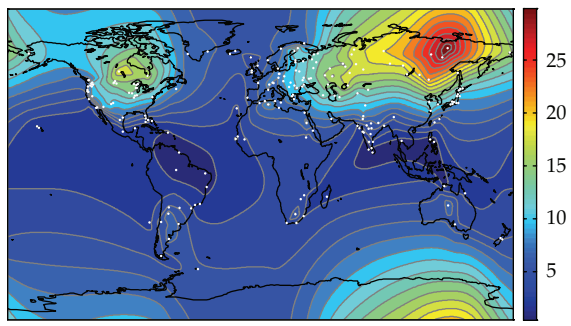

Figure 7: Map of coefficient a_2 of expression (2.1).

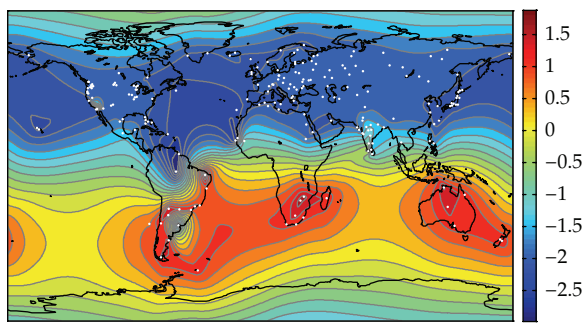

Figure 8: Map of coefficient a_3 of expression (2.1).

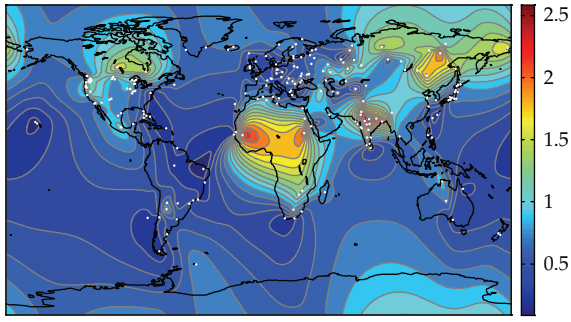

Figure 9: Map of coefficient a_4 of expression (2.1).

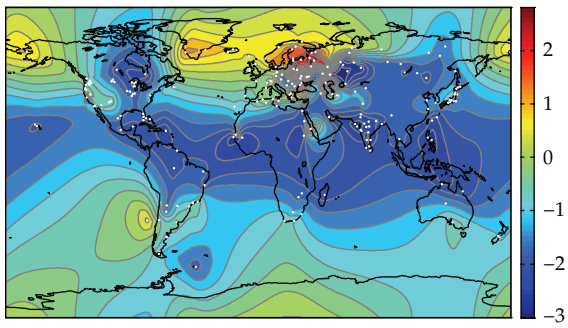

Figure 10: Map of coefficient a_5 of expression (2.1).

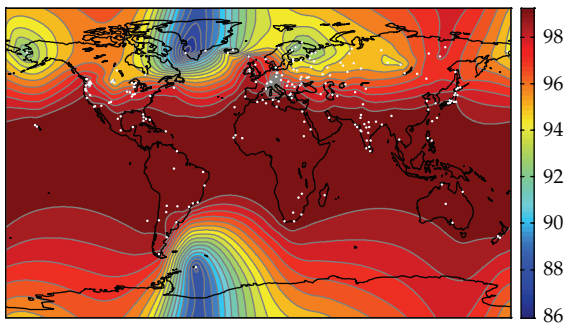

Figure 11: Percentage of energy of the heuristic approximation with reference to the total energy of the original signals.

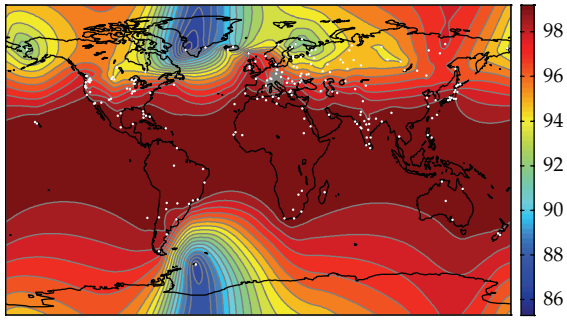

Figure 12: Percentage of energy of the heuristic approximation (without second harmonic) with reference to the total energy of the original signals.

3. Dynamics of the Global Warming

In this section, the global warming phenomenon is analysed in the perspective of a complex system that reacts to stimuli, being the response signals studied by means of the Fourier transform. The methodology is to obtain a representative signal as a manifestation of the system dynamics, process it with the Fourier transform, and, given the characteristics of the resulting spectrum, to approximate its amplitude by means of a power function.

In analytical terms, for a continuous signal $x(t)$, evolving in the time domain t, we have

$$F\{x(t)\} = X(j\omega) = \int_{-\infty}^{+\infty} x(t) \cdot e^{-j\omega t} \cdot dt, \tag{3.1}$$

where F represents the Fourier operator, ω is the angular frequency, and $j = \sqrt{-1}$.

The power law approximation is given by

$$|F\{x(t)\}| = |X(j\omega)| = a \cdot \omega^b, \quad a \in \Re^+,\ b \in \Re. \tag{3.2}$$

The parameters of the power law are the pair (a, b) to be determined by the least squares fit procedure.

Figure 13 depicts the amplitude of the Fourier transform obtained for the meteorological station Tokyo (Figure 4), where a peak value at the angular frequency $\omega = 1.99 \times 10^{-7}$ rad/s that corresponds to a periodicity of one year is well visible.

At low frequencies (Figure 14), it is clear that the spectrum can be approximated by a power law with parameters $(a, b) = (292.1047, -0.8397)$, leading to a fractional value of parameter b.

In the sequel, the values of (a, b) were computed for the whole sample of meteorological stations, using the least squares fit procedure. It was found that there exists a strong correlation between the two parameters. In fact, Figure 15 illustrates clearly the relation between $\log(a)$ and b. It can be seen that a straight line fits quite well into the data. Figures 16 and 17 depict the contour plots of $\log(a)$ and b, respectively. Therefore, we will concentrate our attention on one parameter only, namely, on b that represents the variation of the signal energy versus ω.

The map of parameter b (Figure 17) reveals that climate changes are taking place in the northern hemisphere. Two large regions of Russia and Canada and, in a less extent, central Europe and Western Alaska are being the most affected areas.

As expected, Figure 16 is somewhat "redundant," since Figure 17, with parameter b, is sufficient to characterize the warming dynamics. We verify that $\text{abs}(b)$ varies between 0 and 1 that can be viewed as the cases of white and pink noises, respectively. Therefore, we conclude that equatorial and south hemisphere regions exhibit more "correlated" variation, while the north hemisphere and the two poles have a more "erratic" variation of the temperature.

These results are of utmost importance because we can capture and analyse all information through a single map. In a different perspective, we should also note that the adoption of FC concepts captures large memory effects present in long time series, which is the case of Earth's warming. Therefore, these results encourage further research in this line of thought.

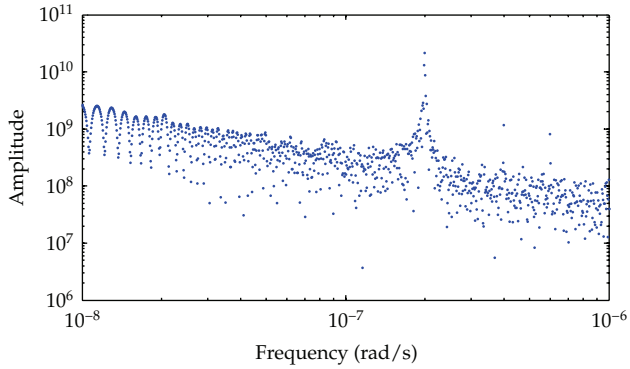

Figure 13: Amplitude of the Fourier transform of the monthly average temperatures of Tokyo.

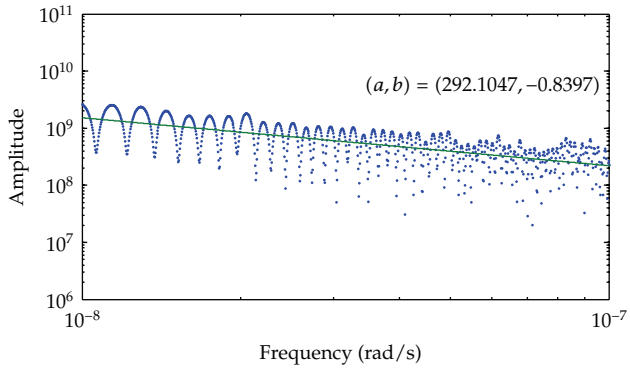

Figure 14: Power law approximation of the amplitude of the Fourier transform of the monthly average temperatures of Tokyo.

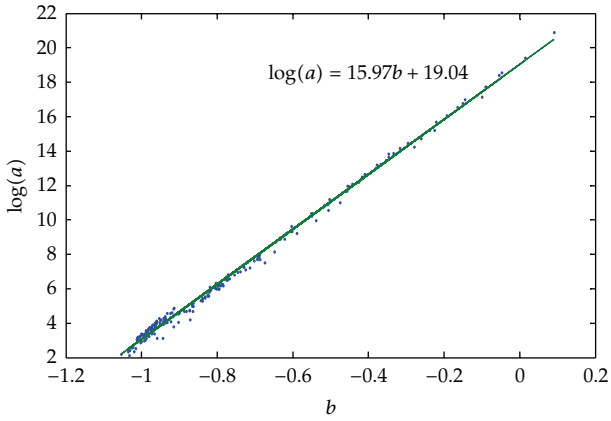

Figure 15: Mapping of the power law parameters $[\log(a), b]$.

4. Conclusions

This paper analysed the global warming in the perspective of complex systems dynamics. The use of Fourier transforms and power law trend lines revealed fractional order dynamics characteristics of the phenomenon. While classical mathematical tools could be adopted,

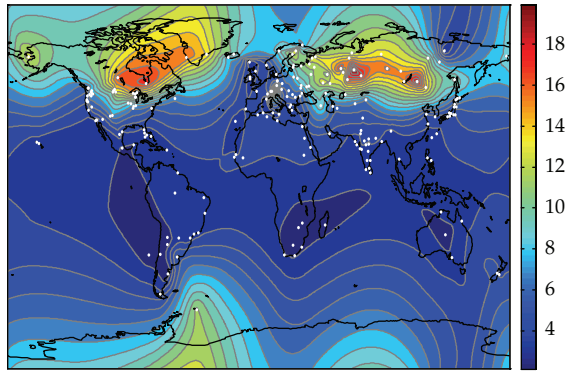

Figure 16: Contour plot of parameter $\log(a)$.

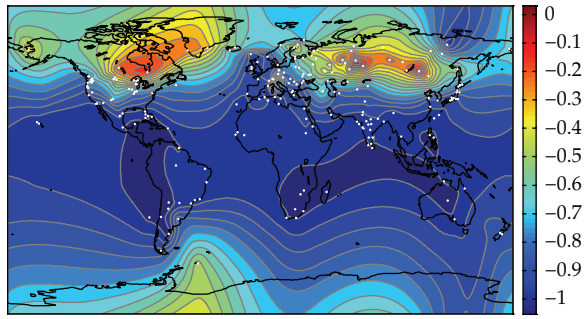

Figure 17: Contour plot of parameter b.

the used methodology based on FC concepts leads to simpler and assertive representation of the global warming dynamics. FC captures inherently long range effects that are overlooked by classical methods. Therefore, this study motivates the analysis of global phenomena with long time histories bearing in mind FC.

References

[1] S. G. Samko, A. A. Kilbas, and O. I. Marichev, *Fractional Integrals and Derivatives: Theory and Applications*, Gordon and Breach Science Publishers, London, UK, 1993.

[2] K. S. Miller and B. Ross, *An Introduction to the Fractional Calculus and Fractional Differential Equations*, John Wiley & Sons, New York, NY, USA, 1993.

[3] I. Podlubny, *Fractional Differential Equations: An Introduction to Fractional Derivatives, Fractional Differential Equations, to Methods of Their Solution and Some of Their Applications*, vol. 198 of *Mathematics in Science and Engineering*, Academic Press, San Diego, Calif, USA, 1999.

[4] A. A. Kilbas, H. M. Srivastava, and J. J. Trujillo, *Theory and Applications of Fractional Differential Equations*, vol. 204 of *North-Holland Mathematics Studies*, Elsevier Science B.V., Amsterdam, The Netherlands, 2006.

[5] K. Diethelm, *The Analysis of Fractional Differential Equations: An Application-Oriented Exposition using Differential Operators of Caputo Type*, vol. 2004 of *Lecture Notes in Mathematics*, Springer, Berlin, Germany, 2010.

[6] D. Baleanu, K. Diethelm, E. Scalas, and J. J. Trujillo, *Fractional Calculus: Models and Numerical Methods*, vol. 3 of *Series on Complexity, Nonlinearity and Chaos*, World Scientific Publishing, Singapore, 2012.

[7] M. D. Ortigueira, *Fractional Calculus for Scientists and Engineers*, vol. 84 of *Lecture Notes in Electrical Engineering*, Springer, Dordrecht, The Netherlands, 2011.

[8] R. R. Nigmatullin, I. I. Popov, and D. Baleanu, "Predictions based on the cumulative curves: basic principles and nontrivial example," *Communications in Nonlinear Science and Numerical Simulation*, vol. 16, no. 2, pp. 895–915, 2011.

[9] D. Baleanu and J. I. Trujillo, "A new method of finding the fractional Euler-Lagrange and Hamilton equations within Caputo fractional derivatives," *Communications in Nonlinear Science and Numerical Simulation*, vol. 15, no. 5, pp. 1111–1115, 2010.

[10] A. Oustaloup, *La Commande CRONE: Commande Robuste d'Ordre Non Entier*, Hermès, Paris, France, 1991.

[11] G. M. Zaslavsky, *Hamiltonian Chaos and Fractional Dynamics*, Oxford University Press, Oxford, UK, 2008.

[12] R. Magin, *Fractional Calculus in Bioengineering*, Begell House Publishers, Redding, Calif, USA, 2006.

[13] F. Mainardi, *Fractional Calculus and Waves in Linear Viscoelasticity: An Introduction to Mathematical Models*, Imperial College Press, London, UK, 2010.

[14] C. Monje, Y. Chen, B. Vinagre, D. Xue, and V. Feliu, *Fractional Order Systems and Controls: Fundamentals and Applications*, Springer, London, UK, 2010.

[15] J. T. Machado, V. Kiryakova, and F. Mainardi, "Recent history of fractional calculus," *Communications in Nonlinear Science and Numerical Simulation*, vol. 16, no. 3, pp. 1140–1153, 2011.

[16] T. Anastasio, "The fractional-order dynamics of brainstem vestibulooculomotor neurons," *Biological Cybernetics*, vol. 72, pp. 69–79, 1994.

[17] J.-G. Lu and Y.-Q. Chen, "Robust stability and stabilization of fractional-order interval systems with the fractional order α: the $0 < \alpha < 1$ case," *Institute of Electrical and Electronics Engineers*, vol. 55, no. 1, pp. 152–158, 2010.

[18] D. Baleanu, A. K. Golmankhaneh, A. K. Golmankhaneh, and R. R. Nigmatullin, "Newtonian law with memory," *Nonlinear Dynamics*, vol. 60, no. 1-2, pp. 81–86, 2010.

[19] C. M. Ionescu, J. A. T. Machado, and R. De Keyser, "Modeling of the lung impedance using a fractional-order ladder network with constant phase elements," *IEEE Transactions on Biomedical Circuits and Systems*, vol. 5, no. 1, pp. 83–89, 2011.

[20] E. Scalas, R. Gorenflo, and F. Mainardi, "Fractional calculus and continuous-time finance," *Physica A*, vol. 284, no. 1–4, pp. 376–384, 2000.

[21] F. B. Duarte, J. A. Tenreiro MacHado, and G. M. Duarte, "Dynamics of the Dow Jones and the NASDAQ stock indexes," *Nonlinear Dynamics*, vol. 61, no. 4, pp. 691–705, 2010.

[22] C. M. Ionescu, P. Segers, and R. De Keyser, "Mechanical properties of the respiratory system derived from morphologic insight," *IEEE Transactions on Biomedical Engineering*, vol. 56, no. 4, pp. 949–959, 2009.

[23] C. Ionescu and J. T. MacHado, "Mechanical properties and impedance model for the branching network of the sapping system in the leaf of Hydrangea Macrophylla," *Nonlinear Dynamics*, vol. 60, no. 1-2, pp. 207–216, 2010.

[24] J. A. Tenreiro Machado, A. C. Costa, and M. D. Quelhas, "Fractional dynamics in DNA," *Communications in Nonlinear Science and Numerical Simulation*, vol. 16, no. 8, pp. 2963–2969, 2011.

[25] W. H. Deng and C. P. Li, "Chaos synchronization of the fractional Lü system," *Physica A*, vol. 353, no. 1–4, pp. 61–72, 2005.

[26] R. R. Nigmatullin, "Fractional kinetic equations and universal decoupling of a memory function in mesoscale region," *Physica A*, vol. 363, no. 2, pp. 282–298, 2006.

[27] O. P. Agrawal, "Fractional variational calculus in terms of Riesz fractional derivatives," *Journal of Physics A*, vol. 40, no. 24, pp. 6287–6303, 2007.

[28] A. Oustaloup, X. Moreau, and M. Nouillant, "The crone suspension," *Control Engineering Practice*, vol. 4, no. 8, pp. 1101–1108, 1996.

[29] A. G. Radwan, A. M. Soliman, and A. S. Elwakil, "Design equations for fractional-order sinusoidal oscillators: four practical circuit examples," *International Journal of Circuit Theory and Applications*, vol. 36, no. 4, pp. 473–492, 2008.

[30] I. Petráš, "A note on the fractional-order Chua's system," *Chaos, Solitons and Fractals*, vol. 38, no. 1, pp. 140–147, 2008.

[31] H. Cao, Z. Deng, X. Li, J. Yang, and Y. Qin, "Dynamic modeling of electrical characteristics of solid oxide fuel cells using fractional derivatives," *International Journal of Hydrogen Energy*, vol. 35, no. 4, pp. 1749–1758, 2010.

[32] J. A. Tenreiro Machado, "Fractional order modelling of fractional-order holds," *Nonlinear Dynamics*, vol. 70, pp. 789–796, 2012.

[33] M. R. Allen, D. J. Frame, C. Huntingford et al., "Warming caused by cumulative carbon emissions towards the trillionth tonne," *Nature*, vol. 458, no. 7242, pp. 1163–1166, 2009.

[34] A. Dai, "Drought under global warming: a review," *WIREs Climate Change*, vol. 2, no. 1, pp. 45–65, 2011.

[35] Q. You, S. Kang, N. Pepin et al., "Climate warming and associated changes in atmospheric circulation in the eastern and central Tibetan Plateau from a homogenized dataset," *Global and Planetary Change*, vol. 72, no. 1–2, pp. 11–24, 2010.

[36] S. Jevrejeva, J. C. Moore, and A. Grinsted, "Sea level projections to AD2500 with a new generation of climate change scenarios," *Global and Planetary Change*, vol. 80-81, pp. 14–20, 2012.

[37] C. Giannakopoulos, P. Le Sager, M. Bindi, M. Moriondo, E. Kostopoulou, and C. M. Goodess, "Climatic changes and associated impacts in the Mediterranean resulting from a 2 ∘C global warming," *Global and Planetary Change*, vol. 68, no. 3, pp. 209–224, 2009.

[38] J. Hansen, R. Ruedy, M. Sato, and K. Lo, "Global surface temperature change," *Reviews of Geophysics*, vol. 48, Article ID RG4004, 2010.

[39] P. Brohan, J. J. Kennedy, I. Harris, S. F. B. Tett, and P. D. Jones, "Uncertainty estimates in regional and global observed temperature changes: a new data set from 1850," *Journal of Geophysical Research D*, vol. 111, no. 12, Article ID D12106, 2006.

[40] M. J. Menne and C. N. Williams, "Homogenization of temperature series via pairwise comparisons," *Journal of Climate*, vol. 22, no. 7, pp. 1700–1717, 2009.

[41] J. H. Lawrimore, M. J. Menne, B. E. Gleason et al., "An overview of the Global Historical Climatology Network monthly mean temperature data set, version 3," *Journal of Geophysical Research*, vol. 116, Article ID D19121, 18 pages, 2011.